9th EUROPEAN CONFERENCE ON

CONTROLLED FUSION AND PLASMA PHYSICS

OXFORD 17 - 21 SEPTEMBER 1979

Contributed Papers

9th EUROPEAN CONFERENCE ON

CONTROLLED FUSION AND PLASMA PHYSICS

OXFORD 17-21 SEPTEMBER 1979

CONTRIBUTED PAPERS

ORGANISED BY UKAEA CULHAM LABORATORY
UNDER THE AUSPICES OF THE EUROPEAN PHYSICAL SOCIETY

Additonal copies of this volume (Price £12.50) are available from:

Public Relations Office
Culham Laboratory
Abingdon
Oxfordshire OX14 3DB
England

Po(T)30

PREFACE

This volume contains the texts of **Contributed Papers** to be presented at the 9th European Conference on Controlled Fusion and Plasma Physics. The papers were selected and arranged by the Papers Selection Committee.

Direct reproduction by photographic processes means that the authors must bear responsibility for their texts. Only the minimum of editorial work was carried out. We wish to thank the authors for complying with the relatively rigorous instructions necessary for this type of publication.

The texts of the **Invited Papers**, together with post-deadline contributions and supplementary pages to papers in this volume, will form a companion volume available before the end of 1979.

LOCAL ORGANISING COMMITTEE

LOCAL ORGANISING COMMITTEE

R J Bickerton (Chairman)
A Gibson
P A Davenport (Scientific Secretary)
J H C Maple (Administrative Secretary)

PAPERS SELECTION COMMITTEE

D Pfirsch	– Max Planck Institut, Garching, FRG
D D Ryutov	– Nuclear Physics Institution, Novosibirsk, USSR
M H Key	– Rutherford Laboratory, Chilton, Oxon, UK
J Tachon	– Centre d'Etudes Nucleaires, Fontenay, France
A Gibson	– JET Joint Undertaking, Abingdon, Oxon, UK
P A Davenport	– Culham Laboratory, Abingdon, Oxon, UK (Scientific Secretary)

CONTENTS

Bumpy torus, stellarators

A2.1 Scaling in ELMO bumpy torus (EBT)
F W Baity, K H Carpenter, J A Cobble, R J Colchin, R A Dandl, H O Eason, J C Glowienka, G R Haste, C L Hedrick, E F Jaeger, R K Richards, T Uckan, T L White, F M Bieniosek*, K A Connor*, R L Hickok*, S P Kuo*, R A Dandl**, S Hiroe†, W H Lazar†† and B H Quon††
Oak Ridge National Laboratory, Oak Ridge, Tennessee, USA
**Rennselaer Polytechnic Institute, Troy, New York, USA*
***Consultant at General Atomic Company, San Diego, California, USA*
†Institute of Plasma Physics, Nagoya, Japan
††TRW Defense Systems, Redondo Beach, California, USA

A2.2 Plasma confinement in Nagoya bumpy torus
M Fujiwara, T Shoji, M Hosokawa, H Iguchi and H Ikegami
Institute of Plasma Physics, Nagoya University

A2.3 Stellarator equilibrium and stability computations in 2 and 3 dimensions
R Chodura, F Hermegger, J. Neuhauser and A Schlüter
Max-Planck-Institut für Plasmaphysik

A2.4 Particle and energy transport in the W VII-A stellarator
W VII-A Team, presented by H Ringler
Max-Planck-Institut für Plasmaphysik

A2.5 Lower hybrid heating in the Wega-stellarator
F Söldner[1], P Brouquet[2], M Durvaux[3], C Gormezano[2], B Gregory[6], W Hess[2], G Ichtchenko[2], H Jaeckel[1], B Jessup[2], R Magne[2], M Moresco[5], T-K Nguyen[2], G Pacher[1], H Pacher[1], H W Piekaar[4], W R Rutgers[4], G-F Tonon[2] and J-G Wegrowe[1]
(1) Association Euratom Max-Planck-Institut für Plasmaphysik, (2) Association Euratom-CEA, Grenoble, (3) Association Euratom-E.R.M., Brussels, (4) Association Euratom-FOM, Jutphaas, (5) University of Padua, (6) On leave: INRS Energy, Quebec, Canada

A2.6 Confinement of low and zero current plasmas in the CLEO stellarators
D W Atkinson, J E Bradley, P J N Davison, A N Dellis, P C Johnson, S Kogoshi, D J Lees, P J Lomas, A C Selden, P A Shatford, I J Spalding, T Stamatakis, P R Thomas, A C Walker and S Ward
Culham Laboratory

A2.7 The quasi-neoclassical law of plasma losses in a stellarator
Yu V Gutarev and V A Suprunenko
The Kharkov Physical-Technical Institute, Acad. Sci. Ukr. SSR, Kharkov, USSR

Tokamak theory

A3.1 Ideal and resistive ballooning modes in axisymmetric toroidal plasmas
A H Glasser, M S Chance and R L Dewar
Plasma Physics Laboratory, Princeton University

A3.3 Beta limits for tokamak experiments
W Kerner*, K Lackner*, R Gruber† and F Troyon†
**Max-Planck-Institut für Plasmaphysik, †CRPP-EPFL, Lausanne, Switzerland*

A3.4 Stability of two dimensional drift waves in a large aspect ratio tokamak
J W Connor, R J Hastie, K W Hesketh and J B Taylor
Culham Laboratory

A3.6 Systematic optimization of tokamaks to all ideal MHD modes
L C Bernard, R L Miller, R.W. Moore and F J Helton
General Atomic Company, San Diego, California

A3.7 Studies on slowing down of energetic ions and transport coefficients by Makokot
H Capes, G Cissoko, C Mercier, J P Morera and F Werkoff
Association Euratom-CEA sur la Fusion

Plasma heating, open traps and miscellaneous topics

AP1 Simultaneous operation experiments of neutral beam injection and lower hybrid heating in JIPP T-11
J Fujita, S Itoh*, K Kadota, K Kawahata, Y Kawasumi, T Kuroda, K Matsuoka, K Matsuura, K Miyamoto, N Noda, K Ohkubo, Y Oka, K Sakurai, K Sato, S Tanahashi, Y Terashima and K Toi
Institute of Plasma Physics, Nagoya University
**Research Institute for Applied Mechanics, Kyushu University*

AP3 Characteristics of the DITE Phase II ion source
R S Hemsworth, D Stork and H C Cole
Culham Laboratory, Abingdon, Oxon.

AP4 Resonances in the ion cyclotron range in toroidal geometries
T Hellsten and E Tennfors
Royal Institute of Technology, Sweden

AP6 Computer simulation of electron cyclotron heating on TFR and T-10
R Cano, A Cavallo and F Werkoff
Association Euratom-CEA sur la Fusion, Fontenay-aux-Roses

AP7 Emission and transmission measurements at the electron cyclotron frequency on TFR
TFR Group
Association Euratom-CEA sur la Fusion, Fontenay-aux-Roses

AP8 MHD resonant hf heating in the R-OM stellatator
A G Kirov, L F Rouchko, A V Sukachov, E A Meleta and I Ya Kadysh
Sukhumi Institute of Physics and Technology of the State Committee on Utilization of Atomic Energy, USSR

AP9 The rf-method for currentless plasma production and heating
S S Kalinichenko, P I Kurilko, A I Lysoivan, N I Nazarov, K N Stepanov, V F Tarasenko and O M Shvets
Physical-Technical Institute of Academy of Sciences of Ukr. SSR, Kharkov, USSR

AP10 Stochastic ion heating by an electrostatic wave in a sheared magnetic field
Y Gell* and R Nakach
Association Euratom-CEA, Grenoble
**Department of Physics and Astronomy, Tel-Aviv*

AP12 Lower hybrid experiments in the PETULA tokamak
PETULA Group
Association Euratom-CEA, Grenoble

AP13 Theoretical and experimental results on the coupled resistive-g/ion temperature gradient instability
J G Cordey, T Edlington, W H W Fletcher, E M Jones, A C Riviere,and D F H Start
Culham Laboratory

AP14 Analysis and Interpretation of Electrostatic fluctuations in the Culham Levitron
D E T F Ashby and E M Jones
Culham Laboratory

AP15 Studies of fuel deposition and penetration depth of a refuelling pellet
C T Chang
Association Euratom – Risø National Laboratory, Denmark

AP16 Suppression of the electron cyclotron instability of a beam-plasma system by selective cyclotron damping
J A C Cabral and C A F Varandas
Laboratório de Electrodinamica, Complexo Interdisciplinar Instituto Superior Tècnico, Lisbon, Portugal

AP17 Anomalous heat transport in a turbulent plasma blanket
D Anderson, M Lisak and H Wilhelmsson
Institute for Electromagnetic Field Theory and Euratom-Fusion Research, Göteborg

AP18 Current transitions in the plasma-wall interface in a tokamak
U Daybelge
Institut für Theoretische Physik, Ruhr Universität Bochum, Federal Republic of Germany

AP19 CO_2 laser scattering from ion-acoustic fluctuations
C M Surko, D Gresillon, J Olivain and A Truc
Laboratorie P.M.I., Ecole Polytechnique, France

AP20 Kinetic theory of the collisional scrape-off layers
U Daybelge
Institut für Theoretische Physik, Ruhr Universität Bochum, Federal Republic of Germany

AP21 Collective scattering of CO_2-laser light by the highly ionized argon plasma of a hollow cathode discharge
B F M Pots, J J H Coumans and D C Schram
Physics Department, Eindhoven University of Technology, The Netherlands

AP22 Space potential measurements with particle beam probes
R L Hickok, W C Jennings, K A Connor and J T Woo
Plasma Dynamics Laboratory, Rensselaer Polytechnic Institute, USA

AP23 Production of plasma currents by means of rotating magnetic fields
W N Hugrass, I R Jones and M G R Phillips
The Flinders University of South Australia

AP24 Screening efficiency of the scrape-off plasma in the shadow of a pololidal limiter
A Nicolai
Institut für Plasmaphysik, Jülich, Federal Republic of Germany

AP25 Experimental studies of scaling laws in a cold-gas mantle
J R Drake and A Kuthy
Royal Institute of Technology, Stockholm Sweden

AP26 The technique or IR holography at 10.6μm for laser-produced plasma diagnostics
E M Barkhudarov, V R Berezovskii, T Ya Chelidze, G V Gelashvili, M I Taktakishvili, and N L Tsintsadze
Institute of Physics, Tbilissi, USSR

AP27 Experimental verification of increased ion confinement in a magnetic mirror field
Y Nishida*, K Ishii** and H Mase***
**Department of Electrical Engineering, Utsunomiya University, Utsunomiya*
***Institute of Plasma Physics, Nagoya University, Nagoya*
****Department of Electronics Engineering, Ibaragi University, Hitachi, Japan*

AP28 The dynamics of alpha particles in tandem mirror plasmas
T Kammash and D L Galbraith
University of Michigan, USA

AP31 Suppression of plasma loss from mirror ends
H Akiyama, O Matsumoto and S Takeda
Nagoya University, Nagoya, Japan

AP32 A possibility of MHD-stable plasma confinement in an axisymmetric mirror machine
V V Arsenin
I V Kurchatov Institute of Atomic Energy, Moscow, USSR

AP33 Electron heating under the influence of the ion-cyclotron instability in a min-B mirror trap
V A Zhil'tsov, P M Kosarev, D A Panov, A A Skovoroda and A G Scherbakov
Kurchatov Institute of Atomic Energy, Moscow, USSR

AP34 Studies of finite gyro-radius effects in a field reversed mirror configuration
G H Miley, J Gilligan, D Driemeyer, E Morse and W C Condit*
University of Illinois, Urbana, USA
**Lawrence Livermore Laboratory, Livermore, USA*

AP35 Two-frequency-bands plasma-density interferometry with oversized microwave waveguide
Ye Youzhang, Hai Shuyuan and Zhang Wenmo
Southwestern Institute of Physics, Leshan, Sichuan, People's Republic of China

Tokamak experiments I

B2.1 Attempts to optimise β in the TOSCA tokamak
R Birch*, C W Gowers*, F A Haas, P A Jones*, K McGuire†, D C Robinson, A Sykes, M Turner and A J Wootton
Culham Laboratory, Abingdon, Oxon.
**AWRE Aldermaston, Berkshire*
†University of Oxford, Oxon.

B2.2 High power neutral beam experiments on ISX-B
D W Swain, S C Bates, C E Bush, R J Colchin, W A Cooper*, J L Dunlap, G R Dyer, P H Edmonds, A C England, C A Foster, J T Hogan, H C Howe, R C Isler, T C Jernigan, H E Ketterer, J Kim, P W King, E A Lazarus, C M Loring, J F Lyon, H C McCurdy, M M Menon, J T Mihalczo, S L Milora, M Murakami, A P Navarro†, R V Neidigh, G H Neilson, D R Overbey, V K Paré, Y-K M Peng, N S Ponte, M J Saltmarsh, D E Schechter, J E Simpkins, W L Stirling, C E Thomas, C C Tsai, J B Wilgen, W R Wing, R E Worsham and B Zurro†
Oak Ridge National Laboratory, Oak Ridge, Tennessee, USA
**University of Michigan*
† Visitors from JEN, Madrid, Spain

B2.3 Fusion neutron production during deuterium neutral beam injection into PLT tokamak
P L Colestock, S Davis, P C Efthimion, H P Eubank, R J Goldston, L R Grisham, R J Hawryluk, J Hovey, D L Jassby, D W Johnson, A A Mirin, G Schilling, R Stooksberry, L D Stewart, J D Strachan, H H Towner
Plasma Physics Laboratory, Princeton University, USA

B2.4 Balance of energy at the L H Heating in the FT-1 tokamak
V E Golant, V K Gusev, V V Djachenko, M M Larionov, A D Lebedev, G T Razdobarin, G A Serebreny and O N Scherbinin
A.F. Ioffe, Physico-Technical Institute, Leningrad

B2.5 Non thermal electron distribution function in the Frascati tokamak
R Bartiromo, P Buratti, L Pieroni and O Tudisco
Associazione Euratom-CNEN Fusione, Frascati, Italy

B2.6 Charge exchange measurements during neutral beam injection and ICRF heating on PLT
S S Medley, K Bol, S L Davis, H P Eubank, R J Goldston, L R Grisham, R Hawryluk, J C Hosea, E B Meservey, G Schilling, W Stodiek, R Stooksberry and M Ulrickson
Princeton University, USA

B2.7 Moderate power ICRF heating characteristics for the two-ion regime in PLT
D Hwang, V Arunasalam, S Bernabei, M Bitter, D Boyd, N Bretz, S Cohen, P. Colestock, S Davis, D Dimock, F Dylla, D Eames, P Efthimion, H Eubank, R Goldston, L Grisham, E Hinnov, J Hosea, H Hsuan, F Jobes, D Johnson, R Kaita, J Lawson, E Mazzucato, D McNeil, S Medley, E Meservey, D Mueller, N Sauthoff, G Schilling, J Schivell, G Schmidt, A Sivo, F Stauffer, W Stodiek, R Stooksberry, J. Strachan, S Suckewer, G Tait and H Thomson
Plasma Physics Laboratory, Princeton University, USA

Open traps and pinches

B3.1 Finite mean-free-path effects on axial particle transport in mirror devices
T D Rognlien and T A Cutler
Lawrence Livermore Laboratory, California, USA

B3.2 Stability of high density plasma in a multiple mirror
M Inutake, A Komori*, R Hatakeyama* and N Sato*
Institute of Plasma Physics, Nagoya University, Japan
**Department of Electronic Engineering, Tohoku University, Japan*

B3.3 The REXIMPLO experiment: conversion from cylindrical to quasi-spherical plasma compression
E Panarella and R P Gupta
National Research Council, Ottawa, Canada

B3.4 Influence of microinstabilities on the MHD stability of field reversed pinches
S Hamasaki, N A Krall* and J B McBride
Science Applications, Inc., La Jolla, California, USA
**JAYCOR, Del Mar, California, USA*

B3.5 Theta-pinch fusion system with liner exploded by thermonuclear neutrons
E A Azizov, Ju A Kareev, I K Konkashbaev and L B Nikandrov
I V Kurchatov Institute of Atomic Energy, Moscow, USSR

B3.6 Spectroscopy of titanium ions injected into a hot plasma by CO_2-laser-radiation
P Greve, J Haumann, M Kato, H-J Kunze and L Ullrich
Institut für Experimentalphysik V, Ruhr-Universitaet, Federal Republic of Germany

General theory, stellarators, torsatrons, bumpy torus

BP1 General theory of kinetic ballooning modes
G Rewoldt, E A Frieman, W M Tang and A H Glasser
Plasma Physics Laboratory, Princeton University, USA

BP2 New theory of wave propagation in nonuniform Vlasov plasmas
T Watanabe, H Hojo, M Watanabe[1], H Sanuki[2], T Ohnuma[3] and Kyoji Nishikawa
Institute for Fusion Theory, Hiroshima University, Japan
[1] *Faculty of Engineering, Kinki University, Japan*
[2] *Institute of Plasma Physics, Nagoya University, Japan*
[3] *Faculty of Engineering, Tohoku University, Japan*

BP3 Saturation of stimulated scattering processes by the nonlinear decay of electrostatic wave
S J Karttunen and R R E Salomaa
Technical Research Centre of Finland, Helsinki, Finland

BP4 Nonlinear theory of the rotational instability in a collisionless FLR plasma
Peter A E M Janssen
Einhoven University of Technology, The Netherlands

BP5 Vortices in laser-produced plasmas
P K Shukla[1], M Y Yu[1], A Hasegawa[2] and K H Spatschek[3]
[1] *Ruhr-Universität Bochum, Federal Republic of Germany*
[2] *Bell Laboratories, Murray Hill, New Jersey, USA*
[3] *Universität Essen, Federal Republic of Germany*

BP6 The influence of parallel viscosity on the resistive 'g' mode
R J Hosking* and D C Robinson
Culham Laboratory
**University of Waikato, New Zealand*

BP7 Magnetohydrodynamic stability criterion for rotating plasmas
G Spies and T Hellsten*
Max-Planck-Institut für Plasmaphysik, Federal Republic of Germany
**Royal Institute of Technology, Stockholm, Sweden*

BP8 On the peeling instability
D Lotz and J Nührenberg
Max-Planck-Institut für Plasmaphysik, Federal Republic of Germany

BP9 Quasilinear evolution of the ion-acoustic turbulence excited by a return current
K Appert, R Bingham, J Vaclavik and E S Weibel
Centre de Recherches en Physique des Plasmas, Lausanne, Switzerland

BP10 On the transport theory of electrostatic microinstabilities
J J Sanderson and S P Gary*
University of St Andrews, Scotland
**Los Alamos Scientific Laboratory, University of California, USA*

BP11 Self-consistent numerical solution of the nonlinear axisymmetric magnetohydrodynamic equilibria
R Bingham, R Gruber and F Troyon
Centre de Recherches en Physique des Plasmas, Lausanne, Switzerland

BP12 Absorption of electromagnetic waves around the electron cyclotron frequency
M Bornatici and F Engelmann
Association Euratom-FOM, The Netherlands

BP14 Spatial structure of gyro-kinetic modes in toroidal geometry
F Pegoraro and T J Schep*
Scuola Normale Superiore, Pisa, Italy
**Association Euratom-FOM, The Netherlands*

BP15 Ion – acoustic solitons with a temperature gradient
W Malfliet
Physics Department, University of Antwerp, Belgium

BP16 Cascade saturation of parametric instabilities in plasma induced by finite-bandwidth driver pump
V Stefan
Boris Kidric Institute of Nuclear Sciences, Yugoslavia

BP17 Reduction and inversion of particle transport due to plasma rotation and ion-neutral friction
D C Schram and B F M Pots
Physics Department, Eindhoven University of Technology, The Netherlands

BP18 Potential small-scale instabilities of an inhomogeneous plasma in crossed fields
Yu A Kirochkin, A G Pokroev and K N Stepanov
Kharkov Physical-Technical Institute, USSR

BP19 Experiments on high pressure plasma in a helical stellarator (Asperator NP-3)
Y Goto, T Asaishi, Y Funato, K Harafuji, S Kitajima, J Neyatani, N Sasaki, K Sugita, I Sakamoto, F Tozuka, H Watanabe and S Nagao
Faculty of Engineering, Tohoku University, Sendai, Japan

BP20 A large stellarator based on modular coils
S M Hamberger, L E Sharp and L F Peterson
Plasma Research Laboratory, The Australian National University, Australia

BP21 Optimization of a stellarator design including modulation of the helical winding geometry
L E Sharp, L F Peterson and S M Hamberger
Plasma Research Laboratory, The Australian National University, Australia

BP22 On toroidal vacuum fields and particle orbits in modified stellarators and torsatrons
W VII A – Team and W Lotz presented by F Rau
Max-Planck-Institut für Plasmaphysik, Federal Republic of Germany

BP23 Dependence of the (2,1) tearing mode on the stellarator field in Wendelstein VII-A
W VII-A Team, presented by R Jaenicke
Max-Planck-Institut für Plasmaphysik, Federal Republic of Germany

BP24 Neutral injection into the W VII-A stellarator
W VII-A Team, Neutral Injection Group
Max-Planck-Institut für Plasmaphysik, Federal Republic of Germany

BP25 Stability of Helical Equilibria
R Gruber*, W Kerner, W Schneider and F Troyon*
Max-Planck-Institut für Plasmaphysik, Federal Republic of Germany
**CRRP Lausanne*

BP26 Observation of poloidal and toroidal asymmetry in line emission in W VII-A stellarator discharges
W VII-A Team, presented by H Hacker
Max-Planck-Institut für Plasmaphysik, Federal Republic of Germany

BP27 Computation of heating efficiencies and deposition profiles for neutral injection into Wendelstein VII-A stellarator
J E Faulkner, G G Lister, W Ott and E Speth
Max-Planck-Institut für Plasmaphysik, Federal Republic of Germany

BP28 Magnetic surfaces, particle orbits and neutral injection in conventional and ultimate torsatrons
D T Anderson, J A Derr, T Kruckewitt, J L Shohet, S Rehker* and J A Tataronis†
University of Wisconsin, Madison, USA
**Max-Planck-Institut für Plasmaphysik, Federal Republic of Germany*
†Courant Institute, New York University, USA

BP29 (a) Ohmic heating discharges in the L–2 stellarator with gas puffing
E D Andrjukhina, M A Bloch, M S Berezhetskii, I S Sbitnikova, G S Voronov, S E Grebenschchikov, K S Dyabilin, O I Fedjanin, N F Larionova, H F Lunin, S V Kladov, S N Popov, A V Khudoleev, Yu V Kholnov and I S Shpigel'
P N Lebedev, Institute of the Academy of Sciences of the USSR, Moscow

(b) Observation of sawtooth fluctuations in ohmic heating discharges in the L–2 stellarator
M S Berezhetskii, S E Grebenshchikov, B I Kornev, J H Harris* and I S Shpigel'
P N Lebedev, Institute of the Academy of Sciences of the USSR, Moscow
**University of Wisconsin, Madison, USA*

BP30 The effect of stochastic electric fields on plasma transport in the range of low collision frequencies in a torsatron with a high helical inhomogeneity
V K Bocharov, P Ya Burchenko, V S Vojtsenya, E D Volkov, A Yu Voloshko, S S Kalinichenko, K S Rubtsov, S I Solodovchenko, O M Shvets and A F Shtan'
The Kharkov Physical-Technical Institute, Kharkov, USSR

BP31 Current turbulent ion heating in modulational instability regime and caviton transport in a stellarator in a high magnetic field
N F Perepelkin, V A Suprunenko, A S Slavny, M P Vasil'ev, A G Dikij, V D Kotsubanov, B V Kravchin, A E Kulaga and Ya Shtöckel*
Physical-Technical Institute of Academy of Sciences, Ukr.SSR, Kharkov, USSR
**IPP, Prague, CZSSR*

BP32 Plasma-wall interaction study in Kharkov stellarators
A B Blank, V S Vojtsenya, E D Volkov, A Yu Gribanov, A G Dikij, Eh S Zolotovitskaya, E M Latsko, V F Rybalko, V P Samoilov and S I Solodovchenko
Physical-Technical Institute of Academy of Sciences, Ukr.SSR, Kharkov, USSR

BP34 Radial transport in the ELMO bumpy torus in collisionless regimes
E F Jaeger, C L Hedrick and D A Spong
Oak Ridge National Laboratory, Oak Ridge, Tennessee, USA

Tokamak experiments II

D2.1 Accumulation of impurities in the high density regime of PULSATOR
W Engelhardt, S Sesnic, K Lackner, G Fußmann, J Gernhardt, E Glock, S von Goeler*, N Gottardi, F Karger, O Klüber, G Lisitano, H M Mayer, D Meisel, H Murmann and F Wagner
Max-Planck-Institut für Plasmaphysik, Garching, Federal Republic of Germany
**Plasma Physics Laboratory, Princeton University, USA*

D2.2 Flux and energy of deuterium incident on a limiter-like probe in PLT
G M McCracken, S A Cohen, H F Dylla, C W Magee, S T Picraux, S M Rossnagel and W R Wampler
Plasma Physics Laboratory, Princeton University, USA

D2.3 Impurity ion sputtering for introducing metal impurity in JFT–2 tokamak
N Suzuki, N Fujisawa, S Konoshima, M Maeno, M Shimada, T Yamamoto, S Kasai and K Uehara
Japan Atomic Energy Research Institute, Tokai, Ibaragi, Japan

D2.5 Initial operation of PDX
D Meade, W Arunasalam, C Barnes, K Bol, S Cohen, H Dalhed, C Daughney, S Davis, J DeLucia, D Dimock, F Dylla, P Efthimion, R Fonck, B Grek, R Hawryluk, E Hinnov, H Hsuan, M Irie, R Jacobsen, D Johnson, L Johnson, H Maeda, D Mansfield, G McCracken, D Mueller, M Okabayashi, O Okada, K Owens, S Picraux*, S Rossnagel, N Sauthoff, G Schmidt, J Schmidt, E Silver, J Sinnis, P Staib, J Strachan, S Suckewer, F Tenney and W Wampler*
Plasma Physics Laboratory, Princeton University, Princeton, USA
**Sandia Laboratories, Albuquerque, New Mexico, USA*

D2.6 Toroidal discharges with cold blankets in RINGBOOG II
The RINGBOOG-Team, presented by L C J M de Kock
Association Euratom-FOM, Jutphaas-Nieuwegein, The Netherlands

D2.7 Magnetic islands and disruptions in a tokamak
K M McGuire* and D C Robinson
Culham Laboratory, Abingdon, Oxon.
**University of Oxford, Oxford*

General theory, REB, atomic processes

D3.1 Axis encircling ion gyro-instability
P J Catto, R E Aamodt, M Rosenbluth*, J A Byers† and L D Pearlstein†
Science Applications, Inc., Laboratory for Applied Plasma Studies, Boulder, Colorado, USA
**School of Natural Sciences, The Institute for Advanced Study, Princeton, USA*
†Lawrence Livermore Laboratory, University of California, Livermore, USA

D3.2 Distribution of particles in stochastic fields
P Rolland
Association Euratom-CEA, Grenoble, France

D3.3 Magnetic field generation in imploding plasmas due to Nernst refrigeration
J H Brownell
Los Alamos Scientific Laboratory, Los Alamos, New Mexico, USA

D3.7 Kink instabilities of a plasma column with elliptical cross-section
Gu Yongnian and Qiu Naixian
Southwestern Institute of Physics, Sichuan, People's Republic of China

Pinches, plasma focus, reactor aspects, inertial confinement, REB

DP1 High current RFP devices and the pulsed RFP reactor
J P Christiansen and K V Roberts
Culham Laboratory

DP2 Modelling ZT-40 with the G2M diffusion code
R N Byrne and C K Chu*
Science Applications, Inc. La Jolla, California, USA
**Columbia University, New York, USA*

DP3 Investigation of microinstabilities in a low density linear theta-pinch plasma
H U Fahrbach, W Köppendörfer, M Münich, J Neuhauser, H Röhr, G Schramm, J Sommer and E Holzhauer*
Max-Planck-Institut für Plasmaphysik, Federal Republic of Germany
**Institut für Plasmaforschung der Universität Stuttgart, Federal Republic of Germany*

DP4 Numerical studies of the RFP
P G Carolan, J W Johnston*, J W Long*, A A Newton, V A Piotrowicz* and M R C Watts*
Culham Laboratory
**Oxford Polytechnic, Headington, Oxford*

DP5 Field reversal experiments
R K Linford, W T Armstrong, J Lipson, D A Platts and E G Sherwood
Los Alamos Scientific Laboratory, Los Alamos, USA

DP6 Z-pinches of intense energy-density driven by high voltage storage lines
P Baldock, P Choi, A E Dangor, A Folkierski, E Kahan, D E Potter, P D Slade and S J Webb
Blackett Laboratory, Imperial College, London

DP7 Pitch programming of the ZT-S reversed-field pinch experiment
A Jacobson, L C Burkhardt, D A Baker, R B Howell, A E Schofield and A G Sgro
University of California, Los Alamos Scientific Laboratory, Los Alamos, USA

DP8 Equilibrium and stability of a screw pinch
J Rem
Association Euratom-FOM, Jutphaas-Nieuwegein, The Netherlands

DP9 Impurity radiation, density and temperature in SPICA
D Oepts, G G Lister*, J W Long†, A F G van der Meer, A A M Oomens and C Bobeldijk
Association Euratom-FOM, Jutphaas-Nieuwegein, The Netherlands
**Max-Planck-Institut für Plasmaphysik, Garching, Federal Republic of Germany*
†Culham Laboratory, England

DP10 Reversed field pinch plasma model
G H Miley, R A Nebel and R W Moses*
University of Illinois, Urbana, USA
**Los Alamos Scientific Laboratory, Los Alamos, USA*

DP11 Optimisation of the Mather type PF devices based on 2D snowplow numerical code and analytical considerations
Z Jankowicz, A Jerzykiewicz, J Nowikowski, B Bartolik, A Matusiak and M Rabinski
Institute of Nuclear Research, Swierk, Poland

DP14 Energy distribution of deuterons in the Frascati 1 MJ plasma focus facility
L Bertalot★, L Bilbao☆, H Bruzzone⊕, A Gentilino○, C Gourlan, R L Gullickson□, H Kroegler, S Podda★, J P Rager, B V Robouch and K Steinmetz●
Associazione Euratom-CNEN, Frascati, Rome Italy
★CNEN Fellow, ☆CNEN Fellow on leave from the University of Buenos Aires, Argentina, ⊕Fellow of the CNICT (Argentina), on leave from the University of Buenos Aires, □AFOSR/NP, Bolling AFB,DC, ●Euratom Fellow

DP15 Pinched high-speed plasma fluxes
A G Tolstolutskij, V G Zykov, I M Zolototrubov and Yu M Novikov
The Kharkov Physical-Technical Institute, Kharkov, USSR

DP16 Direct energy conversion and control of unstable burn by cyclic major radius compression and decompression
K Borrass, K Lackner and E Minardi
Max-Planck-Institut für Plasmaphysik, Federal Republic of Germany

DP17 The influence of plasma edge effects and of impurities on the thermal stability of a tokamak reactor
B K Bein
Uni-Center, D-4630 Bochum, Federal Republic of Germany

DP18 Kinetic theory of neutrals in a bounded plasma slab with inhomogeneous ion temperature and density
M Tendler
Institute of Technology, Uppsala University, Sweden

DP19 Fusion reactors through efficient energy conversion
A Hertzberg, J Dawson* and P Rose†
University of Washington, USA
**University of California, USA*
†Mathematical Sciences Northwest, Inc. USA

DP20 Thermal fluctuations and leaking radiation from laser-produced plasma
S Vukovic, Yu M Aliev*, O M Gradov*, A Yu Kyrie* and A A Frolov*
Institute of Physics, Beograd, Yugoslavia
**Lebedev Physical Institute, USSR Academy of Sciences, Moscow, USSR*

DP21 The wavelength dependence of energy absorption in laser-plasmas
H Schwarz
Rensselaer Polytechnic Institute, Troy, New York, USA and Departamento de Fisica, Universidade de Brasilia, Brazil

DP22 Investigation of laser-produced plasmas in the SM magnetic trap
J Baranowski, S Chyrczakowski, K Melzacki, M Sadowski, E Skladnik-Sadowska, A S Slavnyj and S Ugniewski
Institute of Nuclear Research, Otwock-Swierk, Poland

DP23 Interaction of short 1.06μm laser pulses with low-z plasma
J E Balmer, P Ladrach, A P Schwarzenbach, T P Donaldson and H P Weber
Institute of Applied Physics, University of Berne, Sidlerstrasse, Bern

DP24 A time-dependent study of linear collective ion acceleration
A Sternlieb
Department of Physics and Astronomy, University of Maryland, USA

DP25 X-ray spectrometry of laser compressed microballoons
J G Lunney, M H Key*, J D Kilkenny†, R W Lee†, C L S Lewis and A Moore
Department of Pure and Applied Physics, Queen's University of Belfast
**Rutherford Laboratory, Oxon*
†Imperial College, London

DP26 Transition from isentropic to isothermal expansion in laser-produced plasmas
A Barrero and J R Sanmartin
Escuela Tecnica Superior de Ingenieros Aeronauticos Universidad Politecnica de Madrid, Spain

DP27 Characterization techniques for high quality ICF targets
B W Weinstein and C D Hendricks
University of California, Lawrence Livermore Laboratory, USA

DP28 Axial variation of the energy transfer from an intense relativistic electron beam to a plasma
A E Dangor, A K L Dymoke-Bradshaw, G S Kerslick and P Šunka
Blackett Laboratory, Imperial College, London

DP29 Application of intense relativistic electron beams to steady state tokamaks
V Bailey, J Benford and H Helava
Physics International Company, San Leandro, California, USA

DP30 A numerical study on wave shaping in REB diodes
S Sinman and A Sinman*
Middle East Technical University, Plasma Engineering Laboratory, Ankara, Turkey
**Ankara Nuclear Research and Training Center, Electron Physics Laboratory, Ankara, Turkey*

DP31 Formation of a reversed-field configuration with a rotating relativistic electron beam
J D Sethian, K A Gerber, D N Spector and A E Robson
Naval Research Laboratory, Washington, D.C., USA

DP32 Velocity angle scattering of a relativistic electron beam during transport through a plasma
P H de Haan, H J Hopman, G A M Janssen, E H A Granneman, R Jayakumar*, P S Strelkov† and B Jurgens
FOM-Institute for Atomic and Molecular Physics, Amsterdam, The Netherlands

DP34 The model investigation of the quasispherical liner compression of toroidal plasma
V M Goloviznin, R H Kurtmullaev, V N Semenov, V A Gasilov*, A P Favorsky*, M Yu Shashkov*, N A Sosnin†
I V Kurchatov Institute of Atomic Energy, Moscow, USSR
**M V Keldysh Institute of Applied Mathematics, Ac. Sci., Moscow, USSR*
†M V Lomonosov Moscow State University, Moscow, USSR

DP35 Build-up of antiparallel structure and its stability in systems with magnetic barrier
A G Es'kov, A G Kalygin, R Kh Kurtmullaev, A I Malutin, A P Proshletsov and V N Semenov
Kurchatov Institute of Atomic Energy, Moscow, USSR

DP36 Paramagnetic spheromak formation in a combined zee and theta pinch
G C Goldenbaum, J H Irby, Y P Chong and G Hart
Department of Physics and Astronomy, University of Maryland, USA

Inertial confinement

E1.1 Computational study of laser implosion and comparison with experimental results at ILE Osaka
T Yabe, K Nishihara, K Mirma, N Miyanaga, Y Kato and C Yamanaka
Institute of Laser Engineering, Osaka University, Osaka, Japan

E1.2 Laser fusion experiments at KMSF
R R Johnson, R L Berger, P M Campbell, G Charatis, J G Downward, T M Henderson, F J Mayer, N K Moncur, D L Musinski, L V Powers, S B Segall, L D Siebert, D C Slater, D E Solomon, J A Tarvin and C E Thomas
KMS Fusion Inc., Michigan, Ann Arbor, USA

E1.3 Energy transport from 1.06μm and 0.53μm laser plasmas interactions at 10^{15} W cm^{-2}
J D Kilkenny, D J Bond, D R Gray, J D Hares, R G Evans*, M Key*, W Toner* and J G Lunney†
Blackett Laboratory, Imperial College, London
**Rutherford Laboratory*
†Queen's University, Belfast

E1.4 Acceleration of thin foil targets under intense laser irradiation
G Brederlow, R Brodmann, K Eidmann, P Mulser, R Petsch, R Sigel, G Spindler, G Tsakiris, R Volk and S Witkowski
Projektgruppe für Laserforschung der Max-Planck-Gesellschaft zur Förderung der Wissenschaften e.V., Garching, Federal Republic of Germany

E1.5 Studies of laser driven implosions by time-resolved shadowgraphy
C L S Lewis, L Cooke, J G Lunney, A Moore, J M Ward, R G Evans*, M H Key* and T A Hall†
The Queen's University of Belfast
**Rutherford Laboratory*
†Essex University

E1.6 Laser-matter interaction and implosion studies at Limeil Research Centre
A Bekiarian, A Bernard, E Buresi, R Dautray, M Decroisette, F Delobeau, P Guillaneux, J M Reisse, B Sitt, J M Vedel and J P Watteau
Centre d'Etudes de Limeil, France

E1.7 Recent high density inertial fusion results from the Shiva facility
E K Storm, H G Ahlstrom, J A Glaze, K R Manes and J H Nuckolls
University of California, Lawrence Livermore Laboratory, USA

E1.8 Plasma heating by the amplifier module radiation in thermonuclear installation "Delfin"
N G Basov, Yu A Mikhailov, G V Sklizkov and S I Fedotov
P N Lebedev Physical Institute of Academy of Sciences of the USSR, Moscow, USSR

Plasma heating

E2.1 Nonresonant decay of lower hybrid waves
M Brambilla, B Liberman*, S S Pesic and D Moreau
Association Euratom-CEA, Grenoble, France
**Instituto de Fisica, Porto Alegre-rs-Bresil*

E2.2 The distortion of the thermal ion distribution by neutral injection heating
J G Cordey, M Cox and E Bittoni*
Culham Laboratory, Abingdon, Oxon.
**CNEN Centro Calcola (Bologna)*

E2.3 Ion-ion hybrid resonance damping and heating in the Erasmus tokamak
V P Bhatnagar, G Bosia, M Calderon, I Darius, E Desoppere, R Koch, A M Messiaen, D Pearson, Cl Piret, G Telesca, P E Vandenplas, G van Oost and R R Weynants
Laboratorie de Physique des Plasmas, Ecole Royale Militaire, Brussels

E2.4 The accessibility of the resonant surfaces and the role of surface waves in RF plasma heating
Ernesto Canobbio
Department of Physics, University of California, USA and Association Euratom-CEA, Grenoble, France

E2.5 Characterization of high power neutral beams by optical diagnostics
J F Bonnal, G Bracco, C Breton, J P Bussac, C de Michelis, J Drauaux, M Mittioli, R Oberson and J Ramette
Association Euratom-CEA sur la Fusion, Fontenay-aux-Roses, France

Tokamak experiments, tokamak theory

EP1 Microtearing modes and anomalous transport in tokamaks
J F Drake, N T Gladd, C S Liu and C L Chang
Department of Physics and Astronomy, University of Maryland, Maryland, USA

EP3 Experiments on high-beta tokamak stability
P G Weber, T C Marshall and R A Gross
Columbia University, New York, USA

EP4 Influence of q on stability and confinement in the Garching belt-pinch IIa
G Becker and O Gruber
Max-Planck-Institut für Plasmaphysik, Garching, Federal Republic of Germany

EP5 Limitation of the electron density in the pulsator tokamak
G Fußmann, O Klüber, W Engelhardt, J Gernhardt, E Glock, S V Goeler*, F Karger, N Gottardi, K Lackner, G Lisitano, H M Mayer, D Meisel, H Murmann, S Sesnic, F Wagner and H P Zehrfeld
Max-Planck-Institut für Plasmaphysik, Garching, Federal Republic of Germany
**Plasma Physics Laboratory, Princeton University, USA*

EP6 Tokamak discharges with AC modulation
S von Goeler, J Gernhardt, F Pohl, W Engelhardt and H Murmann
Max-Planck-Institut für Plasmaphysik, Garching, Federal Republic of Germany

EP7 Schlieren measurements of plasma cinematics during current disruptions in tokamaks
G Lisitano
Institut für Plasmaphysik, Euratom-IPP Assoc., Garching, Federal Republic of Germany

EP8 Results from the DITE bundle divertor
S J Fielding, J W M Paul and A J Wootton
Culham Laboratory, Abingdon, Oxon.

EP9 Neutral injection heating in DITE
R D Gill, K B Axon, G A Baxter, W H M Clark, R S Hemsworth, J Hugill, J W M Paul, J B B Percival, R Prentice, B A Powell and A A Mirin*
Culham Laboratory, Abingdon, Oxon.
**Lawrence Livermore Laboratory, USA*

EP11 Low-q discharges in DITE tokamak
J Hugill, A J Wootton, K B Axon, B A Powell, R Prentice, D D R Summers and C M Wilson
Culham Laboratory, Abingdon, Oxon.

EP12 Measurements of electron cyclotron emission on T.10
A A Bagdasarov†, W H M Clark, A E Costley*, E P Gorbunov† and G F Neill*
Culham Laboratory, Abingdon, Oxon.
**The National Physical Laboratory, Teddington, Middlesex*
†I V Kurchatov Institute of Atomic Energy, USSR

EP13 Polarization and millisecond spectral measurements of electron cyclotron emission from DITE tokamak
D J Campbell*, W H M Clark, A E Costley*, P J Fielding, D C Robinson†, G D Tait†† and B Walker*
Culham Laboratory, Abingdon, Oxon.
**The National Physical Laboratory, Teddington, Middlesex*
†University of Sydney, Sydney, Australia
††University of Maryland, Maryland, USA

EP15 D_α spectral profile measurements on TFR plasmas
TFR Group, presented by P Platz
Association Euratom-CEA sur la Fusion, Fontenay-aux-Roses, France

EP16 Nonlinear phenomena by the tokamak helical mode evolution
N V Ivanov and A M Kakurin
I V Kurchatov Institute of Atomic Energy, Moscow, USSR

EP17 Ballooning stable profiles in circular tokamaks
D Lortz and J Nührenberg
Max-Planch-Institut für Plasmaphysik, Garching, Federal Republic of Germany

EP18 Ripple loss of fast ions in a large tokamak
K Tani, H Kishimoto and S Tamura
Japan Atomic Energy Research Institute, Tokai, Japan

EP19 Numerical study of the internal kink mode in tokamaks
W Kerner, R Gruber* and F Troyon*
Max-Planck-Institut für Plasmaphysik, Garching, Federal Republic of Germany
**CRPP-EPFL, Lausanne, Switzerland*

EP20 Electric field and slowing down effects on relativistic charged particle motion in tokamaks
H P Zehrfeld, G Fußmann and B J Green*
Institut für Plasmaphysik, Euratom-IPP Association, Garching, Federal Republic of Germany
**JET Joint Undertaking, Abingdon, Oxon.*

EP21 Control of the radial position of a tokamak plasma in the current rise phase
B J Green, M R Perrone*, P Noll and P Dokopoulos†
JET Joint Undertaking, Abingdon, Oxon
**Universita degli Studi di Lecce, Italy*
†University of Salonika, Greece

EP22 A stable route to the high βp regime
A Sykes and M F Turner
Culham Laboratory

EP23 Pellet refuelling of a divertor tokamak
L Jørgensen and P E Stott
Culham Laboratory

EP24 Nonlinear theory of collisional drift-waves in toroidal geometry and anomalous skin effects in tokamaks
A Rogister and G Hasselberg
Institut für Plasmaphysik der Kernforschungsanlage Julich, Federal Republic of Germany

EP25 Transport calculations for the approach to ignition in JET
M L Watkins and A Gibson
JET Joint Undertaking, Abingdon Oxon

EP26 The loss of injected ions due to spatial field ripple in tokamaks
J G Gordey, W G F Core* and A Gibson*
Culham Laboratory
**JET Joint Undertaking, Abingdon, Oxon*

EP27 A multi-region global transport model for tokamaks
W G F Core and T E Stringer
JET Joint Undertaking, Abingdon, Oxon

EP28 Beam-induced currents in toroidal plasmas
D F H Start, J G Cordey and E M Jones
Culham Laboratory

EP29 Effect of lower hybrid wave turbulence on tearing mode instability
A K Sundaram and A Sen
Physical Research Laboratory, Ahmedabad, India

EP30 Numerical study of the ideal MHD stability of spheromaks
P Gautier, R Gruber, F Troyon, W Kerner*, and W Schneider*
Centre de Recherches en Physique des Plasmas, Lausanne, Switzerland
**Max-Planck-Institut für Plasmaphysik, Garching, Federal Republic of Germany*

EP31 Studies of resonant absorption of Alfven waves by means of an evolution code
B Balet, K Appert, R Gruber, R Keller, F Troyon and J Vaclavik
Centre de Recherches en Physique des Plasmas, Lausanne, Switzerland

EP32 Free-boundary equilibrium of a high-β tokamak
J P Goedbloed
Association Euratom-FOM, Jutphaas-Nieuwegein, The Netherlands

EP33 Numerical studies of MHD instabilities
J L Johnson*, M S Chance, R L Dewar, A H Glasser, R C Grimm, J M Greene, S C Jardin, J Manickam, A E Miller, D A Monticello, A M M Todd, K E Weimer and R B White
Plasma Physics Laboratory, Princeton University, Princeton, USA

EP34 Studies of particle and energy balance of ions in tokamaks T–4 and Tuman-2a by methods of corpuscular plasma diagnostics
V V Afrosimov, E L Berezovsky, A B Izvozchikov, A I Kislyakov, M P Petrov and A V Khudoleev
Ioffe Physico-Technical Institute, USSR Academy of Sciences, Leningrad, USSR

A2.1

SCALING IN ELMO BUMPY TORUS (EBT)*

F. W. Baity, K. H. Carpenter, J. A. Cobble, R. J. Colchin, H. O. Eason, J. C. Glowienka, G. R. Haste, C. L. Hedrick, E. F. Jaeger, R. K. Richards, T. Uckan, T. L. White
Oak Ridge National Laboratory, Oak Ridge, Tennessee, USA

F. M. Bieniosek, K. A. Connor, R. L. Hickok, S. P. Kuo
Rennselaer Polytechnic Institute, Troy, New York, USA

R. A. Dandl
Retired; Consultant at General Atomic Company, San Diego, California, USA

S. Hiroe
Institute of Plasma Physics, Nagoya, Japan

and
N. H. Lazar and B. H. Quon
TRW Defense Systems, Redondo Beach, California, USA

1. INTRODUCTION

The steady-state plasma in the ELMO Bumpy Torus (EBT) is confined in a "bumpy" magnetic field produced by joining 24 magnetic mirror cells into a large aspect ratio torus. Heating power is provided by continuous wave (cw) microwave sources at 28 GHz, 18 GHz, and 10.6 GHz. The magnetic field is adjusted to bring either the 28 GHz or the 18 GHz microwaves into local electron cyclotron resonance near the mirror coils. The two cases are referred to as EBT-S (for Scale) and EBT-I, respectively. The toroidal plasma has been shown to be macroscopically stabilized by the magnetic field modification resulting from diamagnetic annuli of energetic electrons which form in each cell as a result of the microwave heating.

The EBT-S configuration employs a 28 GHz cw gyrotron tube, recently developed by Varian Associates, for the purpose of studying the scaling of the plasma parameters with applied microwave frequency. Experimental documentation of the plasma in EBT-S is a prime objective of the present research group. Documentation of the plasma parameters in the EBT-I mode is more complete.[1]

2. MEASUREMENT OF PLASMA PARAMETERS IN EBT-I

The plasma parameters in the EBT-I mode have been measured by a variety of diagnostic techniques. The results of a typical data run in the macrostable regime (T-mode) of operation are listed in Table 1.

These parameters do not represent the maximum values of any of the parameters, but rather the case for which the greatest amount of diagnostic information is available. As the ambient pressure is reduced (lower collisionality), both the density and electron temperature (and, consequently, the energy lifetime) are observed to increase (see Fig. 1).

In addition, the ion temperature and the depth of the potential well which has been measured in the plasma also are greater at lower collisionality.

The two measurements of electron temperature (soft x-ray and laser scattering) differ significantly. The laser scattering spectrum for the case given in Table 1 is shown in Fig. 2. The analysis of this spectrum indicates an uncertainty of ±75 eV in the temperature determination. The uncertainty in the soft x-ray measurement is estimated to be in the neighborhood of ±50%.

For calculation of the energy lifetime, 10-25% of the applied microwave power was assumed to be absorbed by the plasma electrons. This range is derived from experimental and theoretical estimates of microwave power balance.

TABLE 1. Results of a typical EBT-I run

MACHINE PARAMETERS

Parameter	Value	
Magnetic field	5 kG midplane	10 kG mirror
Major radius	150 cm	
Minor radius, midplane	12 cm	
Plasma volume	300 liters	
Magnetic aspect ratio	9:1	
Microwave power	40 kW at 18 GHz + 5 kW at 10.6 GHz	
Ambient pressure	5.5×10^{-6} torr (outside cavity)	

PLASMA PARAMETERS

Parameter	Diagnostic	Value
Line averaged density, n_e	Microwave interferometer	$6\pm2\times10^{11}$ cm^{-3}
Electron temperature, T_e	Soft x-ray detector	315 eV
	Thomson scattering	120±75 eV
Ion temperature, T_i	Charge exchange	63 eV
Potential well depth, $\Delta\phi$	Heavy ion beam probe	80 V
Energy lifetime, τ		1-2.5 msec

3. EBT SCALING LAWS

The basic plasma parameters in EBT [density (n), electron temperature (T_e), and confinement time (τ)] are predicted to scale in the following manner. The plasma density is limited by microwave cutoff, so the maximum attainable density increases as the square of the microwave frequency. Since the magnetic field required to bring the applied microwave power into resonance increases linearly with the frequency, then the density scales as the magnetic field squared ($n \propto B^2$). A limited number of measurements at 28 GHz support this scaling.[2] The electron temperature, as determined by the soft x-ray detector, has been observed to increase proportional to the square root of the applied microwave power ($T_e \propto P^{1/2}$). The confinement time exhibits two different scaling relations, depending on the regime of collisionality (ν/Ω) in which the plasma operates.

$$\tau \propto \begin{cases} T_e^{-7/2}, & \nu/\Omega \gg 1 \\ T_e^{3/2}, & \nu/\Omega \ll 1 \end{cases}$$

*Research sponsored by the Office of Fusion Energy, U. S. Department of Energy under Contract No. W-7405-eng-26 with Union Carbide Corporation.

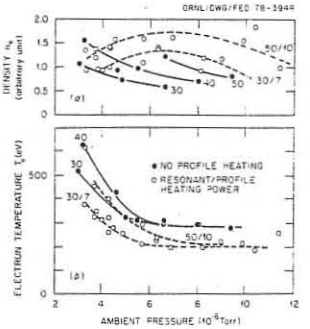

Fig.1. Electron density (a) and temperature (b) versus ambient pressure for various amounts of microwave power in EBT-I. The notation x/y means x kW at 18 GHz and y kW at 10.6 GHz. Single numbers mean power was applied at 18 GHz only.

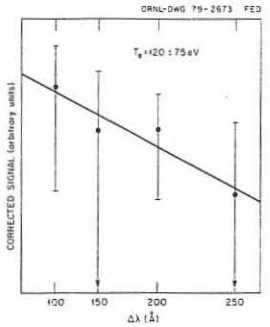

Fig.2. Laser scattering spectrum for the case in Table 1. The temperature is measured on the toroidal axis; the plasma is shifted toward the major axis several centimeters.

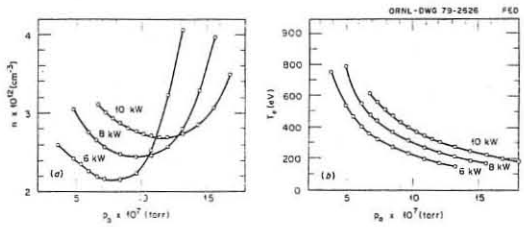

Fig.3. Peak electron density (a) and peak temperature (b) versus edge neutral pressure from the one-dimensional radial transport code for various amounts of microwave power absorbed in the toroidal plasma. Edge neutral pressure (at the toroidal plasma edge) differs from ion gauge pressure which is measured at the cavity wall.

4. RADIAL TRANSPORT CALCULATIONS WITH CONSTANT EDGE NEUTRAL FLUX

Recently, one-dimensional radial transport equations for EBT have been solved assuming a constant flux of cold neutrals at the plasma edge, independent of toroidal plasma parameters.[3] This boundary condition provides a negative feedback mechanism which limits thermal excursions and allows steady-state solutions at low collisionality. Such a boundary condition is appropriate if reflux from the wall occurs on a time scale slow compared to an energy containment time. Experiments[1] indicate that a time on the order of tens of minutes is required for the plasma to reach equilibrium with the wall. Once equilibrium is reached, pumping is balanced by a slight gas feed of about 3×10^{-2} torr liter/sec. This feed rate is small compared to the flux of neutrals required to sustain the plasma, which is about 1 torr liter/sec in the present calculations. The source of these neutrals is assumed to be wall reflux.[1]

The one-dimensional radial transport equations used in these calculations incorporate a self-consistent electric field.[4,5,6] The transport coefficients are assumed to be approximately neoclassical and include lowest order effects of velocity space regions where poloidal drift frequencies are small.[5,7]

Experimental results are often plotted versus ambient neutral pressure as given by ion gauges. For comparison with such data, the numerical results are plotted as a function of $P_o = n_o kT_o$, where n_o is the density of cold neutrals at the plasma edge and $kT_o = E_o \sim 0.5$ eV. Note that p_o is similar to but not equal to the ion gauge pressure. In the collisionless regime (low neutral pressure), the parametric dependence on edge neutral pressure is similar to that observed experimentally; i.e., density, temperature, and potential all increase with decreasing neutral pressure. Compare Fig. 3 with Fig. 1. Experiments apparently do not observe the collisional scaling at high neutral pressures since the electron ring beta is not sufficient to stabilize the toroidal plasma in this regime. We regard the trends shown by this very recent work as encouraging. At this writing, simplified analytic approximations for the ion as well as electron transport coefficients have been used in the modeling. Work is in progress to implement more accurate expressions for the transport coefficients.

ACKNOWLEDGMENTS

The authors gratefully acknowledge the assistance of Bob Livesey, Mack McGuffin, Dick Wintenberg, Carl Becker, George Pierce, and many others who have contributed to the EBT experimental effort.

REFERENCES

1. R. A. Dandl et al., Oak Ridge National Laboratory Report ORNL/TM-6457 (1978).
2. R. A. Dandl et al., in Plasma Phys. and Contr. Nucl. Fus. Research (Proc. Conf. Innsbruck, Austria, 1978).
3. E. F. Jaeger, C. L. Hedrick, and W. B. Ard, submitted to Phys. Rev. Lett. and E. F. Jaeger, C. L. Hedrick, and D. A. Spong, this meeting.
4. E. F. Jaeger and C. L. Hedrick, Nuclear Fusion 29, 443 (1979).
5. E. F. Jaeger et al., Oak Ridge National Laboratory Report ORNL/TM-6806 (1979).
6. E. F. Jaeger et al., Phys. Rev. Lett. 40, 866 (1978).
7. R. D. Hazeltine et al., Science Applications Inc. Report

A2.2

PLASMA CONFINEMENT IN NAGOYA BUMPY TORUS

T. Shoji, M. Fujiwara, M. Hosokawa, H. Iguchi, M. Tanaka and H. Ikegami
Institute of Plasma Physics, Nagoya University, Nagoya 464, Japan

ABSTRACT: Experimental studies are made on the plasma confinement in Nagoya Bumpy Torus (NBT), where plasmas are produced, heated and stabilized by high power microwaves. Plasma characteristics are observed to depend on both microwave power and ambient gas pressure, by which three operating modes are defined. One of many interesting features is the formation of positive electrostatic potential surrounding the toroidal plasma tubing. The potential is peaked at the location of hot electron rings.

Nagoya Bumpy Torus is a bumpy race track consisted of 24 mirrors with 2:1 mirror ratio and two 80 cm long straight sections. The major radius of the circular section is 160 cm with the aspect ratio of approximately 10. The maximum magnetic field strength is 4 kG (midplane) – 8 kG (mirror throat).

Microwave sources are klystron amplifiers with fixed frequencies of 18 GHz (20 kW maximum), 10.5 GHz (30 kW), and 8.5 GHz (75 kW), and the microwave power is divided into 24 equal parts and fed to each mirror section.

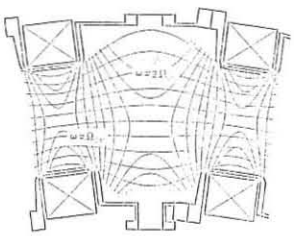

Fig.1. Median horizontal cut view of a single sector of NBT showing the contour of constant |B| and the magnetic field lines.

Magnetic field lines and constant |B| lines in a plane of the median horizontal cut are shown in Fig.1. The hatched regions correspond to the 1st and 2nd cyclotron resonance zone for 8.5 GHz: plasmas are produced and heated at the fundamental resonance and the energetic electrons are generated at the second harmonic resonance to form a hot electron ring in the midplane.

Although the bumpy torus has no rotational transform in the magnetic field lines, particles stay in a closed drift surface as a result of guiding center drifts due to the curvature of field lines and grad-B. Shapes and the axis of the drift surfaces depend strongly on the pitch angle of particles. Figure 2(a) shows a drift surface of a particle with $v_{\parallel}/v = 1$, and Fig.2(b) indicates the effective curvature, <R>, of the field lines

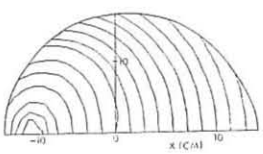

Fig.2(a) Drift surfaces for particles with $v_{\parallel}/v = 1$. Outer circle indicates the shadow of coil casing projected onto the midplane.

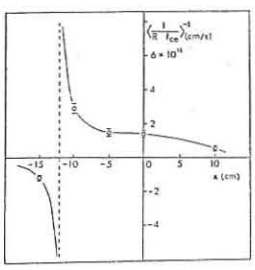

Fig.2(b) Effective toroidal curvature of the magnetic field lines determined from the electron beam tracing.

averaged along the torus which was determined by tracing an electron beam.[1] The position where <R> becomes infinite in Fig.2(b) is the axis of the drift surfaces, which is in good agreement with the computed results.

At present stage, the main diagnostics are listed in the following: (1) Single channel, 8 mm microwave interferometer to determine the average electron density. (2) Scintillator (NaI)-Photomultiplier-Pulse height analyzer system and X-band microwave radiometer to measure the energy and density of the hot electron rings. (3) Diamagnetic coils and Hall elements to estimate the magnetic field produced by diamagnetic currents of the hot electron rings. (4) Visible spectrometer to measure the intensity of H_α line. (5) Movable Langmuir probe for the radial distribution of the density and plasma space potential.

Dependence of various plasma parameters on the ambient hydrogen gas pressure are shown in Fig.3. In higher pressure regime X-ray intensity is weak (the intensity is plotted in logarithmic scale) and the radial magnetic field B_r produced by hot electron rings is not detectable. The plasma is produced and isolated within each simple mirror section with rather poor confinement: C-mode operation which stands for cold plasma. With decreasing

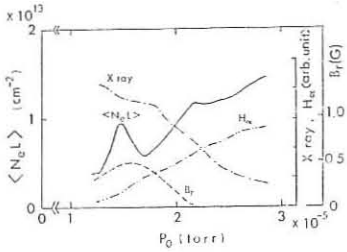

Fig.3. Various plasma parameters as a function of the ambient neutral gas pressure.

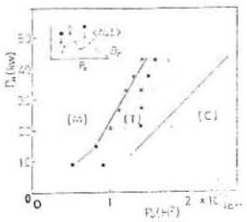

Fig.4. Dependence of the transition between C, T and M modes on the microwave input power and the ambient gas pressure.

the gas pressure, X-ray and microwave radiation are enhanced indicating the formation of hot electron rings, and B_r (≈ 1 gauss) is now detected. In this region the value of $\int n_e d\ell$ increases, while the intensity of H_α line, i.e., $\int n_e n_0 \langle \sigma v \rangle_{ex} d\ell$, decreases with the gas pressure. These facts mean that the plasma confinement time becomes longer associated with the generation of the high β hot electron rings, then the bumpy torus plasma is supposed to be stably confined by means of the average minimum magnetic field owing to the high β hot electron ring encircling the plasma surface. This mode of operation is named T-mode after its toroidal behavior of the plasma.[2] When the gas pressure is further decreased, strong and spontaneous X-ray bursts are observed and the plasma drives macroscopic instabilities as is often observed in a simple mirror plasma, so named M-mode. Conditions for C-T mode transition and T-M mode transition move to higher gas pressure with the increased microwave power input (Fig.4).

Another interesting feature in NBT plasma is the spatial profile of the plasma space potential, which is measured by a Langmuir probe inserted in the linear section where no microwave power is fed. Some profiles of the floating potential with the ambient neutral gas pressure as a parameter are shown in Fig.5. It is evident that a potential well is formed only when the neutral pressure is low enough to operate the T-mode. The radial position of the potential peak, (X_{peak}) when traced back along the magnetic field lines, is found to correspond to the location of the hot electron rings in the midplane of each mirror.

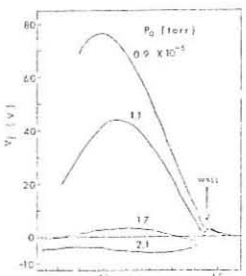

Fig.5. Radial distribution of floating potential for different gas pressures. The potential peaks are traced back to the location of the hot electron ring in the midplane.

In order to examine the relation between the potential peak and the location of hot electron ring, X_{peak} was measured as a function of the toroidal magnetic field strength (Fig.6) with which the location of $\omega = 2\Omega_{ce}$ for the applied frequency ($\omega/2\pi$ = 8.5 GHz) is compared. In Fig.6 the dot-dashed line indicates the cyclotron frequency with the relativistic electron mass with the use of measured hot electron temperature. The result again confirms that the location of the hot ring is the circular drift surface associated with the 2nd electron (nonrelativistic) cyclotron harmonics in the midplane. The mechanism of generating a positive potential peak surrounding the toroidal plasma is considered to be due to the local mirror effect produced by the high β hot electrons trapped in the midplane, where cold electrons are scattered out more than ions. Therefore the potential is positive, several times of electron temperature against the container wall. The potential well edged by this potential peak plays cruicial role for the confinement of bumpy torus plasmas.

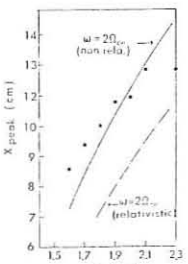

Fig.6. The radial position of the peak of the floating potential as a function of the toroidal magnetic field.

References

1) H. Iguchi, M. Hosokawa, T. Shoji, M. Fujiwara and H. Ikegami: IPP-Nagoya Research Report, IPPJ-385 (1979).
2) R. A. Dandl et al.: Oak Ridge National Lab. Report, ORNL-TM-4941 (1975).

A2.3

Stellarator Equilibrium and Stability Computations in Two and Three Dimensions

R. Chodura, F. Herrnegger, J. Neuhauser, A. Schlüter
Max-Planck-Institut für Plasmaphysik D-8046 Garching, Germany
EURATOM - Association

Abstract

The stability of straight, helically symmetric $\ell = 2$ equilibria with arbitrary longitudinal current is investigated using a 2-D code. The results are compared with those of a 3 D-code applied to the same problem. The 3D-code is used to study the effect of toroidal curvature on the stability of a $\ell = 2$ stellarator. As a further example an 3D-equilibrium with more than one magnetic axis is presented.

1. Introduction

The computation of magnetohydrodynamic toroidal stellarator equilibria is a 3-dimensional problem. Since recently numerical codes are available which are able to determine such equilibria iteratively and to assess their gross stability from the convergence properties of the result.

Due to the complexity of the problem and the restriction in grid size for 3D calculations, it is desirable to get a first estimate of growth rates by 2D calculations for a straight helically symmetric analog. Moreover, when running the 2D and 3D code on a 2D problem, the results from the 2D code can serve to test the reliability and resolution of the 3D code. In the following we give some results of 2D and 3D codes.

2. Helical-Symmetric Results

The 2D straight helically symmetric $\ell = 2$ equilibria are characterized by five parameters: $\beta = 2\, p_o/B^2_{zb}$ at the magnetic axis, the $\ell = 2$ distortion $\delta_2 = (\ell_y/\ell_x - 1)/(\ell_y/\ell_x + 1)$ of that magnetic surface where the pressure is decreased to the 1/e-fold value of the maximum pressure p_o (ℓ_y/ℓ_x is the axes ratio of that flux-surface contour), the compression ratio $\varkappa$, the periodicity number $h = 2\pi/L$, and the longitudinal net current J_{tot}. The mean plasma radius is denoted by a, the mean longitudinal magnetic field at the boundary by B_{zb}. The MHD equilibrium solutions are computed by using a modified version of Marder's helical-symmetric code /1/. The longitudinal current on each magnetic surface is assumed to be a given function $I_z(\psi)$ of the flux function ψ. In Fig. 1 a typical case of a helical $\ell = 2$ equilibrium is shown having no longitudinal net current. In case that a longitudinal current is superimposed such that the rotational transform of the current is added to the rotational transform of the stellarator field, an upper threshold for J_{tot} is found numerically beyond which the solution does not converge to an equilibrium with one magnetic axis (resonance phenomena). Changing the sign of the longitudinal net current, the ellipticity of the magnetic surfaces near the axis decreases.

The numerical stability calculations are carried out by using the stability code by Herrnegger and Schneider /2/. The time-dependent linearized MHD equations are solved as an initial-boundary-value problem. The code is described in Ref. 2 and has been updated to describe $\ell = 2$ configurations. The stability results of a straight helical $\ell = 2$ equilibrium are reported here where the rotational transform ι_p per period is $\iota_p \approx 0.1$, $\beta = 0.25$, $ha = 0.3$, $\varkappa = 2.2$, and negligible net current. We study $m = 2$ modes with an axial wave number k in the vicinity of the resonant value $|k_{res}| = m\, h\, \iota_p$. In our case $|k_{res}\, a| = 0.06$. In Fig. 2 the normalized eigenvalue $(\gamma/h v_A)^2$ is plotted versus the longitudinal wave number ka for different grids ($v_A^2 = B_{zb}^2/\rho_o$; ρ_o is the equilibrium density on axis). A quadratic extrapolation has been applied to get the growth rate for zero mesh size. The peak of the extrapolated curve is rather close to $|ka| = 0.06$ hence this mode is almost a flute mode.

3. Results by the 3D-code

The same problem as in Sec. 2 is treated with our 3D code /3/, i.e. the stability of an $m = 2$ mode in a straight helical $\ell = 2$ configuration. The modes being investigated have a fixed wavelength extending over 5 periods of the equilibrium. The total rotational transform $\iota = 5\,\iota_p$ is varied around the value 1/2 where the resonant interchange mode is expected to evolve. Fig. 3 shows the growth rates for various ι as obtained for different grids, i.e. $10^2 \times 50$, $12^2 \times 60$, $14^2 \times 70$ mesh points, respectively. As may be seen the grid dependence of the dispersion curve is rather strong, the maximum of the growth rate is shifted off the resonant point $\iota = 1/2$ to somewhat smaller values of ι.

Comparing the 2D and 3D results, we find only a factor of two difference in the extrapolated growth rates, though the equilibria are not identical and the boundary conditions are different. For about the same modes the surface current model predicts eigenvalues $(\gamma/h v_A)^2 = \beta(2-\beta)\,\delta_2^2 = 0.044$ for β on axis.

Bending the $\ell = 2$ helix into a torus and keeping the period length of the helix (and of the disturbance) fixed, the equilibrium is changed by the outward displacement of the plasma: a magnetic well with appreciable shear is formed. This leads to a change of the eigenmode (the outer vortex is much stronger than the inner one) and lowers the eigenvalues γ as compared to the straight case. If the aspect ratio A = R/a (R = mean torus radius) is below 30, the configuration is stable in a $14^2 \times 70$ grid; for A=60 γ^2 has about half the value of the corresponding straight case ($A = \infty$). Refining the grid size the same tendency for stability for m = 2 modes may be expected but for a smaller critical aspect ratio.

Since we use a space-fixed grid and not flux coordinates, the code is capable to find equilibria with more than one magnetic axis. Fig. 4 shows 3 cuts, a quarter of a wavelength apart, of flux surfaces for a so-called "double-star" configuration /4/. The aspect ratio is 16 with 16 periods along the torus. This configuration is achieved by superposition of an $\ell = 3$ stellarator with a quadrupole field. The maximum beta is 3%. The outward shift of the magnetic axes is very small as compared to that of a pure $\ell = 3$ stellarator.

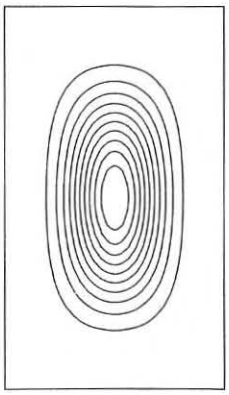

Fig. 1 Contour lines of p = constant surfaces of a straight helical $\ell = 2$ equilibrium: $\beta = 0.25$, $\delta_2 = 0.32$, $ha = 0.30$, $\varkappa = 2.2$, $J_{tot} \simeq 10^{-3}$

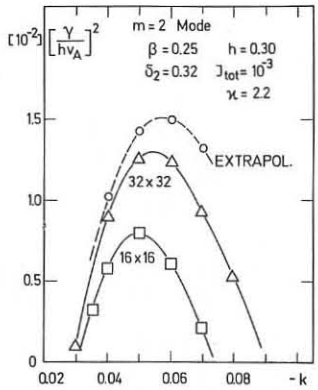

Fig. 2 Normalized eigenvalues $(\gamma/h v_A)^2$ for the equilibrium of Fig. 1 versus longitudinal wave number hk from the 2D code

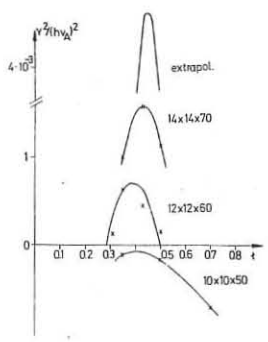

Fig. 3 The same eigenvalues as in Fig.2 versus rotational transform ι from the 3D code

Fig. 4 A configuration with 2 magnetic axes and a separatrix, A = 16, $\beta = 0.03$ (first line: initial condition second line: equilibrium)

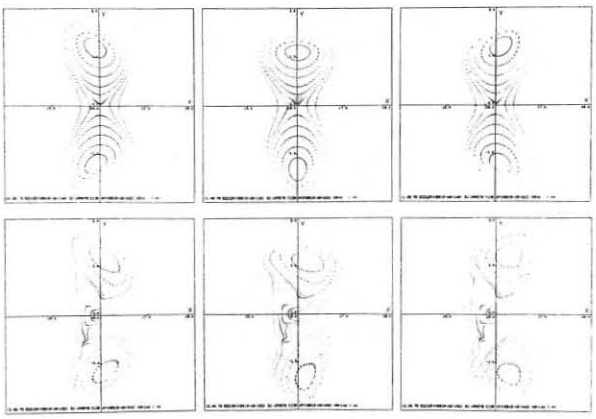

References

/1/ Marder, B., Phys. Fluids 19 (1976) 1395
/2/ Herrnegger, F., Schneider, W., Nucl. Fusion 16 (1976) 925
/3/ Chodura, R., M. Kaufmann, A. Schlüter, Proc. 7th Conf. on Plasma Physics and Contr. Nucl. Fusion Res., Innsbruck, 1978, Vol. 2, p. 335
/4/ Wang, T.S., Jensen, T.H., Nucl. Fusion 18 (1978) 1459

A2.4

PARTICLE AND ENERGY TRANSPORT IN THE W VII-A STELLARATOR

W VII-A Team[+], presented by H. Ringler
Max-Planck-Institut für Plasmaphysik
Association EURATOM-IPP
D-8046 Garching, F.R. Germany

Introduction: Results on plasma confinement of ohmically heated plasmas in the W VII-A stellarator have been reported at the Berchtesgaden [1], Prague [2], and Innsbruck [3] conferences. The energy confinement was shown to deteriorate above a critical current [2]. As a function of electron density the energy confinement time increases; above a critical density depending on plasma current the confinement time decreases again [3]. Radiation losses were found to be an important loss mechanism and closely connected with the limitation of the confinement time. There is however some indication that radiation losses are not the only cause for the deterioration of confinement.

Measurements of Particle and Energy Confinement: We will mainly concentrate here on measurements from a standard 20 kA helium discharge B_o = 3.5 T, external rotational transform ι_o=0.14 [3].

The global particle confinement time $\tau_p(a)$ was determined from the ionization rate which was measured using the 5015 Å HeI line [4]. Contributions of oxygen impurities (<1 %) to the production rate were neglected.

As a function of line density, $\int n_e dl$, the particle confinement time shows a behaviour similar to the global energy confinement time, $\tau_E'(a)$, as derived from the diamagnetic signal (Fig.1): an increase of $\tau_p(a)$ with $\int n_e dl$ followed by a strong decrease. The region of maximum confinement time is shifted to smaller densities by an increase of radiation loss due to small amounts of neon [3]. The decrease of the energy confinement time at high density is still seen if the radiation losses as measured by bolometers are taken into account in the definition of $\tau_E(a)$,

$$\tau_E(a) = \frac{3/2 \int_0^a (n_i k T_i + n_e k T_e) r dr}{\int_0^a (P_{OH} - P_{rad}) r dr}$$

(P_{OH} ohmic power density, P_{rad} radiated power density).

The similarity between particle and energy confinement raises the question whether there is another loss mechanism besides radiation.

Heat Conductivity and Diffusion Coefficient: We have derived local experimental values for the electron heat conductivity $\chi^e_{exp}(r) = \frac{\int_0^r (P_{OH}(r') - P_{rad}(r')) r' dr}{r\, n_e \frac{dT_e}{dr}}$ (contributions of charge exchange and diffusion are small) and the diffusion coefficient $D_{exp}(r) = \frac{\int_0^r (\text{production rate}) r' dr'}{r \frac{dn_e}{dr}}$, using measured profiles for the production rate, n_e, T_e, and the radiated power P_{rad}. In Fig. 2 $\chi^e_{exp}(r)$ and $D_{exp}(r)$ and the calculated neoclassical diffusion coefficient D_{NCl} are plotted as a function of radius for three typical line densities 2, 8, and 11 x 10^{14}cm^{-2}. For comparison the neoclassical values are shown to be 2 - 3 orders of magnitude smaller.

The important point however is that for 11 x 10^{14}cm^{-2} line density χ^e_{exp} and D_{exp} seem to increase again with density.

In Fig. 3 we have plotted in a n_e-T_e plane, curves with χ_{exp} = const. These data were taken outside the q=1 surface from 4 profiles of the 20 kA discharge with different densities and temperatures. In the low density regime the procedure yields the scaling $\chi_{exp} \sim \frac{1}{n_e T_e}$ verifying that the electron thermal conductivity χ^e_{exp} is a function of n_e and T_e only. Impurities such as neon change the electron temperature with the plasma current kept constant, but the data from He-discharges with small additions of neon confirm the assumption $\chi_{exp} = f(n_e, T_e)$ only in the low density regime. In the high density regime with decreasing confinement time these data no longer fit into the results of Fig.3. Therefore, in the high density regime we should consider additional parameters besides n_e and T_e to characterize the local thermal conductivity.

In Fig. 4 $\chi^e_{exp}\, n_e\sqrt{T_e}$ is plotted as a function of radius. Again it is evident that for higher line densities this $\frac{1}{n_e\sqrt{T_e}}$ scaling no longer applies. A thermal conductivity of the form $\chi^e \sim \frac{I}{Br^2} \frac{1}{n_e\sqrt{T_e}}$ was proposed by Guest et al. [5], but the $\frac{1}{r^2}$ dependence is in contradiction with the results above. There is some experimental evidence that χ^e scales with $\frac{I}{B}$ but the data base is too small to prove this dependence.

Discussion and Conclusion: A possible explanation for the deterioration of the confinement at high density is the increase of tearing modes especially of the (2,1) mode [3], and [6]. The strong increase of the MHD activity with increasing density coincides with the observed decrease of τ_p and τ_E and the departure from the $\chi_{exp} \sim \frac{1}{n_e T_e}$ scaling. The same correlation is observed in discharges with addition of impurities (neon), Fig.5. The increase of radiation modifies the temperature and the current profiles in turn. As shown in [6] this gives rise to an increase of the (2,1) mode amplitude. How resulting islands of 1-4 cm width affect in detail the plasma losses cannot be evaluated from the present measurements but according to theory an appreciable effect is expected [7]. At large external transform (ι_o > 0.17) no (2,1) modes are observed, but still there is a deterioration of confinement at large density. Whether stationary islands or the (3,2) mode, which was observed under these conditions, is responsible for the enhanced loss has not yet been investigated in detail.

References

[1] W VII-A Team, Proc.6th Conf.Berchtesgaden II, IAEA, Vienna (1977),81
[2] W VII-A Team, Proc.8th Europ.Conf. Prague 2 (1977), 73
[3] W VII-A Team, Proc.7th Conf. Innsbruck II, IAEA, Vienna (1979), 265
[4] E.Hinnov, H.W. Drawin, private communication
[5] G.D.Guest et al., GA-A 14831 report (1978)
[6] Paper by R. Jaenicke and W VII-A Team, this conference
[7] I.D. Callen, Phys.Rev.Lett. 39, 1540 (1977)

[+] See paper W. Initial Injection into the W VII-A Stellarator, W VII-A Team, Neutral Injection Group, these proceedings

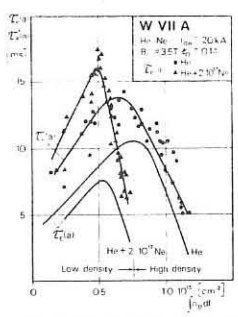

Fig.1: Global particle $\tau_p(a)$ and energy confinement time $\tau_E'(a)$ as a function of line density.

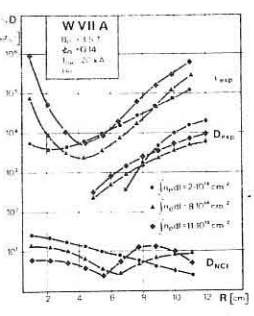

Fig.2: Experimental values for electron heat conductivity and diffusion coefficient vs. radius.

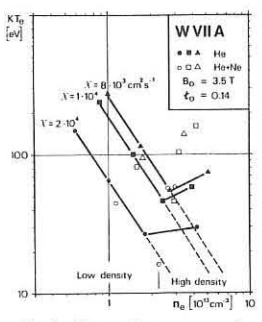

Fig.3: Curves for χ_e = const. plotted in a n_e-T_e plane. Circular, square, and triangular symbols refer to χ=2, 1, and 0.8 · 10^4 cm^2 s^{-1} respectively.

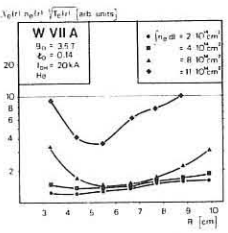

Fig.4: $\chi_e(r)\, n_e(r)\sqrt{T_e(r)}$ versus radius.

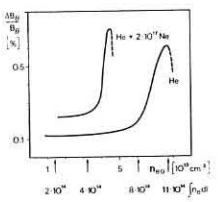

Fig.5: Relative amplitude of poloidal field fluctuations for the 2,1 mode vs. central electron density. A helium discharge is compared with a neon doped discharge.

A2.5

LOWER HYBRID HEATING IN THE WEGA-STELLERATOR

F.SÖLDNER (1), P.BROUQUET (2), M.DURVAUX (3), C.GORMEZANO (2), B.GREGORY (6), W.HESS (2), G.ICHTCHENKO (2), H.JAECKEL (1), B.JESSUP (2), R.MAGNE (2), M.MORESCO (5), T.-K. NGUYEN (2), G.PACHER (1), H.PACHER (1), H.W.PIEKAAR (4), W.R.RUTGERS (4), G.-F.TONON (2), J.-G.WEGROWE (1).

(1) ASS. EURATOM MAX-PLANCK-INSTITUT FUER PLASMAPHYSIK, GARCHING FED. REP. OF GERMANY

(2) ASS. EURATOM-CEA, GRENOBLE, FRANCE

(3) ASS. EURATOM-E.R.M., BRUSSELS, BELGIUM

(4) ASS. EURATOM-FOM, JUTPHAAS, NEDERLAND

(5) UNIVERSITY OF PADOUA, ITALY

(6) ON LEAVE OF I.N.R.S. ENERGY, QUEBEC, CANADA

ABSTRACT : By applying a Ti-getter, the density could be kept constant during LH-heating in stellarator and tokamak discharges. Modest electron and ion heating (by about 40%) was observed. Net-currentfree stellarator plasmas with mean densities up to $0.9.10^{13}$ cm^{-3} were produced by using the HF pulse alone. At 100 kW applied HF power the central plasma remained cold ($T_{io} \approx 9$ eV, $T_{eo} \approx 12$ eV), but a significant population of hot electrons was observed by soft X-rays.

EXPERIMENT : The WEGA device has been transformed from a tokamak into a stellarator by inserting a new shell with l=2, m=5 windings on it for the stellarator current. The experimental set-up is described elsewhere /1/. The particular features of the WEGA stellarator are the small aspect ratio and the "Θ-bridges " between the helical conductors. Tokamak and stellarator discharges are made for comparison with same ι_{tot} (a). Diagnostics used in addition to the existing equipment /2/ are microwave scattering at 2mm, space resolved ω_{ce}-measurements, microwave multichannel interferometry, bolometer measurements and space resolved measurements of the D_α-emission.

STELLARATOR CHARACTERISTICS : The stellarator was normally operated at B=14.4 kG, t_o=0.11 and I_{pl}= 25 kA resulting in ι_{tot} =0.26 (a_{eff} =13cm,R=72cm) and an ellipticity of the plasma b/a=0.7. The main plasma parameters for discharges with and without use of a Ti-getter are given in table 1. Under the non-optimal conditions of the torus wall, gettering reduces the impurity content of the plasma already considerably. Nonthermal ω_{ce}-emission has been studied extensively and a new parameter regime for runaway formation has been deduced /3/.

APPLICATION OF THE HF : The same HF system and the same coupling structure as in earlier tokamak experiments /2/ are used. The decay spectrum measured by probes in the shadow of the limiter shows a bump at about f_o-85 MHz in tokamak discharges. This may be interpreted as penetration of the pump wave into a region of higher density ($n_e \sim 10^{13} cm^{-3}$) required for the decay to modes with this frequency difference to the pump wave /4/, /5/. In the stellarator this bump does not appear. Instead the spectrum is dominated by harmonics of ω_{ci}. An interpretation of this spectrum, however, is difficult because the density between limiter radius and wall is at least an order of magnitude lower in stellarator discharges than in tokamak discharges and might be less than the cut-off density for the slow waves in this frequency range. Phase measurements by probes at the pump frequency of 500 MHz give $N_\perp$ -values only in the nonaccessible region $N_\perp \geq 1.-1.2$.

The main effects of lower hybrid heating at a level of 100 kW on both Stellarator and tokamak plasmas, respectively, were similar to the earlier tokamak results /2/. A strong increase of the electron density and of the loop voltage were observed, as well as electron and ion heating in the central plasma region.

Space resolved D_γ -measurements show a rapid increase of the emission near the plasma edge at the beginning of the HF pulse. No strong toroidal dependence was found for the amount of increased emission indicating that at least a part of the density produced by the HF can not be due to local production near the antenna.

For the purpose of reducing the density increase, a Ti-getter was mounted near the HF antenna. By gettering the torus walls during 6 min before every plasma shot (evaporation of 20 mg Ti), we finally succeded in keeping the density constant during the HF pulse up to the maximum applied power of 170 kW (fig.1). It was still necessary to reduce the flux of the gas injected during the HF, thereby dropping the density without HF to about 70% of its value with HF at the same time.

The D_γ -emission stays nearly constant during HF heating in gettered discharges. The loop voltage (fig.2) still increases slightly. Z_{eff} increases from 3 to about 6. In the limited time of operation with getter, optimisation of the heating was not possible. Present results show, at constant density a modest increase of the bulk temperatures ($\Delta T_{io} \sim$ 50eV, $\Delta T_{eo} \sim$150eV). On charge exchange measurements tangential to the main field, a high energy ion tail is observed in stellarator discharges during the HF. The mean energy of the tail ranges from 250 to 550 eV and increases proportionally to the density which is consistent with ions having a perpendicular energy of 1 keV (as observed in previous tokamak experiments) and scattered by small angle collisions into the observation cone. This cone in tangential observation is closer to the perpendicular in the stellarator than in the tokamak because of the helical mirrors.

HF PRODUCED STELLARATOR PLASMA : The HF pulse alone is used to produce and to heat the plasma in the stellarator. The time evolution of HF power and plasma parameters is shown in fig. 3. The reflection coefficient of HF decreases rapidly from initial 80% to 5%. Complete ionization of the filling gas at the optimal pressure of 3.10^{-4} torr is achieved at 8 ms when the line density saturates at $2.10^{14} cm^{-2}$. This is seen also from the D_α-signal which passes through a maximum at 4ms and reaches a constant level at 8 ms due to recycling. Radial profiles of D_α -emission show rather uniform volume emission during the initial phase and strongly peaked emission from the plasma edge during the later phase. The density profile is hollow with $\tilde{n}_e = 9.10^{12} cm^{-3}$, $n_{eo} = 6.10^{12}$ cm^{-3} (Thomson scattering) and $n_e \geq 10^{13}$ cm^{-3} (microwave interferometry) near the edge. The density corresponding to f_{pi}=500 MHz (transmitter frequency) is $1.1.10^{13} cm^{-3}$ the density corresponding to f_{LH}=500 MHz is $2.6.10^{13} cm^{-3}$. Similar results were obtained in other experiments /6/. The electron temperature measured by the Thomson scattering at the centre and determined from the rise times of the D_α ,OII and CIV lines remains low (fig.3e). Line integrated X-ray measurements as well as the apparition of OVII line emission indicate, however, an electron population with some hundred eV which are not found by Thomson scattering in the central plasma region (r<4 cm). The ion temperature determined from the Doppler broadening of the CIV line (λ = 1548 Å) falls to $T_i \approx 10$eV at $t \geq 6$ ms from the time when CIV appears. About 30 kW of 90 kW HF power incident are detected by the bolometer (assuming isotropic emission). The same ratio of power measured by the bolometer to total inident power (OH+HF) is found in tokamak and hybrid stellarator discharges during HF, whereas about 50% of the Ohmic power are detected without HF. During the density decay, the ion temperature stays constant until at least 5ms after the end of the HF when CIV disappears. This might indicate that convective ion energy loss is larger than heat conduction loss.

SUMMARY : A major problem of lower hybrid heating hitherto, the density increase during the HF pulse, could be overcome by means of Ti-gettering of the torus wall near the antenna. In stellarator discharges a high energy ion tail is observed during the HF in charge exchange measurements tangential to the toroidal main field. Net-currentfree stellarator plasmas (aside from a runaway current of several 100A) with densities of $10^{13} cm^{-3}$ were produced by application of the HF alone. At the low central electron temperatures, the HF power can easily be radiated, assuming a reasonable impurity concentration.

REFERENCES :

/1/ R.FRITSCH et al.,9th Soft, Garmisch-Partenkirchen, 287 (1976)

/2/ H.D.PACHER et al.,7th IAEA Conf. on Pl.Phys.,Innsbruck, Vol.I,p.97 (1978)

/3/ H.W.PIEKAAR, W.R.RUTGERS, internal report Jutphaas, to be published

/4/ M. PORKOLAB, Phys. Fluids 20, 2058 (1977)

/5/ S.PESIC, Heating in Toroidal Plasmas, Grenoble,Vol.I, p.161 (1978)

/6/ P.JAVEL et al., 7th Eur.Conf. on Contr.Fusion,Lausanne, Vol.I,p.147 (1975)

		without getter	with Ti-getter
I_{pl}	/kA /	25	25
t_i (a)		0.15	0.15
U_l	/V /	3.2	2.0
P_{oh}	/kW /	80	50
Z_{eff}		6.7	3
n_{eo}	/cm^{-3}/	$2.4\ 10^{13}$	$2.4\ 10^{13}$
$\bar{n}_e$	/cm^{-3}/	$1.2\ 10^{13}$	$1.15\ 10^{13}$
E_e	/J /	128	120
T_{eo}	/eV /	615	450
T_{io}	/eV /	130	125
τ_E^e	/ms /	1.6	2.4

Table 1 : Plasma parameters in Ohmically heated Stellarator discharges before application of the H.F.

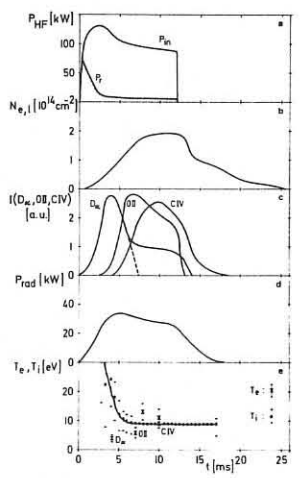

Fig.1 Time evolution of the line density in stellerator discharges with and without getter

Fig.2 Time evolution of the plasma resistance with and without getter

Fig.3 Time evolution of HF power and plasma parameters in HF produced stellarator plasma

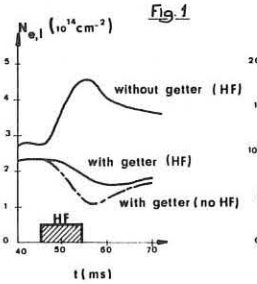

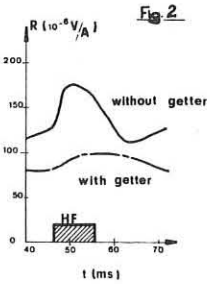

A2.6

CONFINEMENT OF LOW AND ZERO CURRENT PLASMAS IN THE CLEO STELLARATORS

D W Atkinson, J E Bradley, P J N Davison, A N Dellis, P C Johnson, S Kogoshi, D J Lees, P J Lomas, A C Selden, P A Shatford, I J Spalding, T Stamatakis, P R Thomas, A C Walker and S Ward.

Culham Laboratory, Abingdon, Oxon. OX14 3DB, U.K.
(Euratom/UKAEA Fusion Association)

1. INTRODUCTION

CLEO is a 7 field-period $\ell = 3$ stellarator with a 90 cm major radius, and a vacuum-vessel internal minor radius of 14 cm. The outermost magnetic surfaces are triangular giving a mean plasma radius of $\sim$ 10 cm. Previously reported work [1,2] has shown an increasing electron energy replacement time τ_{E_e} as the electron drift parameter $\xi \propto I_g/n_e T_e^{\frac{1}{2}}$ is decreased. The planned experimental programme on CLEO involves neutral injection and electron cyclotron heating of plasmas with no net toroidal gas current I_g. The present paper describes firstly a study of high-density low-current plasmas at $B_\phi = 18$ kG. These offer good confinement properties, with τ_{E_e} up to 10 ms, and should provide a good target plasma for neutral injection. Secondly, work on plasmas produced in the vacuum fields by laser irradiation of solid deuterium pellets is reported.

2. OHMICALLY HEATED PLASMA

In a well-gettered torus, discharges free from runaway electrons are obtained in hydrogen by limiting the gas current to $I_g/B_\phi < 0.4$ (kA/kG) for B_ϕ in the range 6-18 kG and breaking down to line-of-sight mean densities $\bar{n}_e$ of $0.7 - 1 \times 10^{13}$ cm^{-3} at $B_\phi = 18$ kG. With vacuum transforms at the limiter in the range 0.25 - 0.4, breakdown to higher I_g/B_ϕ produces loss of confinement due to the growth of a region of MHD instability at $q = 3$ near to the plasma edge.

Feedback control of $\bar{n}_e$ from the microwave density interferometer using a piezo-electric gas valve, enables reproducible constant-density plasmas to be produced at low values of $I_g < 8$ kA at $B_\phi = 18$ kG. The highest density produced up to the present time is $\bar{n}_e \sim 2 \times 10^{13}$ cm^{-3}, corresponding to an axial value of $n_{e_o} \sim 4 \times 10^{13}$ cm^{-3} with $T_{e_o} \sim 140$ eV. T_e and n_e radial profiles for this discharge are depicted in Fig.1; Thomson scattering was used for T_e and n_e and electron cyclotron emission (ECE) (Fabry-Perot) for T_e, the edge values being given by a Langmuir double-probe. The vacuum transform here was $\iota = 0.4$ (at the magnetic surface in contact with the limiter). The overall profile of $\iota(r)$ is shown in Fig.1. The rotational transform is monotonically increasing with radius, with $\iota < \frac{1}{3}$ at the centre. Also, the resistance anomaly $A_R \simeq 1$ for this discharge, with the fraction of the ohmic power ($P_{OH} \sim 12$-15 kW) detected by a thermopile (radiation + charge exchange neutrals) being less than 5%. The neutral density on axis is $n_o \sim 1$-2×10^8 cm^{-3} (H_α and neutral particle analyser measurements). $T_{io} \sim 125$ eV, indicating that a major fraction of the ohmic power is transferred to the ions. For this discharge $\tau_{E_e} \sim 5$ ms, as expected if neo-classical (plateau) ion thermal conduction is the principal ion energy loss mechanism.

The following effects on confinement are observed:

1. At constant $\bar{n}_e$, I_g, B_ϕ, increasing I_ℓ (the helical winding current) increases T_{e_o}, and reduces V_T (the loop volts). The increase of τ_{E_e} and reduction of ξ are consistent with drift parameter scaling.
2. At constant I_g, B_ϕ, I_ℓ, reducing $\bar{n}_e$ decreases τ_{E_e} and anomalous electron thermal conduction begins to dominate the power balance. Again this corresponds broadly to the drift parameter scaling.
3. At constant $\bar{n}_e$, B_ϕ, I_ℓ, increasing I_g initially depresses τ_{E_e} at a rate much faster than drift parameter scaling. For $B_\phi = 18$ kG, at $I_g \sim 9$-10 kA sawtooth oscillations of n_e and T_e are observed; for the $\bar{n}_e \sim 2 \times 10^{13}$ case, ECE gives $\Delta T_e/T_e \sim 0.2$ - 0.3 at $r = 0$. We associate this with a broad region where $q \simeq 3$ stretching from near $r = 0$ to $r \sim 4$-5 cm (as observed by inversion of soft x-ray sawtooth signals). A similar result is obtained at $\bar{n}_e \sim 1 \times 10^{13}$ cm^{-3}, but with $\Delta T_e/T_e \sim 0.05$ - 0.1 at $r = 0$. The sawtooth relaxations are $m = 0$, $n = 0$ (bulk redistribution of n_e and T_e). There is evidence of a rotating pre-cursor mode, observed on magnetic probes, whose mode number is consistent with $m = 3$, $n = 1$. It is possible to break through this regime by a rapid increase of I_g, with the result that τ_{E_e} again improves, with $3 > q > 2$ at $r = 0$. The overall trend thus follows drift parameter scaling although clearly the MHD effects described produce a detailed deviation from this pattern.

3. CURRENTLESS PLASMAS

1) Afterglow plasmas have been produced for B_ϕ in the range 13-18 kG by terminating the plasma current after 10 ms. The time constant for n_e to decrease is 5-20 ms, the electron temperature falling from 50 eV to $\sim$ 15 eV in about 5 ms. Hydrogen light measurements indicate a neutral density in the range 10^8 - 10^9 cm^{-3}.

2) Plasmas were created by focusing a CO_2 laser, with pulses of 1.5 μs duration with > 1 kJ energy, on to freely falling solid deuterium pellets containing (3-7) × 10^{18} atoms. Preliminary experiments [3] showed absorption of (65 ± 15)% of this energy, generation of 100-2000 eV ions, and possibly complete ionization of the pellet. The trapping of this plasma within CLEO has been found to increase with increasing rotational transform (see Fig.2) to $\sim$ 50% of the pellet if one assumes toroidal uniformity and a nearly flat radial profile. This contrasts with the WIIb results [4]. The risetime to half peak density at a point 165° round the torus from the generation site is $\sim$ 5-10 μs at $B_\phi = 13$ kG and $\iota = 0.6$, which corresponds to the time-of-flight for ion energies of $\sim$ 600 eV and a total energy of order 100 - 140 J.

Fig.3 shows the rather short confinement times observed. The initial density decay (allowing for ionization rates) indicates a particle confinement time of $\sim$ 0.25 ms, and at later times this increases to 1.4 ± 0.4 ms, contrasting with the predicted Pfirsch-Schlüter value of $\sim$ 1 s. The rapid decay of T_e is consistent with a measured neutral density of $\sim 10^{11}$ cm^{-3}, causing charge exchange of most of the energetic ions. Possible neutral production mechanisms are incomplete ionization of the pellet, wall heating by scattering of laser light from the pellet and wall interaction with energetic particles, (the neutrals were localized near the laser-pellet interaction point). Charge exchange losses could be reduced by trapping higher density plasmas.

4. REFERENCES

(1) D W Atkinson et al., Eighth European Conf. on Controlled Fusion and Plasma Physics, Vol. II, Prague (1977), p.93.

(2) D W Atkinson et al., in: Plasma Physics and Controlled Nuclear Fusion Research 1978 (Innsbruck Conf. CN/37 H-1), Vol.II, IAEA, Vienna (1979), p.251.

(3) A C Walker, S Kogoshi, S Stamatakis and I J Spalding, Opt. Commun. 27, 247 (1978).

(4) H Baumhacker et al., Eighth European Conf. on Controlled Fusion and Plasma Physics, Vol.I, Prague (1977), p.133.

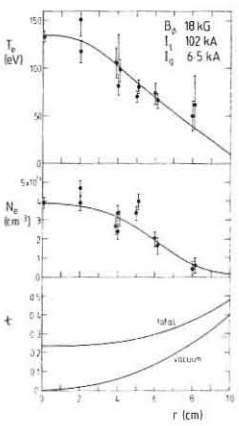

Fig.1

Thomson scattering data only. Points at r = 0 accumulated for 7 shots.

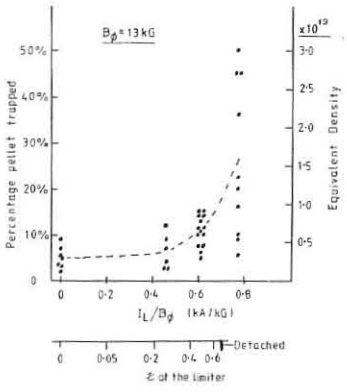

Fig.2

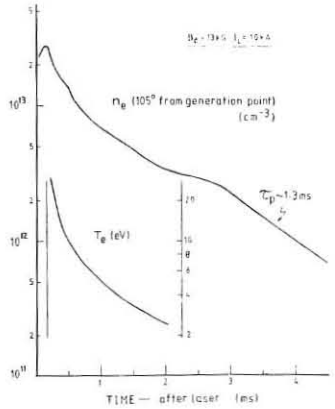

Fig.3

A2.7

THE QUASI-NEOCLASSICAL LAW OF PLASMA LOSSES IN A STELLARATOR

Yu.V.Gutarev, V.A.Suprunenko

The Kharkov Physical-Technical Institute, Acad.Sci.Ukr.SSR
Kharkov, USSR

Investigations of plasma confinement in stellarators with ohmic heating in the region of intermediate collision frequencies (a plateau) showed that anomalously high losses both of particles and energy from a plasma electron component were observed. The study of the ohmical plasma confinement according to various parameters was performed in greatest details on the stellarators URAGAN-1 and URAGAN-2. These experiments showed that the dependence of particle lifetime on electron temperature, confining magnetic field strength, and rotational transform was similar to the neoclassical one for the plateau at confinement of the nonohmic plasma ($\tau_n \sim \frac{H^2 \cdot \ell_\xi^2}{T_e^{3/2}}$), however, in the absolute value it has more than one order less value /1/. In this case the anomality greatly depended on plasma density. This allowed to introduce in the given discussion the quasi-neoclassical formula for the plasma diffusion coefficient in stellarators:

$$D_{exp} = \zeta \cdot D^0_{plateau}, \text{ where}$$

$$D^0_{pl.} = \frac{\sqrt{\pi}}{4} \cdot \frac{R_{Le}^2}{R} \frac{\nu_{Te}}{\ell_\xi^2} \left[1 + (\ell_\xi \frac{a}{R} N)^2 \frac{\ell}{\ell_{-1}}\right] \left[\left(1 + \frac{T_i}{T_e}\right)\frac{n'}{n} + 1.5\frac{T_e'}{T_e} + 1.5\frac{T_i'}{T_i}\right] \cdot \frac{n}{n'} \quad (1)$$

is the diffusion coefficient of nonohmic plasma in stellarators in the plateau region /2/. Here N is the number of magnetic field periods on a by-pass, other notations are universally adopted.

In experiments on the stellarators CLEO and WENDELSTEIN VII-A it was shown that the coefficient in formula (1) was increasing linearly with the growth of the so-called drift parameter ($\frac{U}{\nu_{Te}}$ - the ratio between current drift velocity and thermal velocity of electrons)/3,4/. At the same time, in experiments on the stellarator URAGAN-1 on the confinement of nonohmic plasma produced at the ion cyclotron heating ($T_e \ll T_i \leq 600$ ev) a good numerical and functional agreement with the neoclassical value was observed/5/. A similar result with a cold plasma at ($T_i < T_e \approx 10$ ev) was obtained in the stellarator SATURN, if a shear value exceeded some critical value of ($\theta > 0.05$)/6/.

These results allow to write down a coefficient value in the quasi-neoclassical formula as $\zeta = 1 + \chi\left(\frac{U}{\nu_{Te}}\right)$.

Some considerations about the function $\chi\left(\frac{U}{\nu_{Te}}\right)$ could be gained from paper/7/ in which the plasma turbulent diffusion due to current-drift instability is treated. This kind of instability is excited at a rather high value of a drift parameter when $\frac{U}{\nu_{Te}} > \theta$. It is probably possible to expect that the existence in ohmic discharges of resistive MGD-modes of a restricted amplitude(observed by various methods in all experiments) will result in alleviation of conditions for current-drift instability excitation. Taking into consideration the foregoing and paper/7/, it is possible to write down the following semiempirical expression;

$$\zeta = 1 + 0{,}23 \frac{R^2}{a^2}\left(\frac{M_i}{m_e}\right)^{1/2} \cdot \left(\frac{U}{\nu_{Te}}\right)^{3/2} \quad (2)$$

At rather high values of drift parameter and aspect ratio the unity in formula (2) can be neglected.

At a rather high electron temperature and relatively low density, when it is possible to neglect energy losses from a plasma electron component at the expense of radiation and ion heating, one can believe that thermal losses from an ohmic discharge will be determined mainly by the losses due to particle diffusion/8/.

Therefore, thermal losses can be probably also described by the quasi-neoclassical formula ($\chi^e \approx 5/2\ D_{exp}$).

Figs 1,2 and 3 show in their graphs the values of plasma energetic lifetime obtained in various experiments/3,4/. The heavy line conforms to calculations according to the quasi-neoclassical formula. The calculations were made in neglecting radiation losses and ion heating.

The maximum electron temperature at the ohmic heating obtained under the assumption that $\zeta_\Sigma = \zeta_{cur} + \zeta_n = 1$, can be easily derived from (1) and (2) and given in the form convenient for comparison with the data of paper/3/:

$$T_{emax} = 0{,}82 \cdot 10^{-3} \frac{a^{3/3} H^{3/26} n^{2/3} R^{1/26}}{Z^{1/26} \cdot (1-\ell_n)^{2/26} [1 + (2\pi \frac{a}{R} N)^2]^{6/13}} \sqrt{Z_{eff}} \sigma \frac{H}{R(1-\ell_n)} \quad (3)$$

In this formula the coefficient in front of the root depends rather slightly on parameters, and for experimental conditions in the stellarator WENDELSTEIN VII-A it varies from 3.1 to 3.6, while the measurements offer the value 2.9/9/.

In fig.4 the values of $T_e max$ derived from formula (3) are plotted with the solid curve. Experimental points for stellarators and tokamaks were collected by the authors of paper/9/. Somewhat overestimated values of $T_e max$ derived from the quasi-neoclassical formula are probably associated with the above-mentioned simplifications in calculations which can be easily refined at the expense of the loss in illustrativeness for the sake of numerical calculations.

Thus, the semiempirical, quasi-neoclassical formula derived on the basis of the analysis of experimental results on stellarators describes adequately a rather extensive class of results on the confinement of ohmically heated plasma both in stellarators and tokamaks.

REFERENCES

1. Dikij A.G. et al. Plasma Phys. and Contr. Nucl. Fusion Res. VII, P.45, 1 9 7 4, I A E A, Vienna (1975).
2. Stringer T.E. Plasma Phys., 14, I063 (1972). Galeev A., Sagdeev R., Zh.Eksper.i Teor.Fiz.(USSR), 26, 233 (1968).
3. Atkinson et al. 7-th Conf. on Plasma Phys. and Contr. Fusion. Innsbruck, Paper CN 37/111 (1978).
4. W VII A Team. Ibid, Paper CN 37/112.
5. Dikij A.G. et al. Plasma Phys., 18, 577 (1976).
6. Voitsenya V.S. et al. Nuclear Fusion, 17, 651 (1977).
7. Kadomtsev B.B., Pogutse O.P. Rev. of Plasma Phys., 5, London (1966).
8. Suprunenko V.A. Intern. Symp. on "Heating in Toroidal Plasma", Grenoble, July, 3-3 (1978).
9. W VII A Team. I P P, 2/241, November (1978).

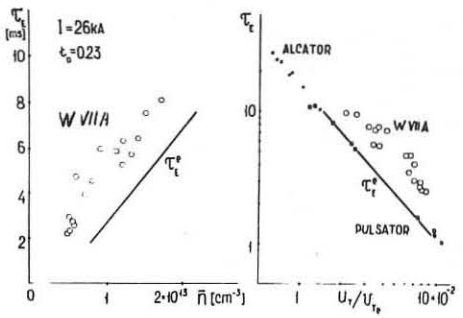

Fig. 1.

Fig.2.

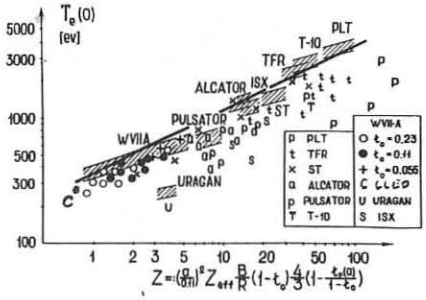

Fig.4.

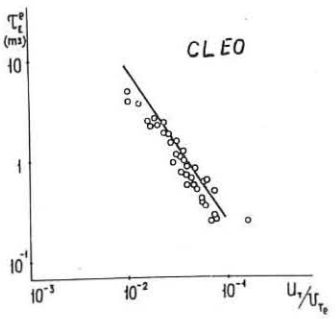

A3.1

Ideal and Resistive Ballooning Modes in Axisymmetric Toroidal Plasmas*

A. H. Glasser, M. S. Chance, and R. L. Dewar
Plasma Physics Laboratory, Princeton University
Princeton, New Jersey 08544 USA

A theory of ideal and resistive MHD ballooning modes with large toroidal mode number n in sheared, axisymmetric, toroidal plasmas has been developed recently.[1] Here we present some new developments in this theory. The poloidal structure of ideal ballooning modes and the role of the continous spectrum are clarified by an application of Floquet theory to the large-θ behavior of the solutions. The radial mode structure is treated by a new numerical code, together with an analytical treatment of the radial boundary conditions which takes account of the more exotic topologies which these modes can exhibit. The effects of resistivity are treated by two numerical codes which solve the full resistive ballooning equations, on one hand, and the equations for the matched asymptotic expansions of the ideal and resistive regions, on the other, and the results of the two methods are compared. The notation of Ref. 1 is used throughout this paper.

Ideal ballooning modes are described in terms of the displacement vector $\vec{\xi} = \vec{B} \times \vec{\nabla}\phi/B^2 + \vec{B}\partial\nu/\partial\theta$, where the parallel and perpendicular stream functions ϕ and ν are expanded in the ballooning representation,[1]

$$\phi = \sum_{\ell=-\infty}^{\infty} \sum_{k} a(V,k)\,\hat{\phi}(V,\theta - \ell,k)\exp[-2\pi n i(\beta + \ell q + \int kq'dV)] \qquad (1)$$

to satisfy toroidal periodicity in the presence of shear. The equations for $\hat{\phi}$ and $\hat{\nu}$ can be written in matrix form,

$$\partial\vec{y}/\partial\theta = \overleftrightarrow{H}\cdot\vec{y}, \qquad (2)$$

where $\vec{y}$ is a 4-vector with components $y_1 = \hat{\phi}$, $y_2 = \hat{\nu}$, $y_3 = (\chi'^2/B^2)\times(\vec{\nabla}\beta + kq'\vec{\nabla}V)^2\,\partial\hat{\phi}/\partial\theta$, $y_4 = [B^2\gamma P/(B^2+\gamma P)][\chi'\partial\hat{\nu}/\partial\theta - 2(\kappa_w + kq'\kappa_s)\hat{\phi}]$, and $\overleftrightarrow{H}$ is a 4 × 4 matrix with $H_{13} = B^2/[\chi'^2(\vec{\nabla}\beta + kq'\vec{\nabla}V)^2]$, $H_{21} = -H_{34} = 2(\kappa_w + kq'\kappa_s)/\chi'$, $H_{24} = (B^2+\gamma P)/(\chi'^2B^2\gamma P)$, $H_{31} = -\rho\omega^2(\vec{\nabla}\beta + kq'\vec{\nabla}V)^2/B^2 - 2P'(\kappa_w + kq'\kappa_s)/\chi'$, $H_{42} = -\rho\omega^2B^2$, and all other components of $\overleftrightarrow{H}$ vanish. The components of $\overleftrightarrow{H}$ contain secular functions of θ.

To study the behavior at large θ, we seek a power series solution of the form

$$y_i(\theta) = \theta^{\lambda_i}\sum_{p=0}^{\infty} y_i^{(p)}(\theta)\,\theta^{-p}, \qquad (3)$$

with $\lambda \equiv \lambda_2 = \lambda_4$, $\lambda_1 = \lambda - 1$, $\lambda_3 = \lambda + 1$. Then the lowest-order terms satisfy the equation $\partial\vec{y}^{(0)}/\partial\theta = \overleftrightarrow{H}^{(0)}\cdot\vec{y}^{(0)}$, where $H_{13}^{(0)} = B^2/(\chi'^2q'^2|\vec{\nabla}V|^2)$, $H_{21}^{(0)} = -H_{34}^{(0)} = -2q'\kappa_s/\chi'$, $H_{24}^{(0)} = (B^2+\gamma P)/(\chi'^2B^2\gamma P)$, $H_{31}^{(0)} = -\rho\omega^2q'^2|\vec{\nabla}V|^2/B^2$, $H_{42}^{(0)} = -\rho\omega^2B^2$, and all other components of $\overleftrightarrow{H}^{(0)}$ vanish. The propagator $\overleftrightarrow{U}(\theta)$, defined as a 4 × 4 matrix such that $\vec{y}^{(0)}(\theta) = \overleftrightarrow{U}(\theta)\cdot\vec{y}^{(0)}(0)$, satisfies the equations

$$\partial\overleftrightarrow{U}/\partial\theta = \overleftrightarrow{H}^{(0)}\cdot\overleftrightarrow{U}, \quad \overleftrightarrow{U}(0) = \overleftrightarrow{I}, \qquad (4)$$

with $\overleftrightarrow{I}$ the identity matrix. Since $\overleftrightarrow{H}^{(0)}$ is periodic, the solution can be expanded in exponentially varying eigenfunctions[2] such that $\vec{y}^{j}(\theta+1) = e^{\alpha_j}\vec{y}^{j}(\theta)$. The characteristic exponents α_j are the roots of the equation

$$\mathrm{Det}[\overleftrightarrow{U}(1) - e^{\alpha}\overleftrightarrow{I}] = 0. \qquad (5)$$

Since $\overleftrightarrow{H}^{(0)}$ is Hamiltonian, $\overleftrightarrow{U}$ is symplectic,[2] and from this it follows that if α is a root, so is $-\alpha$. Since $\overleftrightarrow{H}^{(0)}$ is real, if α is a root, so is α^*. The roots thus form pairs $\pm\alpha$ if α^2 is real, or quadruplets $\pm\alpha, \pm\alpha^*$ if not. If all $\mathrm{Re}\,\alpha \neq 0$, there are two growing solutions as $\theta \to \infty$ and two as $\theta \to -\infty$. Elimination of these solutions provides boundary conditions to determine a discrete number of eigenvalues for the radial wave number $k(V,\omega^2)$, representing the discrete spectrum. If $\mathrm{Re}\,\alpha = 0$ for one or both pairs, there is a 2- or 4-dimensional continuum of divergent solutions, the continuous spectrum. Krein's theorem[2] implies that transitions between these cases can occur only at values of V and ω^2 for which two roots of α are equal Numerical studies show that, for an equilibrium with no zeroth-order flows, all α's are real for $\omega^2 < 0$. For $\omega^2 > 0$, Figure 1 shows a map of a portion of the real $\omega\tau_A$ axis for a typical surface V, with II denoting both pairs imaginary, IR denoting one pair real and one imaginary, RR both real, and C a complex quadruplet.

When all $\mathrm{Re}\,\alpha \neq 0$, we can thus define a multi-valued function $k(V,\omega^2)$, or equivalently a function $\lambda(V,k)$ such that $\lambda(V,k) = \omega^2$ represents a global mode. Figure 2 shows contours of constant λ in the q(V) - Re k plane for a typical equilibrium. Since the eigenfunctions are invariant when $k \to k + 1$, the figure is periodic in k. There are o-points where λ has a minimum, representing the most unstable mode, and X-points on a separatrix, where λ has a saddle point. The propagating region, where k is real, is simply connected inside the separatrix. Outside the separatrix, two propagating regions are separated by an evanescent region through which tunneling occurs.

Different radial mode structures result from the different topologies of the contours in Fig. 2. For the small, closed curves near an o-point V_0, k_0, expansion in powers of $n^{-1/2}$ yields a Weber equation for the slowly varying amplitude a(V). Radial boundary conditions requiring evanescence as $|V - V_0| \to \infty$ then yield the eigenvalue condition[1]

$$\omega^2 = \lambda(V_0,k_0) + \frac{N + (1/2)}{2\pi nq'}\left(\frac{\partial^2\lambda}{\partial k^2}\frac{\partial^2\lambda}{\partial V^2}\right)^{1/2}\Bigg|_{V_0,k_0}$$

with stabilizing n^{-1} corrections. For the larger closed contours inside the separatrix, an expansion in powers of n^{-1} away from single turning points, where $\partial\lambda/\partial k = 0$, $\partial\lambda/\partial V \neq 0$, is matched to expansion in powers of $n^{-1/3}$ about a turning point which yields Airy's equation, to give solutions which evanesce beyond the turning points, and the eigenmode condition[1]

$$\oint kq'dV = (N + \tfrac{1}{2})/n. \qquad (7)$$

This condition quantizes the area inside a closed contour and reduces to Eq. (6) for small N. A similar treatment for a contour far to the left of the sparatrix, neglecting tunneling, yields the condition

$$\int_{V_L}^{V_<} (1 + k_- - k_+)\,q'dV + q_L = N/n, \qquad (8)$$

which quantizes the area to the left of one cycle of the contour. A similar result holds on the right of the separatrix. Finally, tunneling can be treated by matching across the X-point region, where an expansion in powers of $n^{-1/2}$ yields parabolic cylinder functions, and evanescence to the left and right of the two propagating regions yields the eigenvalue condition

$$R_LR_R - (1 + e^{-2\pi\mu})^{1/2}(R_L + R_R) + 1 = 0, \qquad (9)$$

where

$$R_L \equiv \exp\{2\pi ni[\int_{V_L}^{V_<}(1 + k_- - k_+)q'dV + q_L] + i\psi\},$$

$$R_R \equiv \exp\{-2\pi ni[\int_{V_>}^{V_R}(1 + k_- - k_+)q'dV - q_R] - i\psi\},$$

$$\psi \equiv \arg\Gamma(\tfrac{1}{2} + i\mu) - \mu(\ell n|\mu| - 1),$$

$$\mu \equiv 2\pi n\left(-\frac{\partial^2\lambda}{\partial k^2}\frac{\partial^2\lambda}{\partial V^2}\right)^{1/2}\Bigg|_{V_x,k_x}[\omega^2 - \lambda(V_x, k_x)].$$

Equation (9) reduces to Eq. (8) as $\mu \to \infty$ and to Eq. (7) as $\mu \to -\infty$.

Numerical solution of Eqs. (13)-(15) of Ref. 1 governing resistive ballooning modes yields a large variety of different modes. Figure 3 shows eigenvalue curves in the complex $\omega\tau_A$ plane on the same surface as that used for Fig. 1, with arrows denoting increasing values of the small, dimensionless resistivity parameter $\varepsilon \equiv n^{-2}\tau_A/\tau_R$, where τ_A and τ_R the Alfvén transit and resistive skin times. As $\varepsilon \to 0$, these curves converge on the transition lines between the different regions of Fig. 1, where two values of α are equal and the large-θ limit of the ideal modes becomes degenerate. The mode which converges on $\omega\tau_A = 0$ as $\varepsilon^{1/3}$ corresponds to the mode treated in Ref. 1 by matched asymptotic expansions of the small-θ ideal region and the large-θ resistive region. Matching of numerical solutions of these two regions gives excellent agreement with results obtained by solving the full equations, while taking 10-100 times less computer time. A comparsion of the two methods is shown in Fig. 4. Similar matched asymptotic expansions should clarify the behavior of the other modes in Fig. 3, which approach their limit frequencies as $\varepsilon^{1/2}$.

*This work was supported by the United States Department of Energy Contract No. EY-76-02-C-3073.

[1] M. S. Chance, et al., in Plasma Physics and Controlled Nuclear Fusion Research (Proc. 2nd Int. Conf., Innsbruck, 1978) IAEA-CN-37-P-2.

[2] V. A. Yakubovich and V. M. Starzhinskii, Linear Differential Equations with Periodic Coefficients (New York, John Wiley and Sons, 1975).

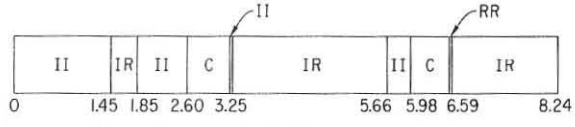

Fig. 1 Regions of the real $\omega\tau_A$ (× 100) axis.

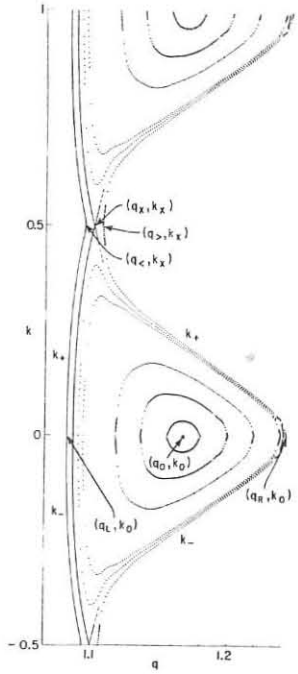

Fig. 2 Contours of constant λ in the q-Re k plane.

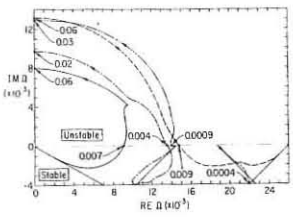

Fig. 3 Eigenvalues in the complex $\Omega \equiv \omega\tau_A$ plane. Arrows denote increasing values of $\varepsilon \equiv n\tau_A/\tau_R$. Numbers denote values of ε. Same surface as Fig. 1.

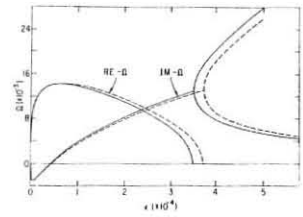

Fig. 4 Comparison of the real and imaginary parts of Ω vs. ε obtained from the fully resistive code (solid) and the matched asymptotic expansion (dashed). Different surface from Figs. 1 and 3.

A3.3

Beta Limits for Tokamak Experiments

W. Kerner, K. Lackner
Max-Planck-Institut für Plasmaphysik, EURATOM-Assoc.
8046 Garching, FRG
R. Gruber, F. Troyon
CRPP-EPFL, Lausanne, Switzerland

Abstract: Numerical MHD stability calculations are performed for tokamak configurations with circular and D shaped cross-sections and parabolic and exponential type current profiles. For relatively flat profiles and β_p values less than A/3 configurations are found which, for an aspect ratio A=2.4 are stable against both low n (n=1,2,3) free surface and high n bollooning modes for average β_t values of about 3% for a circular and 5% for a JET-type cross-section.

Introduction: Extensive numerical investigations using the Garching equilibrium and the Lausanne stability code /1/ have been carried out to determine the maximum β_t-values for tokamak devices compatible with stability against ideal MHD modes.
The motivation of this study is to investigate whether β_t values high enough to allow ignition in planned experiments could be reached with pressure and current profiles close to those of operating tokamaks.
The configurations of interest have circular and JET-like cross-sections and different aspect ratios. Wall stabilization of free surface modes is not assumed, as future expected discharge times will largely exceed the field penetration time through practicable copper shells. The investigation includes perturbations with low toroidal wave numbers n=0,1,2,3 and also high mode number ballooning modes.
The considered equilibria correspond to two different families of pressure and current profiles. The parameters β_t and β_p used to measure the performance of different cases are defined as

$$\beta_t = 2\mu_0 \int p\,dr \Big/ \int B_t^2\,dr \qquad \beta_p = 8\pi \int p\,df \Big/ (\mu_0 I_p^2)$$

Stability: In reference /1/ it had been shown that trying to increase the achievable β_t by flattening the current around the magnetic axis led to the appearance of unstable external kink modes while improving the stability against internal modes. Current distributions are looked for in this paper giving an optimum compromise between these counteracting tendencies.
The first set of equilibria discussed here is characterized by pressure and poloidal current profiles of the type

$$p',\ TT' \sim (\psi - \psi_{limiter})^{\alpha} \qquad (1)$$

with values of α in the range $0.3 \lesssim \alpha \lesssim 1.0$.
Profiles with $\alpha = 1$ yield a very low β_t value ($\approx 1\%$ for A=2.4), which can be increased by decreasing α to flatten the current profile. A minimum value of $\alpha \approx 0.8$ for a circular cross-section is required however as a necessary condition for stability against external kink modes. In the large aspect ratio case this limiting profile gives a ratio of q(limiter)/q(axis) = 2. Optimum β_t values are obtained if β_p is about or less than A/2, leading to $\beta_t \sim 1/A$ and also for $\alpha = 0.8$ - still rather small absolute values ($\beta_t \lesssim 2.1\%$ for A=2.4). For JET-like configurations, stability against non-axisymmetric modes requires only $\alpha \gtrsim 0.6$. resulting in a maximum $\beta_t \lesssim 4.2\%$ for A=2.4.
Considerably larger stable β_t values can be realized by chosing the profiles as proposed in /2/:

$$p' \sim exp\left[-(1-\psi/\psi_{limiter})^{\gamma_{p'}}\right],\quad TT' \sim exp\left[-(1-\psi/\psi_{limiter})^{\gamma_{tt'}}\right] \qquad (2)$$

Profiles of this type, which compared to the previous class contain a flattened region around the magnetic axis, could be thought of being created from more peaked, centrally unstable ones by the action of those localized instabilities themselves. Favourable stability of these cases with respect to external kink modes with n=1 requires for the range of aspect ratios considered ($1.8 \lesssim A \lesssim 4$) $\beta_p < 1$. For an aspect ratio of 2.4 the most favourable cases correspond to $\beta_p \approx 0.5$ and $\gamma_{p'} = \gamma_{tt'} = 4$. Figure 1 shows the eigenvalues (normalized by the Alfven time) of an unstable mode versus q on axis for a circular cross-section with A=2.4 and various β_p-values. For small β_p (0.25 and 0.5) the stability limit is given by values of the safety factor on the boundary $q_s \gtrsim 2$. For the flat q profiles this requires q value considerably above 1. At large β_p values ($\gtrsim 1$) the kink mode remains unstable even for q_s values $\gtrsim 1.7$ corresponding to $q_s > 5$. Increasing the size of the central, flat current density region by increasing the γ-values has a similar, destabilizing effect for external kink modes.
Although the favourable β_p values are less than unity, the kink limit allows high β_t as can be seen from Fig.2. Higher values of β_p result for a given value of γ in a steeper current density gradient on the torus outside which seems to have a destabilizing effect. For A=2.4, this kink stability limit corresponds to $\beta_t \cdot A \approx 9\%$. The results for different aspect ratios A=1.8,2.4 and 4 moreover show this maximum value of $\beta_t \cdot A$ to increase with decreasing aspect ratio, and to occur at progressively larger β_p/A. Stability against n=2,3 and 4 free surface modes has also been examined for these equilibria, showing them less restrictive than the n=1 mode. Ballooning modes however can be a more severe restriction of $\beta_t \cdot A$ values, as can be also seen from Fig.2.

The dependences of $\beta_t \cdot A$ and of the value of β_p/A for which the maximum value of β_t can be realized on the inverse aspect ratio are given in Fig.3 for both kink and ballooning modes. As also axisymmetric modes are stable for circular cross-section in this range of β_p-values, completely MHD stable equilibria with $\beta_t \cdot A$ between 6 and 8% have thus been found.
For JET-type cross-sections a qualitatively similar stability behaviour can be found. Figure 4 shows the beta limits for kink and ballooning modes for A=2.4 in dependence of β_p for different γ-values. The optimum kink limit agrees well with that quoted in Ref. /2/ with β_t up to 7%. The ballooning mode limit is found to be more restrictive. Axisymmetric modes with n=0 are strongly instable and require wall or feedback stabilization. Provided for that, $\beta_t \cdot A$ values of about 10 - 13% could be ideal MHD stable for this class of profiles.

References:

/1/ Gruber,R.; Schreiber,F.; Troyon, F.; Kerner,W.; Lackner,K.; Plasma Physics and Controlled Nuclear Fusion Research (Proc. 7th Int. Conf. Innsbruck, 1978) IAEA-CN-37/K2

/2/ Moore,R.W.; Dobrott,D.; Helton,F.J.; Bernard,L.C. Bull. Am. Phys. Soc. 23, 871 (1978)

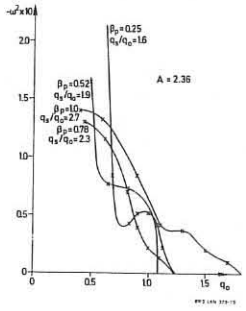

Fig.1 Normalized eigenvalues vs. q at axis for n=1 free boundary mode and circular plasma cross-section

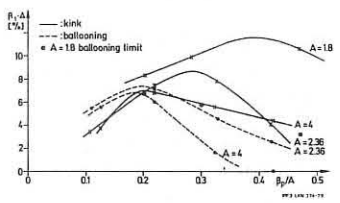

Fig.2 Stability limits on β_t for circular cross-section and $\gamma_{p'} = \gamma_{tt'} = 4$

Fig.3 β_t-limits and corresponding optimum β_p values vs. inverse aspect ratio for circular cross-section

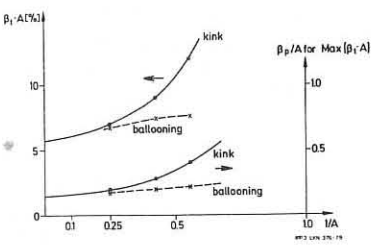

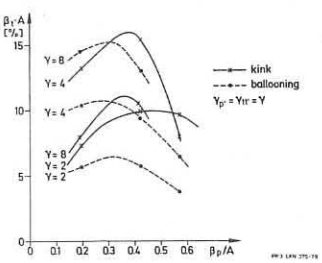

Fig.4 β_t-limits for JET geometry (D-shape, b/a=1.6, A=2.36) for different γ-values as a function of β_p

A3.4

STABILITY OF TWO DIMENSIONAL DRIFT WAVES
IN A LARGE ASPECT RATIO TOKAMAK

J.W. Connor, R.J. Hastie, K.W. Hesketh and J.B. Taylor
Culham Laboratory, Abingdon, Oxon, OX14 3DB, UK
(Euratom/UKAEA Fusion Association)

1. Introduction

In slab geometry with magnetic shear the drift-universal mode is always stable. However new effects arising in toroidal geometry may significantly alter the stability of such modes. For a model without Landau resonances or trapped particles, Hastie, Hesketh and Taylor[1] investigated the shear damping of drift waves in toroidal systems, using the transformation developed in the study of ballooning modes[2]. This transformation reduces the two dimensional eigenvalue problem to an ordinary differential equation in an extended poloidal variable (in leading order of a systematic expansion[1] which leads to an "equivalent plane slab" problem, again in one dimension, in higher order).

For a more complete treatment of stability one must include electron resonance terms, which are the source of the instability. To do this one applies the ballooning transformation directly to the Vlasov equation for each species[3].

2. Solution of Vlasov Equation

Using the notation and coordinates (ψ,χ,ζ) of ref. 2 the ballooning representation for f_j and φ is

$$\left.\begin{matrix} f_j \\ \varphi \end{matrix}\right\} = e^{-i\omega t} \sum_m e^{im\chi/\chi_0} \int_{-\infty}^{\infty} e^{-im\eta/\chi_0} \exp[iN(\zeta - \int_{\eta_0}^{\eta} \nu d\eta)] \left.\begin{matrix} \hat{f}_j \\ \hat{\varphi} \end{matrix}\right\} \qquad (1)$$

where the eikonal $S \equiv N(\zeta - \int_{\eta_0}^{\eta} \nu d\eta)$ satisfies $\underset{\sim}{B}\cdot\nabla S = 0$. Apart from the infinite range of the extended poloidal coordinate η, and its consequences for the boundary conditions, the structure of the problem is then similar to that solved by Taylor and Hastie[4] in multipole geometry. We may therefore take over their solution viz

$$\hat{f} = -\frac{e\hat{\varphi}}{T} F_o + g e^{i\alpha} \qquad (2)$$

where $\alpha = \underset{\sim}{v}_\perp \times \underset{\sim}{e}_1 \nabla S$ and g satisfies

$$v_\parallel \underset{\sim}{e}_1\cdot\nabla g + i(\underset{\sim}{v}_d\cdot\nabla S - \omega)g = -J_o(z)\frac{ie\hat{\varphi}}{T}(\omega - \omega_*) F_o \qquad (3)$$

where $\underset{\sim}{v}_d$ is the guiding centre drift and $z = v_\perp |\nabla S|/\omega_c$.

New features arising because η has infinite range (instead of being periodic) are the repetition of mirror trapped distributions in successive wells and the secular increase of ∇S with η. The boundary condition for passing particles is $g_\pm \to 0$ when $\eta \to \pm\infty$. Thus when $\mathrm{Im}\,\omega > 0$ (analytic continuation for $\mathrm{Im}\,\omega < 0$),

$$g_+ = \frac{-ieF_o}{T}(\omega - \omega_*)\int_{-\infty}^{\eta} \left|\frac{JB}{v_\parallel}\right| d\eta\, \hat{\varphi} J_o(z) \exp(-iM(\omega,\eta',\eta)) \qquad (4)$$

with

$$M(\omega,\eta',\eta) = \int_{\eta}^{\eta'} \left|\frac{JB}{v_\parallel}\right| d\eta\, (\omega - \underset{\sim}{v}_d\cdot\nabla S) \qquad (5)$$

and similarly for g_-. The corresponding expression for trapped particles may be obtained from ref. 4.

The expression (4) conceals the Landau resonance - which is now associated with the infinite range of the η integration. It can be made explicit by introducing the Hilbert transform (again for $\mathrm{Im}\,\omega > 0$) when

$$g_p = (g_+ + g_-) = \frac{eF_o}{\pi T}(\omega - \omega_*)\int_{-\infty}^{\infty} \frac{dt}{(\omega - t)} \int_{-\infty}^{\infty} \left|\frac{JB}{v_\parallel}\right| \hat{\varphi} J_o(z) \cos M(t,\eta',\eta). \qquad (6)$$

so that the imaginary contribution is

$$\mathrm{Im}\, g_p = -\frac{eF_o}{T}(\omega - \omega_*)\int_{-\infty}^{\infty} \left|\frac{JB}{v_\parallel}\right| d\eta\, \hat{\varphi} J_o(z) \cos M(\omega,\eta',\eta) \qquad (7)$$

3. The Drift Wave Eigenvalue Equation in a Tokamak

The general expressions above can be considerably simplified in the limits $\omega_i \ll \omega \ll \omega_e$ where ω_j are the transit frequencies over a typical connection length. Then the ion response can be obtained[4] as an asymptotic series based on $M \gg 1$, $\underset{\sim}{v}_d\cdot\nabla S \ll \omega$. This is equivalent to the approximation of ref. 1; it neglects ion drift resonances and is limited by the secularity of ∇S in η.

For the electrons $M \ll 1$ and, in a Tokamak field $B_\zeta = B_o(1 - \epsilon\cos\eta)$, the passing electron response becomes

$$\delta\hat{\rho}_e = -\frac{e^2 n}{T_e}\left[\hat{\varphi} + \frac{iRq}{2}(\omega - \omega_*)\left(\frac{m}{2\pi T_e}\right)^{\frac{1}{2}} \int_{-\infty}^{\infty} d\eta' \hat{\varphi}(\eta') K(\eta,\eta')\right] \qquad (8)$$

where the integral term is the sought for electron driving term which originates from the Landau resonances in Eq. (6). The kernel is

$$K(\eta,\eta') = \ell n\left(\frac{2}{\epsilon}\right) - 2\ell n\left[\left|\cos\frac{\eta}{2}\right| + \left|\cos\frac{\eta'}{2}\right|\right] \qquad (9)$$

Finally then we obtain a new, one dimensional integro-differential equation representing drift waves in a toroidal system. In the notation of ref. 1 this can be written

$$\frac{d^2\hat{\varphi}}{d\eta^2} + [\lambda - U(\eta)]\,\hat{\varphi} - i\beta\int_{-\infty}^{\infty} K(\eta,\eta')\,\hat{\varphi}\, d\eta' = 0 \qquad (10)$$

where

$$\beta = \frac{1}{2\sqrt{\pi}}\left(\frac{\omega L_c}{v_{Te}}\right)\frac{(\omega_* - \omega)}{(\omega_* + \omega\tau)}\left(\frac{\omega}{\omega_*}\frac{ka_i}{\epsilon_c}\right)^2 \qquad (11)$$

with $L_c = Rq$, $v_{Te} = \left(2T_e/m_e\right)^{\frac{1}{2}}$.

This new equation, which incorporates the electron driving mechanism, replaces Eq. (10) of ref. 1, (where an artificial driving term $i\hat{\varphi}\delta$ was introduced). The electron driving term may be further simplified by replacing $K(\eta,\eta')$ by its dominant contribution $\ell n(2/\epsilon)$.

In the limit $\epsilon_n \equiv \frac{r_n}{Rr} \to 0$, Eq. (10) can be solved analytically to give a dispersion relation equivalent to that of ref. 5 with $\ell n(Mr_n/mL_s)$ replaced by $\ell n(2/\epsilon)$, corresponding to resonances in general geometry rather than a slab.

4. Numerical Results

Because of the integral term in Eq. (10) the "shooting" method of numerical solution used in ref. 1 is no longer convenient. We have instead solved Eq. (10) by expanding in Hermite basis functions, so reducing (10) to a matrix eigenvalue problem. Results have been computed over a range of values of the toroidicity parameter ϵ_n and show the expected decrease in the decay rate γ from its plane slab value at $\epsilon_n = 0$ through a marginally stable point and into a weak instability. An example of the variation of γ with ϵ_n is shown in Fig. 1. Other examples will be presented at the conference.

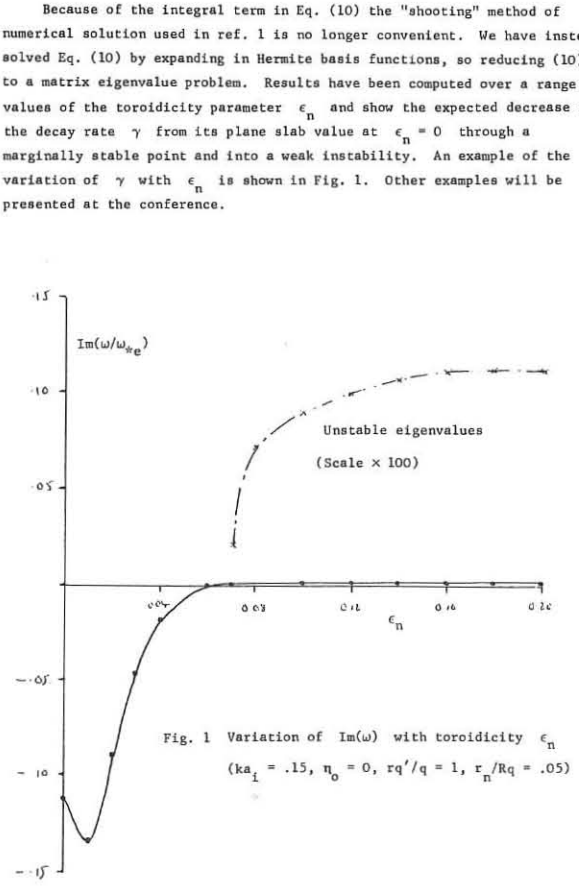

Fig. 1 Variation of $\mathrm{Im}(\omega)$ with toroidicity ϵ_n
($ka_i = .15$, $\eta_o = 0$, $rq'/q = 1$, $r_n/Rq = .05$)

References

1. R.J. Hastie, K.W. Hesketh and J.B. Taylor, to be published in Nucl. Fus. 19(9) (1979).
2. J.W. Connor, R.J. Hastie and J.B. Taylor, Proc. Roy. Soc. A 365, 1, (1979).
3. M. Bornatici, F. Engelmann, A. Nocentini, F. Pegoraro, T. Schep and T. Timmers, Proc. of Seventh Int. Conf. on Plasma Physics and Controlled Nuclear Fusion Research, Innsbruck 1978, vol. 1, p.507.
4. J.B. Taylor, R.J. Hastie, Plasma Physics 10, 479, (1968).
5. K.T. Tsang, P.J. Catto, J.C. Whitson and J. Smith, Phys. Rev. Lett. 40, 327, (1978).

SYSTEMATIC OPTIMIZATION OF TOKAMAKS TO ALL IDEAL MHD MODES

L. C. Bernard, R. L. Miller, R. W. Moore, F. J. Helton
General Atomic Company,
San Diego, California, 92138 U. S. A.

Abstract. Stable plasma equilibria with geometry comparable to the JET device have been found with beta in excess of 12%. External-conductor stabilization is required only for the axisymmetric mode. Higher values of β are reached for higher elongations. We use an automated numerical procedure which maximizes the stable β of tokamak plasmas with respect to all ideal MHD modes. This optimization considers variations in both shape and current profiles.

Investigations which seek to increase the maximum stable β for tokamaks are of fundamental importance. To our knowledge, past studies have been more restrictive than the present work which incorporates: 1) all ideal MHD modes, 2) an automatic and systematic search for optimal parameters, and 3) both arbitrary plasma shapes and current profiles. This work is the culmination of two previous studies.[1,2] In Ref. 1, the current profile was optimized for a fixed plasma shape (JET) with respect to all MHD modes. In Ref. 2, the plasma shape was optimized for a fixed current profile with respect to localized internal modes, using an automated numerical technique. We have now modified this code to optimize the current profile as well as the plasma shape with respect to both external and internal ideal MHD modes. This code automatically searches for optimum equilibrium parameters characterizing both plasma shape and current profile, an approach made possible by efficient ideal MHD codes and Class VI computers.

MHD equilibria are obtained by solving the Grad-Shafranov equation

$$R^2\nabla\cdot(\nabla\psi/R^2) = -\mu_0 R j_\phi = -\mu_0 R^2 p' - ff'$$

using the geometry shown on Fig. 1. For this study:

$$p' \propto \exp\left[1-\left(\frac{\psi-\psi_a}{\psi_\ell-\psi_a}\right)^\alpha\right]-1 \quad ,$$

where index a(ℓ) refers to the magnetic axis (limiter) and α is a measure of the width of the pressure profile (see Fig. 2). For ff' we consider two options: 1) ff' has the same functional form as p', and 2) q(ψ) is specified. The total plasma current is held fixed.

The stability to internal modes is determined by the criterion for localized ballooning modes[3] (close to the magnetic axis, this criterion reduces to the simpler criterion for localized interchange modes[4]). This gives a critical value for the vacuum toroidal field f_ℓ/R_c for marginal stability. The corresponding value of the volume average beta,

$$\beta = 2\mu_0 \int p dV \Big/ \left[(f_\ell/R_c)^2 \int dV\right]$$

is then the value of β for which the equilibrium is marginally stable to localized internal modes. For external modes it is necessary to study only the n=1 kink mode without external conductors. The axisymmetric mode, n=0, can always be easily stabilized by external conductors while such conductors may not be practical for stabilizing kink modes. Under these assumptions the n=1 kink mode is the most restrictive external mode. The stability to external modes is evaluated by the global code ERATO.[5]

The automated optimization is begun by calculating an equilibrium with a given set of values of the independent optimization parameters P_i (poloidal fluxes on the field-shaping coils and current profile parameters). The maximum stable β is determined for this shape and current. Then the value of one of the P_i's is altered with an increment dP_i, and a new equilibrium and a new maximum β are calculated. P_i is incremented until a relative maximum in β is found. Then the next P_i is varied. The optimization cycle is completed by sequentially varying each independent parameter value until a maximum beta is reached.

To reduce the computer time, the optimization is begun with a good equilibrium determined by current profile optimization with fixed plasma shape (see Fig. 3). Figure 4 shows a maximum value of β = 8.2%, corresponding to α = 7.5, β_p = 0.45. The current profiles (Fig. 2) support the qualitative picture that kink instabilities are induced by strong current gradients close to the plasma surface. This picture explains why the current cannot be too flat, and why there is an optimum value of β_p: for large (small) values of β_p, the flux surfaces are shifted outwards (inwards), yielding a strong current at the exterior (interior) of the torus.

By optimizing the plasma shape together with the current profile, we have achieved an increase of β from 8.2% to 12.2%. The profile is slightly changed (new values are α = 7, β_p = 0.7). The new shape is triangular and slightly indented at the inside edge of the plasma. Both effects produce a large triangularity at the magnetic axis, hence the stability to interchange modes is improved. The triangular shape of the outside of the plasma keeps the current well centered inside the plasma surface, which is favorable for stability to the external kink. The indentation helps to stabilize the ballooning mode by reducing (enlarging) the connection length in the bad (good) curvature region of the outside (inside) of the plasma. In contrast to Ref. 2 (limited to internal modes), the plasma shape is not strongly indented at the inside edge. This indentation increases the amount of current flowing close to the plasma surface on the inside edge, which decreases stability to the external kink. With strong indentation, the value of q on axis for stability to localized modes may drop below unity. Then the internal kink, and therefore the external kink, become unstable.

By a combined optimization of plasma and current shaping, we have demonstrated the existence of plasma equilibria which are stable to all ideal MHD modes with a value of β in excess of 12% for plasmas with aspect ratio 2.53 and elongation 1.71. Preliminary computations show an increase of β with elongation and inverse aspect ratio. If time permits, the influence of aspect ratio, elongation, new classes of current profile, and doublet geometries will be discussed in more detail at the conference.

Acknowledgement. This work was supported by Department of Energy, Contract DE-AT03-76ET51011.

References

1. L. C. Bernard *et al.*, General Atomic Company Report GA-A15236, submitted to Nucl. Fusion, 1979.
2. R. L. Miller and R. W. Moore, General Atomic Company Report GA-A15307, submitted to Phys. Rev. Lett., 1979.
3. D. R. Dobrott *et al.*, Phys. Rev. Lett. *39* (1977) 943; J. W. Connor *et al.*, Phys. Rev. Lett. *40* (1978) 396.
4. C. Mercier, Nucl. Fusion *1* (1960) 47.
5. D. Berger *et al.*, in *Plasma Physics and Controlled Nuclear Fusion Research* (Proc. 6th Int. Conf. Berchtesgaden, 1976) Vol. 2, IAEA, Vienna (1977) 411.

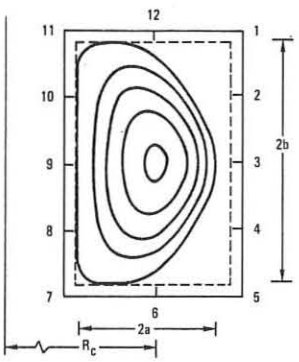

Fig. 1. Equilibrium geometry. Inner rectangle is limiter. ψ is specified on labeled points. R_c/a = 2.53; b/a = 1.71.

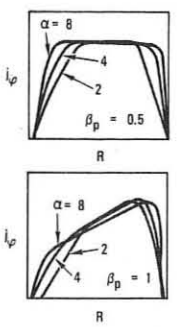

Fig. 2. Current density profile in the equatorial plane. ff' ∝ p'; $\beta_p^{-1} = 1 + ff'/(p'R_c^2)$.

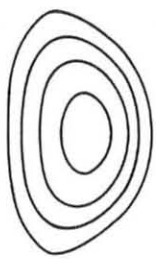

Fig. 3. Initial plasma shape.

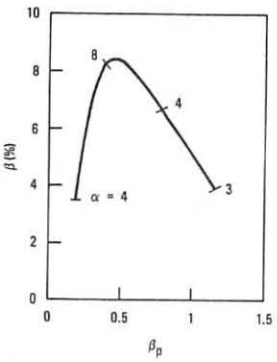

Fig. 4. Optimal value of β for the fixed plasma shape shown on Fig. 3. Stability to all ideal MHD modes is below the curve.

A3.7

STUDIES ON SLOWING DOWN OF ENERGETIC IONS
AND TRANSPORT COEFFICIENTS BY MAKOKOT

H.CAPES, G.CISSOKO, C.MERCIER, J.P.MORERA, F.WERKOFF+

ASSOCIATION EURATOM-CEA SUR LA FUSION
Département de Physique du Plasma et de la Fusion Contrôlée
Centre d'Etudes Nucléaires
Boite Postale n° 6, 92260 FONTENAY-AUX-ROSES (FRANCE)

Numerous numerical models have been proposed for studying the slowing down of energetic ions. Firstly the FOKKER-PLANCK codes study the velocity relaxation of fast ions distribution function without radial diffusion /CORDEY and CORE 1974, FOWLER et al 1976, DNESTROVSKI et al. 1977/. An important improvement have been carried out by averaging the collision operator along magnetic surfaces and including the effects of trapped particles. Secondly the MONTE-CARLO codes [DEI-CAS and MARTY 1974, LISTER 1976] treat the exact particles orbits but are very time consuming.

In order to obtain the power deposited on magnetic surfaces, our starting point will be the bounce-averaged FOKKER-PLANCK equation for axisymetric geometry [CORDEY 1976, ROME 1977]. Assuming that the slowing down time is larger than the bounce time, it is possible to show [ROME 1977] that particle orbits between two collisions are completely determined by one of the two intersection points (r_M, r_I) with the equatorial plane, and by the velocity v at this point. We choose to treat the problem in the 3D space (r_M, v, p_M) where r_M is the more distant intersection point from the magnetic axis and

$$p_M = \frac{v_{//}}{v} \quad \text{for } r = r_M.$$

In the case of cylindrical magnetic surfaces, the following implicit equation must be solved in order to determine intersection points (r_M, r_I) [ROME 1977] :

$$h_M^2 v^2 - h_M h v^2 (1 - p^2) - \left[hpv + \frac{e}{m_j} \left(\int_0^{r_M} B_{\theta_0} \, dr' - \int_0^{r} B_{\theta_0} \, dr' \right) \right]^2 = 0$$

where $h = 1 + \frac{r}{R}\cos\theta$, $h_M = 1 + \frac{r_M}{R}$, $p = \frac{v_{//}}{v}$

This equation allows the determination of the source of energetic ions at the point (r_M, v, p_M). In addition the knowledge of the second intersection point, r_I, give the type of particle orbits and the orbit deviations from magnetic surfaces. Fast ion energy deposition for which the trajectories are included between the two magnetic surfaces (r_M, r_I), will be distributed over ions and electrons of the background localized between the two surfaces (uniformly for each species).

Starting from the bounce-averaged kinetic equation in the drift approximation, we obtain a partial differential equation for the distribution function of energetic ions f (r_M, v, p_M, t) :

$$\frac{\partial}{\partial t} f + \frac{1}{\left\langle \frac{v}{v_{//}} \right\rangle} \frac{1}{r} \frac{\partial}{\partial r} (r \phi_1) = \frac{\langle C dv \rangle}{\langle dv \rangle} + S_0$$

The bracket $\langle \ldots \rangle$ means average along the particle trajectory, C is the Coulomb collision operator with usual approximations [CORDEY 1976] ; S_0 is the source of the fast ions ; ϕ_1 the diffusion flux.

If the deviation from magnetic surfaces is small, quantities as $\langle 1/v_{//} h \rangle$ or $\langle v_{//} \rangle$ have been calculated by CORDEY. In that case it is also possible to evaluate the classical diffusion flux

$$\phi_1^{NC} = - \frac{m_j v p_M}{Z_j e B_\theta} \quad \left(\langle C \rangle = - \frac{\langle C dv \rangle}{\langle dv \rangle} \right)$$

Morever, from the analogy of impurities and light ions [MERCIER - et al 1979] , we include the possibility to use the following anormalous flux

$$\phi_1^A = - D \frac{\partial f}{\partial r_M}$$

(where D is the electron diffusion coefficient) and in a similar way combinations such as $\phi_1 = \phi_1^A + \phi_1^{NC}$. Presently the model uses only ϕ_1^A.

With a low computer time, an application is carried out for a TFR experiment and comparison with the Dei-Cas MONTE-CARLO Code is discussed. No severe discrepancies are observed, which probabily means that ϕ_1^A and ϕ_1^{NC} are of the same order. In another way, we also compare our result with an energy deposition model without ion slowing down and observe some discrepancies in the center of the plasma.

Statistical analysis of a number of Tokomak experiments lead to some different functional dependance for the electron particle coefficients. Such dependances may be studied by Makokot, by simulating experiments with different transport coefficients. In stationnary states, we show the importance for temperature profile of functional dependance in $1/T^{\alpha}q$. In the same way for electron density profile, we find a great sensibility to the functional dependance of the diffusion coefficient at the edge of the plasma.

REFERENCES :

- CORDEY, J.G and CORE, W.G. (1974) Phys. Fluids 17 p 1926

- CORDEY, J.G. (1976) Nuclear Fusion 16 p 499

- DEI-CAS, R. and MARTY, J. (1974) Report EUR-CEA-FC-776
- FOWLER, R.H and al. (1976) Report ORNL/TM-5987
- LISTER, G.G. (1976) in Heating of toroidal Plasma (Proc. 3rd Symposium Varenn

- ROME, J.A. (1977) Private communication

- MERCIER, C. WERKOFF, F. and MORERA, J.P. (1979) Report EUR-CEA-FC-997

+ Present adress Service des Transports thermiques D.T.C.E. CEN/Grenoble

AP1

Simultaneous Operation Experiments of Neutral Beam Injection and Lower Hybrid Heating in JIPP T-II

J. Fujita, S. Itoh*, K. Kadota, K. Kawahata, Y. Kawasumi, T. Kuroda, K. Matsuoka, K. Matsuura, K. Miyamoto, N. Noda, K. Ohkubo, Y. Oka, K. Sakurai, K. Sato, S. Tanahashi, Y. Terashima, K. Toi*
Institute of Plasma Physics, Nagoya University, Nagoya 464, Japan
*Research Institute for Applied Mechanics, Kyushu University, Fukuoka 812, Japan

Abstract — The simultaneous operation of neutral beam injection (NBI) with input power as high as 70 kW and lower hybrid heating (LHH) with rf power of 50 kW into the torus is carried out. We observe effective ion heating of 220 eV whose value is nearly equal to the sum of the temperature increase by each heating method.

Experimental Device, Additional Heating Systems and Diagnostics — The experiments of NBI and LHH have been carried out in JIPP T-II[1] which is operated presently as a tokamak with the resistive shell. Experimental conditions of target plasma are followings: toroidal magnetic field B_t = 21 or 26.4 kG, plasma current I_p = 83 kA, line averaged electron density of hydrogen plasma, $\bar{n}_e$ = (1.4-2.4) × 10^{13} cm^{-3}, ion temperature $T_i(0)$ = 350 eV and electron temperature $T_e(0)$ = 700-800 eV, ion energy confinement time τ_{Ei} = 5-7 msec. A gas puffing system is used to control the plasma density. The neutral beam injector[2] is installed to a tangential port with diameter of 12 cm. The ion source is Berkeley type whose electrodes have 587 holes with the diameter of 3 mm. Equivalent current of NBI is about 5 A at 25 keV with 20-100 ms duration. The rf power of LHH is 180 kW at maximum with frequency of 0.8 GHz and with 20 ms duration. The launcher[3] installed in the movable bellows, whose waveguide is a pair of C-shaped waveguide, is inserted into the torus. The diagnostic instruments used are as follows: ruby laser scattering equipment; 2 mm microwave interferometer; visible and vacuum-ultraviolet spectrometers; TV camera to monitor the plasma cross section. A 6-channel charge-exchange neutral-particle analyzer collimated tangentially is used to measure the parallel ion temperature $T_{i//}$.

NBI — Ion beam are co-injected in the same direction of ohmic current. Time evolutions of ion temperature with and without beam are observed. The increase of ion temperature $\Delta T_{i//}$ at the center reaches about 180 eV in the case of extracted ion beam power of about 120 kW. The estimated neutral beam power injected into the plasma P_{beam} is about 80 kW and is smaller than ohmic power (≈ 200 kW). The increase of ion temperature is proportional to the input power P_{beam} and scales as $\Delta T_{i//}/P_{beam}$ ≈ 1.5 eV/kW. The temperature increases at a heating rate of about 9 eV/msec and the increment $\Delta T_{i//}$ reaches 180 eV. The observed ion temperature rise is roughly consistent with the estimated value. The calculated $\Delta T_{i//}$ shows that the energy confinement time with NBI is equal to the value without NBI. The high energy component of ions is measured in the range up to 8 keV. Typical example of the time evolution of the high energy component of ions is shown in Fig.1. We observe the high energy component during beam injection, which relaxes in about 20 msec that is nearly equal to energy slowing down time of beam. This result shows that injected beam is trapped in the plasma during the time nearly equal to slowing down time and the plasma is heated by the trapped beams. Net electron heating is observed in the case of higher power injection (P_{beam} ≈ 130 kW). In the experiment no appreciable effect of NBI on impurities as well as on the electron density are observed during injection.

LHH — Typical results of the parallel energy spectrum with and without LHH are shown in Fig.2. From the comparison of the temperatures with and without LHH, we see that the ion temperature increases from 317 eV to 410 eV for P_{net} ≈ 40 kW near the end of heating pulse. No high energy tail is observed in the energy spectrum of parallel component in the range up to 5 keV. Since ion temperature increases with the time constant, which closes to the ion energy confinement time of ohmically heated plasma, it suggests that thermalization process has taken place. The experimental results on the increase of temperature show the value of $\Delta T_{i//}/P_{net}$ ≈ 2 eV/kW and $\Delta T_{i//}$ is not yet saturated within the input power level (P_{net} < 55 kW). During LHH, both the loop voltage and the electron density increase by 20 % and plasma current remains unchanged. The time evolutions of electron temperature at the center are measured. At B_t = 21 kG and P_{net} ≈ 42 kW the electron temperature does not change during LHH, but decreases slowly after the end of heating pulse. At the higher magnetic field B_t = 26.4 kG and rf power P_{net} = 55 kW, the temperature increases by 30 % during heating pulse. In this case the electron temperature also begins to decrease after heating pulse. In order to examine the reason on these decreases, emission lines on impurities (oxygen, carbon, iron, molybdenum, gold) are measured. Comparing the ion temperatures with and without LHH in the condition of the same electron density, we estimate the net efficiency of LHH at P_{net} = 41 kW: the value of $\Delta T_{i//}/P_{net}$ is 0.9-1.3 eV/kW and the power to ion by LHH (P_{iLH}) is P_{iLH} ≈ 9-10 kW. In our experiment it may be noted that P_{iLH}/P_{net} does not show any drastic dependence on electron density as far as the turning position of LH wave is located within the half radius of plasma.

Simultaneous Operation of NBI and LHH — When both heating method of NBI with input power of about 70 kW into the torus and LHH with input power of 50 kW is carried out simultaneously, the increase of ion temperature is observed to be about 220 eV as shown in Fig.3. The value is nearly equal to the sum of the increase of each heating method; the increase of ion temperature by NBI only is about 110 eV and the increase by LHH only is about 90 eV. In this heating, increases of loop voltage and electron density by 20-30 % are observed. These effects are resulted from LHH.

Conclusion — The efficiencies of ion heatings by NBI and LHH are 1.5 eV/kW and 2.0 eV/kW, respectively. By the simultaneous operation the increase of ion temperature is nearly equal to the sum of the temperature increases by NBI and LHH. This application does not cause the detrimental effect on plasma.

Acknowledgements — It is a pleasure to acknowledge the assistance in the experiments given by Mssrs. S. Okuno, T. Tabata and K. Yasuda.

References

[1] J. Fujita, S. Itoh, K. Kadota, K. Kawahata, Y. Kawasumi, T. Kuroda, K. Matsuoka, K. Matsuura, A. Miyahara, K. Miyamoto, N. Noda, K. Ohkubo, K. Sakurai, K. Sato, M. Sato, S. Tanahashi, Y. Terashima, K. Toi: Plasma Physics and Controlled Nuclear Fusion Research (Proc. IAEA Conf. Innsbruck, 1978) CN-37-N2, IAEA, Vienna (1979).

[2] T. Kuroda, Y. Oka, T. Kunibe, H. Okamura, A. Miyahara: Proc. of Joint Varenna-Grenoble International Symposium on Heating in Toroidal Plasma, Vol.1, 55 (July 1978, Grenoble).

[3] K. Ohkubo and K. Matsuura: ibid. Vol.1, 145 (July 1978, Grenoble).

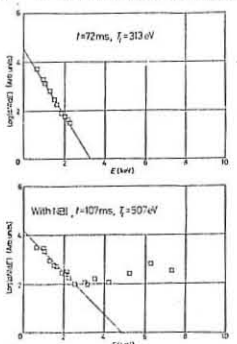

Fig.1. Energy spectra of charge-exchange neutral: upper figure shows the result at 16 msec before the injection and lower figure at 19 msec after the start. (The duration of NBI is 20 ms.)

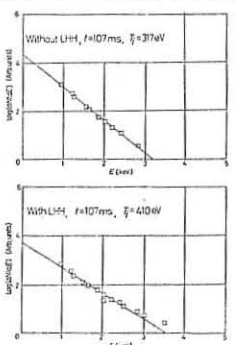

Fig.2. Energy spectra of charge-exchange neutral in the tangential direction: upper figure shows the result without LHH and lower one with LHH at 1 msec before the end of heating pulse.

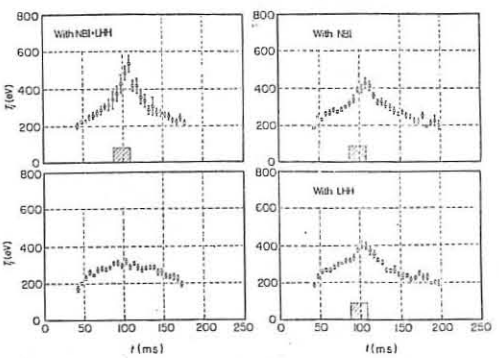

Fig.3. Time evolutions of ion temperature deduced from parallel charge-exchange with and without the additional heatings.

AP3

CHARACTERISTICS OF THE DITE PHASE II ION SOURCE

R.S. Hemsworth, D. Stork and H.C. Cole

Culham Laboratory, Abingdon, Oxon, OX14 3DB, UK
(Euratom/UKAEA Fusion Association)

ABSTRACT

The characteristics of the DITE Phase II plasma source are presented with particular emphasis on the yields of the various hydrogen ion species obtained. We have measured a species mix $H^+:H_2^+:H_3^+$ of (80 ± 4):(18 ± 4):(2 ± 2) at source pressure 4 mT and current density 250 mA/cm^2.

INTRODUCTION

The DITE Phase II neutral injection system has been described in detail elsewhere[1,2]. The ion source, shown in Fig. 1, consists of a plasma source involving a low voltage arc discharge in a rectangular box with one wall replaced by an insulated three electrode extraction grid assembly (65% transparent). The rectangular box (145 mm × 440 mm × 150 mm deep) has rows of Co-Sa permanent magnets mounted orthogonal to the beam axis outside the source walls, adjacent rows of magnets having opposite polarity to form a picket fence magnetic field inside the source[3]. For the studies reported here the source was placed at the end of a 3.6 m beam line, a replica of a DITE beam line, connected to a diagnostic test tank.

PLASMA SOURCE CHARACTERISTICS

The low magnetic field near the extraction system leads to a uniform plasma density in that region. Measurements at the extraction plane show the ion flux to be uniform to within ± 5% over an area of 36 × 8 cm^2 for a 90 V discharge. There is no observed variation with source pressure.

The source operates reliably over a wide range of parameters, arc current 50 - 600 A, pressure 1 - 30 mT. Typical I - V characteristics for the source are shown in Fig. 2. These show that the space-charge limited emission at low arc voltages eventually gives way to thermionically limited emission at high arc voltages and a saturation of arc current.

The source is normally operated with extraction grid at floating potential and in this case the anode current (I_A) is approximately equal to the filament emission current (I_e), thus the ionising efficiency of the source η_I can be defined as $\eta_I = I^+_{ext}/I_A$. Where I^+_{ext} is the extracted current. Increasing the source arc voltage increases η_I due to the increasing ionising efficiency of the primary electrons. η_I is found to fall with increasing arc current at fixed arc voltage (Fig. 3). This phenomenon is not well understood though we have shown that it is not due to the fall in source pressure due to the extraction of more ions. We will return to this point in a future publication[2].

SPECIES

One very interesting parameter for a hydrogen plasma source is the ratio of the various hydrogen species [H^+,H_2^+,H_3^+] produced by the source.

The species from the Phase II source have been measured using a magnetic momentum analyser placed at 4.7 m from the source at the end of an evacuated flight tube. Gas is added to the line in front of the analyser coincident with a beam being extracted from the source. Thus the molecular fractions are broken up and the detector measures peaks at energies E, E/2 and E/3 where E is the extracted beam energy. The signals observed are equated to the infinite target (equilibrium) ion fractions and hence one can obtain the original species fractions.

The results obtained at a beam energy of 24 kV are shown in Fig. 4. It may be seen that the fraction of H^+ ions rises with increasing current density (j^+) in a direct mirror of the fall of the H_3^+ fraction. The amount of H_2^+ produced is largely insensitive to variation in j^+. The H^+ fraction saturates at something over 80% for j^+ values greater than 200 mA/cm^2. The behaviour of the H^+ and H_3^+ signals suggests that direct break-up of the H_3^+ ions is occurring. Most models of species formation[4] whilst predicting the rise in H^+ yield with j^+, usually have break-up occurring via the H_2^+ state. Our observation of a largely invariant H_2^+ fraction casts some doubt on this.

An increase of pressure in the source is expected to yield higher molecular fractions due to an increase in probability for the H_3^+ formation reaction.

$$H_2^+ + H_2 \rightarrow H_3^+ + H_o$$

and this is indeed observed in our results (see Fig. 4).

The absolute species fractions obtained for the DITE Phase II source must be treated with some caution. The method outlined above neglects the fact that the break-up products will have a higher divergence than the H^+ fraction and hence will be preferentially scattered out of a detector with a limited acceptance such as ours (± 20 mrad). Thus the proton yield will be enhanced. We have performed some measurements at low pressure (4 mT) in the source without adding gas. In these measurements the mass analyser sees essentially no break-up products and measures the H^+, H_2^+ and H_3^+ fractions directly. A comparison of 'infinite' and thin target measurements at 4 mTorr source pressure is shown in Fig. 5.

The proton fraction is lower and the H_2^+ and H_3^+ yields are increased. These results can be quoted with confidence and we see that at 4 mT and 250 mA/cm^2 our species fractions are $H^+:H_2^+:H_3^+$ = 80 ± 4:18 ± 4:2 ± 2.

CONCLUSIONS

The DITE Phase II plasma source operates over a wide range of parameters with an electrical efficiency of ~ 1.2 A extracted per kW of arc power. The ionising efficiency increases with arc voltage but falls slowly with arc current. The proton fraction at high current densities, > 200 mA/cm^2, is ~ 80%.

REFERENCES

(1) R.S. Hemsworth et al, Contrib. Paper Joint Varenna-Grenoble Int. Symp. on Ion Heating in Toroidal Plasmas, Grenoble 1978.

(2) R.S. Hemsworth et al, to be submitted to Journal of Physics E.

(3) R. Limpaecher and K.R. McKenzie, Rev. Sci. Instr. 44 (1973) 726.

(4) See for instance A.R. Martin and T.S. Green, CLM-R159 (1976).

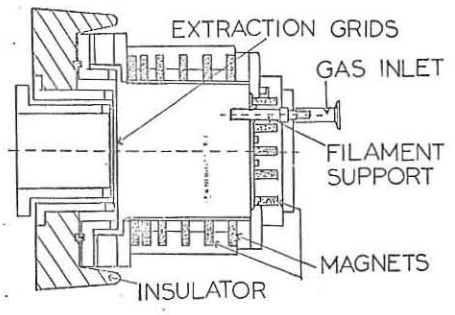

Fig. 1.

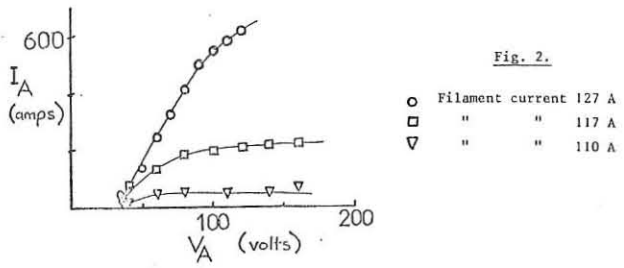

Fig. 2.

Fig. 3. Ionising efficiency vs arc current.

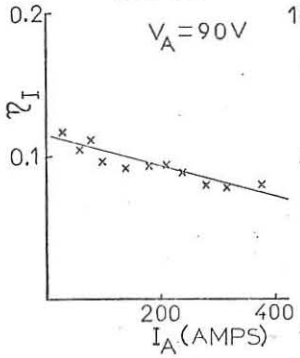

Fig. 4. Species fractions (thick gas target)

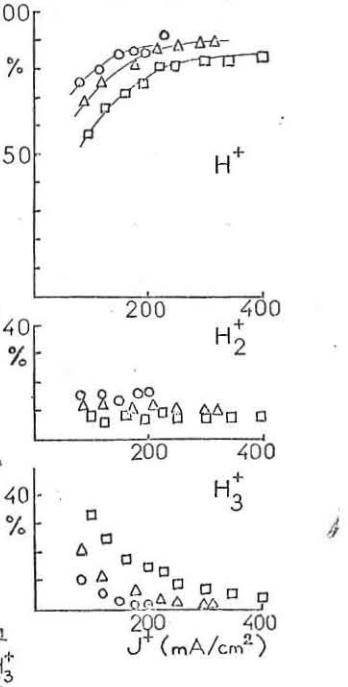

(For Fig. 4 above)

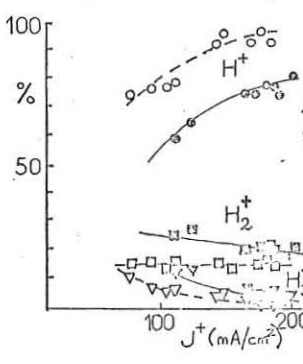

Thick ---- Thin ——

Fig. 5. Effect of gas target thickness on measured species (4 mT).

AP4

RESONANCES IN THE ION CYCLOTRON RANGE IN TOROIDAL GEOMETRIES

T. Hellsten and E. Tennfors

ROYAL INSTITUTE OF TECHNOLOGY, S-100 44 STOCKHOLM 70, SWEDEN

Abstract. Equations for resonances and cut-offs of the fast Alfvén and ion-cyclotron waves have been derived for a multicomponent plasma in a toroidal axisymmetric geometry. Resonance and cut-off frequencies are given by eigenvalues of ordinary differential equations on the resonance and cut-off surfaces, respectively. These surfaces coincide with magnetic surfaces and intersect the fundamental ion-cyclotron and hybrid resonance surfaces.

ICRF heating of toroidal plasmas via the fast Alfvén wave has received increased interest due to the large heating efficiency observed in Tokamaks [1-3]. A crucial problem for estimating the efficiency is to determine the location of various resonance and cut-off surfaces [4,5].

In a cold, axially symmetric multicomponent plasma the resonance and cut-off surfaces of the fast Alfvén and ion cyclotron waves coincide with magnetic flux surfaces. The wave functions at the resonance surface are propagating on the high field side of each fundamental ion cyclotron resonance surface, $\omega=\omega_{c\alpha}$, singular at the surface, and evanescent on the low field side. This is in agreement with the experimentally observed asymmetry with respect to the location of the ion cyclotron resonance surfaces [6,4].

We use a local orthogonal curvilinear coordinate system (χ,ζ,θ) where θ is the toroidal angle, χ and ζ labels two sets of orthogonal axisymmetric surfaces. The metric is defined by $ds^2=g_{\chi\chi}d\chi^2 + g_{\zeta\zeta}d\zeta^2 + r^2d\theta^2$. We linearize the equations of motion for a cold plasma and Maxwells equations about a static equilibrium and then Fourier decompose the perturbations with respect to time and the ignorable toroidal angle 0 and arrive at

$$(\underline{\nabla}\times\underline{\nabla}\times\underline{E})^i = \frac{\omega^2}{c^2}\left(\delta^i_j - \sum_\alpha \frac{\omega^2_{p\alpha}A^i_{\alpha j}}{\omega^2(\omega^2_{c\alpha}-\omega^2)}\right)E^j = \epsilon^i_j E^j \qquad (1)$$

The resonances are recognized by the fact that the equations of motion become singular. Cyclotron resonances are obtained for poles of ϵ. In general, there are other singularities of a system of partial differential equations which cannot be obtained by studying the coefficient in front of the highest order derivative or from poles in ϵ. The set of χ-surfaces is chosen such that one of these surfaces, χ_0, coincide with a singular surface. Furthermore, we assume that E^χ has the same order of singularities as $\partial E^\zeta/\partial\chi$. The leading order terms are denoted by index 0. For Eq. (1) they read

$$\frac{1}{J}\frac{\partial}{\partial\zeta}\left(\frac{r^2}{J}\left(\frac{\partial E_{0\zeta}}{\partial\chi}-\frac{\partial E_{0\chi}}{\partial\zeta}\right)\right) - \frac{in g_{\zeta\zeta}}{J^2}\left(in\,E_{0\chi}-\frac{\partial E_{0\theta}}{\partial\chi}\right) = \epsilon^\chi_\chi E^\chi_0 \qquad (2)$$

$$\frac{\partial^2 E_{0\zeta}}{\partial\chi^2}-\frac{\partial^2 E_{0\chi}}{\partial\zeta\partial\chi}=0 \qquad (3)$$

$$in\frac{\partial E_{0\chi}}{\partial\chi}-\frac{\partial^2 E_{0\theta}}{\partial\chi^2}=0 \qquad (4)$$

Substituting Eqs. (3-4) into Eq. (2) we obtain $\epsilon^\chi_\chi = 0$ where

$$\epsilon^\chi_\chi = 1 - \sum_\alpha \frac{\omega^2_{p\alpha}}{\omega^2_{c\alpha}-\omega^2}\left(\frac{\omega^2_{p\alpha}B_\chi B^\chi}{\omega^2 B^2}-1\right) \qquad (5)$$

which defines the upper hybrid, lower hybrid and Buchsbaum's ion-ion hybrid resonance.

To find the resonances of the ion-cyclotron wave, corresponding to the Alfvén wave resonance, we first note that the coupling between the electrostatic and ion cyclotron wave smooths out the singular behaviour. We eliminate this coupling by taking the limit $m_e \to 0$. In that limit $\omega^2_{pe}\to\infty$ whereas $\omega^2_{pe}/\omega_{ce}$ remains finite. From Eqs.(2,5) we obtain that ϵ^χ_χ is finite and $E^\chi_0 \neq 0$ if and only if $B_\chi = 0$, i.e. the singular surface coincides with a magnetic surface.

We transform the components parallel to the magnetic surfaces of Eq. (1) into components parallel and perpendicular to the magnetic field. The parallel component described the electrostatic waves. In general, the dielectric tensor elements approach infinity when $m_e \to 0$, whereas for the perpendicular component the sum of the terms containing the dielectric tensor elements remains finite. This behaviour justifies the assumption that E^χ varies more rapidly in the neighbourhood of the resonance surface than E^θ and E^ζ. We eliminate the coupling of the electrostatic wave on the other waves by replacing the parallel component of Eq. (1) by $\underline{B}\cdot\underline{E}=0$ we then arrive at

$$\frac{1}{J}\frac{\partial}{\partial\zeta}\left(\frac{r^2}{J}\left(\frac{B^\theta}{B^2}\left(B_\theta\frac{\partial E_{0\chi}}{\partial\zeta} - in\,B_\zeta E_{0\chi}\right)-\frac{\partial E_{0\chi}}{\partial\zeta}\right)\right) -$$

$$-\frac{in g_{\zeta\zeta}}{J^2}\left(in\,E_{0\chi}+\frac{B^\zeta}{B^2}\left(B_\theta\frac{\partial E_{0\chi}}{\partial\zeta}-in\,B_\zeta E_{0\chi}\right)\right) = \epsilon^\chi_\chi E^\chi_0 \qquad (6)$$

The cut-offs are recognized as apparent singularities where the solutions change from an oscillating to non-oscillating ones [7]. The cut-off surfaces can be shown to coincide with the magnetic surfaces with arguments similar to those used for the resonances. The algebra becomes simpler if we do not start with the two components perpendicular to the magnetic field of Eq. (1) but instead replace it with a set of first order equations by utilizing that $i\omega\underline{b} = c\nabla\times\underline{E}$ yielding

$$\frac{i\omega}{J}\frac{\partial b_\theta}{\partial\zeta} - inb_\zeta = \epsilon^\chi_i E^i \qquad (7)$$

$$\frac{i\omega}{J}B^\theta\left(inb_\chi - \frac{\partial b_\theta}{\partial\chi}\right)+\frac{i\omega B^\zeta}{J}\left(\frac{\partial b_\zeta}{\partial\chi}-\frac{\partial b_\chi}{\partial\zeta}\right) =$$

$$= -B^\theta\epsilon^\zeta_i E^i + B^\zeta\epsilon^\theta_i E^i \qquad (8)$$

We write the equations in the following way

$$FE^\chi = G\partial\tau/\partial\chi + H\tau \qquad (9)$$

where F,G and H are differential operators with respect to ζ. The eigenvalues of $FE^\chi = 0$ with periodic boundary conditions will then define apparent singularities corresponding to different kinds of cut-offs depending of the choice of the variable τ.

The fast wave cut-off is obtained for $\tau = E^\theta$ yielding

$$\frac{1}{J}\frac{\partial}{\partial\zeta}\left(\frac{r^2\partial E_\chi}{J\partial\zeta}\right) - \frac{n^2}{J^2}g_{\zeta\zeta}E^\chi + \epsilon^\chi_\chi E^\chi = 0 \qquad (10)$$

The cut-off pair in the neighbourhood of the ion cyclotron wave resonance is obtained for $\tau = \underline{B}\cdot\underline{b}/4\pi$ yielding

$$i\omega b^\chi = \frac{1}{J}\left(\frac{\partial E_\theta}{\partial\zeta}+\frac{inr^2}{B^\zeta}B^\theta E^\theta\right) \qquad (11)$$

$$\frac{i\omega B^\zeta B^\zeta}{J\,B^\theta}\frac{\partial}{\partial\chi}\left(\frac{B^\theta}{B^\zeta}\right)b_\zeta = \left(-B^\theta\epsilon^\zeta_\chi + B^\zeta\epsilon^\theta_\chi\right)E^\chi + \left(B^\theta\epsilon^\zeta_\zeta - B^\zeta\epsilon^\theta_\zeta\right)\frac{B_\theta}{B_\zeta}E^\theta$$

$$-\left(B^\theta\epsilon^\zeta_\theta - B^\zeta\epsilon^\theta_\theta\right)E^\theta - \frac{\omega n}{J}B^\theta b_\chi + \frac{i\omega}{J}B^\zeta\frac{\partial b_\chi}{\partial\zeta}$$

$$-E_\theta\frac{\partial}{\partial\chi}\left(\frac{B^\theta}{B^\zeta}\right) = \frac{\partial E_\chi}{\partial\zeta}+in\frac{B^\theta}{B^\zeta}E_\chi - \frac{i\omega Jb^\zeta B^2}{B^\zeta B_\theta} \qquad (12)$$

$$\frac{-i\omega}{J}\left(\frac{\partial}{\partial\zeta}\left(\frac{B_\zeta b^\zeta}{B^\theta}\right)+inb_\zeta\right) = \epsilon^\chi_\chi E^\chi - \frac{\epsilon^\chi_\zeta r^2 B^\theta}{B_\zeta}E^\theta + \epsilon^\chi_\theta E^\theta. \qquad (13)$$

The authors wish to thank Mr. M. Bureš for valuable discussions. This work has been supported by the European Communities under an association contract between Euratom and Sweden.

References

[1] J. Adam et al., Plasma Physics and Controlled Nuclear Fusion Research, (Proc. 5th Int.Conf. Tokyo, 1979)1, IAEA, Vienna (1975)65.

[2] V.L. Vdovin, V.D. Rusanov and N.V. Shapotski, in Plasma Physics and Controlled Nuclear Fusion Research (Proc. 5th Int.Conf. Tokyo, 1974)1, IAEA, Vienna (1975)217.

[3] N.V. Ivanov, I.A. Kovan and V.S. Svishohev, JETP Lett. 20, 39 (1974).

[4] J. Jacquinot, B.D. McVey and J.E. Sharer, Phys.Rev.Lett. 39, 88(1977).

[5] F.W. Perkins, Nuclear Fusion 17, 1197(1977).

[6] TFR Group, in Plasma Physics and Controlled Nuclear Fusion Research, Proc. 6th Int.Conf. Berchtesgaden, 1976, 3, IAEA, Vienna (1977)39.

[7] D.G. Swanson, Phys. Fluids 18, 1269(1975).

AP6

COMPUTER SIMULATION OF ELECTRON CYCLOTRON HEATING ON TFR AND T-10

R. CANO, A. CAVALLO AND F. WERKOFF

ASSOCIATION EURATOM-CEA SUR LA FUSION
Département de Physique du Plasma et de la Fusion Contrôlée
Centre d'Etudes Nucléaires
Boîte Postale n° 6, 92260 FONTENAY-AUX-ROSES (FRANCE)

Electron cyclotron resonance heating is potentially a very useful method both for plasma heating as well as temperature and current profile control in tokamaks. One great advantage is that coupling the wave energy to the plasma should be independent of conditions at the plasma edge. Also, any region in the plasma can be heated by making the local electron cyclotron frequency equal to the wave frequency, provided the local plasma frequency is less than the wave frequency. Finally, the physical mechanism of energy absorption is theoretically well understood.

For radiation in the ordinary polarization (wave electric field $\vec{E}$ parallel to the toroidal magnetic field $\vec{B}$) propagating along the major radius of the torus at a frequency corresponding to the electron cyclotron frequency in the plasma at a plasma radius r_c, the power deposited in the plasma as a function of radius was taken to be (1) :

$$P(\rho) = \overline{P_i}\ \left(\frac{2\alpha\omega_c}{c}\right) n(\rho)\ \exp - \frac{2\alpha\omega_c}{c}\int_{\rho_c}^{\rho} n(\rho)d$$

$$n(\rho) = \frac{\pi^{\frac{1}{2}}}{8}\ \frac{\omega_p^2(\rho)}{\omega_c^2}\ \left(1 - \frac{\omega_p^2(\rho)}{\omega_c^2}\right)^{\frac{1}{2}}\ Z^{\frac{5}{2}}\ \exp - Z \qquad Z = \frac{c^2 m}{kT_e}\ \left(\frac{1}{\alpha(1+\frac{a\rho}{R})} - 1\right)$$

Here ρ is the normalized radius $\frac{r}{a}$, a the total plasma radius, $\omega_p(\rho)$ the plasma frequency, ω_c the cyclotron frequency at the plasma center, $\alpha\omega_c$ the frequency of the radiation, mc^2 the rest mass energy of the electron, kT_e the electron thermal energy, R the major radius of the plasma. The incident power P_i divided by the volume inside the resonant surface $\pi r_c^2\ 2\pi R$, is denoted by $\overline{P_i}$.

The diameter of the microwave heating beam is assumed to be small compared to the diameter of the plasma ; the absorbed power is assumed to heat an entire toroidal shell of plasma of width $\Delta\rho$ and this is calculated for the region in the plasma $\rho_c \geq \rho \geq 0$. The evolution of the discharge in time and space is then calculated by MAKOKOT (2).

The results of these numerical calculations depend on the assumptions made about the scaling of the energy confinement time τ_E. In particular, in MAKOKOT τ_E is taken to vary as the electron temperature to the three-quarters power.

For TFR (R_o = 98 cm, a = 20 cm) with a toroidal field B_T = 30 kG, a plasma current I_p = 200 kA, a density profile $N(r) = 5\times10^{13}\ (1 - (\frac{r}{a})^2)$ and a given impurity profile, a steady state discharge was calculated using MAKOKOT. The ohmic heating power for the calculated discharge was 350 kW, central electron temperature 1200 eV, and Q(a) = 3.1, in reasonable agreement with the parameters obtained in TFR discharges for the above initial conditions.

Electron cyclotron heating power F_c = 81.5 GHz, P_i = 150 kW, (absorbed power ~140 kW for one transit through the plasma) was applied with the resonance zone close to the plasma center, r_c = 3 cm, and the evolution of the discharge calculated (Fig. 1).

The electron temperature at the center rises very rapidly to 1900 eV ($\Delta T_e \simeq 700$ eV). However, one pays for heating the electrons immediately, and the ohmic heating power decreases substantially. Very little ion heating is observed due to the difference between the energy confinement time τ = 12.2 msec, and the electron-ion equilibration time τ_{eq} = 36 msec for $T_e \simeq 1300$ eV, as calculated from the Spitzer formula. The change in Q at the center of the discharge with time indicates that the current profile is strongly modified by the heating, but on a much longer timescale compared with that for the temperature.

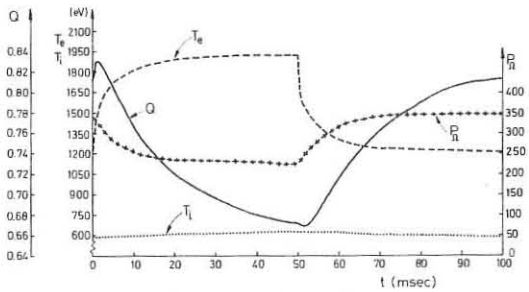

Fig. 1 - TFR with P_i = 150 kW, r_c = 3 cm

Another case considered for TFR was with electron cyclotron heating power approximately equal to the initial ohmic heating power (P_Ω = 350 kW). The effect of the heating power (P_i = 320 kW, F_c = 76.4 GHz, r_c = 9.4 cm) is shown in Fig. 2. The electron temperature at the center of the plasma rises from 1200 eV to 4200 eV for a 200 msec heating pulse, while the ion temperature remains almost unchanged. The ohmic heating power decreases to less than 50 kW, so that such a discharge is really dominated by external heating. The abrupt decrease in the central Q after the heating stops, without a disruption of the discharge, may indicate that the heating should diminish over several tens of milliseconds when such large modifications of the temperature and current profile occur.

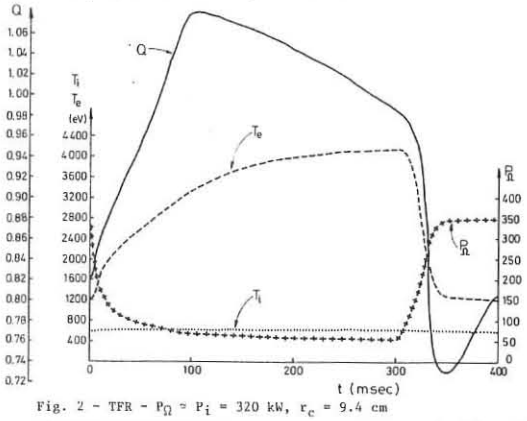

Fig. 2 - TFR - $P_\Omega \simeq P_i$ = 320 kW, r_c = 9.4 cm

Electron cyclotron heating on T-10 (R = 150 cm, a = 36 cm) has also been investigated using MAKOKOT. This is particularly relevant since T-10 is the only large tokamak which is attempting to use this heating method ($P_i \simeq$ 350 kW, 85 GHz, 100 msec pulse).

For T-10 with a toroidal field of 30 kG, a plasma current of 500 kA, a density profile $N(r) = 5\times10^{13}\ (1 - (\frac{r}{a})^2)$ and a given impurity profile, a steady state discharge was calculated using MAKOKOT. The ohmic heating power in this discharge was 750 kW, the central electron temperature about 1200 eV, and Q(a) = 3.1 in reasonable agreement with parameters obtained in T-10 discharge for the above initial conditions.

The evolution of the discharge with a heating power of 340 kW ($F_c \simeq$ 76.4 GHz) and a resonant surface located at r_c = 14.7 cm, is shown in Fig. 3. There is a significant rise in both electron (ΔT_e = 200 eV) and ion (ΔT_i = 160 eV) temperature, as well a decrease in the ohmic heating power for a 100 msec pulse. Due to the longer confinement time in T-10 (τ_E = 308 msec for these plasma conditions) the ions and electron temperatures are closely coupled. The rise in Q(r=0) indicates that the temperature and current profiles are also significantly modified, but that the current profiles modification takes place on a much longer timescale compared to the temperature profile modification.

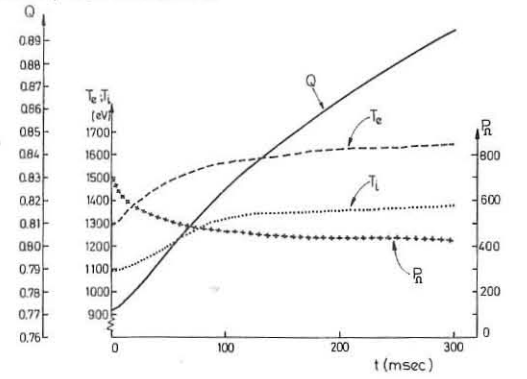

Fig. 3 - T-10 Discharge with P_i = 340 kW, r_c = 14.7 cm

It is well known that electron do not behave classically with regard to heat transport and energy confinement time in tokamak plasmas. This is taken into account in MAKOKOT by multiplying the electron heat conductivity diffusion coefficient inside the Q = 1 surface by a factor of 8 to account for the effect of saw-tooth oscillations and other non-classical effects. For the steady state discharges (the target plasmas) computed by MAKOKOT the Q = 1 surface was located at ρ = 0.5. Thus, it appears that the enhanced heat conductivity which exists in this region does not prevent significant modification of the current and temperature profiles. For all of the cases studied the resonant surface was inside the Q = 1 surface.

The results of the computer simulation clearly show that both plasma heating and profile control are possible with electron cyclotron heating.

/1/ Yu. N. DNESTROVSKII et al., Sov. Phys. Tech. Phys., 8, 691 (1964).
/2/ MAKOKOT Report EUR-CEA-FC-CISI ; EUR-CEA-FC-832 (1977).

AP7

EMISSION AND TRANSMISSION MEASUREMENTS
AT THE ELECTRON CYCLOTRON FREQUENCY ON TFR
TFR GROUP

ASSOCIATION EURATOM-CEA SUR LA FUSION
Département de Physique du Plasma et de la Fusion Contrôlée
Centre d'Etudes Nucléaires
Boite Postale n° 6 , 92260 FONTENAY - AUX-ROSES (FRANCE)

Measurements of the electron cyclotron emission at the fundamental frequency and at the second harmonic have been successfully used for measuring the time and space variations of the electron temperature./1//2//3/

In this paper we report measurements of the emission and transmission at the electron cyclotron frequency carried out on the TFR 600 tokomak. The experimental arrangement consists of a set of two opposite circular horns positioned in the equatorial plane followed by oversize circular waveguides ending in a microwave polarimeter which divides the wave polarization in two perpendicular direction. A microwave superheterodyne receiver with a single end broad band mixer has been used and the location of the emitting or absorbing region has been selected by setting the value of the local oscillator frequency in the interval 113-140 GHz.

In order to obtain absolute values of the electron temperature an accurate calibration of the receiver over the total frequency band has been carried out by using a calibrated noise source emitting like a black body at a known temperature. The overall accuracy in the calibration is not better than 10 % limited by the low frequency drift in the amplifier gain and in the source emission.

A detailed study of the wave propagation through the circular horns and waveguides has been also made to be sure that the polarization of the received radiation is not modified before reaching the microwave polarimeter.

Polarization measurements of the emitted radiation have been performed using the horn positioned in the high toroidal field side of the torus to avoid the evanescent region in the extraordinary mode propagation. It was found that, in agreement with the previous results obtained on PLT, /3/ the amount of the radiation is the same in the ordinary and extraordinary mode both emitting as a black body at the local value of the electron temperature T_e.

With the frequency of the local oscillator fixed to select the emission in the plasma center a vertical scan of the emission has been made by moving shot by shot the receiving horn. The low B field side horn was used and the ordinary polarization was selected. The results are shown in Fig. 1. For one dimensional antenna the output of the receiver is proportional to $P = kT_e\,\Delta f(1 - e^{-\tau})$ where $(\frac{\Delta f}{2}) = 250$ MHz is the band of the receiver and τ is the optical thickness for the ordinary mode given by $\tau = \pi^2 \frac{\omega_p^2}{\omega_c^2}\left(1 - \frac{\omega_p^2}{\omega_c^2}\right)^{1/2} \frac{kT_e}{mc^2} \frac{R}{\lambda_c}$, where ω_p and ω_c are the plasma and electron frequency, R, the major radius and λ_c the wavelength of the measured frequency. In Fig.1 is also shown the radius r_o for which $\tau = 1$ calculated from the electron density and temperature measurements. For $\tau > 1$ ($r < r_o$) it is expected that the measured power is proportional to the local electron temperature and that clearly appears from the good agreement with the values of T_e obtained by laser Thomson scattering. For $r > r_o$, as the radius increases to the limiter radius a = 20 cm, the temperature from cyclotron emission increasingly exceeds the expected one. This result can be explained by wall reflections of the radiation emitted at the same frequency (defined by the receiver local oscillator) by the hottest region of the plasma dominating the radiation emitted by the peripheral (colder) region seen directly by the horn.

This effect is more evident in the results shown on Fig. 2. Here the limiter radius was set at a = 17 cm and the density was 1.8 times less than the previous case. The emission, ordinary polarized, was measured along the major radius R by changing the frequency of the local oscillator and vertically by moving the receiving horn up and down. The emission horizontal profile presents the expected feature of the T_e profile decreasing almost to zero at the limiter radius. Now the wall reflections for $r > r_o$ ($\tau < 1$) play a favourable role bringing the emission to the thermal level since $P = \left[kT_e(1 - e^{-\tau} \right]/1 - \eta e^{-\tau}$ where η is the wall reflectivity. Values of η close to one are expected /4/ for metallic walls, thus the measured power is still proportional to the maximum value of T_e at the radius selected by the receiver. Unfortunately the available measurements of T_e by Thomson scattering are not accurate enough to obtain by comparison with the emission date, a measured value of η.

The vertical profile exhibits the same feature as shown in Fig. 1. Note that measured emission at $r > a$ remains at a constant value which is close to the average plasma temperature in the region $r > r_o$. This can be explained considering that for $r > r_o$ the reabsorption of the radiation reflected by the walls is very efficient giving a small (negligeable) contribution to the radiation collected by the horn.

With the same conditions of Fig. 2 a search has been made for turbulent temperature fluctuations. The power spectrum of the electron temperature signal was observed to be flat in the 0-10 MHz region. This can be explained as follows : for a receiver output voltage V_o (proportional to the square root of the DC output power P_{DC}, the time averaged signal $< V_o >$ is : $< V_o > \propto \sqrt{P_{DC}} = SG\,kT\,\Delta f$ where S is the square law detector constant, G the receiver gain, Δf the bandwidth and kT the electron temperature plus receiver noise temperature. Assuming the signal is integrated for t seconds, the RMS fluctuation in the output is $\sqrt{P_{NOISE}} = SG\,kT\sqrt{\frac{\Delta f}{t}}$. Thus a black body at temperature kT will have a flat noise spectrum with the magnitude of the fluctuations determined by the integration time of the receiver.

This result is in contrast to that observed on the PLT tokamak where a non-flat spectrum was observed out to 0.45 MHz. /5/

In some cases a broad peak was found in the noise spectrum at 30 MHz, which corresponds to the ion cyclotron frequency for deuterium at 40 kG. This feature is not well understood and is being investigated in more detail.

Transmission measurements for the ordinary mode polarization have been performed by two opposite horn in the equatorial plane in the direction perpendicular to the toroidal field. Refraction effects are found to be important only if the peak density is larger than $5 - 6 \times 10^{13}$ cm^{-3}. These can be taken into account by measuring transmission through the plasma at a frequency at which the resonant layer is not present in the machine and comparing to the transmission measured with the resonant layer present. The results are shown in Fig. 3. Density and electron temperature obtained by infrared laser interferometer and Thomson scattering have been used to calculate the normalized transmitted power at the frequency of interest $P_t/P_i = e^{-\tau}$. The good agreement between the calculated and directly measured values of τ is a good check of the hot plasma theory for cyclotron absorption. It is also a further confirmation of the experimental results of the emission previously presented.

Since high directivity horns have been used the transmission measurements are independent of the wall reflection. Then an accurate measurement of τ in the plasma border can be used to obtain a local value of T_e if the density profile is known. This can be of considerable interest because of the lack of T_e measurement in the plasma border where radiation and wall interactions dominate the heat transfer.

REFERENCES

/1/ TFR GROUP - Proceedings 7th European Conf. on Controlled Fusion and Plasma Physics, Lausanne 1, 14b, (1975).

/2/ BROSSIER P., COSTLEY A.E., KOMM D.S., RAMPONI G., TAMOR S., Proceedings of the 6th Intern. Conf. Berchtesgaden (1976) Vienne IAEA 1 (1977) 409.

/3/ HOSEA J., ARUNASALAM V. and CANO R., Phys. Rev. Lett. 39, 408, (1977).

/4/ COSTLEY A.E., HASTIE R.J., PAUL J.W.M., CHAMBERLAIN J., Phys. Rev. Lett., 33, 758 (1974).

/5/ ARUNASALAM V., CANO R., HOSEA J. and MAZZUCATO E., Phys. Rev. Letters 39, 888, (1977).

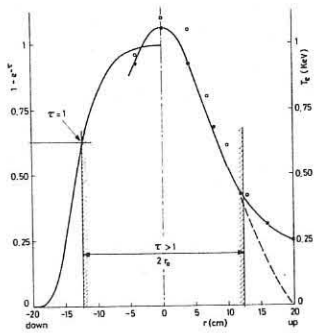

Fig. 1

Electron temperature profile at t = 200 ms obtained by moving vertically the receiver horn (·) compared with the Thomson scattering measurements (o). The absorption factor $A = 1 - e^{-\tau}$ is also shown (solid line) calculated from the experimental density and temperature profiles B = 50 kG, I_p = 300 kA, T_{eo} = 1,1 keV, n_{eo} = 1,16 10^{13} cm^{-3}, a = 20 cm.

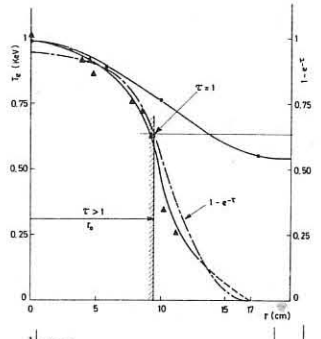

Fig. 2

Electron temperature profiles from cyclotron emission along the vertical (·) and horizontal axis (+). The dotted line is the absorption factor $A = 1 - e^{-\tau}$, B = 42 kG, I_p = 150 kA, T_{eo} = 1 keV, n_{eo} = 6,35 10^{13} cm^{-3}, a = 17 cm.

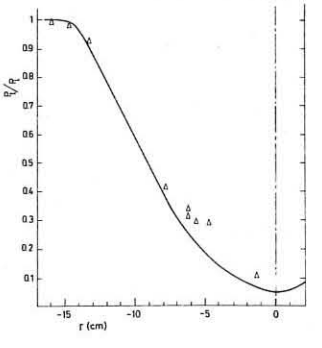

Fig. 3

Measured transmitted power P_t normalized to the incident P_i versus radius (Δ). The solid line is the attenuation $\frac{P_t}{P_i} = e^{-\tau}$ calculated from the experimental density and temperature profiles. B = 45 kG, I_p = 150 kA T_{eo} = 1,4 keV, n_{eo} = 6, 10^{13} cm^{-3}, a = 18 cm.

AP8

MHD RESONANT HF HEATING IN THE R-OM STELLARATOR

A.G.Kirov, L.F.Rouchko, A.V.Sukachov, E.A.Meleta, I.Ya.Kadysh

Sukhumi Institute of Physics and Technology of the State Committee on Utilization of Atomic Energy. Sukhumi, USSR

ABSTRACT: The results on HF plasma heating in the R-OM Stellarator using MHD resonance at $\omega < \omega_{Bi}$ frequencies are presented.

Experimental and theoretical Studies on additional HF heating of thermonuclear plasmas using plasma column MHD oscillations excited at $\omega < \omega_{Bi}$ frequencies are getting sufficiently common at present /1-9/. This method may be conventionally called as MHDR heating (MHD resonance heating). As it follows from the theory /2-4/, the two resonance situated close to each other can be discerned within this frequency range: a locally excited shear Alfven wave and a helical resonance, i.e. excitation of plasma column eigenmodes when the amplitudes of both fast magnetoacoustic wave and the Alfven wave are increasing in the plasma. Both of these resonancies occur provided $\omega/K_{\parallel} > C_A$ for the plasma centre. Experimentally effective plasma heating under above condition was found by us in the R-O device in 1966 /1/.

For the recent years, investigations on efficient MHDR heating were carried out in toroidal devices R-02 /5/, Proto-Cleo /7/ and Heliotron-D /8/. As distinct from the experiments in the R-02 Stellarator ($l=2$) where the HF winding had a spatial $m=2$, $n=6$ structure the HF winding in the R-OM Stellarator ($l=3$) /10/ has a $m=2$, $n=2$ one. The device parameters allowed, as in R-02, to investigate the heating over the wide range parameters: $B_o = 1\text{-}8$ kGs, $\iota = 0,1\text{-}1$, $n_e = 0.5 \cdot 10^{13} - 2 \cdot 10^{14}\,cm^{-3}$, $\omega = 2,5 \cdot 10^6$ and $5 \cdot 10^6\,s^{-1}$, H_2, He and Ar were used. HF generators allowed us to feed up to 1MWT (pulse duration 2,5 ms) into plasma and the HF field could be either travelling ($\pm m, \pm n$) or standing type.

The goals of the experiments have been to investigate the heating efficiency both in Alfven and helical resonance regions, the MHD stability of plasma with the Ohmic current and without it, the plasma density and energy confinement during the heating.

During the experiments, the plasma density was measured by 2.3-mm microwave interferometry; the ion temperature by the Doppler broadening of ion spectral lines and HF fields by magnetic probes. The power absorbed by the plasma and its diamagnetic signal were determined as well. As it follows from the Alfven resonance condition

$$\omega = K_{\parallel} C_A = \frac{B}{R\sqrt{4\pi n_i m_i}}\,(n - mi) \qquad (I)$$

there exists some critical value of the magnetic field and when it is exceeded the Alfven resonance condition is not fulfilled anywhere within the plasma. This fact is well displayed in the experiments when measuring the heating efficiency dependence upon the magnetic field (Fig.I, curve I). The field critical value at which the heating is stopped has to increase on increasing the density (curves I,2). The B_{cr} dependence upon the rotational transform and the frequency is illustrated by curves I,3 where growth of B_{cr} with the frequency is compensated by the rotational transform decrease when the pressure is unchanged. The pressure increase led to the essential growth of B_{cr} (curve 4). On increasing the ion masses (Ar), the heating was initiated at lower initial densities. In the H_2 discharge the heating took place at higher plasma densities. The critical field value rather well coincided quantitevly with that calculated from (I).

The HF field measurements within the plasma by magnetic probes showed the periodic structure. When B_o approaches to the critical field and the resonance point being shifted into the plasma, the internal magnetic probes registered a considerable growth of the HF field. In this region HF field had radially travelling wave structure. With the fields I.5 - - 2 times lower than B_{cr}, when the resonant point had to shift toward the plasma boundary, all of the probes within the plasma showed some increase of the HF field which we relate with the helical resonance. At the same time there appeared some increase in plasma heating (curve 3, Fig. I).

The plasma energy against the HF field grew faster than $\tilde{B}_{\varphi}^2$ which evidently indicates the existence of additional nonlinear dissipation mechanisms at large amplitudes of the HF field. With the HF fields at the plasma boundary 100-150Gs, the HF power absorption reached 10-20 Wt/cm^3 within the plasma The plasma energy content reached 6.10^{15} eV/cm^3 and was close to the limiting equilibrium value. The maximum ion temperature in He measured by broadening of impurity lines was 100-120 eV which was close to the diamagnetic temperature.

The change in the HF field rotation direction did not result in a considerable variation of heating efficiency. However when the wave is rotated in the direction of the electron diamagnetic drift, low frequency oscillations and an increased density decay took place. With the HF field switched on the plasma column stability was considerably improved and the Ohmic current grew 2 or 3 times indicating the electron temperature increase. In optimum regimes with H_2 the energy life time was about 40 μs that was close to the pseudo-classical time (B_o=7kGs, a=3,5cm, ι=0,5).

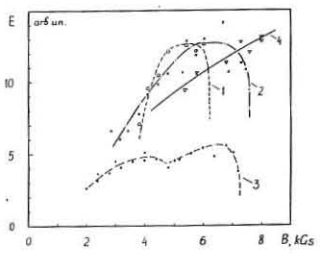

Fig.I. Plasma specific energy vs B_o
1. ι = .26, p=1.3.10^{-3} torr, f=.4 MHz,
2. ι = .26, p=2.6.10^{-3} torr, f=.4 MHz,
3. ι = .06, p=1.3.10^{-3} torr, f=.8 MHz,
4. ι = .37, p=5.2.10^{-3} torr, f=.4 MHz,

The authors are grateful to R.A.Demirkhanov, for his helpful attention and encouragement, N.I.Malykh, A.V.Njushkov and A.M.Abzianidze for their assistance and V.P.Sidorov, S.N.Lozovsky, A.G.Elfimov, F.M.Nekrasov and S.E.Ilyinsky for useful discussions.

1. R.A.Demirkhanov, A.G.Kirov, M.A.Stotland, N.I.Malykh. II Europ.Conf. on Contr.Fus. and Plasma Phys. Stockholm, 1967, Plasma Physics 10, 444 (1968).
2. L.Chen, A.Hasegava, Phys. Fluids 17, 1399 (1974).
3. J.A.Tataronis, W.Grossmann, Nucl.Fusion 16, 667 (1976).
4. А.Г.Елфимов и др. Препринт СФТИ-2, Сухуми, 1976.
5. R.A.Demirkhanov et al. 7-th Europ.Conf. on Contr.Fusion and Plasma Phys., Loussane, Switzerland, 1975, p. 148.
6. A.G.Dikij et al. in Plasma Phys. and Contr. Nucl. Fus. Res., Berchtesgaden, 1976, vol. II, p. 129.
7. S.N.Golovato et al. Phys. Rev. Lett. 37, 1272 (1976).
8. K.Uo et al. in Plasma Phys. and Contr. Nucl. Fus. Res., Berchtesgaden, 1976, vol. II, p. 103.
9. Pochelon, R.Keller, Helv. Phys. Acta 50, 172 (1977).
10. Р.А.Демирханов и др. Препринт СФТИ-4, 1970.

THE RF-METHOD FOR CURRENTLESS PLASMA PRODUCTION AND HEATING

S.S.Kalinichenko, P.I.Kurilko, A.I.Lysoivan,
N.I.Nazarov, K.N.Stepanov, V.F.Tarasenko,
O.M.Shvets

Physico-Technical Institute, the Ukrainian Academy of Sciences, Kharkov, USSR

A B S T R A C T

This experimental study has been carried out to get a better insight of the toroidal plasma production and heating conditions by employing the RF-method within the $\omega \lesssim \omega_{ci}$ frequency range. This has been accomplished by applying various RF power input systems. As a result, slot type antennas have been clearly demonstrated to suit best for the purpose of a high-level RF power input into plasma. Also, the dense toroidal plasma was shown to get produced only when Ion Cyclotron Waves (ACW) and Alfven Waves (AW) are being intensively launched.

INTRODUCTION: Many an experiment on the RF plasma heating within the frequency range of ion-cyclotron order of ($\omega \sim \omega_{ci}$) that we have previously performed on the mirror devices [1,2] , also later on the toroidal ones [3,4] ,demonstrated the feasibility of plasma heating by way of the Fast Magnetosonic Waves (FMSW), Ion-Cyclotron Waves (ICW) and Alfven Waves (AW). The same experiments have proven the effectiveness of the RF plasma producing method, and this is of vital importance for a better look into plasma confinement process in stellarators under currentless conditions. The present paper gives the results of the experimental study of the RF power input efficiency by means of various exciters, and it also looks into the toroidal plasma producing fac tors under ICW and AW exciting conditions as well as those of plasma heating by the above waves. Besides, we have also investigated the influence of the impurity accumulation on the RF heatin process. The ab ove research has been performed on the Omega toroidal device [4] and on the Uragan-2 l=3 stellarator [3]

RESULTS AND DISCUSSION: For experimental investigation of plasma production and wave generation in the vic inity of the ion-cyclotron frequency the RF power was put in through the medium of the low-impedance slot-type wave launching structure (WLS) (Fig.1). Experiments have shown that, voltage in the wave launcher not exceeding U ≈ 20kV, the RF power feed-in is liable to reac h the level of $P_{RF} \approx 1.3$ MW (antenna efficiency 60 %). Fig.2 shows the time relations of plasma density n_e and transversal ion energy $T_{i\perp}$, generated by treating the diamagnetic signal on the assumption that the main contributors to nT_i are ions. The transversal ion energy at the initial phase of RF discharge was of considerable magnitude (several keV) and that was indicative of

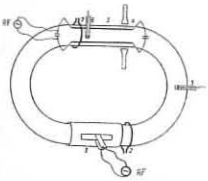

Fig.1. Uragan-2 RF experiment:
1-Slot WLS; 5- Frame WLS;
2,7- Diamagnetic probes;
3,6- RF magnetic probes;
4- Microwave interferometer(λ=4&).

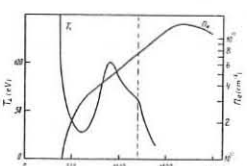

Fig.2.The time behavior of RF plasma transversal energy $T_\perp$ and its density n_e (hydrogen gas, $P_0 = 2 \cdot 10^{-5}$ Torr, H=14.3 kOe, Ω=0.95, f = =20.8 MHz, slot antenna).

the possible neutral (hydrogen) gas ionization by high energy ions. Aside from using the shortlength ICW ($k_\parallel a \sim 1$) the effective plasma heating can be brought about by either a longwave ($k_\parallel a < 1$) FMSW [4] or ion-ionhybride resonance [5]. And also perspective may prove the inhomogeneous plasma heating methods using the AW [6,7]. We have carried out a series of experiments in order to investigate the plasma producing conditions, as well as those of waves excitement and absorption in the alfven frequency range. The RF power input was effected by dint of a quadripolar frame launching structure which had been placed inside the vacuum chamberwithout insulation [3] (Fig.1.).

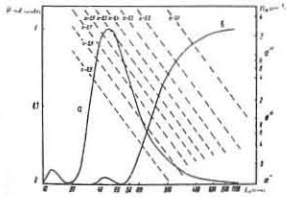

Fig.3. Transversal component longitudinal spectra of the $\bar{H}_\perp$ magnetic field, generated by slot(a) and frame (b) antennas ($P \sim \bar{H}_\perp^2(\lambda_\parallel)$), and alfven resonance lines in the ($n_e, \lambda_\parallel$) coordinates.

As a matter of fact, a discrete number of longitudinal wave modes $\lambda_{\parallel n} = L/n$ is excited in the toroidal plasma resonator, where L is the torus axial length (for the Uragan-2 L=1035 cm) and n is the mode number. The relative amplitude of each mode depends on structural peculiarities of wave launchers and, consequently, on the spectral characteristics of the RF field which they radiate inwards (Fig.3). This spectral variation of the RF field is a predeterminig factor for range variability (along the longitudinal magnetic field) of the RF plasma production (Fig. 4,5). The analysis resulted in the restriction of efficacious ionization and achieved level of high density plasma ($n_e \approx 4 \cdot 10^{12} \div 10^{13}$ cm^{-3}) to the regimes of ICW and AW effic ient excitement. That occurs only when a local alfven wave resonance is existent in plasma for $\lambda_\parallel$ values of considerable spectral intensity.

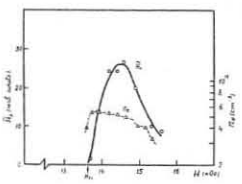

Fig.4. The RF toroidal plasma producing method involving the ese of slot WLS under the conditions of ICWexcitement, where $\bar{H}_\perp$ is wave field amplitude at plasma's center ($a \approx 6.8$ cm).

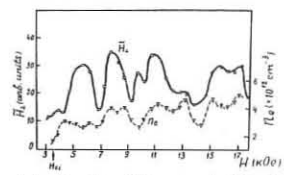

Fig.5. The RF method for toroidal plasma production using frame antenna in the AW excitement regime, where $\bar{H}_\perp$ is wave field amplitude in the proximity of plasma's border-line($a = 6$ cm).

AW, while propagating inside the plasma from the resonance affected area, damps due to Cherenkov distant electron absorption $\Delta z \ll a$, where a is plasma radius and

$$\Delta z \sim a\left(\vartheta_{Te} \cdot \vartheta_A / \vartheta_\parallel a\right)^{2/3} \qquad (\vartheta_{Te} \geq \vartheta_A)$$

However, the AW packet has ample time to make several revolutions round the torus before covering this distance along the radius. Those revolutions number:

$$N \sim \lambda_\parallel \left(\frac{\vartheta_{Te}}{\vartheta_A} \cdot \frac{a^2}{R^2}\right)^{1/3} \gg 1$$

This happens because there exists a great difference between AW radial and longitudinal group velocities. This fact gives us the reason why AW propagate well around the torus and are launched without hindrance (as is the case with our experiments) by the limited range antenna despite a heavy absorption. That is why the antennas do not necessarily surround the entire torus to excite them.

The emerging of the impurities in plasma and the decreasing density of resonant ions during the RF pulse final phase, this all leads to severe restrictions in the RF heating methods employment (Fig.6.). And the interferometrical measurements of the electron concentration indicate its growth at that. Non-linear phenomena may occ ur in plasma when small-(or even medium-) sized devices are used for RF experiments. Those phenomena tend to check the RF heating on account of an energy release on plasma's periphery with ensuing plasma contamination and cooling down by impurities influx from the walls.

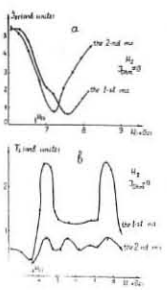

Fig.6. The influence of non-resonant ions concentration increase on the RF power absorbed in plasma:
a - ICW power absorption in the Ohmic plasma at the 1-st and the 2-nd ms from the beginning of RF discharge;
b - same for currentless plasma.

CONCLUSIONS: Thus, the research under consideration has clearly demonstrated that, given the right choice of parameters (wavelength spectrum of the WLS, confining magnetic field strength, RF generator power level and frequency range), both, the dense currentless plasma produc tion under the conditions of ICW and AW intensive excitement, as well as its heating, are quite possible. To serve these purposes the low impedance slot WLS helps resolve the problem of the isulator electric reliability of a high level (~ 1 MW) RF power input nodes as well as use the slots in the chamber's first wall as radiating antennas.

R E F E R E N C E S

1. N.I.Nazarov, et al. Zh.Tekh.Fiz., 32, 536 (1962).
2. O.M.Shvets, et al. Zh.Tekh.Fiz., 35, 2185 (1965); 39,610,(1969)
3. A.G.Dikii, et al. Plasma Physics, 18,577 (1976);
The 6-th Int.Conf. on Plasma Phys. and Contr. Nucl. Fusion Research, V.II,p.*129 (IAEA, Vienna, 1977).
4. S.S.Kalinichenko, et al. Fizika Plasmy, 3, 118 (1977).
5. V.F.Tarasenko, et al. The 5-th Eur. Conf. on Contr. Fusion and Plasma Phys., v.I, p.112 (Grenoble, 1972).
6. V.V. Dolgopolov, K.N.Stepanov. Nuc l.Fusion, 5, 276 (1965).
7. L.Chen, A.Hasegawa. Phys.Fluids, 17, 1399 (1974).

AP10

STOCHASTIC ION HEATING BY AN ELECTROSTATIC WAVE IN A SHEARED MAGNETIC FIELD

Y. GELL* and R. NAKACH

ASSOCIATION EURATOM-CEA
Département de Physique du Plasma et de la Fusion Contrôlée
Service IGn - Centre d'Etudes Nucléaires
85 X - 38041 GRENOBLE CEDEX (France)

* Department of Physics and Astronomy - Tel-Aviv University
TEL-AVIV, ISRAEL

The hot ion tail in the ion velocity distribution observed in lower-hybrid heating experiments[1] has motivated lately a considerable amount of research interest in the mechanism responsible for its formation. Special attention was given to the possibility that stochastic acceleration of ions due to electrostatic waves propagating in the plasma may play an important role in this unexpected and unwanted strong heating of a selective part of the ion population. Considering r.f. electrostatic waves propagating in the plasma perpendicularly to the homogeneous magnetic field, Fukuyama et al.[2], and Karney and Bers[3] have demonstrated the possibility of stochastic ion heating due to nonlinear resonances between the motion in the electrostatic wave and cyclotron oscillations.

However, present day experiments make it difficult to estimate the significance of this heating mechanism when compared with other mechanisms which might lead to the same phenomenon. A first step in understanding and consequently in preventing this undesired effect could be the isolation of an external physical parameter which would affect differently the heating process accordingly to which mechanism is operating. The purpose of this paper is to suggest the shear of the magnetic field as a possible candidate for the above mentioned role. Specifically, we show that magnetic shear effects may be rather important in the stochastic heating process, while as was pointed out by Berger et al.[4], they should not be of great significance in heating effects due to parametric instabilities. Thus, evidence for the dependence of the heating process on the shear parameter should serve as a consistency indicator for the operation of the stochastic heating mechanism.

We consider the motion of an ion in the presence of an electrostatic wave with frequency in the lower-hybrid range $E_o\cos(kY-\omega t)\vec{e}_y$ and a sheared magnetic field $B_o\,(\vec{e}_z + X/L_s\,\vec{e}_y)$ where L_s is the shear length. Normalizing time to Ω^{-1} ($\Omega = eB_o/m_i$) and lengths to k^{-1} we find the equations of motion.

$$\ddot{X} = -\beta u_o X - \frac{\beta^2 X^3}{2} + \dot{Y} \quad ; \quad \ddot{Y} = \alpha\cos(Y-\nu\tau) - \dot{X} \qquad (1)$$

where $\beta = (kL_s)^{-1}$ is the shear parameter, $\alpha = eE_o k/m_i\Omega^2$, $\nu=\omega/\Omega$ and u_o is a normalized constant of integration representing the Z component of the velocity at the plane X = 0.

In order to study the long time behavior of this system, we introduce action-angle variables $(I_i, \theta_i)(i = 1,2)$. A sequence of canonical transformations leads to the following Hamiltonian :

$$K = I_1 + \nu I_2 + \frac{\beta u_o}{2}(r\cos\theta_1 + I_2)^2 + \frac{\beta^2}{8}(r\cos\theta_1 + I_2)^4 - \alpha\sum_{m=-\infty}^{\infty} J_m(r)\sin(m\theta_1 - \theta_2)$$

where $r^2 = 2I_1 = \dot{X}^2 + \dot{Y}^2$, $I_2 = -(X+\dot{Y})$, $\theta_1 = tg^{-1}(\dot{X}/\dot{Y})$ (2)

$\theta_2 = \dot{X} - (Y-\nu\tau)$ and J_m is a Bessel function of order m.

By using this Hamiltonian we proceed to investigate the condition for onset of stochasticity, which is usually considered to be resulting from the overlapping of adjacent resonances. Quantitatively, this condition is expressed by the following inequality

$$T = \frac{\Delta\omega^{(n)} + \Delta\omega^{(n-1)}}{2\delta\omega} \gtrsim 1 \qquad (3)$$

where $\Delta\omega^{(n)}$ and $\Delta\omega^{(n-1)}$ are the widths of the "n" and "(n-1)" resonances respectively, and $\delta\omega$ is the distance in frequency between them. In order to estimate a quantity associated with a "n" resonance we assume that this resonance is isolated which amounts to keep in the infinite sum of the Hamiltonian (2) only the term corresponding to the integer n. Consequently, associated with a "n" isolated resonance there exists an adiabatic invariant $I_o = I_2 + \frac{I_1}{n}$ which can be used to reduce the system to a Hamiltonian system with one degree of freedom.

In our case, we find for the stochasticity criterion the following inequality :

$$T = \frac{2\alpha^{1/2} n(n-1-4I_{2o})}{\nu - I_{2o}(\beta u_o + 4 + \frac{5\beta^2}{2} I_{2o}^2)} \left\{\left[\gamma^{(n)} J_n(I_{\phi s}^{(n)})\right]^{1/2} + \left[\gamma^{(n-1)} J_{n-1}(I_{\phi s}^{(n-1)})\right]^{1/2}\right\} \qquad (4)$$

where $\gamma^{(n)}$ is the nonlinearity parameter and is given by

$$\gamma^{(n)} = \frac{\beta u_o}{n^2} + \frac{3\beta^2}{8}\left(1 - \frac{8I_{2o}}{n} + \frac{4\,I_{\phi s}^{(n)}}{n^2} + \frac{4\,I_{2o}^2}{n^2}\right)$$

Where I_{2o} represents the initial value of the action I_{2o} and $I_{\phi s}^{(n)}$ is the value of the action I_1 corresponding to the location of the elliptic singular point associated with the "n" resonance.

It should be stressed that this criterion is a non rigourous one, simplifying a rather complicated process by emphasizing the overlapping of primary resonances, neglecting correlations among resonances and secondary effects. The approximate nature of the criterion is apparent when considering small values of β. Within these limitations we can predict the threshold value of α for onset of stochasticity and proceed to compare it with the numerical solution of the equations of motion for various initial conditions and different values of the relevant parameters. Using the well known cross section of surface method, fixing the cross plane by the condition $\theta_1 = \pi/2$ we have studied the different patterns of the trajectories crossing points of the cut plane. From the theoretical analysis, as well as from the numerical solutions of the equations of motion, it turns out that the effect of shear is to reduce the threshold for stochasticity.

In order to investigate the possible hot tail structure in the ion velocity distribution, we translate the distribution of the crossing points into a particle velocity distribution by averaging in time over many cyclotron orbits the position of the particles in the velocity space. We have considered the distribution in velocity resulting from stochastic acceleration of 10 particles having the same initial velocity ($I_{10} = 450$, $I_{20} = 0$) but different phases (θ_2) for various values of β fixing $\alpha = 10$. The averaging procedure has been performed over about 1300 cyclotron orbits starting after the first 800 crossings. Normalized distribution functions for representative values of α and β are given in figure I. In this figure we see a pronounced tail in the distribution function depending however on β. As can be seen the effect of increasing the shear is to shift the tail towards a lower velocity range and an opposite effect results from increasing the amplitude of electrostatic wave.

Considering typical plasma parameters B_o=10 kG, T_i=1keV, $k\,a_i \sim 1$, we have $\beta \sim a_i/L_s$, a_i being the gyroradius of the ions, we find that for shearlengths Ls less than $\sim 90\,a_i$ the effect of shear on the stochastic process is noticeable. We conclude that inherently associated with the stochastic heating process is a formation of a hot tail in the ion velocity distribution. Moreover, it turns out that the shear of the magnetic field might provide an efficient mean to indicate whether the stochastic heating mechanism is operating. We find unexpectandly that the shear by shifting the tail to lower values of velocity can diminish the damaging effect of the ion tail formation phenomenon to the RF heating process by lower-hybrid waves.

REFERENCES.

1 - P. BLANC et al., in Plasma Physics and Controlled Nuclear Fusion Research (IAEA, Vienna, 1977), Vol. III, p. 49.

2 - A. FUKUYAMA, H. MOMOTA, R. ITATANI and T. TAKIZUKA, Phys. Rev. letters, 38, 13, 701 (1977).

3 - C.F.F. KARNEY and A. BERS, Phys. Rev. Letters 39, 9, 550 (1977).

4 - R.L. BERGER, LIU CHEN, P.K. KAW and F.W. PERKINS, Phys. Fluids, 20, 11 (1977).

FIGURE CAPTION.

Fig. 1 - The averaged velocity distribution in arbitrary units of ten particles starting with identical values of r (r=30) and evenly distributed in phase θ_2 ; $\alpha = 10$; $\nu = 30.23$, $I_{20}=u_o = 0$, $\theta_1 = \pi/2$ for different values of β (0.000, 0.015, 0.03). The averaging is performed over about 1300 cyclotron orbits starting after the first 800 crossings each curve is normalized by setting its maximum value equal to 1.

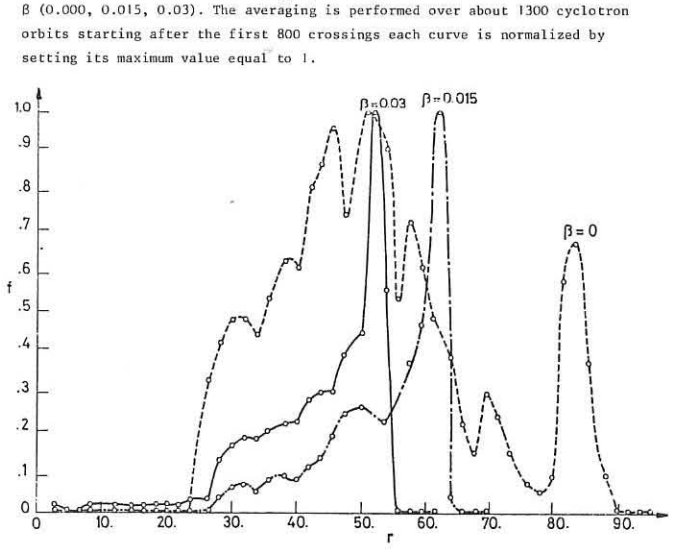

AP12

LOWER HYBRID EXPERIMENTS IN THE PETULA TOKAMAK

PETULA GROUP+

ASSOCIATION EURATOM-CEA
Département de Physique du Plasma et de la Fusion Contrôlée
Service IGn - Centre d'Etudes Nucléaires
85 X - 38041 GRENOBLE CEDEX (France)

The present paper deals with the application of high RF power near the lower hybrid (LH) frequency to a Tokamak discharge. A double waveguide grill antenna has been used to launch a 1.25 GHz-500kW-6 ms RF pulse in PETULA. One of the objectives of this study is to investigate the technological problems associated with LH heating and caused by the high level of RF power involved. Two aspects have been carefully studied : grill conditioning and grill coupling. The latter is strongly dependent on the scrape-off layer of the PETULA plasma and the observations are possibly not significant. The former aspect though not really understood is probably to be expected in other LH experiments. Plasma experiments have been carried out with a wide range of electron density 2. $<n_e$ axis $< 8.10^{13}cm^{-3}$ in both hydrogen and deuterium. For hydrogen this allows theoretically linear mode conversion to take place in the discharge. Although some heating has been observed, the experiments are not, as yet, very conclusive. The actual RF pulse duration is hardly larger than the ion energy confinement time, and the radial plasma displacement caused by the RF is not feedback controlled. The main discharge parameters were the following :plasma radius 14 cm, toroidal magnetic field 27 kG, plasma current 75 kA, loop voltage 1.6 V, $Z_{eff} \lesssim 2.$, $800 \lesssim T_e(o) \lesssim 1100$eV, $200 \lesssim T_i(o) \lesssim 350$ eV.

1 - GRILL BEHAVIOUR AT HIGH RF POWER.

In PETULA the RF power is delivered to the grill through a double window vacuum pumped waveguide. Experiments with grills of different widths have been successfully performed to launch transmitted RF power densities up to 10 kW/cm^2. However power transmission is only obtained once the grill is properly conditioned. Correlation between the incident and the reflected RF power clearly shows that arcing occurs during a conditioning period in two distinct phases : (i) the cleaning of the vacuum pumped waveguide, (ii) the cleaning of the grill extremity. If the machine has been opened to the atmosphere the two cleaning phases are required. Even if the machine has been kept under vacuum but not operated for a few days, still the second phase is required.

The RF network is designed to measure the natural plasma reflection coefficient without a matching system. The reflection coefficient behaviour versus RF power and RF phase ϕ_{RF} between the two waveguides has been extensively studied. The first grill (waveguide width 3.55 cm, total area 117 cm^2) behaves as previously /1/ with 100 µs RF pulse, i.e., the reflection coefficient with $\phi_{RF} = \pi$ decreases as the power increases : at low power it fits the Brambilla's theory /2/ and at 500 kW (4 kW/cm^2) it is quite small. We then tried another grill (w = 1.8 cm, total area 40 cm^2). The reflection coefficient is still better with $\phi_{RF}=\pi$ than any other RF phase as shown on Fig.1, but it increases with increasing power. The main difference with the first grill is the transmitted power density which is close to 10 kW/cm^2 for 500kW. All our observations could be summarized in the following way : at low power density ($\lesssim$ 1 kW/cm^2) the reflection coefficient is described by the theory /2/, at intermediate power density (~ 4 kW/cm^2) it has a minimum, at larger power densities it increases. This behaviour does not depend on either the plasma species (H_2 or D_2) or the plasma density. We do observe a minimum reflection when moving the grill radially (about 1 cm back to the limiter radius).

2 - PLASMA HEATING EFFECTS.

Most experiments were run with the w = 1.8 cm grill which has the following $N_{//}$ spectrum : 12 % of transmitted RF power P_{RF_t} for $N_{//} < 1.3$ (accessibility), 86 % of P_{RF_t} for $1.3 < N_{//} < 8.$ (Flat $N_{//}$ spectrum). As in other LH experiments, a density increase whose origin is not yet fully understood is triggered by the RF pulse. The initial electron density increase scales with P_{RF_t}, $1/P_{RF_t}\ \Delta\bar{n}_e/\Delta t \simeq 4.10^9 cm^{-3}/J$. This scale factor is lower than that observed in WEGA /3/. Here $\bar{n}_e$ is the line averaged electron density. The total density increase does not depend upon $\bar{n}_e$ for a given P_{RF_t}. We also observe a fast ion tail during the RF pulse that makes impossible any measurement of the central ion temperature $T_i(o)$ from our perpendicular charge exchange neutral analyzer. Strong H_β (or D_β) line intensity variations measured at different positions, especially in front of the grill, suggest important RF ionization at the edge of the discharge of the atoms enhanced by outgassing from the grill and the walls. This may explain the discrepancy between the central electron density $n_{e\,axis}$ measured by Thomson scattering and $\bar{n}_e$. Fig. 2 shows the time evolutions of differences with and without RF of the following parameters : H_β intensity in front of the grill, $\bar{n}_e$, radial displacement D_r, P_{RF_t}, and $T_i(o)$ from neutral analysis. During the RF pulse no major impurity contamination is observed. Relative OVI and C IV line intensity variations follow roughly the relative $\bar{n}_e$ time evolution. The plasma current remains constant whereas the loop voltage changes only slightly ($\lesssim$ 20 %). The raw ion temperature rise $\Delta T_i(o)$ is found to fit a $P_{RF}/\bar{n}_e$ scaling for hydrogen data, $\bar{n}_e\ \Delta T_i(o) \simeq 2.10^{15}$eV.cm^{-3} at P_{RF_t} = 350 kW, over a 1. to $5.10^{13}cm^{-3}\bar{n}_e$ range. Deuterium data obtained over a smaller $\bar{n}_e$ range are rather similar. The central electron temperature increase $\Delta T_e(o)$ is about 200 eV at $\bar{n}_e = 2.10^{13}cm^{-3}$ and follows a $1/\bar{n}_e$ scaling law as given by Thomson scattering and soft X-ray analysis. The T_e profile tends to peak and relaxes to the initial profile after the RF pulse. Present experiments do not allow us to conclude much about heating effects. The fact that the RF pulse duration is less or about the ion energy confinement time on axis, and the lack of data in the outer region of the discharge make it difficult to establish a total power balance with RF.

3 - CONCLUSION.

We have demonstrated that high RF power density up to 10 kW/cm^2 can be coupled to a Tokamak using a grill-type antenna. However the power dependence of the coupling is not explained by the present theory. The results in PETULA would suggest that if no RF matching network is used, it is necessary to limit the RF power density to a few kW/cm^2 to minimize the reflection coefficient. Short RF pulse LH experiments are not conclusive in terms of RF heating. More significant heating experiments are under preparation. A longer RF pulse will be used and the plasma discharge equilibrium during R.F. will be controlled to reduce the radial displacement.

REFERENCES.

/1/ - C.M. SINGH et al., Proc. 3rd Top. Conf. R.F. Pl. Heat., paper B3 (1978).

/2/ - M. BRAMBILLA, Nucl. Fus. 16, 47 (1976).

/3/ - H.D. PACHER et al. Proc. VIIth Conf. Innsbruck, Vol. I, 97 (1979).

+ G. MELIN, R. BARDET, M. BERNARD, P. BRIAND, G. BRIFFOD, M. CLEMENT, L. DUPAS, A. GAUTHIER, S.N. GOLOVATO, M. GREGOIRE, P. GRELOT, M. HESSE, R. LEGARDEUR, D. PINET, E. PORROT, C.M. SINGH, G. REY, B. TAQUET, J. WEISSE, S. ZYMANSKI.

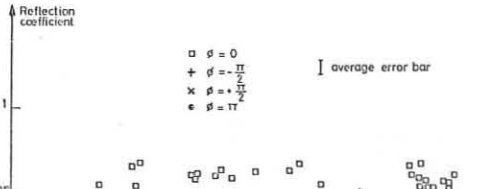

Fig. 1

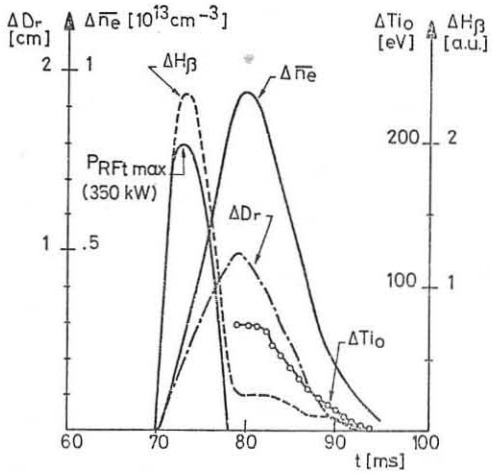

Fig. 2

AP13

THEORETICAL AND EXPERIMENTAL RESULTS ON THE COUPLED RESISTIVE-g/ION TEMPERATURE GRADIENT INSTABILITYTY

J G Cordey, T Edlington, W H W Fletcher, E M Jones, A C Riviere and D F H Start
Culham Laboratory, Abingdon, Oxon, OX14 3DB, UK
(Euratom/UKAEA Fusion Association)

ABSTRACT It is shown that shear in the magnetic field couples the resistive-g mode and ion temperature gradient instabilities to form a single strongly growing mode. For parameters appropriate to the Culham Levitron experiment the calculated mode structure is dominated by its resistive-g nature confirming the previous identification of the observed low frequency fluctuations. The frequency, growth rate and diffusion coefficient (γ/k^2) are compared with the experimental results. The scaling of diffusion with collisionality appears to be faster than predicted.

INTRODUCTION Recent experiments on the Culham Levitron[1] have shown that low frequency, ($\omega<\omega_*$) long wavelength ($k_\perp a_i<<1$) fluctuations are responsible for the diffusion in strongly collisional plasmas. Originally these fluctuations were thought to be drift waves but this seems unlikely since (a) collisional drift waves are stable in slab geometry[2], which is the appropriate geometry for these low m-number modes[1] and (b) the long wavelength is not a drift wave characteristic. Two instabilities which do have the right characteristics are the resistive-g and ion temperature gradient instabilities (see ref.1). These instabilities are similar, requiring $k_\perp a_i<1$ and having Im ω > Real ω. The major difference between them is that the electrons behave adiabatically ($k_\parallel^2 v_e^2<\omega\nu_e$) in the resistive-g instability, and isothermally $k_\parallel^2 v_a^2>\omega\nu_e$ in the ion temperature gradient instability. In a sheared magnetic field, the parallel wave vector of modes which are centred about a mode rational surface depends on the radial distance x from the mode centre; $k_\parallel = k_y x/L_s$. For such modes the electron behaviour in the inner region near the mode centre is adiabatic while in the outer region ($x > \sqrt{\omega\nu_e}L_s/k_y v_e$) the electrons behave isothermally. Thus the question arises as to whether there are two separate unstable modes, one having the character of a resistive-g mode and the other a temperature gradient instability, or whether there is just one unstable mode. By numerically solving the full radial eigenvalue problem it is shown that the modes couple together to form a single strongly growing mode.

THEORY The differential equation describing low frequency electrostatic instabilities can be obtained from the two fluid[3] equations as shown by Horton and Varma[4] and is written in the form

$$Pa_i^2 \frac{\partial^2\phi}{\partial x^2} + (Q + R + S)\,\phi = 0 \qquad (1)$$

where the functions P, Q, R and S are defined in ref.(5). Equation (1) was solved by a standard shooting technique. The dependence on magnetic field curvature is given in Fig.1. For zero curvature the mode is purely the temperature gradient instability. As (r_n/R_c) is increased (destabilising) the growth rate increases dramatically until at the end of the range the mode is resistive-g in character. The effect of shear on the resistive-g mode is shown in Fig.2. For the strongly collisional case the unnormalised growth rate, Im(ω), scales as $(L_s/r_n)^{0.5}$. For the weakly collisional case, $\nu_e/\omega_*=1$, the unnormalised growth rate is almost independent of L_s/r_n.

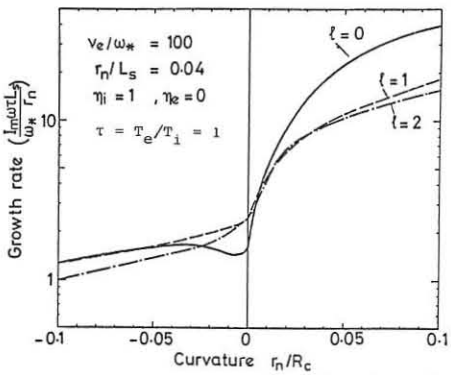

Fig.1 Normalised growth rate as a function of magnetic field curvature for radial mode numbers $\ell = 0$, 1 and 2.

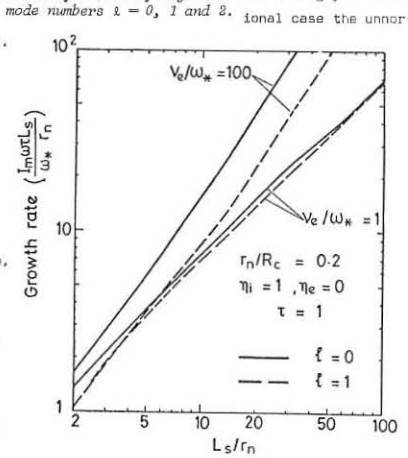

Fig.2 Normalised growth rate of the resistive-g mode as a function of shear parameter L_s/r_n.

EXPERIMENT Floating potential fluctuations were measured[1] in the Culham Levitron experiment (R=30cm, I_R=110kA, I_T=66kA, n(0)$\lesssim 10^{12}$cm^{-3}, $T_e(0)\approx$6eV and $P_{He}=10^{-5}$torr; $L_s^{-1}=I_T/I_R$). Low frequency (LF) waves ($f\lesssim$15kHz, $k_y a_i\lesssim$0.03) are seen on the outer density gradient where $\nabla B.\nabla p>0$ but not on the inner density gradient where $\nabla B.\nabla p<0$. Profiles of $\tilde{\phi}$ recorded as a function of I_T show that the LF waves are strongly damped at large I_T and are localised on mode rational surfaces[1]. As I_T increases changes in r_n mean that r_n/L_s is a slowly varying function whereas the curvature parameter, r_n/R_c, decreases significantly. The strong damping of the mode with I_T is thought to be due to this change in curvature as well as to shear stabilisation. The particle flux, Γ, calculated from the n, T_e profiles, is used to obtain a local diffusion coefficient, $D_{exp}=\Gamma/\nabla n$. It was found[1] that $D_{exp}/D_{class} \propto (I_T/I_R)^{-p}$ where $p\approx 2$ (here $D_{class} = \nu_{ei} a_e^2 (1+T_i/T_e)$). Thus the particle diffusion decreases as the mode amplitude decreases. In this paper further analysis of the data is compared with the theory of the coupled mode. The mode amplitude, $e\tilde{\phi}/kTe$, is compared with γ/ω_{*e} in Fig.3a showing the localisation of the modes is well predicted (the density profile peaks at 1.3cm and the outer edge lies at 4.5cm). In Fig.3b, D_{exp} is compared with D_{QL} ($=\gamma/k_x^2$). Towards the outer edge[6] D_{exp} diverges from D_{QL} where the collision frequency ν_{ei}/ω_{*e} is highest. A plot of $D_{exp}/\omega_{*e}a_i^2$ against ν_{ei}/ω_{*e} for discharges at several ECRH powers but fixed toroidal field (I_T/I_R = .6) is shown in Fig.4. The theory predicts $D_{QL}/\omega_{*e}a_i^2 \propto (\nu_{ei}/\omega_{*e})^{0.7}$ in disagreement with the data. The ranges of the other parameters in this data are $0.36\lesssim\eta_e\lesssim1.3$, $0.42\lesssim\eta_i\lesssim1$, $0.04\lesssim r_n/R_c\lesssim0.13$, $0.025\lesssim r_n/L_s\lesssim0.125$ and $0.65\lesssim T_i/T_e\lesssim0.85$. Inspection of the data shows that these variations together with the theoretical scaling in each case are not sufficient to remove the steep dependence on ν_{ei}/ω_{*e}.

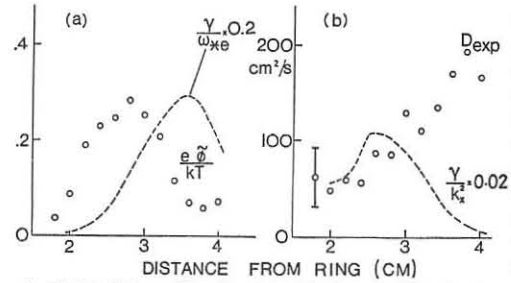

Fig.3(a) Radial profile of mode amplitude, $e\tilde{\phi}/kTe$, (open circles) compared with the theoretical growth rate γ/ω_{*e}. (b) Radial profile of experimental diffusion coefficient, D_{exp}, (open circles) compared with the quasi-linear estimate.

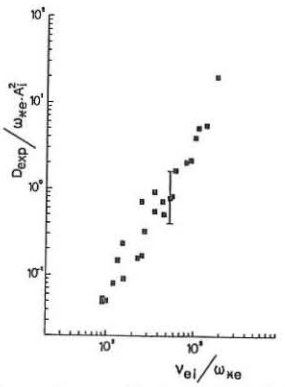

Fig. 4 The normalised experimental diffusion coefficient as a function of normalised collision frequency.

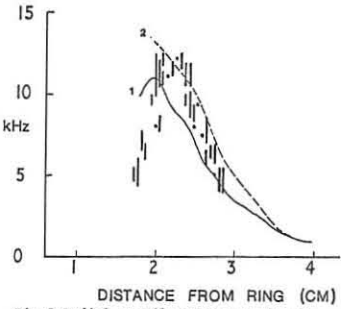

Fig.5 Radial profile of measured mode frequencies (vertical bars). Curve(1) is the predicted doppler frequency with $\omega_R=0$ and curve(2) is the doppler frequency with the theoretical ω_R added on.

Under the reasonable assumption of zero mass motion in the laboratory frame the frequency of the waves undergoes a doppler shift such that $2\pi f_{LAB}=k_y(v_{di}+v_{be})+\omega_R$ where $v_{di}=\nabla p_i/enB$, $v_{be}=2kT_e/eBR_c$. ω_R is the real frequency of the mode and $k_y=m/Rq$. Recent k_y measurements have confirmed that the LF $\tilde{\phi}$ waves have m=1 with lower amplitude m=2 and 3 present. The measured mode frequencies are shown in Fig.5 for the same discharge as in Fig.3. Curve 1 corresponds to f_{LAB} with $\omega_R=0$ and curve 2 to f_{LAB} with the predicted value of ω_R. There is reasonable agreement with the magnitude of the doppler shift and with the sign and magnitude of ω_R.

In summary, the localisation of the mode on the outer density gradient is successfully predicted by theory as are the sign and magnitude of the real frequency. The diffusion is more sensitive to collisions however than the quasi-linear model predicts.

REFERENCES

[1] Ainsworth N R et al, 1979 in Plasma Physics and Controlled Nuclear Fusion Research (Proc. 7th Int. Conf. Innsbruck, Austria 1978) IAEA Vienna to be published.

[2] Cordey J G, Jones E M and Start D F H, Plasma Physics, to be published.

[3] Braginskii S I in Reviews of Plasma Physics edited by M A Leontovich (Consultants Bureau, New York 1965), Vol I, 205.

[4] Horton C W and Varma R K, Phys. Fluids, 15 (1972) 620.

[5] Cordey J G, Jones E M and Start D F H to be published.

[6] An Interpretation of the Data in Terms of Drift-Island-Diffusion is given by Lichtenberg A J, Riviere A C, Edlington T and Todd T N in Proc. Int. Workshop on Intrinisic Stochasticity in Plasmas, Cargese (1979).

AP14

ANALYSIS AND INTERPRETATION OF ELECTROSTATIC FLUCTUATIONS IN THE CULHAM LEVITRON

D E T F Ashby and E M Jones
Culham Laboratory, Abingdon, Oxon OX14 3DB, UK
(Euratom/UKAEA Fusion Association)

ABSTRACT Digitally implemented bispectral analysis shows that a band of waves, typically centred near 50kHz and tentatively identified as drift waves, drive very low frequency fluctuations (~ 3-5kHz) by non-linear interaction.

INTRODUCTION The levitated superconducting ring in the Culham Levitron [1] has major and minor radii of 30 cm and 4.6 cm respectively. High shear axi-symmetric field configurations are produced giving L_s ≈ 10cm, $|B| \approx 3$kG, $B_\theta/B_\phi \approx 10$. Early fluctuation measurements [2, 3] were concerned with decaying plasmas and the effect of ohmic heating. Later measurements[4] dealt with steady-state helium discharges [$n_e \approx 5\times10^{11}$cm^{-3}, $T_i \approx T_e \approx 5$eV] produced by ECRH and made extensive use of digital techniques for spectral analysis [5]. These and more recent measurements together with theoretical work[6] illustrates the diversity of waves and modes possible. This paper is primarily concerned with explaining large amplitude fluctuations of a few kHz which commonly occur.

RESULTS Fig.1 shows fluctuations in floating potential, measured by a high-impedance capacity-compensated probe, together with the corresponding frequency spectra. One signal is from a region of favourable curvature of magnetic field; the other is from a region of unfavourable curvature. In both cases a band of high frequency fluctuations, characterised by $k_\phi a \approx 0.3$, occur together with large amplitude low frequency fluctuations. The high frequency fluctuations are tentatively attributed to collisionless drift waves in the form of wave packets. This identification is based on the value of $k_\phi a$ and the fact that the amplitude drops as $d(\log_e T_e)/d(\log_e n_e)$ increases [4]. The low frequency fluctuations have a measured value of $k_\phi < 2\pi/L_p$ (L_p = pitch length of the magnetic field) indicating that $k_{||} \neq 0$. This characteristic, together with the fact that the fluctuations occur in regions of favourable curvature and also when $d(\log_e T_i)/d(\log_e n_e) < 2/3$, rules out both temperature gradient waves [4] and resistive-g waves [6] as explanations. One possibility is that the low frequency fluctuations result from mode coupling between the high frequency fluctuations causing energy to cascade down the frequency spectrum [7].

This possibility was investigated using bispectral analysis [8]. Conventional spectral analysis resolves a signal into the linear superposition of component waves. Higher order spectral techniques are needed to identify non-linear interaction. For quadratically generated coupling the bispectrum (related to the triple correlation function) is appropriate. The bispectrum $B(\omega_1, \omega_2)$ is $|\langle F(\omega_1)F(\omega_2)F^*(\omega_1+\omega_2)\rangle|$ which when normalised gives the bicoherences $b(\omega_1, \omega_2) = B(\omega_1, \omega_2) \times \{\langle|F(\omega_1)F(\omega_2)|\rangle\langle|F(\omega_1+\omega_2)|\rangle\}^{-1}$ where $F(\omega)$ is a fourier component. If $F(\omega_1+\omega_2) = ZF(\omega_1)F(\omega_2)$ where Z is constant over the region of averaging then $b(\omega_1, \omega_2) = 1$. Frequency averaging was used in this work. Each record of 1024 amplitudes was resolved into 512 complex fourier components and averaged in groups of 8 or 16 to give $b(\omega_1, \omega_2)$. Fig. 2 shows a table of bicoherences typical of the type of power spectra shown in Fig.1 for regions of unfavourable curvature. Since $b \leq 1$ it has been rounded to a single digit and the decimal point dropped. Synthetic random signals give b = 0.1 with a standard deviation of 0.07 so numbers >3 in Fig.2 are highly significant. Four groups of large numbers are discernable. One pair is attributed to frequencies near 50 kHz interacting to give low frequencies near 5-10 kHz and high frequencies near 100 kHz. The third group is attributed to frequencies near 100kHz also generating low frequencies near 5-10kHz and the fourth group to ~50kHz and ~100kHz interacting to give ~150kHz. (Note that the amplitude at 150kHz is too small to show on the spectrum shown in Fig.2.) Similar results are obtained with signals from regions of unfavourable curvature.

DISCUSSION AND CONCLUSION In interpreting fluctuations measured by floating potential it is important to realise that the amplitude is proportional to perturbations of plasma position and not velocity. Consequently the amplitudes squared, as shown by the frequency spectrum, is not a measure of energy in the wave: multiplying the spectrum by ω^2 gives a better indication of energy or power. It is concluded that the fluctuations near 50 kHz are unstable and are responsible for the low frequencies near 5 kHz as well as higher frequencies.

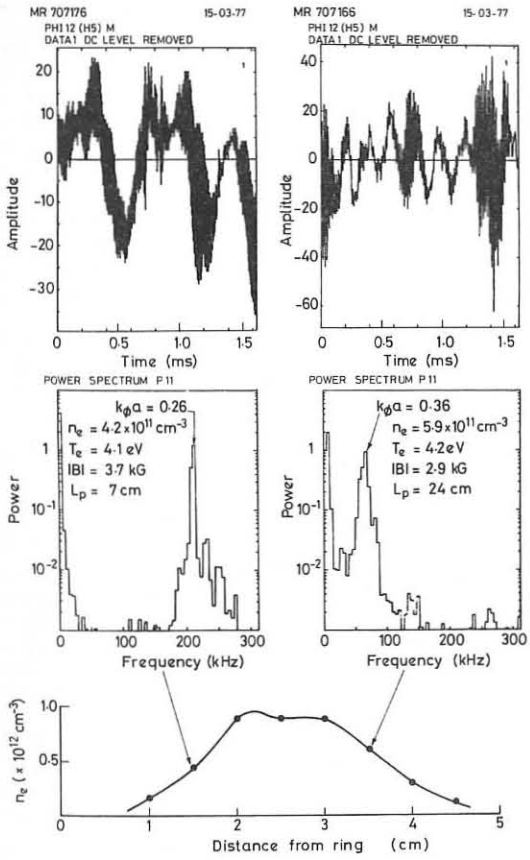

Fig. 1 Signals of fluctuating plasma potential and power spectra for positions of favourable and unfavourable curvature of magnetic field.

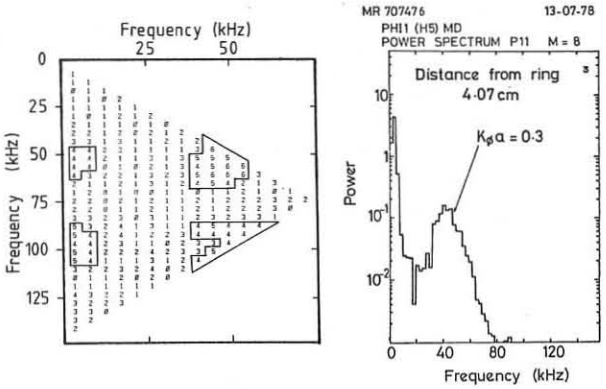

Fig. 2 Frequency spectrum and a table showing the bicoherence $b(\omega_1, \omega_2)$ of a probe signal.

ACKNOWLEDGEMENT The authors gratefully acknowledge the contribution to this work made by the members of the Levitron team led by D R Sweetman.

REFERENCES

[1] Riviere A C and Sweetman D R, Proc. 5th Eur. Conf. on Controlled Fusion and Plasma Physics, Grenoble 1972 p95.

[2] Ainsworth N R et al, Proc. 6th Eur.Conf. on Controlled Fusion and Plasma Physics, Lausanne 2 1975 p 127.

[3] Alcock M W et al, 6th Conf. on Plasma Physics and Controlled Fusion Research, Berchtesgaden 1976 IAEA-CN35/D12.

[4] Ashby D E T F, Jones E M and Start D F H, Proc. 8th Eur. Conf. on Controlled Fusion and Plasma Physics 1, Prague 1977 p 120.

[5] Jones E M and Steed C A, Proc. of the Digital Equipment Computer Users Soc. Copenhagen 1978 p 453.

[6] Cordey J G, Edlington T et al. This conference.

[7] Hasegawa A and Kodama Y, Phys.Rev.Lett. 41 (21) 1978 p1470.

[8] Kim Y C and Powers E J, Phys.Fluids 21 (8) 1978 p 1452.

AP15

Studies of Fuel Deposition and Penetration Depth
of a Refuelling Pellet
C.T. Chang
Association Euratom - Risø National Laboratory
DK-4000 Roskilde, Denmark

Abstract: Neglecting the deceleration of the pellet and the perturbation of the background plasma, the maximum penetration depth and fuel deposition for a pellet injected at a given speed are investigated with respect to the adopted ablation model and the prescribed temperature and density profile of the background plasma.

The penetration depth of a pellet injected at a given speed is affected by the drag experienced by the pellet as well as by the ablation rate itself. If the pellet ablates faster than it decelerates during its journey inside the reactor, one may consider the pellet to be moving at a constant speed [1]. The injection speed required to attain a prescribed penetration depth of a pellet injected at a given speed can be determined from the knowledge of the pellet ablation rate alone provided the temperature and density profiles of the background plasma remain essentially unperturbed. This condition conceivably can be met by restricting the pellet to a sufficiently small size. An estimation of the required injection speed for a prescribed penetration depth has been treated previously [1]. In view of the uncertainty regarding the desired penetration depth, the converse cases, i.e. the maximum penetration depth and the related fuel deposition (prior to the transport of the deposited fuel through its interaction with the background plasma) at a given pellet injection speed, are to be presented in this note.

Under the assumption that both deceleration of the pellet and perturbation of the background plasma are negligible, the ablation of the pellet is governed by

$$U_o \frac{d\zeta}{dx} = \frac{\xi(x)}{n_s h_s} q_{e\infty}(x) \ , \qquad (1)$$

where $x = 1-f$, $f = y/a$, $\zeta = r_p/a$
with y as the penetration distance and a the plasma radius. U_o is the injection speed, $q_{e\infty}(x)$ the electron thermal energy flux of the background plasma, and $\xi(x)$ is the shielding factor with respect to the ablation model being considered. For example, referring to the transonic-flow neutral shielding ablation model of Parks and Turnbull [2], one has for a D_2-pellet

$$\xi(x)/n_s h_s = 3.595 \times 10^{-16} r_p^{-2/3} n_{e\infty}^{-2/3} T_{e\infty}^{0.14} \ , \qquad (2)$$

where r_p is in cm, $n_{e\infty}$, n_s in cm^{-3}, $T_{e\infty}$ and h_s in ev, and referring to Gralnick's ablation model [3], one has

$$\xi = \tfrac{1}{2} h_s/h_i = \tfrac{1}{2} \times 10^{-2}/36 = 1.39 \times 10^{-4} \ . \qquad (3)$$

Anticipating a possible surface/volume effect of the ablation process, we may introduce a modified shielding factor

$$\xi^*(x) = (p+1)\zeta^p \xi(x) \ . \qquad (4)$$

On substituting Eq. (4) into Eq. (1), a direct integration gives

$$\zeta_o^{p+1} - \zeta^{p+1} = (q_{eo}/n_s h_s U_o)\ \Lambda(f,\xi^*), \qquad (5)$$

where

$$\Lambda(f,\xi^*) = \int_{1-f}^{1} \xi^*(x) q_*(x) dx, \quad q_*(x) = n_*(x) T_*^{3/2}(x) \ ,$$

i.e. q_{eo} is the electron thermal energy flux at the torus axis and

$$n_*(x) = n_e(x)/n_e(0), \quad T_*(x) = T_e(x)/T_e(0) \ . \qquad (6)$$

In particular, the maximum penetration fraction, f_{max} is given by

$$\Lambda(f_{max},\xi^*) = \frac{n_s h_s U_o}{q_{eo}} \left[\frac{r_p(0)}{a}\right]^{p+1} \ . \qquad (7)$$

Eq. (7) indicates that apart from the shielding factor ξ^* and the power index p, with respect to a given reactor condition (q_{eo}, a), f_{max} depends on an injection parameter, $U_o r_p^{p+1}(0)$. Using Eq. (7) and $\xi(x)$ given by Eq. (2), the relationship between f_{max} and U_o is computed for two pellet radii with respect to the following modified parabolic profiles:

$$T_*(x) = (1-x^2)^{\alpha_T}, \quad n_*(x) = (1-x^2)^{1.3-\alpha_T} \qquad (8)$$

for $\alpha_T = 1.2$. The result is shown in Fig. 1. As a comparison, the relationship between U_o and f_{max} is also shown for the shielding factor ξ given by Eq. (3) for a pellet with r_p = 2.5 mm. One observes that if the ablated material leaves the pellet surface as a cold plasma instead of in the neutral state, the required injection speed U_o for the same f_{max} will be an order of magnitude lower. Regardless of the ablation model used, the injection speed for $f_{max} = 1/3$ is about an order of magnitude lower for $f_{max} \gtrsim 1$.

Keeping a constant plasma pressure profile of $p_* = (1-x^2)^{1.3}$, the relationship between f_{max} and the temperature profile index α_T is shown in Fig. 2 with respect to the shielding factor $\xi(x)$ of Eq. (2). One observes that for a given combination of U_o and $r_p(0)$, f_{max} is greater for a steeper temperature profile (larger α_T) as compared with a steeper density profile (smaller α_T).

Using Eq. (5), it can be shown that the pellet radius $r_p(f)$ is related to its initial radius $r_p(0)$ through the function $\Lambda(f,\xi^*)$ by

$$\frac{r_p(f)}{r_p(0)} = \left[1 - \frac{\Lambda(f,\xi^*)}{\Lambda(f_{max},\xi^*)}\right]^{\frac{1}{p+1}} \qquad (9)$$

With respect to the two shielding factor, Eq. (2) and (3), the variation of the pellet radius $r_p(f)/r_p(0)$ and the fuel deposition $N_p(f)/N_p(0)$ (where $N_p(0)$ is the total number of particles contained in a pellet of radius $r_p(0)$) with respect to the fraction of penetration, f, is shown in Fig. 3.

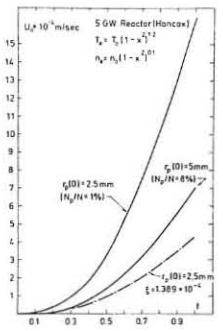

Fig. 1. Injection speed U_o vs. the fraction of penetration, f.

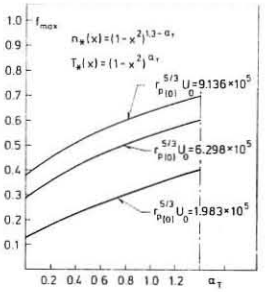

Fig. 2. f vs. for a constant pressure profile $p_* = (1-x^2)^{1.3}$.

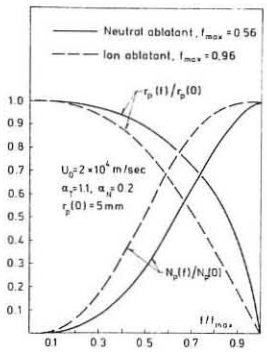

Fig. 3. Variation of the pellet radius $r_p(f)$ and amount of the ablated material $N_p(f)$ with respect to the fraction of penetration, f.

References:

1. Düchs, D.F., Haas, G., Keilhacker, M., Lackner, K., Chang, C.T., Part C, IAEA-CN-37-N-6, 7th Int. Plasma Physics and Cont. Nucl. Fusion Research, Innsbruck, 1978.

2. Parks, P.B., Turnbull, R.J., Phys. Fluids 21, 1735 (1978).

3. Gralnick, S.L., Nucl. Fusion 13, 703 (1973).

AP16

SUPPRESSION OF THE ELECTRON CYCLOTRON INSTABILITY OF A BEAM-PLASMA SYSTEM BY SELECTIVE CYCLOTRON DAMPING

J.A.C. Cabral and C.A.F. Varandas

Laboratório de Electrodinâmica - Complexo Interdisciplinar
Instituto Superior Técnico - Lisbon - Portugal

We study the possibility of suppression of the electron cyclotron instability of a beam-plasma system (ω_o,k_o) through the parallel injection of a secondary electron beam of adequate velocity to induce cyclotron damping ($\omega_o - k_o v_{b2}^x = \omega_{ce}$). The b-p system is conventional and the scd. beam was created by the insertion of a negatively biased fine mesh grid of Tungsten between the filament and the first earthed electrode of the Pierce electron gun. The main beam bombards this grid and so the scd. beam results from thermoionic as well as from secondary electron emission. Typical parameters are: Main beam: 2000 eV, 10 mA, Ø=3 mm; Slow beam: 0 to 180 eV, 0.75 mA; Plasma: 10^9 cm^{-3}, 5 eV; Chamber: L=75 cm, Ø= 8 cm, P_{He}= 4 x 10^{-4} Torr. The spectrum shows a strong cyclotron peak at f_o=450 MHz, k_o=1.30 cm^{-1} with f_{ce}=330 MHz, f_{pe}= 280 MHz, p=1.0 cm^{-1}. The instability appears under the form of rapid bursts with typical durations of 100 ns (CABRAL, 1976). We verified that the passage of the scd. beam changed only slightly the plasma parameters. We measured the total wave power P_w received by a Langmuir pin probe, as a function of the scd. beam energy and Fig.1 shows a typical result:- there is a strong power reduction for U_{b2} ~ 110 eV. Measurements of ω_o and k_o showed that, in every case studied, the velocity corresponding to the minimum of P_w is very close to v_{b2}^x, revealing cyclotron damping (CABRAL et al,1978). Spectral analysis show that the power reduction is mainly due to the decrease in amplitude of the electron cyclotron instability. Figures 2 and 3 show respectively the temporal and the spatial variation of the cyclotron bursts in three situations: 1)- in the absence of the sec. beam; 2)- with a resonant beam (U_{b2}=90 eV); 3)- with a non-resonant beam (U_{b2}=180 eV). As we can observe, the passage of the resonant beam causes the almost

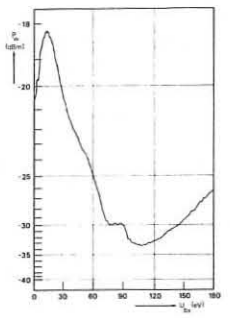

Fig.1

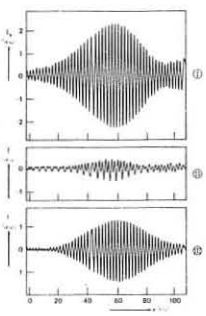

Fig.2

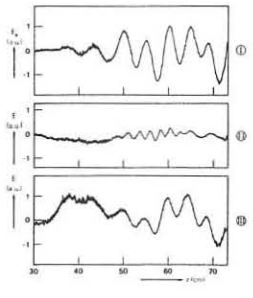

Fig.3

complete disappearence of the cyclotron wave (ω_o,k_o), leaving a clear residual evidence for the excitation of a Trivelpiece-Gould mode developing, by coincidence, around ($\omega_o/2$,$2k_o$). Beams of different velocities (non-resonant) produce only minor modifications in the instability behaviour. In order to explain the experimental results we first consider the transverse dynamics of the scd. beam electrons, acted by the Lorentz force arising from the axial B-field and from the instability E-field. To simulate a continuous electron stream we write $E=E_o \cos(\omega_o t - k_o z + \phi)$ and ϕ is varied from 0 to 2π. Since $v_{b2} \ll v_{ph} = \omega_o/k_o \lesssim v_{b1}$, we neglect the influence of $E_{//}$ on the electron trajectory and so its axial velocity is taken as const. Therefore the E-field can be thought as purely transverse for the calculations. Electrons enter the interaction chamber at z=0 and t=0 and leave it at z=L at $t=L/v_{b2}$. Integration of the equation of motion leads to an expression for the electron transverse energy $U_\perp(\phi, v_{b2})$ at z=L. By an average over ϕ we obtain the mean electron transverse energy $\langle U_\perp \rangle (v_{b2})$ also at z=L. We verified that $\langle U_\perp \rangle$ is sharply peaked at the resonant velocity v_{b2}^x, as expected. A numerical calculation, with the parameters: f_o=450 MHz, k_o=1.30 cm^{-1}, f_{ce}= 330 MHz, L=75 cm and E_o=10 V cm^{-1} leads to a mean transverse energy of 368 eV at resonance. In Fig.4 we plotted the variation of $\langle U_\perp \rangle$ with U_{b2}. Besides the sharp main resonance peak we observe other smaller amplitude peaks. These ones are due to the consideration of the finite w-width of the cyclotron wave packet (resonant interaction with modes to both sides of the main spectral line with amplitudes at -3, -6 and -9 dB). Therefore the global resonant wave-particle interaction is not so sharp. As the dependences of P_w and $-\langle U_\perp \rangle$ on U_{b2} are similar we believe that the wave power decrease observed (Fig.1) is due to the net gain of transverse energy by the scd. beam electrons, as a result of energy conservation. A second approach to the interpretation

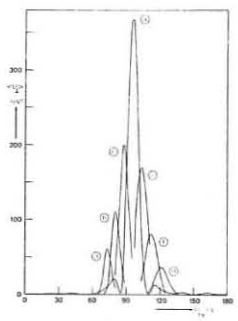

Fig.4

of the experimental results is based on dispersion theory. The computer solution of the dispersion equations, for the three sub-systems, in the cyclotron region of interest ($\omega_{ce} \lesssim \omega \lesssim \omega_{uh}$, $k \sim k_o$), lead to the following results:- (i)- fast beam + plasma: absolute instability; (ii)- slow beam + plasma: evanescence; (iii)- fast beam + slow beam: weak convective instability. The solution of the dispersion equation for the system of a plasma with two beams, when compared with that for the normal system, shows a small decrease in the temporal growth rate ω_i of the absolute instability and an increase in the spatial damping rate k_i of the evanescent modes which appear for the same frequency band with slightly lower real-k values. We can compute the effect of the modification on both ω_i and k_i on the amplitude attained by the instability E-field. Indeed, the ratio E/E_o, where E_o is the field amplitude attained in the absence of the scd. beam, can be calculated from either $E/E_o = \exp[-(\omega_i - \omega_{io})T]$ or $E/E_o = \exp[(k_i - k_{io})Z]$, where T and Z are of the order of one half of the total extension of the bursts respectively in time and in space (T= 50 ns and Z= 20 cm). If we compute the decrease in amplitude due to the changes on ω_i and k_i, with the expressions above, varying the scd. beam energy in steps of 10 eV from 0 to 180 eV, we arrive to the results presented in Fig.5. Curve a) shows the decrease in amplitude (in dB) due to the reduction of the instability growth rate ω_i. As we see the influence of the scd. beam is moderate leading to a maximum decrease of about 7 dB. Curve b) shows the result of the increase of the damping rate k_i which leads to a higher amplitude reduction (some 11 dB). If we combine both effects, that is to say, if we assume that the instability wave packet couples to the evanescent modes with slightly lower k-values, we obtain curve c) which shows a maximum amplitude reduction of about 18 dB and whose dependence on U_{b2} reveals an excelent agreement with the real experimental situation as depicted in Fig.1. Further we note that the energy corresponding to the minimum in Fig.5 is practically coincident with the corresponding value for U_{b2}^x. Therefore the acquisition of

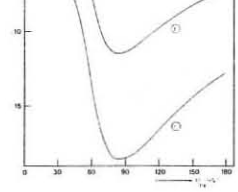

Fig.5

transverse energy by the scd. beam electrons is translated, into dispersion language, as an increase in the spatial damping rate as well as in a decrease of the instability growth rate. As the dispersion diagrams show that the new instabilities caused by the scd. beam are comparatively weak, the passage of this beam through the plasma constitutes indeed an effective suppression mechanism for the electron cyclotron instability. We extend the conclusions of this paper to Fusion research in TOKAMACS since the fast beam can be constituted by the runaway electrons and the slow beam by the hot tail of the electron velocity distribution of the thermonuclear plasma. We finally can foresee a heating mechanism, selective cyclotron damping, based on the adequate injection of powerful waves with $f \gtrsim f_{ce}$.

References:

1.- CABRAL, J.A.C. (1976) - Plasma Physics 18, 719.

2.- CABRAL, J.A.C., SILVA, M.E.F., VARANDAS, C.A.F. - Plasma Physics 20, 21.

AP17

Anomalous Heat Transport in a Turbulent Plasma Blanket

D. Anderson, M. Lisak and H. Wilhelmsson

Institute for Electromagnetic Field Theory (EUR-NE)
Chalmers University of Technology
412 96 Göteborg, Sweden

An analytic investigation is made of the conductive heat transport properties of a plasma blanket, where the heat transport is dominated by anomalous conduction due to a current-convective instability. The scaling of the blanket width with physical parameters is given.

The main purpose of a cold plasma blanket in a fusion reactor is to prevent high-energy neutrals from hitting the wall of the container causing sputtering and subsequent impurity influx. Thus the ion temperature in the blanket must be below the sputtering threshold and the width of the blanket must exceed the penetration depth of highly energetic neutrals from the plasma centre. On the other hand, the width of the blanket is determined by its heat transport properties and for low-beta devices, the corresponding width is usually too small. It was recently suggested, [1], that a wider boundary layer could be obtained by enhancing the conductivity of the blanket through a current-convective instability. In [1] the corresponding highly nonlinear temperature equation was solved numerically and several conclusions were drawn as to the scaling of the blanket width with some of the characteristic physical parameters.

In the present work we reconsider and extend this problem giving explicit analytical solutions for the temperature profile, heat flow, and blanket width, which clearly displays the scaling with all relevant physical parameters. The analysis can also be extended analytically to include the effect of a constant particle flux contributing to the heat flow.

The steady-state heat flux equation determining the temperature profile, $T(x)$, is taken as

$$\frac{d}{dx}\left(n\chi_{\perp}\frac{dT}{dx}\right) = S \tag{1}$$

where the density, n, is assumed constant and the source term, S, is due to Joule heating by the electric field, E_o, which drives the current-convective instability. We consider a situation, where the dominant contribution to the conductivity, $\chi_{\perp}$, is due to turbulence induced by the current-convective instability, [1,2], i.e.

$$\chi_{\perp} \approx 10\,\frac{E_o^4}{\chi_{\parallel}}\left(\frac{R}{B_o}\,\frac{1}{T}\,\frac{dT}{dx}\right)^2 \tag{2}$$

where R is the distance along the major radius, B_o the longitudinal magnetic field, and $\chi_{\parallel}$ the classical thermal conductivity.

Inserting the appropriate expressions, we obtain the highly nonlinear equation

$$\frac{d}{dx}\left[T^{-9/2}\left(\frac{dT}{dx}\right)^3\right] = -\gamma T^{3/2} \tag{3}$$

where the constant γ is

$$\gamma \approx 2\cdot 10^{24}\,\frac{B_o^2}{Z_{eff}^2 n^2 R^4 \ln\Lambda} \tag{4}$$

Z_{eff} being the effective charge and $\ln\Lambda$ the Coulomb logarithm. From eq. (3) the heat flow is obtained after integrating once

$$q(x) = -n\chi_{\perp}\frac{dT}{dx} = q_o\left[1 + \left(\frac{\alpha}{q_o}\right)^{4/3}\frac{4\gamma}{3}\left(T_o - T\right)\right]^{3/4} \tag{5}$$

where $\alpha = 9\cdot 10^{-11}\left(nR^2E_o/B_o\right)^2 Z_{eff}$, q_o denotes the heat flux incident on the blanket from the inner hot plasma core, and T_o is the temperature of the inner boundary. Eq. (3) can be integrated one step further to yield an explicit exact solution involving elliptic functions [3]. As is evident from eq. (5) the character of this solution depends on the single parameter

$$\rho \equiv \left(\frac{\alpha}{q_o}\right)^{4/3}\frac{4\gamma T_o}{3} \tag{6}$$

For most parameters considered here (typically R≈500 cm, B_o=40 kG, Z_{eff}=1, $n=10^{14}\,cm^{-3}$, q_o=10 Wcm^{-2}, T_o=100 eV, and assuming E_o=1 Vm^{-1}) $\rho \ll 1$ in which case we obtain a simple approximate solution corresponding to constant heat flux through the blanket:

$$T = T_o\left(1 + x/x_o\right)^{-2}$$
$$x_o = 2\left(\frac{\alpha}{q_o}\right)^{1/3} T_o^{-1/2} \tag{7}$$

Defining the width of the blanket, x_*, as the distance at which the temperature has dropped to $T = T_* = 10\,ev \ll T_o$

$$x_* \approx 9\cdot 10^{-4}\left(\frac{n^2R^4E_o^2Z_{eff}}{B_o^2\,q_o}\right)^{1/3} T_*^{-1/2} \tag{8}$$

which clearly displays the scaling of the width with all relevant parameters.

Finally, requiring that the blanket width must exceed the penetration length, L, of hot neutrals ($L \sim 10^{15}/n$) implies

$$\left(\frac{n^2R^4E_o^2Z_{eff}}{B_o^2\,q_o}\right)^{1/3} T_*^{-1/2} > 10^{18} \tag{9}$$

For characteristic values as given above one obtains

$$\frac{n}{q_o^{1/5}} > 4\cdot 10^{12} \tag{10}$$

Thus for a heat load of q_o=10 Wcm^{-2}, n must exceed $2\cdot 10^{14}$ cm^{-3} in order to provide sufficient shielding effect.

The analysis can also be extended to include the effect of particle diffusion on the heat transport, [3].

References

[1] Bhadra, D.K., and Gross, L. Nucl. Fus. 17, 622 (1977).

[2] Kadomtsev, B.B., and Pogutse, O.P., Rev. Plasma Phys. (Leontovich, M.A., Ed.) Consultants Bureau, New York 5 (1970).

[3] Anderson, D., Lisak, M., and Wilhelmsson, H., CTH-IEFT/PP-1979-9 (internal report).

AP18

CURRENT TRANSITIONS IN THE PLASMA-WALL INTERFACE IN A TOKAMAK

U. Daybelge

Uni-Center P.O.Box 250149, 4630 Bochum
Federal Republic of Germany

Abstract: The potential variation at the equatorial region of the torus wall, where most of the unipolar arcing tracs have been observed, is calculated by a self consistent method. Secondly, it is shown that certain types of potential perturbations on the wall can lead to self sustaining and moving current transitions.

Although, most of the arcing reported in tokamaks[1,2] occur on surfaces parallel to magnetic field lines, and especially close to the equatorial belt, in the available theoretical studies about unipolar arcs, characteristics of the tokamak plasma in such regions are completely neglected. Among the plasma features close to the torus equator one observes: 1) Due to the magnetic drift, here particles come closest to the wall during their drift-gyro motion. 2) Between two collisions particles can perform many of the fast gyro-motions, so that as far as gyro-motion is concerned, plasma is collisionless. 3) The self consistent electric field near the wall depends on the boundary conditions on the wall, whether the wall is reflecting or absorbing one or both of the particle species. 4) For most tokamaks one can estimate that here electron

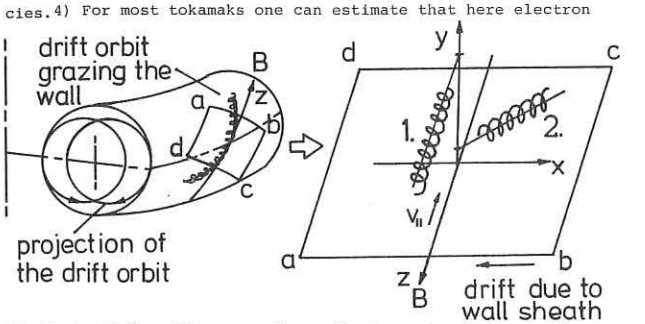

Fig.1 Particle orbits near the wall at equator. Left: Section "abcd" and typical orbits: 1. Outside the sheath, 2. Inside the sheath.

gyro radius ρ_e, is about equal or less than the Debye length λ_D. 5) Since the magnetic drift displacement is larger than the ρ_i and ρ_e, and the direction of the shift depends on the sign of $v_{||}$, inside the wall sheath $v_{||}$ can have only one direction.

In Fig.1 a small section of the region of interest is shown. To calculate the self-consistent sheath potential in the vicinity of the section "abcd" one has to consider the particle dynamics. Neglecting the curvature of the guiding center orbits and considering the potential to depend only on y, we can write for a particle of charge q the equations of motion as

$$m\ddot{x} = q\,\dot{y}\,B \quad ; \quad m\ddot{y} = q\,E(y) - q\,\dot{x}\,B \quad ; \quad m\ddot{z} = 0 \,. \tag{1}$$

Integrating the first equation once we find $\dot{x} = \Omega y + C_1$ where $\Omega = qB/m$, substituting in the second we obtain after integration $\dot{y}^2 - \Omega^2 y^2 + 2\Omega y\dot{x} + 2q\phi(y)/m = C_2$. Here, we used $E = -d\phi/dy$. If we substitute also $\dot{x}$, we find

$$\frac{dy}{dt} = \pm\sqrt{C_2 - 2C_1\Omega y - \Omega^2 y^2 - 2q\phi(y)/m} \,. \tag{2}$$

Contents of the root sign must be positive for a real motion and setting it equal to zero we find the turning points. Hence,

$$\frac{2q\,\phi(y)}{m} \le -\Omega^2 y^2 - 2C_1\Omega y + C_2 \,. \tag{3}$$

Given the potential and the initial conditions, this relation indicates whether or not the particle can exist at the level y.

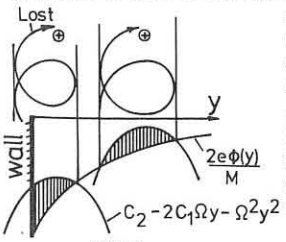

Fig.2.

For a monotonous potential variation the condition for hitting the wall is simply $C_2 \ge 2q\,\phi(0)/m$. Fig.2. illustrates the relation (3) for ions. For an adsorbing surface loss region in velocity space can be therefore easily determined. Setting the value of C_2 we find that the loss region corresponds to

$$\dot{y}^2 + 2y\Omega\dot{x} - \Omega^2 y^2 + \frac{2q}{m}[\phi(y) - \phi(0)] > 0 \tag{4}$$

On normalizing by respective Larmor radii and thermal speeds we rewrite Rel.(4) for plasma components as

Ion loss region: $\dot{y}_i^2 + 2y_i\dot{x}_i - y_i^2 + \eta\Delta\tilde{\phi} > 0$, (5)

Electron loss region: $\dot{y}_e^2 - 2y_e\dot{x}_e - y_e^2 - \Delta\tilde{\phi} > 0$, (6)

where $\eta = T_e/T_i$, $\Delta\tilde{\phi} = \tilde{\phi} - \tilde{\phi}(0)$, and $\tilde{\phi} = e\phi/kT_e$, $(e=|e|)$.

If the particle distributions far from the wall are Maxwellian, then the densities in the vicinity of an adsorbing wall can be calculated by integrating the Maxwellian functions outside the loss regions in the velocity space. The Maxwellian functions are in the form $f = (\sqrt{\pi}v_{th})^{-3}\, N \exp|-(v^2+q\phi/m)/v_{th}^2|$, where the density N is a slowly varying function over the length scales ρ_e and ρ_i, and it reflects the boundary conditions at the infinity, (plasma core, or limiter and divertor effects). Due to guiding center shift, $\dot{z}$ can have a single sign, and transforming all lengths to the ρ_e scale, i.e., $y_e = y$ and $y_i = \varepsilon y$ $(\varepsilon = \sqrt{m/M})$ we find

$$\frac{n_e}{N_e} = \frac{e^{\tilde{\phi}}}{\pi}\int_0^\infty e^{-\dot{y}^2} d\dot{y} \int_{\dot{x}_u}^\infty e^{-\dot{x}^2} d\dot{x} \,, \quad \frac{n_i}{N_i} = \frac{e^{-\eta\tilde{\phi}}}{\pi}\int_0^\infty e^{-\dot{y}^2} d\dot{y} \int_{-\infty}^{\dot{x}_o} e^{-\dot{x}^2} d\dot{x}$$

where $\dot{x}_u = \frac{\dot{y}^2}{2y} - \frac{y}{2} - \frac{\Delta\tilde{\phi}}{2y}$ and $\dot{x}_o = \frac{-\dot{y}}{2\varepsilon y} + \frac{\varepsilon y}{2} - \frac{\eta\Delta\tilde{\phi}}{2\varepsilon y}$.

Thus, we find that

$$\frac{n_e}{N_e} = \frac{e^{\tilde{\phi}}}{4\sqrt{\pi}y}\int_0^\infty dz\ \mathrm{erf}\sqrt{z}\ \exp\{-\frac{1}{4}[\frac{z}{y} - (y + \frac{\Delta\tilde{\phi}}{y})]^2\} \tag{7}$$

$$\frac{n_i}{N_i} \sim e^{-\eta\tilde{\phi}/2} \begin{cases} \mathrm{erf}\sqrt{\varepsilon^2 y^2 - \eta\Delta\tilde{\phi}} & (\text{if } \varepsilon^2 y^2 > \eta\Delta\tilde{\phi}) \\ -\sqrt{2/\pi}\ \dfrac{\varepsilon^2 y^2\ \exp\{-\frac{1}{4}[\varepsilon y + \frac{\eta\Delta\tilde{\phi}}{\varepsilon y}]^2\}}{(\varepsilon^2 y^2 - \eta\Delta\tilde{\phi})\ \sqrt{\varepsilon^2 y^2 + \eta\Delta\tilde{\phi}}} & (\text{if } \varepsilon^2 y^2 < \eta\Delta\tilde{\phi}) \,. \end{cases} \tag{8}$$

Asymptotic expressions in (8) were obtained for $y = O(1)$, $\varepsilon \to 0$. For $y \to \infty$ (ion Larmor radius) one has to use the full integral. Substituting the expressions (7) and (8) in the Poisson's equation $\delta^2 \frac{d^2\tilde{\phi}}{dy^2} = n_e/N_e - n_i/N_i$,

where $\delta \equiv \lambda_D/\rho_e \ge 1$, with $\tilde{\phi}(0)$ fixed, $\tilde{\phi}(\infty) \to 0$, we find the potential variation near a perfectly adsorbing wall. Our initial assumption for a monotonous variation is agreement with the numerical results shown for a hydrogen plasma in Fig.3.

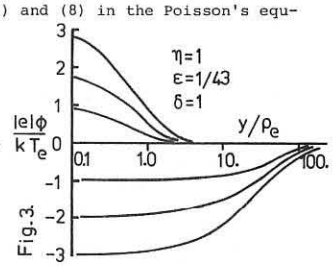

Fig.3.

Results indicate that the alteration of the wall adsorption coefficients change the decay length of the potential without affecting its monotony. These results are contrary to the "potential model with a maximum" suggested in Ref.2.

We have seen that once the wall potential, $\tilde{\phi}(0)$, is given (depending on the discharge history and the diffusion) radial potential variation near the equator region can be determined. Let us, now, assume that a local perturbation locally reduces the potential difference between plasma and the wall (assuming $\Delta\tilde{\phi} > 0$), bending the equipotential surfaces towards this region as seen in Fig.4. (initial perturbation may be due to the starting electron emission): As a result, hot charged particles drifting parallel to the wall at some distance are directed to the disturbance region, hitting and heating the wall they cause more electron emission. The disturbance region will be asymmetrically heated, and the current passing through metal indicate that the initial potential perturbation has to be shifted to the right (so called retrograde direction). With sufficient heating metal evaporation and wall erosion can follow. Neglecting the role of impurity ions in this process, we have determined the amount of energy transferred by plasma ions to the disturbance region, using orbit simulation for a class of perturbations for different wall potentials. Maximizing the heating by varying the shape factors of the perturbation, we have determined necessary ambient conditions for achieving metal erosion during time lengths of a few ms.

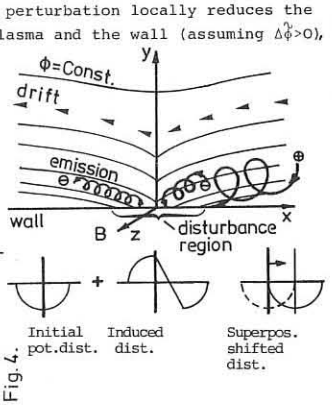

Fig.4.

[1] D. H. J. Goodall and G. M. McCracken, Culham Report CLM R167. November 1977.

[2] G. M. McCracken and D. H. J. Goodall, Culham Report CLM P509 October 1977.

[3] Nedospasov, A. V. and Petrov, V. G., J. Nucl. Mat. 76/77 (1978) 490.

AP19

CO_2 LASER SCATTERING FROM ION-ACOUSTIC FLUCTUATIONS

C.M. SURKO*, D. GRESILLON, J. OLIVAIN** and A. TRUC

Laboratoire de Physique des Milieux Ionisés
Ecole Polytechnique, 91128 Palaiseau, France.

Study of the ion feature in plasmas can yield detailed information about plasma parameters such as ion temperature, electron drifts and impurity content. It is of interest to study details of the thermal ion feature in a well-controlled laboratory plasma. In this paper we describe an experimental study of ion-acoustic fluctuations using CO_2 laser scattering.[1,2] This technique has the advantage that it does not suffer from refraction in plasmas as dense as 10^{15} cm^{-3}, and it requires only a small angular access to the plasma. It also provides enough sensitivity to reach the thermal level in the laboratory plasma described below.

The plasma is produced in one chamber (80 cm diam. by 80 cm long) of a double plasma device with densities of up to 10^{12} cm^{-3} in Ar and 10^{11} cm^{-3} in He, with electron temperatures T_e from 1 to 5 eV. A single-mode C.W. CO_2 laser with a power of 140 W is focussed in the plasma to a diameter $2a_o$ of 4.6 mm to the $1/e^2$ points. A spatial filter consisting of a small aperture and two lenses is placed between the laser and plasma to eliminate nonuniformities in the transverse mode pattern of the laser beam. Scattered radiation is heterodyne detected by beating it with a small fraction of the incident laser beam which is split off and aligned so that it passes through the plasma. The intersection of the two beams defines the interaction volume and assures efficient heterodyning[1]. The detector is a negatively biased Hg Cd Te photodiode which takes a maximum LO power of 1.5 mW. We have been able to work at scattering angles as small as 11 mrad (plasma wavelengths of 0.93 mm) where the stray main beam power on the detector was less than 0.2 mW. The detector noise is found to be close to the photon noise fluctuations of the LO beam in which case the minimum detectable scattered power is given by $P_m = (h\nu/\eta)(\Delta f/\tau)^{\frac{1}{2}}$ where $h\nu$ is the CO_2 radiation photon energy, η the quantum efficiency (0.33), Δf the bandwidth studied, and τ the averaging time.

Shown in figure 1 is the scattered signal I_S (proportional to the fluctuating electron density $\tilde{n}$) from an ion acoustic wave driven by a voltage at frequency ω applied to a 20 cm diameter plane grid in the plasma. The detector signal was mixed with the driving oscillator of frequency ω to produce the interferometer pattern shown. In such an arrangement, the envelope of the signal should be due to the wavevector resolution of the scattering experiment. The rapid oscillations are due to the change in phase produced by the wave traveling between the grid and scattering volume which are separated by a distance X_o. In this case we would expect

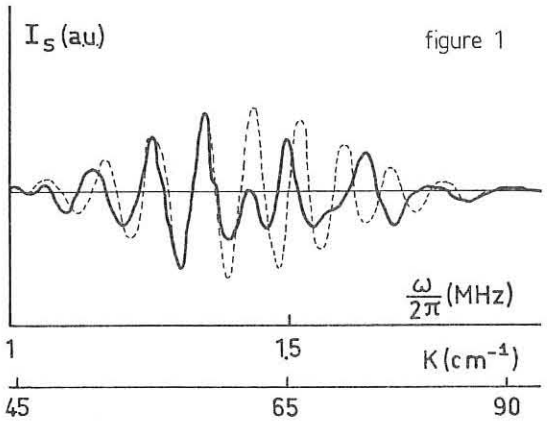

$$I_S(K) \propto \tilde{n}\, e^{-(K-K_o)^2 a_o^2/8} \cos(KX_o) \qquad (1)$$

where K_o is given by the scattering angle θ_o and the wavelength λ of the CO_2 radiation ($K_o = 2\pi\theta_o/\lambda$) and K is the wavevector of the ion acoustic wave. The predictions of (1) are shown by the dashed curve in Fig. 1 using a phase velocity at $\omega/2\pi$ = 1.35 MHz of 1.35×10^5 cm/sec, a plasma density of 1.75×10^{10} cm^{-3} and X_o = 1.85 cm. The observed signal power is about 10 db lower than that predicted from the wave amplitude measured with a probe in the plasma. This may be due to the sensitivity of the scattered signal on grid alignment and flatness.

We have studied naturally occurring fluctuations in Ar plasmas with densities up to 10^{12} cm^{-3}. Shown in Figure 2 is the scattered signal observed in a plasma of density 1.1×10^{11} cm^{-3} with electron temperature 2.2 eV. This spectrum was taken with the interaction volume centered

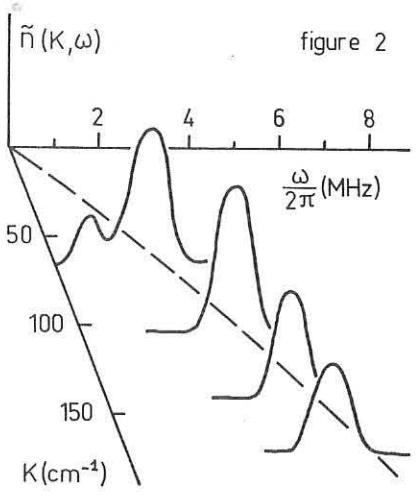

on the edge of the plasma and indicates a fluctuation level far above thermal (by a factor of the order of 10^3 in scattered power). This signal was observed to be a maximum near the plasma edge and is probably related to plasma production and gradients near the wall of the device. The frequencies and wavelengths observed agree reasonably well with the ion-acoustic dispersion relation including finite $K\lambda_{De}$ effects (dashed line). The frequency widths are due mainly to our finite wavevector resolution. In Figure 2, 150 cm^{-1} corresponds to $K\lambda_{De}$ equal to 0.5.

We have attempted to observe the thermal ion feature in Ar plasmas with densities of up to 10^{12} cm^{-3}. We have not observed the thermal spectrum for which we would have expected a signal to noise ratio of 1 to 10 with a 1 second averaging time if S (K) = 1 (a thermal plasma with $T_e \gg T_i$). We have however observed that driven waves in this plasma damp about a factor of 30 faster than expected from electron Landau damping. A 1 % concentration of H in the Ar plasma would produce such a damping and in this case we would expect S (K) $\sim$ 1/30 which is consistent with the negative scattering results. In He plasmas this enhanced damping does not appear to be present. In preliminary experiments in the He we have, depending on plasma conditions, observed superthermal fluctuations similar to those shown in Fig. 2, but we have not yet observed scattering from the thermal ion feature.

We would like to acknowledge useful discussionswith T.D. Mantei and the technical assistance of B. Chapey and R. Vermillard. This experiment was sponsored by D.R.E.T. and C.N.R.S., and one of us (CMS) would like to acknowledge partial support from Bell Laboratories.

* Permanent address : Bell Laboratories, Murray Hill, NJ 07974, USA.

** DPh-PFC, Commissariat à l'Energie Atomique, BP N° 6, 92260 Fontenay-aux-Roses.

(1) C.M. Surko, R.E. Slusher, D.R. Moler and M. Porkolab, Phys. Rev. Letters, 29, 81 (1972) and 36, 674 (1976). R.E. Slusher and C.M. Surko (submitted to Phys. Fluids).

(2) E. Holzhauer, Phys. Lett., 62A, 495 (1977), R.L. Watterson, A.L. Peratt and H. Derfler, Phys. Fluids, 22, 110 (1979).

AP20

KINETIC THEORY OF THE COLLISIONAL SCRAPE OFF LAYERS

U. Daybelge

Institut für Theoretische Physik, Ruhr Universität Bochum,
4630 Bochum, Federal Republic of Germany

Abstract: This paper deals with the boundary value problem of the collisional plasma ion kinetics in the scrape-off layers of poloidal and toroidal limiters.

Under ideal discharge conditions the purpose of the limiter is to intercept all charged particles diffusing out of the discharge and so to prevent them from interacting with the torus wall. It has well been established, however, that in many tokamaks a cool, low density plasma extends outside the limiter and is in contact with the wall. It is reasonable to assume this plasma as collisional. To simplify the problem, one can also assume , that the transition from collisionless to collisional regime at the discharge edge has occured well inside the limiter aperture. These assumptions imply that the boundary conditions imposed at the limiter surface can influence the ions only inside a certain range. However, the plasma-limiter interactions and the related impurity transport largely depend on the kinetic structure of these influence regions.

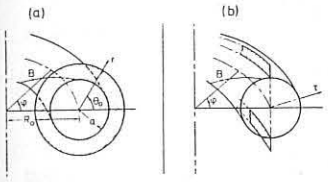

Fig.1 Limiter Configurations and relevant coordinates: (a) poloidal Lim. (toroidal divertor), (b) toroidal Lim.(poloidal divertor).

We consider the ion drift-kinetic equation

$$(\vec{v}_{||} + \vec{v}_D)\cdot \nabla f = C_{ii}(f) \qquad (1)$$

with the particular ordering $\omega << \nu << \Omega$, where ω is a typical transit time, v_{th}/R_0, ν is ion collision frequency and Ω is ion gyro-frequency. According to the maximal ordering of the neoclassical theory[1] the neglected terms in Equ.(1) are $O(\omega^2/\Omega_p^2)$. Our purpose is to solve Equ.(1) with the limiter boundary conditions. The drift velocity in Equ.(1) is $\vec{v}_D = v_{||}\vec{n}\times\nabla(v_{||}/\Omega)$. The effect of the limiter induced electric fields on the particle orbits is assumed small,a point whose consistency needs to be checked. For the collision operator C_{ii} we assume a simple pitch angle scattering operator[2]. Normalizing by the thermal velocity and the aperture radius a, the kinetic equation becomes

$$v\sin\theta\,\frac{1+\xi^2}{2\xi}\frac{\partial f}{\partial\tau} + \frac{\partial f}{\partial\theta} + q(a)\frac{\partial f}{\partial\phi} = q(a)\gamma\,\frac{1}{2v^4\xi}\frac{\partial}{\partial\xi}\left[(1-\xi^2)\frac{\partial f}{\partial\xi}\right] \qquad (2)$$

Here, we have introduced a new radial coordinate $\tau=\frac{(r-a)}{(a/R_0)(v_{th}/\Omega_p)}$ cosine of the pitch angle ξ, the safety factor q, and the parameter of collisionality $\gamma = R_0\nu/v_{th}$. Since γ is assumed to be large, we define new boundary layer coordinates $\tilde{\theta} = \gamma(\theta-\theta_0)$ $\tilde{\phi} = \gamma\phi$ and $\tilde{\tau} = \gamma\tau$. Hence, Equ.(2) can be written as

$$v\,\frac{1+\xi^2}{2\xi}\frac{\partial f}{\partial\tilde{\tau}} + \frac{\partial f}{\partial\tilde{\theta}} + q\,\frac{\partial f}{\partial\tilde{\phi}} = q\,\frac{1}{2v^4\xi}\frac{\partial}{\partial\xi}\left[(1-\xi^2)\frac{\partial f}{\partial\xi}\right] \qquad (3)$$

It is clear that in an axisymmetric case such as a toroidal limiter, f does not depend on ϕ, and the third term on the left drops out. Due to the last transformation, ξ can be treated now as a constant of motion. Allowing ξ to vary in (0,1) we can look at the Equ.(3) as a prescription to determine f^+. Similarly, if $-1\le\xi\le 0$, Equ.(3) determines f^-. In what follows, we consider the equation for f^+ without specifying the superscript. With f_{Neo} we denote the distribution function to this order found via neoclassical theory without limiter[1], and notice that f_{Neo} is a slowly varying function of $\tilde{\tau}$, and it is essentially a Maxwellian[1]. As the collision operator does not couple f^+ and f^-, flow quantities to one plate can only be affected by the distant boundary conditions at the other plate, this effect decreasing with the increasing collision frequency. Hence, using a Maxwellian for f^-_{Neo}, we find that the ion flow to the limiter surface is $\Gamma_i=(T_i/T_e)^{1/2}\,\bar{n}\,c_{is}/2\sqrt{\pi}$ where c_{is} is the ion sound speed and the ion heat flux is $Q_i=2kT_i\Gamma_i$.

On defining $\hat{f} = f^+ - f^+_{Neo}$, it is clear that $\hat{f}$ also satisfies Equ.(3) and vanishes for large values of the $|\tilde{\theta}|$ and $|\tilde{\phi}|$. Now,we take the Fourier transformations of Equ(3) by applying $(2\pi)^{-1}\int_{-\infty}^{\infty}\exp(i\beta\tilde{\tau})\int_0^{\infty}\exp(i\alpha\tilde{\theta})\,d\tilde{\tau}\,d\tilde{\theta}$, and neglecting ϕ dependence

$$\frac{d}{d\xi}\left[(1-\xi^2)\frac{dX}{d\xi}\right] + \left[i\beta\sin\theta_0\frac{v^5}{q}(1+\xi^2) + i\alpha\frac{2v^4}{q}\xi\right]X = -\frac{2v^4\xi}{q\sqrt{2\pi}}\int_{-\infty}^{\infty} e^{i\beta\tilde{\tau}}\hat{f}(\tilde{\tau},\theta_0,\xi)d\tilde{\tau} \qquad (4)$$

The point $\xi=1$ is one of the singular points of the equation (4). The analytic solution at this point can be obtained by substituting $X = \Sigma A_n(\xi-1)^n$ in the homogeneous equation. We find $A_n = A_{n-1}(a+2b-n(n-1))/2n^2 + A_{n-2}(a+2b)/2n^2 + A_{n-3}b/2n^2$, where $a=\frac{2iv^4\alpha}{q}$ $b = i\beta\sin\theta_0 v^5/q$. For the limit $\xi\to1$ we can express the series by the Bessel function $J_0(\sqrt{2(a+2b)(1-\xi)})$. At the other limit, when $\xi\to0$, the solution can be written as $X\sim c_1\,Ai(-a^{1/3}(\xi+\frac{b}{a}))$ $+ c_2\,Bi(-a^{1/3}(\xi+\frac{b}{a}))$. The coefficients c_1 and c_2 can be determined by matching these two limit solutions with an intermediary WKB solution in the middle found for large values of the parameter $|a|$:

$$X_{WKB} = \frac{(1+t^2)[\cos z(t)+\sin z(t)]}{\sqrt{2\pi t}\,[(a+2b)(1+\mu t^4)]^{1/4}} \qquad (5)$$

where $t = \frac{1}{2}\ln\frac{1-\xi}{1+\xi}$ and

$$z(t) = 2\sqrt{a+2b}\int_0^t dt\,\sqrt{1+\mu t^4}/(1+t^2)^2$$

and $\mu=(2b-a)/(2b+a)$. Thus we find $c_1=\sqrt{2}\,a^{-1/6}\cos I$ and $c_2 = \sqrt{2}\,a^{-1/6}\sin I$, with $I=(2b^{3/2}/3a) - z(1)$.

Having thus determined the solution X in the neighbourhood of $\xi=0$, we,now require that $X\to0$ for $\xi\to0$. This is necessary to prevent particle accumulation at the turning points of the orbits. Expanding the Airy functions for large arguments we find that $X\sim\sqrt{2/\pi}\,b^{1/4}\,\sin(\frac{\pi}{4}+z(1))$ when $\xi\to0$. Therefore, we find that the argument of sin must be equal to $k\pi$ with k being an integer. Thus we found a relationship between the two eigenvalues a and b when a is large:

$$\int_0^1 dt\,\sqrt{1+\mu t^4}/(1+t^2)^2 = 3\pi k/8\sqrt{a+2b} \qquad (6)$$

For any value of b, we note that there are many possible values of $a_k(b)$, and for k large $a_k(b)\sim(3\pi k/8\times0.5986)^2$. Hence, by the Fourier inversion formula the solution can be written as

$$f = \frac{1}{2\pi}\sum_1^{\infty}\int_{-\infty}^{\infty}\exp(-i\beta\tilde{\tau})\,d\beta\,\exp(-i\alpha_k(\beta)\tilde{\theta})\left[A_k X_k(\alpha_k,\beta,\xi)+R_k\right] \qquad (7)$$

Here, R_k is the solution of the nonhomogenous term in (4). To determine $A_k(\beta)$ we use the "initial" condition $\hat{f}(\tau,\theta_0,\xi)$. For nonemitting limiter plate it is equal to $-f^{Max}H(\tilde{\tau})$ where H is the step function. For recycling or reflecting plates this value can be accordingly altered. In addition we need the orthogonality of the functions X_j and X_k. It can be shown that

$$\int_0^1 d\xi\,X_j(\beta,\xi)\,X_k(\beta,\xi) = C_j\,\delta_{jk}$$

where δ_{jk} is the Kronecker delta.Hence, $A_k(\beta)=\int_0^1\xi\,d\xi\,X_k(\hat{f}_0-\Sigma R_j)/C_k(\beta)$.

[1] F. L. Hinton and R. D. Hazeltine, Rev. Mod. Phys., 48, 239 (1976).

[2] F. L. Hinton and R. D. Hazeltine,Phys. Fluids, 17,2236 (1974).

AP21

COLLECTIVE SCATTERING OF CO_2-LASER LIGHT BY THE HIGHLY IONIZED ARGON PLASMA OF A HOLLOW CATHODE DISCHARGE

B.F.M. Pots*, J.J.H. Coumans and D.C. Schram
Physics Department, Eindhoven University of Technology, The Netherlands

1. Introduction. We report on collective scattering of CO_2-laser light with optical homodyne detection. The emphasis lies on the measurement of spontaneously appearing turbulence in a medium density plasma ($n_e=10^{19}-10^{20}m^{-3}$) with a c.w. low power CO_2-laser ($P_i=2W$). We compare the fluctuation level measured by scattering with the level at frequencies below 1MHz measured by optical probes. These optical probes measure the plasma light fluctuations.

Collective scattering refers to plasma scattering of electromagnetic radiation, for which the socalled scattering parameter $\alpha=(k\lambda_D)^{-1}>1$. Here $k=|\underline{k}|=|\underline{k}_s-\underline{k}_i|$, where $\underline{k}$ is the wavevector and s and i refer to "scattered" and "incident" respectively (cf. fig. 1); λ_D is the Debye length. The scattered power at frequency ω_s in a band $\Delta\omega_s$ is equal to :

$$P(\underline{k}_s,\omega_s,\Delta\omega_s)=P_i\, n_e\, L\,\sigma\,\Delta\Omega \int_{\omega_s-\frac{1}{2}\Delta\omega_s}^{\omega_s+\frac{1}{2}\Delta\omega_s} S(\underline{k}_s-\underline{k}_i,\omega'_s-\omega_i)\,d\omega'_s \qquad (1)$$

where L is the observation length, $\sigma=8\times10^{-30}m^2/sr$ is the Thomson cross-section and $\Delta\Omega$ is the solid angle. $S(\underline{k},\omega)$ is the spectral density function [1]. By varying the scattering angle θ (cf. fig. 1) and the frequency of observation ω_s, the function $S(\underline{k},\omega)$ can be studied in various parts of the $(\underline{k},\omega)$-space. For a thermal plasma $\int S(\underline{k},\omega)d\omega=1$ and the width of the spectrum can yield information about the ion thermal velocity or the ion acoustic velocity. For a turbulent plasma $\int S(\underline{k},\omega)d\omega\gg1$ is possible.

In homodyne detection the scattered power is mixed optically with a fraction of the original laser beam, called local oscillator (l.o.). The mixing eliminates the stray light problem, shifts the scattered spectrum from the optical to the r.f. range and enlarges the voltage level. No distinction between blue and red shifts can be made. The solid angle of detection is limited by $\Delta\Omega=\lambda_i^2/A$, where A is the effective source area. The ideal signal to noise ratio (SNR) for a photoconductive detector with quantum efficiency η is equal to :

$$SNR^{ideal}=\frac{\eta P_s}{2h\nu\Delta\nu}\sqrt{\Delta\nu\tau} \qquad (2)$$

$h\nu$ is the photon energy, $\Delta\nu$ is the i.f. band of detection and τ is the post detection integration time. The ideal SNR is approached when the shot noise of the l.o. is dominant.

2. CO_2-scattering diagnostic (cf. fig. 1). Our CO_2-laser beam is focussed in the plasma to a spot of 2 mm; a fraction is used as l.o. The scattered radiation is 1) chopped for phase sensitive detection purposes and 2) mixed with the l.o. on a liquid helium cooled Ge:Cu detector (1 mm^2, current 1mA, η=10%). As mentioned for optimum SNR the l.o. shot noise should be dominant with respect to other noise sources. On the other hand low detector dissipation asks for low l.o. power. Therefore,we choose a high load (600 Ω), source follower and ultra low noise components; then 10 mW l.o. power suffices. Passive band pass filters (center frequency 1-50 MHz, relative bandwidth 0.1-0.3, 24 dB/octave) are used for spectral analysis. The scattering angle θ can be varied between 1^o and 7^o ($0.02\lesssim k\lambda_D\lesssim0.1$).

As the l.o. passes through the plasma also "small-k" scattering will be detected in addition to the scattering at angle θ. It can be discriminated by phase sensitive detection and measured seperately. It yields information about $S(\underline{k},\omega)$ in the low frequency region, however, without $\underline{k}$-resolution.

We achieve SNR's about a factor ten below the quantum limit (2). The degradations are due to the use of a chopper, losses in mixing efficiency and remnant noise, including noise contributions of the"small-k"scattering, besides l.o. shot noise.

For the calibration of the diagnostic we refer to reference [2].

3. Plasma facility. We use a low pressure (10^{-3} torr) hollow cathode discharge. The plasma (argon) is cylindrical (radial 10 mm, length 1.5 m), magnetically confined (B<0.5 T), stationary, current driven (10-300 A) and highly ionized. Typical plasma parameters are $n_e=10^{19}-10^{20}m^{-3}$, T_e=3-10 eV, T_i=1-20 eV [2]. The ion plasma frequency is about 200 MHz and the Debye length about 2 μm. The scattering volume is located relatively far from the cathode (0.25 m).

4. Experimental results and discussion. We used two scattering geometries : $\underline{k}\parallel\underline{B}$ and $\underline{k}\perp\underline{B}$. A remarkable result is that we find for all parameter sets a fluctuation level close to thermal for $\underline{k}\parallel\underline{B}$, whereas for $\underline{k}\perp\underline{B}$ the fluctuation level can reach several orders of magnitude above thermal. A typical example of $S(\underline{k},\omega)$ with $\underline{k}\perp\underline{B}$ is shown in figure 2. The measurements show : 1) a linear dispersion corresponding to the ion acoustic velocity; 2) a decay in both $k_\perp$ and ω; 3) the occurance of a peak near the lower hybrid frequency, i.e. Ω_{LH}=40 MHz (drift lower hybrid instability). In figure 3 the relative fluctuation level $\tilde{n}_e/n_e=\sqrt{\int d^3\underline{k}/(2\pi)^3 S(\underline{k},\omega)n_e}$ is given as function of frequency for the same parameter set as in figure 2. The integration refers to the whole $\underline{k}$-space. We assume here that no other turbulence phenomena are present than observed around the ion acoustic velocity line in the $(k_\perp,\omega)$-plane. The points measured by the optical probes are indicated and the overall behaviour is a $1/\omega^2$-decay spectrum. We note that also the optical probes measurements point out fluctuations with a propagation perpendicular to $\underline{B}$.

5. Expectations for Tokamak plasmas. An interesting question is whether supra-thermal drift-wave turbulence levels can be measured in a large sized Tokamak plasma with a low power c.w. CO_2-laser, as Surko and Slusher did with a high power 200 W c.w. CO_2-laser [3]. For a CO_2-laser and λ_D=20 μm, scattering angles between $.1^o$ and 1^o are to be used, with a laser beam diameter of $d=10^{-2}$m; for drift waves the frequencies are relatively low ($\omega=10^6-10^7$ rad/s). Spatial resolution is bad (L=1m). With a fluctuation level of 10^5 times thermal, P_i=20 W, $n_e=10^{20}m^{-3}$, L=1 m, $\Delta\Omega=\lambda_i^2/\pi(d/2)^2=1.4\times10^{-6}$ sr with $d=10^{-2}$m, 10% of the total phenomenon at a specific $\underline{k}$ in a typical frequency band of $\Delta\nu=5\times10^4$ Hz and an optical transmission of 50%, yields $P_s=10^{-10}$ W. With η=10%, a total degradation of a factor ten, and $\tau=10^{-2}$ S, we get SNR=10^4, i.e. fluctuations are measured easily on a time scale of 10 ms. We note that multiplexing both in $\underline{k}$ and ω-space is possible, so that in one plasma shot $S(\underline{k},\omega)$ can be studied as function of time.

References

[1] J. Sheffield, "Plasma scattering of electromagnetic radiation", Academic Press, New York, 1975.
[2] B.F.M. Pots, thesis, Eindhoven University of Technology, 1979, to be published.
[3] C.M. Surko and R.E. Slusher, Phys. Rev. Lett., 37 (1976) 1747.

*) supported by Stichting FOM, the Netherlands.

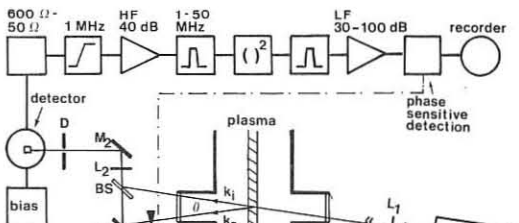

Figure 1

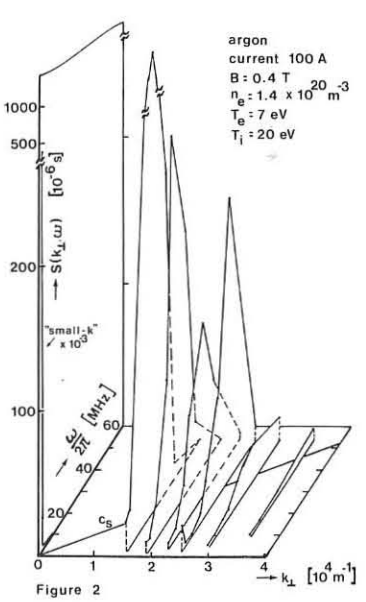

Figure 2

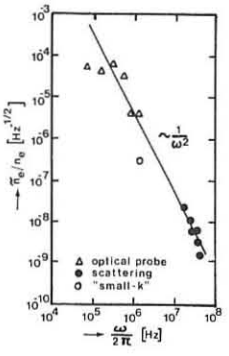

Figure 3

AP22

SPACE POTENTIAL MEASUREMENTS WITH PARTICLE BEAM PROBES*

R. L. Hickok, W. C. Jennings, K. A. Connor, and J. T. Woo

Plasma Dynamics Laboratory
Rensselaer Polytechnic Institute
Troy, New York 12181 U.S.A.

This paper presents a comparison of four heavy ion beam probe diagnostics systems that are in operation or under construction. The beam probes are located at the ELMO Bumpy Torus at Oak Ridge National Laboratory; the Tandem Mirror Experiment at Lawrence Livermore Laboratory; the research Tokamak, RENTOR, and the ALEX Baseball experiment at Rensselaer Polytechnic Institute. The EBT system is fully operational, the TMX and RENTOR systems are completely installed and detailed alignment with the magnetic fields is in progress, and the ALEX system is in the process of being assembled on a test stand. The primary objective of each system is the measurement of the plasma space potential with auxiliary objectives of studying plasma density, electron temperature, magnetic field structure, and fluctuation levels.

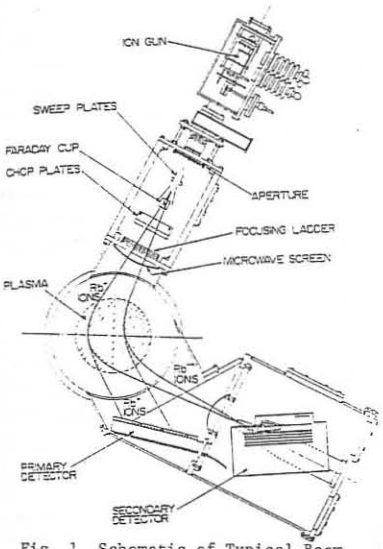

Fig. 1 Schematic of Typical Beam Probe System

The essential features of all four beam probe systems are the same and are illustrated in the schematic diagram of the EBT probe shown in Fig. 1. The basic components consist of a gun chamber to produce the heavy ion beam; an optics chamber that contains auxiliary lens, sweep plates and beam monitors; the plasma region where the charge state of the beam ions is changed by interaction with the plasma electrons; and the detection chamber that houses the energy analyzer to monitor the energy and intensity of the secondary ions. The space potential is determined by measuring the difference in energy between the primary and secondary ions, the intensity of the secondary ion signal provides information on the plasma density and electron temperature and the momentum of the secondary ions can provide information on the magnetic field. Typical primary beam characteristics are a few tens of microamps of alkali metal ions at 10 to 70 KeV and the secondary ion signal is usually of the order of a few tens of nanoamps.

The EBT systems takes advantage of the D.C. operation of this device by using a chopped beam and phase sensitive detection to provide increased sensitivity. With the increased sensitivity we can observe the 1^+ to 3^+ and the 1^+ to 4^+ transitions as well as the usual 1^+ to 2^+ reaction used with beam probing. An analyzer energy scan showing the various secondary ion charged states is shown in Fig. 2. In principle this information can be used to evaluate the electron temperature, but it requires large correction factors that are not well known since the various charged states do not come from the same point in the plasma and they have different sample volumes. The 3^+ and 4^+ signals can be used to measure ϕ. This has the advantage that energy difference between the primary and the 3^+ and 4^+ ions is 2ϕ and 3ϕ respectively, but it has the disadvantage of weaker signals and higher beam energy to probe the same point in the plasma. The 3^+ and 4^+ signals are very useful in making potential measurements at different points in the plasma without changing the beam injection parameters. This provides confirmation of the potential profiles obtained with the 2^+ secondary ions. Figure 3 shows a typical space potential profile measurement on EBT. This is an energy scan along a curved detection line that is more or less vertical.

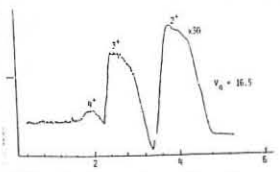

Fig. 2 Secondary Ion Charge States Observed on EBT

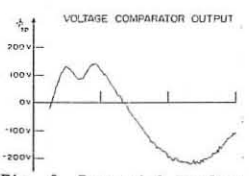

Fig. 3 Potential Profile Observed on EBT

The TMX beam probe system must take into consideration the variation in the beam trajectories with the plasma beta. As beta increases, it will automatically scan the observation point across the plasma without changing either the beam energy or the injection angle. This is illustrated in Fig. 4 where the observation point in the plasma for a given set of injection characteristics is plotted as a function of plasma beta. Unfortunately beta is an unknown parameter, but by monitoring the location of the primary beam after it has traversed the plasma, as a function of the injection parameter, we expect to obtain an evaluation of beta. The calculated scan is for an assumed square well beta extending out to a 30 cm radius with flux conserved inside the solenoid coils. There is only very minor changes in the beta scan if flux conservation is neglected.

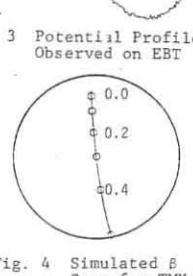

Fig. 4 Simulated β Scan for TMX

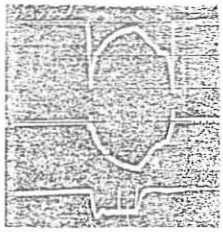

Fig. 5 Primary Ion Signal on TMX

The primary beam has been aligned with the vacuum magnetic field and Fig. 5 shows the beam walking across the primary detector as the magnetic field is pulsed. This is a long resistive detector so that the voltage signal out each end is proportional to the beam location. As the field comes up the beam abruptly appears on the north end (top trace) then this signal decreases while the south end signal (center trace) increases until the field reaches full value. As the field decreases, the beam walks back north and finally off the detector.

On RENTOR one of the major problems is the toroidal deflection of the beam by the poloidal magnetic field. The effect of the vacuum poloidal field can be compensated for by appropriate steering of the beam in the optics chamber, but the field produced by the plasma current gives an unknown amount of toroidal momentum to the beam. The detector in the electrostatic analyzer is split in the toroidal direction and we anticipate using a feedback loop to hold the beam centered on the split plates. This should provide information on the current density distribution, but the accuracy of the results will depend on the signal to noise ratio of the measurements. Figure 6 shows the walking of the beam in the toroidal direction due to the vacuum poloidal field produced by the OH windings. The signals are from a set of radial wires in the bottom of the diagnostic box. The wires are separated by 1 cm. The beam starts to the left of the first wire, walks across it and the second wire, and ends up on the third wire. The toroidal field is also pulsed at the same time so the beam is walking in both the radial and toroidal direction. A programmed toroidal sweep is used to keep the beam centered in the vacuum field. A standard technique for calibrating beam probe systems and to establish the proper slaving conditions, is to bend the primary beam into and through the electrostatic energy analyzer. Figure 7 shows a typical signal when this procedure is carried out with the RENTOR beam probe.

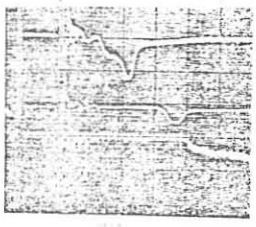

Fig. 6 Toroidal Displacement of Primary Beam on RENTOR

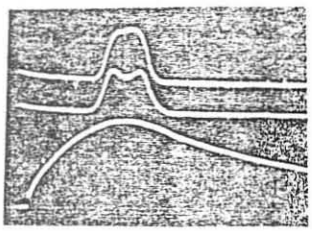

Fig. 7 Primary Beam Signal Through Analyzer on RENTOR

On ALEX a neutral beam rather than an ion beam is used to probe the plasma. A schematic diagram of the primary beam line, showing the alkali metal vapor neutralizing cell and a deflection chamber to remove any unneutralized portion of the beam is shown in Fig. 8. The advantage of this system is that the primary beam is not severely defocused by the strong field gradients of the "baseball" geometry, the required beam energy is reduced by a factor of four and the reaction cross section is higher for the low temperature arc plasma used in ALEX. The disadvantage is the necessity of incorporating the neutralizing cell with its associated inefficiencies and the inability to sweep the beam across the plasma. The plasma can still be scanned in one dimension by sweeping the beam energy.

The present status of all four beam probe systems will be reported and the latest results presented.

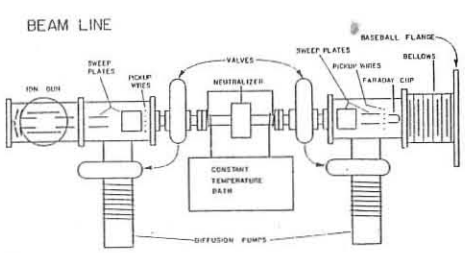

Fig. 8 Schematic of Primary Neutral Beam Line on ALEX

*Work supported by ORNL, LLL, and DOE.

AP23

PRODUCTION OF PLASMA CURRENTS BY MEANS OF ROTATING MAGNETIC FIELDS

W.N. Hugrass, I.R. Jones and M.G.R. Phillips

The Flinders University of South Australia
Bedford Park 5042 South Australia

The technique of generating azimuthal electron currents in a cylindrical plasma column by means of transverse rotating magnetic fields was first investigated by Blevin and Thonemann [1] and Davenport et al [2]. In this paper the results of theoretical and experimental extensions to these early studies are presented and attention is drawn to the merits and versatility of the technique in generating the steady equilibrium currents appropriate to a variety of plasma-field configurations.

In essence, the technique involves applying a rotating magnetic field in a direction transverse to the axis of a cylindrical plasma column. Provided that the angular frequency of the rotating field (ω) lies between the ion and electron cyclotron frequencies, ω_{ci} and ω_{ce} (calculated with reference to the amplitude of the rotating field, B_o), and provided the electron collision frequency, ν_e, is less than the electron cyclotron frequency, the electrons can be considered as "tied" to the lines of force of the rotating field. They circulate synchronously with the angular frequency of the rotating field whereas the ions (at least in the short term) have no nett azimuthal motion. As long as the system remains azimuthally symmetric, no charge separation occurs and the electrons are not prevented from moving by space charge fields. The electrons thus form a steady azimuthal current layer which generates a steady axial magnetic field.

In both the above discussion, and in Refs. [1] and [2], the implicit assumption is made that one is discussing a steady-state situation where a rotating magnetic field completely permeates a plasma column and drives an azimuthal plasma electron current. In practice, the plasma column to which the rotating field is applied is obtained either by preionizing the neutral filling gas or by allowing the induced electric field associated with the rotating field to do the ionizing. In either case the important question arises as to whether or not the rotating field will fully penetrate the plasma column in the first instance. This question has been investigated by means of a numerical study of the initial value problem. The penetration of a transverse rotating magnetic field into an uniform, infinitely long cylindrical plasma column was followed in time. It was assumed that the ions formed a fixed, uniform neutralizing background and that the resistivity, η, was uniform and remained constant in time. Provided that $\omega_{ci} < \omega < \omega_{ce}$ and $\omega < \nu_e < \omega_{ce}$, the appropriate form of Ohm's law is:

$$\vec{E} = \eta\vec{j} + \frac{1}{n_e e}(\vec{j} \times \vec{B})$$

The effect of the non-linear Hall term (which becomes significant when $\nu_e/\omega_{ce} \sim 1$) is to aid the penetration of the rotating field.

These model calculations showed that for small values of B_o the rotating field only partially penetrates the plasma column and only a fraction of the electrons rotate. On increasing the value of B_o, a threshold regime is reached where the number of rotating electrons increases rapidly. Above a certain value of B_o, there is no gain to be obtained by further increasing the amplitude of the rotating field because a situation is already reached where all the plasma electron rotate synchronously with the field. The lower the value of ν_e, the lower is this critical value of B_o.

An experiment was made in which the rotating field technique was used to generate a theta-pinch like distribution of field and plasma. This experiment both illustrated certain features of the numerical calculations and demonstrated the usefulness of the technique. A straight, cylindrical pyrex discharge tube, of 5 cm internal diameter and 70 cm length was equipped on the outside with two longitudinal loops orientated at 90° to each other. R.f. currents of the same frequency and amplitude, but dephased by 90°, were passed through these two loops to produce a transverse magnetic field which rotated about the axis of the discharge tube. The r.f. currents were generated by means of Weibel type r.f. line generators [3] which were modified in such a manner as to reduce substantially the necessary number of spark gaps. Each line generator could produce a short r.f. current pulse consisting of eight periods at a frequency of 0.67 MHz. The equivalent generator impedance and the rms open circuit voltage of each generator was 9.7Ω and 14.1 kV, respectively. No attempt was made to match the generators to the load. In fact, since the load impedance was at all times a small fraction of the generator impedance, the generators behaved essentially as constant current sources. The amplitude of the vacuum rotating field produced in this manner was 220 gauss on axis. An external solenoid was used to produce a steady bias magnetic field, B_a, directed along the axis of the discharge tube. In these experiments, the filling gas was argon. The use of argon ensured that the necessary condition, $\omega_{ci} < \omega < \omega_{ce}$, was easily satisfied.

Provided the conditions set out at the start of this paper are satisfied, the applied transverse rotating field drives a steady azimuthal electron current in a cylindrical plasma. At any radial position r, the electron drift velocity is $r\omega$ and, if all the plasma electrons partake of the rotational motion, $j_\theta(r) = n_e(r)\,|e|\,r\omega$. The component of the total axial magnetic field which is generated solely by the rotating electrons, $B_z(r)$, is

$$B_z(r) = \frac{\mu_o |e|\,\omega\,N(r)}{2\pi}$$

where $N(r) = \int_r^R 2\pi\, n_e(r) r\, dr$ is the line density of electrons lying between r and R; R is the inner radius of the discharge tube. Note that

$$B_z(R) = 0 \quad \text{and} \quad B_z(0) = \frac{\mu_o |e|\,\omega\,N_o}{2\pi}$$

where N_o is the electron line density. The direction of $B_z(r)$ depends on the sense of rotation of the rotating field. For the application we have in mind, we have to consider the case where the axial field component produced by the rotating electrons is in the opposite direction to the applied bias field, B_a. The total axial magnetic field, $B_T(r)$, is therefore given by $B_T(r) = B_a - B_z(r)$.

Experiments were conducted with two filling pressures of argon, namely 3.7 mTorr and 6.0 mTorr. For the 3.7 mTorr experiments it was observed that the rotating field fully penetrated the plasma column and set the electrons rotating. By choosing two different values of B_a it was possible to generate theta-pinch like configurations having different on-axis β-values. Typically, B_a = 740 gauss, $B_z(0)$ = 300 gauss and $\beta(0)$ = 65%. These configurations were sustained for ~ 10 μsec, this being the effective duration of the r.f. pulse. In the 6.0 mTorr experiments, it was observed that the effective electron collision frequency was too high, only partial penetration of the rotating field occurred and only a fraction of the electrons rotated.

The technique discussed in this paper can be used to generate the steady equilibrium currents appropriate to a variety of plasma-field configurations. In particular, the use of it to generate the equilibrium currents corresponding to the spheromak, reversed field pinch and screw pinch/high-β tokamak configurations has already been discussed [4-6] and demonstrated in preliminary experiments.

[1] H.A. Blevin and P.C. Thonemann, Nucl. Fusion, 1962 Suppl., Part I, p.55 (1962)

[2] P.A. Davenport et al., U.K.A.E.A. Culham Report CLM-R65 (1966)

[3] E.S. Weibel, Rev. Sci. Instrum. 35, 173 (1964)

[4] I.R. Jones, Flinders University Report FUPH-R-151 (1979)

[5] I.R. Jones, Flinders University Report FUPH-R-153 (1979)

[6] W.N. Hugrass, I.R. Jones, M.G.R. Phillips, Flinders University Report FUPH-R-155 (1979).

AP24

SCREENING EFFICIENCY OF THE SCRAPE OFF PLASMA IN THE SHADOW OF A POLOIDAL LIMITER

A. Nicolai
Institut für Plasmaphysik der Kernforschungsanlage Jülich GmbH. Association EURATOM-KFA, 5170 Jülich, Federal Republic of Germany

Abstract

The plasma parameters in the scrape off layer of a poloidal limiter are calculated by introducing additional particle and energy loss terms into the six-regime version of Düchs' code /1/. The plasma has two ion components, one hydrogen and one impurity species. The impurity influx from the outside, gasinlet in the oxygen and sputtering in the iron case, is treated by a two-dimensional model. Using TEXTOR data it turns out that the screening efficiency of the scrape off layer is about 25% in the oxygen and 45% in the iron case. The recycling rate of oxygen at the limiter was assumed to be 100% and the gas puffing rate was $\dot{N}=1.35\cdot10^{20}$/sec. The iron ions are supposed to stick at the limiter surface.

1. Impurity built-up

1.1 Oxygen

The oxygen influx ϕ_o consists of two parts, ϕ_{o_1} and ϕ_{o_2}, the first of which

$$\phi_{o_1} = 2\pi R\cdot 2\pi\, r_{lm}\,(n_{o_f}-n_{o_i})/\Delta t$$

is due to the oxygen gaspuff which is supposed to increase the mean oxygen density from n_{o_i} to n_{o_f} linearly during the time Δt. R and r_{lm} are the major and minor radius (Fig. 1). The second contribution

$$\phi_{o2} = 2\pi\,\alpha\,A \int_{r_{lm}}^{r_{ln}} \Lambda_v\, n_v\, v_v\, dr$$

emanates from the impurity recycling processes at the limiter surface. A is the recycling rate. r_{lm} and r_{ln} are the radii of the limiter and liner plane respectively (Fig. 1), n_v is the impurity density summed over all ionization stages. Λ_v is the Boltzmann factor /2/ and α is a constant /3/ and v_v is the impurity ions thermal velocity.

1.2 Iron

The influx of iron atoms has during normal tokamak operation essentially two reasons: charge exchange sputtering at the liner surface and ion sputtering at the limiter surface. Arcing, the ablation of blistered macroscopic iron particles and the selfsputtering evoked by the impurity ions being accelerated in the potential sheath are neglected here though they might be important impurity sources. The flux of sputtered iron due to the escaping charge exchange neutrals reads

$$\phi_{Fe_1} = \sum_{j=1}^{10} \frac{d\Gamma_{hj}}{dE}\,\chi_1(E)\,dE$$

Here the sum runs over the generations of the charge exchange neutrals /3/ and $d\Gamma_{hj}/dE$ is the energy distribution of the hot neutrals. $\chi_1(E)$ is the sputter coefficient /5/.

The flux of sputtered iron released at the limiter surface is obtained as follows:
Before entering the sheath in the hydrogen ions have one half of a Maxwellian as distribution function. The sheath leads to a shift of the energy of the impinging ions of about $|e_oU|$ where U is the sheath potential. By folding the sputter coefficient /5/ for the shifted energy $\chi(E+|e_oU|)$ with the distribution function in front of the sheath, we get the temperature and voltage dependent sputter coefficient

$$\chi_2(T,U) = 4 \int_o^\infty du\, u^3 \exp(-u^2)\,\chi(u^2\cdot kT+|e_oU|)$$

The integration variable is $u=v/v_i$ where $v_i=\sqrt{2m_i/(kT_i)}$ is the ion thermal velocity. Fig. 2 shows a strong dependence of the sputter coefficient on the sheath potential if the temperature is below 200 eV.

The flux of the sputtered iron due to ion impact at the limiter then reads

$$\phi_{Fe_2} = 2\pi\,\alpha \int_{r_{lm}}^{r_{ln}} \Lambda_i n_i v_i \chi_2(T_i,U)\, rdr$$

Here n_i is the ion density, calculated in the diffusion model discussed below, Λ_i is the ions' Boltzmann factor /3/. In analogy to the treatment of the cold neutrals due to the hydrogen recycling at the liner and limiter surfaces /4/, the density of the neutral impurity atoms within the plasma is calculated by means of the expression

$$n_{o_1}(r) = \frac{\phi}{v_o} \int_o^\pi d\vartheta \exp\left(-\frac{1}{v_o}\int_o^l n_e\,\langle\sigma v\rangle_I\, dl'\right)$$

v_o is the velocity of the incoming impurity atoms the distribution function of which is supposed to be isotropic and monoenergetic, $\langle\sigma v\rangle_I$ is the ionization rate coefficient for the first ionization stage /6,7/. The length l is defined in /4/. Integration of the impurity volume source term

$$S_v = n_e n_v \langle\sigma v\rangle_I$$

over the scrape off region and the central core gives the fluxes of impurity atoms being ionized in these regions (Fig. 1):

$$\phi_a = 4\pi^2 R \int_{r_{lm}}^{r_{ln}} rdr\, S_v\,; \qquad \phi_c = 4\pi^2 R \int_0^{r_{lm}} rdr\, S_v$$

The screening efficiency is then given by $\eta_e = \phi_a/(\phi_a+\phi_c)$.
In the oxygen case the fluxes ϕ_a and ϕ_c are calculated analogously.

2. Diffusion model

The diffusion model emanates from the fact that the transport parallel to the magnetic field is caused by MHD processes and by parallel electron heat conduction on a very short time scale (typically 10 - 30 microseconds). On the other hand the time scale for the diffusion processes perpendicular to the magnetic field is 10 - 20 milliseconds. Therefore, if there are closed flux surfaces in the s.o.l., the densities and temperatures are almost constant on them, even in case of the impurity ions. By applying the conservation laws on the region between two infinitesimally neighbouring flux surfaces, additional loss terms occur in the transport equations which are equal to the particle or energy flux densities at the limiter surface divided by some characteristic length l/2, 3/.

3. Sheath potential and secondary emission

The requirement that the net current density due to the influx of hydrogen ions, impurity ions, electrons and due to secondary electron emission should vanish locally results in an equation of the sheath potential /2,3/. As there are strong relaxation processes (two-stream and the mirror instability) in the bulk of the scrape-off region deviations from the Maxwellian distribution function are supposed to be negligible.

4. Results

Various calculations concerning the TEXTOR device (r_{lm} = 50 cm, r_{ln} = 54 cm, R = 175 cm, toroidal field B_t = 20 kG, plasma current I_p = 476 kA, mean density n = $2\cdot10^{13}$ cm) have been done. Some typical results are given below.

4.1 Oxygen

If an oxygen gaspuff which raises the oxygen content from 1% to 3% is applied between 400 and 430 ms, i.e. during the flat top phase, one obtains at the end of the gaspuff the parameters shown in Fig. 3. The hydrogen density deviates strongly from the electron density at the limiter edge, because Z_{eff} is about 4 here. The temperature distribution is very similar to the case without impurity inlet /2/, as the radiation losses are still small compared to the limiter losses. About 85% of the charge flux of the incoming electrons is balanced by the secondaries and only 10% by the hydrogen and 5% by the oxygen ions, so far the limiter edge is concerned. The impurity density there is about 20% of the hydrogen density. The impurity profile deviates considerably from the graphs of the other plasma parameters characterized by an almost exponential decay. The reasons are the strong deposition by the gaspuff and the decrease in the loss term due to the lower thermal speed of the impurities. Fig. 4 shows the different ionization stages of the oxygen which are calculated from a time dependent coronal equilibrium, i.e. by means of the rate equations. Their solutions is interwoven with the solution of the diffusion equation /8/. This procedure seems to be reansonable for the central core, but is somewhat doubtfull for the scrape off region because of the steep gradients and the strong flow parallel to the magnetic field. Nevertheless, the concentrations of the ion species O_2-O_7 shown in Fig. 4 had been calculated by this procedure. The position of the maxima should be typical, whereas the wings of the curves might be not so steep in reality. The density of the neutral oxygen is in the limiter plane about 30% smaller as in the liner plane. 100% recycling at the limiter surface is assumed. At 430 ms the particle fluxes ϕ_{o1}, ϕ_{o2}, ϕ_a and ϕ_c are 22A, 40A, 15A and 47 A, so that the screening efficiency is 24 %.

4.2 Iron

The fluxes ϕ_{Fe_1} = 0.87 A and ϕ_{Fe_2} = 0.61 A, calculated at 430 ms are of the same order of magnitude. The fluxes ϕ_a and ϕ_c turn out to be 0.64 A and 0.85 A respectively so that the screening efficiency is 43%. As expected the screening efficiency for iron is higher than that for oxygen. As it is assumed here that both fluxes ϕ_{Fe_1} and ϕ_{Fe_2} are released in the liner plane the screening efficiency might be somewhat overestimated. As a similar consideration applies also to the oxygen case, the screening efficiency calculated here might be also somewhat too high.

References

/1/ D.M. Meade et al. Proc. 5th Int. Conf., Japan, paper CN-33/1 14-4 (1974)
/2/ A. Nicolai, G. Fuchs, J. of Nucl. Mat. 76, 556 (1978)
/3/ A. Nicolai, G. Fuchs, Proc. 8th Europ. Conf. on Contr. Fus. and Plasma Phys., Vol. 1, paper 26
/4/ D.F. Düchs, D.E. Post. P.H. Rutherford, Nucl. Fus. 17, 565 (1977)
/5/ H.L. Bay, J. Roth, J. Bohdansky, J. Appl. Phys. 48, (1977) 4722
/6/ D. Düchs, NRL Report 7340
/7/ W. Lotz, IPP Report 1/76
/8/ D.F. Düchs et al., 6th Europ. Conf. on Contr. Fus. and Plasma Phys., Vol. I, 29 (1973)

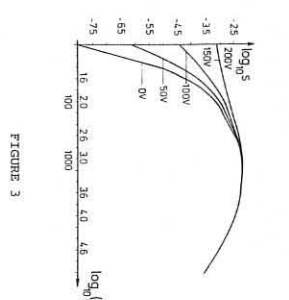

FIGURE 3

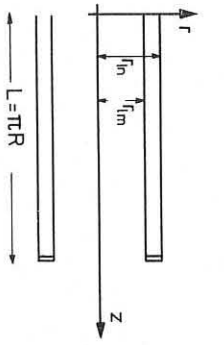

FIGURE 1

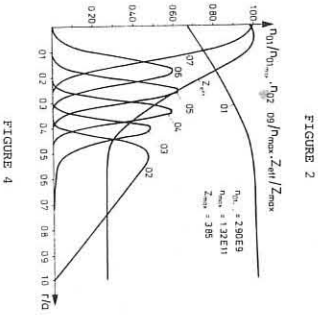

FIGURE 4

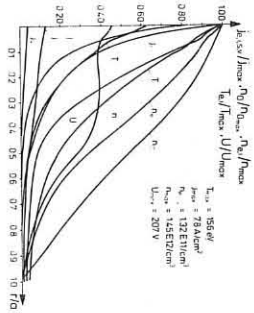

FIGURE 2

FIGURE CAPTIONS

Fig. 1: Geometry

Fig. 2: Sputter yield (Hydrogen - SS)

Fig. 3: Plasma Parameters in the S.o.L.

Fig. 4: Ionization stages of oxygen in the S.o.L.

AP25

Experimental Studies of Scaling Laws in a Cold Mantle
J.R. Drake and A. Kuthy
Royal Institute of Technology, S-100 44 Stockholm 70, Sweden

Abstract: The classical one-third power scaling of the plasma density with the neutral density was observed down to a plasma density of $1.2\times10^{21}m^{-3}$ with a neutral wall density of $2.4\times10^{20}m^{-3}$ and a field strength of 0.5 T.

Introduction: A cold-mantle is a shell of interpenetrating plasma and neutral gas surrounding an impermeable plasma core. In this shell, the neutral density, n_1, is determined predominantly by diffusive penetration of neutrals into the cold mantle from a source region outside the cold-mantle shell. The diffusive scale length is $L_o=(\lambda_{ex}\lambda_{ion})^{1/2}$ where λ_{ex} and λ_{ion} are the neutral mean free paths for charge exchange and ionization respectively. The cold-mantle boundary layer regime is attained if the plasma temperature, T_b, is above 2 eV and the product of the plasma density, n_b, and cold mantle thickness, Δ, satisfies $n_b\Delta \gtrsim 10^{19}m^{-2}$[1]. Experimental studies of scaling laws and observations of plasma density and temperature profiles and neutral penetration were carried out in this parameter regime in the F I rotating plasma device.

In this regime, the observed scaling between n_b and the neutral hydrogen atom density at the wall, n_{1w}, followed the scaling law given by

$$n_b \propto (n_{1w}B^2)^{1/3}$$

where B is the magnetic field strength. In this paper we report verification of this scaling to lower neutral and plasma densities than previously reported [2,3]. This one-third power scaling law implies that n_b is predominantly determined by the particle and momentum balances.

In addition, we have measured plasma n and T profiles at various power input levels and have calculated the neutral profiles using the Boltzmann equation and these measured profiles. The observed plasma density profiles and amplitudes were comparatively intensitive to P, but the temperature profiles and amplitudes were strongly dependent on P. Temperature increased with P. In the calculated neutral profiles, L_o was dependent on P through the strong dependence of λ_{ion} on T in the 2-eV temperature range. In fact, the criterion for sustaining an impermeable-core plasma was maintaining the core temperature above 2eV [4]. For all values of B and n_{1w}, we observed that the penetration of neutrals was determined by these temperature profile effects.

Apparatus: The experiments were carried out on the F I rotating plasma device which has a purely-poloidal spherator magnetic field [3]. The azimuthal $\vec{E}\times\vec{B}$ rotation velocity is sheared and therefore the plasma is heated through ion viscosity. This provides a technique for coupling high power inputs, up to $10^8 W/m^3$, to the plasma. The device has the disadvantage that particle and energy transport parallel to $\vec{B}$ give losses to the internal ring support. However in the experiment discussed here, the rotation parameters and $\vec{B}$ were such that transport perpendicular to $\vec{B}$ dominated and the particle containment scaled classically like B^2. The central plasma density ranged from $1\times10^{21}m^{-3}$ to $6\times10^{21}m^{-3}$ and the central temperature from 2eV to 15eV depending on field strength, filling pressure and power.

The experiments were carried out with a typical poloidal field of 0.5 T. Classical highly collisional ion transport in this spherator device with q=0 is roughly equivalent to that in a tokamak with q=3 and a toroidal field strength of 1.5 T.

One-Third Power Law. The scaling law relating the plasma density at the edge of the impermeable core to the neutral density at the wall is derived by assuming the presence of a steady-state fluid balance between the outward diffusion flux of ions and the inward diffusion flux of neutrals. The friction between ions and neutrals is neglected when considering the ion-fluid momentum balance so that the ion diffusion flux has the classical form $\Gamma_\perp \propto n^2B^{-2}T^{-1/2}(\nabla_\perp n/n + \nabla_\perp T/2T)$.

However, the dominant term in the neutral fluid momentum balance is the friction exerted on the neutrals by the ions through charge exchange collisions. Thus the scaling for the neutral flux in regions where $n>n_1$ is given by $\Gamma_{1\perp}\propto\nabla_\perp(n_1T_1)/n$. If the temperature profile effects are neglected in the cold-mantle boundary layer, a spatial integration of the flux balance gives the one-third power law.

This predicted scaling has been experimentally examined. The plasma density measurements were made using interferometry. The filling pressure was taken as the neutral pressure at the wall. The dense plasma volume represented only about 10% of the vacuum volume so we assumed that the vacuum volume was an infinite reservoir of room temperature neutral hydrogen. In Fig. 1, we show the plasma density versus the filling pressure expressed as a neutral H-atom density. The field strength was 0.5 T and density values were taken at a constant density-normalized power input level of 4×10^4 eV/sec per ion. The scaling followed $n_b\propto n_{1w}^{1/3}$ down to values where the ratio n_b/n_{1w} was 5.

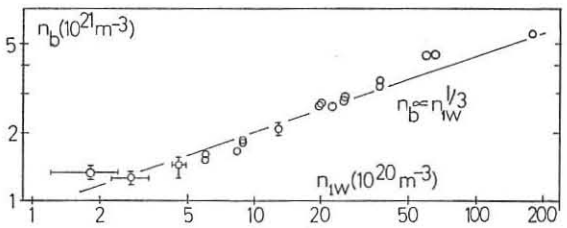

Fig.1. n_b versus n_{1w} showing the one-third power law-scaling.

To demonstrate the classical nature of the particle containment, we show the scaling of n_b versus B at a fixed n_{1w} and fixed power input in Fig.2. The scaling followed the classical expectation, $n_b\propto B^{2/3}$.

Neutral Penetration: We have calculated the neutral profiles for various power inputs by numerically integrating the Boltzmann equation using experimentally measured n and T profiles. These calculated profiles show an increased penetration of the neutrals with decreased power input. A minimum power, P_{min}, was needed to maintain the core temperature above 2eV while also, of course, replacing the energy losses from the system due to enthalpy transport, conduction and radiation [4]. If P was below P_{min}, the core became permeable to neutral penetration.

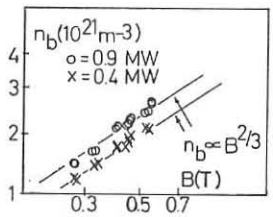

Fig.2. Scaling of n_b versus B.

Figure 3 shows examples of the experimentally measured n and T profiles. The outer half of the profiles on the equatorial midplane are shown as a function of the major radius. Only two power inputs are shown for clarity.

In Fig.4, we show the calculated neutral profiles based on n and T profiles for different power inputs. Note that with higher P, the neutral density decayed rapidly starting immediately inside the limiter. The inner neutral density was determined solely by recombination at these powers. For decreased powers, the neutral penetration was increased and, at P=0.24 MW, the central neutral density was attenuated by less than a factor of 10.

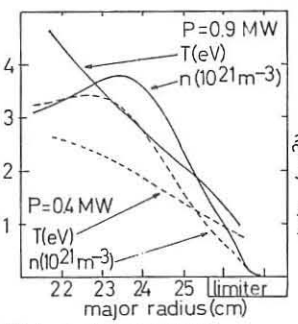

Fig.3. n and T profiles.

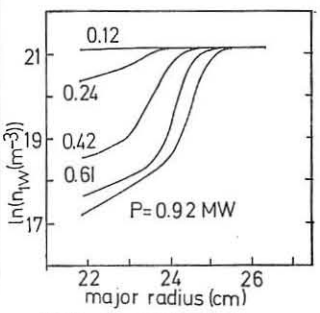

Fig.4. n_1 profiles.

As seen in Fig.4, the plasma core was permeable at P=0.24 MW. In the F I rotating plasma device, this transition to a permeable core was easily seen experimentally. The axisymmetry of the system was lost and the plasma broke up into rotating spokes which were evident on all diagnostics. Thus the calculated neutral profiles are consistent with the other experimentally observed characteristics indicating the transition from an impermeable to a permeable plasma core as a function of power input.

Conclusion: The plasma density amplitude followed the one-third power scaling law for $1\times10^{21}<n_b<6\times10^{21}m^{-3}$ even though the derivation of this law neglects temperature profile effects. However, the temperature amplitude and profile was strongly dependent on the power input and, in turn, the neutral penetration scale length was dominated by the temperature profile effects.

Acknowledgements: This work has been supported by the European Communities under an association contract between Euratom and Sweden.

References:

[1] B. Lehnert, Nucl. Fusion 8, 173(1968).
[2] Ringboog Group, in "Proceedings of the International Symposium on Plasma-Wall Interaction, Jülich, 1976.
[3] B. Lehnert et al, 7th Int.Conf. on Plasma Phys. and Contr.Nucl. Fus.Res., Innsbruck, 1978, paper CN-37-X-3.
[4] B. Lehnert et al., Physica Scripta, 9 109 (1974).

THE TECHNIQUE OF IR HOLOGRAPHY AT 10.6 μm FOR LASER-PRODUCED PLASMA DIAGNOSTICS

E.M.Barkhudarov, V.R.Berezovskii, T.Ya.Chelidze, G.V.Gelashvili, M.I.Taktakishvili, N.L.Tsintsadze

Institute of Physics, Academy of Sciences of the Georgian SSR, Tbilissi, USSR

Abstract: The results of the development of IR holographic interferometry technique utilizing a pulsed CO_2 laser (λ = 10.6 μm) are presented. The possibility of its application to diagnostics of a laser-produced solid target plasma in vacuum, as well as a laser-produced spark in a gas, has been demonstrated.

In studying the high-temperature plasma in devices of Tokamak type, theta-pinch, plasma focus etc. the necessity to measure the electron density of the order of 10^{14}–10^{16} cm^{-3} arises. In this case it is advisable to utilize an infrared (IR) interferometric technique at λ = 10.6 μm wavelength (instead of the visible light) realized using a pulsed CO_2 laser, since it provides essentially higher sensitivity and allows one to attribute the measured interference fringe shift entirely to plasma electrons.

In the present work the possibility of the application of double-exposure IR holographic interferometry technique at 10.6 μm to diagnostics of a laser-produced solid target plasma in vacuum, as well as a laser-produced spark in air, has been demonstrated. The solid target plasma was produced using a pulsed CO_2 laser of microsecond duration. The study of such a plasma is of considerable interest for the problem of magnetic trap filling. Experiments were carried out in a stainless steel vacuum chamber. The double-discharge TE CO_2 laser generated a radiation pulse of a complicated shape – a peak of ≈100 ns width was followed by a "tail" of 1.2 μs width. The laser radiation energy was 60 J. The radiation was focused onto the surface of an aluminum target by a concave copper mirror of 15 cm focal length. The maximum radiation intensity in the focus was $\sim 10^{11}$ W/cm^2.

A pulsed double-discharge TE CO_2 laser was used for obtaining IR holograms of the plasma. The laser was operated using a gas mixture with small nitrogen content, generating a radiation pulse of about 10 J energy, the predominant part of which was concentrated in a peak of $\tau \simeq 100$ ns width. The beam dimensions at the laser output were 2.5 x 4 cm^2. Holograms were recorded using a usual double-beam scheme, on different polymeric materials [1].

Double-exposure IR holograms of the laser-produced solid target plasma in vacuum have been obtained for a series of times up to 2 μs after the initial peak of the plasma-producing laser radiation pulse. Plasma holographic interferograms have been reconstructed from them using a He-Ne laser, one of which, taken at t = = 100 ns, is shown in Fig. 1. The quality of interference fringes is quite satisfactory, indicating, in particular, that temporal resolution of 100 ns is sufficient for studying such a plasma. Figure 2 shows radial electron density profiles at four distances (x) from target surface obtained as a result of a quantitative treatment, using Abel inversion, of fringe shifts measured on the interferogram in Fig. 1. As it follows from Fig. 2, the electron density determined in this experiment at t = 100 ns and at the distance of about 2 mm from target surface varies from the axis to periphery by two orders of magnitude, falling to the value $N_e \approx (2\text{–}3)\cdot 10^{15}$ cm^{-3}.

The technique has been also tested on a laser-produced spark in a wide range of air pressure – from atmospheric to a few Torr. The spark was produced by a ruby laser (radiation energy 0.5 J, pulse width 25 ns), as well as the pulsed CO_2 laser described above. Later stages of the spark development (t > 2 μs after air breakdown) have been studied. Figure 3 shows, as an example, radial electron density profiles in the ruby laser-produced spark plasma at 6.2 and 9.6 μs after breakdown. It should be noted that quantitative results obtained in the present work are well consistent with electron density data obtained in [2-4] for earlier phases of the laser-produced spark development.

Figures 2 and 3 show that IR holographic technique permits to measure, for studied objects, minimum electron densities as low as of the order of 10^{15} cm^{-3}.

As to the pulsed CO_2 laser-produced spark, our results point to rather complicated spark structure due to the existence of several areas of energy release and interaction of produced shock waves. In this connection a quantitative treatment of obtained holographic interferograms is difficult.

Acknowledgements: The authors thank M.O.Mdivnishvili for participation in experiments.

References

[1] E.M.Barkhudarov, V.R.Berezovskii, G.V.Gelashvili, M.I.Taktakishvili, T.Ya.Chelidze, V.V.Chichinadze. Pis'ma v Zhurn. Techn. Fiz., 2, 1079, 1976.

[2] A.J.Alcock, S.A.Ramsden. Appl. Phys. Letts., 8, 187, 1966.

[3] A.N.Zaidel, G.V.Ostrovskaya, Yu.I.Ostrovskii, T.Ya.Chelidze. Zhurn. Techn. Fiz., 36, 2208, 1966.

[4] I.I.Komissarova, G.V.Ostrovskaya, L.L.Shapiro. Zhurn. Techn. Fiz., 38, 1369, 1968.

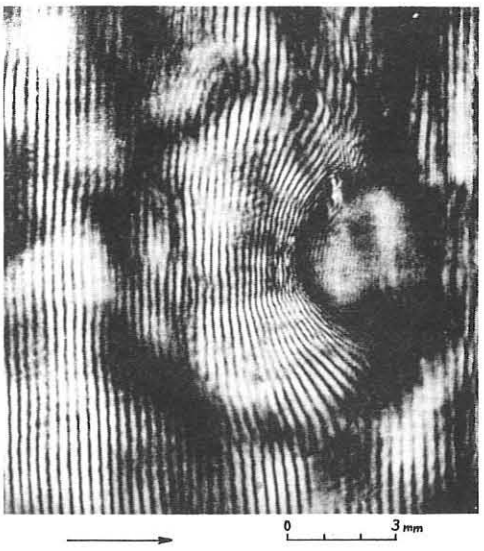

Fig. 1. Holographic interferogram of the laser-produced solid target plasma in vacuum at t = 100 ns.

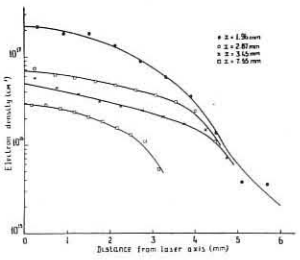

Fig. 2. Radial electron density profiles in the laser-produced solid target plasma in vacuum at t = 100 ns.

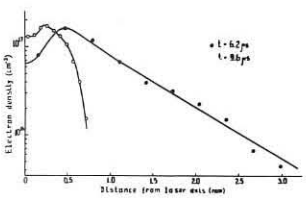

Fig. 3. Radial electron density profiles in the laser-produced spark plasma in air (p = 1 atm) at t = 6.2 and 9.6 μs after breakdown. Distance from the focal plane x = 1.3 mm.

AP27

Experimental Verification of Increased Ion Confinement in a Magnetic Mirror Field

Yasushi Nishida
Department of Electrical Engineering, Utsunomiya University
Hiroshi Mase
Department of Electronic Enigineering, Ibaragi University
Kazushige Ishii
Institute of Plasma Physics, Nagoya University, Nagoya, Japan

Introduction In past years, cross-field-current driven micro-instabilities have been intensively studied, particularly in connection with anomalous ion heating in plasmas produced by relativistic electron beam injection into mirror machines[1] and the modified Penning discharge.[2] Among these instabilities, a lower-hybrid instability, with frequency between the electron and ion cyclotron frequencies, is easily destabilized by ExB current. This instability can play an important role in enhanced ion heating. On the other hand, this heating mechanism has been regarded as the Joule heating due to collisional thermalization of the kinetic energy of ExB drift motion generated by the radial current.[3,4] Thus, the heating mechanism is still not clear.

In the present paper we would like to point out that a basic process of ion heating in the cross-field configuration in a magnetic mirror field is Joule heating due to collisional thermalization of ions, after the investigation of the instabilities. Further, the increased ion confinement is investigated by measuring the confinement time directly.

Experimental device The experimental apparatus is essentially the same as that reported elsewhere,[3] except the diameter of the heating section with 30 cm. The plasma density in steady state is varied berween about 10^{11} to 10^{13} cm^{-3} in a He-gas of a pressure less than 2×10^{-4} Torr. For measuring the transient state, the above plasma is chopped electrically with repetition rate of 10 Hz and about 50% duties. The characteristic decay constant of the plasma current is less than 20 μs. Diagnostics including a floating double probes, a small diameter (5mmΦ) Farady cup and a double monochrometer are used for measuring the plasma particle confinement time, electron and ion temperature and their energy distribution functions. Instabilities are observed by using Langmuir probes in steady state.

Results Ion temperature is measured in steady state by using the monochrometer in a dense plasma, while the Farady cup is used in a dilute plasma. A typical example of the spectrum around HeII(4686 Å) line is shown in Fig.1(a) as a function of the difference in the wave length, Δλ, with a parameter of the heating voltage V_H applied across the magnetic field. The monochrometer is focused on the plasma axis in the middle of the mirror field. From this figure we can easily recognize that when V_H is small, the distribution function shows the equilibrilum state, but it shows two components distribution with higher voltage of V_H. The colder component is suspected to be the plasma flowing into the mirror field region through the orifice without frequent collisions. From the gradient of the curve we can obtain the ion temperature as an example is shown in Fig.1(b). The colder part does not change very much with the increase of the heating voltage, while the hotter one changes in proportional to the squre of V_H.

The particle confinement time is measured directly from the decay curve of the floating double-probe current by chopping the plasma current with a decay time less than 20 μs. A typical example of the decay time, τ, is shown in Fig.2 measured at several points in a radial direction. As clearly seen from the figure, the decay time of about 100-200 μs increases to about 1.5-2 ms at V_H= 100-200 volts without no significant increase of ion temperature, although it depends on the radial positions. Further increase of V_H decreases the decay time and again increases it. This is reasonable because the particles existing in the off center region are trapped electrostatically as this is aimed originally for the present system. At the high voltages of V_H the ion temperature increases and the density also increases because of flattening of the density profile in the steady state operation as already shown in Ref.3. In the transient state, however, the current for heating ions decreases very rapidly compared with the decay time, τ. Thus the ionization within the decaying phase might not be very effective.

The relation of energy balance of ions may be given as follow

$$\frac{d(nT_i)}{dt} = nR_H - \frac{1}{\tau}nT_i = 0 \qquad (1)$$

in a steady state, where the heating rate R_H is given as

$$R_H = \frac{1}{\tau_i}\frac{M}{2}(V_E^2 + V_o^2) \qquad (2)$$

by assuming the collisional thermalization, and τ is the particle confinement time. V_E is ExB/B^2 drift velocity and V_o is the initial particle velocity. Here the particle energy is gained through the cross-field kinetic energy.

Thus;

$$T_i = \frac{1}{2}M(V_E^2 + V_o^2)\frac{\tau}{\tau_i}. \qquad (3)$$

By the crude assumption of $V_H = E_r R_o$, where R_o is the radius of the chamber, T_i changes with V_H^2 as shown in Fig.1(b) by solid line.

The confinement time τ is discussed as follows; If the ions with energies Δϕ are confined in the axial and the radial potential well for a time τ required for them to diffuse upward in energy above the barrier height. For $\phi \geq 2T_i$, τ may be given as follows simillar to the result by Pastukhov[5]

$$\tau = \tau_i \ln R \frac{\phi}{T_i}\exp\frac{\phi}{T_i}. \qquad (4)$$

Inserting Eq.3 into 4, one obtains

$$\tau = \left(\ln R\frac{K}{n}\right)^{\frac{5}{4}} g^{\frac{7}{4}}\left[\frac{M}{2}\frac{n}{K}\frac{1}{(BR_o)^2}\right]^{\frac{1}{4}}\exp\left\{\frac{5}{4}g^{\frac{1}{4}}\left[\frac{M}{2}\frac{n}{K}\frac{\tau}{(BR_o)^2}\right]^{-\frac{4}{5}}\right\} \quad (5\text{-a})$$

for $V_E^2 \gg V_o^2$ and

$$\tau = \left(\ln R\cdot\frac{K}{n}\right)^{\frac{5}{4}} g^{\frac{5}{4}}\left[\frac{M}{2}\frac{n}{K}V_o^2\right]^{\frac{1}{4}}\exp\left[\frac{5}{4}g^{\frac{1}{4}}\left[\frac{M}{2}\frac{n}{K}(V_o^2\tau)\right]^{-\frac{2}{5}}\right] \quad (5\text{-b})$$

for $V_E^2 \ll V_o^2$.

These features are qualitatively in coincidence with the experimental results observedin Fig.2(b), while Fig.2(a) are not explained by this manner because of the plasma near the core flown away by the centrifugal force.

The instabilities are observed with a Langmuir probe in a low density case. Only the ExB type low frequency flute mode has been observed, which frequency is in proportional to ExB drift velocity. No strong instabilities near the Lower Hybrid frequency have not been observed.

Ar gas of about 10% is imposed in the present system to make a mixed Ar and He plasma for intending to observe the ion mass separation caused by the centrifugal force in the radial direction. Preliminary results show that the Ar gas originally concentrated near the column center spreads out toward the chamber wall, while He ions remain near the column center. This shows that the mass separation is possible with the difference of ion mass and the possibility of the gas blanket is suggested in the cross-field rotating type plasma.

References 1: I.Alexeff et al., Phys. Rev. Lett. 25, 848 (1970), 2: J.Roth, Phys. Fluids 16, 231 (1973). 3:Y.Nishida et al., 7th Europ. Con. On Contr. Fusion and Plasma Phys., Lausanne (1975) and Y.Nishida et al., J.Phys. Soc. Japan 43, 1364 (1977). 4: H. Sugai et al., J.Phys. Soc. Japan 43, 1400 (1977). 5: V.P.Pastukhov, Nucl. Fusion 14, 3 (1974).

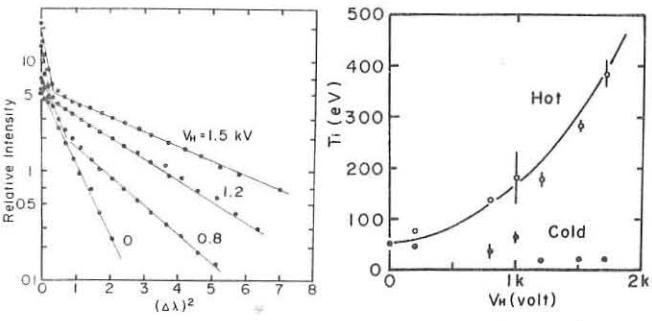

Fig.1. (a) Spectral intensities observed around HeII (4686 Å) line. (b) Ion temperature as a function of V_H. Solid line shows the result of Eq.(3).

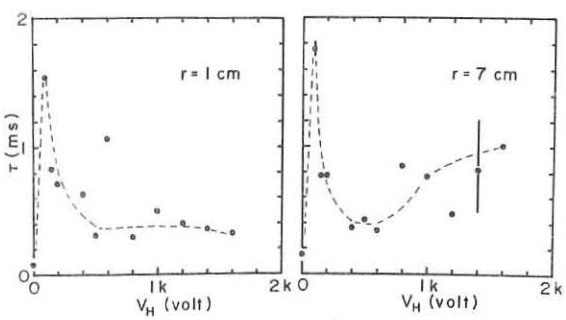

Fig.2. Particle confinement time obtained in a dilute plasma: density of about 10^{11} cm^{-3}.

The Dynamics of Alpha Particles in Tandem Mirror Plasmas*

T. Kammash and D. L. Galbraith
University of Michigan
Ann Arbor, Mich. 48109

Abstract. The Tandem device has been advanced as a mirror confinement scheme with potentially large Q (ratio of fusion power to injected power) value. Several previous calculations have shown that Q values of about 5 are obtainable for realizable fields and sizes if the alpha particles from the D-T reaction are selectively removed. In this paper we solve the full set of particle and energy balance equations that characterize the multispecies plasma including fast and thermal alphas and examine various alpha-associated processes that could impact the Q-value of the system.

Analysis and Results. One of the exciting schemes that have recently been proposed to enhance the Q-value of mirror machines is the Tandem concept.[1,2] This device which consists of a long solenoid in which the magnetic field is nearly uniform, and two end, minimum-B, mirrors that serve as "plugs". By making the electron density in the plugs much larger than that in the solenoid an ambipolar potential is set up which provides the desired confinement for the plasma in the central section. As a reactor it is expected that most of the fusion reactions will take place in the solenoid, and because of their large charge number the alpha particles generated by the D-T fusion reactions will be better confined by the electrostatic potential than the ions. As a result, the Q-value of the system will be significantly affected by the longer confinement of the alphas and some means must be found to selectively remove the alphas without totally destroying their role as a major plasma heating source. In this paper we examine some of the processes that might contribute in a positive manner.

We begin by noting that the system can be characterized by a full set of coupled particle and energy balance equations for each species in the three regions of the device. These equations can be found elsewhere[3], and in the interest of brevity and space we include only those pertaining to the central section. For the ions in this region the particle and energy balance equations are given by

$$\frac{d(n_i)_c}{dt} = S_c\left[1 - \frac{\langle\sigma v\rangle_{cx}}{\langle\sigma v\rangle_{ion}}\right] - \frac{(n_i)_c^2}{(n_i\tau_i)_c} - \frac{1}{2}(n_i)_c^2\langle\sigma v\rangle \qquad (1)$$

$$\frac{d(n_i E_i)_c}{dt} = S_c E_{oc} - (n_i)_k^2 \frac{E_k}{(n_i\tau_i)_c} - n_e(n_i)_c(W_{ie})_c - n_\alpha(n_i)_c W_{i\alpha} - S_c\frac{\langle\sigma v\rangle_{cx}}{\langle\sigma v\rangle_{ion}}(E_i)_c + \frac{1}{4}(n_i)_c^2\langle\sigma v\rangle\left[f Q_{\alpha i} - 2(E_i)_c\right] \qquad (2)$$

where S_c is the ion injection rate, E_{oc} is the ion injection energy, τ_i is the appropriate confinement time, W_{ik} is the energy exchange rate[4] between the two thermal species represented by the indices, f is a non-escape probability of the fusion alphas, and $Q_{\alpha i}$ denotes the energy given to the ions directly by a fusion alpha as it theramlizes. The first term on the right hand side of Eq. (1) represents the net fueling rate by neutral injection that includes ion losses due to charge exchange. If one ignores the atomic processes (i.e., ionization and charge exchange) with the alpha particles and assumes that the electrons and the ions of the plasma have the same temperature then the charge exchange loss term can be written as[5]

$$\frac{\langle\sigma v\rangle_{cx}}{\langle\sigma v\rangle_{ion}} = \frac{2}{3}\left[110\,T^{-0.8} - 1.0\right] \qquad (3)$$

where T is in keV. Since the electron and ion temperatures are not the same and since the atomic interactions with the alphas cannot be ignored we have revised the above formula to read

$$\frac{\langle\sigma v\rangle_{cx}}{\langle\sigma v\rangle_{ion}} = \frac{n_c\langle\sigma v\rangle_{cx}}{n_c\langle\sigma v\rangle_{ii'} + n_e\langle\sigma v\rangle_{ie} + n_\alpha\left[\langle\sigma v\rangle_{i\alpha} + \langle\sigma v\rangle_{x\alpha}\right]} \qquad (4)$$

with the last two terms in the denominator representing alpha ionization and charge exchange respectively. Analytical formulas for all the terms in (4) including dependence on plasma temperature and injection enegy have been developed[6] and checked against experimental data, and subsequently incorporated in the present analysis. The effects of the alpha terms in (4) on the Q-value of the system will be addressed shortly.

Equations similar to (1) and (2) can be written for the alphas in the solenoid while for the electrons in this region the particle balance equation is replaced by one that yields the time evolution of the ambipolar potential[3]. Standard balance equations are written for the electrons and ions in the plugs where it is assumed that no interaction takes place between these particles and the fusion alphas that escape from the solenoid. For the particle and energy confinement times in the plugs we use formulas deduced elsewhere[3] while for the end losses from the solenoid we employ a multispecies modification of Pastukhov's formulas namely[7]

$$\frac{1}{(n\tau)_k} = \frac{4}{n_k C_k^2\sqrt{\pi}\,\tau_{ok}}\left(\frac{R}{R+C_k^2}\right)^{1/2}\frac{e^{-\frac{Z_k e\varphi}{T_k}}}{\ln\left(\frac{4R}{C_k^2}+2\right)}\left(\frac{T_k}{Z_k e\varphi}\right)\int_0^\infty e^{-t}\sqrt{1+\frac{T_k}{Z_k e\varphi}}\,dt \qquad (5)$$

$$\left(\frac{E_L}{n\tau}\right)_k = \frac{6T_k}{n_k C_k^2\tau_{ok}}\left(\frac{R}{R+C_k^2}\right)^{1/2}\frac{e^{-\frac{Z_k e\varphi}{T_k}}}{\ln\left(\frac{4R}{C_k^2}+2\right)}\left\{\frac{2}{3}+\left(\frac{T_k}{Z_k e\varphi}\right)\int_0^\infty e^{-t}\sqrt{1+\frac{T_k}{Z_k e\varphi}}\,dt\right\} \qquad (6)$$

*Work supported by U.S. DOE

where τ_{ok} is the familiar 90° collision time, and R is the appropriate plasma mirror ratio. The constant C_k^2 identified with species k is given in terms of densities and masses[7] and for small alpha densities in the solenoid this constant takes on values of 1, 2, ~ 4 for electrons, ions, and alphas respectively. It must be kept in mind that in applying Eqs. (5) and (6) to the positive species in the central cell the quantity φ should be understood to represent the difference between the solenoid and plug potentials.

In its simplest form, the magnetic field in most of the solenoid (i.e., excluding the transition region) can be viewed as uniform so that in addition to the end losses described above the particles will undergo classical diffusion across the field. However, due to the non-axisymmetry imposed by the minimum-B plugs, Ryutov and his coworkers[8] have recently shown that the particles will undergo neoclassical and enhanced radial transport due to resonant diffusion arising from such field configurations. In this calculation we include only the neoclassical effect which has been shown to be proportional to Bohm diffusion. With this in mind we introduce the following confinement times

$$\frac{1}{(n\tau)_k} = C_{BM}\frac{E_e}{12\lambda_c^2 n_k\left(\frac{eB_c}{c}\right)^2} \qquad (7)$$

$$\frac{E_L}{(n\tau)_k} = C_{BM}\frac{E_k E_e}{12\lambda_c^2 n_k\left(\frac{eB_c}{c}\right)^2} \qquad (8)$$

where the coefficient C_{BM} includes among other things geometric factors.

We have focused our attention in this investigation on three machanisms which the alpha aprticles can participate in and indirectly impact the Q-value. by solving an appropriate Fokker-Planck equation we find that the self-scattering of fast alpha particles in a mirror geometry does not significantly change their lifetime and hence does not contribute measurably to slective removal of these particles.[9] We find that by including alphas in Eq. (4) a sizable increase in the Q-value occurs as shown in Figure 1. This increase can be attributed to the fact that ionization of neutral particles by alphas in a steady state operation leads to a reduction of charge exchange losses which in turn manifest themselves in higher Q. Results based on Eq. (3) are shown in the lower curve.

Although all species are allowed to undergo neoclassical diffusion in the central cell the fact that the step size is proportional to the Larmor radius allows for some measure of preferential diffusion of the alphas. This must, however, be balanced against loss of heating when too many alphas diffuse. Although it does not represent an optimum case Figure 2 shows the dramatic increase of Q with increasing value of the Bohm diffusion coefficient. The same effect can be seen in Figure 1 although loss of heating and possible excessive loss of ions at high diffusion rate will ultimately bring the Q-value down.

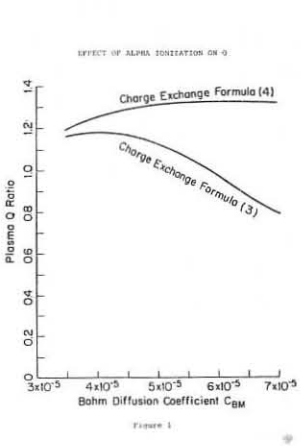

Figure 1

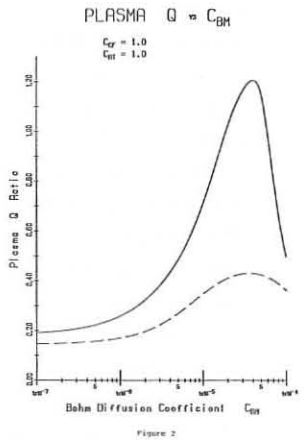

Figure 2

References

1. T. K. Fowler, B. G. Logan, Comments on Plasma Physics and Controlled Fusion, 2, 167 (1977).

2. G. I. Dimov, V. V. Zakajdakov, M. E. Kishinevskij, Plasma Physics and Controlled Nuclear Fusion Research, 3, 177(1977) IAEA, Vienna.

3. D. L. Galbraith and T. K. Kammash, Electric Power Research Institute Report (To be published).

4. T. Kammash, Fusion Reactor Physics, Principles and Technology Ann Arbor Science Pub. (1975) Ch. 4.

5. B. G. Logan, Lawrence Livermore Laboratory Report UCRL-52302 July 15 (1977) Ch. 3.

6. D. L. Galbraith and T. Kammash, Nuclear Fusion (To be published).

7. D. L. Galbraith and T. Kammash, Plasma Physics 20, 959(1978).

8. M. E. Kishinevshij et al. 7th IAEA Int. Conf. Innsbruck (1978) paper CN-37-J3.

9. T. Kammash and J. M. Les (not published).

AP31

SUPPRESSION OF PLASMA LOSS FROM MIRROR ENDS

H. Akiyama, O. Matsumoto and S. Takeda
Department of Electrical Engineering
Nagoya University, Nagoya, Japan

Abstract: The ponderomotive force of r.f. field near the electron plasma frequency is used for stabilizing the drift-cyclotron loss-cone (D.C.L.C.) instability as well as suppressing the plasma loss.

The plasma produced by the lisitano coil flows to both directions, and is reflected by a mirror field at only one side. The operating pressure of Ar or He gas is 10^{-4} Torr, and the electron temperature and the plasma density are the several eV and $10^{9} \sim 10^{10}$ cm^{-3}. The plasma is thought to be collisionless under the experimental conditions with only the half mirror, since the ion-ion mean free path is comparable to the vessel length. The cavity, which has the diameter of 30 cm, the Q value of 2500 and the resonant frequency of 763 MHz without plasma, is mounted near the mirror field. The r.f. power of 200 W is fed to the loop-antenna inside the cavity operated at the TM_{010} mode. As the direction of the electric field inside the cavity is almost parallel to the static magnetic field, the interaction between the two fields is not serious.

After the mirror effect is investigated without r.f. field, the effect of the r.f. field for the suppression of the end loss is studied.[1,2] In Fig.1 are shown the typical experimental results in Ar gas with the r.f. field of 500 V/cm inside the cavity. The incident waveform to the cavity and transmitted one through the cavity are shown by the upper 2 traces. The trace of the electron saturation current I_{se} at the bottom figure shows that the plasma loss at the mirror end is suppressed by the r.f. field. At the same time, the plasma density increases at the mirror center as shown by the third trace. Then the adiabatic confinement without following the ion and electron heating is achieved. In Fig.2 is shown the dependence of the suppression ratio of the end loss on the net input power Pi to the cavity, where I_{seo} is I_{se} without r.f. field and ΔI_{se} is the absolute value of the decreased I_{se}. The theoretical curve is obtained from the explanation of Fig.4.

The spontaneously excited wave with the frequency close to the ion cyclotron frequency is observed in the plasma of He gas.[3] This wave localizing in the radial region with the sharp density gradient propagates in the azimuthal direction of the ion-diamagnetic current. The measured dispersion relation of the wave is in good agreement with the theoretical prediction of D.C.L.C. instability. In Fig.3 are shown the ion saturation current I_{si}, the electron temperature T_e, the space potential and the amplitude of the wave for the mirror ratio 3 as a function of the radial position r. The curves a and b show the amplitude of the wave with and without r.f. field of 65 V/cm. This shows that the D.C.L.C. instability is stabilized by r.f. field.

The mechanisms[3] of the suppression of the end loss and stabilization of D.C.L.C. instability are explained by Fig.4, which shows the velocity space in the mirror center. The dotted region contains the charged particles flowing from the region of the plasma production toward the mirror field. The horizontally and vertically hatched regions contain the particles reflected by only the mirror field and by the ponderomotive force with the mirror field respectively, where ψ and ϕ are the quasi-potential produced by the ponderomotive force and the ambipolar potential. Since the loss-cone velocity distribution is converted into the loss-hyperboloid one by the ponderomotive force, the D.C.L.C. instability is stabilized. The proposed method to stabilize the D.C.L.C. instability does not need the potential of the intense r.f. field which is comparable to the kinetic energy, since the confinement of only the low-energy ions is necessary to change the loss-cone distribution.

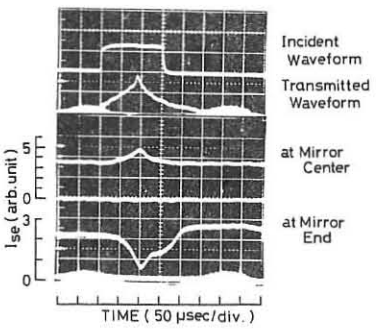

Fig.1

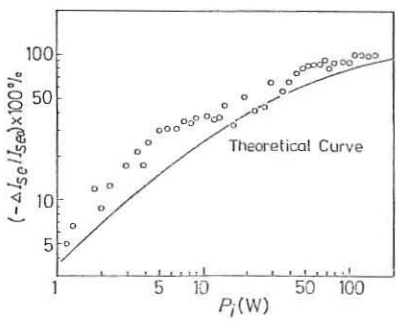

Fig.2

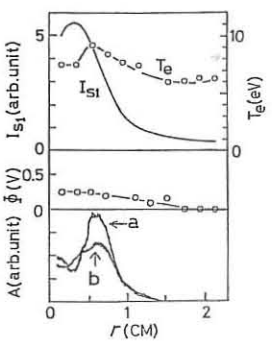

Fig.3

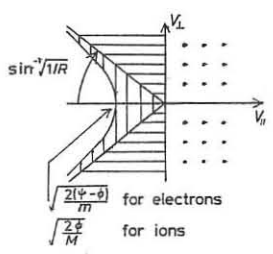

Fig.4

References:

1) H. Akiyama and S. Takeda: J. Phys. Soc. Japan 41 (1976) 1036.
2) H. Akiyama, O. Matsumoto and S. Takeda: J. Phys. Soc. Japan 45 (1978) 1728.
3) H. Akiyama and S. Takeda: J. Phys. Soc. Japan 43 (1977) 1739.

POSSIBILITY OF MHD-STABLE PLASMA CONFINEMENT IN AN AXISYMMETRIC MIRROR MACHINE

V.V.Arsenin

I.V.Kurchatov Institute of Atomic Energy, Moscow, USSR

Stability of a hollow plasma in an axisymmetric mirror machine is investigated in the presence either of an azimuthal current in the near-axis winding, or an axial current in the paraxial approximation. Stability is possible, in particular, in the case without min B in the plasma.

Since the quadrupole geometry of the end mirror in an ambipolar trap [1] gives rise to "neoclassical" transports [2] it is interesting to analyze possibilities of MHD stability in an axisymmetric case. It is sufficient to consider an end trap.

1. A system with a near-axis winding. We proceed from the stability criterion for potential perturbations in rarefied ($\beta \to 0$) plasmas.

$$W = -\frac{1}{2}\int d\varphi \int \frac{d\ell}{B}\left(\vec{\xi}_\perp \nabla \ln B\right)\left(\vec{\xi}_\perp \nabla\right)(p_\perp + p_\parallel) > 0, \qquad (1)$$

in ordinary notations. Eq.(1) is valid also for finite $\beta \ll 1$, provided the plasma radius R is much less than the plasma length L_p (L_p is of the order of the field variation length L if the mirror ratio is ~ 2) [3,4].

Let a nearaxis region of the trap be empty, there is a winding $r = a$, the surface density of the azimuthal current $i(z)$ (Fig.1). Then

$$B_z = \beta(z) - \frac{1}{4}\beta'' r^2 + \frac{a^2}{L} f' \ln\frac{r}{\ell}, \qquad B_r = -\frac{1}{2}\beta' r + \frac{a}{L} f(z)\frac{a}{r}, \qquad (2)$$

where $f = -\frac{2\pi L}{c} i'$, l - is the variation length of $i(z)$ ($l \gg a$).

1.1. m = 1 stability. If the Larmor radius $\rho \gg \frac{R^2}{L}$, only the "first" mode $\xi = \xi_0 \cos\theta$, $\frac{\partial \xi_0}{\partial z} = 0$ can be unstable [5]. For this mode,

$$W = \frac{1}{4}\int d\varphi \int \frac{\xi^2}{\beta^2}\left(\beta'' - \frac{3}{2}\frac{\beta'^2}{\beta}\right) r\,\frac{\partial p}{\partial r}\,dz + \frac{a^4}{2L^2}\int d\varphi \int \frac{\xi^2 f^2}{\beta^3 r^3}\,\frac{\partial p}{\partial r}\,dz, \qquad (3)$$

where $r(z) = \left[r_0^2(0)\frac{\beta(0)}{\beta(z)} + \frac{2a^2}{L\beta}\int_0^z f\,dz\right]^{\frac{1}{2}}$ - denotes the radius of a magnetic force line, $p = p_\perp + p_\parallel$. Two terms in Eq.(3) describe the instability of a hollow plasma in the absence of the inner winding (a suitable mechanical analogy is a rigid ring on the potential mountain with a "flat" top, Fig.2a) and the stabilization effect of positive on the inner boundary of the plasma tube (a ring on the mountain with a sharp top, Fig.2b). Stability is possible if $\overline{f^2} \gtrsim \overline{\beta^2}$. We emphasize that min B is not necessary to stabilize m = 1 mode.

1.2 Stability of other modes. Min B. Only the constancy of ξ with respect to r was essential in the above proof of the "first" mode stability. Therefore, perturbations $m \geq 2$ are also stabilized, provided $\frac{\partial \xi}{\partial r} = 0$. Moreover, a special choice of $i(z)$ gives a possibility to suppress all the perturbations. In fact, we see from

$$B = \beta(z) + \left(\frac{\beta'^2}{8\beta} - \frac{\beta''}{4}\right)r^2 + \frac{a^2}{L} f' \ln\frac{r}{\ell} - \frac{a^2}{2L}\frac{\beta'}{\beta} f + \frac{a^2}{2L^2} f^2 \frac{a^2}{r^2} \qquad (4)$$

that min B can exist at $r = r_1 > a$, provided $f' > 0$. A sufficient stability criterion is

$$W = W_0 - \frac{a^2}{2L}\int d\varphi \int \frac{\xi^2}{\beta r}\left(\frac{f}{\beta}\right)'\frac{\partial p}{\partial r}\,dz, \qquad (5)$$

where W_0 is defined by Eq.(3) (for $\xi = \text{const}$ the latter term in Eq.(5) vanishes). A simple example is a plasma with $L_p \ll L$ (anisotropic pressure). In this case Eq.(5) reduces to the conditions: the roots of quadratic form

$$x^2 \cdot \int \beta'' p\,dz - x \cdot \frac{2}{L}\int f' p\,dz + \frac{2}{L^2}\int \frac{f^2}{\beta} p\,dz, \quad x = \frac{r^2}{a^2}, \qquad (6)$$

are positive and radius r_1 corresponding to the lesser root coincides with the position of max $p(r)$ (the outer plasma radius R must be $< r_2$). These conditions are satisfied, in particular, if 1) the ratio L_p/L is sufficiently small and $f' \sim \frac{|f|}{L_p}$ (for instance $f = \text{const}$. z) or 2) a decrease of the plasma pressure along the axis is slow, for example as $\left|z \mp \frac{L_p}{2}\right|^\alpha$, $\alpha < 1$ ($z = \pm\frac{L_p}{2}$ are the coordinates of the mirrors) and f is localized near the mirrors (for instance, = const). The case $\alpha = \frac{1}{2}$ [6], for instance, can be realized at $\frac{T_i}{T_e} \gg \left(\frac{m_i}{m_e}\right)^{\frac{1}{3}}$ (this inequality does not contradict to the general concept [1]), when i-e cooling is faster than i-i scattering.

The existence of stable axisymmetric configurations has been already pointed out [7,8]. The paraxial approximation used alows us to find a class of long stable configurations. As min B exists both in this approximation and in the limit of short plasma ring removed from the axis [7] a hope arises that it is possible to find a compact configuration suitable for a reactor.

2. Stability in the system with axial current. The existence of a shear in hollow systems with axial current alows the stabilization of all modes. A simple example is a plasma with isotropic pressure (mirror ratio $A \gg 1$). In this case it is sufficient to prove the stability in magnetohydrodynamics [9]. The potential energy

$$W = \int\left\{\frac{1}{m^2 + \kappa^2 r^2}\left[(\kappa r B_z - m B_\theta)\frac{d\xi}{dr} + (\kappa r B_z + m B_\theta)\frac{\xi}{r}\right]^2 + (\kappa r B_z - m B_\theta)^2\frac{\xi^2}{r^2}\right\} r\,dr + 4\pi\int G\,\frac{dn}{dr}\,\xi^2 r\,dr, \qquad (7)$$

where the first term corresponds to perturbations $\cos(m\theta - \kappa z)$ in a cylinder without mirrors and the "gravity" $G \sim AT r/m_i L L_1$ immitates the effect of the field curvature in the presence of mirrors. The stability takes place if the positive minimum of the first integral (this minimum occures on the perturbation localized near r_0 where $m B_\theta - \kappa r B_z = 0$) is larger than the second term:

$$B_\theta^2\left(1 + \frac{2\pi r_0}{B_z^2}\frac{\partial p}{\partial r}\right)^2 \gtrsim \beta\,\frac{AR^2}{L_p L_1} B_z^2. \qquad (8)$$

(L_1 is the mirror length).

It is satisfied if $B_\theta \gtrsim \beta^{\frac{1}{2}}\left(\frac{AR^2}{L_p L_1}\right)^{\frac{1}{2}}$ and quantity $1 + \frac{2\pi r}{B_z^2}\frac{\partial p}{\partial r}$ is nowhere close to zero in the plasma. The latter requirement gives the limit $\beta \lesssim 1$.

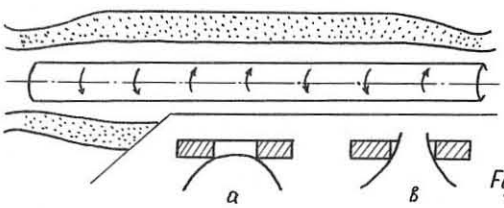

Fig.1

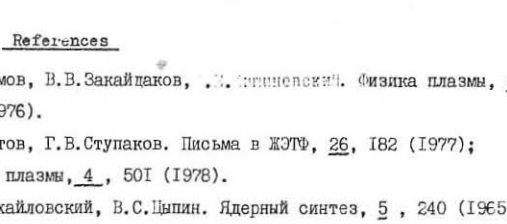

Fig.2

References

1. Г.И.Димов, В.В.Закайдаков, М.Тиунчевский. Физика плазмы, 2, 597 (1976).
2. Д.Д.Рютов, Г.В.Ступаков. Письма в ЖЭТФ, 26, 182 (1977); Физика плазмы, 4, 501 (1978).
3. А.Б.Михайловский, В.С.Цыпин. Ядерный синтез, 5, 240 (1965).
4. J.C.Cordey, C.J.H.Watson. B.N.E.S. Nuclear Fusion Reactor Conf., Sept., 1969, p.122.
5. M.N.Rosenbluth, N.A.Krall, N.Rostoker. Nucl.Fusion, Suppl. 1, 143 (1962).
6. Б.А.Трубников. Plasma Physics and Controlled Nuclear Fusion Research, v.1, p.83. IAEA, Vienna, 1966.
7. J.Andreoletti Comptes rendus, 257, 1235 (1963).
8. H.P.Furth. Phys.Rev.Letters, 11, 308 (1963).
9. M.Kruscal, C.Oberman. The Second Intern.Conf. on Peaceful Use of Atomic Energy, Geneva, 1958.

AP33

ELECTRON HEATING UNDER THE INFLUENCE OF THE ION CYCLOTRON INSTABILITY IN A MIN-B MIRROR TRAP

Zhiltsov V.A., Kosarev P.M., Panov D.A., Skovoroda A.A., Shcherbakov A.G.

I.V.Kurchatov Institute of Atomic Energy

It is well known that neutral beam injection in a mirror machine is accompanied by various types of the ion cyclotron instabilities (ICI). These instabilities are characterized by a comparatively narrow frequency spectrum with maxima arranged in the vicinity of the cyclotron frequency and its harmonics. The enhance losses of particles from a trap are often observed simultaneously with the ICI development. It was shown in the Ogra-3B experiments [1] that the enhance losses actually exist only if at the same time there are low frequency oscillations in the plasma, which were drift oscillations in that particular experiment. When ICI appeared as a series of bursts the low frequency oscillations looked like " ringing after blow". When ICI appeared as a stationary oscillations, then the low frequency activity and particles losses were much lower.

In this report we discuss the behavior of plasma electrons in the presence of ICI in Ogra-3B installation.

It was found out that during each burst of ICI the peak of electron flux along the axis of the trap is detected. As these electrons overcame very high potential barrier (it reached 10-15 electron temperature) and the axial flux of electrons between the bursts was undetectable. It was necessary to suppose the longitudinal acceleration of the electrons in the oscillating field of ICI, the processes well known after the experiments in Ogra-1 installation [2] .

Fig.1. shows the electron temperature dependence on the product of the plasma density and its time of life $n\tau$ with the central field equals 13 kGs. The life time τ in this experiment was limited mainly by charge exchange and was equal approximately 0,3 s. The arrow indicates the threshold of ICI. Electron temperature was calculated from the measured line profile of the super high frequency wave absorption at the electron cyclotron frequency in the minimum B region of the magnetic field [3] . In this case the line profile is described by the Doppler shift, that permits to find easily the longitudinal velocity electron distribution function. It is clear from fig.1 that ICI development followed by significant rise of the electron temperature. In the region of the ICI activity the temperature dependence on $n\tau$ is more steep than classical one proportional to $(n\tau)^{2/3}$.

The time dependence of the electron temperature in one injection impulse is shown on fig.2. Distribution function has some deviation from the maxwellian profile so "the temperature" calculated from the tail of the distribution function (dotted curve) does not coincide with "mean electron temperature". The difference become visible after the appearance of ICI.

Fig.3. shows the limits of ICI on the electron temperature - ion angular anisotropy plane calculated in [4] .Horizontal solid line indicates the region of parameters observed in our experiment. So at highest electron temperature the stable region was reached.

The rise of the electron temperature in the presence of ICI and the delay of the electron heating process may be considered as a cause of a relaxation mechanism of the bursts generation. After the beginning of the ICI oscillations the longitudinal electron temperature with some delay reaches the region of stability and burst stops itself. The electron temperature relatively slow drops down and plasma again gets into unstable region and the next burst begins to develop. Apparently the interval between bursts must be of the order of the electron-electron collision time τ_{ee}. Experimentally measured intervals between bursts as a function of plasma density shown on fig.4 (solid points). Solid line represents the function $2\tau_{ee}(n)$ and it coinsides with experimental points rather well.

Some processes may be responsible for electron heating during the ICI bursts. They are electron heating by high energy ions generated in burstes, resonance phenomena on the plasma boundary where the plasma resonance conditions are fulfild, the resonance between the frequency ω_ℓ of the longitudinal oscillations of electrons in the electrostatic potential well and ICI frequency ω_i. The latter process is rather effective in a parabolic well $\varphi = \varphi_0(1 + (2z/L)^2)$, were frequency of oscillations does not depend on the electron energy (here φ_0 is the plasma potential and L is a characteristic longitudinal dimension of plasma). In our experiments the resonant condition $\omega_i = \omega_\ell$ may be fulfild. The investigations of the longitudinal structure of the ICI waves showed us that two types of waves were excited - symmetrical waves $\tilde{\varphi} = \tilde{\varphi}_0 \cos(\pi z/L)$ and antisymmetrical $\tilde{\varphi} = \tilde{\varphi} \sin(\pi z/L)$, where $\tilde{\varphi}$ is amplitude of ICI oscillations.

If we take into account that in each period of oscillation electrons being in resonance with ICI wave can rise their energy only on a small quantity, it is not difficult to calculate the characteristic time of electrons acceleration. In the case of antisymmetrical waves the process of acceleration takes place not only at fundamental frequency but also at their odd harmonics. The fundamental resonans is most effective and the acceleration time up to energy equals to the well depth φ_0 can be estimated as $t \sim (L/V_{\varphi_0})(\varphi_0/\tilde{\varphi})$, where $V_{\varphi_0} = (2e\varphi_0/m)^{1/2}$. This estimation of acceleration time does not contradict to the experimental observations - the axial flux of electrons was detectable just at the beginning of the bursts.

In the case of symmetrical waves the process of acceleration takes place at even harmonics. Usually ICI generates oscillations at fundamental and some higher harmonics and this gives more possibilities for longitudinal electron acceleration.

So we have seen, that ICI can generate high energy electrons and this process must be taken into consideration in the theory of ICI development.

REFERENCES

1. Zhiltsov V.A. et al, IAEA-CN-37. S-2.; Plasma Phys. Conf. Nuclear Fusion Research, Innsbruck, 1978, IAEA .
2. Kucheriaev Yu., A. et al, Plasma Physics (Journ.Nucl.Energy Part C) 5 ,145, 1963.
3. Skovoroda A.A. et al, JETF, 72, 526, 1977.
4. Timofeev A.V.et al, Plasma Theory, Ed.Leontovich M.A., v.5, p.351, Moscow, Atomizdat, 1967.

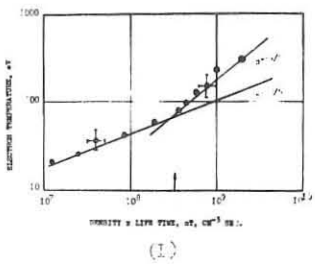

(1)

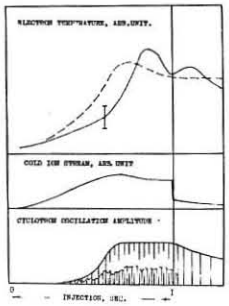

(2)

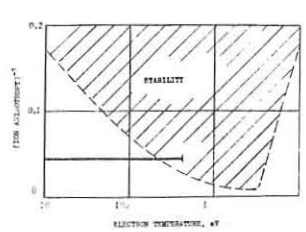

(3)

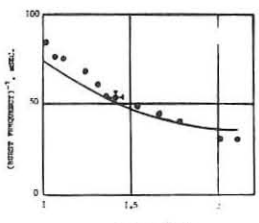

(4)

AP34

Studies of Finite Gyro-Radius Effects in a Field Reversed Mirror Configuration*

G. H. Miley, J. G. Gilligan, D. E. Driemeyer, and E. C. Morse
Fusion Studies Laboratory
University of Illinois, Urbana, IL 61801 USA

and

W. C. Condit
Lawrence Livermore Laboratory, Livermore, CA 94550 USA

The field-reversed mirror (FRM) is characterized by a small size such that finite gyro-radius effects must be considered in both stability and transport analyses. Consequently, such effects are important to the interpretation of both ongoing experiments and extrapolation to future reactor concepts.[1,2] The present work employs an energy principle to study stability of low-frequency ($\omega << \Omega_{ce}$, $\omega \approx \Omega_{ci}$) acoustic modes. Also a Monte Carlo technique has been developed for study of high energy-ion transport.

Stability Studies

Due to the large orbits, FRM stability cannot be determined from a conventional MHD analysis, forcing recourse to the Vlasov equation.[3] In this study, an energy principle based on the Vlasov equation was developed for an axisymmetric field-reversed mirror. With this energy principle, the perturbed energy of the FRM configuration is calculated from an applied electromagnetic perturbation.

A unique aspect of the analysis is that the equilibrium configuration is modeled using the time-dependent orbit kinetics code SUPERLAYER.[4] This code ignores electron physics but computes the ion trajectories in a self-consistent axisymmetric field. Orbital data from SUPERLAYER is used to find the perturbed energy by calculating orbit integrals of the perturbed vector potential of the form $g = \int \vec{v}\cdot\delta\vec{A}dt'$. The energy principle is a functional of g and its time derivative. Consequently, by variations of the trial function $\delta\vec{A}$, instabilities can be found by examining the roots of the energy equation $\delta^{(2)}U = 0$. Here U is the total energy of the plasma and magnetic field.

For a particular equilibrium studied with the SUPERLAYER code, no roots were found for $\ell = 0$, where $e^{i\ell\theta}$ is the azimuthal variation of the perturbation. This corresponds to a lack of tearing instability for a "short, fat" reversed field mirror. For $\ell = 1$ and $\ell = 2$, however, roots were found giving growth rates $\sim 0.05\Omega_{ci}$ and real frequencies on the order of $0.7\ell\Omega$, where Ω is the mean drift frequency of the ions. [These modes are similar to precessional instabilities postulated for Astron.] The growth rates indicated are much lower than those predicted by MHD theory, possibly explaining the relatively long lifetimes observed in some field reversal experiments.[5] Such instabilities are likely to cause magnetoacoustic turbulence, inducing a Bohm-like diffusion. This would not be directly measureable in present low temperature experiments, but could be serious in later devices.

Examination of the theoretical stability properties of reversed-field mirror equilibria with a toroidal field, supplied either externally by a center conductor or internally by poloidal plasma currents,[6] is now in progress. Also, the possibility of using a quadrupole magnetic field is also under consideration, although resulting orbital resonances could enhance transport.[7]

Alpha Particle Transport and the MCFRM Code

For the small FRM configurations, the question of fusion product leakage (i.e., whether or not ignition is possible) becomes crucial. Due to the large, complex orbits involved, a Monte Carlo simulation technique (MCFRM) has been developed where the background plasma is represented by an elongated Hill's vortex, i.e.,

$$\vec{B}(r,z) = \begin{cases} -\frac{3}{2} B_0 \left[\frac{rz}{\kappa^2}\hat{r} + (1-R^2 - r^2)\hat{z}\right] & R \le 1 \\ -\frac{3}{2} B_0 \left[\left(\frac{rz}{\kappa^2 R^5}\right)\hat{r} - \left(\frac{2}{3} - \frac{2}{3R^3} + \frac{r^2}{R^5}\right)\hat{z}\right] & R > 1 \end{cases} \quad (1)$$

Comparison with experiment[1,8] and SUPERLAYER calculations indicate that this is reasonably accurate. Pressure balance then gives the self-consistant plasma density as

$$n(r,z) = n_0 r^2(1-R^2) + n_2, \quad R \le 1; \quad n_2, \quad R > 1, \quad (2)$$

Here κ is the elongation factor, $R = (r^2 + z^2/\kappa^2)^{1/2}$, and based on the good thermal conductivity of the plasma, a uniform temperature has been assumed. Values for the plasma parameters are obtained from an auxilliary global plasma model that incorporates appropriate energy and particle balances.

The fusion product (fp) trajectories are calculated from the equation of motion using a modified leapfrog algorithm. Slowing down and pitch-angle scattering effects are superimposed on this motion through the well-known Spitzer coefficients for drag $\langle dv_\parallel/dt\rangle$, parallel diffusion $\langle dv_\parallel^2/dt\rangle$, and perpendicular diffusion $\langle dv_\perp^2/dt\rangle$. The Gaussian distributions which describe the random change in $v_\perp$ and $v_\parallel$ are approximated by triangular distributions, preserving the standard deviation. The change in the local velocity components during a timestep is therefore

$$\Delta v_{\perp 1,2} = \left[3\left\langle\frac{dv_\perp^2}{dt}\right\rangle \Delta t\right]^{1/2} (\rho_{1,3}-\rho_{2,4}) \quad (3)$$

$$\Delta v_\parallel = \left[6\left\langle\frac{dv_\parallel^2}{dt}\right\rangle \Delta t\right]^{1/2} (\rho_5-\rho_6) - \left\langle\frac{dv_\parallel}{dt}\right\rangle \Delta t\,. \quad (4)$$

where ρ_j-ρ_k are random numbers and Δt is the timestep. The "scattered" velocity vector is then calculated by rotating these changes back into the inertial frame of the particle pusher.

A starting grid is selected which weighs each test particle equally. This requires construction of appropriate grids in both configuration and velocity space. Particle histories are calculated in parallel. Histories are terminated when particles hit the wall, are carried out the mirror throat, or slow down below the cutoff energy. Particles below the cutoff energy are only assigned to the ash buildup if they are confined completely within the closed field region. The remainder are assigned to the leakage plasma that originates on the first few open-field lines.

The primary use of MCFRM has been in conjunction with the SAFFIRE[2] reactor design study. In this design, a cold flowing plasma is introduced on the open-field lines for two purposes. It shields the hot closed-field region from cold neutral charge-exchange interactions,[9] and it aids in the removal of fp ash. This latter effect results from the FRM's small size[9] which allows many fps to interact with both the open and closed-field plasma during slow down. Fig. 1 illustrates this for a 14.7-MeV, D-^{3}He proton in a typical FRM plasma. The large orbit motion carries the proton out into the open-field region. The diverting action of the cold plasma is illustrated by the final gyro-motion which occurs just prior to cutoff, depositing the proton on an outer open flux surface.

References

1. R. K. Linford, et al., Bull. APS, 23, 2781 (1978).
2. G. H. Miley, J. G. Gilligan, D. Driemeyer, Trans. Am. Nucl. Soc. 30, (1978), p. 47. Also see APS, 23 (1978), p. 884.
3. E. C. Morse, Ph.D. Thesis, University of Illinois, 1979.
4. J. A. Byers, Phys. Rev. Lett., 39, 1476 (1977).
5. H. H. Fleischmann, Phys. Rev. Letts., 37, 542 (1976).
6. M. N. Rosenbluth, M. N. Bussac, and H. P. Furth, Controlled Fusion Theory Conference, Gatlinburg, TN, April 1978, DC8.
7. R. Cohen, D. Anderson, C. Sharp, loc. cit., A10.
8. A. G. Es'kov, R. Kh. Kurtmullaev, et al., 7th IAEA Conference on Plasma Physics and Controlled Thermonuclear Research, Innsbruck (1978).
9. J. G. Gilligan, et al., "Divertor Design for the D-^{3}He Field-Reversed Mirror," Proc. Third ANS Topical Mtg. on Fusion, Sante Fe, NM (1978), p. 279.

*This work supported by the U.S. Department of Energy Contract #EY-76-S-02-2218.

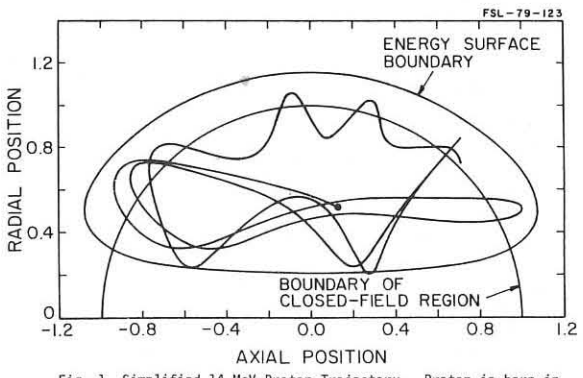

Fig. 1 Simplified 14-MeV Proton Trajectory. Proton is born in the closed field region (dot), confined in its energy surface, but passes thru the open field.

AP35

TWO-FREQUENCY — BANDS PLASMA — DENSITY INTERFEROMETRY WITH OVERSIZED MICROWAVE WAVEGUIDE

Ye Youzhang, Hai ShuYuan, Zhang Wenmo

Southwestern Institute of Physics

P.O.Box 15, Leshan, Sichuan

People's Republic of China

Abstract: A two-frequency-bands interferometer has been used to measure the electron density of a plasma. The two signals with different frequencies (70GHz and 35 GHz) are mixed and divided by a double-prism coupler and interfered independently in the same bridge-type oversized waveguide system. This arrangement permits measurements with overlapping check and greater band width than a conventional single frequency-band interferometer. In the present experiment, a range of electron density from 5×10^{10} to $2 \times 10^{12} cm^{-3}$ is covered.

Arrangements: A two-frequency-bands microwave interferometer with oversized waveguide has been developed on the basis of 4mm-band fringe shift microwave interferometer with oversized waveguide[1]. The principle of this type of interferometer is similar to that of multichannel communication. We use zebra-stripes for 4mm and direct-fringes for 8mm. Components (couplers, bends, phase shifters) are constructed in the same manner as in the 4mm-band fringe shift interferometer with oversized waveguide. A sketch of the interferometer is shown in Fig.1. Microwaves of 4mm and 8mm interfere simultaneously in the same instrument. In principle, it is also possible to realize three or multi-frequency-bands system. After the microwave signals of the two frequency-bands are mixed by an adjustable iris-type power divider (or a double-prism coupler), they are divided into reference path and transmission path by a double-prism coupler, and mixed again by another double-prism coupler, then the interference signals with different frequencies are sent out from different arms, detected, amplified and clipped flat, and finally, two signals are recorded simultaneously on an oscilloscope.

Interferometer: Two microwave beams of 4mm and 8mm wavelength bands are generated by a reflex klystron of type D2012 and K 21. The interferometer can be operated in three different ways: (1) As a 4mm and 8mm microwave absorption-meter. In this case the reference path is shut, the 4mm-band reflex klystron is modulated by 250KHz sawtooth voltage and 8mm-band reflex klystron by 1MHz sinusoidal voltage. (2) As a 4mm zebra-stripe microwave interferometer and 8mm absorption-meter, the reference path is turned on and connected with a high pass filter which allows 4mm wave to propagate but stop the passage of 8mm wave. The 8mm reflex klystron is still modulated by 1 MHz sinusoidal voltage. (3) As a 4mm zebra-stripe interferometer and 8mm direct-fringe (or Mach-Zehnder) interferometer. The reference path is turned on. 8mm reflex klystron operates in c.w. state.

Frequency divider and mixer: The frequency divider and mixer is an important component of this kind of interferometer. Its main function is to incorporate signals of different frequency-bands into the trunk comminication system and then to select different signals from the trunk for different terminals. The frequency divider is a passive network, because it is reversible, it can also be used as a mixer. The frequency dividing system is usually composed of a series of frequency dividers connected in different ways. We use a step-by-step channel shunt filter isolating method. Among the six arrangements suggested, i.e., series diffraction converter[2], series directional coupler, dual frequency diplexer[3], Grating-polarization diplexer, finline coupler[4] and series double-prism coupler[5], we use the double-prism couplers. The basic design of this component and its series-counnected diagram are shown in Fig.2, from which we can see that it can separate three different frequencies. We use only one double-prism coupler as frequency divider. The 4mm and 8mm wave will go out from the vertical and the horizontal arm by adjusting the distance between two prisms of the coupler, and the attenuation of 4mm wave is about 3dB. This kind of coupler is usually used as an attenuator, but it is found to be a good frequency divider too.

Experimental results: The oscillograms of electron density measurement on a plasma produced by discharge tube with the two-bands interferometer are shown in Fig.3, with the direct-fringe oscillogram at frequency 35GHz (top trace) and the zebra-stripe oscillogram at frequency 70GHz (bottom trace). Discharge parameters are: discharge voltage=5Kv, condenser bank capacity=16uf, vacuum pressure$\approx 10^{-3}$ torr, horizontal sweep period of oscillocope=1.1ms. plasma size=72cm. The measured electron density of the plasma is shown in Fig.4. The agreement between the results from the measurements of two frequencies is quite good.

The authers are indebted to Prof. Sun Xiang for her encouragement throughout the research. We are also thankful to the Institute of Electronics Research of the Chinese Academy of Sciences for supplying the reflex klystron.

References:

1) Ye Youzhang et al., Report of the Southwestern Institute of Physics, PRC, 78-11. (1978)

2) **Д.И.Казначеев, Широкополосная Дальняя Связь по Волноводам, Издательство АН СССР. (1959)**

3) M.A.Heald and C.B.Wharton, Plasma diagnostics with microwave. John Wiley & Sons Inc., New York. (1965)

4) S.D.Robertson, The Ultra-Bandwidth Finline Coupler. P.I.R.E. 739. (1955)

5) J.J.Taub et al., IEEE Trans.on Microwave Theory and Techniques, Vol.MTT-11, 338 (1963)

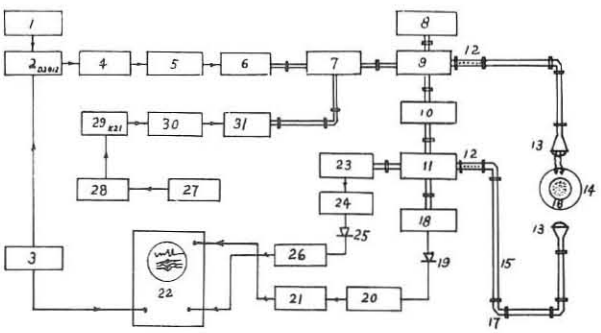

Figure 1

1-power supply (4mm). 2-Reflex klystron (70GHz). 3-Sawtooth generator. 4-Impedance transformer. 5-Isolator. 6-4mm/3cm Taper. 7-Iris type divider. 8-load. 9-Double-prism coupler. 10-Phase shifter or High-pass filter. 11-Double-prism coupler. 12-Filter. 13-Horn antenna. 14-Vacuum chamber. 15-Long path oversized waveguide. 16-Plasma region. 17-Bend. 18-4mm/3cm Taper. 19-Detector. 20-preamp. 21-Amplifier and clipper. 22-Oswilloscope. 23-8mm/3cm Taper. 24-Impedance transformer. 25-Detector. 26-Amp. 27-Modulator. 28-Power supply (8mm). 29-Reflex klystron (35GHz). 30-Isolator. 31-8mm/3cm Taper.

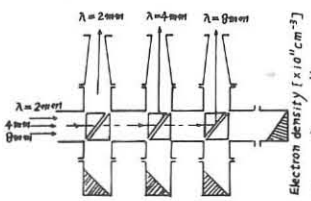

Figure 2

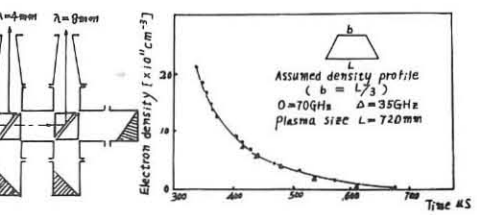

Figure 4

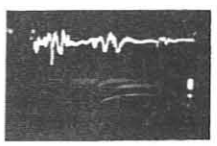

Figure 3

B2.1

ATTEMPTS TO OPTIMISE β IN THE TOSCA TOKAMAK

R Birch*, C W Gowers*, F A Haas, P A Jones*, K McGuire+, D C Robinson, A Sykes, M Turner, A J Wootton

Culham Laboratory, Abingdon, Oxon, OX14 3DB, UK (Euratom/UKAEA Fusion Association)

*AWRE Aldermaston, UK +University of Oxford

ABSTRACT Tokamak empirical scaling laws for an ohmically heated plasma show that the maximum β is obtained in small aspect ratio devices with small major radii. The maximum central value of β obtained by a combination of gettering/gas puffing/shaping on TOSCA is 4%. For a central q value of 1 the maximum theoretical value of central β for the onset of ideal MHD ballooning modes is 3% but for certain profiles higher values are possible. A combination of gettering and the use of a resonant helical coil has permitted stable operation with q_a down to 1.4 and no conducting shell. Triangles show 'jumps' between two equilibria.

INTRODUCTION The small tokamak TOSCA (R=30cm, a/R≤0.27) has been used to investigate the maximum value of β which can be obtained with ohmic heating.

MAXIMUM β SCALING The maximum density for ohmically heated plasmas in tokamaks is observed to be proportional to B_ϕ/R, or as q(0)≈1, the central current density. When this is combined with empirical scaling laws for the energy confinement time, the central value of β can be expressed as $\beta(0) \propto \left(\frac{a}{R}\right)^{\gamma} \frac{Z_{eff}^{\mu}}{R^{\delta} q(0)^{\varepsilon} B_\phi^{\lambda}}$.

If $\tau_E \sim na^2$ then γ=4/5, δ=1, ε=9/5, λ=1/5, μ=2/5, with the Pfeiffer, Waltz[1] scaling γ=0.45, δ=0.55, ε=1.04, λ=0.24, μ=0.46 and with the Mirnov scaling γ=6/5, δ=4/5, ε=2, λ=0, μ=2/5. Fig.1 shows the Pfeiffer, Waltz scaling for central electron β_{Teo} for a number of devices operating at or near the maximum density (Z_{eff} and q(0)=1). The optimum results on TOSCA show that the maximum β is obtained on small aspect ratio devices with small major radius.

OPTIMISING β (a) With circular plasmas the central density rises to 3→3.5 $10^{13}cm^{-3}$ in 3 ms while the central electron temperature is constant from 2→3ms at ∿300 eV. (i) Over the discharge period the toroidal field can be decreased from 5kG to 3kG raising β without any deleterious effects. (ii) When gas puffing is used the density can be raised to 3.5 $10^{13}cm^{-3}$ in 1ms without disruption but higher values of n_e or β are not obtained. (b) With gettered circular plasmas the density can be $5x10^{12}cm^{-3}$ without runaway phenomena and can be raised to 3.5 $10^{13}cm^{-3}$ by gas-puffing but with no further increase in density or β. (c) A triangular plasma has a similar effect with a central β value of 3%[2]. In summary, attempts to increase the density and decrease the toroidal field result in a maximum central electron β value of 4%. The total β value on axis maybe 5%. These discharges trace out trajectories in a normalised current, normalised density diagram as shown in Fig.2. The highest β values are obtained with trajectories which reach high values of $\bar{n}_e R/B_\phi$ i.e. E. Attempts to optimise the average β have also been made by decreasing the value of q by raising the current in a controlled way. Using a combination of gettering which yields low densities with broad current distributions throughout the pulse, and a resonant coil [3] which stabilises the m=2 mode, stable operation is obtained at values of q<2 for times up to 1ms(∿ 2 x τ_E) with no conducting shell (trajectory A, Fig.2). The minimum value of q reaches ∿1.4 where mode activity with m=1, 3 and n=1, 2 is observed, and τ_E is not reduced. The central β value is lower as the density is lower, the average value is ∿1.5%.

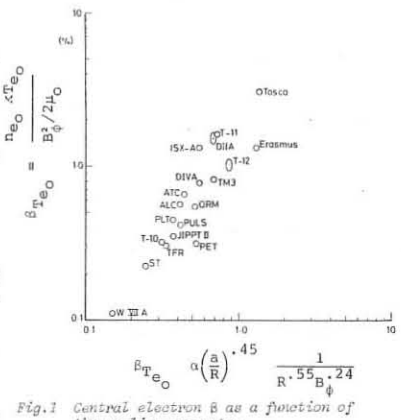

Fig.1 Central electron β as a function of the scaling parameter.

BALLOONING MODES The value of average β for the onset of ballooning modes has already been exceeded on TOSCA[2] with a triangular plasma. Low toroidal mode number instabilities may have a higher critical β, and a second, high β_p region of stability may be accessible. Numerical results for one family of equilibria as the central current profile (characterised by q(0)) is modified are given in Fig.3. This shows the maximum poloidal β, β_p as a function of q(0) for stability to large toroidal mode number modes[2] in the TOSCA device for a circular plasma with $q_a \sim 3$. Two regions of stability (A and B) are apparent. One with $\beta_p<1$ and q(0)≥1 which has a central value of β of 3%, a value which is exceeded in this device, and a region with $\beta_p>>1$. Fig.3 also shows the flux contours, current and pressure profiles for a marginally stable case with β_p=7(B), average β of 2.6% and central value 13%. This high β_p regime maybe accessible if q(0) can be kept at ∿1.5 while heating. Equilibria with $q_a \sim 1.4$ give high average values of β(>4%) with low shear i.e. q(0)≥1.2 although these are in the 'high β_p' regime. In this case the lower region of stability has $\beta_p<0.3$ for q(0)∿1 which has also been exceeded experimentally.

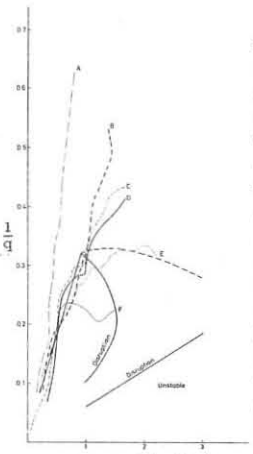

$\frac{1}{q}$

$\frac{\bar{n}_e R\ (10^{19} m^{-2} T^{-1})}{B_\phi}$

Fig.2 Normalised current as a function of normalised density A, B gettered, current rise C, D ungettered current rise E gas puffed, F ordinary.

TRIANGULAR EQUILIBRIA Triangular plasmas are produced by adding a hexapole field, current I_h. Inward pointing plasmas (I_h/I_p<0) are easier to control than outward pointing ones, because of unusual jumps ΔR in major radius. These occur with velocities between 0.02 and 0.2 cm μs^{-1}. Fig.4 shows the magnitude of the jump normalised to the starting position, $\Delta R/R_{pl}$ as a function of the triangularity, I_h/I_p. The results (x) are for plasmas initially near the hexapole centre, R_o, and show small jumps for inward pointing plasmas, large jumps for outward ones. In these jumps the plasma moves from one equilibrium to another, following a small perturbation. Two possibilities are - a neighbouring equilibrium exists or a change in parameters modifies the existing equilibrium. The solid curves in Fig.4 show the predicted jump for a decrease in inductance of 0.07. Two sets of curves are shown for plasmas initially centered (0) or outside by 2.1cm(0.07). The model predicts the variation of the jump size with the ratio I_h/I_p. The new equilibria associated with an outward jump, are not observed experimentally.

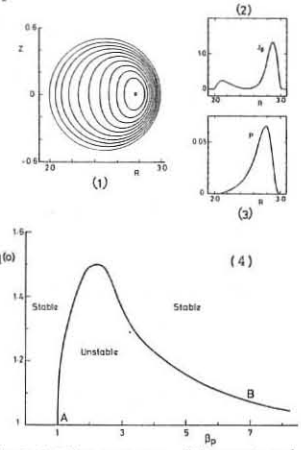

Fig.3 (1)Flux contours, (2)current and (3)pressure distribution for marginally stable equilibrium with β_p=7. (4)Ballooning mode stable region in the q(0), β_p plane.

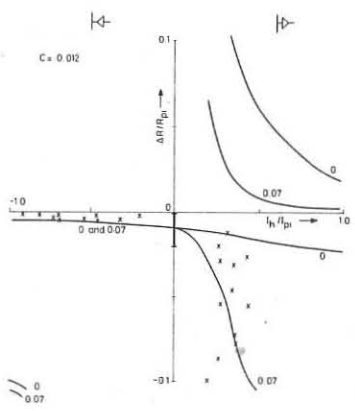

Fig. 4 Major radius jumps as a function of triangularity.

CONCLUSIONS Experimentally the optimised central β of 4% from ohmic heating just exceeds the lower ballooning mode limit. Theoretically a second higher β region of stability maybe accessible. Stable operation at q_a values down to 1.4 has been obtained without a conducting shell.

ACKNOWLEDGEMENT We wish to thank Mr R Peacock for his valuable assistance and reliable operation of TOSCA.

REFERENCES

[1] Pfeiffer W and Waltz R E, Nuclear Fusion 19 (1979) 51.

[2] 7th Int. Conf. on Plasma Phys. Innsbruck 1978, Papers T1-1 and K5.

[3] McGuire K M and Robinson D C. This conference.

B2.2

HIGH POWER NEUTRAL BEAM EXPERIMENTS ON ISX-B*

D. W. Swain, S. C. Bates, C. E. Bush, R. J. Colchin, W. A. Cooper†, J. L. Dunlap, G. R. Dyer, P. H. Edmonds, A. C. England, C. A. Foster, J. T. Hogan, H. C. Howe, R. C. Isler, T. C. Jernigan, H. E. Ketterer, J. Kim, P. W. King, E. A. Lazarus, C. M. Loring, J. F. Lyon, H. C. McCurdy, M. M. Menon, J. T. Mihalczo, S. L. Milora, M. Murakami, A. P. Navarro‡, R. V. Neidigh, G. H. Neilson, D. R. Overbey, V. K. Paré, Y-K. M. Peng, N. S. Ponte, M. J. Saltmarsh, D. E. Schechter, J. E. Simpkins, W. L. Stirling, C. E. Thomas, C. C. Tsai, J. B. Wilgen, W. R. Wing, R. E. Worsham, and B. Zurro‡

Oak Ridge National Laboratory, Oak Ridge, Tennessee 37830 USA

ISX-B is a modification of the ISX-A tokamak [1], which includes neutral beams with injected power $\lesssim$ 1.8 MW, and a poloidal coil system designed to produce circular, elliptical, or D-shaped plasmas with elongations up to 1.8. A major goal of the experimental program is the study of the equilibrium and stability of plasmas with average beta $\langle\beta\rangle$ in the 2-5% range produced by beam heating [2]. Basic machine parameters for ISX-B (shown in Fig. 1) are: R_0 = 0.93 m, a = 0.27 m, B_t = 1.0-1.8 T, I_p = 100-200 kA. Plasma current and position (both vertical and horizontal) are maintained at desired values with feedback control systems. Plasma density is normally controlled by a preprogrammed gas puff. Solid hydrogen pellets 1 mm in diameter moving at speeds up to 1000 m/sec may also be injected into the beam heated plasma to raise the density.

In this paper, we present the results of neutral beam injection experiments carried out on an almost circular plasma (elongation = 1.1-1.2) with neutral beam power of up to 1 MW using gas puffing for density control. We have obtained volume averaged beta values (including the calculated fast ion component from neutral beam injection) of up to 1.8%. Peak beta values of 8-10% have been achieved. The relatively peaked pressure profile observed gives an rms beta ($= \sqrt{\langle\beta^2\rangle}$) = 3% (the parameter of interest for reactor design because burn rate is approximately proportional to pressure squared). Poloidal beta values $\geq$ 3.0 have been obtained. We have not seen evidence of a beta limit caused by ballooning or other instabilities.

Typical Discharge Characteristics: Parameters characteristic of discharges at four injection power levels and several densities for B_t = 1.15 T are shown in Table I. Figure 2 shows the time behavior of plasma current, loop voltage, line average density, central ion temperature, and $\beta_p + \ell_i/2$ during a typical shot with 1 MW of neutral beam injection (at a beam energy of 40 keV). The usual mode of operation is to inject hydrogen neutrals into a deuterium plasma. The increase in plasma current from 110 to 145 kA starting at the beam injection time was preprogrammed into the current feedback control system and is not a result of the beam injection.

The two beams, from two neutral beam injectors designed and built at ORNL, are both co-injected. Significant electron heating is observed, with T_e (0) (determined from Thomson scattering measurements) increasing from 0.6 to 1.5 keV during injection. The value of T_i (0) (from charge exchange analysis) increases from 0.35 to 1.3 keV. As can be seen in Fig. 2, the loop voltage drops from 1.5 to $\lesssim$ 0.5 V when the beams are turned on. In these discharges, the plasma heating is dominated by the neutral beams, the ohmic heating power being < 10% of the total power input during the injection pulse.

As in ISX-A, the plasma impurity concentration is low, with $\langle Z_{eff}\rangle$ between 1.5 and 2.5 typically, both with and without injection. Radiated power is usually < 30% of the input power during ohmic heating. P_{rad} does not increase significantly during injection and is typically $\lesssim$ 10% of the input power during high power injection shots. This is attributed in part to the use of low-Z materials throughout the vacuum vessel and diagnostic devices, with stainless steel used for the limiters. The vacuum vessel is not gettered with titanium.

Beta Results: Figures 3 and 4 plot volume averaged and peak values of beta vs $\bar{n}_e$ for injection powers between 0.3 and 1 MW. For these data, B_t = 1.12 T, and I_p = 110-115 kA. The plasma components of β_0 and $\langle\beta\rangle$ tend to increase linearly with $\bar{n}_e$, in agreement with results reported previously [1]. However, the total beta, which includes the beam component of the pressure addition to the plasma component, does not increase as fast as the plasma component. For the 1 MW cases, which are dominated by the beam contribution to the pressure, the average beta is almost independent of $\bar{n}_e$ because the beam contribution goes down (due to the decrease in the beam slowing-down time) as the electron density goes up. The fast ion contribution to total beta is computed using a Fokker-Planck code [3] to calculate the initial beam deposition profile, using measured T_e and n_e profiles and estimated neutral density. It is in reasonable agreement with results from a Monte Carlo code [4] that computes initial beam ionization and subsequent diffusion. Figure 5 is a graph of the plasma and fast ion contribution to the total beta vs radius for two cases. As can be seen from the curves, the fast ion contribution is a significant fraction of the total beta, particularly near the magnetic axis for the lower density case.

Figure 6 is a plot of T_e (r) and n_e (r) for two cases with the same injected power, gas puff, plasma current, average density, and approximately the same T_i (0), but with different toroidal fields. For the 1.12 T case $\langle\beta\rangle$ = 1.4%, and for the 1.46 T case, $\langle\beta\rangle$ = 0.8%. Although numerical stability calculations using the measured pressure profiles indicate that the interior third of the plasma should be unstable to ballooning modes, the close agreement of the measured macroscopic plasma parameters indicates that no instability that substantially lowers the gross energy confinement time was triggered by the lower toroidal field (i.e., high beta). Distinctive changes in oscillatory signals detected by magnetic pickup coils and collimated PIN diodes are seen as beam power is increased. These may be manifestations of ballooning or other pressure driven modes, but any such identification is uncertain at this time.

Particle and Energy Transport: The behavior of $\bar{n}_e$(t) is altered by injection at powers above approximately 500 kW. For a fixed gas puff flow rate, the density decreases shortly after injection begins, as shown in Fig. 2, and then increases once more after the end of the injection pulse. This is in contrast to a similar shot with no injection, in which $\bar{n}_e$ increases uniformly in time to a value of 4-5 x 10^{13} cm^{-3} until a disruption occurs. This decrease in line average density may be due to a change of the profile or to an increase in average particle loss rate. This could result from a ballooning or other instability, or another mechanism such as a reduction of inward radial transport (e.g., a decrease in the Ware pinch effect) due to the lowered toroidal electric field. More detailed measurements are necessary to resolve these questions. For a fixed value of $\bar{n}_e$, analysis of electron heating by the neutral beam indicates that the beam power has approximately the same effect as the ohmic heating power, causing a change in T_e of $\sim$ 0.5 eV/kW. Although extensive scaling studies have not been done so far, it appears that the electron energy transport is in agreement with Alcator scaling ($\tau_E \sim \bar{n}_e$). Ion thermal conductivity appears to be within a factor of two of neoclassical at the highest densities observed. However, losses associated with charge exchange dominate the ion power balance at low values of $\bar{n}_e$ (<2.5 x 10^{13}).

Summary: 1) Average beta values of 1.8% have been attained in a relatively clean plasma in ISX-B with neutral beam injection power > 10 times the ohmic power input.

2) Total beta has increased smoothly with beam power so far, with no indication that a ballooning or other instability is increasing the energy loss rate significantly.

3) For a given plasma density (>3 x 10^{13}), plasma energy transport processes are in rough agreement with 1-2 times neoclassical for the ions and Alcator transport for the electrons. The effect of T_e on the transport is uncertain.

Acknowledgments: We wish to acknowledge the support of J. F. Clarke, L. A. Berry, O. B. Morgan, J. Sheffield, and the help of the technical and engineering groups, during the design, construction, and operation of ISX-B.

References:

*Research sponsored by the Office of Fusion Energy, U. S. Department of Energy under contract W-7405-eng-26 with the Union Carbide Corporation.

†University of Michigan.
‡Visitors from J.E.N., Madrid, Spain.

[1] M. Murakami et al., Phys. Rev. Lett. 42, 655 (1979).
[2] J. F. Clarke and D. J. Sigmar, Phys. Rev. Lett. 38, 70 (1977).
[3] J. D. Callen et al., Proc. 5th Intl. Conf. on Plasma Physics and Controlled Nuclear Fusion Research, IAEA Tokyo Conf. Paper CN-33/A16-3 (1974).
[4] R. Goldston, private communication (1979).

Table I. Typical discharge parameters in ISX-B

P_{beam} (MW) (±15%)	I_p (kA) (±5%)	$\bar{n}_e$ (10^{13} cm^{-3}) (±10%)	$T_e(0)$ (keV) (±15%)	$\langle T_e\rangle$ (keV) (±10%)	$T_i(0)$ (keV) (±15%)	Volts (±20%)	Z_{eff}	Plasma $\langle\beta\rangle$ (%)	Plasma β_0 (%)	Total $\langle\beta\rangle$ (%)	Total β_0 (%)
0	110	4.1	0.65	0.25	0.40	1.7	1.6	0.42	2.1	0.42	2.1
0	110	1.9	0.84	0.36	0.30	1.1	1.3	0.11	1.0	0.11	1.0
0.3	110	1.5	1.5	0.41	0.80	1.2	0.9	0.35	4.0	0.35	4.8
0.4	120	4.0	1.1	0.40	0.80	1.2	2.0	0.70	3.9	0.81	4.9
0.6	114	2.6	1.5	0.99	0.90	1.1	4.6	0.55	3.2	0.99	6.2
0.7	104	3.6	1.1	0.60	0.65	0.8	2.0	0.62	3.5	0.95	5.5
0.6	111	5.2	1.0	0.50	0.85	0.4	1.3	1.16	4.2	1.40	5.4
0.9	112	5.0	1.4	0.71	0.95	0.6	2.9	1.39	6.3	1.78	8.3
1.1	142	3.0	1.5	0.66	1.30	0.8	2.3	0.87	4.3	1.55	9.5

Figure 1

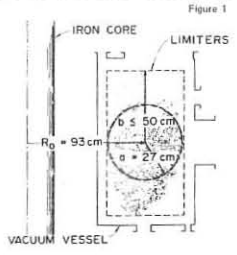

Figure 2

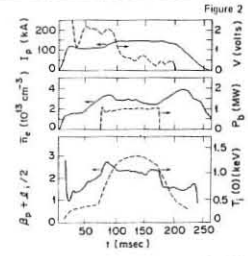

Figure 3

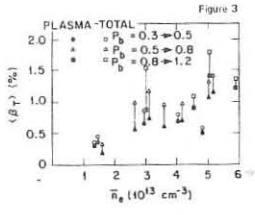

Figure 4

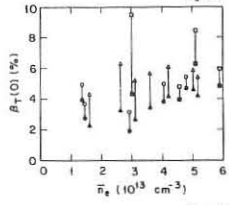

Figure 5

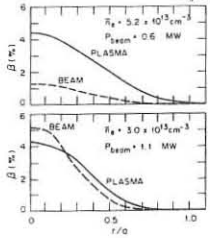

Figure 6

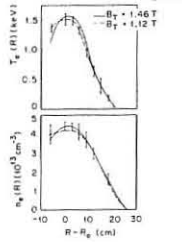

B2.3

FUSION NEUTRON PRODUCTION DURING DEUTERIUM NEUTRAL BEAM INJECTION INTO PLT

P. L. Colestock, S. Davis, P. Efthimion, H. P. Eubank, R. J. Goldston, L. R. Grisham, R. J. Hawryluk, J. Hovey, D. L. Jassby, D. W. Johnson, A. A. Mirin, G. Schilling, R. Stooksberry, L. D. Stewart, J. D. Strachan, and H. H. Towner

Plasma Physics Laboratory, Princeton University, Princeton, New Jersey 08544 USA

The maximum observed fusion neutron intensity (1.5×10^{14} n/sec) from PLT deuterium plasmas heated by deuterium neutral beams[1] is about two orders of magnitude greater than in previous tokamak experiments. The neutron emission is due principally to beam-induced fusion reactions occurring either when the injected deuterons collide with plasma deuterons (beam-target reactions) or when the injected deuterons collide with other beam deuterons (beam-beam reactions). For beam-target reactions, the reacting deuteron pairs have a center-of-mass velocity which was observed on PLT by recording neutron spectra with a collimator viewing the Counter-direction for Co- only and Counter-only injection (Fig. 1). The shape and mean energy of the neutron spectra are reasonably explained by calculated spectra[2] for the energetic beam ions slowing down in a $T_i = 1.5$ keV plasma with $Z_{eff} = 3 \to 5$. The neutron emission is located primarily in the central regions of the plasma (Fig. 2) roughly as expected from the neutral beam deposition.[3]

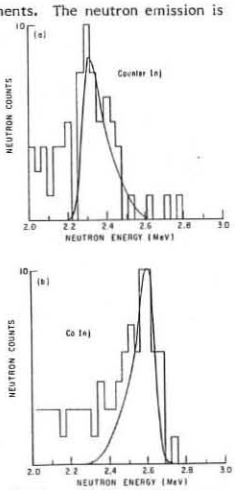

Fig. 1. Collimated neutron spectra obtained looking tangentially in the direction of Counter-injected ions. The shift in mean neutron energy is due to the different center-of-mass velocity of the reacting deuterons for Co-only vs Counter-only injection. The lines are the spectra predicted (Ref. 2) for $T_i = 1.5$ keV, $Z_{eff} = 5$, $W_{CO} = 26$ kV, $W_{CTR} = 30$ kV.

The neutron intensity was measured in the range 10^7 to 10^{15} n/sec with 10 ms time resolution[4] (Fig. 3). The rise time reflects the equilibration of the linearly accumulating fast ions (constant injection current) and their classical slowing down to energies where they no longer contribute to the neutron production. The fall time reflects only the slowing down. In the case of unidirectional injection, where beam-beam collisions can be neglected, both the time behavior and the absolute magnitude of the beam-target neutron flux are well-described by a bounce-averaged numerical calculation of the fast ion behavior.

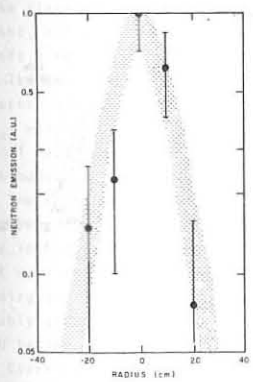

Fig. 2. Radial profile of the neutron emission. The shaded region represents the expected profile (Ref. 3).

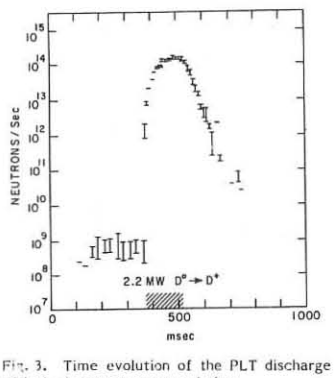

Fig. 3. Time evolution of the PLT discharge with the largest neutron emission.

The absolute calibration of the neutron emission is a difficult problem in the tokamak geometry but we use several different schemes, including the use of PuBe source. Our favored calibration uses the thermonuclear neutron emission predicted from the experimental plasma parameters for high density ohmically heated PLT discharges, where $T_i \simeq T_e$. The expected accuracy is about a factor of two.

Over the entire range of PLT plasma and neutral beam conditions so far obtained the experimental neutron emission varied about two orders of magnitude. The parameter which influenced the neutron production most strongly was the beam voltage (Fig. 4), which reflects the expected dependence of the fusion reaction rate on energy. Empirically, the neutron production rate per unit of injected current (Q') decreased as the density increased (Fig. 5). For the beam-target neutrons, this indicates the influence of enhanced beam trapping in the cooler edge plasma as well as the reduction in central temperature as $\bar{n}_e$ is raised. For the beam-beam neutrons, the direct linear influence of n_e on the decrease in the beam slowing down time, with increasing $\bar{n}_e$ reduces the probability of an energetic collision.

The observed neutron intensity can be predicted reasonably well (Fig. 6) by Fokker-Planck code calculations[5-7] which describe the fast ion population by classical energetic ion slowing down and orbit motion.

A factor-of-two uncertainty is expected, however, in the theoretically predicted neutron rates due to uncertainties in the experimentally measured parameters that are used as input into solving the Fokker-Planck equation.

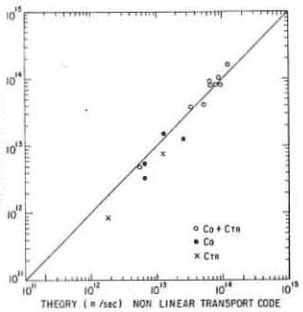

Fig. 6. Comparison of the observed PLT neutron emission with the predicted emission (Ref. 5) for a wide range of plasma and neutral beam conditions.

The most important uncertainties are the magnitude and radial profiles of 1) the ion temperature which contributes a finite T_i enhancement to the relative velocity in calculating the fusion reaction rate,[8] and 2) the neutral density which determines the fast ion charge exchange loss.

These uncertainties in the absolute neutron calibration and the experimental input to the codes are of a magnitude sufficiently large to allow enhanced radial transport of the energetic ions to remain undetected in a simple comparison of the neutron magnitudes. Evidence for the lack of radial transport comes from the fact that injection into both high density and low density plasmas have been equally well described.

At low densities, the neutral beam trapping is centrally peaked, so that enhanced diffusion tends to move energetic ions outward resulting in a reduced neutron emission.[5] However, at higher densities ($\bar{n}_e \geq 5 \times 10^{13}$ cm^{-3}), the neutral beam trapping profile is hollow so that diffusion tends to move energetic ions both inward and outward. In this case the departure of the experimental neutron emission from classically predicted levels even with enhanced radial transport can be expected to be minimal.[5] The agreement between theory and experiment at both high and low densities suggests that no enhanced diffusion was present.

Further evidence for the lack of radial transport comes from the fact that cases where beam-target emission dominates are about equally well described as cases where beam-beam emission dominates (even at the same $\bar{n}_e$). A significant hot ion loss should have had a more pronounced effect on the beam-beam reactions.

During some of these $D^0 \to D^+$ discharges, large density fluctuations observed by microwave scattering were present.[1] The neutron emission from these discharges was equally well described as in all the other cases. Hence, these density fluctuations have apparently no drastic effect on the classical behavior of the energetic beam ions.

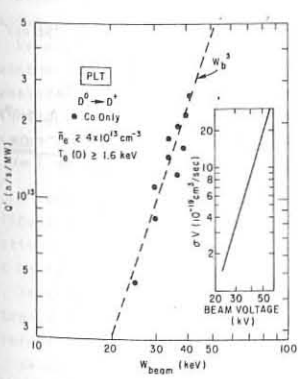

Fig. 4. Dependence of the neutron emission on beam voltage (Ref. 4). The insert shows the dependence of σv on voltage for the D(D,n)He^3 reaction.

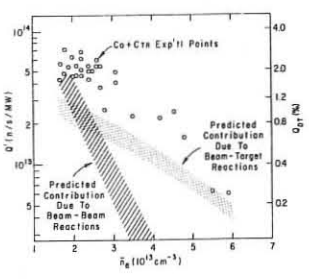

Fig. 5. Dependence of the neutron emission (Co + Counter injection) on plasma density. The shaded regions indicate the predicted levels of beam-beam and beam-target reactions (Ref. 7).

Conclusions

Deuterium beam injection into deuterium PLT plasmas has resulted in D(D,n)He^3 neutron yields of 1.5×10^{14} n/sec and 2×10^{13} n/pulse. This neutron production amounts to 170 watts of fusion power ($Q_{DD} > 6 \times 10^{-5}$) while the equivalent D-T fusion power would reach 50 kW ($Q_{DT} \simeq 2\%$). These results are in agreement with theoretical analyses that assume classical energetic ion behavior and use the experimental profiles of density and temperature.

References

(1) H. Eubank, et al., "Plasma Physics and Controlled Nuclear Fusion Research" (Proc. 7th Int. Conf., Innsbruck, 1978) IAEA-CN-37-C-3.
(2) H. Towner and D. L. Jassby, Trans. Am. Nucl. Soc. 22, 74 (1975).
(3) J. D. Strachan, et al., Phys. Lett. 66A, 295 (1978).
(4) J. D. Strachan, et al., "Joint Varenna-Grenoble Int. Symp. on Heating in Toroidal Plasmas" Vol 1, 25 (Grenoble, 1978).
(5) A. A. Mirin, et al., ibid Vol 1, 18 (Grenoble, 1978).
(6) R. Goldston, Nucl. Fus. 15, 651 (1975).
(7) D. L. Jassby, Phys. Lett. 55A, 225 (1975).
(8) H. Eubank, "Course on Plasma Diagnostics and Data Acquisition Systems" (Varenna, 1975) 377.

B2.4

BALANCE OF ENERGY AT THE LH HEATING IN THE FT-1 TOKAMAK

V.E.Golant, V.K.Gusev, V.V.Dyachenko, M.M.Larionov, A.D.Lebedev, G.T.Razdobarin, G.A.Serebreny, O.N.Shcherbinin

A.F.Ioffe Physical-Technical Institute, Leningrad, USSR

Abstract. When studying the LH heating in the FT-1 Tokamak the increase of electron and ion energy was found. It was shown that up to 50% of HF power was absorbed by electrons in the LHR range and up to 20% was spent for fast ion production. The heating process was accompanied by an increase of energy losses from plasma.

The experiments on the lower hybrid plasma heating at the FT-1 Tokamak (R = 62 cm, a = 15 cm, B_o = 6-10 kG) are described in [1-3]. Now the measurements have been performed to precise the data on the balance of energy at the LH heating. The HF power (400 MHz, 1-3 ms, 80 kW) was coupled to the plasma by the passive slowing structure with N_z = 2-6 [3]. The ohmic heating (OH) power was of the same value (I=30-35kA, U = 2.2-2.5 V). Plasma parameters before the HF pulse were: $T_e(0)$ = 300-400 eV, $n_e(0) = 1\times10^{13}$ cm^{-3} (hydrogen). The LH condition was satisfied at B = 9-10 kG, $n_e = 6\times10^{12}$ cm^{-3}.

The effect of the HF pulse on electron temperature was studied by laser scattering. The average plasma density was controlled by microwave interferometer. Fig. 1 shows the changes in density and temperature profiles when pulse duration was 2.5 ms. The maximum temperature rise (ΔT_e= 100 eV) was registered at r = 4 cm. No changes were observed at $r > 7$cm. The increase in plasma density ($\Delta n = 1\times10^{12}$ cm^{-3}) seems to be connected with the neutral gas flux in the antenna region. The total electron energy store increased from 37 to 50 J, or by 35%. At the longer HF pulses the increase of density is more significant, but the temperature decreases everywhere except the axial region.

The effect of electron heating is more explicit if measurements are made 1 ms after the beginning of the pulse, when the density does not change yet (Fig. 2). It is seen that the increase of T_e is localized in the expected region of wave transformation, which is marked by the black rectangle. The temperature profile was analyzed by the thermal balance equation in assumption that the electron thermal conductivity did not change during LH heating. The increase of temperature gradient at r = 5-7 cm pointed at the additional energy release inside this zone. The comparison with the OH regime showed that up to 40 kW of HF power (about 50%) was absorbed by electrons. The electron temperature in the peripheral region did not rise due to additional energy losses for ionization and emission of impurity ions. This phenomenon spoils the efficiency of HF heating.

The ion energy was studied by charge exchange neutral analyser(CX) [1]. It was found that HF power produced the fast ions with energy 0.5-2.5 keV. Their flux increased sharply when the LH condition was met in the discharge. Fig. 3 shows the evolution of the CX spectra after switch off at B_o = 9 kG. The "tail" of ion distribution has an effective temperature equal to 450 eV. By integration of the CX spectra it was shown that the amount of fast ions reached 4% of total proton density and the energy of ions increased during the HF pulse by 20%.

Fig. 4 represents the time dependence of flux of neutrals with 0.98 keV energy after the HF pulse at B_o= 6.6 kG and 9 kG. In the first case the flux is small and its decay time is close to the ion bouncing time along the banana orbits ($\tau_b \approx$ 70 ms). At 9 kG the flux is 3 times greater and almost 50% of ions are trapped by the magnetic field. their life time is much longer and is determined by collisions with other particles.

Taking data on fast ion density and their life time one can estimate that about 15 kW of input power (20%) goes into the fast ions, but only 2 kW is spent for production of long living component. The rest of the power is lost since the poloidal magnetic field is not strong enough to contain fast ions.

The ion temperature determined by CX without the HF was about 80 eV. But during the HF pulse the CX measurements became inaccurate because of distortion of ion distribution function. The change in ion temperature in this case was defined by Doppler broadening of CV line 2271 A, which is emitted from the central region of the discharge. In ohmic heating stage T_i(CV) = 70 eV, and ΔT_i(CV) = 25-30 eV during HF pulse. The power transferred to ions during OH is evaluated to be 10 kW. So it is clear that only small part of the HF power (4 kW, or 5%) goes into the bulk ion heating. It is quite probable that the bulk ion heating can improve in stronger discharges due to better confinement of fast ions.

In conclusion, it is shown that the efficiency of absorption of HF power is high. Up to 50% of the applied power goes into electrons and up to 20% goes into fast ion production. Some reasons can be noted which limit the plasma heating:

1. The region of energy deposition is not localized at the discharge axis but at $r \approx$ 4-6 cm.
2. Neutral gas injection takes place under the HF pulse which leads to cooling of the plasma periphery.
3. The fast ion containment is rather poor because of low toroidal current in our experiment.

REFERENCES

1. I.P.Gladkovsky, V.E.Golant et al., VIII ECCFPP Prague, 1977, v.1, p.18.
2. V.E.Golant, V.K.Gusev et al., 7-th Int.Conf. PPCNFR, Innsbruck, 1978, IAEA CN-37-A-4-4.
3. V.V.Dyachenko, M.M.Larionov, G.A.Serebreny, O.N.Shcherbinin, Fizika plazmy, 5, 239, (1979).

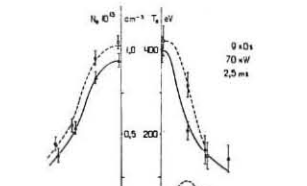

Fig. 1.

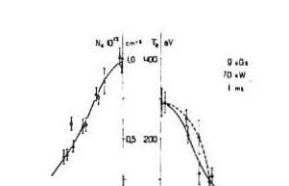

Fig. 2.

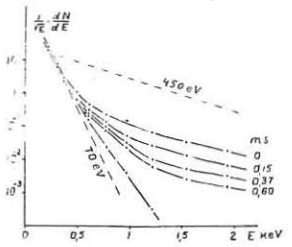

Fig. 3.

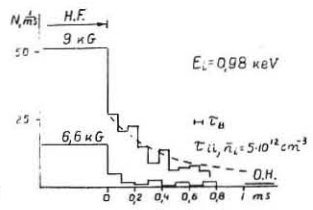

Fig. 4.

NON-THERMAL ELECTRON DISTRIBUTION FUNCTION IN THE FT TOKAMAK

R. Bartiromo, P. Buratti, L. Pieroni, O. Tudisco**

Associazione EURATOM-C.N.E.N. sulla Fusione, Centro di Frascati, C.P. 65 - 00044 Frascati, Rome, Italy

INTRODUCTION

It is well known that the electron distribution function f_e in a tokamak plasma cannot be a maxwellian for the presence of the electric field E driving the toroidal current.

The first order correction in E/E_D, where E_D is the Dreicer field, gives the well known Spitzer-Härm distribution function (1), from which the resistivity is usually computed.

It is also known that the f_e can have other corrections, due to the presence of runaway or slide-away electrons (2,3).

In this work we describe the violations of the Spitzer-Harm model observed in F.T. tokamak by soft x rays, electron cyclotron emission (ECE) and Thomson scattering diagnostics.

In this work we will consider discharges with a low content of runaway electrons (no signal in the hard x rays monitor) in which the streaming parameter $\xi = v_D/v_{th}$ ranged from 1% to 9%. The corresponding plasma parameters range was $\bar{n}_e = .3 \div 2.5\times10^{14}$ cm^{-3}; $I_p = 250 \div 350$ kA; $T_e = 600 \div 1000$ eV; B = 6 T.

We observed non-thermal phenomena developing beyond a value of ξ of the order of a few percent.

In order to explain the observed phenomena we tried a very simple model, based on a deformation of the f_e having a non-zero average over the pitch angle. With our model we cannot explain the details of the deformation, but we can derive the order of magnitude of density and energy of suprathermal electrons.

EXPERIMENTAL RESULTS

In FT we were able to produce very high current density discharges ($\langle J\rangle \sim 300$ A/cm^2) at B = 6T and $\bar{n}_e = .5 \div 3.5\times10^{14}$ cm^{-3}.

The presence of runaway electrons is monitored by a hard x rays detector. In the discharges under examination we had no runaway electrons.

At very high densities and not too high currents the results of the diagnostics measuring the electron temperature were consistent, but for higher currents or lower densities some anomalies in soft x rays and ECE came out.

The emission at the second harmonic of the central cyclotron frequency was no longer correlated with temperature but with $I_p/\bar{n}_e$; which is an anomalous behaviour because the corresponding optical depth was about 4, and the emission was expected to be black-body.

The correlation with $I_p/\bar{n}_e$ suggested a ξ dependence of the phenomenon. We plotted the emission versus ξ and the result is shown in Fig.1. The current density profiles necessary to compute the ξ were derived from Thomson scattering temperature profiles assuming $j \sim T_e^{3/2}$; this is a good assumption for low ξ values; probably above $\xi \sim 10\%$ the deviations from classical resistivity could be important.

Corresponding to anomalous ECE we found anomalous soft x rays fluxes and spectra (Fig.2), due partly to enhanced bremsstrahlung and partly to enhanced line radiation.

In Figure 3 a comparison between ECE, soft x rays flux and $I_p/\bar{n}_e$ is shown.

Anomalies have also been found in Thomson scattering spectra, as shown in Fig.4.

We explored horizontally the discharge section by a ECE; the enhancement came out to be present every where, but the emission is peaked on the center of the discharge, as shown in Fig.5. This again suggests a dependence on the streaming parameter of the emission enhancements.

THEORETICAL MODEL

A complete understanding of non-thermal phenomena is a very difficult task reling on the solution of collisional Boltzman equation in which the correct expression of collisional operator must be taken in account.

In this work we only try to find a tentative form of the electron distribution function which can bring together results of different diagnostics.

We assume that the population of non-thermal electrons can be represented by a displaced maxwellian

$$f_s = n_s\left(\frac{m}{2\pi kT_s}\right)^{3/2}\exp\left[-\frac{m}{2}\,\frac{v_x^2 + v_y^2 + (v_z^2 - v_0)^2}{kT_s}\right]$$

where v_0 is the drift velocity.

From that expression we calculate the x-rays spectrum and ECE enhancement and, from best fit to experimental data, we find values for v_0, n_s and kT_s.

Results of both x-rays and ECE show that, depending on discharge parameters,

$$5 \leqslant \frac{n_s}{n} < 20\%$$

$$E_0 \approx 2\ kT_s$$

$$2 \leqslant kT_s \leqslant 5\ \text{keV}$$

Concluding we stress that such results refer to the center of the discharge; where the suprathermal electrons appear to be concentrated (Fig.5). There f_s can carry an important fraction of the local plasma current and possibly influence the energy balance of the discharge.

BIBLIOGRAPHY

(1) L. Spitzer, R. Härm, Phys. Rev. 89 (1953) 977.

(2) H. Knoepfel, D.A. Spong, Nucl. Fusion 19 (1979) 785.

(3) B. Coppi, F. Pegoraro, R. Pozzoli, G. Rewoldt, Nucl. Fusion 16 (1976) 309.

* C.N.E.N. Fellow

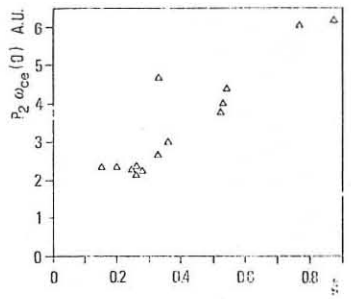

Fig. 1
ECE VERSUS THE STREAMING PARAMETER

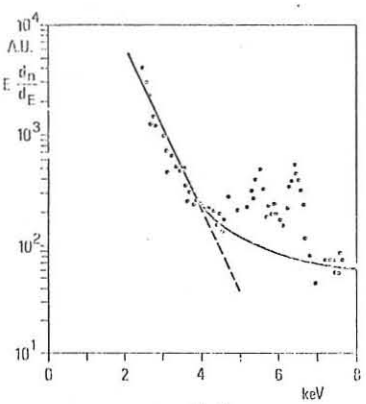

Fig. 2
SOFT X RAYS NON-THERMAL SPECTRUM: THE CONTINUUM IS DUE TO BREMSSTRAHLUNG; THE 5.5 AND 6.5 keV FEATURES ARE DUE TO Cr(Kα) AND F_e (Kα) LINES.

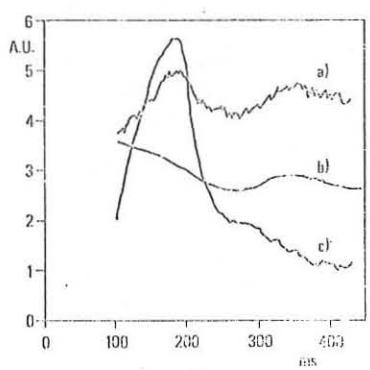

Fig. 3
(a) $2\omega_{ce}$ EMISSION, (b) $\ln I_p/\bar{n}_e$, (c) SOFT X RAYS FLUX.

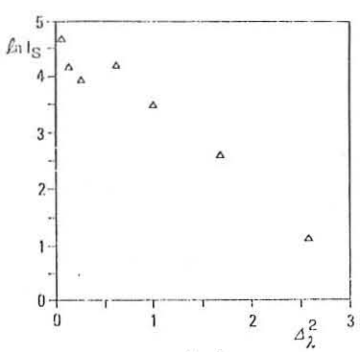

Fig. 4
NON-THERMAL SCATTERING SPECTRUM

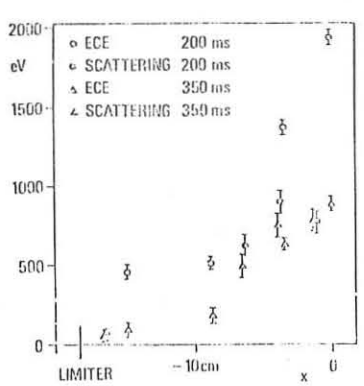

Fig. 5
TEMPERATURE PROFILES FROM ECE AND THOMSON SCATTERING

B2.6

CHARGE EXCHANGE MEASUREMENTS DURING NEUTRAL BEAM INJECTION AND ICRF HEATING ON PLT*

S.S. Medley, K. Bol, S.L. Davis, H.P. Eubank, R.J. Goldston, L.R. Grisham, R.J. Hawryluk, J.C. Hosea, E.B. Meservey, G. Schilling, W. Stodiek, R. Stooksberry,† and M. Ulrickson

Plasma Physics Laboratory, Princeton University
Princeton, New Jersey 08544 USA

ABSTRACT – Ion temperature increases of ~2 eV/kW injected power are observed on PLT for both neutral beam and ICRF heating experiments. Recent results are reported with emphasis on charge exchange diagnostics.

INTRODUCTION – Neutral injection heating experiments performed on PLT [1] using four 40 keV ORNL sources delivered up to 2.4 MW of deuterium beam power to the plasma and source improvements are projected to increase this power to 3.0 MW. Extension of the ICRF coil power level from ~400 kW up to 2.0 MW and combined beam/ICRF heating studies are in progress.

PLT is equipped with two charge exchange diagnostic systems (Fig. 1). A five-channel mass/energy analyzer (MACE) provides measurement of the perpendicular "thermalized" ion energy distribution in the energy range of 0.75 to 40 keV [2]. This system operates in a pulse counting mode, is capable of scanning to ~25 cm in minor radius (a = 40 cm), and uses a Berkeley 15 keV, 10 A diagnostic neutral beam source for localized measurements. A second horizontally scanning multi-sight-line energy analyzer (FIDE) operating in the analog mode provides measurement of both the ion temperature and the injected-ion slowing-down distribution.

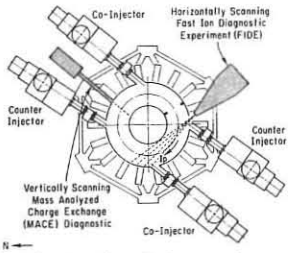

Fig. 1. Location of charge exchange analyzers on PLT.

RESULTS – With the MACE analyzer, ion temperatures were determined (Fig. 2) over a substantial range of electron density and neutral beam power [3]. The peak central ion temperature measurements (Fig. 3) underestimate the true central value by ≲5%. Recent numerical calculations [4] and our previous analysis [1] show that no significant distortion of the Maxwellian thermal tail distribution by beam ions is expected under PLT experimental conditions and, in fact, none was observed.

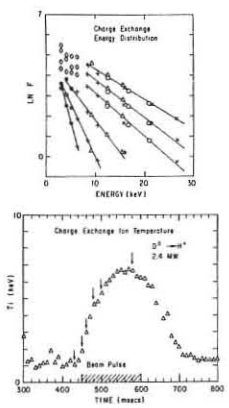

Fig. 2. Energy spectra (top) at selected times (arrows) during T_i time profile (bottom).

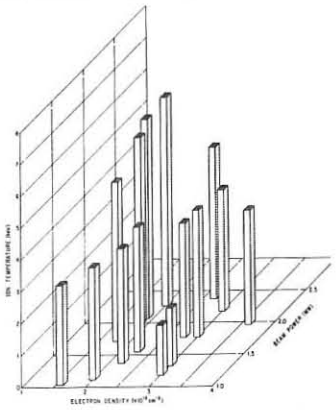

Fig. 3. Peak central T_i during beam heating. Line average electron density is measured at peak T_i.

Ion temperature increases during $H^0 \rightarrow D^+$ and $D^0 \rightarrow H^+$ injection scenarios (Fig. 4) were found to scale with beam power, P_B, and line average electron density, $\bar{n}_e$, as

$$\Delta T_i \text{ (keV)} = 4.5 \pm 0.5\, P_B \text{ (MW)}/\bar{n}_e \text{ } (10^{13}\ \text{cm}^{-3}) \ .$$

The ion temperature scaling does not appear to be affected by the enhanced microturbulence [5] observed during high power injection into low density plasmas. The highest temperature recorded to date (6.5 keV with 2.4 MW $D^0 \rightarrow H^+$ at $\bar{n}_e = 1.9 \times 10^{13}\ \text{cm}^{-3}$) has pushed PLT deep into the collisionless regime with ν_i^* well below 0.1 over much of the plasma radius. Preliminary ion power balance calculations indicate that electron-ion coupling, particle diffusion, and charge exchange losses dominate the power flow with neoclassical thermal conduction contributing a small fraction. Due to the uncertainties in determining particle diffusion and charge exchange losses in a plasma where the ratio of beam-to-plasma ions is no longer small, the possiblity of considerable enhancement of thermal conduction over neolcassical cannot be excluded.

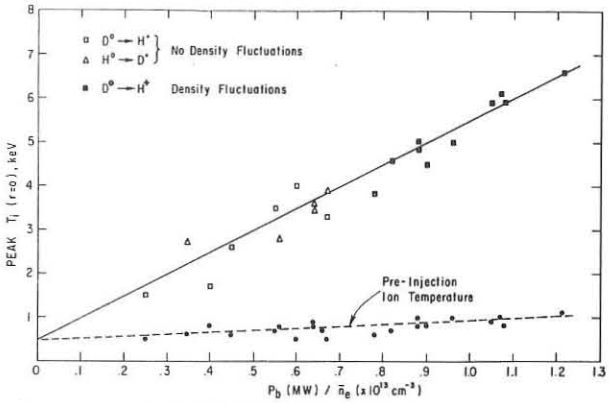

Fig. 4. Scaling of central T_i with the ratio of beam power to line average electron density.

Energy, pitch angle and time resolved measurements of the injected-ion slowing-down distribution are provided by the FIDE analyzer. For example, the slope of the 1/e fall times of the tangential charge-exchange signal as a function of energy (Fig. 5) for a 400 kW $H^0 \rightarrow D^+$ case reflects the fast-ion slowing down rates and agrees well with a numerical solution of the bounced-averaged Fokker-Planck equation. Measurements of the beam ion tail distribution above the injection energy, which is sensitive to the ratio of the drag rate to the rate at which beam ions are heated by the thermal plasma, also agree well with the calculations. Plasma toroidal rotation at central speeds of $v_\phi \approx 10^7$ cm/sec were measured during unbalanced neutral injection by comparing the tangential thermal spectrum with co- and counter-injection.

During ICRF heating, both analyzers were used to study the isotropy of the majority and minority species ion energy distributions. At the maximum power deposition level so far obtained (~260 kW), increase of the majority deuterium ion temperature from 500 to 1200 eV at $\bar{n}_e \sim 1.0 - 1.5 \times 10^{13}\ \text{cm}^{-3}$ was observed. With combined hydrogen beam injection and ICRF heating, the beam tail distribution above the injection energy is strongly enhanced (Fig. 6), indicating direct RF heating of beam ions.

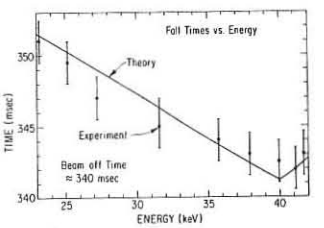

Fig. 5. Plot of the 1/e fall times of the tangential charge exchange flux after beam turn off.

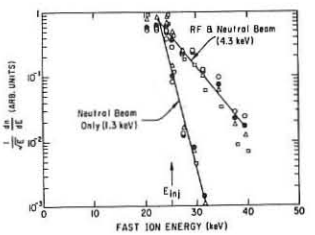

Fig. 6. Fast-ion tail above the injection energy in the counter-direction.

*Work supported by U. S. Department of Energy Contract No. EY-76-C-02-3073.

†Consultant: with Westinghouse Electric Co., Fusion Power Systems Division, Pittsburgh, Pennsylvania.

[1] H. Eubank, et al., IAEA-CN-37-C-3, Innsbruck, Austria (1978).

[2] S. L. Davis, S. S. Medley, and M. Brusati, PPPL-1478 (1979).

[3] S. S. Medley and S. L. Davis, PPPL-1507 (1979).

[4] J. G. Cordey, Culham Laboratory, Private Communication (1979).

[5] V. Arunasalam, et al., Bull. Am. Phys. Soc., 23, 901 (1978).

B2.7

MODERATE POWER ICRF HEATING CHARACTERISTICS FOR THE TWO-ION REGIME IN PLT*

D. Hwang, V. Arunasalam, S. Bernabei, M. Bitter, D. Boyd, N. Bretz, S. Cohen, P. Colestock, S. Davis, D. Dimock, F. Dylla, D. Eames, P. Efthimion, H. Eubank, R. Goldston, L. Grisham, E. Hinnov, J. Hosea, H. Hsuan, F. Jobes, D. Johnson, R. Kaita, J. Lawson, E. Mazzucato, D. McNeil, S. Medley, E. Meservey, D. Mueller, N. Sauthoff, G. Schilling, J. Schivell, G. Schmidt, A. Sivo, F. Stauffer, W. Stodiek, R. Stooksberry, J. Strachan, S. Suckewer, G. Tait, H. Thompson

Plasma Physics Laboratory, Princeton University
Princeton, NJ 08544 USA

ABSTRACT. RF wave powers up to ~260 kW have been applied on PLT for pulse durations exceeding 100 msec. Charge exchange measurements at two radii (0 and 15 cm) indicate that the energetic minority proton distribution is centrally peaked with the two-ion hybrid layer placed on axis and that the majority deuteron heating for this case is approximately the same at the two radii. The central deuteron temperature has been approximately doubled.

Initial heating results obtained on PLT for the two-ion regime in both D-H and He^3-H plasmas for rf wave powers up to ~70 kW have shown that the wave power absorption can be attributed to direct fundamental cyclotron damping by the minority (H) ion species [$\omega \sim \Omega_h(r=0)$].[1] The minority damping, which is aided by the influence of the two-ion hybrid resonance,[2,3] sustains energetic proton distributions which are consistent with Fokker-Planck theory[4] to E ~ 40 keV and heats the deuterons (helium ions) and electrons through ion-ion and ion-electron coupling with the protons. This minority heating regime shows considerable promise for good ion confinement devices.

In our present experiments we are investigating the power deposition and heating characteristics for a single half-turn coil, which excites a broad $k_{||}$ spectrum, to serve as a basis for comparison with multicomponent antennae which will enable placement of the $k_{||}$ spectrum in a range favorable to central heating of the plasma.[5] In this paper we report preliminary results at moderate rf powers in D-H discharges with the parameters:

I_p = 230-300 kA, V_ϕ = 1.3-1.5 V, $\bar{n}_e$ = 1.3-1.7 × 10^{13} cm^{-3}, $\eta_h = \frac{n_h}{n_d} \approx$ 6-10%, $T_e(0) \approx$ 1.2 keV, $T_d(0) \approx$ 0.5-0.6 keV (without rf), $\tau_{E_e} \approx$ 20 msec, and $Z_{eff} \sim$ 3. The excitation frequency is 24.6 MHz and the magnetic field is $B_\phi \approx$ 17.1 kG which places the two-ion hybrid layer on axis for $\eta_h \sim$ 8%.

Hydrogen charge exchange spectra and deuterium temperatures measured with a wave power of ~90 kW applied from t = 360 to 520 msec are given for r = 0 and 15 cm in Figs. 1 and 2, respectively. (The single coil coupling efficiency is ~80%.) The hydrogen spectra indicate that the effective temperature of the energetic proton distribution decreases with radius and that the Fokker-Planck parameter[4] $\xi \propto \frac{\langle P_{rf} \rangle}{n_e n_h} (T_e)^{1/2}$ decreases by the ratio of $\xi(0)/\xi(15) \simeq 1.17$ for this case. Taking the electron density and temperature profiles into account and assuming η_h is constant, gives $\langle P_{rf} \rangle_{r=0} / \langle P_{rf} \rangle_{r=15\ cm} \simeq 1.4$. The increase in T_d at 15 cm is comparable with that on axis indicating a broad heating profile. This result is consistent with $\langle P_{rf} \rangle$ and n_d decreasing with radius (to within the accuracy of the data) but does not exclude charge exchange and diffusion effects.

The deuterium heating measured at a wave power of ~260 kW applied for ~100 msec is given in Fig. 3 along with the neutron emission. T_d is doubled and f_n values of 10^{10} n/sec are obtained. Fig. 4 gives ΔT_d versus wave power divided by $\bar{n}_e$ for the range of wave powers explored. On the average, $\Delta T_d \sim$ 2.3 eV/kW for the present operating regime.

No attempt has been made to control the energetic hydrogen distribution as the power has been increased; so energetic protons are lost more readily at the higher powers as evidenced by increased levels of heavy impurity radiation caused by proton bombardment of the vessel and limiters. (This radiation is comparable with that for counter beam injection for the same conditions.) For the present heating regime at 24.5 MHz, improved proton confinement and deuteron heating is expected at higher levels of η_h and n_e, and for multiple coil excitation. The planned operation in a higher frequency regime with approximately twice the present ohmic heating current capability should provide the additional ion confinement required for power levels up to ~5 MW.

*Work supported by U.S. DOE Contract No. EY-76-C-02-3073.

The authors wish to thank the PPPL Engineering and Technical Support Staffs for their valuable contributions to this program and Drs. F. Perkins and T. Stix for helpful discussions of the theory. The continuing support of Drs. M. Gottlieb, E. Frieman, and H. Furth is gratefully acknowledged.

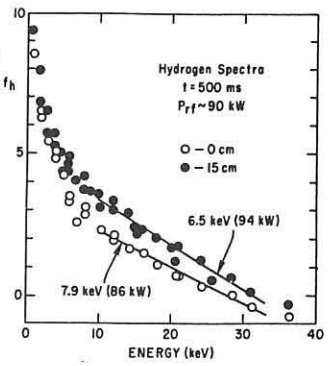

Fig. 1

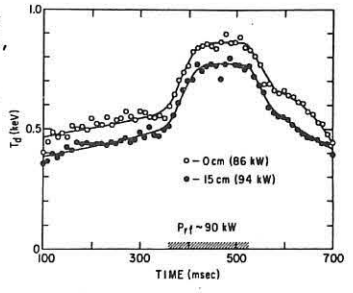

Fig. 2

REFERENCES

[1] J. Hosea et al., Bull. Am. Phys. Soc. 23 (1978) 836; PPPL Report 1554 - submitted for publication.

[2] H. Takahashi, Journal de Physique 38, Sup. C-6 (1977) 171; V. Vdovin et al., Proc. 8th Eur. Conf. on Contr. Fusion and Plasma Physics (Prague, 1977) 19.

[3] F. Perkins, Nucl. Fus. 17 (1977) 1197; J. Jacquinot, Proc. Joint Varenna-Grenoble Int. Symp. on Heating Toroidal Plasmas (Grenoble, 1978) Vol. I, 127.

[4] T. Stix, Nucl. Fusion 15 (1975) 737.

[5] J. Hosea, Proc. 3rd Symp. on Plasma Heating in Toroidal Devices (Varenna, 1976); PPPL Report 1309 (1976).

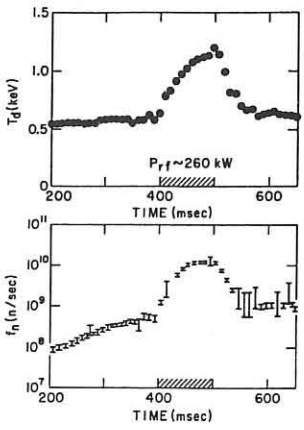

Fig. 3

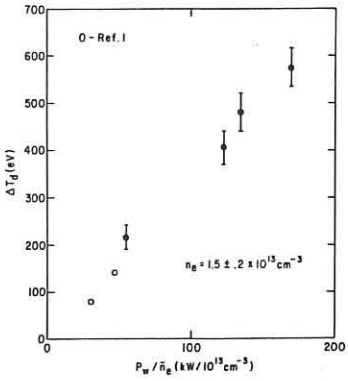

Fig. 4

B3.1

FINITE MEAN-FREE-PATH EFFECTS ON AXIAL PARTICLE TRANSPORT IN MIRROR DEVICES*

T. D. Rognlien and T. A. Cutler
University of California, Lawrence Livermore Laboratory
Livermore, California 94550, USA

We consider the problem of collisional particle and energy transport in open-ended systems where the axial transport is dominant. The Fokker-Planck equation for the distribution function f is

$$\frac{\partial f}{\partial t} + \underset{\sim}{v} \cdot \frac{\partial f}{\partial \underset{\sim}{r}} + \underset{\sim}{a} \cdot \frac{\partial f}{\partial \underset{\sim}{v}} = C \qquad (1)$$

where C is the Coulomb collision operator. This equation has previously been solved in two limits: when the mean-free-path λ_{mfp} is long compared to the system length L[1], and when $\lambda_{mfp} \ll L$.[2] We shall present a Monte Carlo procedure for the solution of Eq. (1) which is formally valid for any range of λ_{mfp}/L, although it is most practical for $\lambda_{mfp} \sim L$. Results are given for two problems relevant to mirror devices at Lawrence Livermore Laboratory, namely, electron confinement in 2XIIB and ion confinement in the tandem mirror TMX.

The Monte Carlo procedure uses a two-part solution to Eq. (1) for an ensemble of test particles. First, the collision term is ignored and the test particle is advanced for Δt according to the left hand side of Eq. (1) which gives the equations of motion

$$m \frac{dv_z}{dt} = -\frac{\partial q\Phi}{\partial z} - \mu \frac{\partial B}{\partial z} \quad , \quad \frac{d\mu}{dt} = 0 \qquad (2,3)$$

Here m is particle mass, v_z is the velocity along the magnetic field B, q is particle charge, Φ is the axial electrostatic potential, and $\mu = mv_\perp^2/2B$ is the magnetic moment. The second part of the solution includes the collision term which is calculated assuming that the distribution of scattering particles is an isotropic Maxwellian locally. The velocity coordinate frame is rotated to the $\underset{\sim}{W}$ frame so that $W_\parallel$ lies along the velocity $\underset{\sim}{v}$ and $W_{x,y}$ are perpendicular to $\underset{\sim}{v}$. Then following Spitzer[2], the velocities after the collision are

$$W_\parallel = W_{\parallel o} + \langle \Delta W_\parallel \rangle \Delta t + \sqrt{3\langle \Delta W_\parallel^2 \rangle \Delta t}\; R_1 \qquad (4)$$

$$W_{x,y} = \sqrt{1.5\langle \Delta W_\perp^2 \rangle \Delta t}\; R_{2,3} \qquad (5)$$

where $W_{\parallel o} = |v|$, $R_{1,2,3}$ are random numbers chosen from a uniform distribution from -1 to 1, and the bracketed terms are collision probabilities[2]. Accumulated density and temperature profiles of the test particles can then be used to update the background scattering profiles. This procedure is repeated until a steady-state is obtained.

As our first example, we consider electron confinement in the 2XIIB mirror device. A gas box located at one mirror throat (z = -.8 m) produces a stream of warm ions for suppression of microinstabilities of the hot confined ions. Two cases with different gas-box currents are presented. The 1-D fluid code PHLOW calculates the final density and potential profiles shown in Figs. 1a,b. The hot ion energy is taken to be 15 keV, and the warm ion temperature is ~ 100 eV. The test electrons have collisions with electrons, warm ions, hot ions, and ionize gas box neutrals. The final test particle temperature profiles are shown in Fig. 1c. For the low-current case, T_e is quite peaked at the midplane and thermal conductivity is not important since a large gradient in T_e is maintained. Here, electron energy is confined primarily by the electrostatic potential.[1] A number of 2XIIB shots at this gas-box current show this behavior with T_e ~ 100-135 eV at the midplane and T_e ~ 30-40 eV in the fan region. For the high-current case, T_e is lower because of increased loss current, and $T_e(z)$ is now nearly uniform. Here thermal conductivity is very important, and one can produce nearly the same profile using a fluid energy equation for T_e with thermal conductivity. The 2XIIB experiment also exhibits lower midplane T_e for high gas-box currents.

The second example studied with the code is the TMX tandem mirror experiment. For this case ions are confined electrostatically in a solenoid by higher density mirror-machine plugs at each end. Confinement time of the ions is generally calculated assuming that $\lambda_{mfp} \gg L$ so that f is zero on the loss-cone boundary.[1,3] However, because TMX has a large mirror ratio (~20) from the solenoid to the plug, ions need scatter only a fairly small angle to fill the loss-cone in a transit-time. In the limit of a Maxwellian the confinement time approaches the collisional value of

$$\tau_c = \frac{\sqrt{\pi}\, RL}{v_i} \exp\left(\frac{e\phi}{T}\right) \qquad (6)$$

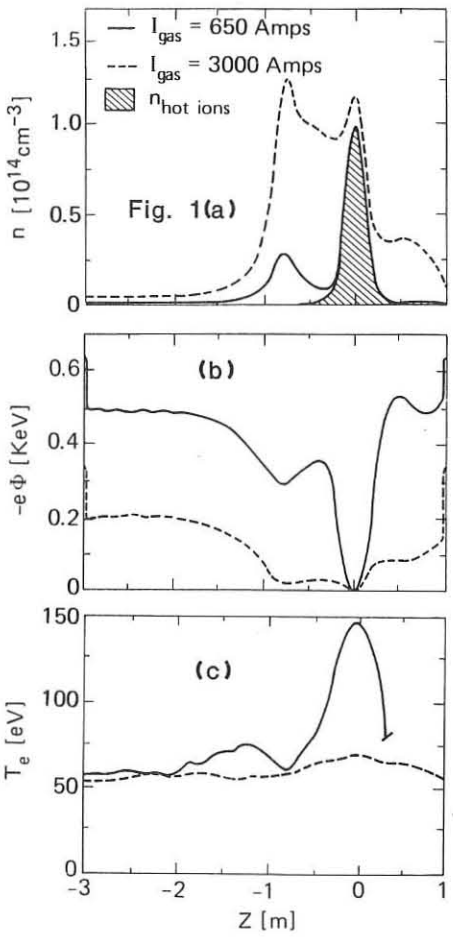

where R is the mirror ratio, L is the effective solenoid length, Φ is the potential barrier, T is the solenoid ion temperature, and $v_i = (2T/m)^{1/2}$.

The code results in Fig. 2 show that TMX has a confinement product $n\tau$ part way between that given by Eq. (6) (45° line) and Pastukhov's result (horizontal line).[1,3] We used the vacuum magnetic field profile of TMX, T = 80 eV and $e\phi/T$ = 3.5. The solenoid density n_c is varied to show the transition between the two regimes. Typical TMX density is $n_c \sim 1 \times 10^{13}$ cm^{-3}. The enhancement in $n_c\tau$ only occurs for devices with moderate λ_{mfp}; for reactor-like plasmas, it is negligible.

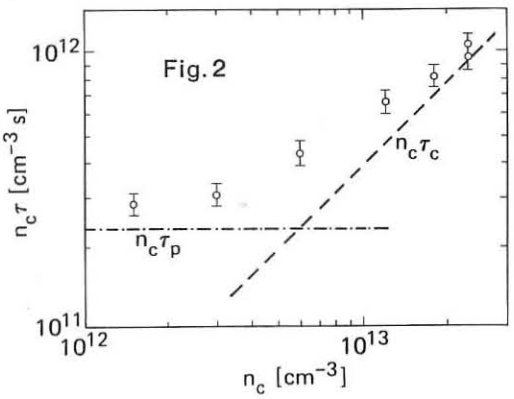

*Work performed under auspices of U.S. Department of Energy at the Lawrence Livermore Laboratory under contract number W-7405-ENG-48.

References

1. V. P. Pastukhov, Nucl. Fusion 14, 3 (1974).
2. L. Spitzer, Jr., Physics of Fully Ionized Gases (Interscience, New York, 1967).
3. R. H. Cohen, M. E. Rensink, T. A. Cutler, and A. A. Mirin, Nucl. Fusion 18, 1229 (1978).

B3.2

STABILITY OF HIGH DENSITY PLASMA IN A MULTIPLE MIRROR

M. Inutake

Institute of Plasma Physics, Nagoya University, Nagoya 464, Japan

and

A. Komori, R. Hatakeyama and N. Sato

Dept. of Electronic Eng., Tohoku University, Sendai 980, Japan

ABSTRACT: Experiments are made on the stability of a quasi-steady, high beta, collisional plasma in a multiple mirror machine. For plasma beta lower than about 15%, a strong density oscillation accompanied by magnetic field fluctuation is observed to propagate with azimuthal mode number m = 1 in the direction of the electron diamagnetic drift. The measured frequency is in a reasonable agreement with the electron diamagnetic drift frequency. It is sure this drift-type instability is due to the periodic structure of the system.

Confinement and stability for a low beta plasma in a multiple mirror have been investigated by using Q-machines at Novosibirsk,[1] Berkeley,[2] and Sendai.[3] Measurements have also been made on gun-produced and θ-pinch[4] plasmas with high beta value. In such transient plasmas with short duration, it is difficult to clarify characteristic behaviors of low frequency plasma instabilities. In this report, we use a quasi-steady (1 msec duration), high-density, helium plasma ($\geq 10^{14}$ cm^{-3}) in order to investigate drift-type instabilities in a high beta plasma.

The plasma is produced by an MPD (magneto-plasma-dynamic) arcjet which is a kind of coaxial plasma accelerator. Typical parameters are as follows: electron and ion temperatures $T_e \sim T_i \sim 10$ eV, plasma flow speed $U \sim 10^6$ cm/sec, ion acoustic Mach number $M \geq 1$, ion mean-free-path λ_{ii} ~ a few cm, plasma beta $\beta \sim$ several %, ionization degree $\geq 80\%$. The plasma coming along a uniform guide field (80 cm long) streams into a multiple mirror region (100 cm long) as shown in Fig.1. The multiple mirror configuration with cell-length 10 cm ($\gg \lambda_{ii}$) is formed by 10 iron rings (10 cm diam.) mounted in a vacuum chamber (15 cm diam. stainless steel) with a uniform external magnetic field ($B_o \leq 3.4$ kG). The mirror ratio R_m is 1.5. The plasma is terminated by a stainless steel plate which can be moved to change the number of cells in the system.

Axial/radial profiles of number density n, floating potential V_F as well as fluctuations of density $\tilde{n}$, potential $\tilde{V}_F$ and magnetic field $\tilde{B}$ are measured by movable double probes and magnetic probes. T_i is determined by the Doppler broadening of He II line. T_e is determined by the double probes and confirmed to agree well with that obtained from the intensity ratio of He I to He II line. The density obtained from the ion saturation current of the double probe is cross-checked by the HCN laser interferometer. In Fig.2 is shown the ion saturation current $J_\perp$ collected by a plane double probe (0.5 mm diam. disk), the surface normal of which is perpendicular to the plasma-flow direction.

A strong low frequency oscillation with 10 - 20 kHz is observed in the multiple mirror configuration (Fig.2(b)). This oscillation does not appear when the iron rings are replaced by aluminum rings in order to check geometrical effect provided by the metal rings (Fig.2(a)). Thus the oscillation is due to the instabilities caused by the multiple mirror configuration. We can also observe this oscillation disappears drastically when the magnetic field decreases below a certain critical level as shown in Fig.2 (c). The results are summarized quantitatively in Fig.3. The suppression of the instability is also observed when the pressure is increased with a fixed magnetic field. According to these results we can say that the threshold of the instability depends on the plasma β value. The threshold beta value is about 15%. Both the oscillation frequency and amplitude increase gradually with an increase in the magnetic field (Fig.3), on the other hand, with an increase in the plasma pressure the frequency increases and the amplitude decreases.

Before describing further details of the instability, we present the plasma properties in the stable operation regime of the multiple mirror system. The axial profile of $J_\perp$ which is roughly proportional to n are plotted in Fig.4 for both the multiple mirror field and the uniform field. It is clearly seen that (i) n in the midplane is higher than that in the throat region. The ratio is nearly equal to R_m., (ii) n in the upstream region is much higher than that for the uniform field and (iii) average density-gradient in the axial direction for the multiple mirror field is steeper than that for the uniform field configuration.

As a result of the instability, the radial diffusion of plasma is enhanced, so that the average density profile has a steeper gradient than that in the stable operation and less increase in n is observed in the upstream region. In order to identify the instability, radial profiles of $J_\perp$ (∝ n), V_F, T_e as well as the oscillation amplitudes of density $\tilde{J}_\perp$, potential $\tilde{V}_F$, three components of magnetic field ($\tilde{B}_r$, $\tilde{B}_\theta$, $\tilde{B}_z$) are measured. in Fig.5 is shown $\tilde{n}$, together with $J_\perp$ (∝ n) at z = 60 cm (upstream region), 100 cm (third mirror point) and 160 cm (8th mirror point). (i) At the first two positions, the density fluctuations are clearly localized near the position of the maximum radial density-gradient. $\tilde{B}_r$, $\tilde{B}_\theta$, $\tilde{B}_z$ and $\tilde{V}_F$ are observed to be localized. At z = 160 cm, n has a broad radial profile and the fluctuation decreases. (ii) The fluctuation propagates with the azimuthal mode number m = 1 in the direction of electron diamagnetic drift velocity. (iii) The phase difference between $\tilde{n}$ and $\tilde{V}_F$ is 180°. $\tilde{B}_z$ and $\tilde{n}$ are out of phase. (iv) The axial phase velocity along the field line is confirmed to be equal to about Alfvén velocity, which is larger than the ion acoustic velocity and less than the electron thermal velocity. (v) The observed oscillation frequency ω is in a resonable agreement with the diamagnetic frequency $\omega^* = k_\theta KT_e \kappa / eB_o$, where $k_\theta = \frac{m}{r}$ (azimuthal wavenumber), $\kappa = -\frac{\nabla n}{n}$ (inverse of radial density gradient). The Doppler frequency due to the radial electric field is less than ω^*. Here the electric field is estimated from the floating potential by taking into account the temperature profile. The increase of ω with an increase in B_o is mainly due to the changes of κ and T_e which are measured in detail. It is to be noted ω is determined by ω^* in the most unstable region, i.e., in the region of first few mirror-cells, although calculated ω^* varies axially.

From the experimental results mentioned above, it is sure that the drift-type instability of high β plasma is caused by the multiple mirror field. A further investigation is necessary to clarify the instability mechanism of such a high β plasma and its stabilization at higher beta value.

References

1) G. I. Budker et al., Plasma Phys. and Contr. Nucl. Fus. Res. IAEA, Vienna, 2, 763, 1975.
2) B. G. Logan et al., Phys. Fluids 17, 1302 (1974).
3) R. Hatakeyama et al., to be published.
4) J. C. Riordan et al., Plasma Phys. 20, 139 (1978).

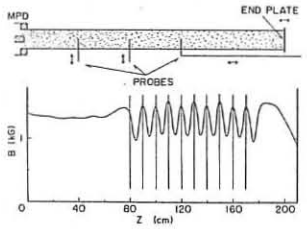

Fig.1 Experimental apparatus. Z is a distance from MPD and vertical lines show positions of mirror throats.

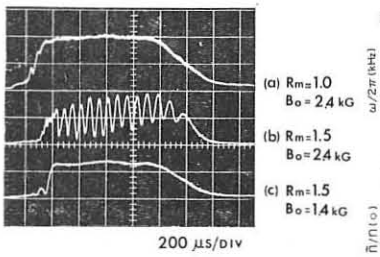

Fig.2 Time evolutions of a plasma density measured by a double probe for typical magnetic configurations.

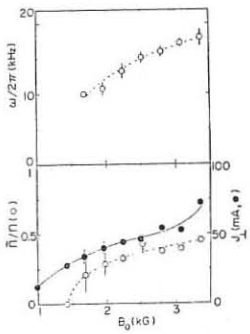

Fig.3 Frequency and normalized amplitude of the instability, and ion saturation current vs. magnetic field.

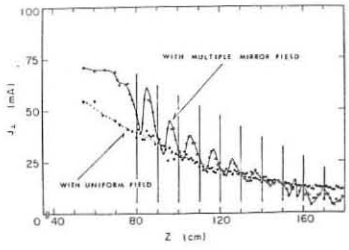

Fig.4 Axial profiles of ion saturation current in cases of R_m = 1.0 and 1.5.

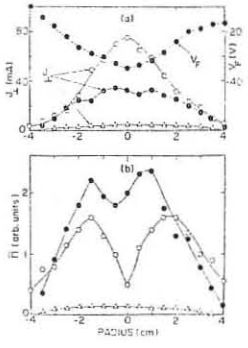

Fig.5 Radial profiles of ion saturation current, floating potential and instability amplitude. Open circles: Z = 60 cm, closed circles: Z = 100 cm, triangles: Z = 160 cm.

B3.3

THE REXIMPLO EXPERIMENT: CONVERSION FROM CYLINDRICAL TO QUASI-SPHERICAL PLASMA COMPRESSION

E. Panarella and R.P. Gupta
National Research Council, Ottawa, Canada, K1A 0R6

Abstract: The conventional theta-pinch device used in the REXIMPLO experiment for plasma compression has been modified from cylindrical to spherical geometry. Under identical conditions of gas pressure (1 Torr) and available condenser bank energy (10 kJ), the conversion resulted in an increase of the electron temperature from 120 eV to over 400 eV and in the production of $\sim 10^6$ neutrons. Moreover, the neutron output increased inversely with the volume of the spherical discharge vessel.

As a continuation of the work reported at the 8th European Conference on Controlled Fusion and Plasma Physics in Prague [1], the theta-pinch discharge system of the REXIMPLO experiment has been converted from cylindrical to spherical geometry. The conversion was motivated by the consideration that the end losses inherent in a cylindrical theta-pinch can be reduced and the confinement improved if the imploding plasma is driven towards a small core volume rather than an extended line.

To illustrate how a spherical implosion can be obtained from the convergence to a core volume of all $\bar{j} \times \bar{B}$ plasma driving forces, consider a spherical surface covered by current lines directed along great circles (meridians) lying on planes perpendicular to the equatorial plane (Fig. 1a). This is the current configuration of a spherical pinch. In order to reproduce it, one first needs to cut half of the sphere along the equator, so that current entering through A can leave the sphere through B (Fig. 1b). However, this arrangement permits the current to flow along any direction on the surface of the sphere. To improve the situation, i.e. to force the current to flow along the meridians, one needs to provide the sphere with a set of slits along a few selected meridians (Fig. 1c). This is the final pinch structure. It has the drawback that the current density $\bar{j}$ (and therefore the plasma driving force $\bar{j} \times \bar{B}$) is larger at the poles P_1 and P_2 than elsewhere, but nevertheless it is capable of driving the plasma towards a small volume.

To see more clearly how this can occur, consider the magnified version of Fig. 1c (Fig. 2). The sphere is provided with two main cuts, one in the equatorial plane QQ and the other in the polar plane P_1P_2. The magnetic field lines in the equatorial and in the polar planes, at a particular instant of time, are represented in Figs. 3 and 4, respectively. It is observed that the plasma is not spherically symmetric because the driving forces $\bar{j} \times \bar{B}$ do not have equal intensity and do not converge towards a point. Nevertheless the plasma is essentially three-dimensional and is better confined than in a cylindrical pinch.

In order to appreciate the effect of the conversion of the discharge geometry from cylindrical to spherical, an experiment was performed with a spherical pinch as shown in Fig. 5. It consisted of a large sphere of $\sim$16 cm diameter which could accommodate a spherical glass vessel containing two diametrically opposite internal electrodes for gas preionization. The condenser bank energy ($\sim$10 kJ) was discharged into deuterium gas at 1 Torr initial pressure. The experiment yielded a large flux of X-rays from the pinched plasma. The electron temperature peaked at over 400 eV, a factor of 4 larger than in the cylindrical pinch. Neutrons were also observed which could not be detected with the cylindrical pinch under identical conditions of initial gas density and condenser bank energy.

The other experiments performed were concerned with the elucidation of the effect of the scaling of the spherical device on the neutron output. By discharging the same condenser bank energy ($\sim$10 kJ) into spherical devices of different dimensions, thus varying the plasma energy density, a variation of neutron output was expected. The experiments were conducted with three fully enclosed spherical pinches similar to that of Fig. 2 of $\sim$15 cm, $\sim$8 cm, and $\sim$5 cm diameter, respectively. The results of the measurements are reported in Table I. One can see that, when the discharge volume decreases by a factor of 8, from 2000 ml (corresponding to the $\sim$15 cm dia. ball) to 250 ml ($\sim$8 cm dia.), the neutron output increases by at least a factor of 5, the uncertainty being due to the limited sensitivity of the counter. When the discharge volume goes down by a factor of 5, from 250 ml to 50 ml ($\sim$5 cm dia. ball), the neutron output increases by a factor of $\sim$7. In short, it seems that the neutron output scales inversely to the volume of the discharge.

TABLE I

n	Volume V_n(mℓ)	Ratio V_n/V_{n-1}	Neutron Output I_n	Ratio I_n/I_{n-1}
1	2000		$<10^5$	
2	250	8	4.41×10^5	>5
3	50	5	2.95×10^6	~ 7

Quite recently, work has been started on the numerical analysis of the spherical implosion. The problem is essentially three-dimensional. The computational analysis considers the following phases:

1. Find the DC current distribution in the spherical conductor and the magnetic field inside it. Since the conductor has several slots for guiding the current and reducing the eddy current losses, it is not convenient to solve the problem analytically. And since ellipsoidal geometries will be considered in future, the finite element method will be adopted.

2. Find the equilibrium plasma configuration, if any, under MHD approximation. For this purpose, either the existing 3D-finite difference schemes or a finite element scheme for the whole system will be adopted. The density of finite elements in a given region will be determined by the complexity of the plasma in that region.

3. Study the dynamics of the plasma from the shock stage through the equilibrium configuration. The plasma equilibrium reached is expected to be a dynamic one so that the plasma oozing out from the regions of low magnetic field will be moved back over itself. This means that the plasma will move from inside to out through the ends, but there it will experience fields which will tend to fold it back over the outer region of the plasma ball and compress it at the same time. If the dynamical calculations confirm this premise, and if the instabilities do not develop too rapidly, then it should be possible not only to generate a three-dimensionally pinched plasma but also to confine it for a significant time.

4. Calculate the containment time of the plasma created in the spherical pinch. The various ellipsoidal modifications of the spherical conductor geometry under varying electrical energy discharge conditions will then be studied in order to maximize the containment time and minimize the losses.

Work is in progress on the computational analysis and will be reported at a later time.

[1] E. Panarella, Proc. 8th European Conference on Controlled Fusion and Plasma Physics, Prague, Czechoslovakia, September 1977, (Vol. 1, p. 59).

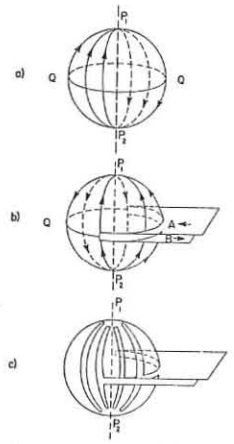

FIG. 1 - Evolution of the spherical pinch concept.

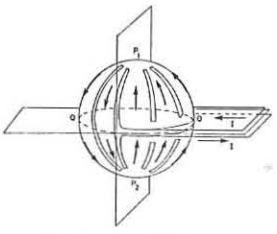

FIG. 2 - Spherical pinch.

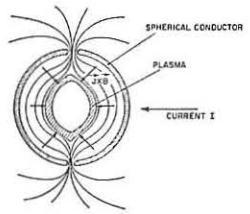

EQUATORIAL SECTION

FIG. 3 - Magnetic field lines distribution and plasma shape in the equatorial plane of the spherical pinch

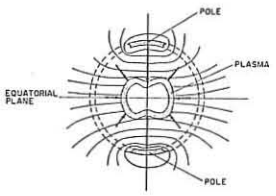

POLAR SECTION

FIG. 4 - Magnetic field lines distribution and plasma shape in the polar plane of the spherical pinch.

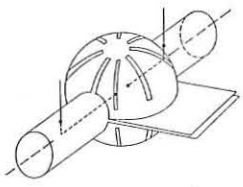

FIG. 5 - Spherical pinch device

B3.4

INFLUENCE OF MICROINSTABILITIES ON THE MHD STABILITY OF FIELD REVERSED PINCHES*

S. Hamasaki, Science Applications, Inc., La Jolla, California 92037

N. A. Krall and J. B. McBride, JAYCOR, Del Mar, California 92014

Reversed field pinches (RFP) are potentially attractive for fusion applications largely because MHD stable configurations have been predicted to exist at relatively high plasma beta with the possibility of purely ohmic heating to ignition. The practical embodiment of the reversed field scheme as a fusion reactor depends on whether a stable equilibrium can be established and maintained for sufficiently long times in the presence of plasma transport from microinstability.

Christiansen and Roberts [1] showed that because of local ohmic heating and consequent rise of plasma β, the central region of low shear can become Suydam-unstable, which results in local MHD turbulence, flattening out the central density and temperature profiles and leading to a quasi-steady state which evolves near Suydam marginal points. This paper addresses the question of whether microinstabilities can occur driven by the ohmic current or by the radial plasma gradients in RFP and thus induce sufficient radial transport to alter an initially MHD stable Z-pinch configuration into an unstable one.

As a starting point, the MHD stable initial profiles of Ref. [2] are chosen as typical RFP profiles and shown in Fig. 1. The maximum local β is about 10%. The magnetic profiles satisfy radial pressure balance and have the form [1] $B_z \approx B_0 J_0(2\theta\, r/a)$, $B_\theta \approx B_0 J_1(2\theta\, r/a)$, $\theta \simeq 1.4$, $a = 16$ cm, $P = P_0 \mathrm{sech}^2(r^2/r_0^2 - 1)$, $r_0 = 6$ cm, for $r < 16$ cm and are the vacuum profiles for $r > 16$ cm. For these given profiles the density gradient length $L_n = [\partial/\partial r(\ell n\, n)]^{-1}$, the magnetic shear length $L_s = [(B_z^2/B^2)\partial/\partial r(B_\theta/B_z)]^{-1}$ and the ion gyroradius ρ_i (assuming constant temperature profile) can be calculated as shown in Fig. 2a. The crossfield drift speed v_d in units of ion thermal speed v_i is plotted in Fig. 2b. Note the drift ion-cyclotron cutoff line [3] below which there is no lower hybrid drift or drift ion cyclotron instability. We see that low frequency drift instabilities may be possible in the inner radius region, while the lower hybrid drift or ion cyclotron instability may occur in the outer regions of plasma where L_n is smaller. The actual occurrence of these microinstabilities, however, depends on the magnetic shear stabilization conditions, which are listed in Table 1 for various important microinstabilities. Table 1 gives the critical shear length requirements for stability of all wave numbers for reasonable temperature ratios of $0.5 \lesssim T_e/T_i \lesssim 2$. The ordinary universal drift or shear Alfvén mode is stabilized with any amount of shear, but may become unstable with trapped particles [10] or some nonlinear turbulence [11]. The effects of high magnetic shear ($L_s \approx L_n$) as in RFP are, however, still unknown for these modes. Other low frequency instabilities like the current driven drift mode which operates when $v_d \gtrsim c_s$ (sound speed) or the ion temperature gradient driven mode seem easily stabilized in RFP devices which have $L_s \approx L_n$. This leaves only lower hybrid drift and drift ion cyclotron instabilities.

The critical shear length L_s^{lh} for both lower hybrid drift and drift ion cyclotron instability is plotted in Fig. 3. The threshold shear length is larger than the actual shear length of RFP indicating complete stability, as shown in Fig. 3. Suydam's criterion can be written as a critical shear requirement

$$L_s^S = \begin{cases} \left[rB^2/B_\theta^2\right] \Big/ \left[B_z/B_\theta + 2\sqrt{B_\theta^2/8\pi(\partial/\partial r)P}\right] & \text{for } \partial P/\partial r > 0 \\ \infty & \partial P/\partial r < 0 \end{cases}$$

L_s^S is also plotted in Fig. 3. Except for a small, outer plasma edge region, Suydam stability requires more shear than microstability. In this outer region the shear is strongest and sufficient for microinstability. Usually Suydam's criterion requires a low $\beta(\beta < 0.2)$ and for low β systems, pressure balance can be written in terms of a shear length as

$$L_s = \left|(\partial B_z/\partial r)/B_\theta + B_z B_\theta/(rB^2)\right|^{-1}.$$

For these typical field reversed profiles, the shear length becomes $L_s < a/\theta$ $(\theta > 1.2)$. Thus we conclude that for low β, Suydam stable RFP systems, the magnetic shear is strong enough to stabilize almost any dangerous microinstability.

Table 1. Critical shear conditions for microstability.

Instability	Critical Shear Condition for Stability	
Lower Hybrid Drift	$\left\|\frac{L_s}{L_n}\right\| < 4.43 \left\|\frac{L_n}{\rho_i}\right\|$	[5]
Drift Ion Cyclotron	$\left\|\frac{L_s}{L_n}\right\| < \left(\frac{m_i}{m_e}\right)^{1/2} \left(\frac{\rho_i}{L_n}\right)^{1/2}$	[5]
Universal Drift	$\|L_s\| < \infty$?	[6]
Shear Alfvén	$\|L_s\| < \infty$?	[7]
Current-driven Drift	$\left\|\frac{L_s}{L_n}\right\| < \sqrt{\frac{m_i}{m_e}} \frac{c_s}{v_d}$ $\left(v_d/c_s > 1\right)$	[8]
Ion Temperature Drift	$L_s < \frac{10\, r}{(1 - 0.95/\eta)^{1/2}}$ $\left(\eta = \frac{d\ell n\, n}{d\ell n T_i}\right)$	[9]

References

[1] J. P. Christiansen and K. V. Roberts, Nucl. Fusion 18, 181 (1978).
[2] D. A. Baker, R. C. Davidson, and J. N. Pimarco, Proc. of the High Beta Workshop at LASL (ERDA-76/108) 528 (1975).
[3] J. P. Freidberg and R. A. Gerwin, Phys. Fluids 15, 657 (1972).
[4] R. C. Davidson et al., Phys. Fluids 20, 301 (1977) and also R. C. Davidson, N. T. Gladd, and Y. Goren, Phys. Fluids 21, 992 (1978).
[5] J. B. McBride and N. A. Krall, Nucl. Fusion 18, 12 (1978).
[6] D. W. Ross and S. M. Mahajan, Phys. Rev. Lett. 40, 324 (1978), K. T. Tsang et al., Phys. Rev. Lett., __, 327 (1978), and also T. M. Antonsen, Jr., Phys. Rev. Lett. 41, 33 (1978).
[7] K. T. Tsang et al., Phys. Rev. Lett. 41, 557 (1978), Y. C. Lee and L. Chen, Phys. Rev. Lett. 42, 708 (1979).
[8] S. Inoue et al., in Plasma Physics and Controlled Nuclear Fusion Research (Proc. Conf. Innsbruck, Austria, 1978) and also S. M. Mahajan and D. W. Ross, Phys. Fluids 22, 669 (1979).
[9] B. B. Kadomtsev and O. P. Pogutse, Rev. of Plasma Phys. 5, 303 (1970).
[10] S. M. Mahajan, D. W. Ross, Phys. Fluids 22, 669 (1979).
[11] S. P. Hirshman and K. Molvig, Phys. Rev. Lett. 42, 648 (1979).

*The work was supported by the U.S. Department of Energy.

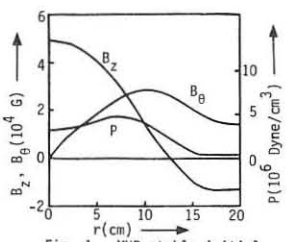

Fig. 1. MHD stable initial profiles. The profiles are chosen in accordance with Ref. [2].

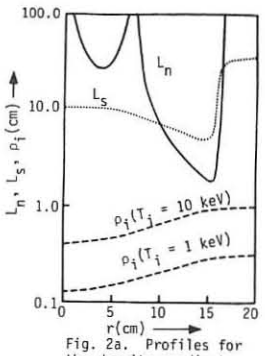

Fig. 2a. Profiles for the density gradient length L_n, the magnetic shear length L_s and the ion gyroradius ρ_i.

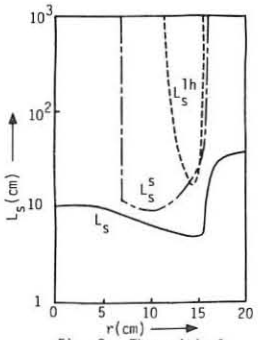

Fig. 3. The critical shear length for the lower hybrid drift or the drift ion cyclotron instability (L_s^{lh}), and for Suydam's criterion (L_s^S), and the actual RFP shear length (L_s).

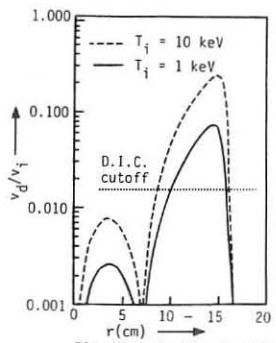

Fig. 2b. Profile for the ratio of the cross-field drift velocity v_d to the ion thermal velocity v_i.

B3.5

THETA-PINCH FUSION SYSTEM WITH LINER EXPLODED BY THERMONUCLEAR NEUTRONS

E.A. Azizov, Ju.A.Kareev, I.K. Konkashbaev, L.B. Nikandrov

I.V. Kurchatov Institute of Atomic Energy

Moscow, USSR

Abstract. The possibility of increasing the inertial confinement time of a pulsed fusion system is discussed. The thermonuclear neutron flux is sufficient for explosion of inner layers of the liner and heating these up to temperature 20 eV, so that the pressure in the liner exceeds the plasma pressure if the conditions $n\tau \geq 10^{15}$ cm^{-3}.sec and $n \geq 10^{21}$ cm^{-3} are fulfilled. Due to increasing the inertial confinement time and additional compression of the burning plasma one can achieve much greater burn-up ($\xi \geq 15\%$) than in the case of "classical theta-pinch with liner". As an example of such exploding liner systems the theta-pinch with closed ends compressed by the fast liner ($V_\ell \approx 10^6$ cm/sec) is considered. The calculations using one--dimensional MHD-code for the plasma and liner are presented.

Good knowledge of liner acceleration and a compression process of the theta-pinch with closed or open ends is the main advantage of the pulse thermonuclear system with inertial confinement. However, the decreasing a large thermal energy of the plasma $Q_p \sim V_1^{-2}$ with liner velosity $V_\ell \sim 10^5$ cm/s requires
1) to compress magnetic traps [1,2] or
2) to increase liner velosity. The problem of increasing of V_1 is connected with a) complicated physics of liner acceleration (the electric explosion of tubes [3] , magnetopressed discharge [4] , the liser or relativistic beams) and b) the low efficiency of energy convertion from energy source into the plasma - η .

For micro-implosion systems (liser, relativistic beam) with $V_1 > 10^7$ cm/s the energy gain should be very large to close energy cycle during inertial confinement time in spite of low η. It is very hard to close energy cycle in traditional "theta-pinch liner system" (if the α-partical self-heating takes place burn-up ξ is equal to 5% only [5]). Still, it is a safe assumption that it is possible to preserve the simplisity and technical practicability of pulse liner system with $V_1 \approx 10^6$cm/s, $Q_p = 10^9$ J.

The idea is based on the fact that if in the liner system $n\tau \geq 10^{15}$ cm/s than thermonuclear flux is suffisient for fast heating the inner layers of the liner. As a result the liner pressure exceeds plasma pressure, and hence the plasma confinement time must increase, because of the compression of the plasma by exploding liner layers hard gas.

In this exploding liner system one can achieve large burn-up $\xi > 10\%$, and it is possible to close energy cycle. The energy gain may be equal to 10.

Three conditions must take place for plasma confinement with help of liner exploded by thermonuclear neutrons:
1) The liner pressure P_1 must exceed plasma pressure P during inertial confinement time $\tau_u \approx R_p/V_\ell$ (after that $P_1 > P$ in spite of plasma self-heating by α-particals):

$$P_\ell = g \cdot \varepsilon_n \cdot (\gamma - 1) \cdot \frac{R_\rho^2}{(R_p + R_L)^2 - R_\rho^2} > P \approx \rho \cdot V_\ell^2$$

where ε_n = 14.1 Mev + binding energy; γ - is the ratio of specific heats of liner material, R_p is the plasma radius, ρ is the liner density, R_L is the absortion length of thermonuclear neutron, g is the intensity of thermonuclear reactions.
2) the inertial confinement time τ_u must be less than $\tau_s \approx R_L/c_s$, where τ_s - is the fall down time of liner pressure; c_s - is the speed of the exploded layers ($C_s \approx V_1$).
3) the liner thickness $\Delta R \gg R_L$.

Fig. 1. shows the region (II) of the existence of thermonuclear system with exploding liner. The curve $n\tau \sim V_\ell^{2/3}$ limits this region from below, and curve $n\tau \sim V_\ell$ from a bove. The minimum liner velosity $V_{\ell min} \approx 5.10^5$ cm/s. As example of this exploding liner system we have considered the "theta-pinch with closed ends" [5] . The longitudinal energy losses will be slight if nL $> 6.10^{22}$ cm^{-2} [5] , the longitudinal magnetic field H_z decreases radial energy losses. The liner velosity $V \leq 10^8$ cm/s can be achieved using cumulation of the thick cooper liner with $\Delta R \gg R_L$.

This liner obtaines kinetic energy after the collision with an other liner called "pusher". The pusher velosity is $V_0 = 10^5$ cm/s. The numerical hydrodynamics calculations show that the velosity of the inner surface $V_\ell(t) = V_0 \cdot (R_2/R_1(t))^{1/2}$ [6,7] (see fig. 2), and heating condition $p \cdot \mathrm{div}\, \vec{V} > W$ is satisfied during compression where W is the energy losses

The basic parameters of the fusion system are obtained using MHD-code. In the MHD-code we take into consideretion transverse and longitidinal thermal conductivity, radiation losses, plasma heating by α - particals and so on; the absorption of thermonuclear neutrons in the inner layers of the liner, nonlinear diffussion of the magnetic field into the liner, real thermodynamic equation of state of the liner [8] . The parameters of a typical system are: liner lenth L = 180 cm; the initial energy of the pusher is 50 MJ/cm, R_{po}=8 cm, R_{pmin} = 0,65 cm, n_{max}=8.10^{20}cm^{-3}, $\beta(r=o)$ = 5, the mean burn-up $\xi \approx 15\%$, $\xi(r=o)$ = 25%, T_{max}= 25 keV, the maximum liner temperature T_{lmax}= 25 eV, $R_p \ll R_L \ll \Delta R$.
Fig.3 illustrates the system parameters as a function of time. It is seen that maximum compression occurs at the moment t= 172 μsec and then weak expansion of the plasma followes (curve 1).

The expansion is stabilized by thermonuclear neutrons heating of the liner. From fig. 4 it is seen that the thermonuclear burning takes place in 60 percent of the plasma amount (where $\xi \approx 25\%$, T $\geq$ 10 keV).

Conclusions. It is possible to create pulse liner thermonuclear system, where plasma is confined by inner liner layers exploded by neutrons. This "recursion" of thermonuclear neutron energy back into the plasma gives considerable burn-up $\xi \approx (15 \div 20)\%$. The burn-up compensates low $\eta = (5 \div 10)\%$, therefore we can consider the liner system as a cleanly thermonuclear system. Moreover, the using verious substances as the liner material (aspesially water) may promote energy utilization, tritium reproduction and defence of reactor structure from neutrons.

References

1. Spalding J. Cusp confinement. Advances in plasma Physics, v. 4, (1971), 80.
2. Boris J.P., et al., Proc. of VI European Conf. on Contr. Fusion and Plasma Physics, Moscow, v. 1, (1973),315.
3. Rioux C., Jablon C., Nuclear Fusion, v. 15, n. 3, (1975), 425.
4. Alikhanov S.G., Glushkov.I.Dokl. Nauk SSSR, v. 242, n. 5, (1978), 1052.
5. Alikhanov S.G., Konkashbaev I.K., Nuclear Fusion, Supplement, (1975), 123.
6. Zababakhin E.I. Nechaev M.N., JETP, v. 33, n. 2, (1957), 442.
7. Zeldovitch Ya.B., JETP, v. 33, n. 3, (1957), 700.
8. Zeldovitch Ya. B. and Raizer Yu.P., Physics of Shock Waves, Academic Press, New York, (1967).

Fig. 1. I - region of the existence of the reactors with cleanly inertial confinement; II - region of the reactors with exploded liner; III - micro-imposion system.

Fig. 2 Liner velosity V_1 as a function of inner radius of liner $R_1(t)$; $V(R_{10}) = 0$, R_{10} is the initial radius of liner, R_2 is the external radius of the liner.

Fig. 3. Time evolution of the plasma parameters (t, 10^6 s): 1 - V_1, 10^6 cm/s; 2 - β ; 3 - n, 10^{18} cm^{-3}; 4 - T, keV - temperature; 5 - P, Mbar - pressure; 6 - ξ .

Fig. 4. The distribution of the P, Mbar; n, 10^{18} cm^{-3}; T, 100 eV; β as a function of the Lagrangian coordinate.

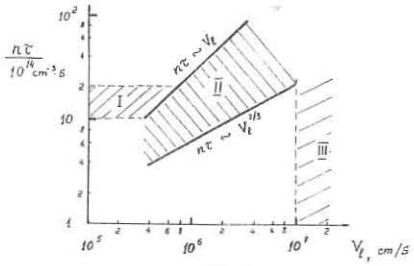

Fig. 1

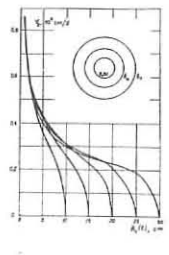

Fig. 2

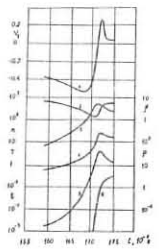

Fig. 3

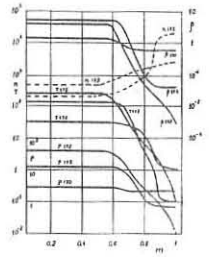

Fig. 4

B3.6

SPECTROSCOPY OF TITANIUM IONS
INJECTED INTO A HOT PLASMA BY CO_2-LASER-RADIATION

P. Greve, J. Haumann, M. Kato, H.-J. Kunze and L. Ullrich
Institut für Experimentalphysik V, Ruhr-Universität
4630 Bochum, F. R. Germany

Abstract: Titanium ions are injected into the plasma of a large-bore theta-pinch by firing a CO_2-laser onto a solid target. After compression and heating of the plasma, the time histories of successive ionization stages are recorded and analyzed.

At the Ruhr-University of Bochum we have started a program to measure rate coefficients for excitation and ionization of positive ions. We employ the plasma spectroscopy method[1]: atoms or ions of interest are introduced into a hot plasma, which is well diagnosed, and excitation rates are deduced from absolute intensities of properly selected emission lines, ionization rates are obtained from the time histories of the ions.

The plasma is produced in a large-bore theta-pinch, which has been constructed specifically for such investigations. It is easily accessible from all sides. The diameter of the single-turn coil is 21 cm, its length is 60 cm. The main capacitor bank stores 140 kJ at a charging voltage of 40 kV. At the time of peak current (the quarter cycle rise time being 5.75 µs), the discharge is crowbarred. The maximum field inside the coil is 4 T. Bias field and preheater banks are discharged through the same coil. For the investigations being reported, the discharge tube was filled to an initial pressure of 12 mTorr hydrogen, and a reverse bias field of 0.06 T was applied.

Titanium atoms and ions are injected into the discharge vessel about 20 µs prior to the preheating discharge by firing a high-power CO_2-laser-beam of 200 MW peak power onto a solid target. The titanium rod of 6 mm diameter protrudes into the discharge tube through a sidearm at a distance of about 6 cm from the end of the coil. The laser beam enters through an opposite sidearm. A schematic of the setup and of the diagnostic instrumentation is shown in Fig. 1.

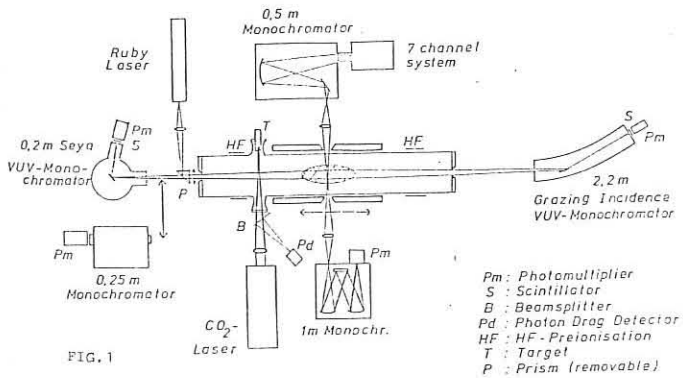

FIG. 1

For the analysis of the spectroscopic observations, the plasma conditions must be known. Electron density and temperature are deduced as function of radius and time in the midplane of the coil using Thomson scattering of light from a ruby laser. The laser beam is directed parallel to the axis of the discharge tube and the scattered light is analyzed at 90° by a seven-channel system. Fig. 2 shows the electron density and temperature as function of time averaged over the diameter of the plasma column. The time history of the C V line at 2271 Å as well as the continuum emission at 5226 Å, both observed side-on, are used to monitor the discharge conditions. The length of the plasma column is deduced from observations of the continuum emission through small holes in the coil. It is obtained to 30 cm. The diameter of the column from the light scattering measurements is about 3 cm.

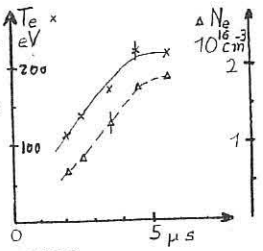

FIG. 2

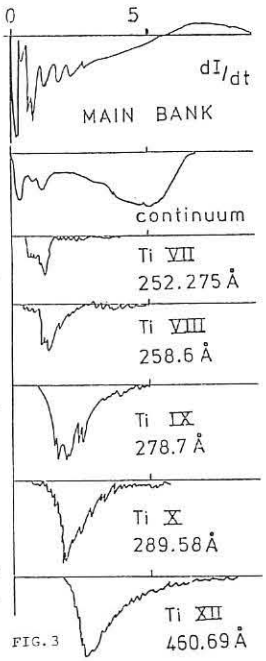

FIG. 3

Spectroscopic observations in the vacuum-uv are made end-on using a 0.2 m Seya-type and a 2.2 m grazing-incidence monochromator, both equipped with a scintillator and a photomultiplier.

Figure 3 shows experimental results. The top trace displays the time derivative of the current of the main discharge through the coil, the second trace the continuum intensity in the midplane of the coil. The sharp drop in the continuum emission at the time of current maximum clearly reveals the break-up of the plasma column caused by an instability. Without injection of titanium this instability does not occur: the continuum emission indicates a stable plasma column lasting for about 10 µs. When the amount of injected titanium is increased from very low levels, the plasma remains stable initially. However, the break-up sets in as soon as the amount of titanium atoms reaches a level, where spectroscopic observations become feasible. Details of the injection are still being investigated.

The remaining traces of Fig. 3 show the time histories of lines from various ionization stages. This time histories are compared with calculated ones, which are obtained from numerical solutions of the coupled set of rate equations and assuming, that the upper levels of the emission lines are populated according to the coronal model. The theoretical rate coefficients, finally, are varied till observed and computed time histories match. The preliminary rate coefficient for ionization of Ti XII thus deduced is

$$I\ (T_e = 180\ eV) \approx 9 \times 10^{-11}\ cm^3 s^{-1}.$$

This can be compared with the semiempirical value of Lotz[2], which is $I \simeq 8 \times 10^{-11}\ cm^3 s^{-1}$.

Acknowlegdements:
The authors wish to thank R. S. Hornady and G. Skopp for the construction of the theta-pinch device. This research was supported by the DFG.

References:
1. Kunze, H.-J., Space Sci. Rev. 13, 565 (1972)
2. Lotz, W., Inst. Plasmaphysik, Garching, Report IPP 1/76

BP1

General Theory of Kinetic Ballooning Modes*

G. Rewoldt, E. A. Frieman, W. M. Tang, and A. H. Glasser
Plasma Physics Laboratory, Princeton University
Princeton, New Jersey 08544 U. S. A.

The recent success in the analytic and numerical treatment of high toroidal mode number ideal MHD stability points toward the utility of similar techniques in the treatment of kinetic stability problems. The general features of the "ballooning representation," which automatically satisfies the requirements in tokamaks of poloidal periodicity and of small effective wavenumber along the equilibrium magnetic field lines, in the presence of finite magnetic shear, apply to the various types of drift modes in axisymmetric geometry in the kinetic regime. The MHD theory[1] reduces the general two-dimensional eigenfunction equation to a one-dimensional differential equation along the lines of force, using a WKB procedure for the radial mode structure. These simplifying features are also present in the kinetic problem, where a one-dimensional integral equation for the behavior of the eigenfunction along the lines of force results, when the effects of trapped particles, magnetic drifts, and finite ion gyroradius are included.

In the past, a general two-dimensional code[2] has been used to generate numerical solutions in the low-β limit. This procedure, while valid, leads to an impractically large expenditure of computer time when all relevant physical features (e.g., spatial variations in the equilibrium gradients) are included. However, a code implementing the one-dimensional ballooning formulation produces results which are in good agreement with those generated by a two-dimensional code containing identical physical assumptions.

We consider here the usual low-β tokamak geometry with circular concentric magnetic surfaces and large aspect ratio, r being the minor radius, θ the poloidal angle, ζ the toroidal angle, R the major radius of the magnetic axis, and q the safety factor. We restrict ourselves for simplicity to the low-β, electrostatic limit for the special case of closely spaced turning points. For this special case, the appropriate expansion is in terms of $\varepsilon^{1/2}$, where $\varepsilon \equiv \rho_i/r_n$, ρ_i being the ion gyroradius and r_n the density gradient scale length. We employ the ballooning representation in the form

$$\Phi = \exp\{-i\omega t + i\ell[\zeta - q(\theta - \theta_o)]\}\eta(\varepsilon^{1/2}r) \sum_{p=-\infty}^{\infty} \hat{\phi}(\theta - 2\pi p) \times \exp(i\ell 2\pi pq) , \quad (1)$$

for the perturbed electrostatic potential. The function η determines the slow radial dependence of the envelope for the eigenfunction, and θ_o is a parameter to be determined. The lowest order (in $\varepsilon^{1/2}$) equilibrium distribution function $F^{(0)}$ is a Maxwellian with temperature T. The nonadiabatic part $h^{(0)}$ of the lowest order perturbed distribution function $f^{(0)} = -(e\Phi/T)F^{(0)} + h^{(0)}$ is decomposed as in Eq. (1) for Φ. After transforming to the guiding center coordinates r', θ', ζ', and then to the banana-center radius r'', the gyrokinetic equation for $h^{(0)}$, obtained at second order in $\varepsilon^{1/2}$, is just

$$\frac{v_\parallel}{qR}\frac{\partial \hat{h}}{\partial \theta'} - i[\omega^{(0)} + iv - \omega_d]\hat{h} = -i\frac{e}{T}F^{(0)}(\omega - \omega_*^T)\langle\hat{\phi}\rangle , \quad (2)$$

where we have used a Krook collision operator,

$$\omega_d \equiv \ell\frac{(\mu B + v_\parallel^2)}{\Omega R}\frac{q}{r}[\cos\theta' + (q'r/q)(\theta' - \theta_o)\sin\theta'] , \quad (3)$$

and the rest of the notation is standard.[3] The gyrophase average $\langle\hat{\phi}\rangle$ may be evaluated as

$$\langle\hat{\phi}\rangle = \hat{\phi}(\theta')J_o\{(v_\perp/\Omega)(\ell q/r)[1 + (q'r/q)^2(\theta' - \theta_o)^2]^{1/2}\} . \quad (4)$$

Equation (2) may be solved by the method of characteristics, to yield $\hat{h}$ in terms of integrals over $\hat{\phi}$, which may be performed by means of Fourier integral transforms for circulating particles and Fourier series transforms for trapped particles. The resulting expression for $\hat{h}$ is substituted into the quasi-neutrality condition,

$$0 = L^{(0)}\hat{\phi} = -\sum_{e,i}(ne^2/T)\hat{\phi} + \sum_{e,i} e\int d^3v\,\hat{h} , \quad (5)$$

to obtain the lowest order eigenmode equation. Here $\hat{h}$ must be transformed back to the particle position, introducing a second factor of J_o. Equation (5) is a one-dimensional integral equation for $\hat{\phi}(\theta)$, whose kernel contains secular functions of θ on the domain $-\infty < \theta < \infty$, and which determines the local complex eigenvalue $\omega^{(0)}(r, \theta_o)$.

The next order ($\varepsilon^{3/2}$) equation locates a double turning point (r_m, θ_m) by the conditions $\partial\omega^{(0)}/\partial r|_{r=r_m} = 0$ and $\partial\omega^{(0)}/\partial\theta_o|_{\theta_o=\theta_m} = 0$, with $\omega^{(1/2)} = 0$. For an equilibrium with up-down symmetry, this yields $\theta_m = 0$. At order ε^2, we obtain a Weber equation for the radial envelope function η,

$$\left.\frac{\partial^2\omega^{(0)}}{\partial\theta_o^2}\right|_{r_m,\theta_m}\frac{d^2\eta}{dz^2} + 2(\ell q')^2\left(\omega^{(1)} - \frac{z^2}{2}\left.\frac{\partial^2\omega^{(0)}}{\partial r^2}\right|_{r_m,\theta_m}\right)\eta = 0 , \quad (6)$$

with $z \equiv r - r_m$. The solution of interest of Eq. (6) is $\eta = c\exp(-\alpha z^2)$, where c and α are constants, with the global eigenvalue

$$\omega = \omega^{(0)}(r_m,\theta_m) + \omega^{(1)} = \omega^{(0)}(r_m,\theta_m) + \frac{1}{2\ell q'}\left(\frac{\partial^2\omega^{(0)}}{\partial\theta_o^2}\frac{\partial^2\omega^{(0)}}{\partial r^2}\right)^{1/2}\Bigg|_{r_m,\theta_m} , \quad (7)$$

for the present case of closely spaced turning points.

The one-dimensional integral equation (5) for $\hat{\phi}(\theta)$ is solved by a Ritz method, as in Ref. 2, decomposing $\hat{\phi}(\theta)$ into a truncated complete set of basis functions, $\hat{\phi}(\theta) = \sum_{n=0}^{N}\hat{\phi}_n h_n(\theta)$. This converts the integral equation into a matrix equation for the $\hat{\phi}_n$'s, which is solved as in Ref. 2, yielding $\hat{\phi}(\theta)$ and $\omega^{(0)}(r, \theta_o)$. Repeating the solution for several values of r and θ_o, in order to compute the necessary derivatives of $\omega^{(0)}$, the global eigenvalue ω is determined by Eq. (7) in the case of closely spaced turning points, as well as the constant α in the solution for η. Then Eq. (1) is used to construct the complete perturbed potential.

This procedure has been carried out for a particular set of equilibrium profiles for n(r), $T_i(r)$, and $T_e(r)$ where the gradients are a maximum at $r = r_o$, and approach zero rapidly as r moves away from r_o. This property facilitates comparison with a two-dimensional calculation[2] which allows for varying equilibrium gradients, but which can only cover a small range of r, for realistic values of the toroidal mode number, because of computer size limitations. For representative parameters,[3] the eigenvalue ω, computed according to Eq. (7), is $\omega/\omega_{*e}(r_m) = 0.194 + 0.070\,i$. The corresponding eigenvalue from the two-dimensional code is $\omega/\omega_{*e}(r_m) = 0.1865 + 0.077\,i$, in acceptable agreement with the one-dimensional ballooning formalism result. Defining $\tilde{\phi}(\theta, S)$ by $\Phi = \tilde{\phi}(\theta, S)\exp(-i\omega t + i\ell\zeta - im^0\theta)$, where $S \equiv \ell q(r) - m^0$, and $q(r_o) = m^0/\ell$, the absolute magnitudes $|\tilde{\phi}(\theta, S)|$ of the eigenfunctions from the two-dimensional (2-D) and one-dimensional (1-D) calculations are shown in the figure. They are in good agreement, both as to the structure along the field line and the radial envelope.

In conclusion, we find that the one-dimensional, "ballooning formalism," calculations can adequately reproduce the results of the earlier two-dimensional calculation, and can be computationally more efficient.

* Work supported by U.S. DoE Contract No. EY-76-C-02-3073.

1. M. S. Chance, et al., in Plasma Physics and Controlled Nuclear Fusion Research, (Proc. Conf., Innsbruck, 1978), (IAEA, Vienna, 1979), paper P-2.

2. G. Rewoldt, W. M. Tang, and E. A. Frieman, Phys. Fluids 21, 1513 (1978) and Bull. Am. Phys. Soc. 23, 785 (1978).

3. E. A. Frieman, G. Rewoldt, W. M. Tang, and A. H. Glasser, Princeton University Plasma Physics Laboratory Report PPPL-1560 (1979).

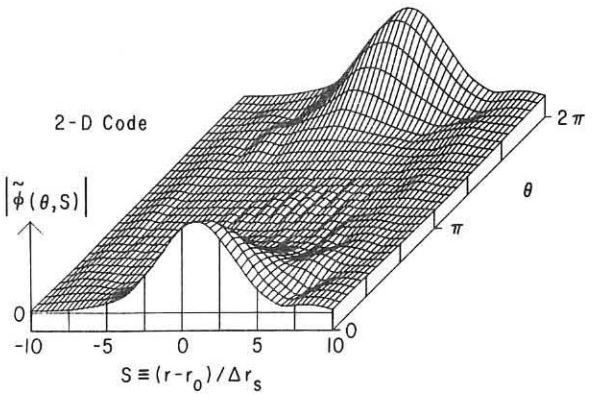

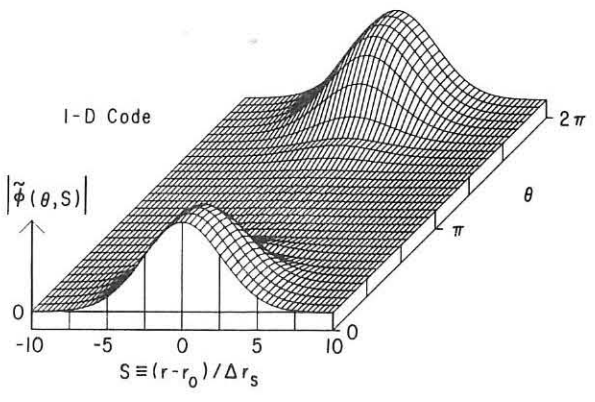

BP2

New Theory of Wave Propagation in Nonuniform Vlasov Plasmas

T. Watanabe, H. Hojo, M. Watanabe*, H. Sanuki**,
T. Ohnuma*** and Kyoji Nishikawa

Institute for Fusion Theory, Hiroshima University, Hiroshima, Japan
* Faculty of Engineering, Kinki University, Kure, Hiroshima
** Institute of Plasma Physics, Nagoya University, Nagoya
*** Faculty of Engineering, Tohoku University, Sendai, Japan

I. Introduction

In fusion research, electromagnetic wave is extensively used for plasma production, plasma heating, rf plugging of open ends of lines of force and plasma diagnostics. In these applications, it is essential to know the wave intensity distribution in plasma. To know the wave intensity distribution, it is important to study the elementary processes such as mode conversion, wave penetration, reflection, reflaction, absorption of the electromagnetic wave in the nonuniform plasma. In the high temperature plasma, thermal motion of plasma particles plays crucial role on these elementary processes through the finite larmor radius effect, cyclotron damping and Landau damping.

Traditional approach to study the wave propagation in the nonuniform plasma is based on the geometrical optic approximation; the wave intensity distribution in plasma is obtained by the ray trace equation and the wave energy conservation equation[1]. In this approach, it is not clear how to derive the local dispersion equation. Furthermore, the wave energy conservation equation is not suitable for the numerical computation since the conservation equation is the partial differential equation.

The present method is based on the linear integral equation in the wavenumber space which includes finite Larmor radius effect, cyclotron and Landau damping. We obtain the solution of the integral equation by the systematic expansion in terms of $(kL)^{-1}$, where k is the typical wavenumber and L, the scalelength of the inhomogenuity of the plasma and the condition $kL \gg 1$ is assumed. The wave intensity is then determined by the ordinary differential equation which is suitable for the numerical computation.

II. Approximate Solution of Integral Equation

We assume that the wave is described by the electrostatic potential $\psi(\vec{x})$ for simplicity. The electrostatic potential $\psi(\vec{x})$ is expanded in terms of the plane waves as

$$\psi(\vec{x}) = \int d^3\vec{k}\ e^{i\vec{k}\cdot\vec{x}}\ \phi(\vec{k}). \tag{1}$$

The integral equation in the wave number space is derived from the Vlasov and Poisson equations as follows:

$$\vec{k}^2\phi(\vec{k}) = \int K(\vec{k},\vec{k}')\ \phi(\vec{k}')d^3\vec{k}'. \tag{2}$$

The range of $\vec{k}'$ which contributes to the integral of R.H.S. of Eq.(2) is limited to

$$|\vec{k} - \vec{k}'| \lesssim L^{-1}.^{2)} \tag{3}$$

When the typical wavenumber k satisfies the condition

$$kL \gg 1, \tag{4}$$

The integral equation (2) can be solved systematically by introducing an eikonal function $S(\vec{k})$[2] in the wavenumber space

$$\phi(\vec{k}) \equiv \exp[-iS(\vec{k})]. \tag{5}$$

The eikonal function $S(\vec{k})$ is determined by

$$H(\vec{k},\vec{G}) = 0 \tag{6}$$

$$\vec{\nabla}_k S_1 \cdot \frac{\partial H(\vec{k},G)}{\partial G} + \frac{i}{2}\sum_{j,l=1}^{3} \frac{\partial^2 H}{\partial G_j \partial G_l}\ \frac{\partial^2 S_0}{\partial k_l \partial k_j} = 0\ , \tag{7}$$

where

$$H(\vec{k},\vec{G}) = \int K(\vec{k},\vec{k}')e^{-i(\vec{k}'-\vec{k})\cdot\vec{G}}d^3\vec{k}' - \vec{k}^2 \tag{8}$$

$$S(k) = S_0(\vec{k}) + S_1(\vec{k}) + O((kL)^{-2}) \tag{9}$$

$$\vec{G} \equiv \vec{\nabla}_{\vec{k}} S_0(\vec{k}). \tag{10}$$

Substituting Eq.(5) into Eq.(1) and performing the integral by the method of the steepest descent, the amplitude $A(\vec{x})$ and the phase $\phi(\vec{x})$ of the wave in real space is found to be

$$\psi(\vec{x}) \equiv A(\vec{x})\ e^{i\phi(\vec{x})} \tag{11}$$

$$A(\vec{x}) = (-2\pi i)^{\frac{3}{2}}\ [\det(P_{jl})]^{-\frac{1}{2}}\ e^{-iS_1(\vec{k})} \tag{12}$$

$$\phi(\vec{x}) = \vec{k}\cdot\vec{x} - S_0(\vec{k}) \tag{13}$$

$$\vec{x} = \vec{G} \tag{14}$$

$$P_{jl} \equiv \frac{\partial^2 S_0}{\partial k_j \partial k_l} \qquad (j,l = 1,2,3) \tag{15}$$

The quantity $\vec{G}$ $(\equiv \vec{\nabla}_{\vec{k}} S_0(\vec{k}))$ corresponds to the observing point $\vec{x}$ and $\vec{k}$ represents the local wavenumber of the wave at the point $\vec{x}$.

Equation(8) can be regarded as the Hamilton-Jacobi equation of the classical dynamics. Therefore, the quantities $\vec{k}$ and $\vec{G}$ are solved by a numerical integration of the"Hamiltonian system"

$$\frac{d\vec{k}}{d\tau} = -H_{\vec{G}} \tag{16}$$

$$\frac{d\vec{G}}{d\tau} = H_{\vec{k}} \tag{17}$$

where τ is an artificially introduced "time".

The quantities ϕ, S_1, and P_{jl} can be obtained by the numerical integration of the ordinary differential equations

$$\frac{d\phi}{d\tau} = \vec{k}\frac{\partial H}{\partial \vec{k}} \tag{18}$$

$$\frac{d\vec{S}_1}{d\tau} = \frac{i}{2}\sum_{j,l=1}^{3} \frac{\partial^2 H}{\partial G_j \partial G_l} P_{jl} \tag{19}$$

$$\frac{dP_{jl}}{d\tau} = \frac{\partial^2 H}{\partial k_j \partial k_l} + \sum_{m=1}^{3}\left(\frac{\partial^2 H}{\partial k_j \partial G_m} P_{ml} + \frac{\partial^2 H}{\partial k_l \partial G_m} P_{mj}\right) + \sum_{m,n=1}^{3} \frac{\partial^2 H}{\partial G_m \partial G_n} P_{nl} P_{mj} \tag{20}$$

Thus we have shown that the distribution of the amplitude and the phase of the wave can be determined by the local dispersion equation $H(\vec{k}\cdot\vec{G})=0$ which is defined by Eq.(6). Numerical calculations for specific examples are now underway.

References

1) I. B. Bernstein: Phys. of Fluids 18 (1975) 320
2) T. Watanabe, H. Sanuki and M. Watanabe: J. of Phys. Soc. of Japan 47 (1979) 286

BP3

SATURATION OF STIMULATED SCATTERING PROCESSES BY THE NONLINEAR DECAY OF ELECTROSTATIC DAUGHTER WAVES

S.J. Karttunen and R.R.E. Salomaa
Technical Research Centre of Finland
Nuclear Engineering Laboratory
P.O. Box 169, 00181 Helsinki 18
Finland

Abstract: A model of a three-wave system which takes into account the parametric decay of the electrostatic daughter wave predicts efficient saturation of anomalous laser reflectivity. Stimulated Brillouin scattering remains small for $n \lesssim 0.1\, n_{cr}$. Backscattering due to Raman process saturates to a level proportional to $(v_e/c)^2$.

Several recent experiments with underdense plasma targets have revealed unexpectedly low reflectivity due to stimulated Raman (SRS) or Brillouin scattering (SBS) [1]. The laser intensities have been well above the instability thresholds which fact implies the presence of some efficient saturation mechanism. Many alternative explanations have been suggested and studied. In this work we investigate the effects introduced by the nonlinear parametric decay of the electrostatic daughter waves created by the external pump field. The backscattered EM wave may act also as a secondary pump, but its further decay does not seem to account the low reflectivities observed [2]. A stronger coupling to the plasma is provided by the ES waves because of the nearer coincidence between the secondary ES pump and its decay products.

A theoretical model is derived from the familiar three-wave equations by introducing a nonlinear decay term into the ES wave equation and the two additional equations for the secondary decay products [3,4]. For mathematical simplicity we have neglected further cascading (five wave system) and assumed a homogeneous plasma slab. Coupling between the secondary ES waves and the EM waves is excluded by off resonance.
In SBS the primary ES wave is an ion acoustic wave (IA) which can further decay into two new IA waves only. Phase matching conditions in the process IA → IA' + IA" are satisfied in the linear region of the dispersion relation ($\omega \approx c_s k$ if $k\lambda_D \ll 1$). In dimensionless form the steady state equations for the slowly varying amplitudes read (for details see [3])

$$e_0' + \alpha e_0 = -e e_- \tag{1}$$
$$e_-' - \alpha e_- = -e_0 e^* \tag{2}$$
$$e' + \beta e = e_0 e_-^* - \kappa e_1 e_2 \tag{3}$$
$$e_1' + \beta_1 e_1 = \kappa e e_2^* \tag{4}$$
$$e_2' + \beta_2 e_2 = \kappa e_1^* e \tag{5}$$

where e_0 and e_- are the EM pump and backscattered waves, respectively, and e the primary ES wave, e_1 and e_2 the ES decay products. α and β represents phenomenological damping. The coupling coefficient κ is given by $\kappa = 4(k_1 k_2/k^2)^{1/2}(n_{cr}/n - 1)$ where k_i is the wave number corresponding to e_i. It is maximum for $k_1 = k_2 = \frac{1}{2}k$ and for $n \ll n_{cr}$ we have $\kappa \gg 1$ which indicates the strength of the secondary decay. The latter feature becomes evident also if we compare the linearised growth rates of the original SBS instability and the secondary decay.

Neglecting damping and assuming real amplitudes we can solve (1)-(5) analytically by making use of the conservation laws $e_-^2 = e_0^2 + \varepsilon - 1$, $e_0^2 = 1 + 2\varepsilon - e^2 - e_1^2$, $e_1^2 = e_2^2$, and $(e_0 + e_-)e_1^{1/\kappa} = (1 + r^{1/2})e^{1/2\kappa}$ where $r\ (= e_-^2(0))$ is the reflectivity and ε describes ES noise. The solution $r(L/L_c, \varepsilon)$ where L is the plasma length and L_c the critical length is shown in the Figure ($\varepsilon = 10^{-3}$). The broken line corresponds to a three-wave reflectivity [5,6]. A most remarkable feature is the low value of the saturation level r_∞ at densities $n < 0.1\, n_{cr}$. This can be evaluated from the equation

$$\frac{n_{cr}}{n} = 1 + \frac{1}{2}\frac{\ln(2+r_\infty/\varepsilon)}{\ln[(1+r_\infty^{1/2})/(1-r_\infty^{1/2})]} \tag{6}$$

where we have assumed $k_1 = k_2 = \frac{1}{2}k$. Note also that the onset of the secondary decay requires a finite ES noise level ε.

For heavy IA damping the primary ES wave intensity will level off at the threshold of the secondary decay ($e^2 = \beta_1\beta_2/\kappa^2$). If the IA waves are Landau damped we find for the time-dependent backscattered intensity at the entrance plane

$$I_-(t) = I_0(t)\left[\frac{ct-L}{ct+L}\right]\tanh^2\left\{\frac{LK}{2c}\left[\left(\frac{ct+L}{ct-L}\right)^{1/2} + \left(\frac{ct-L}{ct+L}\right)^{1/2}\right]\right\} \tag{7}$$

where $K = (\pi/16)^{1/2}(\omega_p/\omega_0)\omega_{pi}$ and $I_0(t)$ is the incoming intensity. Backscattering begins at $t = L/c$ which is the time the pump wave needs to propagate through the plasma slab.

In SRS the ES daughter wave is a Langmuir wave, which can further decay parametrically into another Langmuir wave and an IA wave (phase mismatch prevents the process L → L' + L"). In the long wave length region ($k_i\lambda_D \ll 1$) the Langmuir wave number is $k_1 \approx (8m_e/9m_i)^{1/2}\lambda_D^{-1} - 2k_0$ (typically $k_1 < 0$, note $k = 2k_0$) and for the IA wave we have $k_2 \approx 4k_0 - (8m_e/9m_i)\lambda_D^{-1}$ ($k_2 > 0$). The set of equations for the five wave system is very similar to (1)-(5) except for some sign changes and that now the coupling coefficient κ equals $\kappa = (|k_2|/3|k_1|)^{1/2} \times (c/v_e)^2$ (v_e electron thermal velocity). Even in the keV-region κ is very large which implies a strong effect of the secondary decay on the SRS saturation. In the weak damping limit we find for the maximum reflectivity

$$r_\infty = \tanh^2(\pi/2\kappa) \tag{8}$$

This depends mainly on the plasma temperature and is very small for $\kappa \gg 1$ (a weak dependence on density is caused by k_1 and k_2). In the solution (see [4]) we can put phenomenological noise sources equal to zero which indicates that the process is an absolute instability. For heavily damped IA and Langmuir waves the steady state reflectivity is given by

$$r = \tanh^2\{(L^2/L_s L_p)^{1/2}/\kappa\} \tag{9}$$

where L_p and L_s are the absorption lengths. We have also studied the effects of a nonlinear damping of the (secondary) IA wave on the SRS saturation (cf. SBS). It turns out that only minor corrections enter the dominant role being played by the Langmuir wave decay.

The simplified model calculation suggests that the secondary decay processes provide a very efficient saturation of SBS and SRS in underdense plasma. This is in good qualitative agreement with experiments. Near the critical density anomalous reflectivity remains large. There, however, additional processes are operational which are not included into our model.

References:

1. F.F. Chen, pp. 62-101 in Plasma Physics, Nonlinear Theory and Experiments (Ed. H. Wilhelmsson), Plenum, New York 1977.
2. S.J. Karttunen and R.R.E. Salomaa, Plasma Physics 21, 247 (1977).
3. S.J. Karttunen and R.R.E. Salomaa, Phys. Lett. (to be published).
4. S.J. Karttunen, Parametric Instabilities in Laser Heating of Fusion Plasmas, Thesis, Helsinki University of Technology. 1979.
5. D. Andersson and H. Wilhelmsson, Nucl. Fusion 14, 537 (1974).
6. D.W. Forslund, J.M. Kindel and E.L. Lindman, Phys. Fluids 18, 1002 (1975).

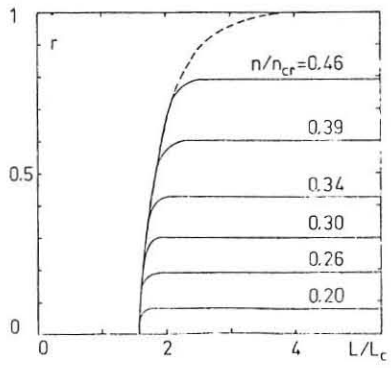

BP4

NONLINEAR THEORY OF THE ROTATION INSTABILITY IN A COLLISIONLESS F.L.R. PLASMA

PETER A.E.M. JANSSEN, DEPARTMENT OF ELECTRICAL ENGINEERING, EINDHOVEN UNIVERSITY OF TECHNOLOGY, EINDHOVEN, THE NETHERLANDS.

I. Introduction

For some fifteen years now there has been interest in low-frequency oscillations which arise in a cylindrical plasma confined by an axial magnetic field. The presence of a radial electric field gives rise to an $\vec{E} \times \vec{B}$-drift and a centrifugal force on the ions which drives these azimuthally propagating waves unstable (rotation instability). Recently, the interest in this instability has increased because large electric fields are expected in tandem mirror systems [1].

A theory which describes low-frequency waves is given by Rosenbluth and Simon [2] in which they assume that the electric force is of the same order of magnitude as the pressure gradient (Finite Larmor Radius Ordering). Many papers were devoted to the linear stability of a rotating plasma, and as a result, F.L.R. effects were found to give rise to a threshold for instability [2]-[6]. Near this threshold two time scales can be distinguished, and we therefore determine the nonlinear evolution in time of the rotation instability by means of the multiple time scale formalism. Here, we consider the special case of an isothermal, uniformly rotating plasma with a weakly-varying density profile.

II. Linear Theory

Rosenbluth and Simon [2] have obtained a closed set of macroscopic equations for low-frequency, azimuthally propagating waves in a collisionless F.L.R. plasma in the so called flute approximation. The flute approximation assumes a) a low-β plasma, so that the magnetic field $\vec{B}$ is constant in time and b) a two-dimensional problem; the magnetic field is also a constant in space and points in the third direction.
Because of a) the $\vec{E} \times \vec{B}$ drift $\vec{V}$ is divergence free. Only wave propagation perpendicular to the magnetic field is considered and the waves are electrostatic.
From the closed set of equations, found in Ref. 2, we obtain for a quasi-neutral, isothermal plasma the following coupled set of equations for the density n and the electric potential ϕ:

$$\frac{D}{Dt} n = 0,$$
$$\nabla.\left(n \frac{D}{Dt} \frac{e}{M} \vec{E} - v_{th}^2 \frac{D}{Dt} \nabla n\right) = 0, \tag{1}$$

where $\frac{D}{Dt} = \frac{\partial}{\partial t} + \vec{V}.\nabla$, $\vec{V} = \vec{E}x\vec{B}/B^2$, $\vec{E} = -\nabla\phi$ and $v_{th}^2 = kT/M$.

All the symbols have their usual meaning.
The set of equations (1) is the starting point of the linear and nonlinear stability analysis of a cylindrical plasma with a gaussian density profile and an uniform rotation profile. Linearizing Eq. (1) around this cylindrical equilibrium we obtain for normal modes $\sim \exp i(\omega t + m\varphi)$ (where m is the mode number and ω its frequency) an eigenvalue equation for the perturbed electric field E_ϕ,

$$\frac{1}{r}\frac{d}{dr}\left(n_o r^3 W\bar{W} \frac{d}{dr} E_\phi\right) + \left[(1-m^2) n_o W\bar{W} + r\omega^2 \frac{dn_o}{dr}\right] E_\phi = 0, \tag{2}$$

where $W = \omega + m\omega_E$, $\bar{W} = \omega + m(\omega_E + \omega_D)$, $\omega_E = -E_o/rB$, $\omega_D = v_{th}^2 \frac{dn_o}{dr} / r n_o \omega_c$ and ω_c is the ion cyclotron frequency.
The boundary conditions read

$$E_\phi(r=0) \text{ is finite}, \quad E_\phi(r=a) = 0, \tag{3}$$

since at the wall (r=a) the plasma displacement is assumed to vanish. For our special case the eigenvalue problem (2)-(3) can be solved in terms of Whittaker functions ([4],[6]). A relatively simple solution can be found, however, for slowly-varying density profiles,

$$n_o = \tilde{n}_o \exp -\delta r^2, \tag{4}$$

where δ is small in some sense. Then, the eigenvalue ω and the unknown E_ϕ can be expanded in powers of δ and the lowest order result reads [7]

$$\phi_1 = \Phi \exp \tfrac{1}{2}\delta r^2 J_m(\gamma_{mn} r), \quad \gamma_{mn} = \frac{j_{mn}}{a}, \tag{5}$$

where J_m is the Besselfunction of the first kind and m^{th} order, while j_{mn} is its n^{th} zero. The amplitude Φ is still undetermined. The dispersion relation is then given by

$$\omega = -m(\omega_E + \tfrac{\omega_D}{2})(1 - \tfrac{1}{p}) \pm \frac{m}{p}\sqrt{(p-1)\left[p\frac{\omega_D^2}{4} - (\omega_E + \tfrac{\omega_D}{2})^2\right]}, \tag{6}$$

where $p = -1 + \tfrac{1}{2}\delta^{-1}\gamma_{mn}^2 + O(\delta)$.
The solution (5)-(6) can be shown to be valid for

$$\mu^2 \equiv \frac{1}{3}\frac{a^2\delta^2}{\gamma_{mn}^2} << \frac{1}{1 + \frac{2(m^2-1)}{j_{mn}^2}}. \tag{7}$$

To proceed, we label a particular mode with the numbers (m,n-1), where m is the mode number and n-1 the number of nodes in the interval (o,a). A particular (m,n-1) mode is stable if

$$|\omega_E/\omega_D + \tfrac{1}{2}| \leq \tfrac{1}{2}\sqrt{p}, \tag{8}$$

i.e. F.L.R. effects give rise to a threshold for instability. The stability criterion (8) shows that the first mode to become unstable is the (1,0) mode since then p is minimal. Hence, there is a critical diamagnetic drift frequency ω_{DC} for which all modes are still stable. Consider now a plasma with a diamagnetic frequency which is a fractional amount below ω_{DC},

$$\omega_D = \omega_{DC}(1-\Delta^2), \qquad \Delta << 1 \tag{9}$$

then all modes remain stable, except the (1,0) mode. The dispersion relation for this mode is given by

$$\omega = \frac{(p-1)}{2\sqrt{p}}\omega_{DC} \pm i\Delta\{\tfrac{1}{2}\sqrt{2}\omega_{DC} + O(\mu^{\frac{1}{2}})\}, \tag{10}$$

thus, two time scales can be distinguished in the problem of the nonlinear evolution in time of the slightly unstable (1,0) mode. This is therefore an appropriate opportunity to apply the multiple time scale method in solving this problem.

III. Nonlinear Theory

In this section we discuss the results of the multiple time scale method applied to the slightly unstable (1,0) mode of the rotation instability. We have seen in sec. II that the (1,0) mode is slightly unstable if the plasma has a diamagnetic drift frequency given by Eq. (9). Inserting the expansion

$$\frac{\partial}{\partial t} \Rightarrow \sum_{\ell=0}^{\infty} \Delta^\ell \frac{\partial}{\partial \tau_\ell}; \quad n = \sum_{\ell=0}^{\infty} \Delta^\ell n_\ell; \quad \phi = \sum_{\ell=0}^{\infty} \Delta^\ell \phi_\ell \tag{11}$$

in the basic set (1) we get the following hierarchy of equations

$$\Delta^\ell: \; L\vec{\psi}_\ell = \vec{S}_\ell \qquad \ell = 0,1,2,\ldots, \tag{12}$$

where $\vec{\psi}_\ell = \begin{pmatrix} n_\ell \\ \phi_\ell \end{pmatrix}$ and L is the linear matrix operator occuring in linear theory. The source term $\vec{S}_\ell$ contains only lower order $\vec{\psi}_p$ with $p \leq \ell-1$. Usually $\vec{S}_\ell$ generates higher harmonics, but may also have terms which oscillate with the eigenfrequency in the τ_o scale of $L\vec{\psi}_\ell = 0$, giving secular terms in $\vec{\psi}_\ell$. Since many time scales are introduced sufficient freedom is introduced to prevent this secular behaviour.
In the limit $\mu << 1$ (i.e. $\delta << 1$) we have solved the hierarchy (12) order by order [7]. Here, only the results are briefly discussed.
In first order we obtain the linear result, as found in sec. II, but now the amplitude Φ is still a function of $\tau_1, \tau_2, \ldots$ Growth and saturation of the (1,0) mode occurs on the τ_1 scale, so that to this order there is no radial plasma transport.
In second order higher harmonics are generated; in addition, a phase difference between density and potential fluctuation is found giving a third order radial transport,

$$nu_r = -\frac{\Delta^3 n_o'}{(rBW)^2}\frac{\partial}{\partial \tau_1}|\Phi|^2. \tag{13}$$

In third order we obtain from the condition that secularities are absent equations for the modification of the equilibrium: e.g. the density on the axis starts to decrease due to the radial transport given by Eq. (13). In addition, an equation for the τ_1-dependence of the amplitude Φ is found,

$$\frac{\partial^2}{\partial \tau_1^2}\Phi - \gamma^2\Phi + \beta^2\Phi|\Phi|^2 = 0, \tag{14}$$

where γ is the growth rate of the (1,0) mode and $\beta^2 = 1.6\gamma_{11}^2/a^2B^2$. In the limit $\mu << 1$ the instability is quenched due to modification of the equilibrium. Clearly, the rotation instability in a collisionless F.L.R. plasma does not exhibit limit cycle behaviour, but in stead a modulation in the amplitude is found. For this reason, the time-asymptotic method of Simon [8] does not provide a proper solution of the problem under consideration, because in this method the amplitude is assumed to be independent of time for large t.

Acknowledgement

The author is pleased to acknowledge useful discussion with M.P.H.Weenink and P.P.J.M. Schram. This work was performed as part of the research programme of the association of Euratom and the foundation F.O.M.

References

[1] J.P. Freidburg and L.D. Pearlstein, Phys.Fluids 21, 1207 (1978).
[2] M.N. Rosenbluth and A. Simon, Phys. Fluids 8, 1300 (1965).
[3] F.W. Perkins and D.L. Jassby, Phys. Fluids 14, 102 (1971).
[4] T.D. Rognlien, J. Appl. Phys. 44, 3505 (1973).
[5] G.I. Kent, N.C. Jen and F.F. Chen, Phys. Fluids 12, 2140 (1969).
[6] M.N. Rosenbluth, N.A. Krall and N. Rostoker, Nucl. Fusion supplement part I, 143 (1962).
[7] P. Janssen, Ph.D. thesis Eindhoven University of Technology (1979).
[8] A. Simon, Phys. Fluids 11, 1181 (1968).

BP5

VORTICES IN LASER-PRODUCED PLASMAS+

P.K. Shukla*, M.Y. Yu*, A. Hasegawa×, and K.H. Spatschek××

* Institut für Theoretische Physik 1, Ruhr-Universität Bochum 4630 Bochum, F.R. Germany

× Bell Laboratories, Murray Hill, New Jersey 07974, U.S.A.

×× Fachbereich Physik, Univ. Essen, 4300 Essen, F.R. Germany

In the presence of the baroclinic vector, $\nabla n \times \nabla p$, where n and p are the number density and pressure of the plasma, mega-Gauß magnetic fields have been observed [1,2]. Such magnetic fields are considered to play an important role in the electron transport properties in laser-pellet interactions. The aim of this paper is to show [3] that the baroclinic vector simultaneously creates an ion vortex, and that the formation of a stationary vortex is essential to the creation of the magnetic fields.

By taking the curl of the equations of motion of a plasma in a magnetic field, and assuming two-dimensional incompressible flow ($\nabla \cdot \vec{v} = 0$) in the plane perpendicular to the magnetic field $\vec{B}$ and the vorticity vector $\nabla \times \vec{v}$, one can derive for each plasma species the equation for vorticity,

$$d(\nabla \times \vec{v} + \vec{\omega}_c)/dt = (1/mn^2)\nabla n \times \nabla p , \qquad (1)$$

where $\vec{\omega}_c$ ($= q\vec{B}/m$) is the cyclotron frequency and m is the mass of the species. If we ignore electron inertia, we obtain for electrons $d\vec{B}/dt = -(1/en)\nabla n \times \nabla T_e$, which was obtained by Tidman and used to discuss magnetic field production. On the other hand, the inertia of ions cannot be ignored. Hence, we see from (1) that vorticity is generated simultaneously. This is true even if the ion baroclinic vector is zero, for in this case $d(\nabla \times \vec{v} + \vec{\omega}_{ci})/dt = 0$.

We consider a stationary vortex solution under these circumstances. We assume that the baroclinic vector has existed for a definite period of time and disappeared at t=0 as the plasma gets heated and becomes collisionless. Thus the plasma has a certain initial total vorticity $\nabla \times \vec{v} + 2\vec{\omega}_{ci}$. We take as an example a cylindrically symmetric vortex with only radial variation. We treat the plasma as collisionless. First, we consider the ion dynamics. The constants of ion motion are the Hamiltonian, $H = e\varphi + [(p_\Theta/R - eA)^2 + p_R^2]/2m_i$, and the canonical angular momentum, $p_\Theta = m_i R^2 \dot{\theta} + eRA$, where $p_R = m_i \dot{R}$, A is the θ component of the vector potential, φ is the electrostatic potential, and R and θ are the radial and azimuthal coordinates. We choose the ion distribution function $f_i(p_\Theta, p_R, \Theta, R) = f_i(H, p_\Theta)$ to be $f_i = (n_o/2\pi m_i T_i)\exp[-(H + \alpha p_\Theta^2/2m_i)/T_i]$, where T_i is the ion temperature and α is a constant. Thus, the ion density $n_i(R)$ and the θ component of the current density $J_i(R)$ are $n_i = \int f_i \, dp_R \, dp_\Theta / R$, $\mu_o J_i = \mu_o e \int R\dot{\theta} f_i \, dp_R \, dp_\Theta / R$, respectively. Here, μ_o is the vacuum permeability.

For electrons, we assume the Larmor radius to be much smaller than the scale size, and use the guiding-center Hamiltonian, $H = \mu\omega_{ce} - e\varphi$, where $\mu (= m_e v_\perp^2/2\omega_{ce})$ is the magnetic moment. The canonical variables are then μ, $\theta = \int \omega_{ce} dt$, R, and θ. Note that for electrons, R and θ correspond to the guiding-center coordinates. The constants of motion are H and R. Hence, we choose the electron distribution function $f_e(\mu, \theta, R, \Theta) = f_e(H, R)$ to be $f_e = (n_o \omega_{ce}/2\pi T_e)\exp[-(1/T_e)(\mu\omega_{ce} - e\varphi) + g(R)]$, where the function g(R) will be determined later. This gives the electron number density, $n_e = \int f_e \, d\mu \, d\theta$, and the electron current density J_e is the sum of the g.c. ($\mu_o J_g = -e\mu_o \int R\dot{\theta} f_e \, d\mu \, d\theta$), and the magnetization ($\mu_o J_m = \int \mu f_e \, d\mu \, d\theta$) currents, where $R\dot{\theta} = -(\partial H/\partial R)/eB$.

The necessary field equations are the quasineutrality condition, $n_i = n_e$, and Ampère's law for the θ component of the vector potential,

$$\frac{1}{R}\frac{d}{dR}\left(R\frac{dA}{dR}\right) - \frac{A}{R^2} = -\mu_o(J_i + J_e) . \qquad (2)$$

The magnetic field is then given by $(1/R)(d/dR)(RA) = B$. When a vortex is set up, the centrifugal force of ions should be balanced by the pressure gradient. The self-generated magnetic field should vanish at $R \to \infty$. The density at the core of vortex is hence reduced and n should approach $n_o (\neq 0)$ at $R \to \infty$. If $B \to 0$ as $R \to \infty$, A should be bounded there. Hence, in n_i we must have $\varphi \to -(T_i/2e)\ln(1 + \alpha R^2)$ as $R \to \infty$. The quasineutrality condition then gives $g(R) = \frac{\eta}{2}\ln(1 + \alpha R^2)$, where $\eta = T_i/T_e$. The density and potential are now given by

$$n_i = n_e = n_o \exp\left(-\frac{\eta}{1+\eta}\frac{\alpha e^2 R^2 A^2}{2m_i T_i (1 + \alpha R^2)}\right), \qquad (3)$$

$$\frac{e\varphi}{T_e} = -\frac{\eta}{2}\ln(1 + \alpha R^2) - \frac{\eta}{1+\eta}\frac{\alpha e^2 R^2 A^2}{2m_i T_i (1 + \alpha R^2)} . \qquad (4)$$

Substituting the above results into Eq.(2) we have the equation for the vector potential A. Equation (2) can be simplified by using the variables: $u \equiv eRA/m_i \lambda c_s$, $\xi = R^2/\lambda^2$, $\bar{\alpha} \equiv \alpha\lambda^2$, where $\lambda = c/\omega_{pi}$ is the linear spatial scale, and $c_s = [(T_e + T_i)/m_i]^{1/2}$ is the sound speed. Then Eq.(2) becomes

$$4\frac{d^2u}{d\xi^2} = \frac{\bar{\alpha}}{1 + \bar{\alpha}\xi}\left[u - \frac{\eta}{2(1+\eta)}\left(\frac{du}{d\xi}\right)^{-1}\right]\exp\left(-\frac{\bar{\alpha}u^2}{2(1 + \bar{\alpha}\xi)}\right) . \qquad (5)$$

The asymptotic value of its vortex solution, which is obtained by neglecting the left hand side, is $u \sim [\eta\xi/(1+\eta)]^{1/2}$. Thus, at large R, the vector potential becomes constant, while the density becomes $n_\infty = n_o \exp[-\eta/2(1+\eta)]$. Using the asymptotic solution for u, we have integrated Eq.(4) radially inwards from $R/\lambda = 80$. A typical vortex result is shown in Fig. 1. Note that in general the electron and ion currents do not vanish outside.

Next, we discuss the effect of collisions. The electron-ion collision time for $T_e = 10$ keV, $n = 10^{20}$ cm^{-3}, is approximately 1 ns. Hence in the absence of the baroclinic vector (driving force), the current and the magnetic field will die off rather quickly. However, the ion vorticity which can be dissipated only by the ion viscosity remains for a much longer period. The viscous damping rate for $k_i\rho_i > 1$ (k_i^{-1} is the typical scale size) is given by $\nu_{ii}(k_i\rho_i)^{-1}$, where $\rho_i = v_{Ti}/\omega_{ci}$ is the ion gyroradius. Hence for $T_i = 10$ keV, $n = 10^{20}$ cm^{-3}, $B \simeq 1$ MG, we obtain the lifetime of the vorticity to be 10^2 ns.

Vortex formation in the laser-pellet interaction has several important implications: (1) If the vorticity is made large, light leading to the enhanced transparency.

+ Supported by SFB "Plasmaphysik Bochum/Jülich".

[1] D.A. Tidman, Phys. Rev. Lett. 32, 1139 (1974).

[2] C.E. Max, W.M. Manheimer, and J.J. Thomson, Phys. Fluids 21, 128 (1978).

[3] A. Hasegawa et al., Phys. Rev. Lett. 41, 1656 (1978), ibid. 42 (E), 412 (1979).

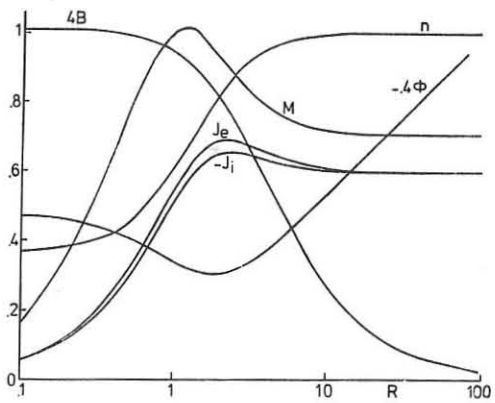

Fig. 1. An example of a stationary vortex solution. The density n has been renormalized to 1 at $R \to \infty$, and the radius R is normalized by λ; $\bar{\alpha} = 1$, $\eta = .5$.

BP6

THE INFLUENCE OF PARALLEL VISCOSITY ON THE RESISTIVE 'g' MODE

R J Hosking*, D C Robinson
Culham Laboratory, Abingdon, Oxon, OX14 3DB, UK
(Euratom/UKAEA Fusion Association)

*University of Waikato, Hamilton, New Zealand

ABSTRACT

In both the reverse field pinch and spheromak the most dangerous instability is the resistive 'g' mode. If the pressure gradient is much smaller than the value given by the Suydam criterion then the parallel viscosity is found to reduce the growth rate significantly so that configurations with $\bar{\beta}\sim 10\%$ can be obtained with the maximum growth rate less than the field diffusion rate for specific pressure profiles.

INTRODUCTION Tearing mode stable distributions of the current exist for both the reverse field pinch [1] and the spheromak with a small vacuum region between the plasma and the conducting wall. Fig. 1 shows such a configuration with zero β. Previous work [2] has shown that resistive interchanges or 'g' modes grow rapidly in such high β, high shear configurations. The modes dominate unstable Suydam modes[3] at realistic values of the magnetic Reynolds number, S, and are not stabilised by viscosity or finite Larmor radius effects [4]. Non-linear calculations [5] show that such modes in these configurations do not readily saturate. The influence of the parallel viscosity on the resistive tearing mode has been investigated [6,7].

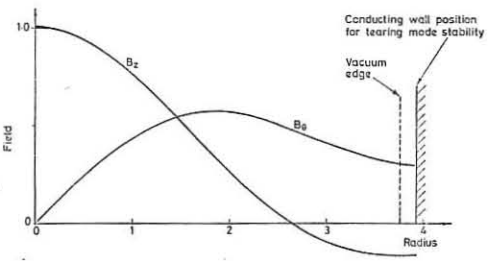

Fig. 1 Tearing mode stable field configuration.

CALCULATIONS The code GNSTAB is used to solve the generalised resistive equations of motion which include a full stress tensor in cylindrical geometry. Fig.2 shows the growth rate p (normalised to the field diffusion rate) of pressure driven resistive modes with m=1 and 0 as a function of the ion Larmor radius, r_{Li}, (the incompressible inviscid value is indicated). Perpendicular and parallel viscosities are included in this calculation but not the finite Larmor radius terms, the m=0 results show that the perpendicular viscosity plays no role. The modes are essentially stable for $r_{Li}/a\sim 0.1$ for this value of S or when r_{Li} becomes comparable with the resistive layer thickness (this condition can be written as $S>(a/r_{Li})^3\beta^{\frac{1}{2}}$), however the equations are of doubtful validity in this domain. In addition the drift to sound speed ratio is greater than unity which will presumably lead to other instabilities. At lower values of β the m=1 mode is found to be stable if $r_{Li}/a\geq 0.03$ (and the equations are applicable) however the long wavelength m=0 mode is much more difficult to stabilise and demands a low pressure gradient in the region of field reversal. We can construct pressure profiles which are grossly 'stable' in the sense that p<1 for all modes for a given value of S. Such a profile is shown in Fig.3 which has a central β value of 5% and an average value of 10%. Inclusion of all the finite Larmor radius terms leads to a broadening of the resistive layer thickness and increased growth. The equations used in these calculations do not reduce simply to those of slab geometry and field curvature effects are dominant. In these calculations we have assumed that the pressure gradient is associated with a density gradient to avoid producing rippling modes associated with the resistivity gradient. Though the finite Larmor radius terms tend to cancel the stabilising effect of the parallel viscosity, if the value of β is decreased further, stabilisation is achieved. Fig.4 shows the growth rate p, as a function of central β value for a calculation including all terms. Stability is possible for $\beta(0)\lesssim 4\%$. β values for the 'cylindrical' spheromak are about a factor of two lower than for the reverse field pinch.

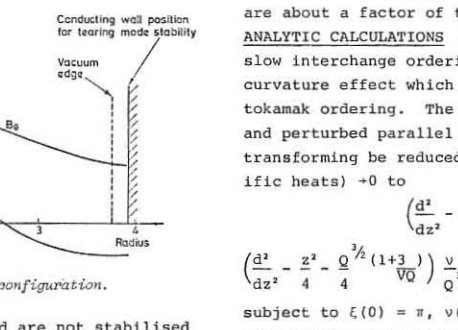

Fig.2 Growth rate as a function of the ratio of ion Larmor radius to plasma radius for two unstable 'g' modes.

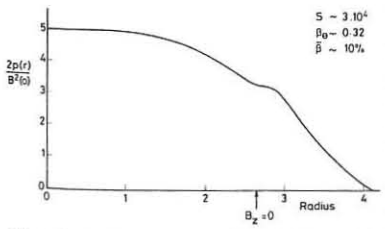

Fig.3 'Stable' pressure profile indicating the flattening required where $B_z=0$.

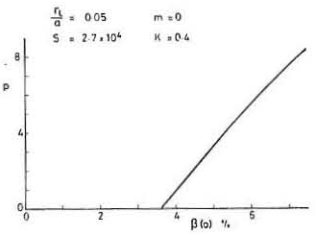

Fig.4 Growth rate as a function of central β value for the m=0 mode including all terms.

ANALYTIC CALCULATIONS The ion parallel viscosity enters the slow interchange ordering resistive equations as a cylindrical curvature effect which is zero in slab geometry and small in tokamak ordering. The equations for the radial displacement ξ, and perturbed parallel field component ν, can after fourier transforming be reduced in the limit that γ (the ratio of specific heats) →0 to

$$\left(\frac{d^2}{dz^2} - z^2 + \frac{3D}{2Q^{3/2}}\right)\xi - \frac{\nu}{2Q^{3/2}} = 0$$

$$\left(\frac{d^2}{dz^2} - \frac{z^2}{4} - \frac{Q^{3/2}}{4}\left(1+\frac{3}{\sqrt{Q}}\right)\right)\frac{\nu}{Q^{3/2}} - \left[\frac{3D}{2Q^{3/2}}\frac{d^2}{dz^2} - \left\{\frac{H}{8} + \frac{D}{4}\left(1+\frac{3}{\sqrt{Q}}\right)\right\}\right]\xi = 0 \quad (1)$$

subject to $\xi(0) = \pi$, $\nu(0) = \pi D$ and ξ, ν→0 as z→∞. z and Q are the length and frequency normalised to the slow interchange scaling parameters. V is related to the parallel viscosity ($V\sim r_{Li}r_{Le}/L_R^2$, L_R is the resistive scale length), D the Suydam parameter and H is related to the shear and field curvature. (We have chosen the limit γ→0 as this gives the most pessimistic results). In the limit V→0 (and Δ'→0) we obtain $Q=D^{2/3}$ as the maximum growth rate for the slow interchange mode. If we expand in V in the electrostatic limit (i.e $b_r\to 0$) then we obtain

$$Q = D^{2/3}\left(1 - \frac{V}{18D^{1/3}}(1+H)\right)$$

and $\xi = \pi e^{-z^2/2}(1+z^2V/D^{1/3})$. The coefficient $V(1+H)/D^{1/3}$ can be expressed as $\frac{(1+4k^2B_\theta^2)}{r^2F'^2}\frac{r_{Li}r_{Le}}{L_R^2}$ where $F = mB_\theta/r + kB_z$, $F'=\frac{dF}{dr}$

r_{Le} is the electron Larmor radius and k is the axial wavenumber. The stabilising effect indicated by this coefficient is not as strong as that shown in Fig.2. However in the calculations γ=5/3 and the more complete form of equations(1) with γ≠0 indicates the stabilising nature of non zero γ which may explain the discrepancy. No general solution has been obtained.

CONCLUSIONS The presence of parallel ion viscosity is found to reduce the growth rate of the slow interchange or resistive 'g' mode significantly so that reverse field pinch configurations with $\bar{\beta}\sim 10\%$ can be obtained with the maximum growth rate less than the field diffusion rate for specific pressure and current profiles. A similar stabilisation is indicated by analytic calculations.

ACKNOWLEDGEMENT We would like to thank T Hender and B Mudford for assisting in the analytic calculations.

REFERENCES

[1] Robinson D C, 1978 Nuclear Fusion, 18, 939
[2] Robinson D C, Proc. 8th Euro. Conf. on Controlled Fusion, Prague (1977) 78
[3] Gowers C W et al, Proc. 7th Conf. on Plasma Phys. & Controlled Nuclear Fusion, Innsbruck (1978), E1-2
[4] Ortolani S and Robinson D C, Bulletin American Phys. Soc. 22 (1977) 1190
[5] Killeen J, Schnack D, Ann. Controlled Fusion Theory Conf. Gatlinburg, Tenn. USA, A25 (1978)
[6] Marinoff G M, 1974, Plasma Phys. 11, 253.
[7] Hosking R J, 1975, Plasma Physics 13, 27.

BP7

MHD Stability Criterion for Rotating Plasmas

G.O. Spies
Max-Planck-Institut für Plasmaphysik,
8046 Garching, Federal Republic of Germany
and
T. Hellsten
Royal Institute of Technology, Stockholm 70,
Sweden

Abstract: A necessary stability criterion is derived for axially symmetric stationary equilibria with a purely toroidal rigid plasma rotation, a purely poloidal magnetic field, and constant entropy along the field lines. The criterion imposes a complex requirement upon the field line curvature and the mass distribution. If it is violated, unstable eigenvalues accumulate at the harmonics of the rotation frequency; the eigenfunctions are flute-like, and have many radial nodes.

Since significant plasma flow perpendicular to the magnetic field appears in a number of laboratory experiments (e.g. plasma centrifuges, homopolars, Astron, rotating multipoles, linked mirrors, or reversed field theta pinches) as well as in cosmical objects (e.g. the earth's magnetosphere, rotating stars), a stability theory for rotating plasmas offers a wide variety of interesting applications. In the present contribution we consider axially symmetric equilibria with a purely poloidal magnetic field and a purely toroidal flow. While the energy principle has been applied to this geometry to give a complete solution of the stability problem in the absence of flow [1], it can give only a sufficient stability criterion in the presence of flow [2]. Here, we perform a normal mode analysis which gives a relatively simple necessary criterion if the rotation is rigid and if the entropy is constant along the field lines.

To describe an equilibrium, we put $\underset{\sim}{B} = \nabla\phi\times\nabla\psi$ and $\underset{\sim}{V} = r^2\Omega\nabla\psi$ for the magnetic field and the flow velocity, where (r, ϕ, z) are cylindrical coordinates. The rotation frequency Ω must then be a function of the flux ψ, and

$$\frac{\partial^2\psi}{\partial r^2} - \frac{1}{r}\frac{\partial\psi}{\partial r} + \frac{\partial^2\psi}{\partial z^2} + r^2\frac{\partial P(\psi, r)}{\partial\psi} = 0, \tag{1}$$

$$- N\Omega^2 r + \frac{\partial P(\psi, r)}{\partial r} = 0, \tag{2}$$

where N and P are the mass density and the plasma pressure. Assuming that $\partial S(\psi, r)/\partial r = 0$, where $S = PN^{-\gamma}$ (this implies that the continuous spectrum is stable) [3], we can solve Eq. (2) to obtain

$$P = P_o(1 + \frac{\gamma-1}{\gamma}A)^{\gamma/\gamma-1},\quad N = N_o(1 + \frac{\gamma-1}{\gamma}A)^{1/\gamma-1}, \tag{3}$$

where P_o and N_o are arbitrary functions of ψ, and $A=N_o\Omega^2r^2/2\,P_o$ is the ratio of kinetic energy and thermal energy. An equilibrium is now determined if one prescribes the functions $\Omega(\psi)$, $P_o(\psi)$ and $N_o(\psi)$ (along with a boundary condition upon ψ), because Eq. (1) then is elliptic.

The MHD equations, when linearised about such an equilibrium, and when Fourier decomposed by putting the perturbations proportional to exp i(- ωt + mϕ), can be written as

$$\sigma^2 N\underset{\sim}{v} + 2\sigma L\underset{\sim}{v} + Q\underset{\sim}{v} = 0, \tag{4}$$

where $\sigma = \omega - m\Omega$, L and Q are the self-adjoint operators given by

$$L\underset{\sim}{v} = iN\Omega\nabla z\times\underset{\sim}{v}, \tag{5}$$

$$Q\underset{\sim}{v} = \nabla(\underset{\sim}{v}\cdot\nabla P + \gamma P\,\mathrm{div}\,\underset{\sim}{v}) - \underset{\sim}{B}\times\mathrm{curl}\,\mathrm{curl}\,(\underset{\sim}{v}\times\underset{\sim}{B}) - \mathrm{curl}\,\underset{\sim}{B}\times\mathrm{curl}\,(\underset{\sim}{v}\times\underset{\sim}{B}) - (\underset{\sim}{v}\cdot\nabla N + N\,\mathrm{div}\,\underset{\sim}{v})\Omega^2 r\nabla r, \tag{6}$$

and $\underset{\sim}{v}$ is the perturbing velocity. If Ω is constant (rigid rotation), σ is a constant, too, and can be viewed as an eigenvalue parameter replacing the frequency ω. Being quadratic in σ, the eigenvalue problem (4) - (6) is not self-adjoint, and investigating stability (Im$\sigma \lesseqgtr 0$) requires a normal mode analysis.

The necessary stability criterion whose derivation we sketch here arises from putting $\sigma = 0(\epsilon)$ and $\partial/\partial\psi = 0(1/\epsilon)$, and expanding Eq. (4) in powers of ϵ. To lowest order we find, among other relations, that the quantity $X = \underset{\sim}{v}\cdot\nabla\psi$ is an arbitrary function of ψ alone. In the next order a solubility condition appears, imposing a constraint upon X which can be written as

$$\sigma^2\frac{d^2X}{d\psi^2} + K(\psi)X = 0, \tag{7}$$

where K is an equilibrium quantity. The eigenvalues of Eq. (7) are real, and they accumulate at the origin from the positive, the negative, or both sides depending on whether K is positive, negative, or takes both signs. Hence $K \gtreqless 0$ is a necessary criterion for stability. When written out, this criterion is

$$\langle F\rangle\langle G\rangle - \frac{\Omega^2}{\gamma S}\frac{dS}{d\psi}\left[\langle H\rangle\left\langle\frac{N\nabla r\cdot\nabla\psi}{rB^2}\right\rangle - \frac{1}{2}(\langle F\rangle\langle Hr^2\rangle - \langle Fr^2\rangle\langle H\rangle)\right] \gtreqless 0, \tag{8}$$

where $\langle\ldots\rangle = q^{-1}\oint dl\ldots/B$ is the usual field line average (with $q = \oint dl/B$),

$$F = \frac{N}{r^2B^2}\nabla\psi\cdot(-2\underset{\sim}{\kappa} + \frac{N\Omega^2 r}{\gamma P}\nabla r), \tag{9}$$

$$G = \frac{N}{r^2B^2}\nabla\psi\cdot(-2\underset{\sim}{\kappa} - \frac{N\Omega^2 r}{\gamma P}\nabla r + \frac{B^2+\gamma P}{\gamma PB^2}\nabla P), \tag{10}$$

$$H = \frac{N^2(B^2+\gamma P)}{\gamma PB^2}, \tag{11}$$

and $\underset{\sim}{\kappa}$ is the curvature vector of a field line. The calculations leading to Eqs. (7) - (11) are formidable, and will be given elsewhere.

The criterion (8) is rather unintuitive. To provide some insight, we consider two special cases: (1) If Ω = 0, the criterion reduces to

$$\left\langle\frac{\kappa\nabla\psi}{B^2r^2}\right\rangle\left(2\left\langle\frac{\kappa\nabla\psi}{B^2r^2}\right\rangle - \frac{dP}{d\psi}\left\langle\frac{B^2+\gamma P}{\gamma PB^2}\right\rangle\right) \gtreqless 0, \tag{12}$$

thus requiring that the curvature vector, on the average, is opposite to the pressure gradient. The criterion (12) is the closed-line counterpart [4] of Mercier's criterion; it reduces to the well-known interchange condition $d(Pq^\gamma)/dq \gtreqless 0$ in the low beta limit, and then also becomes sufficient for stability. (2) If the curvature vanishes (rotating theta pinch), the criterion reduces to the well-known [5] condition

$$\frac{dN}{dr} \gtreqless \frac{N^2\Omega^2 r}{B^2+\gamma P}, \tag{13}$$

thus requiring that the density gradient points away from the rotation axis.

References:

[1] I.B. Bernstein, E.A. Frieman, M.D. Kruskal, and R.M. Kulsrud, Proc. R. Soc. Lond. A244, 17 (1958)

[2] E.A. Frieman and M. Rothenberg, Rev. Mod. Phys. 32, 898 (1960)

[3] T.A.K. Hellsten and G.O. Spies, Phys. Fluids 22, 743 (1979)

[4] G.O. Spies, Nucl. Fusion Lett. 11, 552 (1971)

[5] G.O. Spies, Phys. Fluids 21, 580 (1978)

This work was performed under the terms of the agreements on association between Max-Planck-Institut für Plasmaphysik und EURATOM and between Sweden and EURATOM.

On the peeling instability

D. Lortz, J. Nührenberg

Max-Planck-Institut für Plasmaphysik, 8046 Garching bei München, Federal Republic of Germany

Abstract: The stability of a toroidal magnetohydrostatic equilibrium configuration surrounded by vacuum is re-investigated. An improved form of the peeling criterion together with the ballooning mode equation is evaluated for certain classes of axisymmetric equilibria.

If a toroidal MHD equilibrium configuration with a continuous pressure profile is separated from a perfectly conducting wall by a vacuum region, then a disturbance of the peeling type can be found which is localized near the free boundary. The system is unstable unless near the free boundary (for notation see [1]):

$$\langle |\nabla V|^2 A \rangle = \langle |\nabla V|^{-2} \mathcal{J}^2 + \dot{\mathcal{I}}\ddot{\Phi} - \dot{\mathcal{J}}\ddot{\mathcal{X}} \rangle \le 0 , \qquad (1)$$

$$A = 2|\nabla V|^{-6}(\vec{\mathcal{J}} \times \nabla V)\cdot(\vec{B}\cdot\nabla)\nabla V ,$$

$$\langle \cdots \rangle = \Big[\oint B^{-1} d\ell\Big]^{-1} \oint \cdots B^{-1} d\ell .$$

The criterion (1), the proof of which will be published elsewhere, is more stringent than the form in [1]. For axisymmetric equilibria described by the equation

$$\frac{\partial^2\Psi}{\partial r^2} - \frac{1}{r}\frac{\partial\Psi}{\partial r} + \frac{\partial^2\Psi}{\partial z^2} + \frac{d\bar{f}}{d\Psi}\bar{f} + r^2\frac{d\bar{p}}{d\Psi} = 0$$

we have in dimensionless form

$$\mathcal{L}T + 4\iota_o^{-2}\left[f'f + (1+x)^2 p'\right] = 0 \qquad (2)$$

where

$$\mathcal{L} = \frac{\partial^2}{\partial x^2} - \frac{1}{1+x}\frac{\partial}{\partial x} + \frac{\partial^2}{\partial y^2} , \quad \cdots' = \frac{d}{dT}\cdots , \quad T(0,0) = 0 ,$$

$$\mathcal{L}T(0,0) = 2(\varepsilon + \varepsilon^{-1}) , \quad \Psi = -\tfrac{1}{2}\iota_o R B_o T , \quad f(0) = 1 ,$$

$$\bar{f} = B_o R f , \quad \bar{p} = B_o^2 p , \quad x = (r-R)/R , \quad y = z/R ,$$

and ι_o, B_o, ε are the rotational transform, field strength, and half-axis ratio on the magnetic axis with radius R. Here, the peeling condition is of the form

$$\langle |\nabla V|^{-2}\mathcal{J}^2\rangle + \dot{\mathcal{I}}\ddot{\Phi} - \dot{\mathcal{J}}\ddot{\mathcal{X}} = B_o^2\iota_o^{-2}\pi^{-4}R^{-6}U_1^{-1}\left[p'^2 W_3 + 2p'f'f W_1 + f'^2 f^2 W_{-1} - \tfrac{1}{4}\iota_o^2 f'f U_{-1}' - \tfrac{1}{4}\iota_o^2 p' U_1'\right] \le 0 \qquad (3)$$

$$U_m = \frac{1}{\pi}\int_0^{2\pi} S_T S (1+x)^m d\varphi , \quad W_m = \frac{1}{\pi}\int_0^{2\pi} (S_T S)^3 (S^2 + S_\varphi^2)^{-1} (1+x)^m d\varphi ,$$

$$x = S\cos\varphi , \quad y = S\sin\varphi .$$

For a convex contour $U_n > 0$, $W_n > 0$, and in the neighbourhood of a separatrix at $T = T_s$ we have $U_{-1}' , U_1' \sim (T_s - T)^{-1}$. Since $p = 0$, $p' \le 0$ on the free surface, it is found from the criterion (3) that the paramagnetic case $f'f < 0$ is always peeling unstable. Specializing the profiles to

$$f'f = \gamma_0 + \gamma_1 T , \quad p' = -p_0 + p_1 T , \qquad (4)$$

where

$$\gamma_0 = -\iota_o^2[1 - \beta_p(0)](\varepsilon + \varepsilon^{-1})/2 , \quad p_0 = \iota_o^2\beta_p(0)(\varepsilon + \varepsilon^{-1})/2 , \quad \beta_p = 1 - \dot{\mathcal{I}}\dot{\Phi}/\dot{\mathcal{J}}\dot{\mathcal{X}} ,$$

we can solve eq. (2) in the form $T = v(x) + w(x)\cos ky$ and obtain

$$\left.\begin{aligned} v'' - (1+x)^{-1}v' + 4\iota_o^{-2}\left[\gamma_0 + \gamma_1 v + (1+x)^2(-p_0 + p_1 v)\right] = 0 \\ w'' - (1+x)^{-1}w' - k^2 w + 4\iota_o^{-2}\left[\gamma_1 w + (1+x)^2 p_1 w\right] = 0 \end{aligned}\right\} \qquad (5)$$

The expansion to 4th order in ρ yields

$$T = \rho^2\left[\varepsilon\cos^2\varphi + \varepsilon^{-1}\sin^2\varphi\right] + \rho\left(T_{30}\cos^3\varphi + T_{12}\cos\varphi\sin^2\varphi\right) + \rho^2\left(T_{40}\cos^4\varphi + T_{22}\cos^2\varphi\sin^2\varphi + T_{04}\sin^4\varphi\right)\Big] + O(\rho^5)$$

$$= \tfrac{1}{2}\rho^2\left[\varepsilon + \varepsilon^{-1} + (\varepsilon - \varepsilon^{-1})\cos 2\varphi\right] + \rho^3\left(S_{31}\cos\varphi + S_{33}\cos 3\varphi\right) + \rho^4\left(S_{40} + S_{42}\cos 2\varphi + S_{44}\cos 4\varphi\right) + O(\rho^5) .$$

If the shear is defined by $S(V) = -2\pi R^3\dot{\iota}/\iota$, then the quantities ε, ι_o, $\beta_p(0)$, S_{33}, S_{44}, $S(0)$, p_1 can be prescribed and it is found that

$$\left.\begin{aligned} &\frac{d}{2}\left(\varepsilon + \frac{1}{3\varepsilon}\right) = \frac{3}{2}\varepsilon - \beta_p(0)\left(\varepsilon + \frac{1}{\varepsilon}\right) - 2S_{33} , \\ &T_{30} = \varepsilon\left(1 - \tfrac{1}{3}\alpha\right) , \quad T_{12} = -2\varepsilon + 2\beta_p(0)\left(\varepsilon + \frac{1}{\varepsilon}\right) + \varepsilon\alpha , \\ &12T_{40} + 2T_{22} + 4\iota_o^{-2}\varepsilon(\gamma_1 + p_1) = 3T_{30} - 2\varepsilon + 4\iota_o^{-2}p_0 , \\ &2T_{22} + 12T_{04} + 4\iota_o^{-2}(\gamma_1 + p_1)\varepsilon^{-1} = T_{12} , \\ &3\varepsilon^{-2}T_{40} + T_{22} + 3\varepsilon^2 T_{04} = \frac{3}{4}\varepsilon^{-1}\left(5\varepsilon^{-2}T_{30}^2 + 2T_{30}T_{12} + \varepsilon^2 T_{12}^2\right) \\ &\qquad + 3\varepsilon^{-2}T_{30} + T_{12} + 2\varepsilon^{-1} + 4\gamma_0 - 4S(0) , \\ &T_{40} - T_{22} + T_{04} = 8S_{44} , \\ &k^2 = -12\varepsilon T_{04} . \end{aligned}\right\} \qquad (6)$$

The initial conditions for the equations (5) are

$$w(0) = -2\varepsilon^{-1}k^{-2} , \quad w'(0) = -2k^{-2}T_{12}$$

For the case of the simplest geometry ($\varepsilon = 1$, $S_{33} = S_{44} = 0$) eqs. (6) reduce to

$$-\tfrac{1}{2}\iota_o^{-2}(\gamma_1 + p_1) = -\iota_o^2 + 29/32 + (\iota_o^2 + 5/4)\beta_p(0) + \tfrac{3}{2}\beta_p^2(0) - S(0) .$$

For this case the evaluation of the criterion (3) is represented in Fig. 1 for $\iota_o = 1$ and $p_1 = 50\,\beta_p(0)$.

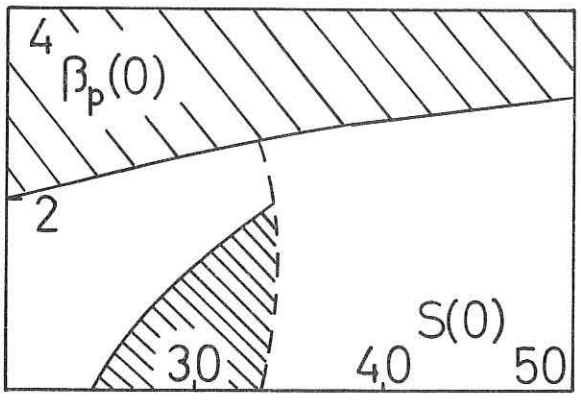

Fig. 1

The dotted line has $p'(T_s) = 0$ such that in the region left of the dotted line we can choose the T-value T_b of the free boundary with $p'(T_b) = 0$. It is then found that outside the coarsely hatched region the system is completely ballooning stable, while inside the coarsely hatched region it is ballooning unstable on the magnetic axis according to the results in [3]. However, there is peeling instability everywhere except in the finely hatched region, leading to a value $\beta_c \sim \frac{1}{2}\%$ ($\beta = 2\int \bar{p}\,d^3\tau / \int B_t^2 d^3\tau$). If one drops the condition $p'(T_b) = 0$, higher β_c - values can be reached. An example with $\beta_p(0)$ above the ballooning unstable band [3] is: $\varepsilon = 1$, $S_{33} = S_{44} = 0$, $\beta_p(0) = 5$, $S(0) = 0$, $\gamma_1 = 50$. Here, the system is ballooning stable everywhere between the magnetic axis and the separatrix, is peeling stable near the separatrix, and has $\beta = 8.5\%$. This case, however, is unstable with respect to external global modes with $n = 1$ according to the numerical code ERATO [4].

Finally, if one relaxes the profile conditions (4) to

$$f'f = \gamma_0 + \gamma_1 T + \gamma_2 T^2 , \quad p' = -p_0 + p_1 T + p_2 T^2$$

such that eq. (2) becomes nonlinear, the results are more encouraging. Magnetic surfaces of the example

$$\beta_p(0) = .4 , \quad \iota_o = 1 , \quad \varepsilon = 1 , \quad S_{mm} = 0 , \quad p_2 = 10 , \quad \gamma_2 = 15 , \quad \beta = 3\,\%$$

are shown in Fig. 2. This configuration is peeling stable and everywhere ballooning stable.

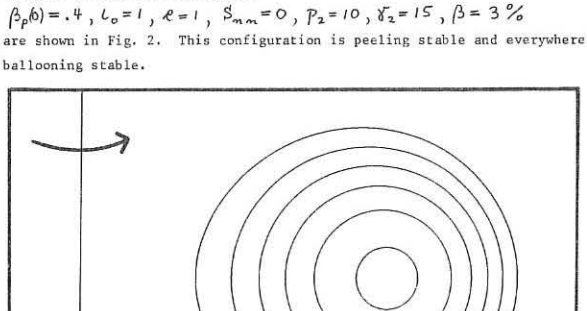

Fig. 2

References

[1] Lortz, D., Nucl. Fusion 15 (1975) 49.

[2] Lortz, D., Rebhan, E., Spies, G., Nucl. Fusion 11 (1971) 583.

[3] Lortz, D., Nührenberg, J., Nucl. Fusion (1979) to appear

[4] Berger, D., Bernard, L., Gruber, R., Troyon, F., paper C3, 2nd European Conf. on Comput. Phys., Garching (1976).

Acknowledgement. Discussions with Drs. R. Gruber and W. Kerner on the use of the ERATO stability code are gratefully acknowledged.

"This work was performed under the terms of the agreement on association between Max-Planck-Institut für Plasmaphysik and EURATOM".

BP9

QUASILINEAR EVOLUTION OF THE ION-ACOUSTIC TURBULENCE EXCITED BY A RETURN CURRENT

K. Appert, R. Bingham, J. Vaclavik, and E.S. Weibel
Centre de Recherches en Physique des Plasmas
Ecole Polytechnique Fédérale de Lausanne
21 Av. des Bains, CH-1007 Lausanne / Switzerland
Association "Confédération Suisse - EURATOM"

ABSTRACT : Current-driven ion-acoustic turbulence is investigated numerically within the context of a quasilinear model. It is found that the turbulent wave energy and the plasma heating exhibit features similar to those observed in particle simulation.

1. Introduction

Experiments on relativistic electron beam heating of plasmas in controlled fusion devices indicate that the return current of drifting plasma electrons gives rise to ion-acoustic turbulence which enhances the dissipation of the beam energy [1,2]. An objective of the present paper is to investigate the evolution of this turbulence and the associated heating of the plasma within the context of a quasilinear model that includes nonresonant ion diffusion. This type of interaction was neglected in previous theories of ion-acoustic turbulence [3] although it is a simple one, and the results of computer simulation [4] indicate that the interaction is essential for the determination of quasi-saturation mechanisms.

2. Model

The plasma under consideration is assumed to be collisionless, uniform and nonmagnetized. The electrons are hot ($T_e \gg T_i$) and drift with a constant velocity $\vec{v}_d = v_d \vec{e}_x$ relative to a cold ion background which results in the generation of an ion-acoustic turbulence in the system. Since the problem exhibits axial symmetry with respect to the current axis we confine ourselves, for convenience, to a two-dimensional model. As one can see below, the structure of the ion nonresonant diffusion term is rather formidable. In order to make it amenable to a numerical procedure we take the motion of ions as one-dimensional. However, in their resonant terms, where 2-D behaviour is important, we replace the 1-D δ-function obtained by averaging the 2-D δ-function over the angles assuming that the ion distribution is isotropic. With this stipulation, the quasilinear equations describing the problem can be given in the form [5,6]

$$\frac{\partial f_e}{\partial t} + E \frac{\partial f_e}{\partial v_x} = \frac{\partial}{\partial \vec{v}} \cdot \int \frac{d^2\vec{k}}{4\pi} \frac{\vec{k}\vec{k}}{k^2} I_{\vec{k}} \delta(\omega_{\vec{k}} - \vec{k}.\vec{v}) \cdot \frac{\partial f_e}{\partial \vec{v}}, \tag{1}$$

$$\frac{\partial f_i}{\partial t} - \alpha E \frac{\partial f_i}{\partial v_x} = \alpha^2 \frac{\partial}{\partial v_x} \int \frac{d^2\vec{k}}{(2\pi)^2} \frac{k_x^2}{k^2} I_{\vec{k}} \left(\frac{\omega_{\vec{k}}}{k_x v_x} \frac{2}{\sqrt{(k_x v_x)^2 - \omega_{\vec{k}}^2}} + \frac{\gamma_{\vec{k}}}{2(\omega_{\vec{k}} - k_x v_x)^2} \right) \frac{\partial f_i}{\partial v_x}, \tag{2}$$

$$\frac{1}{2I_{\vec{k}}} \frac{\partial I_{\vec{k}}}{\partial t} = \gamma_{\vec{k}} \equiv \frac{1}{k^2 \partial\varepsilon/\partial\omega_{\vec{k}}} \{ \pi \int d^2\vec{v}k . \frac{\partial f_e}{\partial \vec{v}} \delta(\omega_{\vec{k}} - \vec{k}.\vec{v}) + 2\alpha\omega_{\vec{k}} \int dv_x \frac{\partial f_i}{\partial v_x} \frac{1}{v_x \sqrt{(k_x v_x)^2 - \omega_{\vec{k}}^2}} \} \tag{3}$$

$$k^2 \frac{\partial \varepsilon}{\partial \omega_{\vec{k}}} = 2\left(\frac{\alpha k_x^2}{\omega_{\vec{k}}^3} + \frac{k_x v_d}{k^2 T_e} \right), \quad \omega_{\vec{k}} = - \frac{(\alpha T_e)^{\frac{1}{2}} k_x}{(1 + k^2 T_e - k_x^2 v_d^2 / (k^2 T_e))^{\frac{1}{2}}} \tag{4}$$

where f_e and f_i are the electron and ion distribution functions, respectively, $I_{\vec{k}}$ is the spectral distribution of the fluctuating electrostatic field, E is the electric field associated with the current, and $\alpha = m_e/m_i$ is the electron-to-ion mass ratio. Equations (1)-(4) are in dimensionless units; the units of time, space, distribution function, electric field and temperature are, respectively, ω_{pe}^{-1}, λ_D, $m_e n/T_{eo}$, $(4\pi n T_{eo})^{\frac{1}{2}}$ and T_{eo}. Here n and T_{eo} are the electron density and initial temperature, respectively, and λ_D is the Debye length. Equations (1)-(4) are solved numerically using the finite-element method [7]. The initial conditions are

$$f_e(t=o) = \frac{1}{2\pi} \exp\{ -\frac{1}{2} ((v_x - v_d)^2 + v_y^2) \}$$

$$f_i(t=o) = \frac{1}{(2\pi\alpha T_{io})^{\frac{1}{2}}} \exp\{ -\frac{v^2}{2\alpha T_{io}} \}, \quad I_{\vec{k}}(t=o) = \text{const.}$$

3. Computational results and conclusion

We have performed a series of computations with different values of the parameters α, v_d and T_{io}. In general, all runs gave a similar overall picture. In the accompanying figures we show the results of the run with $\alpha = .01$, $v_d = .75$ and $T_{io} = .02$, which are values used in particle simulation by Dum et al. [4]. Figure 1 shows the time evolution of the electrostatic wave energy W, the electron and ion temperatures, and the electric field. We observe that the electric field, which is a measure of the turbulent resistivity, begins to saturate as soon as the wave energy reaches approximately 1 %. Since the resistivity is proportional to $\partial f_e/\partial v$, this implies that the electron distribution function begins to flatten as a result of diffusion. At about this time ($t \sim 10^3$) the heating of the electrons and ions sets in. The latter is connected with the fact that a significant fraction of suprathermal ions is produced due to a combined dynamical effect of the quasilinear nonresonant and resonant diffusions. The formation of the high-energy ion tail is clearly demonstrated in Fig. 2, which shows the ion distribution function at three instants in time. As the wave energy grows further, the ion tail starts extending to larger velocities and the number of particles in the tail increases. At the same time the electron distribution function flattens more and more as is evidenced by the decrease of the electric field. This leads to a further reduction of the wave growth rate. Finally, when the number of high-energy ions reaches about 2% of the total population, the growth of the wave energy is quenched by Landau damping in the ion tail ($t \sim 4.10^3$). From this moment on the wave energy decreases, the electrons and ions being further heated. The spectral distribution of the fluctuations at the saturation time is displayed in Fig. 3. One can see that the spectrum peaks roughly around $k \sim .4$ with an angular width greater than 45°. With such a broad spectrum one may expect that the electron distribution function remains quite isotropic. Fig. 4, which shows the electron distribution function at several times, indicates that this is the case except for a small runaway tail along the current direction.

In general, all these features compare favourably with those observed in particle simulation [4]. However, the time scales for the evolution of the macroscopic quantities and their values are somewhat different. In our opinion, this discrepancy is due to particle discreteness effects which, of course, are not included in our treatment.

In conclusion, we have found that the evolution of the ion-acoustic turbulence excited by a constant current may be satisfactorily described within the frame of the quasilinear approximation that includes nonresonant ion diffusion.

This work was supported by the Swiss National Science Foundation.

References

[1] J. Benford et al., Proc. 6th International Conf. on Plasma Physics and Controlled Nuclear Fusion Research, Berchtesgaden 1976, Vol. II, p. 543.

[2] A.K.L. Dymoke-Branshow, A.E. Dangor and J.D. Kilkenny, in Ref. 1, p. 555.

[3] W. Horton, Jr. and Duk-In Choi, Phys. Rep. 49, No 3, 273 (1979).

[4] C.T. Dum, R. Chodura and D. Biskamp, Phys.Rev.Lett. 32, 1231 (1974).

[5] A.A. Vedenov, E.P. Velikhov and R.Z. Sagdeev, Nucl. Fusion, Suppl. 2, 465 (1962).

[6] W.E. Drummond and D. Pines, Nucl. Fusion, Suppl. 3, 1049 (1962).

[7] K. Appert, T.M. Tran and J. Vaclavik, Comput. Phys. Commun, 12, 135 (1976).

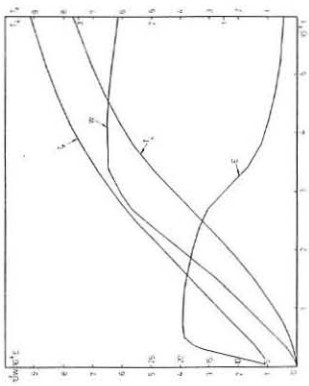

Fig. 1

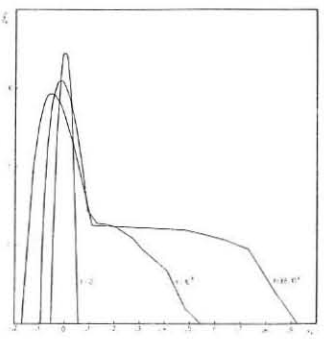

Fig. 2

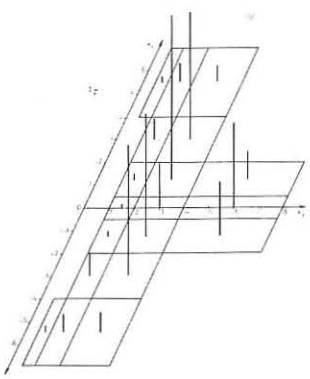

Fig. 3

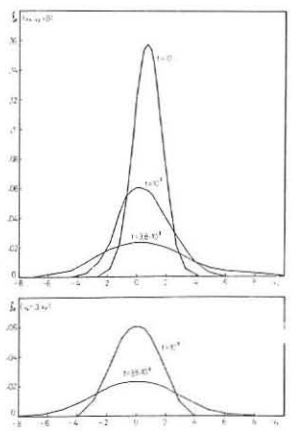

Fig. 4

BP10

ON THE TRANSPORT THEORY OF ELECTROSTATIC MICROINSTABILITIES

J. J. Sanderson
(Dept. of Applied Mathematics, University of St. Andrews, St. Andrews, Scotland)
and
S. P. Gary
(Los Alamos Scientific Laboratory, University of California, Los Alamos, N.M., U.S.A.)

A general second order perturbation theory for electrostatic microinstabilities in an infinite, Vlasov plasma is applied to the case of density and temperature gradients perpendicular to a uniform magnetic field. The momentum and energy exchange rates are expressed in terms of integrals over wave vector space, each integrand being a product of the fluctuation energy density and another factor involving the contribution of the relevant species to the linear dielectric function. These exchange rates and the heat flux are then derived by the same two-step process used in earlier papers [1,2], namely, a perturbation expansion followed by a velocity integration of the ensemble-averaged second order Vlasov equation. If the results are used with estimates of the maximum fluctuation level, wave-particle transport coefficients may easily be determined.

The perturbation expansion is valid only if the fluctuation energy density is much less than the thermal energy density and is really useful only if the linear Vlasov equation correctly describes the species response to the fluctuating fields through all phases of the instability (growth, saturation, and post-saturation). The integration over velocity space requires that the wave-particle interaction be either broadly resonant or else nonresonant.

Results are presented for the application of the theory to the temperature gradient driven ion acoustic instability [3,4,5] of relevance to laser produced plasmas. The theory has also been applied to other instabilities driven by diamagnetic drifts [6,7,8] which may be due to a density gradient [9] or both density and temperature gradients [10].

GENERAL THEORY

The distribution function satisfies the Vlasov equation

$$\frac{\partial f_j}{\partial t} + \underline{v}\cdot\frac{\partial f_j}{\partial \underline{x}} + \frac{e_j}{m_j}\left[\underline{E}(\underline{x},t) + \frac{\underline{v}\times\underline{B}}{c}\right]\cdot\frac{\partial f_j}{\partial \underline{v}} = 0$$

and the fluctuating electric field is determined by Poisson's equation

$$\underline{\nabla}\cdot\underline{E}(\underline{x},t) = 4\pi\sum_j \rho_j(\underline{x},t).$$

We carry out a perturbation expansion using the ratio of the magnitude of the fluctuating fields to the mean kinetic energy as the small parameter

$$f_j(\underline{x},\underline{v},t) = f_j^{(0)}(\underline{x},\underline{v}) + f_j^{(1)}(\underline{x},\underline{v},t) + f_j^{(2)}(\underline{x},\underline{v},t) + \ldots.$$

$$\underline{E}(\underline{x},t) = \underline{E}^{(1)}(\underline{x},t) + \underline{E}^{(2)}(\underline{x},t) + \ldots.$$

and with the usual definitions of density n_j, charge density ρ_j, particle flux density $\underline{\Gamma}_j$, momentum density $\underline{P}_j \equiv m_j\underline{\Gamma}_j$, current density $\underline{J}_j \equiv e_j\underline{\Gamma}_j$, drift velocity $\underline{v}_{d_j} \equiv \underline{\Gamma}_j/n_j$, energy density tensor

$$\underline{\underline{W}}_j \equiv \frac{m_j}{2}\int d^3v\, \underline{v}\,\underline{v}\, f_j, \qquad W_j \equiv \frac{m_j}{2}\int d^3v\, v^2 f_j$$

pressure tensor

$$\underline{\underline{\Pi}}_j \equiv m_j\int d^3v(\underline{v}-\underline{v}_{d_j})(\underline{v}-\underline{v}_{d_j})f_j$$

scalar pressure

$$\Pi_j \equiv \frac{m_j}{3}\int d^3v(\underline{v}-\underline{v}_{d_j})^2 f_j$$

temperature $T_j \equiv \Pi_j/n_j$, kinetic energy flux density

$$\underline{q}_j \equiv \frac{m_j}{2}\int d^3v\,\underline{v}\,v^2 f_j$$

and heat flux density

$$\underline{Q}_j \equiv \frac{m_j}{2}\int d^3v(\underline{v}-\underline{v}_{d_j})(\underline{v}-\underline{v}_{d_j})^2 f_j$$

one obtains the following set of second order equations:

$$\frac{\partial\langle n_j^{(2)}\rangle}{\partial t} + \underline{\nabla}\cdot\langle\underline{\Gamma}_j^{(2)}\rangle = 0$$

$$\frac{\partial\langle \underline{P}_j^{(2)}\rangle}{\partial t} + \underline{\Omega}_j\times\langle\underline{P}_j^{(2)}\rangle + 2\underline{\nabla}\cdot\langle\underline{\underline{W}}_j^{(2)}\rangle - e_j n_j\langle\underline{E}_j^{(2)}\rangle = e_j\langle\underline{E}^{(1)}n_j^{(1)}\rangle \equiv -\nu_{P_j}\underline{P}_j$$

$$\frac{\partial\langle W_j^{(2)}\rangle}{\partial t} + \underline{\nabla}\cdot\langle\underline{q}_j^{(2)}\rangle - e_j\langle\underline{E}^{(2)}\rangle\cdot\underline{\Gamma}_j = e_j\langle\underline{E}^{(1)}\cdot\underline{\Gamma}_j^{(1)}\rangle$$

$$\frac{\partial\langle\underline{\underline{\Pi}}_j^{(2)}\rangle}{\partial t} + \frac{2}{3}\underline{\nabla}\cdot\langle\underline{Q}_j^{(2)}\rangle + \underline{\nabla}\cdot(\underline{v}_{d_j}\langle\underline{\underline{\Pi}}_j^{(2)}\rangle) + \frac{2}{3}(\underline{\Omega}_j\times\underline{v}_{d_j})\cdot\langle\underline{P}_j^{(2)}\rangle$$
$$= \frac{2e_j}{3}(\langle\underline{E}^{(1)}\cdot\underline{\Gamma}_j^{(1)}\rangle - \underline{v}_{d_j}\cdot\langle\underline{E}^{(1)}n_j^{(1)}\rangle) \equiv -\nu_{T_j}\underline{\underline{\Pi}}_j$$

and

$$\frac{\partial\langle\underline{Q}_j^{(2)}\rangle}{\partial t} + \underline{\nabla}\cdot\langle\frac{m_j}{2}\int d^3v\,\underline{v}(\underline{v}-\underline{v}_{d_j})^2 f_j^{(2)}\rangle + \underline{\Omega}_j\times\langle\underline{Q}_j^{(2)}\rangle$$
$$+ 2(\underline{\Omega}_j\times\underline{v}_{d_j})\cdot\langle\underline{\underline{W}}_j^{(2)}\rangle + \frac{3}{2}(\underline{\Omega}_j\times\underline{v}_{d_j})\langle\underline{\underline{\Pi}}_j^{(2)}\rangle - \underline{v}_{d_j}(\underline{\Omega}\times\underline{v}_{d_j})\cdot\langle\underline{P}_j^{(2)}\rangle$$
$$- \frac{e_j}{m_j}\langle\underline{E}^{(2)}\rangle\cdot(\frac{3}{2}\underline{\underline{\Pi}}_j + \underline{\underline{\eta}}_j) = \frac{3e_j}{2m_j}\langle\underline{E}^{(1)}\Pi_j^{(1)}\rangle + \frac{e_j}{m_j}\langle\underline{E}^{(1)}\cdot\underline{\underline{\Pi}}_j^{(1)}\rangle$$
$$\equiv \langle\underline{R}_j^{(2)}\rangle \equiv -\nu_{Q_j}\underline{Q}_j$$

where we have omitted the superscript 0 on steady state quantities, $\underline{\Omega}_j = e_j\underline{B}/m_j c$, and $\langle\ \rangle$ denotes an average over an ensemble of waves with random phases.

It then follows from the usual linear theory applied to a slab model with $\underline{\nabla} \equiv (d/dx,0,0)$ and $\underline{B} = (0,0,B)$ that the wave-particle exchange frequencies defined by the second order equations are given by:

$$\nu_{P_j} = -\frac{2v_j^2}{v_{d_j}}\sum_{\underline{k}} k_y\frac{\mathcal{E}(\underline{k},t)}{nT_j}\,\mathrm{Im}[K_j(\underline{k},\omega)] \tag{1}$$

$$\nu_{T_j} = -\frac{4}{3}\sum_{\underline{k}}\frac{\mathcal{E}(\underline{k},t)}{nT_j}\,\mathrm{Im}[(\omega-\underline{k}\cdot\underline{v}_{d_j})K_j(\underline{k},\omega)] \tag{2}$$

$$\nu_{Q_j} = -\frac{1}{Q_j}\sum_{\underline{k}}\mathcal{E}(\underline{k},t)\,\mathrm{Im}[k_y M_j(\underline{k},\omega) + 2i\Omega_j L_{jx}(\underline{k},\omega)] \tag{3}$$

where $v_j^2 \equiv T_j/m_j$, $\mathcal{E}(\underline{k},t) = |\underline{E}^{(1)}(\underline{k},t)|^2/8\pi$, and K_j, $\underline{L}_j$ and M_j are the first three moments of the dielectric function:

$$\begin{bmatrix} K_j \\ \underline{L}_j \\ M_j \end{bmatrix} = -\frac{i\omega_j^2}{k^2 n_j}\int\begin{bmatrix}1\\ \underline{v}\\ v^2\end{bmatrix} d^3v\int_{-\infty}^{t} dt'\,\underline{k}\cdot\frac{\partial f_j^{(0)}}{\partial \underline{v}'}\exp(i[\underline{k}\cdot(\underline{x}'-\underline{x}) - \omega(t'-t)] \tag{4}$$

$$\omega_j^2 = 4\pi n_j e^2/m_j,$$

the time integration being the usual integration over unperturbed orbits.

STEADY STATE DISTRIBUTION FUNCTION

Assuming gradient scale lengths much greater than an ion gyroradius an appropriate zeroth order distribution function is [3]

$$f_j^{(0)}(x,\underline{v}) = \frac{n_0}{(2\pi v_j^2)^{3/2}}\left[1+\varepsilon_n(x+\frac{v_y}{\Omega_j}) + \varepsilon_{T_j}(x+\frac{v_y}{\Omega_j})(\frac{v^2}{2v_j^2}-\frac{3}{2})\right]\exp(-v^2/2v_j^2)$$

from which it follows that

$$n_j(x) = n_0(1+\varepsilon_n x)$$

$$\underline{v}_{d_j} = (v_{n_j} + v_{T_j})\hat{y}$$

$$T_j(x) = T_j(1+\varepsilon_{T_j}x)$$

$$\underline{Q}_j = \frac{5}{2}n_0 T_j v_{T_j}\hat{y}$$

so that ε_n and ε_{T_j} may be identified as the inverse scale lengths for the density and temperature gradients and $v_{n_j} \equiv \varepsilon_n v_j^2/\Omega_j$ and $v_{T_j} \equiv \varepsilon_{T_j} v_j^2/\Omega_j$ are the diamagnetic drift velocities.

Note that the distribution function may be written as

$$f_j^{(0)}(x,\underline{v}) = [1 + \varepsilon_{T_j} T_j\frac{\partial^2}{\partial T_j\partial\varepsilon_n}]f_j^{(0)}(x,\underline{v},\varepsilon_{T_j}=0)$$

where the operator in the square brackets commutes with the velocity and time integrations of equation (4). This reduces substantially the algebra involved in calculating the wave-particle exchange frequencies.

RESULTS

We present here the results of this theory applied to the electron temperature gradient driven ion acoustic instability; results for other instabilities driven by diamagnetic drifts are presented elsewhere [9,10], together with a full description of the derivations.

On evaluating K_e, $\underline{L}_e$ and M_e from equation (4) for the ion acoustic instability and inserting the results in equations (1) to (3) we obtain for the wave-electron exchange frequencies:

momentum:
$$\nu_{P_e} = \frac{\sqrt{2\pi}k_e^2}{m_e n_0 v_{d_e}}\sum_{\underline{k}}\frac{\mathcal{E}(\underline{k},t)k_y}{k^3}\left(\frac{k_y(v_{d_e}-\frac{3}{2}v_{T_e})-\omega_r}{v_e}\right)$$

heating:
$$\nu_{T_e} = -\frac{2\sqrt{2\pi}k_e^2}{3n_0 T_e}\sum_{\underline{k}}\frac{\mathcal{E}(\underline{k},t)}{k^3 v_e}(\omega_r - k_y v_{d_e})(\omega_r - k_y(v_{d_e}-\tfrac{3}{2}v_{T_e}))$$

heat flux:
$$\nu_{Q_e} = \frac{2\sqrt{2\pi}k_e^2}{5m_e n_0 v_{T_e}}\sum_{\underline{k}}\frac{\mathcal{E}(\underline{k},t)k_y}{k^3}\left(\frac{k_y(v_{d_e}-\frac{1}{2}v_{T_e})-\omega_r}{v_e}\right)$$

where $k_e^2 \equiv 4\pi n_0 e^2/T_e$. The first two results are appropriate modifications of earlier results [2] for the ion acoustic instability accounting for the fact that the instability is here driven by the electron temperature gradient rather than a current parallel to the magnetic field.

REFERENCES

1. Gary and Feldman, Phys. Fluids 21, 72 (1978).
2. Gary, J. Plasma Phys. 21, 361 (1979).
3. Priest and Sanderson, Plasma Physics 14, 951 (1972).
4. Allan and Sanderson, Plasma Phys. 16, 753 (1974).
5. Manheimer, Max and Thomson, Phys. Fluids 21, 2009 (1978).
6. Gary and Sanderson, Phys. Fluids 21, 1181 (1978).
7. Gary and Sanderson, Phys. Fluids (to be published).
8. Gary and Gerwin, Phys. Fluids (to be published).
9. Gary, Nuc. Fusion (to be published).
10. Gary and Sanderson (in preparation).

BP11

Self-Consistent Numerical Solution of the Nonlinear Axisymmetric Magnetohydrodynamic Equilibria.

R. Bingham, R. Gruber and F. Troyon

Centre de Recherches en Physique des Plasmas - EPFL Lausanne
21, Av. des Bains, CH - 1007 Lausanne
Association "Confédération Suisse - EURATOM".

Abstract : A self-consistent solution of the inverse nonlinear Grad-Shafranov equation describing magnetohydrodynamic equilibria in toroidal geometry is obtained. This equation is solved iteratively by a finite hybrid element expansion scheme of the weak form of the linearized equation.

1. Introduction

An important problem in the pursuit of controlled thermonuclear fusion is the fast calculation of M.H.D. equilibria. Not only is knowledge of M.H.D. equilibria important for determining the position of the poloidal field coils and the currents flowing in them, but it is also an essential part of M.H.D. stability calculations and 2-D transport codes. The overall accuracy of the stability calculation is usually limited by the accuracy of the equilibrium calculation itself. In this paper we only consider the fixed boundary case.

2. Model

Conventional codes for M.H.D. equilibrium calculations are based on solving the Grad-Shafranov equation (equation 1.) in an r,z coordinate system [1,2].

$$4x\frac{\partial^2\psi}{\partial x^2}+\frac{\partial^2\psi}{\partial z^2}=-xp'-TT' \qquad (1)$$

where $x=r^2$ and p and T are the plasma pressure and toroidal field function, respectively. They are both functions of the poloidal flux function ψ. The prime denotes differentiation with respect to ψ.
As a solution we obtain $\psi(r^2,z)$ or $\psi(r^2,z^2)$ when up-down symmetry is included. However, stability calculations are carried out by choosing ψ as an independent variable. The purpose of this paper is to invert equation (1) and calculate the polar variable $\rho(\psi,\theta)$, (θ is the polar angle), at the given (ψ,θ) mesh points (see Fig. 1). Introducing the geometrical variable s ($\psi=\psi_s s^2$, $\psi_s=\psi$ at the plasma surface and $0\le s\le 1$), multiplying eq. 1 through by $\frac{\rho}{2\psi_s}\frac{\partial\rho}{\partial s}$ we obtain the quasi-linear differential equation :

$$\frac{\partial}{\partial s}\left(\frac{s}{\rho\frac{\partial\rho}{\partial s}}\left(\rho^2+\left(\frac{\partial\rho}{\partial\theta}\right)^2\right)\right)-\frac{\partial}{\partial\theta}\left(\frac{s\frac{\partial\rho}{\partial\theta}}{\rho}\right)-$$

$$\frac{s}{r}\left(\rho\cos\theta+\frac{\partial\rho}{\partial\theta}\sin\theta\right)+\frac{\rho}{2\psi_s}\frac{\partial\rho}{\partial s}\left(r^2p'+TT'\right)=0\ . \qquad (2)$$

3. Numerical Approach and Results

Equation (2) is solved iteratively by writing at each step

$$\rho^{(K+1)}=\rho^{(K)}+\Delta \qquad (3)$$

assuming $\Delta\ll\rho^{(K)}$. After substitution the resulting equation is solved by a finite hybrid element approach [3] on its weak form $\delta L(\Delta)/\delta\Delta=0$ [4], where

$$L(\Delta)=\int\left(A\Delta^2+B\Delta\frac{\partial\Delta}{\partial s}+C\Delta\frac{\partial\Delta}{\partial\theta}+D\left(\frac{\partial\Delta}{\partial s}\right)^2+E\frac{\partial\Delta}{\partial s}\frac{\partial\Delta}{\partial\theta}+F\left(\frac{\partial\Delta}{\partial\theta}\right)^2\right.$$
$$\left.+2G\Delta+2H\frac{\partial\Delta}{\partial s}+2I\frac{\partial\Delta}{\partial\theta}\right)dsd\theta \qquad (4)$$

and

$$A=\frac{s}{\tau}\cos\theta-\frac{s\rho}{\tau^2}\cos^2\theta-\frac{s}{\tau^2}\frac{\partial\rho}{\partial\theta}\cos\theta\sin\theta-\frac{\tau^2p'}{2\psi_s}\frac{\partial\rho}{\partial s}-\frac{\tau p'\rho}{\psi_s}\frac{\partial\rho}{\partial s}\cos\theta-\frac{TT'}{2\psi_s}\frac{\partial\rho}{\partial s}\ ;$$

$$B=\frac{s}{\frac{\partial\rho}{\partial s}}-\frac{s}{\rho^2\frac{\partial\rho}{\partial s}}\left(\frac{\partial\rho}{\partial\theta}\right)^2-\rho\frac{\tau^2p'}{2\psi_s}-\rho\frac{TT'}{2\psi_s}\ ;\qquad C=\frac{s}{\tau}\sin\theta\ ;$$

$$D=-\frac{s}{\rho\left(\frac{\partial\rho}{\partial s}\right)^2}\left(\rho^2-\left(\frac{\partial\rho}{\partial\theta}\right)^2\right)\ ;\qquad E=\frac{2s}{\rho}\frac{\frac{\partial\rho}{\partial\theta}}{\frac{\partial\rho}{\partial s}}\ ;\qquad F=-\frac{s}{\rho}\ ;$$

$$G=\frac{s\rho}{2\tau}\cos\theta+\frac{s}{2\tau}\frac{\partial\rho}{\partial\theta}\sin\theta-\frac{\rho}{4\psi_s}\frac{\partial\rho}{\partial s}\left(\tau^2p'+TT'\right)\ ;\qquad \rho=\rho^{(K)}\ ;$$

$$H=\frac{s}{2\rho\frac{\partial\rho}{\partial s}}\left(\rho^2+\left(\frac{\partial\rho}{\partial\theta}\right)^2\right)\ ;\qquad I=-\frac{s}{2\rho}\frac{\partial\rho}{\partial\theta}\quad\text{and}\quad\tau=R+\rho\cos\theta.$$

The "variation" over all the unknows Δ_{ij} then gives a system of linear algebraic equations to be solved. Numerically, there are two problems to be overcome. The first consists of the determination of the magnetic axis ($r=R$) which has to remain at the centre of the inner-most s surface. The second problem consists of the determination of ψ_s which plays the role of the eigenvalue of the original problem (eq. 1). ψ_s is determined iteratively by fixing the ellipticity ε around the magnetical axis such that $\frac{\partial\varepsilon}{\partial s}=0$. A study of the influence of ψ_s on the ellipticity around the axis has been performed on the analytic Solov'ev equilibrium [5]. We have chosen as a test case, ellipticity $\varepsilon=2$, aspect ratio 3 and $\psi_s=2/9$. Using these values and a mesh size $N_s\times N_\theta=20\times 40$ we converge to the solution in a few steps. By increasing (decreasing) ψ_s, the ellipticity around the axis decreases (increases). After 20 interation steps and a change of 10% in ψ_s we obtain the results shown in Fig. 2. As an example of a more difficult equilibrium calculation the following forms for p' and TT' are used

$$p'=\alpha_1(\psi-2\psi^2)\ ;\quad TT'=\alpha_2\psi^2+\alpha_3\psi^4$$

where $\alpha_1=-0.701$, $\alpha_2=-17.89$, $\alpha_3=-17.51$. This particular case has been found to be very difficult to compute by the standard procedure [6], however, our method is extremely efficient in computing this case. The numerically computed flux surfaces are shown in fig. 3.

This work was supported by the Swiss National Foundation.

References

[1] Callen, J.D. and Dory, R.A., Phys. Fluids 15 1523 (1972).
[2] Lackner, K., Computer Physics Communications 33 (1976).
[3] Gruber, R., J. Comp. Phys., 26 339 (1978).
[4] Strang, G. and Fix, G., An Analysis of the Finite Element Method. Prentice Hall, Englewood Cliffs, N.J., (1973).
[5] Solov'ev, L.S., JETP. 26 400 (1968).
[6] Gruber, R., et al. Plasma Physics and Controlled Nuclear Fusion (Proc. 8th Int. Conf. Innsbruck, 1978) IAEA 1 593 (1979).

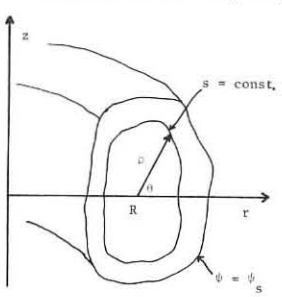

Fig. 1 : Cylindrical coordinate system used to define flux surfaces. $r=R+\rho\cos\theta$, $z=\rho\sin\theta$, $0\le\theta\le 2\pi$.

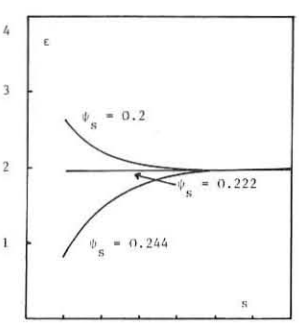

Fig. 2 : Variation of ellipticity $\varepsilon(s)$ for different values of ψ_s. $\psi_s=0.222$ is the correct value.

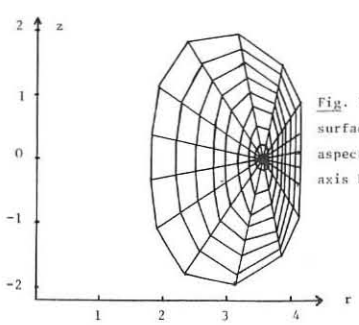

Fig. 3. Numerically computed flux surfaces with $N_s\times N_\theta=8\times 16$, aspect ratio = 3 and magnetic axis R = 3.55.

BP12

ABSORPTION OF ELECTROMAGNETIC WAVES AROUND THE ELECTRON CYCLOTRON FREQUENCY

M. Bornatici*) and F. Engelmann
Association Euratom-FOM, FOM-Instituut voor Plasmafysica
Rijnhuizen, Jutphaas, The Netherlands

ABSTRACT
It is shown that finite Larmor radius effects affect the absorption of electromagnetic waves at the electron cyclotron frequency. Moreover, the role of polarization in reducing the absorption of the extraordinary mode at finite plasma densities is displayed on the basis of the energy conservation law.

INTRODUCTION
For plasma densities and magnetic fields such that $\omega_p \approx \omega_c$, ω_p and ω_c being respectively the plasma and the cyclotron frequency of the electrons, the absorption of electromagnetic waves around ω_c is strongly affected by the plasma dielectric properties[1]. In particular the absorption of the extraordinary (X) mode has been found to scale as $(\omega_c/\omega_p)^2$ in the limit in which finite Larmor radius (FLR) effects are neglected. Here, we discuss how FLR effects affect the absorption coefficient of the ordinary (O) and the X mode in a way that clarifies the physics of the absorption, namely, we evaluate the absorption coefficient on the basis of the energy conservation law (an evaluation of the absorption by solving the dispersion relation has been given in[2], but in this approach the reason for the reduced absorption of the X mode remains obscure and, in particular, a cancellation of terms appearing can not be interpreted physically). This allows also to understand the way in which the electromagnetic and reactive kinetic ("sloshing") energy of the wave enter into the absorption process. Moreover, for the X mode the role of FLR effects in both the wave polarization and absorption is exhibited.

Under steady-state conditions the conservation law of electromagnetic energy (Poynting theorem) has the form[3]

$$2\underline{k}'' \cdot \left[\frac{c}{4\pi} \mathrm{Re}\,(\underline{E}\times\underline{B}^*) - \frac{\omega}{8\pi} \frac{\partial \varepsilon_{ij,h}}{\partial \underline{k}'} E_i^* E_j \right] = \frac{\omega}{4\pi} \underline{E}^* \cdot \underline{\varepsilon}_a \cdot \underline{E} \ , \qquad (1)$$

if the (slow) spatial variations associated with the energy absorption are dominant with respect to the variations due to the plasma inhomogeneities. In (1), $\underline{k}'' \equiv \mathrm{Im}\underline{k}$ and $\underline{k}' \equiv \mathrm{Re}\underline{k}$ denote respectively the imaginary and real part of the wave vector; ω is the (real) wave frequency; $\underline{E}$ and $\underline{B}$ are the Fourier components of the wave electric and magnetic field (the asterisk denotes the complex conjugate); $\underline{\varepsilon} = \underline{\varepsilon}_h + i\underline{\varepsilon}_a$ is the dielectric tensor, $\underline{\varepsilon}_h$ and $i\underline{\varepsilon}_a$ being the Hermitian and anti-Hermitian part of $\underline{\varepsilon}$, respectively. A further condition for the validity of (1) is $|\underline{k}''| < |\underline{k}'|$, but no smallness assumption is required for $\underline{\varepsilon}$ or $\underline{\varepsilon}_a$. For the high frequencies considered here, it is only the electron dynamics that matters, so that $\underline{\varepsilon}$ is to be taken as the dielectric tensor of the electrons. We will make use of (1) to evaluate the absorption coefficient of both the O and X mode around ω_c for propagation perpendicular to $\underline{B}_o$ in a weakly relativistic ($v_t^2 \ll c^2$) Maxwellian plasma ($v_t = (T/m)^{\frac{1}{2}}$ is the thermal velocity of the electrons).

O MODE
For perpendicular propagation, $\underline{E} = \hat{z}E_z$ and the wave propagation and absorption are described by the zz-element of $\underline{\varepsilon}$,

$$\varepsilon_{zz} = 1 - \frac{\omega_p^2}{\omega^2} - \frac{1}{2}\frac{\omega_p^2}{\omega_c^2} N_\perp^2 F_{3/2}(z) \ , \qquad (2)$$

with

$$F_q(z) \equiv -i \int_0^\infty \frac{e^{izt}}{(1-it)^q}\, dt, \qquad z \equiv \frac{c^2}{v_t^2}\frac{\omega-\omega_c}{\omega} \ ,$$

$N_\perp \equiv \frac{k_\perp' c}{\omega}$ being the refractive index. The term proportional to $F_{3/2}$ in (2) is due to FLR effects[2] and contributes to the electromagnetic energy balance equation (1) both via the flux of sloshing energy

$$\underline{Q}_s \equiv -\frac{\omega}{8\pi} \frac{\partial \varepsilon_{ij,h}}{\partial \underline{k}'} E_i^* E_j = \frac{1}{2}\frac{\omega_p^2}{\omega_c^2} F_{3/2}' (N_\perp c) \frac{|E_z|^2}{4\pi} (\underline{k}_\perp'/k_\perp') \qquad (3)$$

and the power absorption $\frac{\omega}{4\pi} \underline{E}^* \cdot \underline{\varepsilon}_a \cdot \underline{E} = -\frac{1}{2}\frac{\omega_p^2}{\omega_c^2} N_\perp^2 F_{3/2}'' \omega \frac{|E_z|^2}{4\pi}$, ($F_q' \equiv \mathrm{Re}F_q$ and $F_q'' \equiv \mathrm{Im}F_q$). Together with the Poynting vector

$$\underline{P} \equiv \frac{c}{4\pi} \mathrm{Re}\,(\underline{E}\times\underline{B}^*) = (N_\perp c) \frac{|E_z|^2}{4\pi} (\underline{k}_\perp'/k_\perp') \qquad (4)$$

equation (1) yields the absorption coefficient of the O mode,

$$2k_\perp'' = \frac{1}{2} k_\perp' \frac{\omega_p^2}{\omega_c^2} \frac{(-F_{3/2}'')}{1 + \frac{1}{2}\frac{\omega_p^2}{\omega_c^2} F_{3/2}'} \ , \qquad (5)$$

in agreement with the result obtained by solving the dispersion relation[1] for $|\underline{k}''| < |\underline{k}'|$. Note that for $\omega_p^2 \approx \omega_c^2$ and near the resonance, i.e., $|F_{3/2}| \approx 1$, one has $k_\perp'' \approx k_\perp'$, so that (1) and, as a consequence, (5) reach their validity limit.

X MODE
For perpendicular propagation, the X mode is elliptically polarized in a plane perpendicular to $\underline{B}_o$, i.e., $\underline{E} = \hat{x}E_x + \hat{y}E_y$. By making use of the explicit expressions for ε_{xx}, ε_{yy} and ε_{xy} with corrections of order v_t^2/c^2 included, i.e., taking both FLR effects and relativistic corrections into account[2], one gets for the power absorption

$$\frac{\omega}{4\pi} \underline{E}^* \cdot \underline{\varepsilon}_a \cdot \underline{E} = \frac{\omega}{4\pi} \left(\varepsilon_{5/2}'' |E_x - iE_y|^2 - \lambda \varepsilon_{3/2}'' S_1 + \lambda^2 \varepsilon_{3/2}'' S_2 \right) \ , \qquad (6)$$

where

$$\varepsilon_q = -\frac{1}{2}\frac{\omega_p^2}{\omega_c^2}\frac{c^2}{v_t^2} F_q \ ,$$

$$\lambda = \frac{\omega^2}{\omega_c^2}\frac{v_t^2}{c^2} N_\perp^2 \simeq 2\left(1 - \frac{\omega_p^2}{2\omega_c^2}\right)\frac{v_t^2}{c^2} \ ,$$

$$S_1 \equiv 2|E_x - iE_y|^2 + |E_y|^2 - |E_x|^2 \ ,$$

$$S_2 \equiv \frac{15}{8}|E_x - iE_y|^2 + \frac{5}{4}(|E_y|^2 - |E_x|^2) + \frac{3}{2}|E_y|^2 \ .$$

It appears that the absorption mechanism has to do with both the deviation from circular of the polarization of the mode and the finiteness of the electron Larmor radius. In fact, the first and second term on the right-hand side of (6) are zero in the limit of circular polarization, whereas the second and the third vanish for zero Larmor radius. For the wave amplitudes, $E_x = -(\varepsilon_{xy}/\varepsilon_{xx}) E_y$ holds, so that the mode polarization is given by

$$\frac{E_x - iE_y}{E_y} \simeq iN_\perp^2 \frac{v_t^2}{c^2} \frac{1}{F_{5/2}} \left(\frac{\omega_c^2}{\omega_p^2} - F_{3/2}' \right) \ , \qquad (7)$$

for $|\varepsilon_{5/2}| \gg 1$, which is the case close to resonance for plasma densities and magnetic fields of practical interest, i.e., $\omega_p^2/\omega_c^2 > v_t^2/c^2$. (A noticeable exception to the condition $|\varepsilon_{5/2}| \gg 1$ appears for the runaway electrons of a tokamak for which $|\varepsilon_{5/2}| \ll 1$ so that the tenuous-plasma approximation[3] is appropriate). From (7) it appears that the mode polarization deviates from circular by terms of order v_t^2/c^2, FLR effects, proportional to $F_{3/2}'$, contributing as well as the term, proportional to ω_c^2/ω_p^2, that leads to the anomalous scaling of the wave absorption with respect to density[4]. It is in fact the value of ω_c^2/ω_p^2 which weighs the importance of FLR effects, and neglecting these effects, as usually done, is incorrect for $\omega_p^2 \approx \omega_c^2$. It is interesting to note that $(E_x - iE_y)/E_y \approx (\varepsilon_{3/2}'')^{-1}$, with $\varepsilon_{3/2}''$ ($\approx \varepsilon_{3/2}'$) the anti-Hermitian part of the dielectric tensor to lowest order in v_t^2/c^2. It is just the fact that $|\varepsilon_{3/2}''| \gg 1$ which makes the polarization of the X mode almost circular (in the direction opposite to the gyration of the electrons) and hence the resulting absorption much weaker than that corresponding to the tenuous-plasma limit. This almost circular polarization is also the physical reason for the cancellations found when solving the dispersion relation[2]. Note also that all terms on the right-hand side of (6) are of the same order, viz. $O(v_t^2/c^2)$, and, hence, the FLR terms must be consistently retained. Inserting (7) into (6) yields

$$\frac{\omega}{4\pi} \underline{E}^* \cdot \underline{\varepsilon}_a \cdot \underline{E} = B\alpha^{(o)} (N_\perp c) \frac{|E_y|^2}{4\pi} \ , \qquad (8)$$

with

$$B \equiv \left| 1 - \frac{\omega_p^2}{\omega_c^2} F_{3/2} \right|^2 + 2\frac{\omega_p^2}{\omega_c^2}\frac{F_{3/2}''}{F_{3/2}''}\left[F_{3/2}' - \frac{\omega_p^2}{\omega_c^2} \mathrm{Re}\,(F_{3/2}^* F_{3/2}) \right] + \frac{3}{2}\frac{\omega_p^4}{\omega_c^4}\frac{F_{3/2}''}{F_{5/2}''} \ , \qquad (9)$$

$$\alpha^{(o)} \equiv \sqrt{2}\left(1 - \frac{\omega_p^2}{2\omega_c^2}\right)^{3/2} \frac{\omega_c^2}{\omega_p^2}\frac{v_t^2}{c^2}\frac{(-F_{5/2}'')}{|F_{5/2}|^2}\frac{\omega_c}{c} \ , \qquad (10)$$

Noting that to lowest order in v_t^2/c^2 the flux of electromagnetic energy of the X mode is simply the Poynting vector $(N_\perp c)|E_y|^2/4\pi$, (the flux of sloshing energy is associated with FLR effects and is of order v_t^2/c^2), (1) combined with (8) yields the absorption coefficient

$$2k_\perp'' = B\alpha^{(o)} \qquad (11)$$

in agreement with the result obtained by solving the dispersion relation[2]. In the limit of zero Larmor radius, which according to (9) is appropriate for $\omega_p^2/\omega_c^2 \ll 1$, $B = 1$ and the absorption coefficient reduces to $\alpha^{(o)}$ as given by (10), the result deduced earlier (cf. Ref. 1). The function B has been studied in detail in Ref. 2. Since $B \approx 1$, FLR effects, although modifying the scaling of absorption with plasma density and magnetic field as well as the line profile for $\omega_p \approx \omega_c$, do not change the order of magnitude of the absorption coefficient. Finally, let us note that $k_\perp'' \approx \alpha^{(o)} \sim (\varepsilon_{3/2}'')^{-1}$, i.e., the larger is the anti-Hermitian part of the dielectric tensor the smaller is the absorption coefficient and, consequently, $|\underline{k}''| \ll |\underline{k}'|$ for $\varepsilon_{3/2}'' \gg 1$.

ACKNOWLEDGEMENT
This work was performed under the Euratom-FOM association agreement with financial support from ZWO and Euratom.

REFERENCES
1) M. Bornatici and F. Engelmann, Radio Science 14, 309 (1979) - and references therein.
2) M. Bornatici, F. Engelmann and G. Lister, I.R. 78/047, Instituut voor Plasmafysica, Jutphaas (1978), to be published in Phys. Fluids.
3) G. Bekefi, Radiation Processes in Plasmas, (Wiley, New York, 1966).
4) M. Bornatici and F. Engelmann, Comments Plasma Phys. Cont. Fusion 4, 139 (1979).

*) On leave of absence from the University of Pavia, Italy.

BP14

SPATIAL STRUCTURE OF GYRO-KINETIC MODES IN TOROIDAL GEOMETRY

F. Pegoraro

Scuola Normale Superiore, Pisa, Italy

T.J. Schep

Association Euratom-FOM, FOM-Instituut voor Plasmafysica Rijnhuizen, Jutphaas-Nieuwegein, The Netherlands

Abstract

The spatial structure of modes with high toroidal mode numbers is investigated. Exploiting the radial translational invariance and the poloidal periodicity of the gyro-kinetic and Maxwell equations, the two dimensional mode structure is expressed in terms of a single extended poloidal variable. The dispersion equations for modes with phase velocities larger than the ion thermal velocity are given for a general toroidal geometry. Compressional effects are retained. A new form of the nonadiabatic electron response is discussed in connection with electrostatic drift waves and an asymptotic limit of electromagnetic modes is analyzed.

We consider an axisymmetric toroidal equilibrium configuration described by $\underline{B} = \nabla\zeta \times \nabla\psi + I(\psi)\nabla\zeta$. We use the orthogonal coordinates (ψ,ϑ,ζ) with Jacobian J, where ψ is the poloidal flux function, ϑ the poloidal angle-like variable, and ζ the toroidal angle. Refering to any perturbed quantity $\tilde{\xi}$, we write

$$\tilde{\xi} = \xi(S,\vartheta)\exp -i\left(\omega t - n^{o}\zeta + \int_{o}^{\vartheta} q\,d\vartheta'\right), \qquad (1)$$

where n^{o} is the toroidal mode number, $S = n^{o}(\bar{q}-\bar{q}^{o})$ the short scale radial variable, $\bar{q} = (2\pi)^{-1}\oint q\,d\vartheta$, $q = JB_{\zeta}/R$ and $\bar{q}_{o}$ labels a reference mode rational surface. The mode form (1) is valid in the large n^{o} limit where the equilibrium scale length is long compared to the distance between adjacent mode-rational surfaces. Although $\tilde{\xi}$ is periodic in ϑ, the amplitude $\xi(S,\vartheta)$ is not and must satisfy the constraint $\xi(S,\vartheta+2\pi) = \xi(S,\vartheta)\exp(i2\pi S)$. The components of the wave vector corresponding to the mode form (1) are given to leading order in $1/n^{o}$ by $k_{\chi} = -n^{o}B/(RB_{\vartheta})$, $k_{\psi} = k_{\chi}\hat{k}_{S} = k_{\chi}\hat{s}\left[\vartheta + i\partial\ell n\,\xi/\partial S + (d\bar{q}/d\psi)^{-1}\partial/\partial\psi\int_{o}^{\vartheta} d\vartheta'(q-\bar{q})\right]$ and $k_{\parallel} = i/(BJ)^{-1}\partial\ell n\xi/\partial\vartheta$, where k_{χ} is the component in the magnetic surface and perpendicular to the magnetic field lines and $\hat{s} = (RB_{\vartheta})^{2}B^{-1}d\bar{q}/d\psi$. Thus $k_{\parallel}/k_{\chi,\psi} = O(1/n^{o}q)$ so that these modes have long parallel wavelengths and vary rapidly perpendicularly to the field lines. We consider modes with frequencies below the ion gyrofrequency and obtain the perturbed particle and current densities from the gyro-kinetic equations (GKE). To leading order in $1/(n^{o}q)$ the GKE and Maxwell's equations are a system of coupled differential equations for the perturbed electric potential $\Phi(S,\vartheta)$ and the vector potential $\underline{A}(S,\vartheta)$, of first order in ϑ through $k_{\parallel}$ and of infinite order in S through the operator k_{s}, which enters the GKE to first order through the magnetic drift frequency and to infinite order through the finite ion gyroradius effects. The coefficients in these equations are either periodic in ϑ or depend on the combination $\vartheta+i\partial/\partial S$ and do not depend on S explicitly. Hence, the equations are invariant under continuous translations of S. The poloidal periodicity constraint restricts this invariance to the discrete translations $S \to S+m$, with m integer. Then, the amplitude $\xi(S,\vartheta)$ can be expanded [1] on a basis of radially periodic amplitudes $\xi_{\alpha}(S,\vartheta)$, $-\pi < \alpha \leq \pi$,

$$\xi(S,\vartheta) = \int_{-\pi}^{+\pi} d\alpha/(2\pi)\,C_{\alpha}\xi_{\alpha}(S,\vartheta)\exp(iS\alpha), \qquad (2)$$

where $\xi_{\alpha}(S,\vartheta)$ is periodic in S with period one. Expanding $\xi_{\alpha}(S,\vartheta)$ in a Fourier series and exploiting the poloidal constraint we can write

$$\xi_{\alpha}(S,\vartheta) = \sum_{m=-\infty}^{+\infty}\hat{\xi}_{\alpha}(\vartheta+2\pi m)\exp(-i2\pi mS). \qquad (3)$$

With the expansions (2) and (3) k_{S} becomes $\hat{k}_{S} = \hat{s}\left[(\hat{\vartheta}-\alpha) + (d\bar{q}/d\psi)^{-1}\int_{o}^{\hat{\vartheta}}(q-\bar{q})\,d\hat{\vartheta}'\right]$, where $\hat{\vartheta} = \vartheta + 2\pi m$ is the extended poloidal variable, so that the infinite order differential operators in S are converted into algebraic expressions in $\hat{\vartheta}-\alpha$. The GKE and Maxwell equations become a set of ordinary differential equations in the single variable $\hat{\vartheta}$ on the domain $(-\infty,+\infty)$. All coefficients are either periodic in $\hat{\vartheta}$ or depend on $\hat{\vartheta}-\alpha$ through $\hat{k}_{S}$.

The dispersion equations for modes with phase velocities larger than the ion thermal velocity are a system of two coupled second order differential equations for the electric potential $\hat{\Phi}_{\alpha}(\hat{\vartheta})$ and the potential $\hat{\Psi}_{\alpha}(\hat{\vartheta})$ defined by $(JB)^{-1}\partial\Psi/\partial\vartheta = -i(\omega/c)A_{\parallel}$, and are valid for arbitrary ratios of the thermal ion gyroradius to the perpendicular wavelength. For simplicity we consider the limit of small ion gyroradii (b<1) and take equal temperatures, and obtain [2]

$$0 = \left[1-\frac{\omega_{*}}{\omega_{\alpha}} + \frac{\beta}{4}\left(1-\frac{\omega_{*}^{2}}{\omega_{\alpha}^{2}}(1+\eta)^{2}\right) + \frac{A\,T}{m_{i}\omega_{\alpha}^{2}J}\frac{d}{d\hat{\vartheta}}\frac{1}{JB^{2}}\frac{d}{d\hat{\vartheta}}\right)\left(\hat{\Phi}_{\alpha}+\hat{\Psi}_{\alpha}\right) + \Lambda\left[b+\hat{\varepsilon}\,\frac{\omega_{*}}{\omega_{\alpha}}\right]\hat{\Phi}_{\alpha} + \hat{N}_{\alpha}, \qquad (4)$$

$$\frac{Tc^{2}}{4\omega_{\alpha}^{2}ne^{2}}\frac{1}{J}\frac{d}{d\hat{\vartheta}}\frac{k_{\chi}^{2}(1+k_{s}^{2})}{JB^{2}}\frac{d}{d\hat{\vartheta}}\hat{\Psi}_{\alpha} = A\left[b\hat{\Phi}_{\alpha} + \hat{\varepsilon}\,\frac{\omega_{*}}{\omega_{\alpha}}\left(\hat{\Phi}_{\alpha}+\hat{\Psi}_{\alpha}\right)\right] - 2\hat{\varepsilon}\,\frac{\omega_{*}}{\omega_{\alpha}^{2}}\frac{L_{n}}{L_{p}}\hat{\Psi}_{\alpha}, \qquad (5)$$

where $\omega_{*} = k_{\chi}cT/(eBL_{n})$, $\eta = L_{n}/L_{T}$, $L_{n,T}^{-1} = -[e_{\psi}\cdot\nabla\ell n\,n,T]$, $L_{p}^{-1} = L_{n}^{-1}+L_{T}^{-1}$, $A = 1+(1+\eta)\omega_{*}/\omega_{\alpha}$, $b = \hat{b}(1+\hat{k}_{s}^{2})$, $\hat{b} = k_{\chi}^{2}T/m_{i}\Omega_{i}^{2}$, $\Omega_{i} = eB/m_{i}c$, $\beta = 8\pi p/B^{2}$, $\hat{\varepsilon}(\hat{\vartheta}) = -L_{n}B^{-2}(e_{\psi}-\hat{k}_{s}e_{\chi})\cdot\nabla(B^{2}+8\pi p)$ represents the curvature of the magnetic field lines and $\hat{N}_{\alpha} = \hat{N}_{\alpha}(\hat{\Phi}_{\alpha}+\hat{\Psi}_{\alpha})$ is the non-adiabatic response of trapped and circulating electrons. The term proportional to β in Eq.(4) represents compressional effects due to the perturbed parallel magnetic field and the non-curvature part of the magnetic drift frequency. Two quadratic forms are obtained by subtracting $\hat{\Psi}_{\alpha}$ or $\hat{\Psi}_{\alpha}^{*}$ times Eq.(5) from $(\hat{\Phi}_{\alpha}+\hat{\Psi}_{\alpha})$ or $(\hat{\Phi}_{\alpha}+\hat{\Psi}_{\alpha})^{*}$ times Eq.(4), respectively and by integrating over $\hat{\vartheta}$. The first is variational but generally complex. The second is related to the usual electromagnetic Lagrangian and is variational for real frequencies.

The dispersion equations are invariant under the transformation $(\hat{\vartheta},\alpha)\to(-\hat{\vartheta},-\alpha)$, which in terms of the amplitudes $\xi_{\alpha}(S,\vartheta)$ is $(\vartheta,S,\alpha) \to (-\vartheta,-S,-\alpha)$ and implies $\omega_{\alpha} = \omega_{-\alpha}$. No symmetry relation involving only ϑ or only S exists. This invariance derives from the general properties of equilibria that are even in ϑ and from the additional symmetry in the gyro-kinetic ordering.

The plane slab model is obtained in the limit of zero curvature, keeping the connection length finite and neglecting trapped particles. In this model the α-modes are degenerate. In this limit, except for the compressional and η terms, Eqs.(4) and (5) are equivalent to the Fourier transform of the equation given in Ref.(3). For modes that are localized on a poloidal length scale $\Delta\hat{\vartheta} < \bar{\omega}_{te}/\omega = v_{the}/(qR\omega)$, taking $\eta = 0$, $\hat{N}_{\alpha}$ can be approximated by

$$\hat{N}_{\alpha} = \frac{i}{\pi^{\frac{1}{2}}}\frac{\omega}{\bar{\omega}_{te}}\left[1-\frac{\omega_{*}}{\omega}\right]\int_{-\infty}^{+\infty} d\hat{\vartheta}'\left[\hat{\Phi}_{\alpha}(\hat{\vartheta}')+\hat{\Psi}_{\alpha}(\hat{\vartheta}')\right]\left[-\ell n\left[\frac{\omega}{\bar{\omega}_{te}}|\hat{\vartheta}-\hat{\vartheta}'|\right]-\frac{3}{2}\gamma+i\frac{\pi}{2}\right]. \qquad (6)$$

The $\pi/2$ arises from non resonant electrons, whereas Euler's constant γ and the logarithm originate from resonant ones. The contribution of the latter is very sensitive to the structure of the mode around $\hat{\vartheta} = \alpha$. To illustrate this we consider electrostatic drift waves in the limit $\beta \to 0$. The complex variational quadratic form, using Eq.(6) and the trial function $\hat{\Phi}_{\alpha} = \exp i\sigma(\hat{\vartheta}-\alpha)^{2}/2$ with $\mathrm{Im}\,\sigma > 0$ for the lowest order even eigenmode, yields $\lambda + (i/2)\left[\mu^{2}\sigma^{-1}+\sigma\right] + iC(-i\sigma)^{-\frac{1}{2}}\left(-2\gamma + i\pi/2 + \ell n(\bar{\omega}_{te}^{2}\omega^{-2}\sigma)\right) = 0$. Here, $\lambda = 2\omega^{2}/\bar{\omega}_{ti}^{2}\left[\hat{b} + (1-\omega_{*}/\omega)/A\right]$ with $\bar{\omega}_{ti} = v_{thi}/qR$, $\mu = (\omega/\bar{\omega}_{ti})\hat{s}(2\hat{b})^{\frac{1}{2}}$ and $C = 2\omega^{3}/(\bar{\omega}_{te}\bar{\omega}_{ti}^{2}A)\left[1-\omega_{*}/\omega\right]$. Except for a small contribution, this form is equivalent to the one given in Ref.(4). In the same way, with the trial function $\hat{\Phi}_{\alpha} = (\hat{\vartheta}-\alpha)\exp i\sigma(\hat{\vartheta}-\alpha)^{2}/2$, we obtain $\lambda + (3i/2)(\mu^{2}\sigma^{-1}+\sigma) + 2iC(-i\sigma)^{-\frac{1}{2}} = 0$ for the lowest order odd mode. The quadratic forms for even and odd modes given above can be used to determine σ and the frequency variationally [4].

The asymptotic solutions of Eqs.(4) and (5) with $k_{\parallel} \to 0$ for $|\hat{\vartheta}| \to \infty$ correspond to drift-Alvén waves with frequencies such that $[1-\omega_{*}/\omega] < \hat{b}\hat{A}s^{2}(\hat{\vartheta}-\alpha)^{2}$. Disregarding $\hat{N}_{\alpha}$ for $1 < \hat{\vartheta} < \bar{\omega}_{te}/\omega$ as a first approximation, the asymptotic solutions are $\hat{\Psi}_{\alpha} \sim (\hat{\vartheta}-\alpha)^{-\rho}$ and $\hat{\Phi}_{\alpha} \sim (\hat{\vartheta}-\alpha)^{-\rho-2}$, where $\rho \simeq 1-\varepsilon_{s}^{-2}(\omega/2\omega_{*})^{2}(1-\omega_{*}/\omega)$, $\varepsilon_{s} = \hat{s}L_{n}/qR$, and compressional effects have been neglected. The amplitude $\hat{\Psi}_{\alpha}(S,\vartheta)$ together with $A_{\parallel\alpha}$, and the perturbed fields and current $B_{\psi\alpha} = ik_{\chi}A_{\parallel\alpha}$ and $J_{\parallel\alpha} = (c/4\pi)k_{\chi}^{2}(1+k_{s}^{2})A_{\parallel\alpha}$, are then calculated from Eq.(3). For $\rho \simeq 1$, odd modes have current sheaths on mode rational surfaces while $J_{\parallel\alpha}$ for even modes has simple poles. This behaviour is a consequence of the contribution of the higher m-terms in the series (3). However, the approximation breaks down because $k_{\parallel} \sim \hat{\vartheta}^{-1}$ so that for higher m-numbers the phase velocity approaches the electron thermal velocity and $\hat{N}_{\alpha}$ must be retained in the evaluation of the asymptotic limit.

This work was performed under the Euratom-FOM association agreement with financial support from ZWO, Euratom and from the Scuola Normale Superiore, Pisa, Italy.

REFERENCES

1) F.Pegoraro and T.J.Schep, Rijnhuizen Report 78-116 Fom-Instituut voor Plasma fysica, Rijnhuizen, Jutphaas, The Netherlands.

2) F.Pegoraro and T.J.Schep, Rijnhuizen Report 79-119 Fom-Instituut voor Plasma fysica, Rijnhuizen, Jutphaas, The Netherlands.

3) P.J.Catto, A.M.El Nadi, C.S.Liu and M.N.Rosenbluth, Nucl.Fus. 14 (1974), 405.

4) D.W.Ross and S.M.Mahajan, Phys.Rev.Lett. 40 (1978), 324.

BP15

ION-ACOUSTIC SOLITONS WITH A TEMPERATURE GRADIENT.

by

W. Malfliet

Physics Department, University of Antwerp, U.I.A.,
B-2610 Wilrijk-Antwerp, Belgium.

Abstract.
With the aid of the reductive perturbation (RPT) methods, the nonlinear propagation of warm ion-acoustic waves is analysed in the case of a small temperature gradient. When the temperature profile is linearly space-dependent or arbitrarily time-dependent we are able to find again KdV-like equations.

The nonlinear propagation of an ion acoustic wave in a collisionless plasma with a temperature gradient is investigated.
Then, in one dimension, the normalized set of equations can be written as

$$\frac{\partial n}{\partial t} + \frac{\partial}{\partial x} nu = o \qquad \text{(continuity eq. for the ions)} \tag{1}$$

$$\frac{\partial u}{\partial t} + u \frac{\partial u}{\partial x} = - \frac{\partial \varphi}{\partial x} - \frac{\gamma_i}{n} \sigma \frac{\partial n}{\partial x} - \gamma_i \frac{\partial \sigma}{\partial x} \tag{2}$$

(eq. of motion for the ions)

with $\sigma = \frac{T_i}{T_e}$,

$$\frac{\partial^2 \varphi}{\partial x^2} = e^{\varphi} - n \qquad \text{(Poisson's eq.)}. \tag{3}$$

It seems appropriate to start first with the case of a fixed ion temperature.

$$\text{I.} \qquad \sigma = \frac{T_i}{T_e} = \sigma_o = \text{constant}. \tag{4}$$

Then the last term on the r.h.s. of eq. (2) disappears. If we introduce new space-time variables

$$\xi = \varepsilon^{1/2}(x - \lambda_o t) \quad \text{and} \quad \tau = \varepsilon^{3/2} t \tag{5}$$

$$\text{with } \lambda_o^2 = 1 + \sigma_o \gamma_i \tag{6}$$

and if we moreover expand the relevant physical quantities:

$$n = 1 + \varepsilon n_1 + \varepsilon^2 n_2 + \ldots \tag{7a}$$
$$\varphi = \varepsilon \varphi_1 + \varepsilon^2 \varphi_2 + \ldots \tag{7b}$$
$$u = \varepsilon u_1 + \varepsilon^2 u_2 + \ldots \tag{7c}$$

we arrive in first-order at the relations $\varphi_1 = n_1$ and $\lambda_o n_1 = u_1$ and in second-order at the KdV equation

$$\frac{\partial \varphi_1}{\partial \tau} + \lambda_o \varphi_1 \frac{\partial \varphi_1}{\partial \xi} + \frac{1}{2\lambda_o} \frac{\partial^3 \varphi_1}{\partial \xi^3} = 0 \quad . \tag{8}$$

This analysis is known as the RPT-method[1]. The one-soliton solutions of eq. (8) reads like

$$\varphi_1 = \frac{3c}{2^{1/3} \lambda_o^{4/3}} \operatorname{sech}^2 \left[\frac{1}{2} \sqrt{c} \left((2\lambda_o)^{1/3} \xi - c\tau \right) \right] \quad . \tag{9}$$

If we should increase the ion temperature σ, for instance

$$\sigma = \sigma_o + \delta \quad (0 < \delta \ll 1), \tag{10}$$

we obtain the following result for the one-soliton solution:

$$\varphi_1 \cong \frac{3c}{2^{1/3} \lambda_o^{1/3} (1 + \frac{2}{3}\delta b)} \operatorname{sech}^2 \left[\frac{1}{2} \sqrt{c} \left((2\lambda_o)^{1/3} (1 + \frac{1}{6}\delta b)(\xi - \frac{\delta}{\varepsilon} \frac{\gamma_i}{2\lambda_o^2} \tau) - c\tau \right) \right] \tag{11}$$

where $b \equiv \frac{\gamma_i}{\lambda_o^2}$.

Hence, a higher ion temperature reveals the following properties: it lowers the amplitude of the corresponding soliton and it moves manifestly faster than the colder one.

$$\text{II} \qquad \sigma = \frac{T_i}{T_e} = \sigma_o + \varepsilon^3 \frac{x}{a} \qquad \text{for} \quad o \leqslant x \leqslant a \ . \tag{12}$$

In this case we have to take into account the last term of eq. (2). If we use again the RPT-method, we get the following KdV equation with a correction term.

$$\frac{\partial \varphi_1}{\partial \tau} + \lambda_o \varphi_1 \frac{\partial \varphi_1}{\partial \xi^1} + \frac{1}{2\lambda_o} \frac{\partial^3 \varphi_1}{\partial \xi^{1\,3}} = - \varepsilon^{1/2} \frac{\gamma_i}{2a\lambda_o} \tag{13}$$

$$\text{with } \xi^1 = \xi - \frac{\gamma_i}{4a} \varepsilon^{1/2} \tau^2 \text{ and } - \frac{\lambda_o \tau}{\varepsilon} \leqslant \xi \leqslant - \frac{\lambda_o \tau}{\varepsilon} + a \varepsilon^{1/2} \ . \tag{14}$$

A solution of this equation can be found with the aid of Miura's transformation[2]. The result is

$$\varphi_1 = \frac{4c}{2^{1/3} \lambda_o^{4/3}} \operatorname{sech}^2 \left[\frac{1}{2} \sqrt{c} \left((2\lambda_o)^{1/3} (\xi + \lambda_o c_1 \tau + \lambda_o c) - c\tau \right) \right] - 2C\tau - c_1 \tag{15}$$

$$\text{where } C = \frac{\varepsilon^{1/2} \gamma_i}{4\lambda_o a} \ , \quad c_1 = \frac{\varepsilon^{3/2} \gamma_i}{2a\lambda_o^2} \xi \text{ and } c = \frac{\varepsilon^{5/2} \gamma_i}{2a\lambda_o^3} \xi^2 \ .$$

The constants c_1 and c_2 are determined by the condition that for $x = o$ (or $\xi = - \frac{\lambda_o \tau}{\varepsilon}$) the solution (15) reduces to the soliton (9). We remark that the argument of the sech^2 term consists of a nonlinear combination of ξ and τ variables.
Further, the term $-2C\tau - c_1$ (proportional to x) causes an unstable situation and, if the temperature would have no upper limit, our perturbation analysis would break down.
At $x = a$, the solution is related to that one of the region $x \geqslant a$ where $\sigma = \sigma_o + \varepsilon^3$ (i.e. the eq. (11) with $\delta = \varepsilon^3$).

$$\text{III} \qquad \sigma = \frac{T_i}{T_e} = \sigma_o + \varepsilon f(t). \tag{16}$$

For this case, the last term in eq. (2) cancels. By changing the variable ξ into

$$\xi_1 = \xi - \int_o^\tau \frac{\gamma_i}{2\lambda_o} f(\tau^1)\, d\tau^1. \tag{17}$$

We arrive again at a KdV equation with ξ_1 and τ as the independent variables.
Clearly, if $f > o$ ($f < o$) the corresponding soliton moves faster (slower), but with the same amplitude as in the case where $f = o$.
We remark also that this analysis can be formalised by an extension of the RPT method, if we introduce the following variables[3]

$$\xi = \varepsilon^{1/2} (x - \lambda\,(x,t)\, t) \tag{18a}$$

$$\text{and} \qquad \varepsilon = \varepsilon^{3/2} t \ , \tag{18b}$$

$$\text{where} \qquad \lambda = \lambda_o + \varepsilon \lambda_1\,(x,t) + \varepsilon^2 \lambda_2 + \ldots \tag{18c}$$

References:

1. a) H. Washimi and T. Tanuitti, Phys. Rev. Letters 17 (1966) 996.
   b) Y. Ichikawa, T. Mitsuhashi and K. Konno, J. Phys. Soc. Japan 41 (1976) 1382.
2. R.M. Miura, J. Math. Phys. 9 (1968) 1202.
3. S. Caenepeel, private communication.

BP16

CASCADE SATURATION OF PARAMETRIC INSTABILITIES IN PLASMA INDUCED BY FINITE-BANDWIDTH DRIVER PUMP

V. STEFAN

Boris Kidrič Institute of Nuclear Sciences-Vinča,

Beograd, Yugoslavia

The nonlinear saturation of parametrically turbulent plasma state, initiated by nonmonochromatic driver pump, is considered. Parametrically excited electron Langmuir wave is saturated by secondary decays to new electron Langmuir wave and ion-sound wave, transfering, in that way, energy from the domain of primary excitation to the domain with lower frequencies. It is shown that the excistence of a finite-bandwidth pump leads in nonlinear phase of evolution of parametric instabilities, to decreasing of electron Langmuir and ion-sound oscillation energy and also of effective collision frequency (turbulent dissipation frequency).

The excitation of parametrically unstable plasma oscilations by intense electromagnetic radiation [1] leads to variety of nonlinear phenomena, observed experimentally. Linear theory [2-4] of parametric decay instability in plasma interacting with the nonmonochromatic pump wave $E(t) = E_0(t)\exp(-i\omega_0 t) + c.c.$ with descrete frequency spectrum

$$E_0(t) = E_{00}\sum_{n=-\omega}^{+\omega} f_n \exp(-in\Omega t)\ ;\ E_{00} = \max E_0(t) \qquad (1)$$

shows the possibility for excitations of electron Langmuir and ion-sound waves with the frequencies ω_{Le} and ω_S and decrements $\tilde{\gamma}$ and γ_S, respectively, in the case when modulation frequency satisfies $\Omega \ll \omega_S$. Let us consider secondary decays $(\ell \to \ell' + S)$ leading to the cascade transfer of Langmuir wave energy from the domain of primary excitations to the domain where frequencies decrease, and restrict ourselves to the domain of high enough modulation frequency Ω $(\Omega > \gamma)$ where γ is parametric increment in the case of monochromatic driver pump. In the opposite case instabilities reach nonlinear phase of evolution during one modulation period, making possible use of monochromatic driver pump parameteric theory. This mechanism was first used in [5] for consideration of isotermal plasma.

For the description of plasma upon the action of the external finite-bandwidth driver pump $E(t)$, a system of hydrodinamical equation averaged over the frequency ω_{Le} (see for example 5)

$$i\frac{\partial E}{\partial t} + \frac{3}{2}\omega_{Le}r_{De}^2\frac{\partial^2 E}{\partial x^2} = \frac{\omega_{Le}}{2n_0}\delta n\left[E + E_0(t)\exp(-i\Delta\omega t)\right] \qquad (2)$$

$$\frac{\partial^2 \delta n}{\partial t^2} - V_S^2\frac{\partial^2 \delta n}{\partial x^2} = \frac{1}{16\pi m_i}\frac{\partial^2}{\partial x^2}\left[|E|^2 + E^* E_0\exp(i\Delta\omega t) + EE_0^*\exp(i\Delta\omega t)\right]$$

is used. Here V_S is ion-sound speed, r_{De} -electron Debye radius, m_i -mass of ions and n_0 nonperturbed plasma density. For the effective collision frequency in the case of weak linear damping rate of electron Langmuir waves $\gamma_S > \gamma > \tilde{\gamma}$, $\Omega > \gamma$ and for large enough spectral width ($\delta\omega > \gamma_S$, Ω, $\tilde{\gamma}$) of driver pump

$$\nu_{eff} = \frac{\omega_{Le}\omega_S}{16\gamma_S}\frac{E_0^2}{4\pi n_0 T_e}\left(\frac{\gamma_S}{\delta\omega}\right)\frac{\gamma_S}{\Omega}\,d\|^2\,\frac{\pi\gamma_S}{\Omega} \qquad (3)$$

is obtained. Factor $\left(\gamma_S/\delta\omega\right)$ in the right-hand side of (3) shows significant decreasing of nonlinear dissipation rate for a finite-bandwidth driver pump. In the case when $\Omega \gg \gamma_S$ is valid for

$$\nu_{eff} = \frac{\omega_S\omega_{Le}}{16\gamma_S}\frac{1}{4\pi n_0 T_e}\frac{\sum_{n=-\omega}^{+\omega}|E_{00}f_n|^4}{\sum_{n=-\omega}^{+\omega}|E_{00}f_n|^2} \qquad (4)$$

is obtained. If modulation frequency Ω is small compared to the linear damping rate of ion-sound wave γ_S $(\Omega \ll \gamma_S)$ spectral distribution of driver pump could be considered as continuous. For the effective colusion frequency in this case,

$$\nu_{eff} \sim \frac{\omega_{Le}\omega_S}{16\delta\omega}\frac{E_0^2}{4\pi n_0 T_e} \qquad (5)$$

is obtained. The effective collision frequency given in (5) is of the order of parametric increment in the case of nonmonochromatic driver pump [2].

If the intensity of driver pump is assumed to be strong enough so that $\gamma > \gamma_S > \tilde{\gamma}$ is valid, every sattelite of electron Langmuir wave has finite spectral width and every line from spectral expansion (1) could be considered as separate driver pump. In this case for

$$\nu_{eff} \sim \gamma\frac{\tau}{T} \qquad (6)$$

is obtained. Here τ and T are rectangular pulse duration and repetition period, respectively. On the upper limit $\tau\gamma/T \sim (\gamma\omega_s)^{1/3}$ of the applicability of (6), defined by the stability of Langmuire sattelites with respect to the aperiodic excitations, ν_{eff} exceeds electron-ion collision frequency ν_{ei}, ω/γ times, the same as in the case of monochromatic pump wave.

REFERENCES

1. V.P.Silin, "Parametric Effect of High Power Radiation on Plasma", Nauka, Moscow, (1973)
2. V.V.Pustovalov, V.P.Silin, D.A.Chernikov, Quantum Electronics 5, No 9,(1978)
3. Yu.M.Aliev, O.M.Gradov, D.Zünder, Beträge aus der Plasma Physik, B.17, H.6, 353 (1977)
4. Yu.M.Aliev, A.A.Chernikov, O.M.Gradov, V.V.Pustovalov, V.P.Silin, V.Stefan, Eight European Conference on Controlled Fusion and Plasma Physics, C.P., v.1, p.146 (1977)
5. W.L.Kruer, E.J.Valeo, Phys. Fluids, 16, 675,(1974)
6. V.E.Zaharov, Zh.Eksp. Teor. Fiz. 62, 1745, (1972)

BP17

REDUCTION AND INVERSION OF PARTICLE TRANSPORT DUE TO PLASMA ROTATION AND ION-NEUTRAL FRICTION

D.C. Schram, B.F.M. Pots,
Physics Department, Eindhoven University of Technology, The Netherlands
and P.A.E.M. Janssen,
Department of Electrical Engineering, Eindhoven University of Technology, The Netherlands.

1. Introduction. In the past several studies have been devoted to the measurement and calculation of pressure enhancement in magnetized arcs with Hall parameter $\Omega_e\tau_e >> 1$. In several of these studies the measured pressure enhancement was partially ascribed to the Nernst-effect. Originally, the effects of ion rotation and friction on the momentum balance, particle transport and pressure enhancement were ignored. Klüber [1] in his study on the potential distribution in symmetrical arcs and later Schüller [2] in his study on toroidal arcs did include these effects. This paper concerns an analysis of the momentum equations of electrons and ions in a rotating plasma volume, including ion viscosity and ion-neutral friction. Moreover, anomalous diffusion due to unstable flute waves is considered. Results are compared with experiments.

2. Theory. In magnetized arcs the radially directed electric field can be of the order $E_r = kT_e/e\Lambda$, where Λ is the radial scale length. This field may result in large rotational velocities of the ions and electrons, approaching the ion thermal velocity $v_{thi} = \sqrt{kT_i/M_i}$. Then, the effect of rotation in the contributions from inertia, ion viscosity, ion-neutral friction and finite source term to the ion momentum balance cannot be neglected. A systematic ordering of the momentum equations with small parameters $(\Omega_e\tau_e)^{-1}$, Λ/L (L is the axial scale length), and λ_{ii}/Λ yields for $\Omega_i\tau_i < 1$ the following expression for the diffusion flux :

$$n_e w_{ri} = -D^{total}\frac{\partial n_e}{\partial r} = \frac{1}{\Omega_e\tau_e eB_z}\left(1+\frac{1}{\Omega_i r}\frac{\partial}{\partial r}(rw_{\theta i})\right)\cdot\Big[-$$

$$\frac{\partial(p_e+p_i)}{\partial r} + (\nabla\cdot\underline{\pi}_i)_r - m_i n_e\frac{w_{\theta i}^2}{r} + j_z B_\theta - \frac{3}{2}\frac{kT_e}{\partial r}\Big] + \cdot$$

$$\Omega_e\tau_e\left[-(\nabla\cdot\underline{\pi}_i)_\theta + (\underline{R}_{ia})_\theta + (\underline{S}_i)_\theta\right]\Big] \qquad (1).$$

In the experimental case considered we may neglect the pinch term and ion terms in the first part of the right hand-side of equation (1). Since also $\frac{1}{2T_e}\frac{\partial T_e}{\partial r} << \frac{1}{n_e}\frac{\partial n_e}{\partial r}$, the first term between square brackets leads to the the classical contribution $-D^{class}\frac{\partial n_e}{\partial r}$, where the classical diffusion coefficient is $D^{class} = \frac{1}{\Omega_e\tau_e}\frac{kT_e}{eB_z}$.

The second term of nw_{ri}, which we call "rotational" diffusion, may be important as it is multiplied by $\Omega_e\tau_e$. It contains contributions from ion viscosity $(\nabla\cdot\underline{\pi}_i)_\theta$, ion neutral friction $(\underline{R}_{ia})_\theta$ and momentum loss due to a finite source term $(\underline{S}_i)_\theta$.

The direction of the "rotational part, depends on the sign of $w_{\theta i}$; if it is positive ($E_r<0$) it is directed inward and extra confinement occurs; if it is negative extra diffusion results.

The pressure enhancement can be calculated from equation (1). We can deduce that i-a friction is more important than the Nernst effect if :

$$\frac{n_a}{n_e} \gtrsim 3\times 10^{-4}\frac{1}{T_e^{\frac{1}{2}}\{eV\}T_i^{\frac{1}{2}}\{eV\}B_z\Lambda}$$

We note, that for 1 torr pressure arcs this is usually the case.

3. Experiment procedure and results. We investigated the transport in the argon plasma of a hollow cathode discharge in an axially directed magnetic field B_z; n_e and T_e were measured by Thomson scattering, the neutral density from ArI and ArII lines and Collisional Radiative Models and subsequent calibration by the relation p_a=constant for low electron density conditions [3]; this neutral density is consistent with the classical ion energy balance.

The particle flux was determined from the continuity equation for ions

$$n_e w_{ri} = \frac{1}{r}\int_0^r n_e n_a \langle\sigma v_e\rangle_{ion}\, r'\, dr' = -D^{meas}\frac{\partial n_e}{\partial r}.$$

In figure 1 the measured diffraction coefficient is compared with the classical diffusion coefficient. For low values of $\Omega_e\tau_e$ we observe indeed a large reduction of transport compared to classical diffusion. This reduction can be explained by the rotational confinement, which for low values of $\Omega_e\tau_e$ is mainly due to the i-a friction and for somewhat larger values due to ion viscosity. This is equivalent to the conclusion that these effects contribute to the pressure enhancement, more than the Nernst effect. The effect of i-a friction may be even larger for higher pressure arcs.

For larger values of $\Omega_e\tau_e$, the rotational part is expected to become so strong that even an inward flux is expected; however, the experiment shows an increase of the D^{meas}. In reference [4] this was ascribed to drift waves, the levels of which are in the order of maximal a few %. Besides drift waves also rotational instabilities are present in all but four conditions, the level is about 15%. In the next section we indicate which anomalous diffusion contribution follows from these instabilities.

4. Anomalous diffusion. In combination with a radial density gradient, the ExB drift drives flute waves unstable, giving large amplitude, low frequency oscillations in a rotating plasma column. In the presence of these low frequency oscillations enhanced transport is possible. The dominant contribution to this "turbulent" transport stems from the average of the ExB drift.

In a hollow cathode discharge the most unstable low frequency wave has mode number m=1, and if this mode is only taken into account the following expression for the total radial plasma transport results :

$$n\, w_{ri} = \langle nw_{ri}\rangle_{eq} - D_w\frac{\partial n_e}{\partial r},\quad D_w = \alpha\gamma\left(\frac{\tilde{n}_e}{n_e}\right)^2 \qquad (3)$$

where γ is the growth rate, $\tilde{n}_e$ is a measure for the amplitude of the density oscillation, and α a geometrical factor. The radial transport in equilibrium, given by $\langle nw_{ri}\rangle_{eq}$, has been discussed in the previous section.

The saturation value of the m=1 mode in a collisionless plasma is given in Ref. [5], and according to Ref. [6], for flute waves the saturation is not affected by collisions. Inserting this in eq. (3) we obtain for D_w on the axis

$$D_w = \frac{5\sqrt{2}}{8}\Delta^3\left(\frac{a}{\Lambda}\right)^2\frac{kT_i}{eB} \qquad (4)$$

where Δ is the ratio of growthrate γ to the oscillation frequency ω and a is the plasma radius. To appreciate the effect of the enhanced diffusion we added in Fig. 1 a plot of D_w/D^{class} versus the Hall parameter. For the unknown parameter Δ we have taken Δ=0.20, resulting in a relative fluctuation level of about 20%, hence a reasonable agreement between theory and experiment is obtained.

5. Conclusions and implications. We have shown that for low values of $\Omega_e\tau_e$ rotational confinement is important. For larger values of $\Omega_e\tau_e$ we find an anomalous diffusion which can be explained in terms of transport due to the rotational instability.

Though in Tokamaks the plasma is much more collisionless still in the outer layers the rotational contribution may be significant. Since here $\Omega_i\tau_i >> 1$, ion viscosity is unimportant; the dominant contribution comes from the source term [7]:

$$n\, w_{ri}^{rot} = (1+2q^2)\frac{n_i m_i w_{\theta i} \nu_{ion}}{eB_z} \qquad (5)$$

The potential is again of the order T_e/Λ and negative in the centre, though slightly positive in the limiter shadow. This may lead to rotational velocities in the outer layer of a few times 10^4 m/s, in the order of the local ion thermal velocity. For neutral densities larger than $10^{17}m^{-3}$, we get an inwardly directed radial velocity of about 10 m/s, which is of the same order as the observed inward velocities.

Acknowledgement. This work was partly supported by the Stichting FOM.

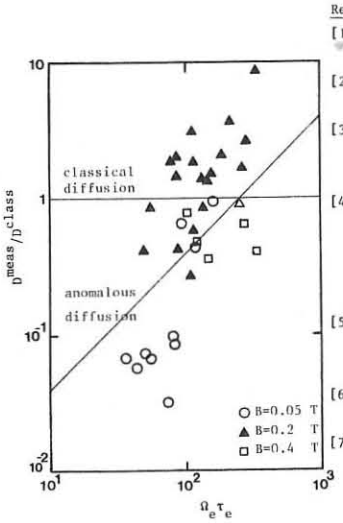

References

[1] O. Klüber, Z. Naturforsch., 25a (1970) 1583.
[2] F.C. Schüller, thesis, University of Utrecht, 1974.
[3] B.F.M. Pots, thesis, Eindhoven University of Technology, 1979, to be published.
[4] D.C. Schram, B.F.M. Pots and J.J.A.M. van der Mullen, Proc. 14th ICPIG, Grenoble, 1979; J.J.A.M. van der Mullen, B.F.M. Pots, D.C. Schram, to be published.
[5] P. Janssen, this conference; P. Janssen, thesis, Eindhoven University of Technology, 1979.
[6] A.M. Sleeper and J. Weinstock, Phys. Fluids 15 (1972), 1507.
[7] A. Boozer, Physics Fluids, 19 (1976) 149.

BP18

POTENTIAL SMALL-SCALE INSTABILITIES OF INHOMOGENEOUS PLASMA IN CROSSED ELECTRIC AND MAGNETIC FIELDS.

Yu.A.Kirochkin, A.G.Pokroyev, K.N.Stepanov.
Physical-Technical Institute of the Ukrainian Academy of Sciences, Kharkov, USSR.

Abstract. The effect of inhomogeneity of particle drift velocity in crossed fields and of finiteness of their Larmor radius on inhomogeneous plasma instabilities is considered.

Introduction. Crossed electric and magnetic fields are inherent to many thermonuclear devices : surface magnetic confinement systems, in particular, electromagnetic trap, theta-pinches, adiabatic traps with radial electric field, etc.

Transverse current which is due to the electric drift is the cause of a series of small-scale plasma instabilities in such systems [1-4]. The present paper shows that the inhomogeneity of the electric drift velocity $V_E = -c(E/B)$ essentially influences the cyclotron and ion-sound plasma instabilities.

Steady state. Consider flat-layer plasma in weakly inhomogeneous $\vec{E}$ and $\vec{B}$ fields. In such fields a charged particle describes an ellipse with the modified cyclotron frequency $\Omega = \omega_B[1+(1/\omega_B)(dV_E/dx)]^{1/2}$. The ellipse has $\rho_x = V_\perp/|\Omega|$ and $\rho_y = |\omega_B/\Omega|\rho_x$ half-axes and it drifts cross to $\vec{E}$ and $\vec{B}$ with a velocity being the sum of the velocities of electric V_E and modified magnetic V_M drifts, where $V_M = (\omega_B/2\Omega^2)V_\perp^2 \varkappa_\Omega$ $\varkappa_A = d\ln A/dx$, $V_\perp$ is oscillating velocity amplitude. (Note that $V_M \neq 0$ even for a homogeneous magnetic field if $d^2E/dx^2 \neq 0$. This fact for a weak E case is noted in papers [5,6].)

The distribution over $V_\perp$ and $V_\parallel$ is considered locally Maxwellian with the temperature Θ .

Dispersion equation. For perturbations $\sim \exp(i\int\kappa_x dx + i\kappa_y y)\cdot \exp(-i\omega t)$ in the local approximation the dispersion equation is $1+\delta\varepsilon_e+\delta\varepsilon_i=0$ where

$$\delta\varepsilon_e = (\omega_p/\kappa_\perp v_T)^2\cdot\left[1+i\sqrt{\pi}(\omega'-\hat{\omega}^*)(1/\sqrt{2}\,\kappa_\perp v_T)\cdot\sum_{s=-\infty}^{\infty}\Phi_s\right], \qquad (1)$$

$\omega' = \omega - \kappa_y V_E$, $\kappa_\perp^2 = \kappa_x^2 + (\omega_B/\Omega)^2\kappa_y^2$, $\hat{\omega}^* = \kappa_y v_T^2(\omega_n/\Omega^2)(\varkappa_n + \varkappa_\Theta\Theta\frac{\partial}{\partial\Theta})$.

In the short wavelength limit ($\kappa_\perp r_L \equiv \kappa_\perp v_T/|\omega_B| \gg 1$) if $|dV_E/dx| \ll |\omega_B|$ we have

$$\Phi_s = i(\sqrt{2\pi}\,\kappa_\perp r_L\zeta)\cdot\sum_{n=-\infty}^{\infty}(-1)^n J_n(a_s)\,\zeta_s^{-(n+\frac{1}{2})}\,e^{\zeta_s}\cdot\Gamma\left(n+\tfrac{1}{2},\zeta_s\right) \qquad (2)$$

where

$$\zeta = \kappa_y r_L \varkappa_B/\sqrt{2}\,\kappa_\perp\,,\quad \zeta_s = -(a_s+z_s/\zeta)\,,\quad z_s = (\omega'-s\omega_B)/\sqrt{2}\,\kappa_\perp v_T,$$

$$a_s = (\kappa_s\kappa_x/\sqrt{2}\,\kappa_\perp^2\zeta)^2\,,\quad \kappa_s = (\kappa_y/\omega_B)(dV_E/dx) + s\varkappa_B\,,$$

$J_n(a)$ is the Bessel function, $\Gamma(n+\frac{1}{2},\zeta)$ is the incomplete gamma function. The validity conditions of the local approximation have the form

$$|d\kappa_x/dx| \ll \kappa_x^2\,,\quad |\kappa_x| \gg |\varkappa_A|\,,\quad \frac{v_\perp^2}{v_T^2}r_L^2|d\kappa_x/dx| \ll 1\,. \qquad (3)$$

If $(\kappa_y/\omega_B)(dV_E/dx) \gg s\varkappa_B$, $|z_s/\zeta| \ll 1$ and $|a_s| = |a| \ll 1$, then retaining in the sum (1) only resonant term with $s=n$ gives as a result

$$\delta\varepsilon_e = (\omega_p/\kappa v_T)^2\cdot\left[1+i(\omega'-\omega^*)/2\kappa_\perp r_L\sqrt{\kappa_y\bar{V}_M(\omega'-n\omega_B-\Omega^*)}\right] \qquad (4)$$

where $\omega^* = \kappa_y v_T r_L(\varkappa_n - \varkappa_\Theta)$, $\bar{V}_M = v_T^2\varkappa_B/2\omega_B$,

$$\Omega^* = -(\kappa_y\kappa_x^2/2\kappa_\perp^2\varkappa_B\omega_B)(dV_E/dx)^2.$$

The feature of this paper in contrast to papers [1-4, 7-8] is the presence in resonant denominators of the expression for the perturbed distribution function, $\omega-\omega_{res}$, the terms which are due to the Doppler shift because of particle drift velocities V_E and V_M as well as the terms which are due to V_E and ω_B inhomogeneities: $\omega_{res} = \kappa_y V_E + n\omega_B + \kappa_y\bar{V}_M\cdot V_\perp^2/v_{Te}^2 + ((\kappa_y/\omega_B)(dV_E/dx) + n\varkappa_B)V_y$. These terms lead to appearance of the frequency Ω^* in eq.(4).

Results. In highly inhomogeneous plasmas ($r_{Li} \gg L_A \gg r_{Le}$, $L_A = 1/|\varkappa_A|$) the growth rate $\gamma = \mathrm{Im}\,\omega \gg \omega_{Bi}$. In this case the ions may be considered unmagnetized and for them we may put $\delta\varepsilon_i = (\omega_{pi}/\kappa v_{Ti})^2\cdot[1+i\sqrt{\pi}\,z_i W(z_i)]$ where $z_i = \omega/\sqrt{2}\,\kappa_\perp v_{Ti}$, $W(z)$ is the Kramp function whereas for $\delta\varepsilon_e$ we may use expressions (1),(2) and (4).

To evaluate the growth rate of the electron cyclotron oscillations of a plasma with $\beta \sim 1$ under the resonant condition $\kappa_y V_E \approx -n\omega_{Be}$ we use eq.(4). Then we have

$$\gamma \sim (r_{Le}/L)^2\cdot|\omega_{Be}| \qquad (\gamma/\kappa_\perp v_{Ti} < 1). \qquad (5)$$

It is assumed that $|\varkappa_B| \sim |\varkappa_n| \sim |\varkappa_\Theta| \sim 1/L$, $V_E \sim V_M \sim v_{Te}(r_{Le}/L)$. The instability discussed is due to the resonant interaction between cyclotron waves and the particles having the velocities $V_\perp \sim v_{Te}(r_{Le}/L)$.

The expression (4) corresponds to one found in paper [8] where only the magnetic drift was involved. Note that in the case considered $|a| \sim 1$ and the formula (4) and therefore the estimate (5) are valid only to the order of magnitude. It is necessary to say that the eventual breaking of the resonance $\kappa_y V_E \approx -n\omega_{Be}$ in an inhomogeneous plasma leads to the violation of the local approximation criterion $r_{Le}^2|d\kappa_x/dx| \ll 1$ too. It means that the electron cyclotron instabilities of a plasma with $\beta \sim 1$ necessitate a non-local approach.

To describe the ion acoustic oscillations of the inhomogeneous plasma with $\beta \sim 1$ we retain in eq.(1) only the term with $s=0$. Then we obtain that $\mathrm{Re}\,\omega = \omega_s = \kappa v_s(1+\kappa^2 r_{De}^2)^{-1/2}$ and

$$\gamma \sim (|\omega^*|\omega_s/\kappa_\perp r_{Le}\sqrt{|\kappa_y\bar{V}_M|})^{2/3}. \qquad (6)$$

The growth rate approaches its maximum at $|\kappa_y\bar{V}_M| \sim |\omega_{Be}|$

$$\gamma_{max} \sim (m_e/m_i)^{1/3}\cdot|\omega_{Be}|. \qquad (7)$$

This growth rate exceeds that found in [2] . In contrast to the electron cyclotron oscillations all of the validity conditions (3) of the local approach hold for the ion acoustic oscillations.

Conclusions. The investigation performed shows that the inhomogeneities of the drift velocity V_E and the frequency ω_{Be} effects essentially the development of electron cyclotron instability and it may change the resonant conditions of ion sound excitation.

Acknowledgements. The authors are very grateful to V.D.Yegorenkov for his help.

References

1. R.C.Davidson, N.A.Krall, Nucl.Fusion, 17, 1313 (1977).
2. V.L.Sizonenko, K.N.Stepanov, Nucl.Fusion, 18, 1081 (1978)
3. V.V.Dolgopolov et al., Ukr.Fiz.Zhurn., 18, 18 (1973).
4. Yu.A.Kirochkin et al., Ukr. Fiz.Zhurn., 18, 621 (1973).
5. A.V.Timofeev, Nucl.Fusion, 6, 93 (1966).
6. A.Nocentini, J.Plasma Physics, 3, 543 (1969).
7. D.G.Lominadze. Cyclotron waves in plasma (In Russian), Tbilisi, "Metzniereba", 1975.
8. J.J.Sanderson, E.R.Priest, Plasma Physics, 4, 959 (1972).

BP19

Experimentals on the High Pressure Plasma in a Helical Stellarator (Asperator NP-3)

Y.Goto, T.Asaishi, Y,Funato, K.Harafuji, S.Kitajima, J.Neyatani, N.Sasaki, K.Sugita, I.Sakamoto, F.Tozuka, H.Watanabe and S.Nagao.

Faculty of Engineering, Tohoku University, Sendai, Japan.

Abstract: It was found that there is a distinct "forbidden region" of toroidal discharge in a stellarator with a closed helical magnetic axis(Asperator NP-3).This phenomenon is therefore tentatively explained by the assumption of 1/2 resonance of the magnetic field lines near the axis. The measurements of the plasma column resistance suggest that in the allowed region but the vicinity of boundary of both regions the plasma is stabilized by the formation of magnetic well.

Asperator NP-3[1] is a toroidal device with a helical magnetic axis of which the major radius is 80cm, the aperture radius of plasma limiter 3cm, radius of axial helix 5cm and period number N=16(Fig.1). The important differences between Asperator NP-3 and other high beta $\ell=1$ stellarators or Figure 8 stellarator are in such points that the pitch angle of the helix of magnetic axis is about 45°, which is much larger than those of other stellarators and the period number N=16 is much larger than 2 of Figure 8. These characteristic features in our device are intently in order to guarantee a helical symmetry of the field configuration as good as possible.

In Fig.2, the time variations of the plasma current J, its time derivative dJ/dt and the one turn voltage V of the discharge are shown. Each phase corresponds to each Region of the stability criterion, given by Safranov[2].

Region	I	$0 > 1/q$	unstable
Region	II	$1 > 1/q > 0$	unstable
Region	III	$1.84 > 1/q > 1$	stable
Region	IV	$1/q > 1.84$	unstable

(1)

where $q=B_B k/\mu_0 j_0$ and B_B, j_0 and k are the axial magnetic field, the plasma current density near the axis and the curvature of the axis respectively.

The peak currents and the column resistances in the RegionI and II , both measured in the second half-cycle of the discharge are compered in Fig.3 as function of the condenser voltage of $\ell=1$ helical windings. Then it was eventually found that the discharge currents increase slightly as the increase of $\ell=1$ helical winding current I_1, which may shift the location of discharge current axis. Above a certain value of I_1 however there is a distinct region where the toroidal discharge does not occur at all, which will be called hereafter as "the forbidden region" of toroidal discharge against the allowed region.

It is to be noted that the boundary of both regions can be defined and reproduced experimentally very well and that the resistances of plasma column decrease in the vicinity of the boundary in the allowed region.

Then the shifts of the plasma current axis Δ were roughly estimated by two magnetic probes, which were set outside the vacuum chamber. The results of measurements are shown in Fig.4, where the positive of I_1 denotes that the helicalwinding current in the direction of the principal normal is parallel to the longitudinal main field and vice versa. When I_1 is negative, the inward shift in the direction of the principal normal of the axis $\Delta > 0$ was observed. It is very obvious in this case that the radius of axial helix decreases as the increase of the absolute value of I_1 and so the current path around the torus will become shorter to give a smaller resistance of the plasma column than otherwise and the discharge will be finally forbidden above a certain critical value of I_1.

In the case of positive I_1 however, which is expected to shift the plasma current axis outward in the opposite direction to the principal normal, apparent shifts of the plasma current axis were not observed and nevertheless there exists the current forbidden region of toroidal discharge with a small value of negative I_1.

In order to clarify these phenomena above described, the boundary between the allowed and forbidden regions(in Region II discharge) was measured next in the plane of I_1 versus I_2, where I_2 is the current of helical winding $\ell=2$ to give the elliptical deformation of the magnetic surfaces. The results are shown in Fig.5. However it has been known by the numerical calculations of magnetic surfaces for given I_1 and I_2 [3] that the I_1 current has some component to give the elliptical deformation of magnetic surfaces besides the shift of magnetic axis, while the I_2 current has some component to give the shift of magnetic axis as well as the elliptical deformations of the magnetic surfaces. These are of course due to the fact that the currents in the direction of the principal normal are less effective to produce the helical field near the axis than the currents in the opposite direction, by the curvature effect of the helical axis. By means of the results of numerical calculations above mentioned, Fig.5 was transformed onto the Δ and ε plane, as shown in Fig.6, where Δ and ε denote the shift of magnetic axis and ellipticity of magnetic surfaces respectively.

It was also measured that the plasma column resistance obtained by the current decay of L/R type varies as functions of pure Δ and pure ε , as shown in Fig.7.

To explain the existance of the forbidden region of toroidal discharge, it may be assumed here that the vacuum magnetic surfaces are disrupted at the boundary of both regions by the 1/2 resonance of field lines by the toroidal effect, which corresponds to the resonance of the safety factor q=2 in tokamak.

The discharge allowed region is approximated by

$$\sqrt{\frac{1-\varepsilon^2}{2}}\left(1-\frac{3}{2}\frac{\Delta}{r_0}\right) > \frac{1}{2} \qquad (2)$$

where Δ , r_0 and ε are the shift of the magnetic axis, the radius of the axial helix and the ellipticity of the magnetic surfaces respectively.

Thus it is remarkable that the decrease of plasma column resistance in the vicinity of the boundary of both regions also agrees well with the plasma stability near the field line resonance, as predicted theoretically by C.Mercier[4].

The definite conclusion on the mechanism of current forbidden phenomena and well formation near the boundary should be postphoned till father experiments with reinforced ohmic heating are excuted in near future.

References

[1] S.Nagao and Asperator group:Proc.7th Symp. Eng. Prob.Fusion Res.Vol.I p.841(Knoxville, Tennessee,U.S.A.Oct.25-28, 1977)
[2] L.S.Soloviev and V.D.Shafranov:Rev. Plasma Phys. Vol.5, Consultant Bureau,N.Y. and London (1970)
[3] N.Sasaki and Asperator Group: to be published elsewhere.
[4] C.Mercier: Nucl. Fusion, Vol.4, p.213 (1964)

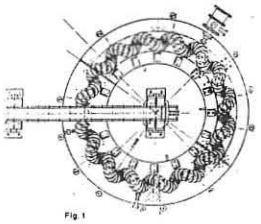

Fig.1

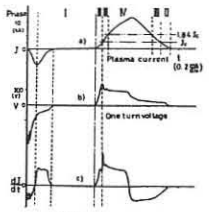

Fig.2

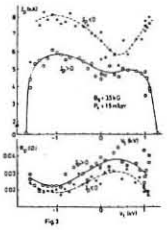

Fig.3

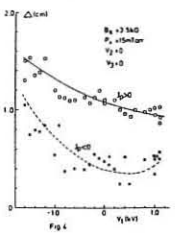

Fig.4

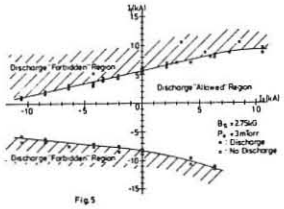

Fig.5

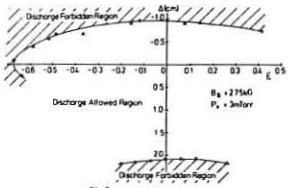

Fig.6

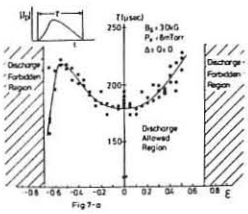

Fig.7-a

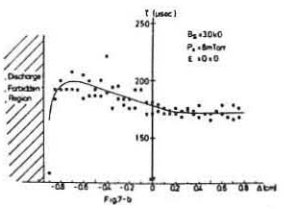

Fig.7-b

BP20

A LARGE STELLARATOR BASED ON MODULAR COILS

S.M.Hamberger, L.E.Sharp, and L.F.Peterson

Plasma Research Laboratory,
The Australian National University, Canberra.

Although stellarators offer some considerable advantages over tokamaks, (e.g. in continuous operation, better confinement properties, ab initio equilibrium, freedom from disruptions) difficulties arise in designing large devices due, for instance, to poor plasma access as well as to constructional, electromechanical and maintenance problems associated with continuous helical windings. This paper describes a design for a fairly large device (major radius 2.1 m), based on a set of discrete coil modules arranged in a toroidal configuration to provide the required closed magnetic surfaces, having gaps for unobstructed access to the plasma for diagnostics, etc, and allowing for easy removal for maintenance.

The provisional design parameters, which have been obtained as part of a detailed computational study aimed at optimisation of this type of configuration[1], are as follows: $B \leq 4$ T, $R = 2.1$ m, $\ell = 3$, 8 field periods (each consisting of two modules), $\iota_{max} = 0.59$, mean helical winding radius 0.33 m, separatrix radius $a = 0.25$ m. The equivalent current $I_{eq} = \iota a^2 B/2R = 0.35$ MA. It is intended to use ohmic heating currents $I_H \leq 0.2$ MA. The arrangement is shown in Figs. 1 and 2: the helical conductors within each module are to be connected in series with each other and with the toroidal coils, the links between helical conductors contributing to the toroidal field. Mechanical strength is obtained by using large cross-section, single-turn conductors (hard Cu or Cu-Cr alloy), and by fixing the helical windings to the toroidal coils to form a rigid assembly. No azimuthally encircling conductors are used: the transverse field components required to centre the magnetic surfaces, including the separatrix, within the vacuum chamber will be obtained by using a different pitch angle modulation ($\theta = m\phi + \alpha_{1,2} \sin\theta$, $\alpha_1 \neq \alpha_2$) for each polarity of helical conductor. Fig. 3 shows the separatrix computed for the above arrangement, but with $\alpha_1 = \alpha_2 = +0.05$.

The low impedance electrical characteristics of the assembly form a suitable load to the Canberra Homopolar Generator (stored energy 0.5 GJ, 400 V). With the windings all in series, this will produce $B \approx 3$ T for a 2 sec. 'flat-top' ($I_w \approx 0.3$ MA) and with half the windings in parallel $B \approx 4$ T for 1 sec. ($I_w \approx 0.4$ MA).

From extrapolation of the results from existing ohmically heated stellarators, which suggest $\tau_E \propto I_{eq}^2$, we expect $\tau_E \sim 100$ ms, while experience, e.g. on CLEO[2], suggests that optimum confinement will be obtained at low ohmic current density such that the drift parameter $\xi \equiv v_d/v_e \leq 10^{-2}$. From simple power balance, taking $\bar{n} = 5.10^{19}$ m^{-3}, $z = 3$, $r_p = 0.21$ m, an ohmic heated current of 200 kA should produce temperatures $T_e \approx T_i \approx 1.3$ keV, ($\xi \approx 10^{-2}$) with a loop voltage ≈ 1 V. Generous space exists (see Fig. 1) for the use of a sufficiently large iron core (say, 5 Vs) with the primary windings close-wound on the central limb to allow long pulse operation (> 1 s) without introducing stray fields due to core saturation.

An engineering design study of this device, supported by the National Energy Development and Demonstration Commission, is under way.

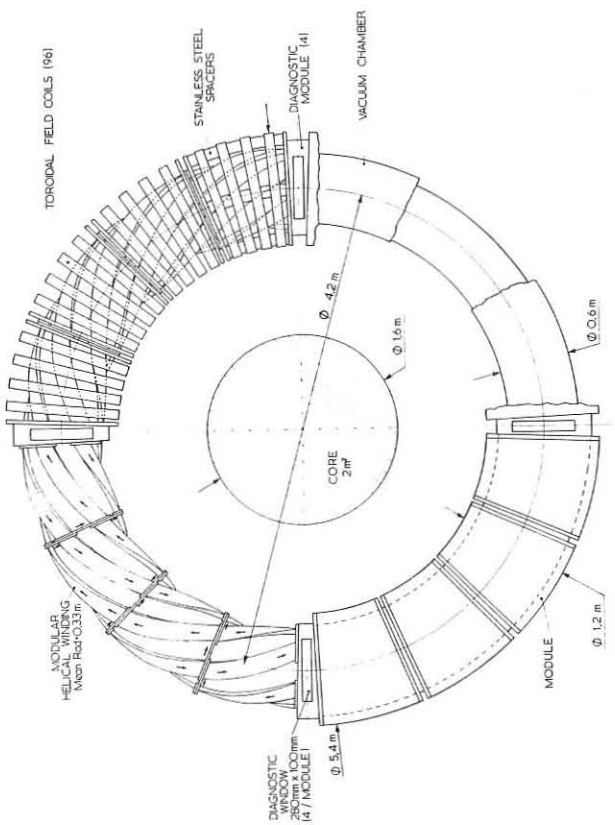

Fig.1. Schematic layout of Canberra Modular Stellarator windings. The 'diagnostic gaps' are 13 cm wide at the mean major radius and offer access to the plasma from all four directions.

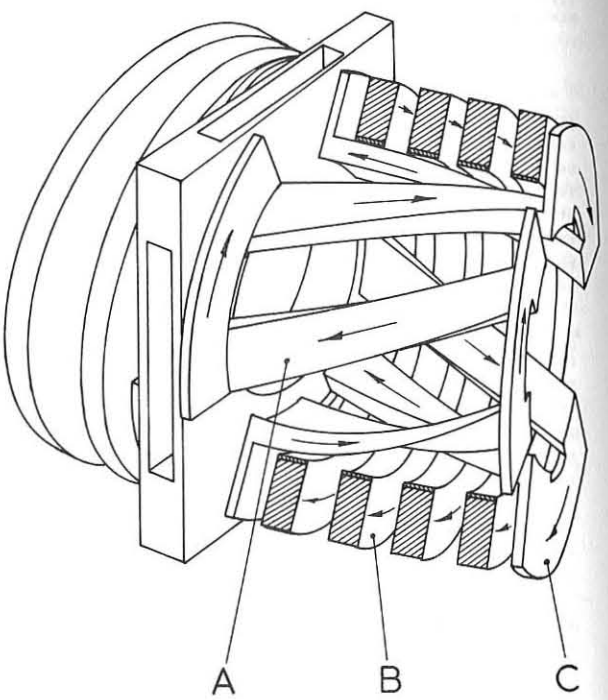

Fig.2. Arrangement of windings in one module (connections now shown). Two modules (of different type) form each field period. The conductor cross-sections and mean minor radii are: A - 17 x 6 cm, 33 cm; B - 20 x 7.5 cm, 48 cm; C - 3 x 20 cm, 48 cm.

References

(1) SHARP, et. al., "Optimization of a Stellarator Design Including Modulation of the Helical Winding Geometry": this conference.

(2) ATKINSON, et. al., 7th Int. Conf. on Plasma Physics and Controlled Fusion, IAEA/CN/37 H.1, 1978.

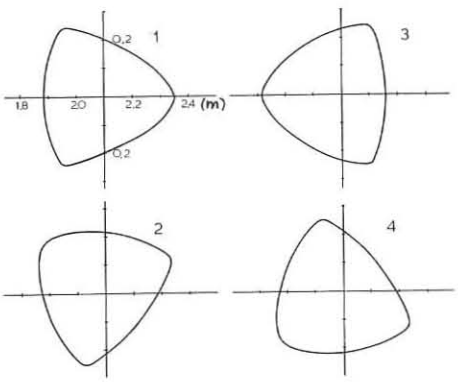

Fig.3. Computed separatrix cross-sections at four positions in one field period. Each conductor is approximated by 3 filaments. There are 4 x 4.5° diagnostic gaps with 1° gaps between each module. 1. - main gap. 2 - 4, quarter, half, three quarter period.

OPTIMIZATION OF A STELLARATOR DESIGN INCLUDING MODULATION OF THE HELICAL WINDING GEOMETRY

L.E.Sharp, L.F.Peterson and J.W.Blamey

Plasma Research Laboratory,
The Australian National University, Canberra

The optimization of the helical winding geometry of the next generation of high performance stellarators is of critical importance as the current in the helical conductors must be kept to a minimum to reduce the very large electromechanical forces on the conductors.

General Optimization

Using a modified version of the Culham computer code MAGBAT[1] we have calculated the separatrix r_s as a fraction of the helical winding radius a and the parameter, $\iota_s(a/R)$ calculated at the separatrix, as functions of the helical winding pitch angle $\psi = \tan^{-1}(m\,a/R)$, for $\ell = 3$ stellarators with aspect ratios $4 < a/R \leq 16$. The results are plotted in Figs. 1 and 2 respectively for different values of the ratio I/Ba, where I is the helical conductor current and B is the toroidal magnetic field. The width of the helical conductors has been approximated by 3 current filaments each carrying I/3 and spaced poloidally 10^o apart. The graphs show an optimum ψ for a given value of I/Ba which increases with increasing I/Ba. Examination of the poloidal rotation of field lines (e.g. see Fig. 3) shows that surfaces will

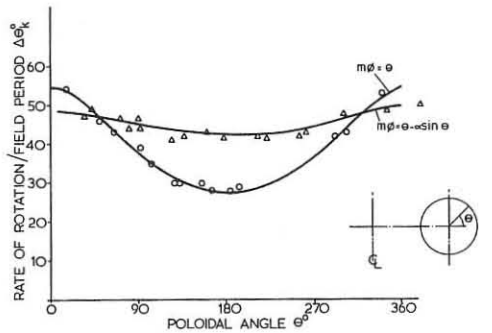

Fig. 3. The rate of rotation of a magnetic field line starting at $\theta = 0$, r = 26 cm for modulated stellarator with $\alpha = 0.05$ and unmodulated stellarator $\ell = 3$, m = 7/3, R = 2.15 m, a = .34, B = 40 kG, I = 330 kA.

open when the *local* pitch of the field line (corresponding to 2 to 3 times the *average* value) approaches ψ. Thus as the winding pitch is decreased below the optimum value the separatrix shrinks and as a consequence $\iota_s a/R$ falls. Nevertheless, as the electromechanical forces on the helical conductor increase with ψ it is advisable to choose the lowest acceptable winding pitch angle.

Taking the set of curves for which I/Ba = 0.25 as an example, the effect of toroidicity can be seen to be important for small aspect ratios $R/a \gtrsim 4$ and to become negligible when $R/a \sim 12$. It is thus important when comparing the curves of Figs. 1 and 2 to use the actual value of R/a if ≤ 12.

The influence of toroidicity can be reduced if the helical winding pitch is modulated according to the equation

$$m\phi = \theta - \alpha \sin\theta$$

where α is a constant found by computer iteration. The effect of α on the helical winding geometry is to make the winding on the outer circumference steeper, and shallower on the inner circumference, thus causing the field line to rotate more uniformly with poloidal angle. This is illustrated in Fig. 3, where the case of constant pitch winding is shown for comparison with the parameters $\ell = 3$, m = 7/3, R = 2.15 m, a = 0.34, B = 40 kG, I = 330 kA. For these calculations the conductors were approximated by single filaments. The effect of modulation is to increase the rotational transform by ~ 20%.

It should be noted from Fig. 2, that little improvement can be expected using modulation when $R/a > 12$. By using different values of α for the forward and return helical conductors, a local vertical field which is modulated in phase with the winding is introduced. This produces both a finite rotational transform on the magnetic axis (Fig. 4) and its displacement in major radius without causing break-up of the outer surfaces. This is in contrast to the distortion of the surfaces and serration near the separatrix found by Gibson[2] when a uniform vertical field was added to a constant pitch stellarator.

Modular Configuration

Fig. 5 compares magnetic surfaces of a continuously wound stellarator with that in which a number of azimuthal gaps (4 diagnostic gaps of 4.5^o and 12 gaps of 1^o for finite conductors and insulation) have been introduced, and shows little effect on the gross features of the magnetic surfaces. The helical winding modules are oriented so that the end points of the conductors are rotated in azimuth with the same poloidal coordinates across the gap.

The case chosen is that of the Canberra Modular Stellarator[3]. Fig. 6

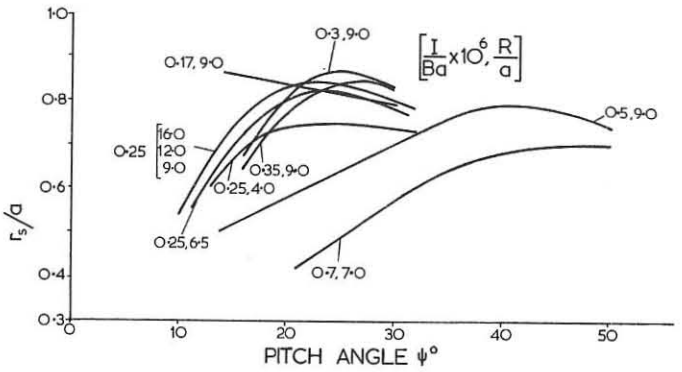

Fig.1. r_s/a as a function of winding pitch angle ψ for various I/Ba and aspect ratios.

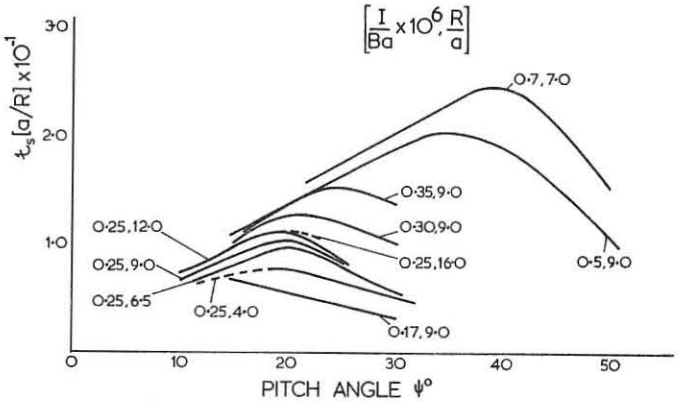

Fig.2. $\iota_s a/R$ as a function of ψ, for various I/Ba and aspect ratios.

shows the effect of varying the total gap width up to 45^o varying the ratio of the above two types of gaps. The main effect is a decrease in the rotational transform with the outer surfaces themselves remaining intact. This appears to hold provided the individual gap width is not large compared with the winding-separatrix distance.

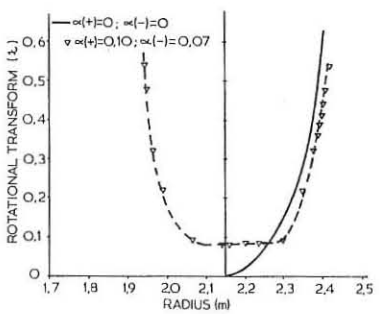

Fig.4. ι as a function of the initial radius of a field line for constant pitch (solid) and modulated stellarator (dashed) with $\alpha(+) = 0.10$ and $\alpha(-) = 0.07$ showing finite ι on the magnetic axis.

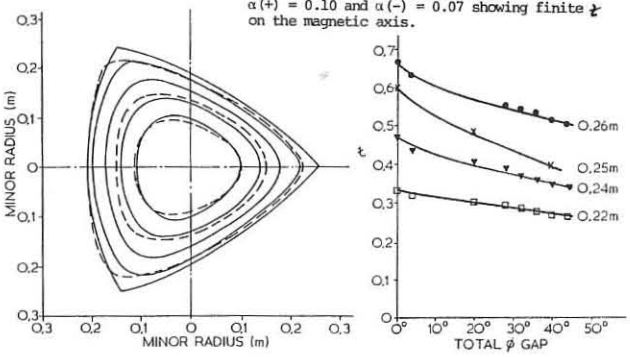

Fig.5. Magnetic surfaces (i) - - - for modular stellarator with 4x4° and 12x1° gaps. (ii) —— continuous helical winding. $\ell = 3$, m = 8/3, R = 2.0 m, a = 0.34 m, B = 40 kG and I = 370 kA.

Fig.6. ι as a function of total azimuth gap angle with 4 large and 12 small gaps, helical windings approximated by single filaments $\ell = 3$, m=7/3, α=0, R=2.2m, a=0.34, B=40 kG, I=330 kA.

REFERENCES

(1) MARTIN,T., Culham Laboratory, UKAEA, Private Communication.
(2) GIBSON, A., Phys. Fluids, 10 (1967) 1553.
(3) HAMBERGER, S.M., SHARP, L.E., PETERSON, L.F., "A large stellarator based on modular coils", these Proceedings.

BP22

ON TOROIDAL VACUUM FIELDS AND PARTICLE ORBITS IN MODIFIED STELLARATORS AND TORSATRONS

W VII-A Team[+] and W. Lotz, presented by F. Rau
Max-Planck-Institut für Plasmaphysik, Ass.EURATOM-IPP
D-8046 Garching, Federal Republic of Germany

Abstract: Superimposing magnetic fields on the vacuum fields of stellarators or torsatrons can reduce, usually at the expense of aperture, the poloidal variation of $q = \int_0^L dl/B$ which is a measure of the diamagnetic current parallel to B, L being the length of a field period. So far, large reduction factors have been obtained only for $\ell=2$ torsatrons with V" > 0. In certain regions of such a configuration drift orbits of charged particles are closed within one field period.

Introduction: In non-axisymmetric configurations trapped particles (collisionless plasma without electric fields) perform complicated spatial drifts (superbananas) which induce additional losses when touching the limiter or the wall. The drift velocity out of the surface is correlated with the variation of |B| on the surface. Instead of minimizing this variation, the poloidal variation of q is minimized. Therefore, a drift-optimized magnetic surface s is characterized [1] by a minimum of $Q_s = \frac{\Sigma|q - \bar{q}|^2}{\bar{q}^2} \frac{R_A^2}{\phi_T}$. The sum Σ is taken over one poloidal transit of the field line (major radius R_A of its axis, toroidal flux ϕ_T, $\bar{q} = \oint dl/B$ normalized to one field period). A minimum of Q_s simultaneously the secondary currents are minimized [1]. The rotational transform ι enters implicitly in the sum; large ι causing Σ to consist of a few terms only. The quality factor Q of nested surfaces is taken to be the linear average of their values Q_s. Since a large aperture A is useful for confinement we consider a configuration as drift-optimized at minimum Q/A.

Configuration Studies: Vacuum fields of stellarators (ℓ= 2,3) and torsatrons (ℓ=2) with m= 2 - 20 field periods are modified by homogeneous, axisymmetric (dipole to octopole) or m-fold symmetric magnetic fields. It is aimed to maintain compatibility with structure and toroidal field of the W VII-A stellarator [2]. Depending on the topology and the magnitude of the superimposed field, the values of Q and Q/A are obtained, along with the radial dependence of ι and $\bar{q}$, as well as the position and helicity of the magnetic axis.

Stellarators: Modified ℓ=2 m=5 stellarator configurations are shown for two azimuthal positions in Fig.1 (quadrupole field) and Fig.2 (m=5 field). As given in the table below, Q is moderately reduced, but Q/A stays constant to within 10% and V" < 0.

Configuration	Q	Q/A	ι axis	ι edge	$\bar{q}$ axis	$\bar{q}$ edge
ℓ=2 m=5 stell.	5.3	31	0.21	0.22	4.2	3.8
Fig.1	2.9	32	0.25	0.28	4.5	4.3
Fig.2	3.9	35	0.31	0.31	4.7	4.4
	T^{-1}	$T^{-1}m^{-2}$			$T^{-1}m$	

Dipole fields [3] have a similar effect, but octopole fields introduce smaller changes in Q than quadrupoles; vertical fields shifting the surfaces outwards improve Q via an increase in ι; low m provides large ι (low Q) at small A (separatrix limit); large m requires large helix current for reasonable ι and Q.

Quadrupole fields at ℓ=3 stellarators cause an internal separatrix (Fig.3), similar to the "double star"[4]. The X-point is situated between the quadrupole stagnation point and the axis of the ℓ=3 system. At large quadrupole current the internal separatrix would touch the limiter. No particular improvement in Q has been seen.

ℓ=2 Torsatrons, m=10 - 20: Even in the case of a relatively large external toroidal field ~1/R added to the torsatron configuration a reduction of Q by factors ≥100 is obtained by shifting the magnetic surfaces radially inward by a strong B_z. The minima of Q and Q/A nearly coincide (Fig.4a); A and V" > 0 are reduced but ι is increased (Fig.4b) due to a strong increase of the poloidal field when periodically approaching the helix. The "reduced Q" configuration of Fig.4a is shown in Fig.5. The aperture A is about three times that of the W VII-A stellarator. In an effort to keep B_z within technical limits the helix is modulated in the poloidal (θ) direction, $d\theta/d\varphi \sim (1-0.3\cos\theta)$. Helical mirrors are large but toroidal mirrors are nearly absent.

The "min Q" configuration of Fig. 4a has a very small A and no shear and appears to be less interesting.

Particle Orbits: Drift orbits of charged particles (mass M, energy W) are calculated in the absence of electric fields and collisions using the adiabatic constants $\mu = \frac{W_\perp}{B}$ (= $\frac{W}{B_m}$ at a mirror point with B = B_m), and $J = \oint v_\parallel dl = \sqrt{\frac{2\mu}{M}} \oint \sqrt{B_m - B}\, dl$. In a space grid covering one field period numerical values of B and of $J^* = \oint \sqrt{B_m - B}\, dl$ are computed. Intersecting the surfaces B = const. and J^* = const. and integrating the spatial line of intersection yields the spatial curve of one of the mirror points. The analysis is faster in computation compared to an explicit calculation of the complete guiding center trajectory.

In the W VII-A stellarator and the centered torsatron case, the particles are azimuthally untrapped or drift out of the confinement region. In contrast to this result drift orbits of the "reduced Q" torsatron are closed for certain mirror points in the configuration. An example of a closed superbanana is shown in Fig. 6 (10 keV deuteron starting at $\varphi = \pi/10$). The dashed contours in the figure are obtained by the analysis described above. This example demonstrates a correlation between a reduction of Q and an optimization of drift orbits. Particles starting in a mirror point at φ = 0 perform several bananas and eventually leave the considered field period in the azimuthal direction.

The "min Q configuration" yields particle orbits similar to those at reduced Q.

References

[1] A. Schlüter, private communication, and IPP Annual Report 1978, 58
[2] W VII-A Team , Proc.8th Eur.Conf. II,73, Prague 1977
[3] R.P. Freis et al., Nucl.Fusion 17,281, 1977
[4] T.S. Wang, T.H. Jensen, Nucl.Fusion 18,1459, 1978

[+] See paper Neutral Injection into the W VII-A Stellarator, W VII-A Team, Neutral Injection Group, these proceedings

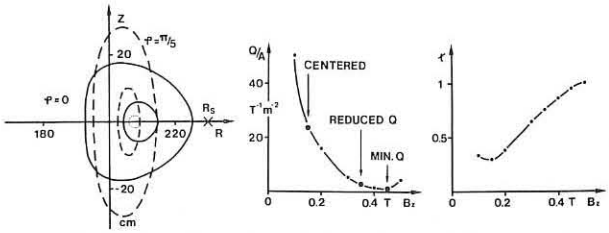

Fig.1: ℓ=2 stellarator modified by quadrupole field, current < 20% of helix current, stagnation point at R_S.

Figs.4a, 4b: Variation of Q/A and ι with vertical field B_z; ℓ=2 m=10 torsatron, helix 1 MA additional toroidal field ~1/R 1.5 T

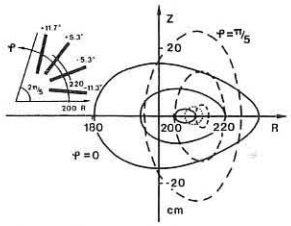

Fig.2: ℓ=2 stellarator modified by m=5 field of toroidal field coils shown in the insert.

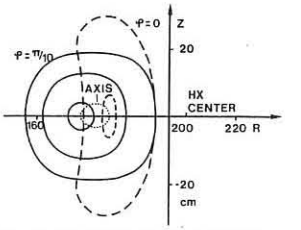

Fig.5: Reduced Q configuration of Fig. 4a at B_z = 0.35 T.

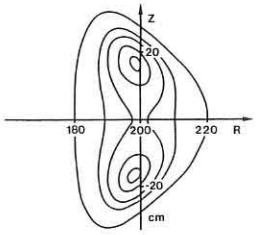

Fig.3: ℓ=3 stellarator modified by quadrupole with stagnation point at stellarator axis.

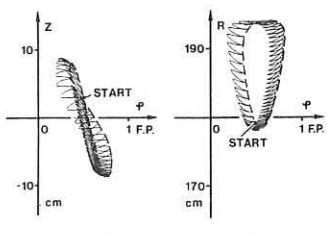

Fig.6: Guiding center trajectory localized within one field period (F.P.) shown as curves Z(φ) and R(φ); "Reduced Q" configuration.

BP23

DEPENDENCE OF THE (2,1) TEARING MODE ON THE STELLARATOR FIELD IN WENDELSTEIN VII-A

W VII-A Team[+], presented by R. Jaenicke

Max-Planck-Institut für Plasmaphysik
Association EURATOM-IPP
D-8046 Garching, F.R. Germany

Abstract: In the W VII-A stellarator it has been found experimentally that the m=2, n=1 or (2,1) tearing mode is stabilized by increasing the external rotational transform beyond $\iota_o = 0.17$. Numerical calculations confirm that this stabilization is mainly due to the radial shift of the resonant q=2 surface with respect to the current density profile by the stellarator field. The width of the (2,1) islands is calculated following the theory of P.H.Rutherford. The resulting magnetic field perturbations outside the plasma agree quite well with the measurements from Mirnov coils.

Introduction: The ℓ=2, m=5 helical windings of the W VII-A stellarator produce an external rotational transform ι_o with negligible shear [1]. Operated with ohmic heating the radial profiles of the current density j(r) and the safety factor $q(r) = 1/(\iota_p(r)+\iota_o)$ are similar to those of tokamaks ($\iota_p(r)$ is the transform produced by the plasma current I_p).

In a previous paper [2] experimental results on the dependence of the (2,1) mode on the parameters ι_o, I_p, electron density n_e, and working gas have been presented. The main result was that the (2,1) mode is no longer observed provided the stellarator field is strong enough ($\iota_o > 0.17$).

In the following, experimental results are compared with numerical calculations based on a paper of A.H. Glasser et al. [3]. The only stellarator effect included in this cylindrical approximation is the additional ι_o in the safety factor q(r) which shifts the resonant surface outwards. The current profile $j(r) \sim T_e^{3/2}$ is calculated from the temperature profile

$$T_e(r) = T_e(o) \quad \frac{1}{1+(\frac{r}{r_o})^{2\alpha}}$$

with Z_{eff}= const. r_o defines the width of the $T_e(r)$ and therefore j(r) profiles and increases mainly with I_p. α indicates the steepness of j(r) and increases mainly with n_e. The width w of the tearing mode islands is approximately determined by $dw/dt \sim \Delta'(w) \to 0$ [4,5]. From the radial field perturbation $B_r \sim w^2$ on the resonant surface [6] the relative amplitude $\delta\hat{B}_\theta/B_\theta$ of the poloidal field fluctuations at the Mirnov coils is calculated (B_θ is the poloidal field of the plasma current).

Dependence on Electron Density: In Fig. 1 the measured $\delta\hat{B}_\theta/B_\theta$ of the (2,1) mode is given as a function of the central density n_{eo} (derived from the microwave line density by assuming a parabolic profile). The theoretical curve is shown as a function of α (upper scale). α is taken from profile measurements for four different n_{eo} by fitting the data from Thomson scattering. The second parameter in j(r), r_o, is always determined by q(r=o) = 1 resulting from sawtooth oscillations. The experimental values of r_o from the T_e profiles are unreliable because of the elliptic cross-section of the current channel.

The theoretical values of $\delta\hat{B}_\theta/B_\theta$ agree quite well with the experimental results. Thus, the strong increase of the (2,1) mode amplitude with n_e can be understood by the cooling of the outer plasma region and the resulting steepening of the current profile inside the q=2 surface (compare Fig.2, profile (5) characterizes the situation of $n_{eo} > 8.5 \cdot 10^{13}\,cm^{-3}$ with no (2,1) mode).

Dependence on External Rotational Transform:

(1) At constant current I_p a superposition of ι_o on ι_p shifts the q=2 surface towards the outside, where j(r) and j'(r) are smaller. The solid lines in Fig. 3 show the theoretical $\delta\hat{B}_\theta/B_\theta$ as a function of ι_o with α as parameter. For W VII-A α varies approximately between 1.5 and 4. In fact, the experimental values taken at ι_o = const. and I_p = 20 kA lie quite well inside this shaded region. $\delta\hat{B}_\theta/B_\theta$ again increases with α corresponding to increasing electron density and/or impurity content for $\iota_o \leq 0.14$.

(2) At constant q(a) (a plasma radius) the position of the q=2 surface remains nearly fixed. With increasing ι_o the plasma current has to decrease from 46 kA to 16.4 kA (ι_o= 0 → 0.17) which again results in a smaller j(r) and j'(r) around the resonant surface. Fig. 4 shows theoretical and experimental values of $\delta\hat{B}_\theta/B_\theta$ for q(a) = 2.9. Again the experimental data lie quite well inside the shaded area given by the numerical calculation.

Conclusions: Numerical calculations to compute the width of tearing mode islands from $\Delta'(w) = 0$ are in good agreement with experimental observations on the (2,1) mode in the W VII-A stellarator. This suggests that the increase of the (2,1) mode amplitude with electron density (or impurity content) is due to the resulting modification of the current profile. The stabilization of the (2,1) mode for $\iota_o \geq 0.14$ is sufficiently well explained by the shift of the q=2 surface with respect to the current density profile by the stellarator field. The island width ranges between 1 - 4 cm for a ≈ 11 cm. Under certain conditions ($\iota_o \leq 0.05$, large I_p and n_e, see Fig. 4) the islands extend up to the limiter. Whether islands of that size affect the plasma loss will be discussed in another paper [7].

Acknowledgements: The authors wish to thank K. Lackner for the modifications of his numerical code and D. Biskamp for valuable discussions.

References

[1] W VII-A Team, Proc.6th Int.Conf.Berchtesgaden (1976) 2, IAEA, Vienna (1977) 81

[2] W VII-A Team, Proc.7th Int.Conf.Innsbruck (1978) 2, IAEA,Vienna (1979) 277

[3] A.H.Glasser, H.P.Furth, and P.H.Rutherford, Phys.Rev.Lett.,38 (1977) 234

[4] P.H.Rutherford, Phys.Fluids 16 (1973) 1903

[5] J.D.Callen et al.,Proc.7th Int.Conf.Innsbruck (1978) 1, IAEA, Vienna (1979) 415

[6] S.Matsuda and M.Yoshikawa, Jap.J.Appl.Phys.,14 (1975) 87

[7] W VII-A Team, this conference, paper presented by H. Ringler.

[+] See paper Neutral Injection into the W VII-A Stellarator, W VII-A Team, Neutral Injection Group, these proceedings

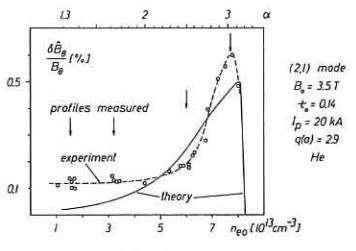

Fig.1

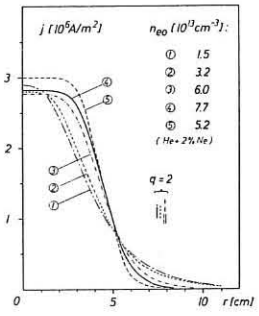

Fig.2

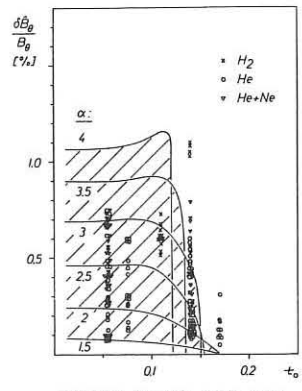

Fig.3

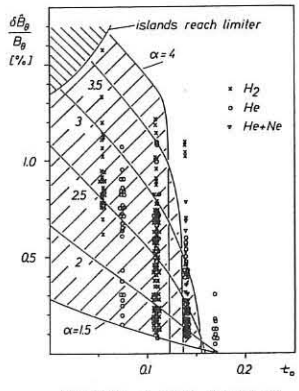

Fig.4

BP24

NEUTRAL INJECTION INTO THE W VII-A STELLARATOR

W VII-A[+] Team, Neutral Injection Group[++]
Max-Planck-Institut für Plasmaphysik
Association EURATOM-IPP
D-8046 Garching, F.R. Germany

Introduction: Three neutral injectors (30 kV, 30 A) [1] have been installed on the W VII-A stellarator (major radius R = 2.0 m, plasma radius a = 0.1 m; helical windings: ℓ=2, m=5 shearless; main field B_o < 4 T). A neutral beam power of $P_b \leq 600$ kW is available for hydrogen, this exceeds the ohmic power of $P_{OH} \leq 400$ kW. The beam is injected radially into the plasma 6° from the perpendicular direction to the magnetic field. Therefore, the fast injected particles are mainly captured in the toroidal and helical mirrors and this affects the heating efficiency appreciably [2].
The interaction length with the plasma is very short (L = 0.2m), therefore a high density plasma ($\bar{n} > 5 \cdot 10^{19}$ m^{-3}) with $kT_e <$ 400 eV is necessary for sufficient absorption.

Hydrogen Injection Into a Helium Plasma: As shown at the Innsbruck conference [3] He discharges are more suitable for producing high density discharges for the following reasons:

1) The capture efficiency for fast hydrogen atoms (for a given electron density) is nearly the same in He^{++} plasma as in a H^+ plasma.

2) The release of oxygen from water absorbed at the wall is very small in helium discharges. Oxygen, even in low concentration, deteriorates the confinement and reproducibility of high density discharges.

3) During the interaction of the hydrogen beam with He Z_{eff} remains practically constant in spite of the unavoidable influx of impurities during injection.

Mode of operation: The high density plasma as discussed in [2] could not be reproduced after the installation of injectors since the Mo calorimeters, which measure the power of the neutral beam, introduce an additional impurity influx in spite their position 2 cm behind the limiter radius.

With the use of Ti gettering the following target plasma could be achieved: $\int n_e dl = 1.5 \cdot 10^{19}$ m^{-2}, $\bar{n}_e = 7 \cdot 10^{19}$ m^{-3}, $T_e(o) =$ 260 eV, $B_o = 3.5$ T, $I_p = 35$ kA, $t_o = 0.14$, $P_{OH} = 350$ kW, q(a) = 2. These parameters are only possible because the external transform $t_o \geq 0.14$ prevents the disruptive instability.

With the density feedback system it is possible to keep the density constant during the injection phase. So far only one injector has been used, the two others are in the conditioning phase at present.

First Results with Injection: An injection pulse of 25 kV/26 A and 75 ms duration is applied during the stationary plateau of the ohmic discharge (Fig. 1). Following the Lister code [2] only 40 % of the neutral power of 200 kW at the port may be fed to the plasma. An increase of the energy content is measured by means of the diamagnetic loop. This energy increase is mainly due to a heating of the electrons and was confirmed by laser scattering data and soft X-ray measurements. The ohmic power slightly decreases at the beginning of the injection pulse, but later on it increases above the pre-injection level indicating some accumulation of impurities during the pulse. The oxygen emission does not increase during the injection pulse, but radially resolved energy flux measurements with a bolometer exhibit an additional radiated power of $P_{rad} \sim 100$ kW. (Fig.2).

Further results will be given at the time of the conference.

References

[1] J.H.Feist et al.,Proc.7th Symp.Eng.Probl.Fusion Res.,Knoxville 1977,527
[2] J. Faulkner, G.G.Lister, W.Ott, E.Speth, this conference
[3] W VII-A Team, Proc. IAEA Innsbruck (1978) IAEA-CN-37-H-2

[+] Bartlett,D.V., Cannici,G., Cattanei,G., Dorst,D., Elsner,A., Grieger,G., Hacker,H., How,J., Jäckel,H., Jaenicke,R., Javel,P., Junker,J., Kick,M., Lathe,R., Leuterer,F., Mahn,C., Marlier,St., Müller,G., Ohlendorf,W., Rau,F., Renner,H., Ringler,H., Saffert,J., Sapper,J., Smeulders,P., Tutter,M., Weller,A., Würsching,E., Wobig,H.

[++] Faulkner, J., Feist,J.-H., Ott,W., Speth,E., Vollmer,O.

Acknowledgements

The authors would like to thank the technical crew who operatesthe machine, our computer programmers and secretaries. The assistance of the technicians in developing and maintaining the diagnostics is also gratefully acknowledged.

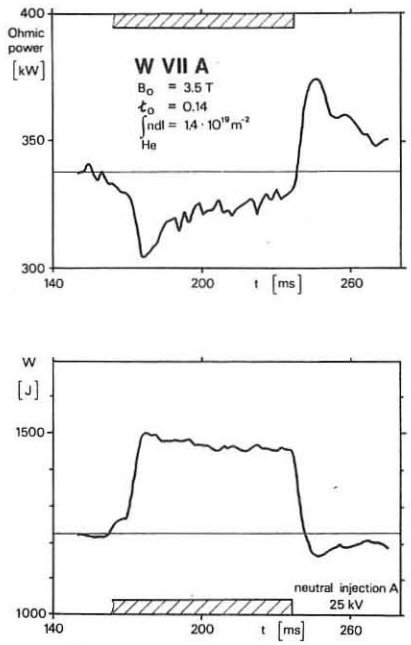

Fig.: 1 Energy content W (diamagnetic coil) and ohmic power during injection (25 kV, 26 A; 75 ms). Plasma current 35 kA at B_o = 3.5 T, t_o = 0.14, $\int ndl = 1.4 \cdot 10^{19}$ m^{-2}.

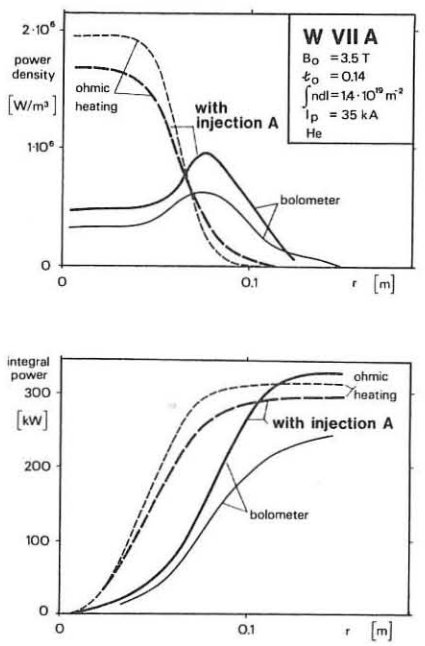

Fig. 2: Power density of ohmic heating (from laser scattering data) p_{OH} and radiation power density p_{rad} obtained by bolometer at 150 ms and during injection at 200 ms. The integral power is also calculated:

$$P_{OH} = 4\pi^2 R \int_o^r p_{OH}\, r dr$$

$$P_{rad} = 4\pi^2 R \int_o^r p_{rad}\, r dr$$

BP25

Stability of Helical Equilibria

R. Gruber[++], W. Kerner[+], W. Schneider[+], F. Troyon[++]

+) Max-Planck-Institut für Plasmaphysik, D-8046 Garching, Germany;

++) Centre de Recherches en Physique des Plasmas, Ecole Polytechnique Fédérale de Lausanne, 21 av. des Bains, CH-1007 Lausanne, Switzerland.

Abstract

The stability code ERATO has been modified to treat the more general class of helically symmetric equilibria.

1. Variational Form of Ideal MHD for Helical Geometry

A helically symmetric plasma equilibrium /1/ is characterized by the flux function $\psi(r, \varphi - hz)$, the invariant shape of the cross-section, the distance δ_1 between the magnetic axis and the geometric axis of the helix, and the wave number $h = 2\pi/L$, where L is the period length (see Fig.1). The flux function satisfies the equilibrium equation

$$r \frac{\partial}{\partial r}\left[r u^2 \frac{\partial \psi}{\partial r}\right] + \frac{\partial^2 \psi}{\partial \xi^2} = rj - 2r^2 h T u^4 \qquad (1)$$

where $\xi = \varphi - hz$, $u^2 = \frac{1}{1+h^2r^2}$; the current density $j = -r\frac{dp}{d\psi} - u^2 r\, T\frac{dT}{d\psi}$; T and p are arbitrary functions of ψ /2/

The ideal MHD spectrum of such equilibria is obtained by variation of the Lagrangian $L \equiv \delta W(\underline{\xi}, \underline{\xi}) - \omega^2 K(\underline{\xi}, \underline{\xi})$, where δW is the usual expression for the potential energy and $K = 1/2 \iiint d^3x\, \rho |\underline{\xi}|^2$. It is convenient to replace the angular variable χ by a new local variable $\mathcal{X} = \int_0^l \frac{dl}{u J |\nabla\psi|}$, where the integration runs along a constant ψ-surface, and l designates the arclength (see Fig.1). The Jacobian J is defined as $J = \frac{q}{u^2(r - hr\frac{\partial \xi}{\partial r})}$. The "safety factor" q is obtained by normalizing $\mathcal{X}$ to 2π. For the sake of numerical accuracy, ψ is substituted by the geometric variable $s: \psi = s^2 \psi_s$, $0 \le s \le 1$, $\psi_s = \psi/\text{surface}$.

In the rotating coordinate system (x^1, y^1), or, equivalently (r, ξ), the equilibrium quantities are independent of z; the displacement $\underline{\xi}$ can be expanded as

$$\underline{\xi}(r, \xi, z) = \frac{1}{2\pi}\int_{-\infty}^{+\infty} dk\, \underline{\xi}(r, \xi)\, e^{ikz}$$

For a specific k the potential energy in the Lagrangian then reduces to the two-dimensional expression

$$\delta W = \iint \frac{ds}{4 s \psi_s u^2 J} d\chi \left\{ a|I_1|^2 + d|I_2|^2 + c|I_3|^2 + d|I_4|^2 - e|k|^2 \right\} \qquad (2)$$

where $a = \frac{4\psi\psi_s}{J^2|\nabla\psi|^2}$, $b = T^2u^2$ (longitudinal magnetic field pressure),

$c = |\nabla\psi|^2 u^2$ (poloidal magnetic field pressure), $d = \rho$,

$$e = \rho\psi\psi_s\left[\frac{j^2}{|\nabla\psi|^2} - ju\frac{\partial}{\partial\psi}\left(a_1|\nabla\psi|\right)_n + \frac{dp}{d\psi}\frac{\partial}{\partial\chi}\left(a_1 u\right)_n + 2hu^3\left(u\frac{dT}{d\psi} - \frac{jT}{|\nabla\psi|^2}\right)\right],$$

$I_1 = F[X] + GX$, $I_2 = D - \frac{4s\psi_s\, hu^2}{T} X$,

$I_3 = D + \beta_\chi\, F[X] - F[V] + HX$,

$I_4 = D - X\frac{\partial}{\partial s}(a_1 u^2) - V\frac{\partial}{\partial\chi}(a_1 u^2) + u^2 F\left[\frac{Y}{u^2}\right] = \nabla\cdot\underline{\xi}$,

$D = \frac{\partial X}{\partial s} + \frac{\partial V}{\partial\chi} + ikX(\beta_z - \alpha\beta_\chi) + ik\alpha V$,

$F \equiv \frac{\partial}{\partial\chi} + ikq$, $G = -q\frac{\partial}{\partial\chi}\left(a_1(u^2 J)\right)$,

$H = -\frac{\partial}{\partial s}\left(a_1(u^2 J)\right)_n - \frac{2s\psi_s\, j}{u|\nabla\psi|^2}$, $\alpha = q - Tu^2 J$.

The new vector components X, V, Y are related to the displacement $\underline{\xi}$ through

$$(X, V, Y) = \left(u^2 J/|\nabla\psi|\ \xi_s,\ \frac{2s\psi_s u}{|\nabla\psi|}\xi_\chi - Y + \zeta_\chi X,\ 2s\psi_s u\, \xi_\xi/T\right).$$

The quantities

$$\beta_\chi = 2s\psi_s\left(\frac{\partial\chi}{\partial s}\right)_n = \left(\frac{\partial\chi}{\partial s}\right)_n$$

$$\beta_z = 2s\psi_s\frac{(e_\xi\cdot\nabla\psi)}{|\nabla\psi|^2} = -2s\psi_s\frac{h}{|\nabla\psi|^2}\frac{\partial\psi}{\partial\xi}$$

measure the non-orthogonality of the (ψ, χ, z) coordinate system.

The variational form for axisymmetric geometry (tokamak) /3/ is obtained by replacing $u^2 = \frac{1}{r^2}$, and then setting h = 0 and k = n.

2. Ballooning Mode Criterion

From the expression above for δW, it is possible to derive the ballooning stability criterion. It can be written as

$$\delta W_B = \int_{-\infty}^{+\infty} \frac{d\chi}{u^4 J}\left\{ A\left(\frac{\partial X_0}{\partial\chi} + BX_0\right)^2 + CX_0^2\right\} > 0 \qquad (3)$$

where $A = a + \frac{bc}{b+c}(\beta_\chi - M)^2$, $B = \frac{1}{A}\left(aG + \frac{bc}{b+c}(\beta_\chi - M)E\right)$,

$C = \frac{abc}{A(b+c)}(E - (\beta_\chi - M)G)^2 - e$, $M = \frac{1}{Ju^2T}\left(\beta_z - \alpha\beta_\chi - \frac{d\alpha}{ds}(\chi - \chi_0)\right)$,

$E = H - \frac{\partial M}{\partial\chi} + \frac{4s\psi_s\, hu^2}{T}$;

X_0 is the amplitude of X, $X = X_0(\chi)e^{-ikq(\chi - \chi_0)}$

Just like in the axisymmetric case this criterion has to be verified independently on each magnetic surface.

3. Discretization

The variational problems (eqs. 2 and 3) are discretized using finite hybrid elements /4/ which prevent the pollution of the eigenvalue spectrum.

The eigenvalue problem arising from eq. (2) is solved by an inverse vector iteration technique. The resulting code is an extension of the axisymmetric ERATO code. It is suitable to study long-wave length perturbations, $kq \lesssim 3 \div 5$. For the ballooning stability criterion (eq. (3)), corresponding to the limit $kq \to \infty$, we check the positive definiteness of the resulting matrix.

4. Results

The first application of the code was for a homogeneous screw-pinch with a conducting wall tight to the plasma surface. For this configuration the growthrate Γ can be calculated analytically and furthermore by a 1D stability code /5/ (see Fig.2). This case is reproduced by our helical code when setting h = 0, $\frac{dp}{d\psi} = -0.4$, $T\frac{dT}{d\psi} = 0$, q = 5 and varying k from 0.18 to 0.22.

The growthrates Γ of the first three fundamental m = 1 modes are plotted versus k. The results of the helical ERATO code, plotted as (x) in Fig. 2, are in very good agreement with the "exact" solutions (solid curves).

The next step will be to calculate the eigenvalues of fixed boundary modes for straight $\ell = 1$ helical equilibria and compare them with results of an initial-boundary-value code /6/.

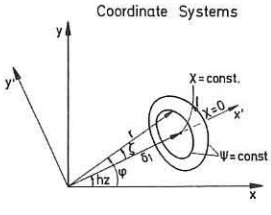

Fig. 1: Plasma cross-section in a plane perpendicular to the geometric axis z showing the various coordinate systems.

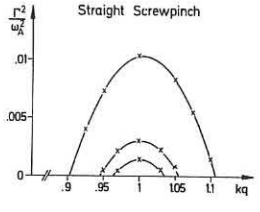

Fig. 2: Comparison between the "exact" solution, calculated by THALIA /5/ (solid curves), and the results of the helical ERATO code (x).

This work has been carried out in close cooperation between CRPP Lausanne and IPP Garching under the auspices of EURATOM.

References

/1/ B. Marder, Phys. Fluids 19, 379 (1978)

/2/ C. Mercier, Nucl. Fusion 1, 47 (1960)

/3/ D. Berger, L.C. Bernard, R. Gruber, F. Troyon, Proc. 6th Int.Conf. on Plasma Phys. and Contr.Nucl. Fusion, Berchtesgaden (1976), IAEA-CN-35/BII-4

/4/ R. Gruber, J. Comp. Phys., 26, 379 (1978)

/5/ K. Appert et al., Computer Phys. Commun., 10 (1975), 11

/6/ F. Herrnegger, W. Schneider, Nucl. Fus. 16 (1976), 925

BP26

OBSERVATION OF POLOIDAL AND TOROIDAL ASYMMETRY IN LINE EMISSION IN W VII-A STELLARATOR DISCHARGES

W VII-A Team[+], presented by H. Hacker
Max-Planck-Institut für Plasmaphysik
IPP-EURATOM Association
D-8046 Garching, F.R. Germany

Abstract: Space and time resolved measurements of the intensity of line radiation of O, Ne, and the working gas have been made in H- and He-discharges. A survey of the main and some detailed features of the complicated pattern of asymmetric profiles and their origin are given.

During a long period of experiments ($\sim 10^4$ shots) the time and space resolved line radiation of impurity and working gas ions was measured in H- and He-discharges of the ohmically heated W VII-A stellarator at two diagnostic planes. At the horizontal port of plane 3 (108° from the limiter) a 2.2 m grazing incidence monochromator (magnetic multiplier, 15-120 nm) and a 0.25 m quartz monochromator (300-650 nm) with a movable mirror unit were used. By scanning the angle of incidence from 70 to 88° on a shot-to-shot basis, a profile could be obtained with a space resolution of 0.5 cm over the entire plasma cross-section. A 1 m normal incidence monochromator (channeltron, 50-150 nm) and a 1 m grating monochromator (300-650 nm) on the horizontal (or by means of an additional mirror, the vertical) port of plane 7 (-180° from limiter) allowed radial profiles to be obtained with 0.5 cm resolution of the 45° two mirror unit. Both systems (mirror unit, monochromator, detector) were absolutely calibrated.

The elliptic cross-section of the W VII-A plasma is viewed at 45° with respect to the major axis. The angular scan of the light emission exhibits a natural asymmetry due to the elliptical shape of the plasma. This geometrical effect is taken into account during the evaluation of the measured profiles; plasma current and external transform determine the shape of the magnetic surfaces. All profiles shown in the following section are transformed profiles and show the light flux [phot·cm^{-2}·s^{-1}·sr^{-1}] along a line of sight as a function of minor radius r in circular geometry. The limiter is about 10 cm.

As is well known from H_α-measurements and side-on observation of the limiter, strong asymmetries, up to a factor of 10, exist in the radial distribution of light fluxes. This also happens in other planes around the torus with internal diagnostic structures. In contrast to this fact resonance lines of higher ionization states of O, C and additional elements, such as Ne or Kr - observed in the VUV region - show only small asymmetries within experimental accuracy (≤10%) during the stationary phase of a discharge (Fig.1). This observation also made on PLT [1], was verified on W VII-A in many cases by measuring profiles at plane 7 with no additional structure inside. If asymmetries appeared at plane 7 they were of small order (a factor 2 greater at the bottom) in the profiles of working gas lines (H, HeI, HeII), whereas those of OII to OVI showed an increased light flux only up to a factor of 1.5 in the upper half of the profile. In contrast to this all profiles observed at plane 3 (H, HeI, HeII, OII to OVI), where an internal structure is only 10 cm from the port, are dominated by a bottom-to-top asymmetry up to a factor of 5. In order to simulate the influence of such inhomogeneities in the wall, a rod of Mo was moved into the torus through the bottom port at plane 7. The observed asymmetric profiles of HeII, OIII, OV, and OVI, shown in Fig.2, are quite similar to those of plane 3. The top of the rod at r = 8.5 cm acts as a strong source of He and O as well. The light fluxes exceeded those of the unperturbed discharges (line density constant) by a factor of 5.

In order to study the location of poloidal asymmetry in more detail, radial profiles were measured in the same plane through both the horizontal and the top vertical ports. Fig.3 shows that the strong bottom-to-top asymmetry of HeII-radiation may be explained by an increased light flux in the lower part of the elliptical plasma cross-section, simulating a bell shape distribution in the case of observation from the top. In addition a horizontal asymmetry was found. The horizontally measured profile of the OV-line is trapezoidal while the vertically observed distribution is asymmetric and exhibits the usual hollow shape (Fig.4).
The OV-profiles, given in Fig.5, were observed simultaneously at planes 3 and 7. The distribution detected at plane 3 is strongly asymmetric, while that of plane 7 is symmetric. The light flux, determined from the upper half in plane 3, was equal to that from the symmetric profile of plane 7 within the error of absolute calibration (50%). In most cases when asymmetric profiles were seen at both planes, differences in the integrated light fluxes of 100 to 300 % existed.

Up to now it is unknown which effect is responsible for the asymmetries in light emission and which effect prevents the impurity ions from achieving a constant concentration on magnetic surfaces. The asymmetries mainly occur in those planes with inhomogeneities of the wall. Increase of asymmetries towards lower ionization states indicates that the inhomogeneity of the neutral component is the source of the asymmetries. This idea is supported by the fact that in H-discharges the asymmetries occur more often and are more pronounced than in He-discharges where recycling from the wall is nearly 100%. The $\vec{B} \times \vec{\nabla}B$-drift of ions [2] can be excluded as an explanation since the asymmetry can change its sign around the torus (Fig.4) and during the discharge as demonstrated by the history of a OIII-line (Fig.6). The initial top-bottom asymmetry is reversed by changing the plasma current from 36 kA (160 ms) to 16 kA (230 ms) during the discharge.

In conclusion, the results presented above caution against the use of quantitative statements for radiation loss balance studies if no detailed spatial information is available.

References

[1] Suckewer, S., et al., PPPL Report PPPL-1430 (1978)
[2] Terry, J., et al., Phys.Rev.Lett. 39, 1615.

[+] see paper Neutral Injection into the W VII-A Stellarator, W VII-A Team, Neutral Injection Group, these proceedings

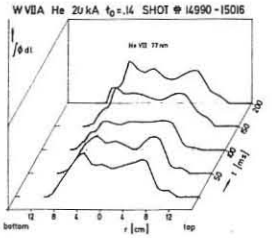

Fig.1: Time history of Ne VIII - 77 nm radiance during current plateau of a helium discharge

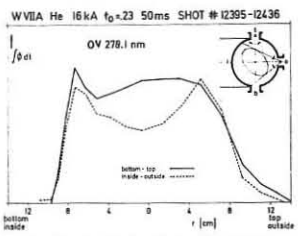

Fig.4: Radial distributions of O V - 278.1 nm radiance observed horizontally and vertically

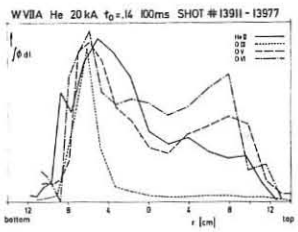

Fig.2: Profiles of various ionization states with the Mo rod at 8.5 cm at plane 7

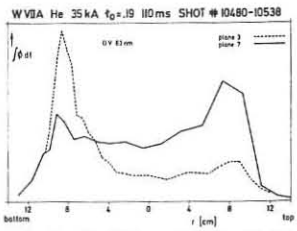

Fig.5: Profiles of O V - 63 nm radiance observed simultaneously at planes 3 and 7

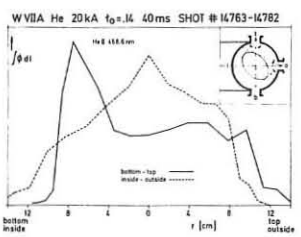

Fig.3: Radial distributions of He II - 468.6 nm radiance observed horizontally and vertically

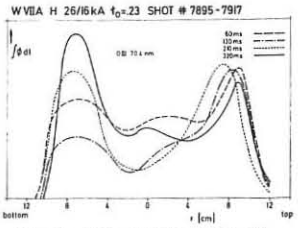

Fig.6: Time development of O III - 70.4 nm profiles in a H-discharge with a current step around 200 ms. Line density remained constant.

BP27

COMPUTATION OF HEATING EFFICIENCIES AND DEPOSITION PROFILES FOR NEUTRAL INJECTION INTO WENDELSTEIN VII A STELLARATOR

J.E. Faulkner, G.G. Lister, W. Ott, E. Speth
Max-Planck-Institut fuer Plasmaphysik
D-8046 Garching, Fed. Rep. of Germany

A series of computer studies of the effects of neutral injection has been performed for Wendelstein VII A. This device is a stellarator but may be run also as a pure tokamak or as a hybrid.

The purpose of these studies is to optimize the parameters of the experiment as well as later on to be able to interpret the results of the experiments on Wendelstein VII A. Computations indicate that the efficiency of neutral beam injection may be greatly improved by the addition of a toroidal current ("hybrid" fields) or with a small vertical magnetic field. The efficiency as a function of injection angle and plasma parameters has also been studied.

A brief description of the device is as follows: Major radius = 200 cm. Minor radius of plasma = 10 cm. Limiter radius = 13 cm. The device is an $\ell = 2$, $m = 5$ stellarator with an $\iota_0 = 0.23$ for maximum current in the helical field windings. The field on axis has a value of 35 kG for maximum current. For operation as a hybrid, the value of the maximum ohmic heating current is 35 kA. Space restrictions limit the maximum angle of neutral injection to 6^0 to the perpendicular.

The studies were performed using an extended version of the computer program FREYA[1] modified to include stellarator fields[2]. This program first calculates the trapping of the injected neutral beam and then follows the subsequent ion motion by a guiding center calculation. The Fokker-Planck equation for the slowing down and scattering of the ions is solved as follows: The slowing-down of the ions is calculated by integrating the differential equation resulting from the usual slowing-down time for ions. The scattering is calculated by a Monte-Carlo method. The program is thus able to calculate the fraction of the neutral beam not ionized, the orbit losses, the charge exchange losses, and the energy delivered to the plasma. The energy given to the plasma ions and electrons is calculated separately. The spatial energy deposition profile is also calculated.

In the computer studies, the injector is represented by an 8 cm diameter circle located 223.5 cm from the major axis. The angular distribution of the neutrals as they emergy from the circular injector face is such that they are uniformly distributed between $\pm$ 7° in the vertical direction and $\pm$ 1.53° in the horizontal. Since the ion beam consists of three species (H^+, H_2^+, and H_3^+), there are three energy components in the injected neutral beam.

Since high density plasmas can be achieved more easily in helium, most of the studies were done for a neutral hydrogen injected into a helium plasma. The plasma electron density is chosen so that $\int n_e d\ell = 2 \times 10^{15}$ cm^{-2}. The density and temperature variations with radius were taken from experimental measurements. The central value of the electron density is 1.06×10^{14} cm^{-3} while the central ion and electron temperatures are 200 eV. The neutral density profile was fitted to measurements at the minor radius 6 cm ($n_0 = 3 \times 10^9$) and 10 cm ($n_0 = 3 \times 10^{10}$) such that the radial derivative of the neutral density vanished in the center. The neutral density was extrapolated to the 13 cm limiter radius ($n_0 = 10^{11}$ cm^{-3}).

The helical windings of the stellarator give the orbits a different character from those in a pure tokamak. The stellarator orbits are rosette rather than circular or "banana" as in a pure tokamak. The stellarator field also has local mirrors. The initial orbit losses in the pure stellarator are from the orbit size rather than from local mirror trapping. However, an ion can be lost by scattering into a local mirror.

Fig. 1 shows the efficiency of neutral beam heating for a pencil beam in a pure stellarator as a function of injection angle. Results obtained from two computer codes, FREYA and a code developed by Dei-Cas[3], are shown and are in good agreement. For the case shown, the density profiles were taken to be parabolic and the temperature profiles flat. The results show that high (80 %) efficiencies may be obtained for angles of injection $\geq 20^0$ to the perpendicular.

Fig. 2 shows the efficiencies of neutral injection into stellarator and "hybrid" magnetic fields as a function of the source voltage of the injection. In this case flat profiles were used for both density and temperature. The single point represents a result for the pure stellarator field with the addition of a 100 G vertical field and it can be seen that the increase in efficiency is equivalent to that obtained using a hybrid field.

The spatial energy deposition is highly sensitive to the plasma profiles. It can be seen from Fig. 3 that the energy deposition profile is parabolic for parabolic temperature and density profiles (case a) whilst for broad plasma profiles (case b) the energy deposition is peaked near the edge. This difference is due both to the poorer beam penetration and the faster slowing down time at the edge for the broad plasma profiles.

Conclusion

We conclude that the efficiency of neutral beam heating for the Wendelstein VII A experiment should be of order 50 % but this could be greatly improved if the injection angle could be increased.

1) G.G. Lister, D.E. Post, R.J. Goldston, Proc. Third Symp. on Heating in Toroidal Plasmas, Varenna 1976, p. 303

2) G.G. Lister, J.E. Faulkner, to be published

3) R. Dei-Cas, D. Marty, Fontenay-aux-Roses Report, EUR-CEA-FC-726, Jan. 1974

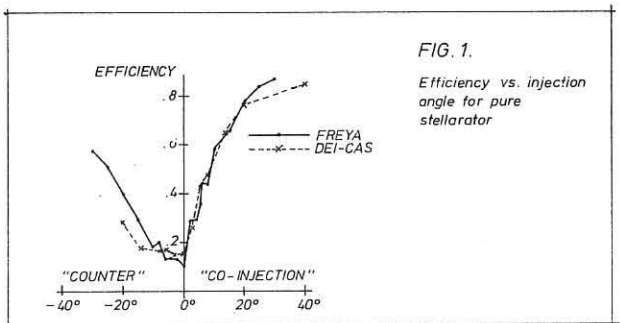

FIG. 1.
Efficiency vs. injection angle for pure stellarator

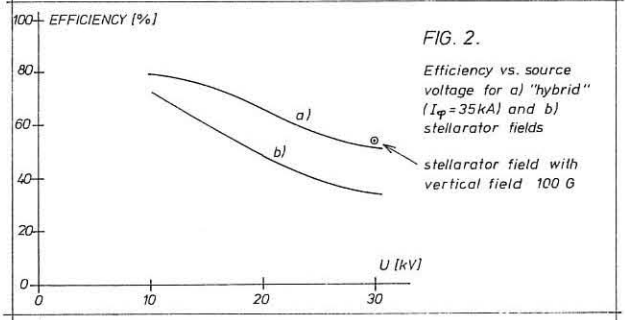

FIG. 2.
Efficiency vs. source voltage for a) "hybrid" (I_{φ}=35kA) and b) stellarator fields

stellarator field with vertical field 100 G

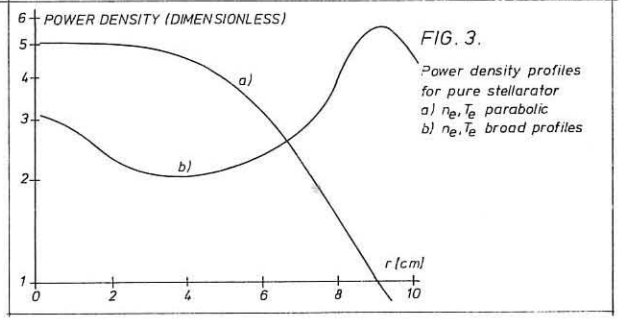

FIG. 3.
Power density profiles for pure stellarator
a) n_e, T_e parabolic
b) n_e, T_e broad profiles

BP28

MAGNETIC SURFACES, PARTICLE ORBITS AND NEUTRAL INJECTION IN CONVENTIONAL AND ULTIMATE TORSATRONS

D. T. Anderson, J. A. Derr, T. Kruckewitt and J. L. Shohet
University of Wisconsin-Madison
Madison, Wisconsin 53706 (USA)

S. Rehker
Max Planck Institut fur Plasmaphysik, Garching-bei-Munchen,(FRG)

and J. A. Tataronis
Courant Institute, New York University, New York, NY (USA)

ABSTRACT. Capabilities in fully non-axisymmetric numerical methods have resulted in a parametric study of various conventional and ultimate torsatron configurations. No superbananas are found in torsatrons without local magnetic wells. Neutral injection calculations show that, if the vacuum magnetic surfaces are well defined, tangential injection is very efficient.

In a conventional torsatron, the nature of the magnetic surfaces are well known[1]. However, in an ultimate torsatron, nested magnetic surfaces are produced without the use of vertical field compensating coils. This is achieved by using a modulated helical coil winding law of the form $\phi = m\theta + \alpha\sin\phi$ where α is the modulation constant. An analytical expression for an α which produces no net vertical field within the torus was derived by Gourdon, et al.[2], as a function of the inverse aspect ratio ε:

$$\alpha_{analytic} = \varepsilon\left(\log\frac{8}{\varepsilon} - \frac{1}{2}\right) \qquad (\varepsilon < 1) \qquad (1)$$

Numerical studies show that such values of α produce surfaces of high transform at the separatrix (typically $\iota > 1$) but often with more than one magnetic axis causing the formation of internal separatricies. The qualitative shape of the magnetic surfaces is principally determined by aspect ratio, ℓ number, and number of field periods. Variations of α of up to ±20% move the magnetic axis inward or outward in the radial direction but do not directly affect surface shape. It is found that an ultimate torsatron of multiplicity ℓ produces surfaces resembling those of the conventional torsatron of multiplicity $\ell + 1$. In an $\ell = 2$ ultimate torsatron this results in magnetic surfaces having both high shear and non-zero rotational transform on the magnetic axis. For a 12 field period $\ell = 2$ ultimate torsatron with $\alpha = .63$ (Fig. 1) well-behaved surfaces are formed with the magnetic axis located at the geometric axis of the torus. No evidence of island formation has been found.

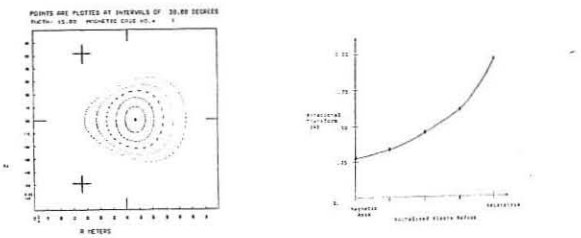

Fig. 1: Magnetic surfaces and transform profile in a 12 field period $\ell = 2$ ultimate torsatron ($\alpha = .63$, $\varepsilon = .224$)

Orbit study and classification must precede transport theory development for torsatrons. Orbit classification is made on the basis of drift surface boundary intersections with flux surfaces. These curves are computed from the condition $E - \mu B = 0$ on flux surfaces, where E is energy, μ is magnetic moment, and B is the value of magnetic field for which particle reflection occurs. Regions where $B > E/\mu$ are inaccessible to the particle. The orbit classifications follow from topological variations of the forbidden regions as a function of the normalized magnetic moment $\delta = \mu B_0/E$ (Figure 2). The surface accessibility A is a function of the ripple $R(\psi)$, where ψ is the flux and

$$R(\psi) = \frac{B_{max}(\psi) - B_{min}(\psi)}{B_0(\psi)}$$

where $B_0(\psi)$ is the average B on the surface ψ.

The firmness of the assumed adiabatic invariants, the magnetic moment and the action, must also be investigated for different orbit types. A study of these quantities for 3.5 MeV alpha particles, using the Lorentz force equation of motion for vacuum fields, has shown good invariance of the magnetic moment. The action, however, has been found to be conserved on a piece-wise basis only, for a significant portion of the trapped particles (Figure 3). This is due to the predominance of the transitional orbit types in the torsatron geometry.

A related result is the absence of superbananas in the torsatron, which lacks the closed helical magnetic wells found in stellarators. Analytic predictions of superbananas are invalid due to the non-conservation of the action in the predicted superbanana regime.

Neutral beam injection is the next large step that must be taken in the heating of torsatron/stellarator type devices, especially in the light of drift parameter scaling previously reported on the Cleo stellarator, and now reported in L-2. We have examined neutral injection into two large proposed devices, one a "classical" torsatron, and the other an "ultimate" torsatron, using a modified version[3] of the Dei-Cas code. This code uses a single-particle guiding center model to follow the fast ions down to thermalization with the inclusion of Monte-Carlo type collisions. It is fully three dimensional in both orbits and fields.

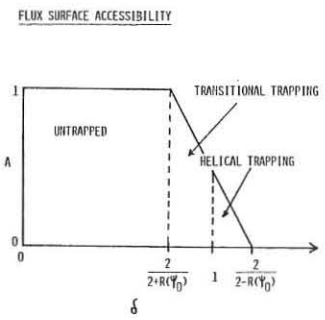

Figure 2

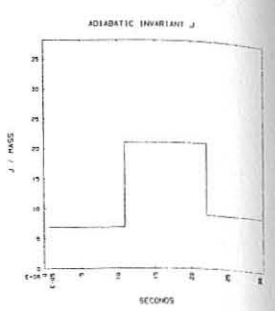

Figure 3

The machine investigated had the following parameters:

Classical: $\ell = 3$, 16 field periods, BT = 30kG, R = 306 cm, r = 50 cm, $\phi = m\theta$ winding law

Ultimate: $\ell = 2$, 12 field periods, BT = 30kG, R = 250 cm, r = 56 cm, $\phi = m\theta + \alpha\sin\phi$ winding law $\alpha = .63$

Similar plasma parameters were assumed for the two devices: $\bar{T}_e$ = 500 eV $\bar{N} = 5 \times 10^{13}$, $z_{eff} = 1$, $N = 7 \times 10^{-8}$ Torr. One of the beam parameters studied was the injection angle with respect to the magnetic axis. In both cases, the difference in efficiency between tangential and perpendicular injection was a factor of 3-4, with tangential being the most efficient.

The reason for this can be seen as follows: trapped particles are poorly contained compared to circulating particles. Tangential injection puts all of the particles in with a relatively low pitch angle. Since $\tau_{slowing\ down} \leq \tau_{90\%scattering}$ for the parameters chosen, most of the tangentially injected particles slow down before they are scattered into trapped states (Figure 4). As the angle is moved toward perpendicular, the velocity space angle to the trapped states is reduced, with a corresponding reduction in the amount of energy deposited before a particle becomes trapped (Figure 5).

These calculations show the importance of tangential injection for a large, beam heated device, where efficiencies as high as 94% can be attained with tangential injection.

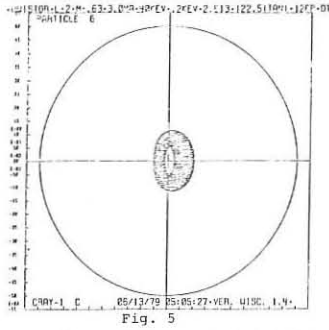

Fig. 5

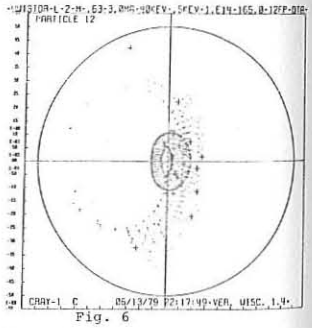

Fig. 6

Figure 5. Tangentially injected particle
Figure 6. Non-tangentially injected particle

This work is supported by the National Science Foundation under grant ENG-77-14820 and the U.S. Department of Energy under contract No. ET-78-S-02-5069.

1. C. Gourdon, D. Marty, E. K. Maschke, J. P. Dumont, in Plasma Physics and Controlled Nuclear Fusion Research (Proc. 3rd Int. Conf., Novosibrisk, 1968) 1, IAEA, Vienna 877 (1969).

2. C. Gourdon, P. Hubert, D. Marty, C.R. Acad. Sc. Paris, Vol. 271, p. 843 (1970).

3. Modified by S. Rehker, Max Planck Institute fur Plasmaphysik, Garching-bei-Munchen, FRG.

OHMIC HEATING DISCHARGES IN THE L-2 STELLARATOR WITH GAS PUFFING

E.D.Andrjukhina, M.A.Bloch, M.S.Berezhetskii, T.S.Sbitnikova, G.S.Voronov, S.E.Grebenshchikov, K.S.Dyabilin, O.I.Fedjanin, N.F.Larionova, H.F.Lunin, S.V.Kladov, S.N.Popov, A.V.Khudoleev, Yu.V.Kholnov, I.S.Spigel

P.N.Lebedev Institute of the Academy of Sciences of the USSR, Moscow

Ohmically heated plasma with gas puffing was investigated on the L-2 stellarator. The machine and plasma parameters are as follows: the stainless steel vacuum vessel has major and minor radii R=100 cm and r=17.5 cm, the plasma mean radius is a=11.5 cm, helical winding l=2, N=14, the vacuum rotational transform on the axis is ι (0) = 0.185 and at the plasma edge is ι (a)=0.8, B=14 + 16 kG, I_p=18 ÷ 22 kA and gas puffing was used in hydrogen discharges. Fig.1 illustrates the time history of the plasma parameters for typical discharges both without and with gas puffing. With gas puffing (Fig. 1b) the plasma density increased linearly with time while the radiation power P_{wall} grew proportionally to the electron density. The central electron temperature showed weak dependence on the mean plasma density up to $n_e \sim 2 \cdot 10^{13} cm^{-3}$ and above this value dropped

Fig.1

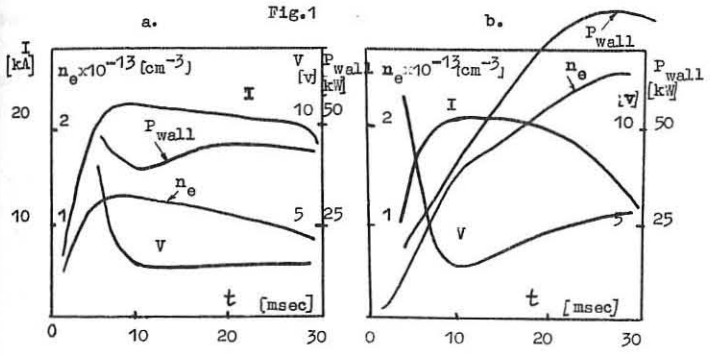

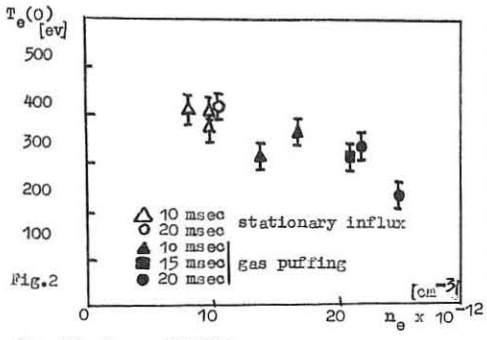

Fig.2

sharply (Fig. 2). The central ion temperature changed only negligibly with density and agreed essentially with those discharges without gas puffing. The intensity of soft X-ray decreased monotonously with plasma density.

During the density increase no instabilities were observed but plasma resistivity increased. It is possible that these phenomena are caused by cooling of the plasma edge due to the influx of cold gas and impurities from the wall. The increase of plasma resistivity in L-2 leads to the change in the operation of the primary circuit of the ohmic heating transformer. The ohmic impedance became equal to the reactive impedance and the primary circuit source cannot maintain constant plasma current. The high level of radiation losses and the current generator impedance are possibly the main upper limit to the neutral flux and plasma density. The decrease in the soft X-ray intensity while the electron temperature remaines constant can be explained by decrease in impurity concentration in the plasma column. At first sight, this appears in contradiction with the observations at the increase in the intensity of light impurities of the plasma edge. These phenomena can be connected with the diminution of electron temperature at the plasma edge, simulteneously with the increasing plasma density but not the increase of impurities. The independence of the central ion temperature on the plasma density does not agree with the Artsymovich formula. It is possible that these phenomena are connected with the neutral density increasing and the increase flux P_{ex}. The measurements of the charge-exchange flux (on the site of the torus opposed to the gas puffing pot) showed that 30% of the ion power input were lost with charge-exchange flux.

There appears to be no decrease in the central electron temperature at higher densities obtained with gas puffing into target hot plasma while the quasi-steady-state discharge indicate monotonously diminishing of the electron temperature as the density grows. It seems that gross energy confinement time increases with gas puffing.

[1] D.K.Akulina et al, Fizica Plasmy 4, 1022 (1978).
[2] V.S.Vlasenkov et al. Proc. 7th Int.Conf. (Innsbruck, 1978), CN-35-D-5.

OBSERVATION OF SAWTOOTH FLUCTUATIONS IN OHMIC HEATING DISCHARGES IN THE L-2 STELLARATOR

M.S.Berezhetskii, S.E.Grebenshchikov, B.I.Kornev, J.H.Harris*, I.S.Shpigel

In this paper we report the results of investigations of fluctuations in OH plasma in the L-2 stellarator. Soft X-ray radiation along different chords of the plasma cross-section was detected with two movable silicon surface-barrier detectors. In some operating regimes in a well cleaned vacuum chamber usual sawtooth oscillations were observed. Fig. 1 shows typical radial distribution of amplitude $\frac{\Delta \tilde{U}}{U}$ sawtooth modulations of the soft X-ray flux.

The amplitude of fluctuationshas the maximum value at the centre of plasma column, decreases with radius and goes practically to zero at some surface. Out of this surface the amplitude of fluctuations grows again and changes its phase. Sawtooth period is 0.2-0.3 msec and the amplitude increases with plasma density (Fig.2). Assuming that fluctuations of X-ray intensity is mainly due to the change in electron temperature we found that $\Delta \tilde{T}_e$ at the centre of the plasma column is up to 20 eV (Te(0) = 400 - 500 eV, $n_e \sim 10^{13} cm^{-3}$). The radius of the surface at which the change in the phase of sawtooth fluctuations took place at the given value of

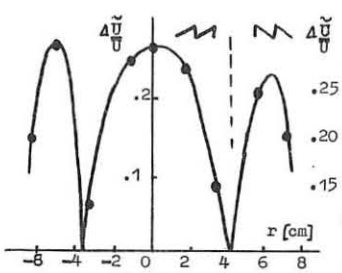

Fig.1

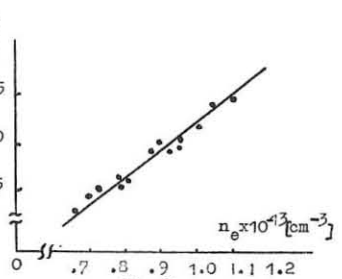

Fig.2

a confining magnetic field increased with ohmic heating current(Fig.3)

In the L-2 experiments we did not succeed in the fluctuation mode analysis due to the small value of X-ray signal. We analysed the possibility of appearance of sawtooth oscillations due to development of m=2, n=1 mode at a resonance surface with t=0.5. It is possible only at the flat current density distributions and does not agree with the measured electron temperature distribution. The appearance of m=1 at the t=1 surface r=4 cm requires peaked current profile which may be due to the effect of stellarator-trapped particles on the plasma conductivity [2] .

The thermal flux from the plasma central part through the resonance surface due to the sawtooth fluctuations gave ~ 5 KW power losses that is 20% of the ohmic power input in these conditions.

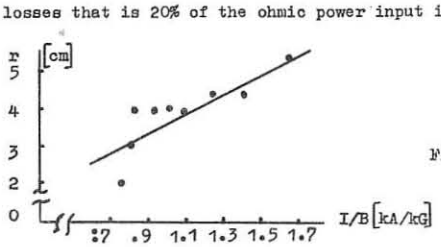

Fig.3

[1] D.K.Akulina et al.IAEA Plasma Phys. and Contr.Nucl.Fusion 11, 115 (1976)
[2] D.K.Akulina et al.IAEA,Innsbruck,CN-37-H-4 (1978)

BP30

THE EFFECT OF STOCHASTIC ELECTRIC FIELDS ON TRANSPORT OF LOW COLLISION FREQUENCY PLASMA IN TORSATRON WITH A HIGH HELICAL INHOMOGENEITY.

V.K.BOCHAROV, P.Ya.Burchenko, V.S.Voitsenya, E.D.Volkov, A.Yu.Voloshko, S.S.Kalinichenko, K.S.Rubtsov, S.I.Solodovchenko, O.M.Shvets, A.F. Shtan'.

THE KHARKOV PHYSICAL-TECHNICAL INSTITUTE, ACAD. SCI., UKR. SSR, KHARKOV, USSR.

ABSTRACT

In the l=1 torsatron "Vint-2o" [1] the presence of high inhomogeneities of a magnetic field results in the increase of low-collisional currentless plasma losses and the anomaly of current-carring plasma electric conductivity at low electric fields. The excitation in a plasma of R.F. fields with a broad spectrum gives an appreciable effect in the improvement of plasma confinement.

One of results of the neoclassical theory is an increase of transport coefficients due to the trapping of some part of charged particles between magnetic field local inhomogeneities: helical ones - in a stellarator [2] and longitudinal ones - in a tokamak[3]. The most substantial increase of losses was detected in model experiments at those stellarators where helical inhomogeneities are especially high[4]. For example, as seen from fig.1a, the change of collision frequency of injected plasma in the l=1 torsatron "Vint-2o" resulted in 5-fold change ($\tau \sim \nu_e^{0,4}$) of the lifetime.

The measurements with the current-carrying plasma in this machine show that rather strong anomaly of electric conductivity takes place in the low electric field range (low-collisional regime of plasma diffusion).

Fig.1b shows the comparison of dependences, on the electric field value, of plasma electric conductivity anomaly, $\frac{\sigma_{coul}}{\sigma_{exp}}$, measured both on Sirius (curve 1) and Vint-2o (curve 2) machines. Magnetic configurations of both machines differ in values of magnetic field inhomogeneities associated with toroidality (ε_t) and helical currents (ε_h) for the stellarator Sirius ε_t= 0,04 and ε_h=0,01, and for the torsatron Vint -2o ε_t=0,25 and ε_h=0,65 (for the outer - most magnetic surfaces).

The coincidence of dependences $\frac{\sigma_{coul}}{\sigma_{exp}}$ in the high electric field range ($E/E_{cr} > 1$), where noises are excited with the electric field strength $\tilde{E} \sim$1-1o kv/om [5], could be interpreted as the result of the effective collisional frequency increase due to this fluctuating noise field.

It was shown in the stellarator Saturn [6] that the excitation in a plasma of fluctuating electric fields with a broad spectrum ($\Delta f \sim 2$ MHz) resulted in decreasing the effect caused by trapped particles.

The initial data used for the estimation of a generator frequency range for the Vint-2o torsatron are shown in Fig.2: the radial dependences of a plasma density (n_e), quantity of localised electrones (δn) and the frequency of electron reflections from the local magnetic mirrors (f_g). It is seen that the total calculated frequency range is rather wide ($\Delta f_g / \bar{f}_g \approx \frac{1}{2}$), however, for a high portion of localised electrons (the volume with $r > 4$ cm, Fig.2) the difference of calculated frequencies does not exceed $\sim$1 MHz. As a result of this, it would be possible to have at this machine a significant effect of transfering of localised particles into passing ones in such conditions when the frequency range of RF generator is quite narrow : $\frac{\Delta f}{\bar{f}} \ll 1$.

Experiments were performed with a plasma produced by the ECR in quasi-stationary conditions (the magnetron frequency $f_e \simeq 2{,}5 \cdot 10^9 sec^{-1}$, the discharge duration $\simeq$2 sec), and the effect of changing of plasma confinement was registered by the change of plasma density.

For the excitation of RF electric fields with a broad spectrum in a plasma the pairs of elements were used. They were placed near outer regions of the outermost magnetic surface in five (out of thirteen) magnetic field periods. As in work [6], the spectrum of excited oscillations in a plasma differed slightly from the spectrum of the generator.

The measurements showed: the effect of R.F. field excitation to depend greatly on the spectrum of the RF generator and the plasma density. The best results were obtained when the mean spectrum frequency was approximately two-three times of the frequency found from the simple estimation, Fig.2: $\bar{f}_{est} \simeq$ 8 MHz, $\bar{f}_{exp} \simeq$ 18 ÷ 28 MHz.

The maximum change of the plasma density during RF field excitation has been obtained under minimum background pressure ($\sim 10^{-6}$ torr) when it was still possible to maintain an ECR discharge.

The dependence of amplitudes of the electric probe signals obtained with (A_{RF}) and without (A_o) RF field excitation is shown in Fig.3. It is seen, that the "positive" effect value decreases very fast with the increase of plasma density (A_o), that is with the increase of the electron collision frequency.

This fact, together with an optimum on RF voltage found, is an indication that the effect of improvement of plasma confinement does not relate to the additional ionization of the background gas, but is caused by an untrapping of some portion of localized electron into passing trajectories.

REFERENCES

1. A.V.Georgievskii at.al., "3d Intern.Symp.on Toroidal Plasma Confin.", Garching, 1973, paper D-11.
2. B.B.Kadomtsev, O.P.Pogutse, Nucl.Fus., 11,67 (1971).
3. T.E.Stringer, Ibid [1], paper F1-1.
4. V.S.Voitsenya et al., IAEA, Tokyo, 1974, vol. 2, p.63, Vieenna, 1975.
5. A.P.Barkov at al., Ibid [1], paper E - 18.
6. V.S.Voitsenya, et al., "7th Europ. Conf. on Plasma Phys. and Nucl. Fus.", Prague, 1977, 1, p.124.

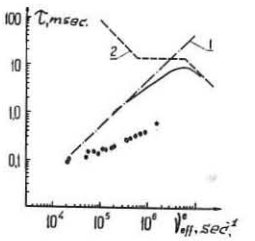

Fig. 1a.

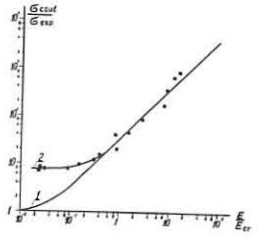

Fig.1b

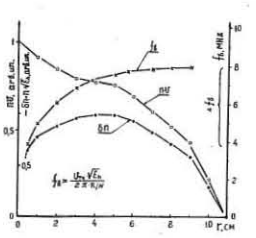

Fig. 2

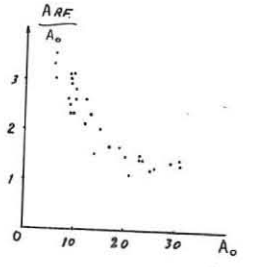

Fig. 3

CURRENT TURBULENT ION HEATING IN MODULATIONAL INSTABILITY REGIME AND CAVITON TRANSPORT DYNAMICS IN A STELLARATOR IN A HIGH MAGNETIC FIELD

N.F.Perepelkin, V.A.Suprunenko, A.S.Slavny, M.P.Vasil'ev, A.G.Diky, V.D.Kotsubanov, B.V.Kravchin, A.E.Kulaga (Phys.-Techn. Inst. Acad. Sci., Ukr.SSR, Kharkov, USSR); Ya.Shtöckel (IPP, Prague, CZSSR)

Identification of turbulent discharge modulational regime has been performed on combinative spectra of thermal radiation of the cyclotron harmonic $2\omega_{ce}$ and epithermal sporadic radiation near Langmuir frequency ω_{pe}. The dynamics of turbulent discharge transfer into modulational regime and ion heating effect have been investigated.

The nonmaxwellian ohmic heating of ions in stellarators and tokamaks arises in strong electric field $E \sim E_{Dr}$ against the background of intensive low-hybrid oscillations. The excitation mechanism for oscillations and the conditions of effective transforming of turbulent energy over to particles are not enough studied. For such low-density discharges with run-away electrons the "slide-away" regime term has become strong enough, here preference is being given to the instability on the Doppler anomalous effect [1] .

In the URAGAN-2 stellarator in the fields $E > E_{Dr}$ the growth of ion noise intensity ω_{pi} results in disruption of quasi-stationary electron acceleration. At low heating efficiency of electrons the transverse electron temperature $T_e^{\perp}$ does not strongly depend on electric and magnetic field strength. The contradiction implies the fact that the increase of plasma turbulization degree in a strong magnetic field leads to the decrease of plasma resistance. As a result, the plasma anomalous resistance depends on the magnetic field $R \sim 1 - \frac{H}{H_{max}}$, and the noise energy is effectively pumped over to ions.

In the given work the regimes of ion heating and the dynamics of current discharge transfer into the strong-turbulence regime with low impedance have been studied in order to identify instabilities. The dependences of various parameters of ohmic heated plasma on electric and magnetic fields have been obtained for two gases H_2, D_2 at $n_e = \text{const} = 6 \cdot 10^{12}\,cm^{-3}$ and H=5-20 kOe on the basis of laser-$T_e^{\perp}$; microwave $T_{Br}^{\omega_{pe}}$ measurements, and the spectra $\omega_{pe}, 2\omega_{pe}$ and $2\omega_{ce}$; X-ray γ (5--100 keV); spectroscopy and neutral charge-exchange atoms- $\langle n_i T_i^{\perp} \rangle$, as well as magnetic measurements of noise intensity- $P_{\omega_{pi}}$.

Phenomenology of discharges in the stellarator is the following: in low $\omega_{ce} \ll \omega_{pe}$ and high $\omega_{ce} > \omega_{pe}$ magnetic fields the nature of anomalous resistance is different. In both cases with the electric field rise, near the threshold $E = E_{Dr}'' \sim n_e/T_e''$, there takes place the excitation of noises ω_{pi} and the intensity of hard X-radiation γ both from the target in a plasma and chamber walls sharply drops. The stripping of quasy-stationary acceleration of electrons does not lead to the stripping of epithermal sporadic UHF radiation ω_{pe} , its brightness temperature $T_{Br}^{\omega_{pe}}$ is maximum in the regime of noise excitation ω_{pi} . In an unmagnetized plasma $\omega_{ce} \ll \omega_{pe}$ from the data of laser scattering and thermal UHF radiation ω_{pe} , in the fields $E > E_{Dr}''$ it is observed a strong anisotropy of temperatures $T_e'' \gg T_e^{\perp}$, so that $T_{Br}^{\omega_{pe}} = T_e'' \sim E$ at $T_e^{\perp}$ and $n_e = \text{const}$. Fig. 1 shows the dynamics of discharge transfer into a strong-turbulence regime with the magnetic field rise. It is seen that the excitation of epithermal sporadic radiation ω_{pe} and ion noises ω_{pi} , the change of anomalous resistance R nature, the drop of thermal component of the plasma UHF radiation $T_{Br}^{\omega_{pe}}$ and the associated with it jump of the drift parameter U/U_{Te} take place in the field $E > E_{Dr}''$ near the threshold $\omega_{ce}/\omega_{pe} \approx 1$. The exponential growth of total energy of ion hot component $\langle n_i T_i^{\perp} \rangle$ with the supercritical magnetic field rise is an essential fact. In this case the three-temperature energetic ion spectra arise, and with the magnetic field increase a number of particles and their energy grow. The spectra of synchrotron $2\omega_{ce}$ and epithermal ω_{pe} radiation allow to draw a number of important conclusions about turbulence nature and the extent of energy localization in the low-hybrid frequency range $\omega_L = \omega_{pi}(1 + \omega_{pe}^2/\omega_{ce}^2)^{-1/2} \sim \omega_{pi}$. In fact, the bumping of run-away electrons with the electric field rise leads to instability stripping on the anomalous Doppler effect and to the vanishing of transient synchrotron spectrum with the characteristic "red" shift $\omega < 2\omega_{ce}$. An anomalously broadened stationary combinative spectrum arises near the frequency $2\omega_{ce}$. As seen from Fig. 2, its fine structure depends on the gas mass, as frequency intervals between satellites are equal to $\Delta\omega \approx 2\omega_{pi}$; $4\omega_{pi}$ and $\Delta\omega \sim (M_i)^{-1/2}$. Here the dashed path shows the magnetic broadening in a stellarator in a radiation detection zone where $\Delta H/H = 1{,}5\ \%$.

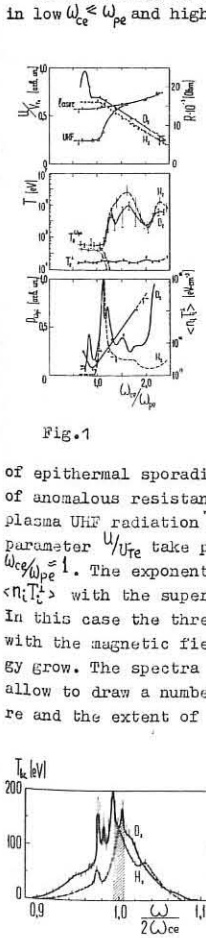

Fig.1

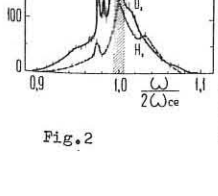

Fig.2

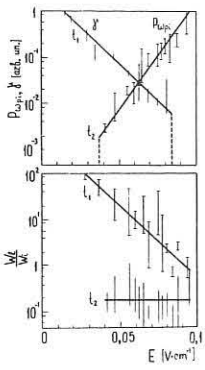

Fig. 3

The epithermal sporadic radiation spectrum where strong energy concentration near the Langmuir frequency ω_{pe} is observed is quite typical [2]. The harmonic ratio in the spectrum is $P_{2\omega_{pe}}/P_{\omega_{pe}} \approx 3(K/K_0)^2 W_t/W_i \sim 3 \cdot 10^{-4}$, which according to [3], allows to estimate redistribution of oscillation energy in a plasma in a wide frequency range. As the scale of turbulence satisfies the condition $K < K_0 \ll K_D = \omega_{pe}/U_{Te}$ at $K = 3 \cdot 10^{-2} K_D$ and it can decrease only with the density rise of oscillation energy due to energy pumping over to a long-wave region, so even for small changes in $K_0 \ll K_D/2$, the density of ions oscillation energy greatly exceed the density of Langmuir oscillations $W_i > 10 W_t$.

Investigations showed that in the high magnetic field $\omega_{ce} \approx 2{,}2\,\omega_{pe}$ the ratio W_t/W_i depended on the electric field strength and the number of accelerated electrons which can, for example, appear in a for-plasma with low field strength $E \ll E_{Dr}$, and then their bumping in a turbulent phase at $E > E_{Dr}$ takes place. Fig. 3 shows the dependences of W_t/W_i , $P_{\omega_{pi}}$ and γ on the electric field in the bumping $t_1 = 200\ \mu$sec and turbulent $t_2 = 400\ \mu$sec discharge phases. It is seen that an exponential decrease of X-radiation intensity $\gamma < 100$ keV in the bumping phase t_1 (when the noise level $P_{\omega_{pi}}$ is low) correlates with the intensity decrease of Langmuir oscillations $W_t/W_i \approx 10^2 \div 1$. In the turbulent phase t_2 when hard X-radiation $\gamma > 10$ keV does not exist, the exponential rise of ion noises $P_{\omega_{pi}}$ stabilizes the ratio at the level $W_t/W_i < 10^{-1}$. The estimation of Langmuir turbulence extent from the data $P_{2\omega_{pe}}$ gives the value which is much less than the threshold of modulational instability excitation [4] : $W_t/nT \ll (K/K_0)^2 \sim 10^{-3}$.

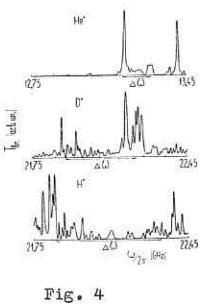

Fig. 4

At the same time, a high radiation level on plasma frequency $P_{\omega_{pe}} \sim 2 \cdot 10^{-6}\ W \cdot cm^3$ can be well associated with the phenomenon of cavitation in low-hybrid spectrum range , as $W_t/nT > (K/K_0)^2 (\omega_{ce}/\omega_{pe})^2 m/M_i \sim 5 \cdot 10^{-6}$.

The combinative spectra of the synchrotron $2\omega_{ce}$ (Fig.2) and epithermal ω_{pe} radiations are the confirmation of the given hypothesis. Fig.4 shows the fine structure of sporadic bursts near ω_{pe} for various gases and plasma densities : He ($n_e \approx 2 \cdot 10^{12}\,cm^{-3}$) , D_2 and H_2 ($n_e \approx 6 \cdot 10^{12}\,cm^{-3}$) obtained during $5\ \mu$sec. Here the minimum frequency shift between satellites is equal to $\Delta\omega \approx \omega_{pi}$. The basic radiation power is enclosed in a doublet of lines with frequency difference $2\Delta\omega \approx 2\omega_{pi}$.

Thus, it has been stated that in the electric field $E > E_{Dr}''$ the stripping of quasi-stationary electron acceleration in the URAGAN-2 stellarator is caused by the excitation of intensive ion oscillations, the energy of which is much more than that of Langmuir ones $W_i \gg W_t$. Under conditions of plasma magnetization, when $\omega_{ce} > \omega_{pe}$, this probably results in formation of low-hybrid cavitons with the scale $K_0 < K_D/2$.

The turbulent discharge transfer into the modulational regime near the threshold $\omega_{ce}/\omega_{pe} \approx 1$ is followed by an effective heating of ions and electrons from the tail of their energy distributions. Along with stationary perturbations of plasma density and a magnetic field which were observed earlier in these conditions [2] , the stationary combinative spectrum of the synchrotron radiation $2\omega_{ce} \pm n2\omega_{pi}$ and sporadic bursts near the frequencies $\omega_{pe} \pm n\omega_{pi}$; $\omega \sim \omega_{pi}$ and $2\omega_{pi}$ are the direct indication to the modulational instability excitation in the low-hybrid spectrum. It is the modulational processes in the low-hybrid spectrum which lead to production of fast ions and electrons and which can be the reason of radiation of combinative spectra ω_{pe} and $2\omega_{ce}$.

It is supposed that due to cavitation the longitudinal transport increases and the anomalous plasma resistance drops with the magnetic field rise.

REFERENCES

1. B.Coppi et al. Nuclear Fusion, 16, 309, 1976.
2. N.Perepelkin et al. 8-th Europ.Conf.Contr.Fusion, 144, Prague 1977.
3. A.Ivanov, D.Ryutov, Zh.Eksper.i Teor.Fiz.(USSR), 48, 684, 1965.
4. V.Sotnikov, V.Shapiro, V.Shevchenko. Fiz.Plasmy (USSR), 4, 450, 1978.

BP32

PLASMA-WALL INTERACTION STUDY IN KHARKOV STELLARATORS

A.B.Blank, V.S.Vojtsenya, E.D.Volkov, A.Yu.Gribanov, A.G.Dikij, Eh.S.Zolotovitskaya, E.M.Latsko, V.F.Rybalko, V.P.Samoilov, S.I.Solodovchenko

The analysis of vacuum chamber inner surfaces of the Uragan-2 and Sirius stellarators shows that strongest plasma-wall interaction is realized in the regions close to the separatrix apexes where the major plasma flux to the wall is localized, which azimuthal distribution has been measured by means of special multilamellar probes.

From year to year the importance of plasma-wall interaction studies in the fusion program is growing. This type of study is usually carried out with tokamaks and special devices [1] but there are practically no results obtained for stellarators though plasma wall interaction here has some peculiarities. In this paper we report some experimental results concerning plasma-wall interaction in the stellarators Uragan-2 [2], Saturn [3] and Sirius [4] of the Kharkov Physico-Technical Institute. All these devices are, so called, "classical" stellarators with l=3 helical windings. In Table 1 the parameters of these devices and ranges of n_e and T_e (under principal operating regimes) are shown.

The measurements, performed with special multilamellar electrostatic probes, indicate that plasma fluxes to the vacuum walls of the Uragan-2 and Saturn stellarators are concentrated near apexes of the separatrix (Fig.1). The apexes, as it is known, are placed under helical conductors with the current direction opposite to the main magnetic field. The halfwidth of azimuthal distributions is only an insignificant portion of the minor perimeter of the vacuum chamber, for the Saturn stellarator ~1/20, for example.

At the same time, plasma flux values between separatrix apexes do not exceed 1% of maximum amplitudes shown in Fig.1. When comparing values of plasma flux to the wall at different positions of separatrix apexes one can see that there is a considerable difference between those of them directed to the inner and outer torus perimeters (apexes 1 and 4, respectively, in the insert of Fig.1). This difference is due to the toroidal inhomogeneity of magnetic field.

Thus, our measurements indicate that plasma-wall interaction regions in stellarators are restricted of by rather narrow helical bands placed under the "negative" helical conductors. The density of plasma contacting with the surface, due to strongly localized plasma fluxes, must be rather high. Evaluations made for the "Uragan-2" stellarator give values $\Gamma_w \lesssim 5 \cdot 10^{17}$ cm^{-2} sec^{-1} for the plasma flux and $n_w \lesssim 5 \cdot 10^{10}$ cm^{-3} for the density of plasma in contact with a surface.

The analysis of the vacuum chamber walls state in Uragan and Sirius, made of stainless steel, after several years of exploitation shows that areas of the heaviest erosion coincide with plasma flux outlet regions. The main reason for the erosion is unipolar arcs. In some regions of the Sirius vacuum chamber the density of arc tracks is so high that they are overlapping and form almost continuous strips going helically just under the "negative" helical conductors (Fig.2). The arc tracks cover $\lesssim$10% of the total surface area of the vacuum chamber and the density of arc tracks on the outer perimeter of torus is much higher than on the inner one, as Fig.3 shows. The difference is much greater than the difference between plasma flux amplitudes measured in the Uragan-2 and Saturn stellarators (Fig.1).

The arc length varies from several mm to several cm and the longest tracks (up to ~10cm) are observed on the outer part of the straight section of Uragan-2. These long tracks appearing here are ascribed to training discharges.

We estimated the formation of $\lesssim$10 arcs and the injection of $\sim 5 \cdot 10^{16}$ metal atoms per a discharge. Analysing the chemical composition of a deposit on the alumina break (Table 2) one can see that only small portion of metal atoms arrive into the plasma subsequently distributing all over the surface of the vacuum chamber. This fact is in agreement with data obtained from studies of the composition of sputtered matter in the vacuum arc [5]: the major portion of sputtered products is distributed along the electrode surface in the form of small metal drops.

The peculiarities of plasma-wall interaction described above (in particular, very strong localization of the interaction region near separatrix apexes) are typical of a stellarator configuration when the magnetic limiter plays an important part in the formation of a plasma volume. Consequently, transferring the zone of the active plasma-wall interaction into a special burial chamber (e.g. by means of torsatron configuration with a divertor [6]) and the use of special measures to suppress the arcing there [7] can guarantee an essential decrease of impurity content in a plasma.

Evaluations made for the torsatron Uragan-3 [8] show that in this case even the unloading divertor (with efficiency 90%) will give quite low metal (Fe) impurity concentration in the confining volume: $\frac{n_{Fe}}{n_e} < 3 \cdot 10^{-4}$ by the end of a discharge pulse.

References

1. Proceed. of 3rd Int. Conf. on Plasma Surface Int. in Thermonucl Devices, Culham 1978, J.Nucl.Mat., 76-77, 1978.
2. A.V.Georgievskij et al., Ukr.Fiz.Zh., 21, 422 (1976).
3. V.S.Vojtsenya et al., IAEA (Madison 1971), Vienna 1971, 3, 131.
4. P.Ya.Burchenko et al., Zh.Ehksper. Teor.Fiz., Pis'ma, 3, 243(1966).
5. J.E.Daalder, J.Phys.D, Appl.Phys., 9, 2379 (1976).
6. C.Gourdon et al., Nucl.Fus., 11, 161(1971).
7. G.H.Milley, J.Nucl.Mat., 63, 331(1976).
8. O.S.Druj et al., Proceed. of 7th Int.Vac.Congress, Vienna, 1977.

Table I

Devices	R_0 (cm)	r_0 (cm)	$\bar{r}_{pl}$ (cm)	H(kOe)	$\bar{n}_e (10^{12} cm^{-3})$	T_e (ev)	Δt (s)
Uragan-2	110	10	6,3	20	2-8	50-200	10^{-2}
Sirius	60	5	2,6	16	4-20	10-500	10^{-3}
Saturn	36	8,7	5,5	3	0,2-0,8	5-15	1

Table II

Devices	Chem. elements (10^{16} at/cm^2)			
	Fe	Ni	Cu	Mn
Uragan-2	2,5	1,2	0,13	0,3
Sirius	1	0,45	0,3	1

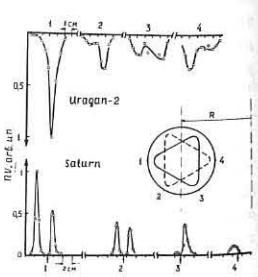

Fig.1.

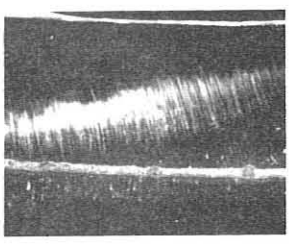

Fig.2.

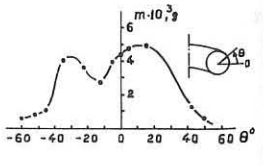

Fig.3.

BP34

RADIAL TRANSPORT IN THE ELMO BUMPY TORUS IN COLLISIONLESS REGIMES*

E. F. Jaeger, C. L. Hedrick, and D. A. Spong

Oak Ridge National Laboratory, Oak Ridge, Tennessee, USA

Introduction: Fully classical, thermally stable solutions for radial transport in the ELMO Bumpy Torus (EBT) have recently been achieved in the collisionless electron regime by changing the treatment of the cold neutrals at the plasma edge [1]. Previous one-dimensional (1-D) radial transport calculations for EBT have assumed a variable flux of cold neutrals at the plasma edge determined by instantaneous reflux of toroidal plasma particles at the wall [2]. This assumption gives thermally unstable solutions to the 1-D radial transport equations [3,4] for EBT in the collisionless electron regime, where experiments apparently operate stably [5]. An alternate boundary condition has now been applied that assumes constant flux of cold neutrals at the plasma edge. This provides a negative feedback mechanism to limit thermal excursions by reducing the power deposited per plasma particle [1].

Transport Coefficients: In these calculations diffusion is assumed to be neoclassical. Direct, or nondiffusive, losses are neglected. Transport coefficients include lowest order effects of velocity space regions where poloidal drift frequencies are small [2,6]. For particles that experience cancellation of electric and magnetic drifts in the bulk of the velocity space distribution (ions in EBT), the flux is dominated by slowly orbiting particles on noncircular drift orbits. In the moderate collisionality (plateau) regime, this gives transport coefficients independent of collision frequency [2,6]. Specifically, the plateau result of Eq. (14) in Ref. 2 is used for ions. For particles that do not experience such a bulk cancellation of drifts (electrons in EBT), the flux is dominated by particles with large poloidal drift frequencies and nearly circular orbits. For convenience, the large electric field result of Kovrizhnykh [7] is used for electrons. Conservation of charge requires that enhanced ion particle losses in the plateau regime increase the radially inward pointing electric field, thus broadening the regime in which such negative electric field solutions exist.

Radial Transport Calculations: Stability results for two neutral boundary conditions are illustrated in Fig. 1, which shows radial profiles of plasma density n, ambipolar potential ϕ, ion temperature T_i, and electron temperature T_e at 4-ms time intervals as the 1-D transport calculation proceeds from the initial parabolic profiles at time t = 0 to the collisionless electron regime. The calculations in Fig. 1 are for typical EBT-I parameters with 24 mirror sectors, plasma radius a = 10 cm, major radius R_T = 150 cm, bounce-averaged magnetic field on axis $B_o \sim 6.4$ kG, cold neutral energy $E_o \sim 0.5$ eV, electron ring beta $\beta_a \sim 37\%$, microwave power absorbed by toroidal electrons P_μ = 6 kW, and power absorbed by toroidal ions P_b = 0 kW. At the edge, r = a, plasma density and temperature are fixed at $n = 3 \times 10^{10}$ cm^{-3}, and $T_e = T_i$ = 13.5 eV.

In Fig. 1(a), the flux of cold neutrals at the plasma edge is assumed to be determined by the toroidal plasma through instantaneous reflux of plasma particles at the wall. In this approximation the total number of plasma particles remains constant in time. In the collisionless regime, energy containment time increases with electron temperature, and for a constant total number of particles, there is a net positive feedback, causing electron temperature to become arbitrarily large. Steady-state solutions exist if the temperature dependence of the energy lifetime is modified artificially at low collisionalities [2].

In Fig. 1(b), the flux of cold neutrals at the plasma edge is assumed constant independent of toroidal plasma parameters. Such a boundary condition is appropriate if reflux from the wall occurs on a time scale that is slow compared to the energy containment time. As the temperature and lifetime increase, so does the total number of particles, thus reducing the power deposited per particle. This provides a negative feedback mechanism that limits the thermal excursion and yields thermally stable results in the regime of the experiment, i.e., collisionless electrons with negative electric fields.

Figure 2 shows thermally stable, steady-state solutions with constant edge neutral flux as in Fig. 1(b) and 8 kW of power deposited in the toroidal plasma. In the solid curves all power is assumed absorbed by the electrons (P_μ = 8 kW, P_b = 0 kW). In the dashed curves, one-fourth of the power is assumed absorbed directly by the ions (P_μ = 6 kW, P_b = 2 kW). Edge neutral pressure is varied as a parameter along the curves. In all cases the shape of the potential is such as to produce a negative or radially inward pointing electric field [3]. In Fig. 2(a), steady-state values of energy containment time τ_E and electron and ion temperatures on axis are plotted vs central plasma density. In Fig. 2(b), the steady-state product of energy containment time τ_E and central electron temperature is plotted vs electron collisionality $\nu_e/\Omega_{o,e}$ on axis. Two distinct collisionality regimes are evident in Fig. 2. In the collisional regime, τ_E varies as $T_e^{-7/2}$, and edge neutral pressures are high. In the collisionless regime, τ_E varies as $T_e^{3/2}$, and edge neutral pressures are low. Also, in the collisionless regime density, temperature, potential, and lifetime all increase with decreasing neutral pressure [1], as observed experimentally [5]. A discontinuity in the variation of T_i with n occurs when cancellation of poloidal drifts becomes possible for thermal ions at some radius within the plasma.

The effect of direct ion heating is shown by the dashed curves in Fig. 2, where one-fourth of the power is absorbed directly by ions. In this case for the same plasma density, both energy containment time and ion temperature increase. Also, for the same electron collisionality, the product of electron temperature and energy containment time increases with direct ion heating.

References:

*Research sponsored by the Office of Fusion Energy (ETM), U.S. Department of Energy under contract W-7405-eng-26 with the Union Carbide Corporation.

[1] E. F. Jaeger, C. L. Hedrick, and W. B. Ard, submitted to Phys. Rev. Lett.

[2] E. F. Jaeger et al., Oak Ridge National Laboratory Report ORNL/TM-6806 (1979).

[3] E. F. Jaeger et al., Phys. Rev. Lett. 40, 866 (1978).

[4] E. F. Jaeger and C. L. Hedrick, Nucl. Fusion 19, 443 (1979).

[5] R. A. Dandl et al., Oak Ridge National Laboratory Report ORNL/TM-6457 (1978); F. W. Baity et al., this meeting.

[6] R. D. Hazeltine et al., Science Applications, Inc., Report SAI-02379-664LJ (1979); submitted to Nucl. Fusion.

[7] L. M. Kovrizhnykh, Sov. Phys. — JETP 29, 475 (1969).

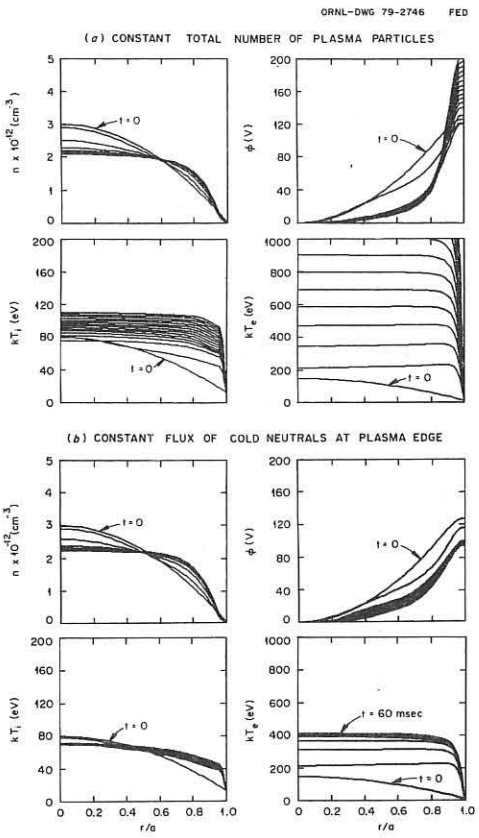

Fig. 1. Plasma profiles at time intervals Δt = 4 ms for two neutral boundary conditions: (a) constant total number of plasma particles; (b) constant flux of cold neutrals at the plasma edge.

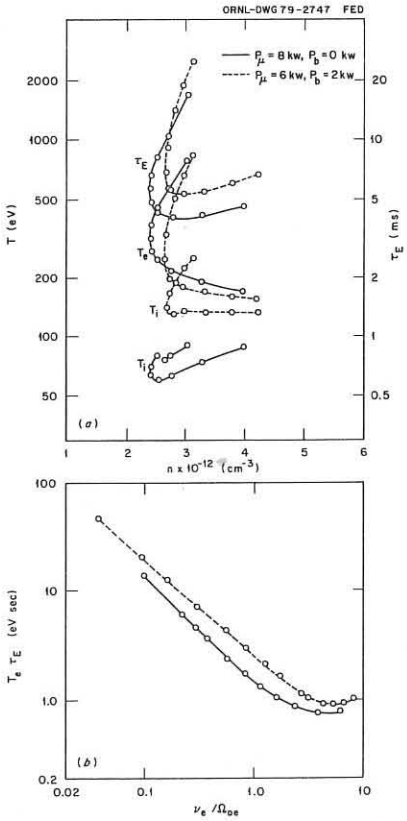

Fig. 2. (a) T_e, T_i, and τ_E vs n in steady state with the boundary condition of Fig. 1(b) and P_μ = 8 kW, P_b = 0 kW (solid); P_μ = 6 kW, P_b = 2 kW (dashed). T_e, T_i, and n are evaluated on axis. (b) Confinement scaling with electron collisionality for the boundary condition of Fig. 1(b) and power deposition as in (a).

D2.1

Accumulation of Impurities in the
High Density Regime of PULSATOR

W.Engelhardt, S.Sesnic, K.Lackner, G.Fußmann, J.Gernhardt,
E.Glock, S.von Goeler[+)], N.Gottardi, F.Karger, O.Klüber,
G.Lisitano, H.M.Mayer, D.Meisel, H.Murmann, F.Wagner
Max-Planck-Institut für Plasmaphysik, EURATOM-IPP Assoc.
D-8046 Garching, F.R.G.

I. Introduction: The accumulation of impurities as predicted by neoclassical theory has been observed in the high-density regime of Pulsator /1,2/. The effect was deduced from the time evolution of the signals from an X-ray diode array which integrated over the spectral range from photon energies of 1 to 10 keV. In order to investigate the effect at lower photon energies as well, we extended the spectral range of the diodes down to 100 eV. The results, which confirm the accumulation hypothesis, are presented in Sec.II. A systematic parameter study of the conditions leading to accumulation was performed. It showed that the accumulation depends on the density build-up, the plasma position, and the safety factor q(a). The results are given in Sec.III. Finally, an attempt is made in Sec.IV to explain all observed features of the accumulation effect in terms of a model which includes the interaction of neoclassical diffusion and anomalous transport caused by sawtooth activity.

II. Spectral Resolution of the Impurity Radiation During Accumulation: By means of X-ray diodes it is possible to measure the radiation over a large spectral range. A rough spectral resolution can be achieved by placing different Be foils in front of the diodes. Using five different filters (0, 0.5, 2, 12.5, 25 μm Be in addition to 0.02 μm Au on the diodes), we obtained five spectral channels by subtracting the transmission curves of the individual filters. The half-widths of these spectral windows are indicated in Fig. 1. The radial intensity profiles with different filters were taken 1 ms as well as 20 ms before disruption of a $I_p = 60$ kA, $B_t = 2.7$ T discharge. After Abel inversion of the intensity profiles the emissivity measured by diodes with different filters is subtracted in the same way as the filter curves and normalized by the integral over the transmission curve of the spectral window. The resulting spectra are displayed in Fig. 1 for five radial positions. For reference we have included the slope of a bremsstrahlung spectrum taking the measured electron temperature. It is obvious that these spectra depend on the plasma radius, and that they are strongly dominated by line emission. Comparing the two points in time, it is seen that the whole spectrum peaks within $r \leq 4$ cm at the disruption. This effect is not due to peaking of the temperature or density of the electrons, as shown by the Thomson scattering measurements. It is very likely that an accumulation of iron, which has many lines between 0.7 and 1.2 keV, is responsible for the emissivity increase in the centre of the plasma. It cannot be excluded, however, that oxygen with strong lines at 0.57 keV and above 0.65 keV accumulates, too.

III. Conditions Leading to Accumulation: It has been reported in /1/ that the accumulation can be controlled by the hydrogen influx. In order to investigate this effect systematically, the gas influx was programmed in such a way as to yield constant $d\bar{n}_e/dt$. It was found that the critical density at which accumulation occurs depends on $d\bar{n}_e/dt$, as shown in Fig. 2. Below a certain threshold density of 5×10^{13}cm^{-3} no accumulation is observed. With increasing $d\bar{n}_e/dt$ the critical density for accumulation rises. In these cases the sawteeth disappear when $\bar{n}_{e\ crit}$ is reached and 5 to 20 ms later the discharges disrupt probably because of an unfavourable current density profile characterized by $q(o) > 1$ /3/. Above a threshold in $d\bar{n}_e/dt$ of 1.8×10^{15}cm^{-3}s^{-1} accumulation is no longer observed. The sawtooth activity continues until the high density limit /1/ is reached.

These results refer to well centred discharges. If the plasma is shifted inward or outward by more than ± 0.5 cm, accumulation is prevented and the discharges disrupt at $\bar{n}_e < \bar{n}_{e\ crit}$ without the sawteeth disappearing. High current discharges with $q \approx 2.8$ show a weaker tendency to accumulation. The sawtooth activity is much stronger in these discharges /1/. The increase of the diode signals before disruption is moderate and the time between the last internal and the main disruption is too short in order to decide whether $q(o) > 1$ has been reached.

IV. Transport Model: In the absence of temperature gradients the impurity flux with ionic charge Z may be written as

$$\Gamma_I = D_{neocl} \left(Z n_I \frac{1}{n_H} \frac{\partial n_H}{\partial r} - \frac{n_I}{r} \right) - D_{anom} \frac{\partial n_I}{\partial r} .$$

The first term describes the neoclassical diffusion where the inward convection dominates for peaked proton density profiles. The second term is due to some anomalous transport mechanism which produces an outward flux. As D_{neocl} is proportional to n_H and D_{anom} is probably proportional to n_H^{-1}, it is clear that accumulation can only occur above a certain critical density. This is in accordance with the experimentally found threshold density for accumulation (Fig. 1). It is difficult to understand, however, why $\bar{n}_{ecrit}$ increases with $d\bar{n}_e/dt$ and why the accumulation develops on a short time scale during which the density varies insignificantly. These findings may be explained qualitatively as follows: The sawtooth activity usually prevents accumulation in two ways: It increases D_{anom} and flattens the proton density gradient in the centre. On the other hand, the accumulation has a tendency to prevent sawteeth because it increases the central resistivity with a consequent reduction of the current density and an increase of q(o). Both effects, sawtooth activity and accumulation, counteract each other. Whenever the accumulation is strong enough, the sawteeth will disappear and the further development of the accumulation process can occur unhampered on a short time scale. If slight changes in the plasma parameters favour accumulation, it will therefore prevail. On the contrary, if there exist conditions in favour of sawtooth activity, accumulation will not be observed. A stronger influx of hydrogen, for example, may cool the edge of the plasma to some degree with a consequent slight peaking of the current density and a reduction of q(o). In this case a higher critical density would be necessary, so that accumulation can overcome the outward transport caused by the sawteeth. This picture fits to the following experimental findings:

- sudden occurrence of accumulation
- dependence of $\bar{n}_{ecrit}$ on $d\bar{n}_e/dt$ (Fig. 2)
- prevention of accumulation by an influx of krypton /1/ (edge cooling)
- weak accumulation at low q discharges (stronger sawtooth activity)
- prevention of accumulation by plasma displacement (reduction of q, edge cooling by impurity release from the wall)

V. Conclusion: Spectrally and radially resolved measurements of the impurity radiation show a strong radial peaking of the emissivity in the whole spectrum at constant or decreasing electron temperature before disruption. The most obvious explanation is an accumulation of impurities (probably iron) in the centre of the plasma. Other observations concerning the experimental conditions for the peaking of the emissivity are consistent with this assumption.

References:
/1/ W.Engelhardt et al., 7th Int.Conf. on Plasma Physics and Contr. Nuclear Fusion Research, Innsbruck 1978, IAEA-CN-37-A5.
/2/ W.Engelhardt et al., Proc.of Symp. on Disruptive Instability in Toroidal Devices, Garching, 1979, to be published by IAEA.
/3/ G.Fußmann et al., "Limitation of the Electron Density in the Pulsator Tokamak", this conference.

Figure Captions:
Fig.1: Spectrum of the emissivity of the plasma on five radii at two points in time measured by X-ray diodes with different Be filters.

Fig.2: Dependence of the critical mean density for accumulation on the density rise.

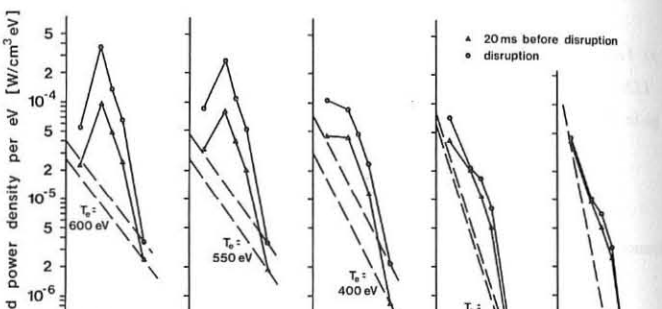

Fig. 1

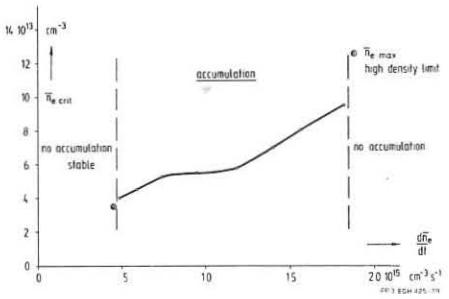

Fig. 2

[+)] On leave from Plasma Physcis Laboratory, Princeton University

D2.2

FLUX AND ENERGY OF DEUTERIUM INCIDENT ON A LIMITER-LIKE PROBE IN PLT

G.M. McCracken†, S.A. Cohen, H.F. Dylla, C.W. Magee+, S.T. Picraux*, S.M. Rossnagel, W.R. Wampler*

Plasma Physics Laboratory, Princeton University
Princeton, N.J. 08544 USA

Introduction. In tokamaks, the energy distributions of ions and neutrals striking surfaces of the vacuum chamber are important parameters in the overall power balance and impurity generation processes. Furthermore, the energies of the hydrogenic particles determine the saturation level of hydrogen isotopes in the walls and hence the tritium inventory in DT devices. Data on the energy distribution are available for neutrals at high energies from stripping cell analyzers, but there is little data on ions or low energy neutrals. The energies of ions cannot simply be deduced from plasma parameters as the ion energy may be modified by sheath potentials before striking the wall. New techniques for measuring the energy of hydrogen isotopes have been proposed based on depth distribution and saturation trapping value of the ions implanted in carbon and silicon collectors [1]. Some experimental results have been reported for TFR [2] and PLT [3]. The present paper reports the energy and fluence of deuterium as a function of radial position and evaluates the role of these particles in power balance and impurity generation.

Experiment. A set of carbon and silicon samples were mounted in PLT on a grounded, rotatable cylindrical probe behind a shield which had 3 mm slits on both the ion and electron drift sides, (Fig. 1). The samples were positioned on the torus mid-plane, with those nearest the plasma being just at the position of the outside limiter (45 cm). Those furthest from the plasma were behind the nominal wall position (50 cm). The plasma radius was determined by top and bottom carbon mushroom limiters at r =± 40 cm. The horizontal position of the plasma center was feedback stabilized at R = 137 ± 2 cm (Fig. 1). A series of exposures were made on each set of samples by rotating the cylinder. The exposures were to 1,2,3,6 and 12 low density discharges typical of those used for ICRF heating, i.e. I = 230 kA, $\bar{n} = 0.9 \times 10^{13}\,cm^{-3}$, $T_e(0) = 1.1$ keV, B = 17 kG, $V_L = 1.6$ V, and the pulse length was 0.4 sec. No auxiliary heating was applied during the present exposures. After exposure to the plasma, the samples were removed and analysed using both secondary ion mass spectrometry and ^3He (d,p) ^4He nuclear reaction analysis [3] for the amount of deuterium retained as function of the number of discharges. From this data and using the theoretical model [1], the mean energy, $\bar{E}$, and flux, Γ, of the incident ions were obtained under the assumption of a Maxwellian energy distribution. The depth profiles indicate that the ions have a broad energy distribution. The saturation behavior of the trapped deuterium as a function of incident flux gives another indication that the flux is not monoenergetic. [4] But because of the uncertainty about the detailed energy distribution we will refer to a mean energy for the deuterium rather than a temperature.

Results. The incident flux is determined from the absolute amount of retained deuterium after corrections for reflection and saturation. Figure 2 shows fluxes calculated for both cos θ and normal incidence impact angle distributions. The flux falls off monotonically with radius. At radii greater than 50 cm, in a recess in the vacuum wall, the flux drops by more than an order of magnitude. A low flux in this region is expected due to charge exchange neutrals, some being backscattered from the walls.

The results for the mean ion energies obtained as a function of radial position are shown in Fig. 3. In the range of the data, the energies are insensitive to whether a normal incidence or cos θ distribution is chosen. The energies and fluxes on the electron drift side are consistently below those on the ion drift side. Electron temperature profiles were not measured during the discharges which were used for sample exposure, but results obtained from Thompson scattering in similar discharges at a later date indicate values of T_e of 180 ± 50 eV at r = 36 cm [5]. If T_e were still above 100 eV at r = 45 cm and a sheath potential $-3T_e$ developed at the surface, then the sheath would have contributed a large fraction of the total energy.

Discussion. The high energies, although initially surprising, are only two times higher than energies observed in the divertor of the relatively cool C stellarator [6]. The power flux is calculated from the ion flux and mean energy and equals $\frac{4}{3}\Gamma\bar{E}$. We have also included the angle of the probe with respect to the toroidal field. The power falls off exponentially with an e-folding distance of 2.4 cm (Fig. 4). Integrating over the radius from 45 cm to 51 cm and over 2π in poloidal angle gives the total power flow in this annulus of

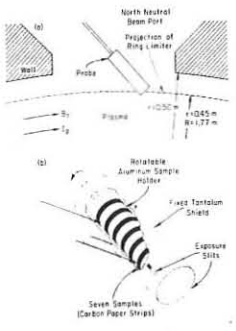

Fig. 1. Schematic of probe: (a) in the plasma boundary, plan view and (b) details of probe.

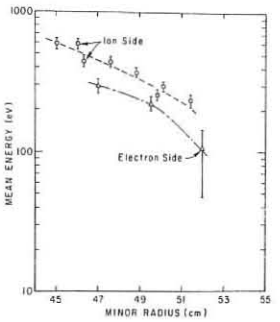

Fig. 3. Mean energy, $\bar{E}$, of incident deuterium obtained from saturation behavior (Δ,O) and from depth profiles (□) For a Maxwellian distribution $E = \frac{3}{2}kT$.

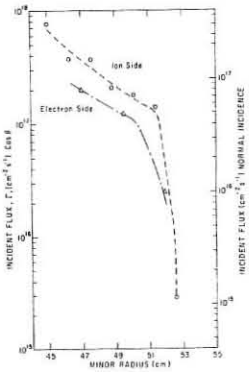

Fig. 2. Incident deuterium flux to the probe calculated from the trapped flux assuming (a) cos θ incident distribution (b) normally incident flux.

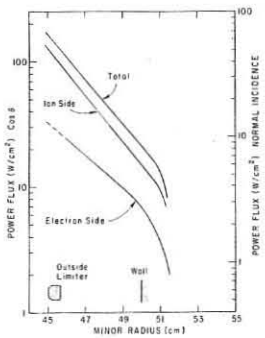

Fig. 4. Power flux to probe due to deuterium bombardment, calculated from the smoothed curves in Figs. 2 and 3. Correction has been made for the angle of probe with respect to B_T.

40 to 100 kW. The lower end of this range corresponds to normal incidence impact as would occur if a large sheath were present. The upper end corresponds to a cos θ distribution of impact angles. Over half the power is lost between 45 and 47 cm.

Making an integration over the same area for the sputtering due to these ions and using Bohdansky's sputtering yields [7], we obtain an erosion rate of 0.6 - 1.5 x 10^{19} atoms s^{-1} for stainless steel, and 1.2 - 3.0 x 10^{19} atoms s^{-1} for carbon. If the impurities were uniformly distributed through the plasma, this would be equivalent to an injection rate of 1.3 - 3.5 x 10^{12} and 2.6 - 7.0 x 10^{12} atoms cm^{-3} s^{-1} for Fe and C respectively. Again, more than half the yield comes from the annular region between 45 cm and 47 cm, the location of the PLT stainless steel ring limiter.

If we assume that deuterium arriving at the ion side target at r = 51.6 cm is representative of the charge exchange outflux, then integrating over the whole torus wall gives an estimated charge exchange rate of 10^{21} deuterons s^{-1}. This would produce sputtering comparable to that of the charged particle flux to the limiter. Such an extrapolation is, however, hazardous as the poloidal and toroidal asymmetries are known to be large.

Conclusion. The use of surface probes in the plasma edge has provided information about the flux and energy of particles arriving at the limiter. The values obtained in low density PLT discharges indicate that sputtering by ions at the limiter and by charge exchange neutrals produce comparable impurity flux rates. Assuming poloidal symmetry, the power loss to the radial scan accessible to the probe was ~11-28% of the ohmic power.

*This work was supported by the U.S. Department of Energy Contracts No. EY-76-C-02-3073 and AT(29-1) 789.

+RCA Laboratories, Princeton, N.J.
†Culham Laboratory, Abingdon, U.K.
*Sandia Laboratory, Albuquerque, N.M.

References

[1] S.A. Cohen & G.M. McCracken, PPPL 1529 (1979) J. Nucl. Mat. to be published.
[2] G. Staudenmaier et al. Bull APS 23 (1978) 802, and private communication.
[3] W.R. Wampler et al., J. Nucl. Mat. to be published 1979.
[4] W.R. Wampler et al. (in preparation).
[5] D. McNeill, Private Communication.
[6] H.P. Eubank, MATT Q22, Princeton 1964.
[7] J. Bohdansky et al., 7th Int. Vac. Congress Vienna 2 (1977) 1509.

D2.3

IMPURITY ION SPUTTERING FOR INTRODUCING METAL IMPURITY IN JFT-2 TOKAMAK

N.SUZUKI, N.FUJISAWA, S.KONOSHIMA, M.MAENO, M.SHIMADA, T.YAMAMOTO, S.KASAI and K.UEHARA

Japan Atomic Energy Research Institute, Tokai, Japan

Abstract. Origin of metal impurity in the JFT-2 tokamak was investigated experimentally and it was concluded that a predominant mechanism for metal contamination is the sputtering by highly ionized light impurities.

Introduction. The problem of metal contamination has been pointed out early from the viewpoint of radiation loss[1] and in the research to reduce metal impurity three mechanisms responsible for introducing metal impurity into a plasma were considered, that is, ion sputtering[2], unipolar arcing[3] and evaporation. On the JFT-2 tokamak we investigated experimentally which mechanism is the dominant one. Typical parameters of the JFT-2 tokamak are as follows; Bt= 14 - 18 kG, R= 90 cm, a= 20 - 25 cm, q_a= 2 - 4, $\bar{n}_e$= 1 - 6 x10^{13} cm^{-3}, Te(0)= 0.6 - 1.0 keV and Zeff= 1.5 - 6.

Firstly, thermal evaporation is not a predominant source because the surface temperature of Mo limiter measured with a infrared camera (AGA 680) was 400 - 600 °C at the end of discharges[4] and so it is too low to evaporate Mo. Residual two processes have similar dependence on the electron temperature of scrape-off plasma (Tes). But the sputtering yield depends strongly on incident ion species, so this difference was noticed for identification. We investigated the relation among the metal impurity (mainly Mo), light impurity and the Tes. Impurity densities were measured with a VUV monochromator and checked by the soft x-ray measurement, the Tes was measured with a electrostatic probe.

Tes dependence. The Tes scaling[5] shows that a simple way to change the Tes is in control of the peripheral radiation cooling by light impurities. In this experiment the Tes was varied by adjusting the injection rate of working gas (H_2) through a piezoelectric valve at a stationary state of a discharge. Results are shown in Fig.1. At a higher injection rate, as the electron density rose up and increase of the radiation loss was followed, the Tes was reduced to about half and the Mo density was also reduced. In contrast, at a lower injection rate the Tes increased a little and the Mo density also increased. In this experiment Ti-gettering was not used , so main impurity determining the radiation loss and the Zeff is oxygen[6], and in spite of the change of $\bar{n}_e$ oxygen density was kept nearly constant. These results confirm that the Tes is one of the important factors to determine the metal impurity concentration. The Mo density was estimated to be 10^9 - 10^{10} cm^{-3} spectroscopically[7].

Light impurity effect. Light impurities (mainly oxygen) and their radiation loss were reduced by 1/3 - 1/10 with Ti-gettering[6] (one Ti-ball) and simultaneously metal impurities were also reduced by about the same factor as shown in Tab.I. Titanium impurity was also observed, but its density was the same order of Mo density or less (10^9 cm^{-3}) and so no bad effect on a plasma was observed. In this experiment the Mo limiter and about half of the vacuum wall (SUS 304) were not coated by titanium geometrically. It is to be noted that the Tes was almost the same in two cases; with and without Ti-gettering. This data is not strange because the reduction of light impurity leads to decrease of joule input power. So the reduction of Mo density comes from cleanliness for light impurity. These results are summarized as follows; under the same Tes the metal concentration depends on the light impurity one. This phenomenon may be different apparently in comparison with other experiments[8], but a key point of this result is probably that the Tes is not so high as to bring about the self-sputtering of metal impurity.

Dependence on working gas species. Under the same operation conditions working gas species was changed from H_2 to D_2 or He. In these experiments Ti-gettering was used to reduce the effect of light impurity. Results are shown in Tab.II. Hydrogen and deuterium plasma have almost the same plasma parameters, but helium plasma has a different characteristics , namely the Mo density is higher than by one order and the radiation loss increases by about 6 and one-turn voltage rises from 1.2 to 2.0 volt. Here oxygen density and the Tes are nearly the same. So the increase of one-turn voltage comes from He itself and the rise of radiation loss is brought about by the increase of Mo density because of the center peaked profile of radiation loss. These results show clearly that the sputtering by He ion is the dominant source of Mo contamination. In the normal H plasma the Mo density can be explained as the sputtering by oxygen ion, because the sputtering yield of oxygen ion ∿10^{-1}, which is necessary to explain the Mo density in comparison with the He sputtering yield, seems a reasonable value.

Rare gas injection. In order to simulate the effect of light impurity and the Tes, neon gas was injected into a clean plasma produced by Ti-gettering. Quantity of injected neon corresponds to 2 - 4 % of the electron density, which is consistent with the electron density increase. Results are shown in Fig.2. At the injection phase, the Tes decreased abruptly to half and the Mo density also decreased in spite of existence of neon ions. But at the following steady state of neon density, as the Tes returned gradually to the original value, the Mo density increased up to about 7 times. This time evolution of the Mo density is in agreement with that of the sputtering yield of neon ion. These results confirm again that the metal impurity concentration depends on the light impurity one and the Tes.

Summary. It is concluded from these results that in normal JFT-2 discharges a predominant mechanism for introducing metal impurity into a plasma is the sputtering by highly ionized light impurity. The self-sputtering of metal impurity is considered to be a sub-process because the Tes was comparatively low; 10 - 30 eV. The arcing was not observed in these experiments, a reason may be that the conditioning effect of the discharge cleaning suppresses the probability of arcing.

References.

1) J.L.CRASTON, et al., Proc. 2nd Int. Conf. Geneva,1958 P/34
2) K.OHASA, et al., Nucl. Fusion 18 (1978) 872
3) G.M.McCRACKEN, et al., Nucl. Fusion 18 (1978) 537
4) Y.GOMAY, et al., Nucl. Fusion 18 (1978) 849
5) DIVA GROUP, Nucl. Fusion 18 (1978) 1619
6) S.KONOSHIMA, et al., J. Nucl. Mater. 76 (1978) 581
7) M.SHIHO, et al., Nucl. Fusion 18 (1978) 1705
8) E.B.MESERVEY, et al., MATT 1175 (1975)

TFR GROUP, Nucl.Fusion 17 (1977) 1297
J.HUGILL, et al., Proc. 8th Eur. Conf. Prague, 1977 p.39

Table I. Effect of light impurity (mainly Oxygen).

	V_1 (Volt)	OVI (cm^{-3})	OVIII (cm^{-3})	MoXIII (a.u.)	Tes (eV)	Zeff	P_R (kW)
without Ti-getter	2.7	3x10^{10}	1x10^{12}	28	30	5.5	60
with Ti-getter	1.5	3x10^{9}	2x10^{11}	2.6	30	2.0	20

Table II. Dependence on working gas species.

Working Gas	V_1 (Volt)	OVI (a.u.)	MoXIII (a.u.)	Tes (eV)	P_R (kW)	Sputtering Yield (atoms/ion)
H_2	1.2	2.3	∿1.5	∿12	12	< 10^{-4}
D_2	1.2	2.5	∿2.5	∿13	15	< 10^{-4}
He	2.0	2.7	∿22	∿12	83	∿10^{-2}

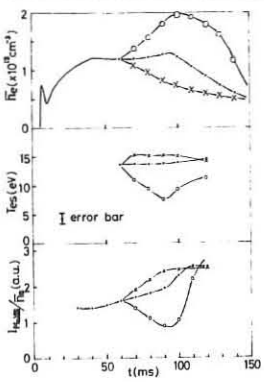

Fig.1. Tes dependence.

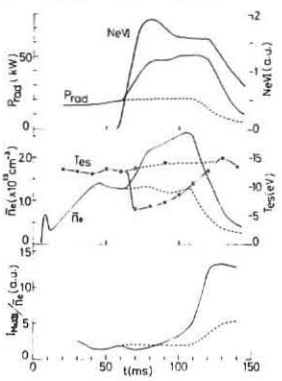

Fig.2. Neon injection.

INITIAL OPERATION OF PDX

D. Meade, W. Arunasalam, C. Barnes, K. Bol, S. Cohen, H. Dalhed, C. Daughney, S. Davis, J. DeLucia, D. Dimock, F. Dylla, P. Efthimion, R. Fonck, B. Grek, R. Hawryluk, E. Hinnov, H. Hsuan, M. Irie, R. Jacobsen, D. Johnson, L. Johnson, H. Maeda, D. Mansfield, G. McCracken, D. Mueller, M. Okabayashi, O. Okada, K. Owens, S. Picraux*, S. Rossnagel, N. Sauthoff, G. Schmidt, J. Schmidt, E. Silver, J. Sinnis, P. Staib, J. Strachan, S. Suckewer, F. Tenney, W. Wampler*

Plasma Physics Laboratory, Princeton University
Princeton, NJ 08544 USA

Introduction PDX was brought into operation initially with a circular cross-section plasma. Extensive glow discharge cleaning, feedback control of plasma position, current and density, and the use of titanium limiters and gettering allowed PDX to produce plasmas with reasonably low q, low $\bar{Z}$ and long confinement times in a relatively short time of operation.

Machine Description For these initial experiments, PDX was operated as a circular cross-section undiverted tokamak with the following parameters, B_T = 20 - 25 kG, a = 37 - 40 cm, R_o = 132 - 142 cm, q_L ~ 3, I_p = 350 - 500 kA, $\bar{n}_e$ = 2 - 5 x 10^{13} cm^{-3}, $\bar{Z}$ = 2 - 4, and pulse lengths ~ 1 sec. Internal vacuum vessel components that were exposed to the plasma (such as limiters, protective plates, microwave horns, etc.) were fabricated from 99% pure titanium. Titanium gettering was done using one 0.3 gm/hr sublimator in the divertor burial chamber that deposited titanium on an area of ≈ 4 m^2. The vertical field power supply was feedback controlled using an internal saddle coil detector and held the radial position of the outer flux surfaces to ± 3 mm during the plasma current flattop. The vertical position of the outer flux surfaces was also positioned to ~ ± 3 mm. In addition, the ohmic heating power supply was feedback controlled during the plasma flattop, which allowed the plasma current to be held constant to ± 3% during a pulse and from pulse to pulse. Diagnostics included magnetic measurements of I_p, R_o, $\beta_\theta + \ell_i/2$, δB_p, a three channel 2 mm at y = 0 and ± 15 cm for n_e, a four radial position soft x-ray system for $T_e(r)$ and impurity measurements, microwave measurements of $T_e(r)$, hard x-ray measurements of energetic electrons, visible and vacuum ultraviolet measurements of impurities, charge exchange and neutron production measurements of ion temperature, bolometric measurements of radiation profiles and surface analysis measurements of the "plasma-wall" interaction.

Discharge Cleaning Conventional low power Taylor-type discharge cleaning was applied for only 16 hours due to difficulties with discharge initiation at low fields in the presence of stray fields produced by induced currents in the divertor coil vacuum jackets. This problem was solved by reconnecting poloidal coils to passively cancel the error fields and allow discharges to be started at steady-state 3 kG toroidal fields. Intensive conditioning was undertaken with a d.c. glow discharge (G.D.C.) in which H_2 at a pressure of 3 x 10^{-2} torr flowed through the vacuum chamber at 10 torr-ℓs^{-1}. One or two anodes located on the midplane provided a discharge current of 2 to 4 amps at 400-500 volts.

Impurity production was monitored with a differentially pumped residual gas analyzer and by in-situ surface analysis. Impurities produced were mainly CH_4, C_2H_4 and CO with an initial gas phase removal rate of 1.5 x 10^{18} molecules s^{-1}. The rate decreased roughly inversely with time over 120 hours with a total removal of ~ 15 gm or ~ 120 monolayers of carbon. Surface removal rate of carbon and oxygen at the surface analysis station was ≈ 6 x 10^{10} atoms $cm^{-2}s^{-1}$.

Initial G.D.C. was accompanied by frequent arcing, but this gradually decreased and the discharge occupied an increasing proportion of the vacuum vessel as the impurity level and arcing decreased. The relatively low level of oxygen and carbon ($\bar{Z}$ ~ 2.5) after a short period of operation, is attributed largely to the efficacy of G.D.C.

Circular Plasma Results Typical plasma parameters for a circular deuterium plasma discharge with titanium gettering are: V_ℓ = 1.25V, I_p = 360 kA, $\bar{n}_e$ = 2.10^{13} cm^{-3}, $T_e(o)$ = 1.4 keV, $T_i(o)$ = 0.6 keV, $\bar{Z}_{eff}$ ≅ 2.4, τ_E ≈ 37 ms and q_L = 3.2. The electron density profile was measured at r = 0 and 0.4 a, the remainder of the profile and the T_i profile were estimated using a transport calculation. This confinement time is in the same range as those for PLT under similar conditions.[1] The soft x-ray spectrum indicates the presence of Cl, Ti and Cr impurities.

The effective ion charge was determined from the soft x-ray continuum intensity as Z_{eff} ≈ 2.5 - 3.2, in good agreement with the measured plasma resistance,[2] and spectroscopic measurements of the impurity concentrations. The latter gave typical values as Z_{eff} ≈ 1.0 + 0.25 + 1.0 + 1.0 for the H, C, O and T_i contributions, with negligible additions from Cl and Cr. The impurity concentrations appear to be fairly homogeneous, with no observed evidence of spatial accumulations on the time scale of about 0.5 sec. Surface physics measurements of oxygen and titanium fluxes to a probe 5 cm behind the limiter in a similar hydrogen discharge are typically 0.6 - 5.0 x 10^{15} and 0.2 - 0.4 x 10^{15} atoms cm^{-2} $discharge^{-1}$.

Several new spectrum lines of magnetic dipole transitions in the ground configurations of Ti XIV - XVII ions have been observed,[3] and their measured intensities have been used to test the adequacy of recent theoretical calculations.[4] These lines are expected to be very useful in local plasma diagnostics in the 0.8 - 2.0 keV range of temperatures.

Runaway electrons have reached energies greater than 8 MeV indicating single particle confinement for over 10^6 transits of the torus. Mean runaway electron confinement times are in the range of 10 to 100 ms as measured by hard x-ray spectra. The energetic runaway electrons have caused photoneutron production at the titanium limiters. The neutron flux had maximum steady-state levels of 10^9 m/sec on some discharges. Radioactivity was observed on the limiters, coming primarily from Sc^{47} caused by runaway electron induced $Ti^{48}(\gamma,p)$ reactions. The outside limiter had the highest dose of about 10 nCi. The PDX runaway electron photoneutron levels are considerably lower than were observed on early PLT discharges.

The total power radiated from this discharge was measured with a scanning bolometer at a position 100° azimuthally away from the limiter and found to be 200 - 280 kW out of a total of 450 kW. Estimates of the power radiated by the spectroscopically measured impurities are $P_R(C)$ ≈ 5 - 20 kW, $P_R(O)$ ≈ 70 kW, and $P_R(Ti)$ ≈ 150 - 190 kW giving a total power radiated of 225 - 280 kW. The radial distribution of power radiated from the discharge was essentially flat with a ≈ 50% peak at r = a/2 (T_e ≈ 600 eV) and second peak near the plasma surface.

A sequence of low q experiments was run using a plasma current waveform that increased in time from an initial value corresponding to q_L ≈ 3.5 to a final value q_L = 2.4 700 ms later. In this case the radial position of the plasma was adjusted to minimize the fluctuations in the poloidal field (presumably m = 2), and this allowed the line average electron density to be increased by gas puffing from 0.8 to 5.0 x 10^{13} cm^{-3}. Parameters of this discharge were I_p = 500 kA, V_ℓ(resistive) ≈ 1.5 V, $\bar{n}_e$ ≈ 1 → 5 x 10^{13} cm^{-3}, $T_e(O)$ = 1.2 → 0.8 eV, $\bar{Z}_{eff}$ ≈ 3 → 1.5 and τ_E ~ 30 ms. There appears to be some degradation of confinement relative to the low density discharge if τ_E α n, however the error bars were large for this early measurement.

Poloidal Divertor Experiments The poloidal divertor experiments are just beginning. The first experiments will concentrate on particle and energy transport in the divertor scrape-off region and the efficiency of the divertor in reducing impurities. In addition, the effects of plasma cross-section shaping on transport and MHD behavior will be studied.

Acknowledgments

The continuing support of M. B. Gottlieb and H. P. Furth is gratefully acknowledged. In addition, the technical assistance of D. Muschal, S. Hand and the PDX operating crew has been invaluable.

This work was supported by the U.S. Department of Energy, Contract No. EY-76-C-02-3073.

References

1. K. Bol et al, "Radiation, Impurity Effects, Instability Characteristics, and Transport in Ohmically Heated Plasmas in the PLT Tokamak", (Proceedings 7th Int. Conf., Innsbruck, Austria, 1978) IAEA-CN-37-A-1.
2. S. P. Hirschman, R. J. Hawryluk and B. Birge, Nucl. Fus. 17, (1977) 611.
3. S. Suckewer, R. Fonck and E. Hinnov (to be published).
4. U. Feldman et al, J. Appl. Phys. (1979) to be published.

* Sandia Laboratories, Albuquerque, New Mexico, 87185, USA

D2.6

TOROIDAL DISCHARGES WITH COLD BLANKETS IN RINGBOOG II

The RINGBOOG-Team*, presented by L.C.J.M. de Kock
Association Euratom-FOM, FOM-Instituut voor Plasmafysica
Rijnhuizen, Jutphaas-Nieuwegein, The Netherlands

Abstract:

The measurements on toroidal discharges in RINGBOOG II with electron densities ranging from $5\times10^{19} \div 3\times10^{21}$ m^{-3} indicate that the particle balance is mainly determined by hydrogen transport, whereas the energy balance seems to be dominated by oxygen line radiation.

General:

In RINGBOOG II[1] (R = 0.56 m, a = 0.075 m, $B_T \leq 4$ T), grossly stable toroidal discharges in hydrogen are produced to study plasmas surrounded by cold blankets. Discharges are mainly characterized by the filling pressure: between $3\div100\times10^{-3}$ torr, resulting in electron densities ranging from $5\times10^{19} \div 3\times10^{21}$ m^{-3}. Plasma currents (I_p) are approximately 17 kA and loop voltages (V_ℓ) range from 10÷250 V at B_T = 1.4 T. In Fig. 1 various discharge parameters are shown as functions of the density. The equilibrium of the plasma toroid is mainly provided by a copper shell; the equilibrium position may be influenced by an externally applied vertical magnetic field B_v.

The results presented here are obtained after overnight bakes at 100 °C and daily discharge cleaning of the stainless steel vessel with $p_0=5\times10^{-3}$ torr, $B_T \approx 0.5$ T, and $I_p = 300$ A at 8 kHz in pulse-trains of 1 sec. duration. The residual gas pressure is approximately 10^{-8} torr (mainly H_2 and H_2O).

It may be stressed that a continuous transition is found from resistive arc discharges at high density to modest tokamak discharges at the lower end of the density range studied.

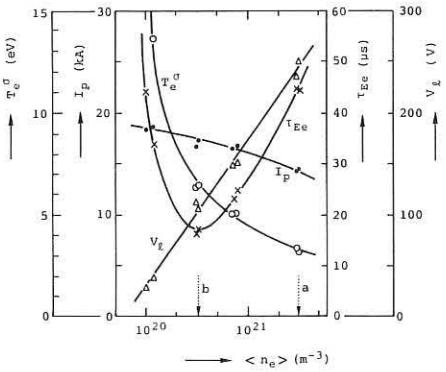

Fig. 1. Parameters of RINGBOOG II discharges at B_T = 1.4 T. I_p, V_ℓ, conductivity temperature T_e^σ, and electron energy replacement time τ_{Ee} as functions of line-averaged electron density $\langle n_e \rangle$. Assumptions: flat profiles and Z_{eff} = 1.

Profiles:

Various profiles have been studied in detail: Local measurements of T_e^{sc} and n_e^{sc} are taken by means of laser scattering at various different vertical positions, z, at fixed R = 0.56 m. The n_e^{inf} profiles have been inferred by Abel inversion[2] of the line-density measurements $\int n_e^{inf} d\ell$ at different radial positions R done with a CO_2-laser interferometer, c.f. [3]. The line densities of excited hydrogen, $\int n_3 d\ell$ and $\int n_4 d\ell$, are derived from simultaneous measurements at different horizontal chords of the H_α- and H_β-emission respectively. All parameters vary in time during one shot. In particular, the electron density, certainly in the lower range, decreases with time. The measurements presented in Fig. 2 are taken at t = 2.4 ms after the start of the discharge and are averaged over 0.3 ms, except for the laser-scattering data (20 ns). The results are obtained in shot-to-shot measurements; the data are averaged over several runs with identical external parameters. Run-to-run variations are generally small in the laser-scattering measurements, and less than 20% in the interferometer data, but can be as large as 70% in H_α- and H_β-measurements. However, the general shape of the profiles remains unchanged. Typical variations within one run are indicated by bars.

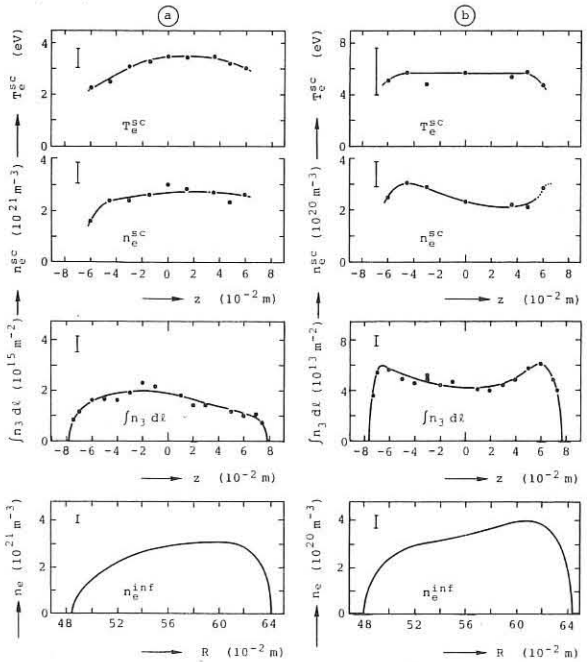

Fig. 2. Typical profiles of T_e^{sc}, n_e^{sc}, $\int n_3 d\ell$ and n_e^{inf}.
(a): $\langle n_e \rangle \approx 3\times10^{21}$ m^{-3}; B_v = 0 ; (b): $\langle n_e \rangle \approx 3\times10^{20}$ m^{-3}; $B_v \approx 0.002$ T.

Particle and energy balances:

To describe the particle and energy balances a computational model[4] is used in which emission and reabsorption of hydrogen line radiation as well as diffusion of neutrals in the ground state and enthalpy transport are taken into account. Self-consistent profiles are found when transport coefficients for the highly collisional regime[5] are used. Moreover, it is possible to calculate $\int n_3 d\ell$ and $\int n_4 d\ell$ with this model, when the experimental profiles of T_e^{sc} and n_e^{sc}, extrapolated to the walls, are introduced. The results are sensitive to the actual value of the neutral density at the outside of the plasma. To obtain agreement between the calculated and the measured values of $\int n_3 d\ell$ and $\int n_4 d\ell$, the neutral density n_1 near the wall (T_e = 1 eV) must be $n_1 \approx 1 \div 3\times10^{20}$ m^{-3} for $\langle n_e \rangle \approx 3\times10^{20}$ m^{-3} (b). No satisfactory agreement could be found for $\langle n_e \rangle \approx 3\times10^{21}$ m^{-3} (a).

According to our model L_α-radiation produced in the central part of the discharge is resonantly absorbed in the outer layers of high neutral density. With decreasing density the blanket starts to be optically transparent to L_α-radiation, but on the other hand, the emission decreases. As a result of these two competing effects, a maximum in the L_α-emission should occur. In Fig. 3 the 'window' as predicted by our model is shown as a function of n_e on axis, together with the L_α-intensity measured with a vacuum UV spectrometer. The experimental profiles and the self-consistent profiles from the model are different, but nevertheless, a reasonable agreement is found: the power predicted to be emitted in the forward direction in the maximum is approx. 3 kW m^{-2} sr^{-1}, against a measured value on the order of 10 kW m^{-2} sr^{-1}.

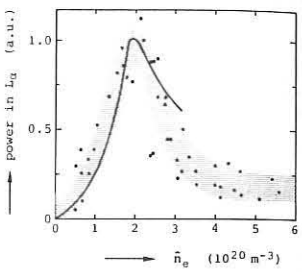

Fig. 3. L_α-emission versus n_e on axis.
Full line: prediction according to model. Shaded area and points: experimental observations.

The measured energy replacement time τ_{Ee} = 20÷50 μs, is at least one order of magnitude smaller than expected. The total ohmic power input of several MW can neither be accounted for by hydrogen line-radiation losses (< several 10 kW) nor by conduction and convection (~ 100 kW according to the model). Moreover, MHD activity is always found to be too small to explain the power losses.

Since measurements in the vacuum UV (at $\langle n_e \rangle \approx 10^{20}$ m^{-3}) show only oxygen lines, mainly O IV, it is tentatively concluded that oxygen line radiation is the dominant energy loss mechanism. Taking the experimental data (cf. Fig. 1), assuming that all ohmic power is radiated away by oxygen, and inserting temperature-dependent radiative energy loss coefficients[6], we calculate the oxygen density in all discharges over the whole range of densities studied to amount to $n_{ox} \approx 2\times10^{18}$ m^{-3}. This hypothesis for the energy loss mechanism is further corroborated by the observation that when T_e is lowered (by decreasing I_p) an increase in τ_{Ee} is found in high-density cases and a decrease in τ_{Ee} at low densities. This can be explained as excursions in temperature on both sides of the maximum (near T_e = 20 eV) of the radiative energy loss by the oxygen contamination. A dominant influence of the oxygen radiation, even at this low concentration, would also explain the broad T_e-profiles.

This work was performed under the Euratom-FOM association agreement with financial support from ZWO and Euratom.

References

1. RINGBOOG Team, Proc. 10th Symp. on Fusion Technology, Padova 1978, paper A-5.
2. N. Gottardi, IPP III/39, Max Planck-Institut für Plasmaphysik, Garching, December 1977.
3. C.A.J. Hugenholtz, B.J.H. Meddens, Rev. Sci. Instr., accepted for publication 1979.
4. W.J. Goedheer, Rijnhuizen Report 78-110 and Rijnhuizen Report 78-111, also part of Thesis, University of Utrecht, 18-9-1978.
5. F. Engelmann, A. Nocentini, Nucl. Fusion 17 (1977) 761.
6. V.L. Jacobs et al., JQSRT 19 (1978) 591.

* E.P. Barbian, C.J. Barth, W. van den Boom, G.J. Boxman, J.J. Busser, W.J. Goedheer, C.A.J. Hugenholtz, L.C.J.M. de Kock, O.G. Kruyt, H.A. van der Laan, J. Lok, B.J.H. Meddens, L.Th.M. Ornstein, R.W. Polman, A. Ravestein, W.J. Schrader, F.C. Schüller+, H.W. van der Ven.

+ Present address: JET, Culham, United Kingdom.

MAGNETIC ISLANDS AND DISRUPTIONS IN A TOKAMAK

K M McGuire*, D C Robinson
Culham Laboratory, Abingdon, Oxon, OX14 3DB, UK
(Euratom/UKAEA Fusion Association)
*University of Oxford

ABSTRACT Experiments with an external m=1 coil show that sawtooth oscillations are suppressed when the current in the coil exceeds 2kA. The application of an m=2 helical field suppresses m=2 activity and permits operation at $q_a \approx 2$. At higher fields irregular m=2 oscillations are produced which can lead to soft disruptions. An m=3, n=2 coil wound around the torus shows the presence of 3/2 mode activity just before a major disruption, at the time of an internal disruption and when operating at low q_a. Energising the coil produces soft disruptions if m=2 activity is present above a certain level.

m=1 COIL EXPERIMENT To obtain a better understanding of the internal disruption and the transport properties of the m=1, n=1 magnetic island, an m=1 coil was fitted onto the TOSCA device. This is a first order helical approximation coil with no net helicity which completely covers the torus. This coil was powered by a capacitor bank, with a pulse length of 2ms. The experimental results are shown in Fig.1, where $I_{m=1}$ is the coil current and $\frac{\Delta A}{A}$ is the relative amplitude of the sawtooth oscillation. It was observed that the m=1 coil interfered with the sawtooth oscillations and reduced the amplitude. The suppression of the oscillation occurred about 500μs after the application of the field, corresponding to the field penetration time. The stabilisation could be due to the coil produced island, reducing the effective radius of the q=1 surface or decreasing the current gradient at this surface. Field line tracing calculations show that the interaction of the externally produced m=1 island and the internal island produces an island of larger width - Fig.2. Because the m=1 coil is an approximation it also produces an m=2, n=1 island of small size. For a current distribution of the form $j=j_o(1-(\frac{r}{a})^2)^2$ corresponding to the experimental ratio of q_a to q(0), the island width of the m=1 mode would be some 3.7 times larger than that obtained from the current filament approximation used in Fig.2, if the radius at which q=1 is taken to be 1cm, as measured experimentally. From these considerations the maximum size of the magnetic island is about 3cm when the sawtooth oscillations are completely suppressed. The m=1 coil was observed to produce a stabilising effect on the 2/1 mode. It is probable that the m=1 coil produces a fixed island structure within the plasma which hinders the rotation of the 2/1 mode and/or decreases $\frac{dj}{dr}$, $\frac{dT_e}{dr}$ and because of this, affects the growth of the perturbation. The density as measured by a two channel 1.4mm microwave interferometer, showed no detectable profile changes. The central electron temperature as inferred from x-ray emissivity, also showed little change when the m=1 coil was activated.

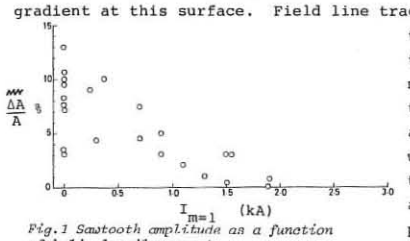

Fig.1 Sawtooth amplitude as a function of helical coil current.

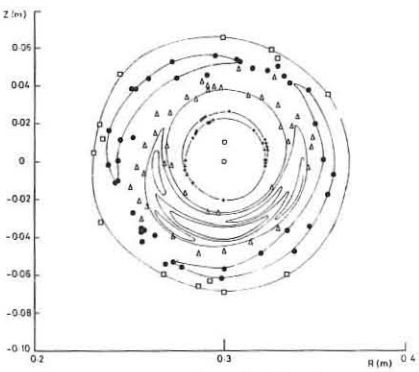

Fig.2 Magnetic islands produced by internal MHD activity and applied external m=1 field.

m=2 COIL EXPERIMENT An m=2, n=1 coil was fitted to TOSCA. This coil was again an approximation coil, but a correction to the position of the coils was made to produce the correct quadrupole field for a tight torus. For these experiments the plasma parameters were I_p=12kA, V_L=2.5V, $\bar{n}_e = 1.5\times10^{13}$cm^{-3} and $T_e(0)$=300eV (from Thomson scattering and soft x-ray spectra). The m=2 coil was activated at 1.0ms with a pulse length of 1.5ms. The experimental results obtained with a coil current of 2kA are shown in Fig.3. The main effect of the m=2, n=1 coil is to stabilise the 2/1 mode[1]. The integrated sin 2θ signal demonstrated that the coil did not produce an additional stationary island, associated

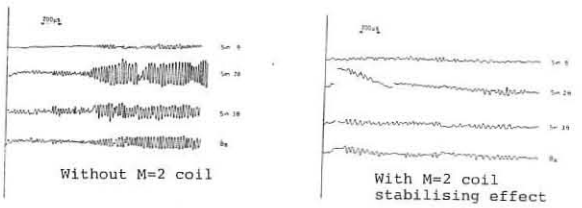

Fig.3 Mode suppression observed when a m=2 helical field is applied.

with the plasma rotation ceasing. The stabilisation of the 2/1 mode made it possible to operate at values of $q_a \sim 2$[2]. However, at very low q_a (below 1.8) the 2/1 coil was observed to produce major disruptions. Under normal conditions ($q_a \approx 3.5$) the 2/1 coil did not produce a major disruption even with coil currents of 3kA, though the time evolution of the m=2 mode disruptions was irregular, giving rise to soft disruptions.

Fig. 4 shows a field line tracing calculation for a filamentary current but with a radial field perturbation as measured[3]. Large regions around the islands become ergodic at the measured perturbation levels, apparently associated with the coupling between toroidicity and the mode. From measurements with the x-ray detectors and a Langmuir probe it is doubtful if ergodisation takes place at all.

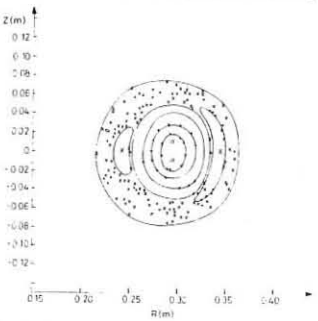

Fig.4 Magnetic islands and ergodic regions produced by mode activity.

MAJOR DISRUPTIONS A recent theory[4] indicates that the major disruption could be due to the destruction of magnetic surfaces by the non-linear interaction of magnetic islands of different helicity. An m=3, n=2 coil was constructed for TOSCA to produce another island which could interact with the 2/1 island. This saddle coil was used to detect the 3/2 mode, which is predicted to appear before a disruption. Fig.5 shows the time sequence of a major disruption on TOSCA. A large 2/1 island is believed to develope, which flattens the current profile at the q=2 surface, then a fast 3/2 mode starts, which appears from soft x-ray detectors to destroy the centre core of the plasma, the current distribution broadens and then the negative voltage spike is observed. The 2/1 and 3/2 modes may not be the only modes involved in the disruption process. The frequencies of approximately 100kHz and 50kHz for the 3/2 and 2/1 mode respectively imply that the plasma is rotating in the toroidal direction. The growth rate of the 3/2 is approximately three times faster than the 2/1 mode. The 3/2 mode is also observed when internal disruption occurs and when operating at low q_a. Energising the 3/2 coil produces soft disruptions if 2/1 activity is present above a certain level. Energising both the 2/1 and 3/2 coils produces a major disruption.

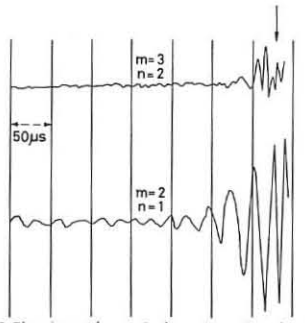

Fig.5 The detection of the m=3, n=2 mode at a major disruption, the arrow indicates the time of disruption.

CONCLUSIONS The m=1 coil reduces the amplitude of the sawtooth oscillation. Stabilisation of the 2/1 mode is possible with a m=2 coil which permits low q operation. A 3/2 mode is detected with a helical saddle coil just before disruption and this mode seems to play an important part in the disruptive process on this device.

ACKNOWLEDGEMENT We wish to thank Mr R Peacock for overcoming the problems with fitting the helical coils to the TOSCA device.

REFERENCES

[1] Fussman G et al, in Plasma Physics and Controlled Nuclear Fusion Research (Proc. 7th Int.Conf. Innsbruck 1978 CN37-T4. and Karger F et al, Proc. 8th Eur.Conf. Contr.Fusion and Plasma Phys., 1 Prague 1977 3.
[2] Birch R et al, this conference.
[3] McGuire K M and Robinson D C, Nuc.Fus. 19 (1979) 115.
[4] Waddell B V et al, Phys. Rev. Lett. 41 (1978) 1386.

D3.1

AXIS ENCIRCLING ION GYRO-INSTABILITY

Peter J. Catto, R. E. Aamodt, and Marshall Rosenbluth[a)]
Science Applications, Inc.
Laboratory for Applied Plasma Studies
Boulder, Colorado 80302

J. A. Byers and L. D. Pearlstein
Lawrence Livermore Laboratory
University of California
Livermore, California 94550

ABSTRACT. An idealized plasma model in which all the ion guiding centers lie along the magnetic axis of a cylindrically symmetric plasma is investigated. The radial eigenvalue equation is derived and solved for this strongly unstable limit.

INTRODUCTION. When a large fraction of ions encircle the magnetic axis in a small radius plasma, their gyratory motion results in a substantial azimuthal mean velocity. In an inhomogeneous plasma this flow can lead to an ion cyclotron instability which cannot be treated by a radially local analysis. Furthermore, the axis encircling ions which are the source of this instability are not retained in the usual slab models of drift cyclotron instabilities.[1] This axis encircling ion gyro-instability may be excited in some operating regimes of the 2XII-B mirror machine,[2] and in configurations with plasma radii the order of a few ion gyroradii or less.

The effect of axis encircling ions in a cylindrical plasma is considered in the limit in which all the ion guiding centers lie along the magnetic axis. Neglecting variations along the magnetic field, a radial eigenvalue equation is derived and solved for a family of model density profiles capable of representing both a Maxwellian and a class of loss cone velocity space distributions. The resulting gyro-instability typically has a growth rate and real frequency on the order of the azimuthal mode number ℓ times the ion gyrofrequency Ω.

DERIVATION OF THE EQUATIONS. For a cylindrical plasma immersed in a uniform magnetic field $\underline{B} = B\hat{z}$, the response of the ions and the electrons is calculated from the species continuity and momentum equations by treating the electrons as cold and assuming that all the ion guiding centers are on axis. In obtaining the equations, only flute modes are considered so that all dependent variables are functions of time and the cylindrical spatial coordinates r and θ only ($\partial/\partial z = 0$).

By considering the special limit in which all the ion guiding centers are along the axis of symmetry, the unperturbed ion density N_0 and the mean ion velocity $\underline{V}_0$ are such that $N_0 = N_0(r)$ and $\underline{V}_0 = V_{0\theta}\hat{\theta} = -\Omega r\hat{\theta}$ with $\Omega = eB/Mc$ and M the ion mass. In addition, because all the guiding centers are on axis, only a single velocity is present at any point in space so that the ion pressure is zero and remains zero even when the plasma is perturbed. Note, however, that the ions are not cold since there is a distribution of velocities.

Seeking solutions of the form $\exp(-i\omega t + i\ell\theta)$ and denoting differentiation with respect to r by a prime, the linearized continuity and momentum equations for a neutral unperturbed plasma become

$$-i(\omega - \ell V_{0j}/r)n + N_0' v_r + (N_0/r)[(rv_r)' + i\ell v_\theta] = 0 \tag{1}$$

$$-i(\omega - \ell V_{0j}/r)v_r + \Omega_j v_\theta = -(Ze/M_j)\Phi' \tag{2}$$

$$-i(\omega - \ell V_{0j}/r)v_\theta - \Omega_j v_r = -i(Ze\ell/M_j r)\Phi \ , \tag{3}$$

where Φ is the perturbed electrostatic potential, and species subscripts (j = i,e) are suppressed on n and $\underline{v} = v_r\hat{r} + v_\theta\hat{\theta}$. For the ions ($j$ = i, Z = +1, $M_i = M$, and $\Omega_i = \Omega$), $V_{0j} = -\Omega r$; while for the electrons (j = e, Z = -1, $M_e = m$, and $\Omega_e = -eB/mc$), $V_{0e} = 0$. Combining Eqs. (1) to eliminate $\underline{v}$ and inserting the resulting expressions for n into Poisson's equation gives

$$(4\pi e)^{-1}\nabla^2\Phi = n_e - n_i = \left\{\frac{e}{M}\left[\frac{m}{M\Omega^2}\nabla\cdot(N_0\nabla\Phi) + \frac{\ell N_0'\Phi}{r\omega\Omega}\right]\right\} - \left\{\frac{-(e/M)}{\omega + \ell\Omega}\left[\frac{(\omega + \ell\Omega)\nabla\cdot(N_0\nabla\Phi) + (\ell\Omega/r)N_0'\Phi}{(\omega + \ell\Omega)^2 - \Omega^2}\right]\right\} , \tag{4}$$

where $\Omega_e^2 >> \omega^2$ is assumed.

Defining

$$g = \frac{(\ell/\omega\Omega)\left[(\omega + 2\omega)^2 - \Omega^2\right] - \left[\ell\Omega/(\omega + \ell\Omega)\right]}{\left\{1 - (m/M\Omega^2)\left[(\omega + \ell\Omega)^2 - \Omega^2\right]\right\}} \tag{5}$$

and

$$\alpha = \frac{-M\left[(\omega + \ell\Omega)^2 - \Omega^2\right]}{4\pi e^2\left\{1 - (m/M\Omega^2)\left[(\omega + \ell\Omega)^2 - \Omega^2\right]\right\}} \ , \tag{6}$$

and making a change of dependent, $\Phi = (N_0 + \alpha)^{-\frac{1}{2}}\Psi$, and independent, $r = L\exp(x)$, variables, gives the desired form[3] for Eq. (4), namely,

$$\frac{\partial^2\Psi}{\partial x^2} - V(x,\omega)\Psi = 0 \ , \tag{7}$$

with

$$V = \ell^2 + \frac{rN_0'g}{N_0 + \alpha} + \frac{r(rN_0')'}{2(N_0 + \alpha)} - \left(\frac{\frac{1}{2}rN_0'}{N_0 + \alpha}\right)^2 . \tag{8}$$

The constant L is some typical scale length for the model density profile of interest. For the density profile employed here,

$$N_0 = n_0(r/L)^p \exp(-r^2/2L^2) , \qquad p = 0,2,4,... \tag{9}$$

L is a measure of the width of the gaussian. For this density profile there are only two turning points. Denoting x_1 or $r_1 = L\exp(x_1)$ and x_2 or $r_2 = L\exp(x_2)$ as the inner and outer turning points, respectively, the WKB phase integral expression for the eigenvalue equation obtained by demanding $\Psi(|x| \to \infty) \to 0$ is simply

$$\int_{x_1}^{x_2} dx\,[-V(x,\omega)]^{\frac{1}{2}} = \int_{r_1}^{r_2}\frac{dr}{r}\,[-V(r,\omega)]^{\frac{1}{2}} = \pi(n + \tfrac{1}{2}) , \tag{10}$$

with $n = 0,1,2,...$, V given by Eq. (8), and r_1 and r_2 given by $V(r_1,\omega) = 0 = V(r_2,\omega)$.

ANALYSIS OF WKB EIGENVALUE EQUATION. In the limit of a shallow, parabolic well the location of the bottom of the well $r_0 = r_0(\omega_0)$ and the lowest order eigenvalue ω_0 may be obtained by solving $V(r_0,\omega_0) = 0 = \partial V(r_0,\omega_0)/\partial r_0$. When $\ell^2 >> 1$ only the first two terms in Eq. (8) need be retained. Eliminating r_0 and employing the $p = 0$ form of Eq. (9), the eigenvalue equation (10) reduces to

$$g(\omega_0) = \ell^2/2\ell n[2n_0 g(\omega_0)/e\alpha(\omega_0)\ell^2] , \tag{11}$$

where $e = 2.718...$. Assuming $\omega_0 = -\ell\Omega(1 + \delta)$ with $|\delta| << 1$, then for $\ell^{2/3} >> |1/\delta| >> 1$, Eq. (11) gives

$$\omega_0 = -\ell\Omega\left\{1 \mp i\left[2\ell n(2\omega_{p0}^2/e\ell^2\Omega^2) - (m\ell^2/M)\right]^{-\frac{1}{2}}\right\} , \tag{12}$$

where $\omega_{p0}^2 \equiv 4\pi e^2 n_0/M$. Consequently, the axis encircling gyro-instability has a growth rate and real frequency on the order of the azimuthal mode number for $1 << \ell^2 << M/m$. In addition, the electron polarization drift correction results in stabilization for $\ell^2 \geq (2M/m)\ell n[2\omega_{p0}^2/e\ell^2\Omega^2]$, while for lower densities stabilization occurs for smaller ℓ ($\ell << M/m$) because $2\omega_{p0}^2/e\ell^2\Omega^2$ becomes of order unity or less. As a result, the polarization stabilization occurs in the high density limit $2\omega_{p0}^2/e\Omega^2 > \ell^2 > (2M/m)\ell n(2\omega_{p0}^2/e\ell^2\Omega^2)$, while the low density limit requires $\ell^2\omega_{p0}^2/e\Omega^2$ for stability. For $p \neq 0$ the analysis is somewhat more involved; however, the only effects are a slight lowering of the growth rate and a small shift in the range of unstable ℓ. Finally, the radial mode number corrections to the shallow well approximation can be evaluated to find that the higher radial eigenmodes are becoming more unstable with increasing n. In order to see that this behavior does not persist for $n >> \ell$, a treatment of the radial mode number dependence which permits widely spaced turning points is required.

In order to obtain a simple approximate form for Eq. (10) that is valid when $\ell^2 >> 1$ in the widely spaced turning points limit, note that in $V \approx \ell^2 - [(r^2/L^2) - p]gN_0/(N_0 + \alpha)$, $N_0/(N_0 + \alpha)$ decays exponentially fast beyond $N_0 \sim \alpha$. Consequently, again defining r_0 via $\partial V(r_0,\omega)/\partial r_0 = 0$ so that for $4\ell n(n_0/\alpha) > p \sim 1$

$$(r_0/L)^2 \approx 2\ell n\left\{\frac{(n_0/\alpha)[2\ell n(n_0/\alpha)]^{\frac{1}{2}p}}{\ell n(n_0/\alpha) - (p + 1)}\right\} ,$$

then Eq. (10) may be approximated by

$$\pi(n + \tfrac{1}{2}) \approx \int_{r_1}^{r_0}\frac{dr}{r}\left[g\left(\frac{r^2}{L^2} - p\right) - \ell^2\right]^{\frac{1}{2}} = \frac{g^{\frac{1}{2}}}{L}\left[(r_0^2 - r_1^2)^{\frac{1}{2}} - r_1\cos^{-1}(r_1/r_0)\right] , \tag{13}$$

with r_1 found from $V \approx \ell^2 - g(r_1^2/L^2 - p) \approx 0$. For the widely spaced turning point limit $(r_1/r_0)^2 < 1$ may be used to simplify the righthand side of Eq. (13) to $(g^{\frac{1}{2}}/L)(r_0 - \frac{1}{2}\pi r_1)$. Then for $1 << \ell^2 << [(2M/m)\ell n(2\omega_{p0}^2/e\ell^2\Omega^2)]^{\frac{1}{2}}$ and $2\omega_{p0}^2/e\Omega^2$, $g \approx \ell(\omega + \ell\Omega)^2/\omega\Omega$ may be employed in resulting form to obtain

$$\omega/\Omega \approx -\ell + (S/2\ell) \pm [-S + (S^2/4\ell^2)]^{\frac{1}{2}} , \tag{14}$$

where

$$S \equiv \left[\frac{\pi(n + \frac{1}{2})}{r_0/L} + \frac{\pi(\ell^2 + pg)^{\frac{1}{2}}}{2r_0/L}\right]^2$$

Consequently, stability occurs for $S > 4\ell^2$ or $n > \ell(2r_0/\pi L)$. In addition, the fastest growing radial eigenmode occurs for $S = 2\ell^2$ which gives the fastest growing n to be the integer nearest $\ell(2^{\frac{1}{2}}r_0/\pi L)$ and results in $\mathrm{Im}\,\omega/\Omega \sim i\ell$. Because of the approximations employed to evaluate Eq. (10), the results in this paragraph should be viewed as qualitative.

In addition to the large ℓ results of the preceding two paragraphs, a form of the eigenvalue equation can be obtained which is valid for small ℓ, n, and p and/or high density. Such a limit is obtained by noting that in the $\alpha \to 0$ limit there exist two turning points of the full V that are independent of density. Evaluating Eq. (10) for $\alpha \equiv 0$ gives the simple eigenvalue equation

$$g = 2n + (\ell^2 + 2pn)^{\frac{1}{2}} \equiv Q . \tag{15}$$

Equation (15) is valid provided the outer turning point r_2 occurs before N_0 becomes as small as α, that is, $N_0(r_2) > \alpha$. This condition restricts Eq. (15) to the lowest values of ℓ, n, and p unless ω_{p0}^2/Ω^2 is extremely large. When $\ell = 1$ Eq. (15) predicts stability for all n and p, while for $\ell >> 1$ it yields

$$\omega/\Omega = -[\ell - (Q/2\ell)] \pm [-Q + (Q^2/4\ell^2)]^{\frac{1}{2}} . \tag{16}$$

This last equation predicts results similar to Eq. (14), however, Eq. (16) can only be satisfied if $\omega_{p0}^2/\Omega^2 \to \infty$. As ω_{p0}^2/Ω^2 is decreased, only Eq. (14) is able to predict the qualitative behavior of an increase in the growth rate and a decrease in $|\mathrm{Re}\,\omega/\Omega|$.

Many of the physical features predicted by the preceding simple analytic limits of the WKB phase integral condition have been verified for $p = 0$ by a comparison with the results of a linearized particle simulation which is being developed to treat the transition region between the on axis and slab limits.[4] In particular, the $\ell = 1$ mode is observed to be stable for all densities.

DISCUSSION. The preceding paragraphs have sketched an investigation of an instability driven by the flow associated with a large fraction of ions encircling the magnetic axis in an inhomogeneous, cylindrical plasma. In the limit in which all the ion guiding centers are on axis, the instability typically has a growth rate and real frequency on the order of $\ell\Omega$. The fastest growing radial mode is found to be roughly purely growing with $\omega \sim i\ell\Omega$ and with $n \sim \ell$. In this on axis limit a large range of $\ell \geq 2$ are found to be unstable. Roughly speaking, in the higher density limit $\omega_{p0}^2/\Omega^2 > \ell^2 > M/m$ is necessary for stability, while at lower densities $\ell^2 > \omega_{p0}^2/\Omega^2$ is required. Furthermore, the fastest growing ℓ modes occur just before stabilization. In addition, the results are found to be relatively insensitive to the details of the density profile near the magnetic axis since the modes are centered away from $r = 0$.

REFERENCES

1. R. F. Post and M. N. Rosenbluth, Phys. Fluids 9, 730 (1966); and A. B. Mikhailovskii and A. V. Timofeev, Zh. Eksp. Teor. Fiz. 44, 919 (1963) [Sov. Phys. - JETP 17, 626 (1963)].
2. T. C. Simonen et al., Lawrence Livermore Laboratory, Report UCRL-80634, July 10, 1978. Also, Proceedings of the Seventh International Conference on Plasma Physics and Controlled Nuclear Fusion Research, Innsbruck, Austria, August 1978 (IAEA-CN/J-1).
3. J. Heading, An Introduction to Phase-Integral Methods (Methuen, London, 1967), pp. 127-131.
4. J. Byers, work in progress.

ACKNOWLEDGMENT. This work was supported by the U. S. Department of Energy.

a)Permanent Address: School of Natural Sciences, The Institute for Advanced Study, Princeton, New Jersey 08540.

DISTRIBUTION OF PARTICLES IN STOCHASTIC FIELDS

P. ROLLAND

ASSOCIATION EURATOM-CEA
Département de Physique du Plasma et de la Fusion Contrôlée
Service IGn - Centre d'Etudes Nucléaires
85 X - 38041 GRENOBLE CEDEX (France)

It has already been noted that the distribution of particles in a stochastic field is generally not a gaussian one.[1,2] The rates of diffusion, heating, etc... depend strongly upon the kind of law the stochastic field obeys. Besides, the deviation of the equilibrium distribution from a gaussian one may be of importance in renormalized turbulence theory.[3] Several aspects of this problem are examined in this paper : what is the probability p (x, v) to find a particle at the point x, v in a field E which varies according to different laws ? What kind of solution is then obtained for boundary or initial value problems ? In what conditions does a stationary and homogeneous distribution exist in a stochastic field ?

1 - Suppose that $\{x,v,t\}$ can be regarded as a markov process, that is to say :

$$p\{x,v,t\,|\,x',v';t'\ ..\ x'',v'';t''...\} = p\{x,v,t\,|\,x',v';t'\} \quad \text{for any } t''<t'<t \qquad (1)$$

Then p satisfies Chapman-Kolmogorov's equation (C-K equation)

$$p(x,v;t\,|\,x_o,v_o;t_o) = \int dx'dv'\,p(x,v;t\,|\,x',v';t')\,p(x',v';t\,|\,x_o,v_o;t_o) \qquad (2)$$

Expanding $p(x,v;t\,|\,x',v';t')$ as a Taylor series in $(x'-x)$, $(v'-v)$ and considering the limit $t-t'=\tau\to 0$ yields the partial differential equation (PDE) :

$$\partial_t p(x,v;t\,|\,x_o,v_o;t_o) = I_x\partial_x p(x,v;t\,|\,x_o,v_o;t_o) + I_v\partial_v p + \tfrac{1}{2}I_{xx}\partial_x^2 p + I_{xv}\partial_x\partial_v p + \tfrac{1}{2}I_{vv}\partial_v^2 p \ ... \qquad (3)$$

where

$$I_x = \lim_{\tau\to 0}\frac{1}{\tau}\int dx'dv'(x'-x)\,p(x,v;t\,|\,x',v';t') \qquad I_v = \lim_{\tau\to 0}\frac{1}{\tau}\int dx'dv'(v'-v)\,p$$

$$I_{xx} = \lim_{\tau\to 0}\frac{1}{\tau}\int dx'dv'(x'-x)^2 p \qquad I_{xv} = \lim_{\tau\to 0}\frac{1}{\tau}\int dx'dv'(x'-x)(v'-v)p \qquad I_{vv} = \lim_{\tau\to 0}\frac{1}{\tau}\int dx'dv'(v'-v)^2 p \ ... \qquad (4)$$

Under this markovian assumption, the initial value problem in which $p(x_o,v_o;t_o)$ is given is easily solved, since we have :

$$p(x,v;t) = \int dx_o dv_o\, p(x,v;t\,|\,x_o,v_o;t_o)\,p(x_o,v_o;t_o) \qquad (5)$$

which gives the local density $N(x;t)=\int dv\,p(x,v;t)$, the local velocity distribution $f(v;t)=N^{-1}(x;t)p(x,v;t)$, generally different from the total velocity distribution $F(v;t)=\int dx\,p(x,v;t)/\int dx\,N(x,t)$, with the evident simplifications if $p(x,v;t\,|\,x_o,v_o;t_o)$ depends on $x-x_o$ and if the initial state is homogeneous. The question is now to know if $\{x,v;t\}$ can be regarded as a markov process and what the good approximation for $p(x,v;t\,|\,x_o,v_o,t_o)$ is.

2 - Let us first consider the following simple model : the field E is constant in space but it undergoes pulses with amplitudes $E_i\tau_\varepsilon/\Delta t$ during small intervals of time Δt separated by periods τ_ε. E_i is stochastic and obeys a gaussian law $p(E_i)=\frac{1}{\sqrt{2\pi}\bar{E}}e^{-\frac{E_i^2}{2\bar{E}^2}}$. An exact formula has been obtained[4] for p. It gives (when $\tau=t-t_o\gg\tau_\varepsilon$) $\sqrt{2\pi}\bar{E}$ the asymptotic limit : (valid for a larger class of fields with correlation time τ_E)

$$p(x,v;t\,|\,x_o,v_o;t_o) = \frac{\sqrt{3}}{\pi\tau_E\tau^2}\left(\frac{m}{e\bar{E}}\right)^2 e^{-\frac{2}{\tau_E\tau}\left(\frac{m}{e\bar{E}}\right)^2\left\{(v-v_o)^2-\frac{3}{\tau}(v-v_o)(x-x_o-v_o\tau)+\frac{3}{\tau^2}(x-x_o-v_o\tau)^2\right\}} \qquad (6)$$

This probability satisfies C-K's equation (2) as well as the equation :

$$\partial_t p + v\partial_x p - \frac{\tau_\varepsilon}{2}\left(\frac{e\bar{E}}{m}\right)^2\partial_v^2 p = 0 \qquad (7)$$

i.e. the equation (3) with $I_x=v$, $I_{vv}=\tau_\varepsilon\left(\frac{e\bar{E}}{m}\right)^2$, $I_v=0$, etc...

There is no trapping, and the process $\{x,v;t\}$ is markovian.

The mean deviations are :

$$\langle v-v_o\rangle = 0 \qquad \langle x-x_o-v_o\tau\rangle = 0 \qquad \langle(v-v_o)^2\rangle = \tau_\varepsilon\tau\left(\frac{e\bar{E}}{m}\right)^2$$

$$\langle(x-x_o-v_o\tau)^2\rangle = \frac{\tau_\varepsilon\tau^3}{3}\left(\frac{e\bar{E}}{m}\right)^2 \qquad \langle(v-v_o)(x-x_o-v_o\tau)\rangle = \frac{\tau_\varepsilon\tau^2}{2}\left(\frac{e\bar{E}}{m}\right)^2 \qquad (8)$$

in agreement with trajectory method results[5,6] with $\int_{-\infty}^{\infty}d\tau\langle E_t E_{t-\tau}\rangle = \tau_\varepsilon\bar{E}^2$ and $\partial_{v_o}\int_0^\infty d\tau\langle E_t E_{t-\tau}\rangle = 0$. The kinetic energy increases with a rate $\partial_t\langle v^2\rangle = \tau_\varepsilon\left(\frac{e\bar{E}}{m}\right)^2$ which is invariant in uniform translation. A gaussian homogeneous initial distribution remains a gaussian one with a linearly growing thermal energy $v_{th}^2(t)+\tau_\varepsilon\left(\frac{e\bar{E}}{m}\right)^2\tau$. When the initial distribution is localized in space, the local heating rate is larger than the total heating rate beyond the diffusion front. An initial wave with wave number k is damped with an increment $-k^2\tau_\varepsilon\tau^3\left(\frac{e\bar{E}}{m}\right)^2/6 = -k^2\langle\Delta x^2\rangle/2$.

3 - Let us now consider a time independent stochastic field, constant in intervals i of length ℓ_ε with random amplitudes E_i with probability $p(E_i)=\frac{1}{\sqrt{2\pi}\bar{E}}e^{-\frac{E^2}{2\bar{E}^2}}$. One obtains[4] the asymptotic limit :

$$p(w;n\,|\,w_o;n_o) = \frac{1}{\sqrt{2\pi(n-n_o)}}\left\{e^{-\frac{(w-w_o)^2}{2(n-n_o)}} - e^{-\frac{(w+w_o)^2}{2(n-n_o)}}\right\} \quad \text{where } W=\frac{mv^2}{2e\ell_\varepsilon\bar{E}}\ ,\ n=\frac{x}{\ell_\varepsilon} \qquad (9)$$

This probability satisfies C-K's equation as well as a simple PDE. The process $\{w;n\}$ is a markov process. Things are quite different with the process $\{w;t\}$ since reflected particles cross over again the same intervals i so that $p(w;t\,|\,w';t')$ is not independent of the realisations for $t<t'$. $\{w;t\}$ is not a Markov process. However, if $\frac{\sqrt{2n}}{w_o}e^{-\frac{w_o^2}{2n}}\ll\frac{n}{w_o^2}\ll 1$ one can neglect the very small number of reflected particles and nevertheless take the deviation from the gaussian process into account. Indeed, the calculation of the integrals (4) shows that $p(x,v;t\,|\,x_o,v_o;t_o)$ satisfies the equation :

$$\partial_t p + v\partial_x p + \frac{\ell_\varepsilon}{2v^2}\left(\frac{e\bar{E}}{m}\right)^2\partial_v p - \frac{\ell_\varepsilon}{2v}\left(\frac{e\bar{E}}{m}\right)^2\partial_{v^2}^2 p = 0 \qquad (10)$$

An expansion in powers of $(v-v_o)/v_o$ leads to a hierarchy which can be solved using Fourier and Laplace transforms. The first two terms of this expansion are[4] :

$$P_o = \frac{\sqrt{3}\,\alpha^2}{2\pi\tau^2}\,e^{-\frac{\alpha^2}{\tau}\left\{v^2-3vx+3x^2\right\}}$$

$$P_1 = \frac{P_o}{4v_o}\left\{(x-v\tau)\left[\frac{\alpha^2v^2}{\tau}+\frac{8}{5}-\frac{36}{5}\frac{\alpha^2}{\tau}(x-\tfrac{v}{2})^2\right]+v\left[2-\frac{\alpha^2v^2}{2\tau}-\frac{6\alpha^2}{\tau}(x-\tfrac{v}{2})^2\right]\right\} \qquad (11)$$

where $\alpha^2=\frac{2|v_o|}{\ell_\varepsilon}\left(\frac{m}{e\bar{E}}\right)^2$; $\tau=t-t_o$; $v=v-v_o$; $x=\frac{x-x_o}{\tau}-v_o$. $v,x\ll v_o$.

The mean deviations are :

$$\langle v-v_o\rangle = -\tau/\alpha^2v_o \qquad \langle x-x_o-v_o\tau\rangle = -\tau^2/2\alpha^2v_o \qquad \langle(v-v_o)^2\rangle = 2\tau/\alpha^2$$

$$\langle(x-x_o-v_o\tau)^2\rangle = 2\tau^3/3\alpha^2 \qquad \langle(v-v_o)(x-x_o-v_o\tau)\rangle = \tau^2/\alpha^2 \qquad (12)$$

in agreement with trajectory method results with $\int_{-\infty}^{\infty}d\tau\langle E_t E_{t-\tau}\rangle = \ell_\varepsilon\bar{E}^2/v_o$ and $\partial_{v_o}\int_0^\infty d\tau\langle E_t E_{t-\tau}\rangle = -\ell_\varepsilon\bar{E}^2/v_o^2$. We observe that $\partial_t\langle v^2\rangle = 0$ in this reference frame, where dispersion and drag effects cancel. However, in a frame with velocity U with respect to the field configuration, we have $\partial_t\langle(v-U)^2\rangle = 2U/\alpha^2v_o$ $\left(=\ell_\varepsilon(e\bar{E}/m)^2/v_o=\tau_c(e\bar{E}/m)^2\ \text{when } U=v_o\right)$.

4 - The results (11) can be extended to the mixed case where independent periods of spatial stochasticity regime succeed with time intervals $\tau_\varepsilon\ll v_o^2\alpha^2$. Now consider an initially homogeneous maxwellian plasma with a shifted distribution $f=b^{1/2}\pi^{-1/2}\exp-b(v_o+U)^2$ immersed in such a stochastic field with correlation length ℓ_ε and correlation time τ_ε . Suppose $\tau_\varepsilon\ll(m\ell_\varepsilon/e\bar{E})^{1/2}$. Then particles with velocities $v_o\ll\ell_\varepsilon/\tau_\varepsilon$ obey eq. 6 whereas particles with velocities $v_o\gg\ell_\varepsilon/\tau_\varepsilon$ obey eq. 11 . When U = 0 one obtains $\langle v\rangle = 0$ and $\partial_t\langle v^2\rangle = \tau_\varepsilon(e\bar{E}/m)^2 e^{\ell_\varepsilon^2 b^{1/2}/\tau_\varepsilon}$: The energy growth rate $\partial_t\langle v^2\rangle$ vanishes when $\ell_\varepsilon/\tau_\varepsilon\ll v_{th}$ and reaches its maximum $\tau_\varepsilon(e\bar{E}/m)^2$ when $\ell_\varepsilon/\tau_\varepsilon\gg v_{th}$. When $U\gg\ell_\varepsilon/\tau_\varepsilon$, v_{th} one obtains $\partial_t\langle v+U\rangle = \partial_t\langle v\rangle = \ell_\varepsilon(e\bar{E}/m)^2/2U|U|$ and $\partial_t\langle(v+U)^2\rangle = \partial_t\langle v^2\rangle + 2U\partial_t\langle v\rangle = \ell_\varepsilon(e\bar{E}/m)^2/|U|$: the energy growth rate in the field reference frame $\partial_t\langle v^2\rangle$ vanishes ; in the plasma reference frame its expression is analogous to that of § 2 in which τ_ε is replaced by the correlation time in this frame $\tau_c=\ell_\varepsilon/|U|$.

5 - The following question may be asked : What conditions must satisfy the law obeyed by the stochastic field in order to permit the existence of a homogeneous and stationary distribution of particles ? When it exists a reference frame in which E is stationary , it is shown[4] that the condition is that $\int_0^\infty\int_0^\infty dvdx\,p(v;x)$ must exist (where $p(v;x)$ is the probability that a particle starting from x_1 with V = 0 reaches $x_2=x_1+x$ with a velocity V.) In the above models, like in Ref.1 chap. VIII this integral diverges. However, small effects (viscosity collisions) may restore the convergence.

REFERENCES.

1 - P. ROLLAND, rapport EUR-CEA-FC 757 (1974).

2 - P. ROLLAND, Proc. 2nd Int. Conf. on Plasma Theory Kiev (1974).

3 - P. ROLLAND, J. of Plasma Physics 21, 341 (1979).

4 - P. ROLLAND, Rapport EUR-CEA-FC (to be published).

5 - P.A. STURROCK, Phys. Rev. 1, 141 (1966).

6 - P. ROLLAND, Rapport EUR-CEA-FC 975 (1978).

D3.3

MAGNETIC FIELD GENERATION IN IMPLODING PLASMAS DUE TO NERNST REFRIGERATION

J. H. Brownell
Los Alamos Scientific Laboratory, University of California
Los Alamos, New Mexico 87545, U.S.A.

ABSTRACT

It is shown that the Nernst effect may generate a large magnetic field in a high density plasma on a very short time scale, even in initially symmetric systems. Such a field would have implications for pellet fusion.

It has been pointed out that self-generated magnetic fields may be produced by the interaction of directed energy beams with target plasmas. These fields are caused by thermal currents generated by nonparallel temperature and density gradients, [1,2,3] by radiation pressure, [4] by resonant absorption, [5,6] and by thermal instability. [7] Such fields could affect the performance of pellets intended for use in inertial confinement fusion because they alter the ideal hydrodynamics of the implosion process. For example, for a pellet composed of concentric, homogeneous layers these processes may produce magnetic fields in the beam deposition region which can decrease the electron thermal conductivity between the absorption region and the ablator surface.

The present work was originally motivated by asking if a magnetic field could be produced in a pellet with concentric, homogeneous layers and which is initially symmetric in the sense that $\nabla n \times \nabla T = 0$. Upon considering that part of the electron temperature distribution where $\partial T_e/\partial r > 0$ such as might occur in the interior of a pellet at the beginning of an implosion or at the ablation surface, it was noticed that a thermoelectric effect similar to the Nernst effect could indeed produce an abrupt change in the magnetic field.

To isolate the Nernst effect's influence on the evolution of the magnetic field for small time, we look at the induction equation only [8]

$$\frac{\partial \vec{B}}{\partial t} = \nabla \times \left(\vec{v}_i \times \vec{B}\right) - \nabla \times \left(\frac{\vec{j} \times \vec{B}}{en}\right) - \frac{c}{en}\left(\nabla n \times \nabla T\right) - \frac{c}{e}\nabla \times \left(\frac{\vec{R}_T}{n}\right) - \frac{c^2}{4\pi}\nabla \times \left(\nabla \times \vec{B}\right)\Big/\sigma \qquad (1)$$

where $\vec{v}_i$ is the ion drift velocity, $\vec{j}$ is the current, n is the electron density, $\vec{R}_T$ is the thermal force, and σ is the conductivity.

We consider the case where $\nabla n \times \nabla T = 0$ and compare the magnitudes of the terms. For small time the Hall term is small, being of $O(B^2)$, and, anticipating cases where growth times are short compared to L/V_i (L is the initial scale length of the problem), the term involving V_i can be neglected.

Rewriting then, we have

$$\frac{\partial \vec{B}}{\partial t} - \frac{c^2}{4\pi\sigma}\nabla^2 \vec{B} = -\frac{c}{e}\nabla \times \left(\vec{R}_T/n\right) \qquad (2)$$

Now the relevant part of R_T is proportional to $(-n\omega_c \tau \hat{h} \times \nabla T)$ ($\hat{h}$ is the unit vector of the magnetic field) and constitutes a source term whose strength is a function of the unknown. Here $\tau \propto T^{3/2}/n$ and $\sigma \propto ne^2\tau/m$.

Consider the solution of Eq. (2) for a slab of plasma between $x = -a$ and $x = a$ with a symmetrical temperature distribution. The Nernst effect creates a source of emf that drives a current in the direction $\hat{n} \times \nabla T$ (a ring current in cylindrical or spherical geometry). Assume that the density is uniform and constant for times of interest and that $T = T_o(1 + x^2/L^2)$. The boundary condition is that $B(\pm a) = B_o$ where B_o is the initial field. The solution may be expressed in terms of integrals of parabolic cylindrical functions and for time and a/L small it can be shown that $B(x=0) \sim B_o \exp(\Gamma t)$ $[1 - 2/\sqrt{\pi}\ \exp(-\xi^2)/\xi]$, where $\xi = \sqrt{t_D/4t}$, $t_D = 4\pi\sigma a^2/c^2$ is the diffusion time and $\Gamma = .82\ \tau T'/m$. For example, if $n = 10^{21}$ cm^{-3}, T = 1 keV, and the gradient length is 100 μm, the e-folding time is 2×10^{-11} seconds. It is important to note that exponential growth occurs only for $\omega_c\tau \ll 1$. If $\omega_c\tau > 1$ initially, the Nernst coefficient changes form and $\dot{B}$ is much smaller. [8]

Thus, the Nernst effect is capable of producing exponentially growing fields both within the core of a pellet and in the ablation region even if the pellet is symmetrically irradiated.

From energy conservation the field grows at the expense of electron thermal energy, and one might describe the effect as Nernst refrigeration. Noting that energy is being transformed from an incoherent form to a coherent form, it is necessary to check that the entropy production is positive. This can be shown to be so for small time, principally because of rapid heat conduction. One can estimate that electron thermal conduction occurs on a time scale similar to that of the field growth, and so a more correct solution to the problem must follow $T(\vec{r},t)$.

This magnetic field amplification effect may have implications for fusion pellet implosion schemes, since with a proper temperature profile any initial field (or temperature perturbation [9]) may cause the B-field to grow. Once the field reaches a significant level, it will affect the symmetry of the implosion. In addition, the plasma temperature at the pellet's center will be lower than would otherwise be supposed.

Finally, the self-generated magnetic field may be important to the thermonuclear burn process, as it will decrease the ρR requirement and increase the distance that reaction products travel in the plasma, aiding in bootstrapping the reaction. Thus, while this effect may hinder the attainment of thermonuclear conditions, once a proper assembly is formed, the magnetic field may help ignition to occur.

REFERENCES

1. J. A. Stamper et. al. Phys. Rev. Letters 26, 1012 (1971).
2. J. Chase, J. LeBlanc, and J. Wilson, Phys. Fluids 16, 1142 (1973).
3. J. A. Stamper and B. H. Ripin, Phys. Rev. Letters 34, 138 (1975).
4. J. A. Stamper and D. A. Tidman, Phys. Fluids 16, 2024 (1973).
5. J. J. Thomson et. al., Phys. Rev. Letters 35, 663 (1975).
6. B. Bezzerrdes et al., Phys. Rev. Letters 38, 495 (1977).
7. D. A. Tidman and R. A. Shanny, Phys. Fluids 17, 1207 (1974).
8. S. I. Braginskii, JETP 6, 358 (1958).
9. J. Brownell, Comments Plasma Phys. Cont. Fusion 4, 131 (1979).

KINK INSTABILITIES OF A PLASMA COLUMN WITH ELLIPTICAL CROSS-SECTION

Gu Yongnian and Qiu Naixian

Southwestern Institute of Physics
P.O.Box 15,Leshan,Sichuan,People's Republic of China

Abstract: Kink instabilities of a sharp boundary plasma column with elliptical cross-section are studied,with arbitrary ellipticity and wavelength. For finite wavelength perturbations, numerical calculations are carried out by using Mathieu functions directly.

If the plasma is assumed to be incompressible, the perturbed total pressure in the plasma P_t and the scalar potential of perturbed vacuum magnetic field Φ_e are described by Laplace's equations[1]:

$$\nabla^2 P_t=0 \quad , \quad \nabla^2 \Phi_e=0 \qquad (1)$$

In the co-focal elliptical-cylinder coordinate(u, e, z), the inner and outer solutions of Laplace's equations are[2]:

$$P_t=\sum_m (C_m Ce_m(u,-q)ce_m(e,-q)+iS_m Se_m(u,-q)se_m(e,-q))e^{ikz} \qquad (2)$$

$$\Phi_e=\sum_m (F_m iFek_m(u,-q)ce_m(e,-q)+G_m Gek_m(u,-q)se_m(e,-q))e^{ikz} \qquad (3)$$

If there is a conductive shell at $u=u_1$,the Fek_m and Gek_m in eq. (3) should be replaced by the following functions respectively:

$$\widetilde{Fek}_m=Fek_m(u,-q)-Fek'_m(u_1,-q)Ce_m(u,-q)/Ce'_m(u_1,-q)$$

$$\widetilde{Gek}_m=Gek_m(u,-q)-Gek'_m(u_1,-q)Se_m(u,-q)/Se'_m(u_1,-q)$$

where $q=k^2d^2/4$; d is half focal length; $ce_m(e,-q)$ and $se_m(e,-q)$ are Mathieu functions with negative q ; $Ce_m(u,-q)$,$Se_m(u,-q)$ and $Fek_m(u,-q)$, $Gek_m(u,-q)$ are the first kind and third kind of modified Mathieu functions respectively; C_m, S_m, F_m, and G_m are constants to be determined; the primes and dots refer to differentials with respect to u and e respectively. This form of solutions is general and it is slightly different from that given by Coppi et al[1].

From the boundary conditions on the plasma column surface and using properties of Mathieu functions, we have obtained a general form of the dispersion relation:

$$|D_{mn}|=0 \qquad (4)$$

here $D_{mo}=F_{mo}-\sum_{s=1,j=1}\sum F_{mj}G_{js}^{-1}G_{so}$, $D_{mn}=H_{mn}-\sum_{s=1,j=1}\sum F_{mj}G_{js}^{-1}U_{sn}$ $(n\geqslant 1)$,

$$F_{mn}=(w+x_p^2-\nu^2x_p^2(Ce'_m(u_o,-q)/Ce_m(u_o,-q))\widetilde{Fek}_m/\widetilde{Fek}'_m)\delta_{mn}$$
$$-(Ce'_m(u_o,-q)/Ce_m(u_o,-q))\sum_j(\widetilde{Gek}_j/\widetilde{Gek}'_j)MS_{mj}MS_{nj}$$
$$-thu_o(Ce'_m(u_o,-q)/Ce_m(u_o,-q))NC_{mn} \quad ,$$

$$U_{mn}=(w+x_p^2-\nu^2x_p^2(Se'_m(u_o,-q)/Se'_m(u_o,-q))\widetilde{Gek}_m/\widetilde{Gek}'_m)\delta_{mn}$$
$$-(Se'_m(u_o,-q)/Se_m(u_o,-q))\sum_j(Fek_j/Fek'_j)MC_{mj}MC_{nj}$$
$$-thu_o(Se'_m(u_o,-q)/Se_m(u_o,-q))NS_{mn} \quad ,$$

$$H_{mn}=\nu x_p(Ce'_m(u_o,-q)/Ce_m(u_o,-q))(MC_{nm}\widetilde{Fek}_m/\widetilde{Fek}'_m-NS_{mn}\widetilde{Gek}_n/\widetilde{Gek}'_n) \quad ,$$

$$G_{mn}=\nu x_p(Se'_m(u_o,-q)/Se_m(u_o,-q))(MC_{mn}\widetilde{Fek}_n/\widetilde{Fek}'_n-NS_{nm}\widetilde{Gek}_m/\widetilde{Gek}'_m) \quad ,$$

$$MC_{mn}=\pi^{-1}\int_o^{2\pi} se_m(ce_n)'/h_o\,de \quad , \quad NC_{mn}=\pi^{-1}\int_o^{2\pi} ce_m ce_n/h_o^4\,de \quad ,$$

$$MS_{mn}=\pi^{-1}\int_o^{2\pi} ce_m(se_n)'/h_o\,de \quad , \quad NS_{mn}=\pi^{-1}\int_o^{2\pi} se_m se_n/h_o^4\,de \quad ,$$

$\delta_{mn}=G_{mn}(m,n\geqslant 1)$, $h_o=(1-k_1^2\cos^2 e)^{1/2}$, $k_1^2=1/ch^2u_o$,

$\nu=B_v/B_p$, $x_p=\alpha_p ka$, $\alpha_p=D_p/B_\perp$, $w=4\pi\rho_o a^2\omega^2/B_\perp^2$,

in which B_p and B_v are uniform longitudinal magnetic fields inside and outside the plasma column respectively, $B_\perp$ is the magnetic field on the boundary,which is produced by plasma current, a is the half major axis of the elliptical column, b the half minor axis.

The order of the determinant which expresses the dispersion relation corresponds to the number of perturbation modes existing in the system. Modes are generally coupling. Coupling occurs only among even modes or among odd modes. Accordingly, the dispersion relation can be divided into two kinds, one with even modes and the other with odd modes. The more stringent one of them should be taken as the stability condition of the system.

In the first order in ellipticity ϵ , the stability criteria are the same as that obtained in the case of a circular cylinder plasma with the same cross-sectional area. For n=1 mode,$\bar{q}_c\geqslant 2/(2-\beta)$.

In the second order in ϵ , the stability conditions for interior single-mode perturbation are ($\nu=1$)

n=1, $\bar{q}_c\geqslant(1+3\epsilon^2/32)$,

n=2, $\bar{q}_c\geqslant(1+\epsilon^2/8)(1+(6\epsilon^2)^{1/2}/4)$or $\bar{q}_c\leqslant(1+\epsilon^2/8)(1-(6\epsilon^2)^{1/2}/4)$,

$n\geqslant 3$, stable.

For an arbitrary ellipticity, numerical calculations have been carried out for the stability conditions of the first few modes and for its maximum instability growth rate. The results are shown in Fig.1 and 2. It follows that the number of instable modes increases with ϵ and β , and the maximum growth rate of high n modes is greater than that of the low n modes.

In the second order in ϵ , the stability condition for the case of coupling between n=1 and 3 modes is ($\nu=1$)

$$\bar{q}_c\geqslant(1+9\epsilon^2/32).$$

It shows that the coupling has a destabilizing effect.

Numerical calculations have been carried out for the case of multiple-modes too. The results are as follows: $\bar{q}_c$ required for stability increases rapidly with ϵ . Accordingly, the number of coupled modes to be taken into account increases too. When the coupled modes for a given ϵ increases to a certain number, $\bar{q}_c$ approaches a limit (Fig.3). At a/b > 2 and in the absence of a conductive shell, we obtain approximately $\bar{q}_c-1\propto(a/b)^2$. If ϵ is small, the value of $\bar{q}_c$ for the perturbation with finite wavelength is slightly larger than the value for perturbation with long wavelength (Fig.4). A conductive shell close to the plasma has a stabilizing effect to some extent. However, if a/b is large enough, either perturbation with finite wavelengths or any conductive shell has hardly any effect on the value of $\bar{q}_c$ (Fig.5). In addition, in the presence of a conductive shell, $\bar{q}_c$ changes abruptly at certain values of a/b .

The stability condition is more stringent in high-β system than in low-β system.

The analytical treatment and the results in long-wavelength approximation in this paper are found to be the same as those in papers /3/ and /4/, our work was done independently [5].

References:

/1/ B.Coppi, R.Dajazian and R.Gajewski, Phys.Fluids 15(1972) 2405.

/2/ N.W.McLachlan, Theory and Application of Mathieu Functions, Oxford, (1947)

/3/ J.P.Freidberg,and F.A.Haas, Phys.Fluids 17(1974) 440.

/4/ B.M.Marder, Phys.Fluids 17(1974) 447.

/5/ Gu Yongnian and Qiu Naixian, Report of the Southwestern Institute of Physics, PRC (1974).

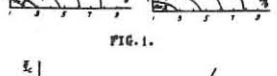

FIG.1.

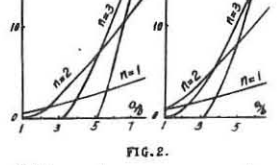

FIG.2.

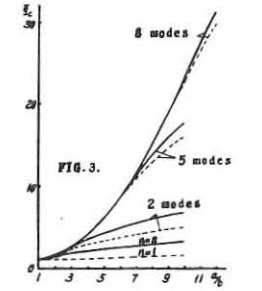

FIG.3.

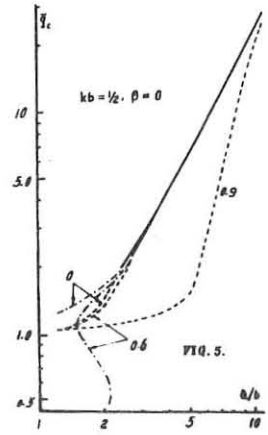

FIG.5.

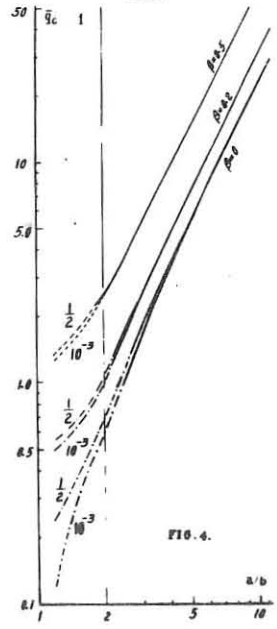

FIG.4.

DP1

HIGH CURRENT RFP DEVICES AND THE PULSED RFP REACTOR

J P CHRISTIANSEN and K V ROBERTS
Culham Laboratory, Abingdon,Oxon. OX14 3 DB, UK.
(Euratom/UKAEA Fusion Association)

Abstract. Results from calculations with a 1-dimensional equilibrium transport code on high-current medium-sized RFP devices are presented. Three devices of minor radii a = 0.6, 0.7, 0.8m respectively are computed with toroidal currents in the Megamp regime and the line density for optimum ion temperature found. Secondly a study of the operation of a Pulsed RFP reactor (PRFPR) is made. One reactor cycle is divided into 5 phases and a simple analytic model for the energy balance is used to show that ignition by Ohmic heating alone is feasible subject to certain assumptions.

1. High current RFP devices. Any present RFP simulation model is bound to be incomplete due to lack of empirical knowledge of anomalous transport processes. The RFP model used in the ATHENE 1 code normalizes the electron thermal conductivity to the empirical scaling laws for Tokamaks by choosing the diffusion as $D = c\ a^2/\tau_E^*$, where τ_E^* is the energy containment time for a Tokamak expressed in terms of the operating parameters. To achieve the value τ_E given by the Tokamak scaling the constant c is chosen such that $\tau_E(t = \tau_c) = \tau_E^*$, where τ_c is the RFP configuration time.

1.1 Parameters. The toroidal current is varied as I=(2.5,5,7.5,10)a[MA] corresponding to 4 different values of the axial field. The line density is varied as $N = (1,2,3,4,8)N_o$ where $N_o = 2.5\ 10^{19}[m^{-1}]$. The effective atomic Z is Zeff = 1.35 corresponding to Hydrogen and 0.65% fully ionized Oxygen. The standard initial and wall conditions of ATHENE 1 are used.

1.2 Results. The optimum value of N for each (I,a) value is related to the collisionality of the plasma. When the performance parameters for the optimum N values are studied as a function of current I it is found that the ion temperature appr. reaches 1keV per MA. It would thus appear that a medium-sized high current RFP could get close to ignition by Ohmic heating with I > 5MA although the Lawson parameter is $n\tau \sim 0.2\ 10^{20}[m^{-3}sec]$. It should be noted that the drift parameter is higher by a factor 1-2 than the value at which anomalous effects are expected.

2. The pulsed RFP reactor. One cycle of operation of the PRFPR is divided into 5 phases characterized by the setting-up of the RFP, the heating of the plasma to ignition, gas puffing, thermonuclear burn-up and pump-out. Of these 5 the gas puffing and thermonuclear burn-up phases are studied for the Lawson RFP reactor design [1]. A low-density (N_o) plasma is heated beyond the ignition point T_o and cold gas puffed into the discharge. The energy balance equation for the plasma is

$$\lambda\frac{\partial\mu}{\partial t} + \mu\frac{\partial\lambda}{\partial t} = \omega_\gamma\mu^2\lambda^2 + \omega_\Omega\lambda^{-3/2} - \omega_R\mu^2\lambda^{\frac{1}{2}} - \omega_E^*\lambda\mu \qquad (1)$$

where $\lambda = T/T_o$, $n = n/n_o$ (assume $T_e = T_i$, $n_e = n_i$) and the 4 terms represent α-heating ($\langle\sigma v\rangle_D \sim T^2$), Ohmic heating, Bremsstrahlung and thermal losses respectively. The time constant $\omega_E^* = 1/\tau_E^*$ is considered either constant or $\sim n^{-1}$. During the gas puffing phase it is envisaged that $\partial\lambda/\partial t$ is small and solutions for programmed puffing, $\mu(t)$ are found. Similarly during thermonuclear burn-up $\partial\mu/\partial t$ is small and solutions for $\lambda(t)$ are found. The solutions μ and λ are characterized by time constants τ_p (gas puffing) and τ_b (burn-up) which depend on (n_o, T_o, τ_{Eo}^*). The successful completion of the 2 phases requires $n_o = 3\ 10^{19}[m^{-3}]$, $T_o = 10[keV]$ $\tau_{Eo} > 20[sec]$. One cycle of operation will thus produce the average power level of 2[GW][1] subject to 5 basic conditions: 1) heating to T_o, 2) spatially uniform puffing, 3) local α-heating, 4) Gross MHD stability during cycle time, 5) perfect pump-out such that Zeff = 1. The conditions are relaxed somewhat in calculations with the ATHENE 1 code since the terms of (1) now have a spatial dependence. In these calculations it is however still assumed that cold gas can be puffed into the centre and furthermore that the empirical Tokamak scaling for τ_E^* applies.

[1] J D Lawson Culham Report CLM-R171 (1977).

DP2

MODELLING ZT-40 WITH THE G2M DIFFUSION CODE*

R. N. Byrne
Science Applications, Inc., La Jolla,California 92038

C. K. Chu
Columbia University, New York, New York 10027

Abstract. The G2M tokamak diffusion code [1] has been modified to include the model of anomalous diffusion developed for the ATHENE code[2,3] to model the slow evolution of reversed field pinches. The resulting code thus includes neutral and impurity transport, impurity radiation, and various anomalous transport models developed for tokamaks. We intend,following Christiansen and Roberts, to normalize the code to ZETA data, then use it to investigate the late-time behaviour of ZT-40.

1. ZETA. The following three points are established with respect to ZETA:

1.1 The Christiansen/Roberts/Suydam transport model (CRS)[3] doesn't much affect the temperatures in our simulations, since classical transport gives flattish profiles anyway. The density profiles are somewhat affected, but the overall calculation is little changed.

1.2. The calculated temperatures do depend on the level of impurity assumed. They increase with the amount of oxygen added, due to the increase in Zeff. Five per cent give Zeff about 2.5 and a central temperature of 210 eV.

1.3 Two dimensional calculations show that the currents that evolve produce mirroring fields. The mirror ratio on a flux surface rises to 1.3 at 0.35 m, falling to 1.2 at the wall. Since neither classical nor CRS transport models depend on this, the plasma evolution is almost the same as in the 1D - simulation. -

2. ZT-40. Turning to ZT-40, we find that the CRS transport strongly affects the calculated results. The temperatures tend to peak sharply off-axis, classically, and this tendency is reduced by CRS. Oddly, the central temperatures are higher with the enhanced transport, even thought the losses are much larger. This is partly because the central density falls with CRS and partly because the temperature profiles are smoother. The classical case does have more energy in the plasmas, but it is concentrated in the off-axis peak. A further prediction of the model is a large reduction in configuration time, since the field at the wall passes through zero at about 3.5 ms with CRS, but not for tens of ms classically, assuming perfect crowbarring.

Even with the help of CRS, ZT-40 cannot burn through oxygen in the central core at the highest densities envisioned ($10^{21}\ m^{-3}$) with as little as 1 per cent oxygen. If a way is found to preheat the electrons to, say, 50 eV, the device can support that much oxygen. At half the density, the problem disappears, and, as in ZETA, increased oxygen levels result in increased heating.

Finally, the 2D calculations show that there is less mirroring in ZT-40 than in ZETA, not unreasonable in view of the larger aspect ratio of the former device. The ratio of fields outboard to inboard is still as much as 1.2 near the peak of the poloidal field, however.

[1] Byrne, R. N., Klein, H. H., J.Comp.Phys. 28(1978) 352.

[2] Roberts,K. V., Christiansen, J. P., Long, J.W., Comp. Phys. Comm. 10(1975)264.

[3] Christiansen, J. P., Roberts, K.V., Nucl. Fusion 18(1978)181.

DP3

Investigation of Microinstabilities in a Low Density Linear Theta-Pinch Plasma

H.U. Fahrbach, W. Köppendörfer, M. Münich, J. Neuhauser, H. Röhr, G.Schramm, J. Sommer
Max-Planck-Institut für Plasmaphysik, D-8046 Garching, Germany, EURATOM Association, - and
E. Holzhauer, Institut für Plasmaforschung der Universität Stuttgart, 7000 Stuttgart, Germany.

1. Introduction

Current-driven microinstabilities can exist in post-implosion theta-pinch plasmas and cause anomalous diffusion. Linearized theory /1/ predicts the lower hybrid drift (LHD) instability if the density gradient extends over a few ion gyroradii for $T_e < T_i$. The wave is found to grow fastest at a wavelength $\lambda_{LHD} = 2\pi a_e \left(\frac{T_i}{2T_e}\right)^{1/2}$ with a_e the electron gyroradius. The saturated fluctuation level of the wave and anomalous diffusion were estimated using thermodynamic considerations /2/. Anomalous diffusion was deduced from the time behaviour of the magnetic field profile in the theta-pinch experiment Helix /3/ but conclusions on the cause of this diffusion could not be drawn. In order to identify the LHD instability and to measure its fluctuation amplitude a small-angle CO_2 laser light-scattering experiment was set up at the theta-pinch INTEREX in Garching. In sect. 2, this experiment, its diagnostic , the parameters and the behaviour of the plasma are described. Sect. 3 gives the scattering arrangement and results for two typical filling pressures. A discussion of these results follows.

2. The INTEREX Experiment and the Plasma Properties

INTEREX is a 8.75 m long theta-pinch with a coil of 0.19 m diameter. The magnetic field produced by a power-crowbarred capacitor bank rises in 0.6 µsec to 0.7 T and then stays nearly constant for 20 µsec. At filling pressures between 3 and 10 mTorr deuterium a hot low-compressed plasma is produced this way. Image convertor cameras, diamagnetic loops, infrared interferometers at 3.4 and 10.6 µ, 90° Thomson scattering, neutron detectors and monochromators for impurity line measurements are used to analyze the plasma. The magnetic field, neutron flux, electron temperature and diamagnetic flux signals are shown in Fig.1 from 5 mTorr discharges. Fig.2 shows electron density profiles measured with the CO_2 interferometer in the midplane of the coil. An ion temperature of 700 eV was deduced from the neutron flux assuming a two-dimensional velocity distribution. The beta on axis varies from $\beta = 0.8$ to 0.9. Although the plasma is grossly stable and contained for more than 20 µsec, the diamagnetic flux and the line density show irreproducible deviations (Fig.1).They are of the m=0 type with about 20 cm axial wavelength and can be assigned to mirror anisotropy instabilities. They do not allow to derive diffusion coefficients from density profiles. At half density radius a LHD wave with maximum growth rate $\gamma = 2.2 \cdot 10^7\ sec^{-1}$ $\lambda = 0.7$ mm and $\omega = 2.4 \cdot 10^8\ sec^{-1}$ should be excited according to linear theory. The ion gyroradius is about 1 cm in this region and the ion-ion collision time 50 µsec. Plasma produced at 3 and 8 mTorr give about the same condition for LHD instabilities since the ratio of the diamagnetic drift velocity to the ion sound velocity is about the same in the boundary layer, $\frac{v_d}{v_i} = 0.2$.

3. CO_2 Scattering

The arrangement for collective scattering at 10.6 µ with optical heterodyning is shown in Fig.3. The optical components are mounted on a moveable carriage. At small angles θ_s the direction of $\vec{k}_\Delta$ is nearly perpendicular to L_i /4/. If fluctuations propagate only in a narrow gradient region, radial scanning allows the separation of azimuthal and radial $\vec{k}_\Delta$ components. The accessible wavenumber range is determined by the windows ($k_\Delta \perp B = 60 - 600\ cm^{-1}$; $k_\Delta \parallel B = 60\ cm^{-1}$).
The single-mode, single-frequency output of the pulsed CO_2 laser has constant power during the plasma lifetime. The detector signal is amplified behind a 7 MHz high-pass. Finally spectral analysis within the detector bandwidth (300 MHz) is performed with filters of 20 MHz bandwidth.
The alignment of L_i and LO in the experiment is controlled with a novel method using nonlinear absorption in SF_6 at low pressures /5/. The angle θ_s is varied by changing position and angle of mirror M_1.
For all filling pressures the scattered power increased strongly with decreasing k_Δ (halfwidth in k_Δ space $200\ cm^{-1}$). The results quoted below were all measured at $k_\Delta = 82\ cm^{-1}$ ($\theta_s = 13$ mrad), close to the maximum growthrate expected from linear theory. Radial scanning up to 6.5 cm radius indicated azimuthal and radial fluctuations of comparable intensity and frequency spectrum.
In Fig.4 the signal amplitude proportional to $\tilde{n}_e$ is shown (double sensitivity for 75 MHz). At 8 mTorr strong initial fluctuations damp out within 5 µsec. Lateron scattered signals can be detected only in the two lowest frequency channels.
No signals could be detected at any pressure for $k_\Delta \parallel B$ ($k_\Delta = 82\ cm^{-1}$). A lower bound for the value of $\tilde{n}_e$ is obtained by integrating over the scattering volume (gradient thickness 2 cm) and a range of $\vec{k}_\Delta$ vectors which is specified by the beam geometry, corresponding to $\tilde{n}_e = 10^{10}\ cm^{-3}$ ($P_s = 7.2 \cdot 10^{-10}$ W) at 8 mTorr and $\tilde{n}_e = 6 \cdot 10^{10}\ cm^{-3}$ ($P_s = 2 \cdot 10^{-8}$ W) at 3 mTorr. An upper bound for the value of $\tilde{n}_e$ results if the k_Δ -spectrum is assumed isotropic in the r-θ-plane yielding $\tilde{n}_e = 4 \times 10^{10}\ cm^{-3}$ ($\frac{\tilde{n}_e}{n_{eo}} = 4 \times 10^{-5}$) at 8 mTorr and $\tilde{n}_e = 2.4 \times 10^{11}\ cm^{-3}$ ($\frac{\tilde{n}_e}{n_{eo}} = 6 \times 10^{-4}$) at 3 mTorr.

4. Discussion

The results obtained so far show strong fluctuations in the wavenumber range in which LHD instabilities should be excited. The wave vector parallel to the magnetic field is found small ($k_\parallel \ll k_\vartheta$) in accordance with theory /6/. The radial wave vector, however, seems comparable in size with the azimuthal one ($k_r \approx k_\vartheta$) a case not treated by theory. The fluctuation amplitude fits within an order of magnitude the saturation level as estimated in /2/.
At 3 mTorr a frequency spectrum $\Delta f \approx 100$ MHz was measured which is broader than expected from theory /7/. The observed discrepancies can depend on the fact that the experiment may not fit the simplified theoretical models. Especially at low pressures the ion velocity distribution will deviate considerably from a Maxwellian distribution.

References

/1/ Krall, N.A. and Liewer, P.C., Phys.Rev. A4 (1971) 2094
/2/ Davidson, R.C. et al. in Plasma Physics and Contr.Nuclear Fusion Research Proc. 6th Int.Conf. Berchtesgaden 1976, Vol.3 (IAEA, Vienna, 1977) p.113
/3/ Bogen, P., et al. in Plasma Physics and Contr. Nuclear Fusion Research, Proc. 6th Int.Conf. Berchtesgaden 1976, Vol.1 (IAEA, Vienna, 1977)p.539
/4/ Holzhauer,E., Massig, J.M., Plasma Phys. 20, 867 (1978)
/5/ Holzhauer, E., - to be published
/6/ Gary, P.S., Sanderson, J.J., Phys. Fluids 21 (1978) p. 1181
/7/ Gladd, N.T., Plasma Phys., Vol. 16, p. 27 (1976)

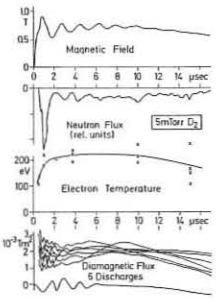

Fig. 1 Magnetic field, neutron flux, electron temperature and diamagnetic flux signals

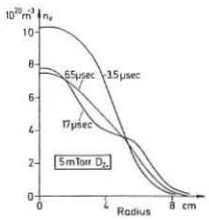

Fig. 2 Electron density profiles

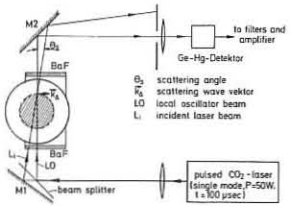

Fig. 3 CO_2-laser scattering arrangement

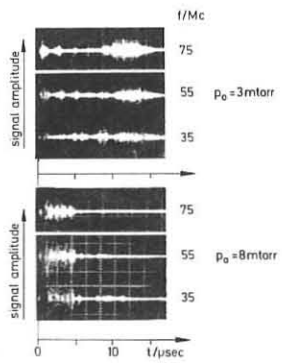

Fig. 4 Scattered signal amplitude for 3 different center frequencies

DP4

NUMERICAL STUDIES OF THE RFP

P G Carolan, J W Johnston,* J W Long,*
A A Newton, V A Piotrowicz,* M R C Watts
Culham Laboratory, Abingdon, Oxfordshire OX14 3DB, UK
(*Euratom/UKAEA Fusion Association*)
* *Oxford Polytechnic*

ABSTRACT

The evolution of the magnetic field profile of a pinch to a reversed field state has been simulated by a 1-D code modified to include 'dynamo' effects. The effective thermal conductivity K_F due to the dynamo has been estimated. We find that $K_F \propto T_e/n_e^{\frac{1}{2}}I$ in the collisional regime and $K_F \propto n_e^{\frac{1}{2}}a/I\ T_e$ in the collisionless case. A 0-D power balance code has been used to simulate the behaviour of the RFPs, HBTXI and ZETA.

INTRODUCTION

1-D and 0-D codes have been used to study the formation of, and energy losses from, reversed field pinch (RFP) plasmas, such as ZETA and HBTXI.

FIELD DIFFUSION DURING THE CURRENT RISE PHASE

Calculations of the magnetic field profile during the current rise phase have been performed using a modified version of the 1-D code 'ATHENE'.[1] The non-axisymmetric perturbations necessary for spontaneous field reversal were included using a 'dynamo model'.[2] We assume that the plasma β is small, and that the current rise time, τ_i, is much larger than the Alfvén transit time, τ_A. The magnetic field then evolves through a series of force free states satisfying $J \times B = 0$. The plasma resistivity, η, is assumed constant in space and time. Results are given as F-θ curves, where $F = B_{\phi\,\text{wall}}/B_{\phi\,\text{average}}$ and $\theta = B_{\theta\,\text{wall}}/B_{\phi\,\text{average}}$. Figure 1 shows the curves obtained without a dynamo for several values of η. In spite of large variations in the field profiles, the F-θ curves are very similar for all values of η. The effect of non-axisymmetric fluctuations is to add the extra term $\partial B/\partial t = -\nabla \times (\alpha B - \eta_T/\mu_o\ \nabla \times B)$ to the field diffusion equation, where α and η_T depend upon the parameters of the turbulence. If α is chosen as $\mu\,\eta_T/\mu_o + f(\bar{\mu} - \mu)$, where $\mu = \nabla \times B.B/B^2$, f is any positive function and $\bar{\mu}$ is the average of μ with weighting function f, then the conditions for Taylor's minimisation theorem[3] are satisfied and the field relaxes to the Bessel Function Model (BFM). We describe this choice of α as the 'Mean μ Model'. As a demonstration, we take $f = \eta_T/\mu_o$ = constant. Figure 2 shows the F-θ curve for three values of η_T. For $\theta < 1.2$ the F-θ curve is scarcely altered by the dynamo, but for $\theta > 1.2$ the dynamo allows the field to reverse and to follow the BFM curve. This is similar to the behaviour observed experimentally.[4]

FLUCTUATIONS AND HEAT LOSSES DURING THE CURRENT SUSTAINMENT PHASE

Using the dynamo model we have estimated the fluctuation level required to prevent the resistive decay of the reversed field. Assuming equipartition of energy between velocity and magnetic field fluctuations, we find $\delta B/B \propto S^{-\frac{1}{2}}$, where S is the ratio of resistive diffusion to Alfvén timescales. It is interesting to note that this is the same scaling as that found for reversal due to MHD modes.[4] The model can be extended to include heat losses due to electron thermal conduction along the perturbed field lines.[5] In the collisional regime, typically $T_e \lesssim 40$eV for ZETA-like conditions, the transverse thermal conductivity, K_F, is proportional to $T_e/n_e^{\frac{1}{2}}I$, which is essentially a Bohm scaling. In collisionless conditions we obtain a classical scaling, with $K_F \propto n_e^{\frac{1}{2}}a/I\ T_e$. If ohmic heating and conduction losses dominate the energy balance then a scaling law for the electron temperature may be found. In the collisionless case, appropriate for large devices, we find $T \propto I^2/n_e$, corresponding to constant electron beta.

0-D CALCULATIONS

A 0-D power balance code has been used to simulate the behaviour of the RFP experiments, ZETA and HBTXI.[6] The model includes the electrical circuit and energy losses due to ionisation, radiation, diffusion and convection associated with field fluctuations. The impurity charge state distribution and radiation losses are determined from the corona model.[7] The effect of relaxation of the discharge to a reversed field is included by allowing the plasma model to pass through a series of tearing mode stable (TMS) states.[8] These define an F-θ curve close to that observed and the corresponding plasma inductance values are used. Simulations of ZETA have been extended to include cases where the filling gas was deuterium mixed with known quantities of argon to study the radiated energy losses. The steady state coronal model was assumed to be valid for the argon and iron impurities considered in these calculations and values of mean charge etc were taken from Post[9] with extrapolations where $T_e < 30$eV. Bolometer measurements of the radiated energy were 57kJ without argon and 140kJ on the addition of 0.4% argon. Assuming that 0.15% iron was also present the code produced corresponding results of 55kJ and 157kJ. In Fig 3 is shown the experimentally measured current and the computed current for 0.15% iron and 0.4% argon. In order to extend the calculations to HBTXI, the code was modified to take account of this experiment's large 'dead space', i.e. the area between the vacuum vessel and the ϕ flux conserver. Using the experimental result that the plasma follows a universal F-θ curve where F and θ are measured at the plasma edge (not at the ϕ flux conserver) the actual θ and thus the plasma inductance and resistance factor can be calculated. Agreement with the experimentally observed current in HBTXI can only be obtained if the model plasma inductance is increased above that of the TMS model. Even in this case only reasonable agreement is obtained with the experimental results, as shown in Fig 4, where 4% of oxygen impurity and the measured values p_o = 40mTorr and $\delta B/B$ = 10% are used. The electron temperature reaches 7eV, comparable with values measured by Thomson scattering for similar discharges. A possible reason for the poorer agreement of the predicted current with HBTXI results is that the plasma is not in a fully relaxed state during the discharge, thus the model values of plasma inductance will differ from the actual values.

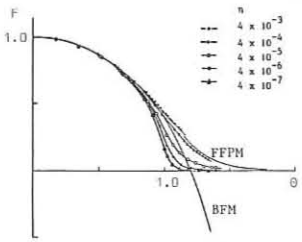

Fig 1 F-θ curves for five values of η, corresponding to values of τ_i/τ_η between 0.1 and 1000. The Bessel Function and Force Free Paramagnetic Models are shown for comparison.

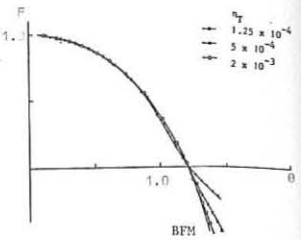

Fig 2 F-θ curves for $\tau_i/\tau_\eta = 10$ including dynamo terms. As the strength of the dynamo is increased the F-θ curve approaches that of the Bessel Function Model.

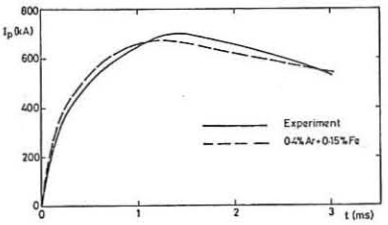

Fig 3 Experimental (solid line) and computed plasma current in ZETA as a function of time.

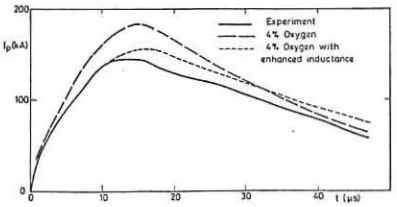

Fig 4 HBTXI plasma current as a function of time (dashed lines computed).

CONCLUSIONS

The experimentally observed F-θ curves can be simulated using an axisymmetric field diffusion equation, with non-axisymmetric fluctuations included using a dynamo model. The enhanced thermal conductivity associated with the dynamo is found to have a classical scaling under collisionless conditions. The 0-D simulations were extended to cases where argon was present in ZETA. Good agreement was obtained with radiation and current measurements. The code was modified to include a dead space region for HBTXI simulations. By increasing the inductance to values greater than those of the TMS model reasonable agreement was made between the currents.

REFERENCES

[1] J Christiansen, K V Roberts, J W Long: Comp Phys Comm 14 (1978) 423

[2] C G Gimblett, M L Watkins: in 'Controlled Fusion and Plasma Physics' (Proc 7th European Conf, Lausanne, 1975) 1 (1975) 103

[3] J B Taylor: in 'Pulsed High Beta Plasmas' ed D E Evans, Pergamon (1976) p59

[4] C A Bunting et al: in 'Controlled Fusion and Plasma Physics' (Proc 8th European Conf, Prague, 1977) 1 (1977) 79

[5] A B Rochester, M N Rosenbluth: Phys Rev Letts 40, 38 (1978)

[6] P G Carolan et al: 7th Int Conf on Plasma Physics and Controlled Nuclear Fusion Research, Innsbruck (1978)

[7] R W P McWhirter: in 'Plasma Diagnostic Techniques' ed Huddlestone and Leonard, New York, Academic Press (1965)

[8] D C Robinson: Nuclear Fusion 18 (1978) 939

[9] D E Post et al: At Data and Nucl Data Tables (USA) 20 (1977) 397

Field Reversal Experiments*

W. T. Armstrong, R. K. Linford, J. Lipson, D. A. Platts, and E. G. Sherwood

I. Introduction

The equilibrium, stability, and confinement properties of the reversed field configuration are being studied in two theta pinch facilities referred to as FRX-A, and FRX-B. The configuration is a toroidal plasma confined in a purely poloidal field configuration containing both closed and open field lines. The FRX system produces highly elongated tori with major radius R=3-5 cm, minor radius a ~ 2 cm, and a full length ℓ ~ 35 cm. Plasma conditions have ranged from T_e ~ 150 eV, T_i ~ 800 eV, and $N_{max} \sim 10^{15}/cm^3$ to T_e ~ 50 eV, T_i ~ 50 eV, and $N_{max} \sim 4 \times 10^{15}/cm^3$. The plasma remains in a stable equilibrium for up to 50 μs followed by an n=2 rotational instability which results in termination of the reversed field configuration (RFC). The plasma behavior with respect to equilibrium, stability, and rotation is consistent with recent theoretical work in these areas.

II. Recent Experimental Results

Before proceeding with a detailed review of experimental data and their consistency with theory, we shall first briefly describe our most recent experimental results. Independently driven, crowbarred mirror coils were recently included on FRX-A. With optimum mirror timing, it was found that the particle inventory increased as compared with plasmas created with passive mirrors or without any mirrors, the increase being largely due to greater plasma length. It is thought that the mirrors produce a more localized tearing and reconnection of field lines during the formation phase by providing more favorable field curvature at the ends. This should contribute to increased inventory. After the first few microseconds, the mirrors act more like an extension of the implosion coil which would also increase plasma length. An increase in plasma lifetime from 20 to about 35 μs is also observed but has not yet been fully explained.

An experiment in plasma translation was performed by disconnecting one of the driven mirrors. Where the remaining mirror was activated 0-5 μs before the implosion, the plasma was observed to translate towards the opposite end with an initial drift velocity of 3.3 cm/μs, exiting the coil in 15 μs. This time is intermediate between the plasma stable time (t_s) and an Alfvén transit time (T_A) so that the plasma can undergo a collective translation prior to instability. A 6328 Å fractional fringe interferometer, external field probes, and a side on streak camera all indicated a well defined plasma column forming in the center of the implosion coil and then drifting uniformly out of the system.

End-on framing photography indicated retention of an annular equilibrium as the plasma moves axially.

Thomson scattering has recently been added to FRX-B. The system has all its components rigidly mounted to a single table surface such that all relative alignments remain fixed. To shift the experiment either radially or axially, the table is translated by means of air bearings. This versatility is permitted because a three grating polychromator[1] has been employed. This instrument has sufficient rejection at 6943 Å to obviate the necessity of a beam or viewing dump.

Observations were made on the axial midplane at a constant filling pressure of 17 mtorr. Over the stable lifetime of the plasma, the electron temperature was essentially constant in both time and space at about 100 eV for radii interior to the seperatrix. Relative density was also fairly constant as a function of time at these radii. The ion temperature on the axial midplane was determined by Doppler broadening of the 2271 Å line of CV and after the first 10 μs was also 100 eV as required by fairly rapid equipartition. These data indicate that the energy density at any given radial position on the axial midplane is nearly constant in time. This implies that the equilibrium adjusts axially to compensate for losses from this region. The data also reconciles pressure balance quantitatively (to within 20%) where previous interferometric data at 17 mtorr has been used. The determination of an energy confinement time must await detailed axial scans.

III. Equilibrium

Great progress has been made in modeling the FRX equilibrium both analytically and by means of computer codes.

A 2D sharp boundary calculation by Linford[2] has yielded results similar to earlier calculations by Wright et al[3], and by Kadish[4]. The model indicates how the equilibrium varies under adiabatic compression, either by the addition of vertical flux, or by a perfectly conducting moving liner. The plasma length ℓ is found to be proportional to $r_s^{14/5}$ (r_s is the seperatrix radius) for the first case, and $r_s^{2/5}$ for the latter case. These findings are in excellent agreement for moderate compressions with a 2D time dependent ideal M.H.D. code developed by Grossmann[5]. The results diverge for large compressions because the equilibrium looses information about the walls and changes from an elongated to a roughly circular configuration as described by Kadish, and Stevens[6].

IV. M.H.D. Stability Review

The situation concerning M.H.D. stability has been greatly clarified. No pure M.H.D. modes are observed during the stable lifetime even though $t_s > 100\, t_A$ the latter being the minimum time scale for M.H.D. growth. Further, it has been observed that the stable time increases with increasing a/ρ (ρ is the ion gyro-radius) for our experimental range $3 < a/\rho < 10$. This is precisely the opposite scaling if finite Larmor radius (FLR) effects were contributing to the stability significantly.

The 3D M.H.D. simulation work of Anderson[7] et al, and the analytical work of Barnes and Seyler[8] has been largely consistent with experimental observations. The n=o mode (n= toroidal mode number) is found to be stable for reasonable pressure profiles in the fixed boundary model but is wall stabilized in the free boundary model. The n=1 sideways mode was found to be stable even without a wall except where very strong mirror fields are included. The n=1 tilting mode is never observed in the 3D computer modeling.

For n=2, 3D computer simulations show stability except for pressure profiles characteristic of over-compressed plasmas. Here the n=2 mode was found to have a relatively small growth rate $\gamma^{-1} \sim 30\, T_A$. For n >2 but still not large, the simulations indicate stability.

Local modes have also been considered. For $n+\infty$ the m=o mode (m is the poloidal mode number) was found to be stable for closed field line configurations (no shear), and for proper pressure profiles and boundary conditions. Indications are that finite pressure on the seperatrix is also required. The m=1 axial and radial kink modes have been examined by Pearlstein and Newcomb[9] for a Hill's vortex equilibrium. The growth rates both scale as a/ℓ so for highly elongated RFC's the growth is small. FLR effect should also help stabilize these modes. For m >2 all modes were stable. In all cases, elongation of the equilibrium was favorable for stability.

V. Rotation

The plasma lifetime is limited by the onset of an n=2 rotational instability which has been treated theoretically by Seyler[10] using a Vlasov fluid code, and by Freidberg and Pearlstein[11] using an FLR expansion. In Seyler's model $-\omega_r/\Omega^* = 1.64$ where ω_r is the real part of the perturbation frequency, and Ω^* is the diamagnetic drift frequency. For FRX, this ratio is about 2.0 where ω_r is determined by end on framing photography. The Vlasov fluid model also indicates a critical value of $\alpha \equiv -\Omega/\Omega^* = 1.55$ for stability where Ω is the ion rotational frequency. This is not in agreement with the experimentally determined value of 0.4, however Ω is determined experimentally by measuring the doppler shift of the 2271 Å line of CV. It is thought that the impurity profile is much more diffuse than the deuterium ion profile and that the CV measurement is not reflective of the deuterium rotational velocity. This is supported by the theoretical criterion that $\omega_r < n\,\Omega$ an inequality not satisfied for the experimental data. The critical Ω however has been observed to scale with Ω^* as predicted.

The most plausible explanation for the spin-up of the plasma has also been advanced by Seyler[12] where the preferential loss of particles with negative angular momentum is considered. These particles are found to be located either outside the seperatrix or encircling the axis, precisely the locations of anticipated large losses.

VI. Transport/Scaling

Transport has been the least satisfactorily studied area both experimentally, and theoretically. The energy confinement time during the stable period is of the order of tens of microseconds which is significantly shorter than a classical diffusion time. One candidate for enhanced transport is like particle (ion-ion) diffusion[13] which can proceed rapidly when the density gradient length is of the order of an ion gyro-radius. Also possible is anomalous transport due to the lower hybrid drift instability[12] which is driven by strong pressure gradients. A 1D hybrid code is being developed by Hamasaki[14] to consider both classical and anomalous transport but has not yet yielded definitive results.

Experimentally, the study of transport and scaling is limited by the relatively restricted parameter range of existing machines. A larger experiment called FRX-C has been proposed to alleviate the difficulty.

VII. Conclusions

Considerable progress has been made in defining the equilibrium, stability, and rotational properties of the RFC. These efforts have been aided by the addition of Thomson scattering to FRX-B, and by substantial new results from the theoretical community. Much remains to be done both experimentally and theoretically in understanding transport and scaling with respect to micro-turbulence, resistive instabilities, M.H.D. stability, and equilibrium.

*Work performed under the auspices of the U. S. Department of Energy.

References

1. R. Siemon, Appl. Optics 13, 697 (1974)
2. R. K. Linford to J. Lipson, private communication
3. J. K. Wright, R. D. Medford, and B. Chambers, Plasma Physics 12, 242 (1961)
4. A. Kadish, Conf. Record of 1979 IEEE Intl. Conf. on Plasma Science, p. 140
5. W. Grossmann, W. Hameiri, Proc. of the Sherwood Meeting on Theoretical Aspects of CTR Research, paper 2B9 (1979)
6. A. Kadish, D. C. Stevens, Nuclear Fusion 14, 821 (1974)
7. D. V. Anderson, W. A. Newcomb, D. C. Barnes, C. E. Seyler, Proc. of the Sherwood Meeting on Theoretical Aspects of CTR Research, paper 2A4 (1979)
8. D. C. Barnes, C. E. Seyler, LASL Rpt, LA-UR-79-13 (1978)
9. W. Newcomb to D. C. Barnes, private communication
10. C. E. Seyler, LASL Rpt. LA-UR-79-185 (1979)
11. J. P. Freidberg, L. D. Pearlstein, Phys. Fluids 21, 1207 (1978)
12. C. E. Seyler to R. K. Linford, private communication
13. M. Tuszewski, A. J. Lichtenberg, Phys. Fluids 20, 1264 (1977)
14. S. Hamasaki, Conf. Record of 1979 IEEE, Intl. Conf. on Plasma Science, p. 143

DP6

Z-PINCHES OF INTENSE ENERGY-DENSITY DRIVEN BY HIGH VOLTAGE STORAGE LINES

by

Baldock,P., Choi,P., Dangor,A.E., Folkierski, A., Kahan, E., Potter, D.E., Slade, P.D and Webb, S.J.
Blackett Laboratory, Imperial College,London SW7.

The high power pinched discharges described earlier (1) have been further investigated with the use of holographic interferometry to obtain information on number density, and spectroscopic technique in the visible to obtain temperatures. The holographic interferometry has been carried out in the double path configuration parallel to the axis of the discharge, with a 10ns ruby laser. Pinches in hydrogen, having lengths 5cm and 3cm, radii 1cm and 0.5cm and filling pressures 350 mTorr and 1 Torr respectively, were examined. Ring electrodes were used, and current waveforms were similar to those in ref.1. The interferograms show a cylindrically symmetric collapse down to approx. $\frac{1}{3}$ of tube diameter, after which the diameter remains constant for an appreciable time, and the plasma appears confined, until fringes begin to grow near the wall at times greater than 350ns. Fig.1 shows a hologram taken 350ns after onset of current in the larger tube; fig.2 shows the corresponding n_e profile, and - for comparison - the fringe pattern computed from it. The measured electron density of $1.5 \times 10^{17} cm^{-3}$ taken together with the filling pressure of 350 mTorr and the assumption of full ionization yields a compression ratio of 6.

Spectroscopic measurements were carried out on a 10cm long, 2cm radius tube, and the current pulse was 80kA for 150ns. Time resolved line profiles were obtained using a polychromator. In most cases 6 channels were used. The six simultaneous photomultiplier outputs were fed to an electronic time-editing unit constructed by one of us (PC), and were displayed sequentially on an oscilloscope. The discharge column was observed side-on, and the Balmer Hβ line, the He II 468.6 nm line and various nitrogen impurity lines were used.

The pre-ionization stage of the discharge was examined using the Hβ line. This line was predominantly Stark broadened and its width showed that preionization was 75% or more in the filling pressure range of 30-100 mTorr of H_2. As soon as the main current came on the Hβ line "burnt out".

The collapse stage was investigated with helium filling, and the evolution of the He II 468.6nm line profile was obtained for a range of filling pressures. This is shown in fig.3 for a pressure of 45mTorr. Both Doppler and Stark broadening contribute to the profile. The Stark profile was calculated using Kepple's tabulation (2) and n_e values inferred from compression ratios obtained from streak photography (single ionization being assumed). Then the Doppler width was obtained using the unfolding procedure described by Wiese (3) and a Voigt profile. This procedure yields ion temperatures of about 100eV.

After some 300ns - the precise value depending on the pressure - the 468.6nm line is burnt through. To study the discharge after this stage we reverted to a hydrogen discharge and used nitrogen impurity which did not exceed 2%. In particular the lines NII 460.1nm and NV 460.4nm were monitored simultaneously in a 50 mTorr hydrogen discharge. The NII line appeared as soon as the main current came on, and burnt through in about 150ns, while the NV line appeared at about 200ns.

In conclusion, both interferometric holography and nitrogen impurity spectroscopic measurements confirm that the quiescent stage after pinch formation is hot and dense as was surmised in ref (1).

References

(1) Choi P., Dangor A.E., Folkierski A., Kahan E., Potter D.E., Slade P.D., and Webb S.J. Plasma Physics and Controlled Nuclear Fusion Research (Proc.7th Int.Conf.Innsbruck 1978) Vol.2. IAEA, Vienna (1979)69.

(2) Kepple P.C., Phys.Rev. A.6, 1(1972).

(3) Wiese W.L. p.265, "Plasma Diagnostic Techniques", Academic Press, New York (1965).

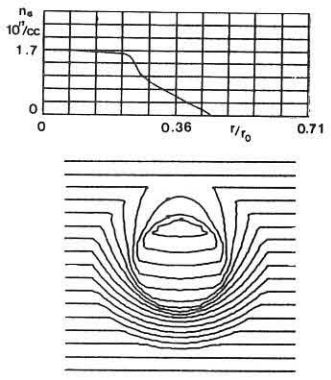

FIG. 2

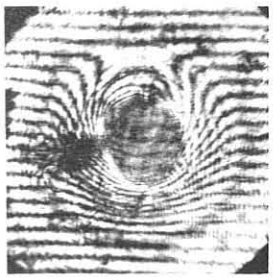

FIG. 1

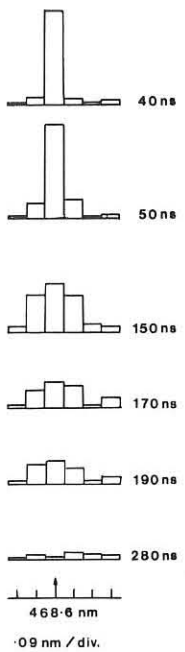

FIG. 3

PITCH PROGRAMMING OF THE ZT-S REVERSED-FIELD PINCH EXPERIMENT*

A. Jacobson, L. C. Burkhardt, D. A. Baker,
R. B. Howell, A. E. Schofield, A. G. Sgro

University of California
Los Alamos Scientific Laboratory
Los Alamos, New Mexico, U.S.A.

I. INTRODUCTION

The ZT-S experiment is a small, (R/a = 40 cm/7.7 cm) toroidal pinch experiment that uses the favorable MHD stability properties[1,2] of a high shear, reversed toroidal field configuration (RFP). This experiment provides guidance for the medium-sized ZT-40 RFP experiment presently under construction at LASL. The ZT-40 experiment has been designed to allow much flexibility in current rise time (2.5 μs-1 ms). This capability will be used to study (1) the confinement and scaling properties of a high-beta RFP at elevated temperatures, (2) the production and ohmic heating of RFP configurations at longer rise times. The first objective will begin with a study of the desired RFP configurations that are produced using field programming with tens of microsecond current rise times and the second will be accomplished by examining the production of the RFP and associated losses with increasing rise times up to ~ 1 ms. In the latter case, self-reversal and relaxation processes will play an important role as the fields are applied on slower time scales. This paper reports studies made on ZT-S to provide guidance for the programming of ZT-40 for the first objective. The suggestion has been made[3] that the pitch programming concept may be a useful guide for producing the desired field profiles in an RFP. This method has been extensively used for programming the nearly constant-pitch profiles into the screw-pinch experiments at Jutphaas since 1963. The purpose of the present study on ZT-S is to examine the utility of the concept for producing RFP configurations.

II. THE PITCH PROGRAMMING CONCEPT

A. Ideal

The pitch programming concept was first introduced by Colgate, et al.[4] The basic idea of the pitch programming is that, when both the poloidal and toroidal fluxes are conserved during the pinch-formation phase, the pitch P of the field lines ($P = rB_z/B_\theta$)** will stay constant on each inward moving magnetic surface. To the extent that the field is frozen into the plasma, as it is produced at the wall, it should be possible with this ideal model to map a given radial-pitch profile into the plasma with a proper choice of the time history of the pitch applied at the wall. The concept of injecting gas and continuously producing the plasma at the wall during the pinch formation has been proposed by the Culham group.[5] The radial pitch and pressure profiles obtained from this model will depend upon the subsequent plasma motion and heating, which is not easily predicted, and normally computer calculations are needed to complete the picture.

B. Non-Ideal

(1) General

In the ZT-S experiments the departure from the above idealized picture is considerable. (1) The primary part of the plasma is born throughout the volume by ionization of the initial gas fill. (2) Diffusion of the fields due to finite resistivity is important. (3) The energy loss processes during the programming are not easily predicted. (4) The production of a desired pitch history is limited by available ZT-S circuitry and is complicated by the interaction of the plasma motion with the driving circuits.

(2) Effect of Resistivity on the Motion of the Constant Pitch Surfaces

To get an idea of the effect of non-zero tensor resistivity $\vec{\vec{\eta}}$ on the motion of the constant pitch flux surfaces, we deduce an expression for the radial velocity of such a surface. The radial velocity v_p of a surface of constant pitch is obtained from the expression for the convective derivative acting on the pitch function P(r,t).@ Using $P(r,t) = rB_z/B_\theta$, and calculating $v_p = -(\partial P/\partial t)/(\partial P/\partial r)$ yields

$$v_p = v_r + \frac{B_\theta \partial(rK_\theta)/\partial r + rB_z \partial K_z/\partial r}{2B_\theta B_z - \mu_o r \vec{J} \cdot \vec{B}}$$

where v_r is the plasma radial fluid velocity and $\vec{K} = \vec{\vec{\eta}} \cdot \vec{J}$. We see that the constant pitch surfaces move with the fluid only if the added correction term vanishes as it does for the case of zero resistivity. For finite resistivity there can be a motion of the constant pitch surfaces to the axis, and some values of the pitch programmed into the plasma will be lost. The correction to the mapping is complicated by the time and space dependence of the resistivity making predictions difficult.

C. Initial Preliminary Computer Calculations

The preliminary calculations for the idealized current waveforms shown in Fig. 1 were used to guide the experimental programming. The corresponding $q(t) \equiv P(t)/R$ behavior at the wall is shown in Fig. 2a (R is the major radius). The q(r) profile at t = 4 μs is shown in Fig. 2b. The q(r) profile is qualitatively quite similar to the q(t) profile, and qualitatively similar to desirable equilibrium q profiles. The loss of the pitch values corresponding to values of q in the interval ~ 0.07-0.2 programmed at the wall results from the finite value of v_p at the axis.

*Work performed under the auspices of the U.S. Department of Energy.

**A cylindrical approximation used since ZT-S has a rather large aspect ratio (5.3).

@It is assumed that the pinch remains cylindrically symmetric and smoothly varying during the programming time.

III. COMPARISON OF THE EXPERIMENTAL RESULTS WITH FINAL COMPUTER CALCULATIONS

In the experimental results the waveforms were somewhat different from the idealized version due to constraints of the circuit inductance and bank capacity. The results are divided into two cases. In case (a) the field waveforms at the wall are shown in Fig. 3. The computed q(r) profile at 4 μs is shown in Fig. 4 by a dashed line and the experimental q(r) values are plotted as circles. The q(t) profile is shown as a solid line. The plots of q(r) correspond to the computed and measured field profiles in Fig. 5. Calculated electron temperatures ranged from 10 eV in the plasma to 100 eV in a hot corona surrounding the plasma, to 2 eV near the wall.

In case (b) the field waveforms at the wall are shown in Fig. 6. The experimental q(r) profile at 10 μs is shown in Fig. 7 along with the computed q(r) which is indicated by a dashed line. The corresponding field profiles exhibit an off-axis shift, which was used to recenter the experimental q(r) profile in Fig. 7 (as evident from the horizontal bars) so that the q(r) plots have common centers. The lower solid curve is q(t) showing the mapping of q(t) into q(r).

In the two cases shown here the computed pitch profiles resemble the experimental profiles. The resistivity and thermal conductivity chosen have thus been able to provide a useful mapping from the q(t) at the wall to q(r) inside the plasma.

IV. CONCLUSIONS

Preliminary studies of pitch programming have been made, both experimentally and computationally. In either case there is a rough qualitative mapping between radial pitch profiles (at the conclusion of the programming phase) and time histories of the pitch (at the wall) during the programming phase. An effect of resistivity is to reduce the total range of pitch values in the resulting radial profile below the corresponding range programmed at the wall. It is still unknown whether pitch programming will be appropriate to larger bore experiments (such as ZT-40), and the present work indicates the need for more investigation of this matter.

REFERENCES

1. D. C. Robinson, Plasma Phys 13, 439-462 (1971).
2. D. A. Baker and L. W. Mann, Proc. 2nd Top. Conf. on Pulsed High-Beta Plasmas, Garching 1972 (Max-Planck Institut fur Plasma physik bei Munchen, 1972) pp 69-72.
3. A. G. Sgro and P. C. T. Van der Laan, "Computer Modeling of Reversed-Field Pinch Formation," Bull. Amer. Phys. Society 22, 9, 1155, Oct 1977.
4. S. A. Colgate, J. P. Ferguson, and H. P. Furth, "External Conductivity Theory of Stabilized Pinch Formation," UCRL 5086 (1958).
5. A. A. Newton, "The Formation of Stable, High Beta Reversed Field Pinches," Bul. Amer. Phys. Soc., Sept 1973, p 1327.

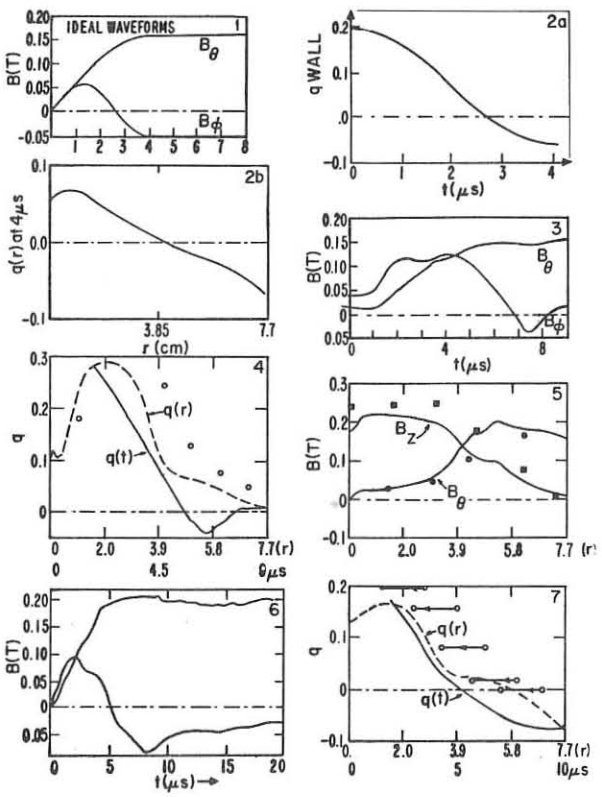

DP8

EQUILIBRIUM AND STABILITY OF A SCREW-PINCH

J. Rem

Association Euratom-FOM, FOM-Instituut voor Plasmafysica
Rijnhuizen, Jutphaas, The Netherlands

ABSTRACT

An analytic solution for the equilibrium fields in the force-free field region surrounding a high-beta tokamak has been found. This solution was used to determine which combination of the equilibrium parameters describing the stability of a high-beta tokamak corresponds to the screw-pinch.

In a screw-pinch the plasma is shock-heated and compressed in such a manner that force-free currents in the tenuous plasma outside the plasma give rise to a special q-profile: a q that is uniform in space. This makes a direct application of the stability theory of the sharp boundary model of a high-beta tokamak impossible because this has just the attractive feature of involving only the equilibrium fields on the plasma boundary. To determine which combination of the equilibrium parameters leads to such a special q-profile one must solve for the equilibrium fields in the force-free field region.

In Ref. 1 it was shown that the high-beta ordering reduces the problem of determining the force-free fields to a two-dimensional problem for the poloidal field. A simple dependence on the equilibrium parameters - beta, q^* the parameter related to the current and the force-free current parameter Γ - is obtained when a dimensionless field is introduced:

$$\underline{\hat{b}}_p = \underline{\hat{B}}_p \, q^*/\varepsilon B_o = -\underline{\hat{e}}_z \times \underline{\nabla}\psi \ , \qquad (1)$$

where:
$$q^* = \varepsilon L B_o / I_{tor} \approx \varepsilon B_o \left[\oint_S d\ell \, \hat{B}_p / L\right]^{-1} \ . \qquad (2)$$

The various quantities appearing here are: ε the inverse aspect ratio a/R_o, B_o the toroidal field on S at x = 0, R_o the major radius, "a" the half-width of S, L the length of the circumference and I_{tor} the toroidal plasma current [Fig. 1].

Expressed in terms of the flux function the problem is that of determining the solution to the Poisson equation:

$$\nabla^2\psi = -\Gamma \qquad (3)$$

in V^{ff}. This equation must be solved with Cauchy boundary conditions on S,

$$\hat{b}_p \ (\text{on S}) = -\underline{n}\cdot\underline{\nabla}\psi \overset{\psi=0}{=} 2\sqrt{\varepsilon\beta_p}\left[1 - 0.5k^2\left(1 - x_s(t)\right)\right]^{\frac{1}{2}}/k \ , \qquad (4)$$

where $\varepsilon\beta_p = \beta q^{*2}/\varepsilon = 0.25k^2/\langle[1 - 0.5k^2(1 - x_s(t))]^{\frac{1}{2}}\rangle^2$, so that it belongs to the category of "ill-posed" problems; $\langle A\rangle = \oint_S d\ell \, A/L$. Observe that the flux function depends only on Γ, and the parameter k, i.e. on $\beta q^{*2}/\varepsilon$; k = 0 corresponds to β = 0 and k = 1 corresponds to the equilibrium limit. The same dependence is found in the safety factor q when it is normalized with respect to q^*:

$$q/q^* = \int d\ell^* \ (2\pi\hat{b}_p)^{-1} \ , \qquad (5)$$

where ℓ^* is the length along a ψ = constant surface in the dimensionless coordinates of Fig. 1.

In Ref. 2, Kerner et al. showed that a conformal transformation of the vacuum region in the (x,y)-plane to a semi-infinite strip in the ω-plane enables one to find the solution to the poloidal field by analytic continuation of the field on the boundary. This method has been extended to a plasma surrounded by force-free currents[3]. When the shape of S is given in a parametric form, i.e., $x_s = f(t)$ and $y_s = g(t)$, the desired conformal transformation is:

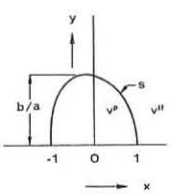

Fig. 1.

$$z = f(\omega) + i\,g(\omega) = h(\omega) \ ; \quad \omega = u + iv \ . \qquad (6)$$

In the (x,y)-plane the (u,v)-lines represent an orthogonal coordinate system in which the surface S coincides with v = 0. Decomposing the field in components along these coordinates the following analytic expression for the poloidal field is obtained:

$$\hat{b}_u + i\,\hat{b}_v = \sqrt{\frac{h'(\bar{\omega})}{h'(\omega)}}\ \hat{b}_p(\bar{\omega}) - i(\Gamma/2)\left\{\sqrt{h'(\bar{\omega})}/|h'(\omega)|\right\}[h(\bar{\omega}) - h(\omega)] \ , \qquad (7)$$

where $\bar{\omega}$ denotes the complex conjugate of ω. The first term corresponds to the vacuum term of Kerner et al. and the second one arises from the force-free currents. Observe that the current distribution inside the plasma influences the fields only through $\hat{b}_p(\bar{\omega})$. The flux distribution around S is determined from Eq. (7) by integration.

The vacuum solution shows a number of peculiarities: stagnation points occur where $h'(\bar{\omega}_1) = 0$, $\hat{b}_p(\bar{\omega}_2) = 0$ or $h'(\omega_3) = \infty$ and these points are also branch points unless the zero at ω_1 and the pole at ω_3 are even or when near $\bar{\omega}_2$ the function $\hat{b}_p(\bar{\omega})$ is multi-valued. For the sharp boundary model only the first and second type of stagnation points occur and both are branch points. Only the stagnation points arising from $\hat{b}_p(\bar{\omega})$ depend on beta so that at least one of these should correspond to the usual stagnation point that approaches the inside of the toroid when k → 1. The branch cuts starting at the stagnation points are physical boundaries with currents along them and their position is determined by Eq. (7). Fig. 2a shows the flux surfaces around an ellipse with an elongation of 1.5 for k = 0 and Γ = 0. The same surfaces for k = 0.9 and $e\Gamma$ = 1 are shown in Fig. 2b (e = L/2πa). Due to the increase in k the branch point from $\hat{b}_p(\bar{\omega})$ has moved from $x = -\infty$ to P while the one originating from $h'(\bar{\omega})$ has remained at the same position: Q. As expected the force-free currents removed the stagnation points but cannot affect the presence of the singularities.

A number of shapes were investigated - ellipses and D-shapes - and the resulting q-profiles were found to depend weakly on the shape. Over a large range of k- and Γ-values the ψ-dependence of q was approximately linear. Therefore a good indication of the dependence of $q(\psi)$ on k and Γ can be obtained from $dq/d\psi$ on S. For an ellipse with an elongation of 1.5 this is shown in Fig. 3. For each value of Γ there is one value of k (or $\varepsilon\beta_p$) that yields $(dq/d\psi)_s = 0$. Since k corresponds to $\beta q^{*2}/\varepsilon$ = constant the equilibrium q-profile is the same for all points on this curve in the stability diagram (β/ε versus q^*). The intersection point of this curve with the one corresponding to marginal stability (for the same value of Γ) thus corresponds to a screw-pinch plasma, i.e. a plasma with a uniform q-profile in V^{ff}. Fig. 4 shows the marginal stability boundaries for the ellipse b/a = 1.5. The curves a, b, d, e correspond to the values of $e\Gamma$: 0, 1, 2, 3, and the points 1, 2, 3, 4 indicate the equilibria with $(dq/d\psi)_s = 0$. Point 1 has $e\Gamma \approx 0.1$ and lies on the equilibrium boundary while the other points lie on the marginal stability curves: $e\Gamma$ = 1, 1.5 and 2. The figure points out that values of Γ larger than 2 cannot yield a screw-pinch and that higher values of β/ε are possible when negative values of $(dq/d\psi)_s$ are permitted.

ACKNOWLEDGEMENT

This work was performed under the Euratom-FOM association agreement with financial support from ZWO and Euratom.

REFERENCES

1. D'Ippolito, D.A., et al., Phys. Fluids 21 (1978) 1600.
2. Kerner, W., et al., Nucl. Fusion 12 (1972) 433.
3. Rem, J., to be published.

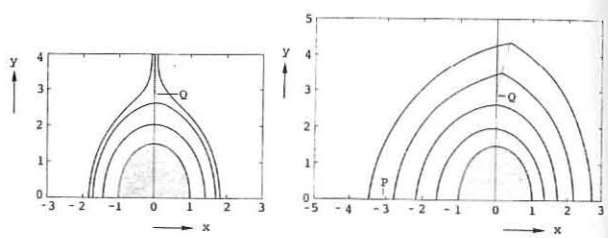

Fig. 2a. Fig. 2b.

Flux surfaces around the ellipse b/a (e = 1.26) for two conditions: a) k = 0, $e\Gamma$ = 0 and b) k = 0.9, $e\Gamma$ = 1. The branch cuts starting at P and Q are indicated by the shaded lines.

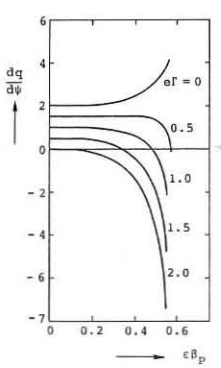

Fig. 3. Values of $dq/d\psi$ on S for the ellipse b/a = 1.5 as function of $\varepsilon\beta_p$ and $e\Gamma$.

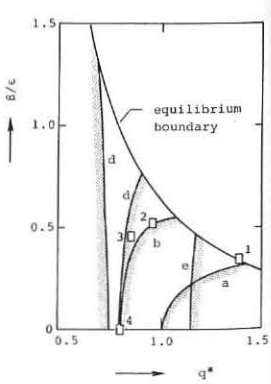

Fig. 4. Stability diagram for the ellipse b/a = 1.5. The curves a, b, d, e correspond to marginal stability for the following values of the force-free parameter $e\Gamma$: 0, 1, 2 and 3. The stable region is indicated by shading. The points 1, 2, 3 and 4 indicate a screw-pinch plasma: $dq/d\psi/s = 0$, for the values of $e\Gamma$: 0.1, 1, 1.5 and 2.

IMPURITY RADIATION, DENSITY AND TEMPERATURE IN SPICA

D. Oepts, G.G. Lister*, J.W. Long**, A.F.G. van der Meer
A.A.M. Oomens, and C. Bobeldijk
Association Euratom-FOM, FOM-Instituut voor Plasmafysica
Rijnhuizen, Jutphaas-Nieuwegein, The Netherlands

Abstract

Profiles of electron temperature and density have been measured in crowbarred discharges at times up to 120 μs. In stable discharges plasmas with an average $\beta \sim 0.2$ are observed up to 50 μs. A comparison with computed profiles shows remarkable differences. The first results of an investigation of impurity radiation are reported.

Introduction

Screw-pinch discharges with type L predischarge[1] (characterized by a homogeneous density profile and an ionization degree of 40%) have been investigated. These discharges reproduced poorly and, therefore, definite conclusions cannot easily be drawn. Nevertheless, stable discharges can be produced with interesting discharge properties. Two causes for the irreproducible character can be mentioned:
- the predischarge itself is irreproducible,
- the conflicting demands of β below 20% (stability) and an effective implosion without excessive skin broadening leave only a narrow range of useful operating conditions.

Density and temperature profiles

A new 90° Thomson-scattering detection system has been installed to enable the measurement of electron density and temperature profiles in a single shot. A 150 mm long section of the laser beam traversing the plasma is imaged onto the entrance slit of a spectrometer and the spectrum is viewed with a sensitive camera tube (ISIT vidicon, optical multichannel analyzer). The optical image of the scattering volume is transferred to the spectrometer in the screened room by means of a 12 m long image guide consisting of a coherent bundle of 300 optical fibres. The spectral image at the vidicon is scanned in successive tracks corresponding with 11 positions in the plasma. Each track is divided into 500 spectral channels. This number is reduced during read-out by adding together the signals from groups of successive channels. The resulting spectral resolution is 5 nm; the spatial resolution elements measure 14 mm in the radial direction. Figure 1 shows an example of the recorded signals. Temperatures and densities are determined by fitting gaussian curves to the spectral profiles.

Measurements have been done of discharges with p_0 = 8 mtorr D_2, B_ϕ = 1.2 T, $I_{zp} \approx 250$ kA and 0.14 T bias field at times 7.5, 10, 20, 50, 70, 100 and 120 μs after the start of the main discharge.

The following observations can be made:
At 7.5 μs, the density frequently shows a hollow profile. In the central region, with a width varying from 20 to 40 mm, the density is lower than $\sim 3\times10^{21}$ m^{-3} and often even too low to observe the Thomson-scattering signal. When the density is sufficiently high to determine the temperature, values from 20 to 50 eV are found in this region. In the "skin" regions, which have a width of 40 to 70 mm, n_e is in the range 5 to 15×10^{21} m^{-3} and T_e ranges from 40 to 100 eV. A rough sketch of such profiles is given in Fig. 2. The density minimum is not always as pronounced as shown and the temperature values usually show considerable scatter which cannot always be explained by inaccuracy of the measurement. At 10 μs hollow profiles are less frequently observed, but the general appearance is similar; while the density falls off rather sharply at the boundaries, the temperature does not.

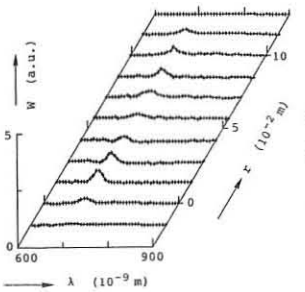

Fig. 1. Example of Thomson-scattering signals after correction for background light.

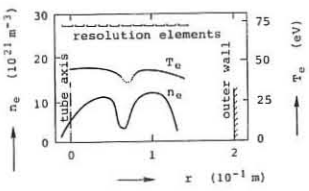

Fig. 2. Sketch of n_e and T_e radial profiles at 7.5 μs.

The measurements at later times indicate that in stable discharges the temperature and density decay approximately at the same rate. When a column is still present, its temperature profile is usually rather flat (e.g., 40 eV at 50 μs), while the density ($\sim 7\times10^{21}$ m^{-3}) is somewhat asymmetric, with a steeper gradient at the outside. The diameter of the column appears to decrease from about 100 mm at 10 μs to about 40 mm at 100 μs. Remnants with density $\approx 2\times10^{21}$ m^{-3} and temperature 20 - 50 eV have been detected at 120 μs; a reasonably dense but cold (T_e < 20 eV) column has never been observed.

Integration of the densities, obtained from the profile measurements, along the radius did agree well with the interferometric measurements.

An investigation of the region near the outer wall, using the older single-position scattering set-up, indicates the presence of a plasma with $n_e \approx 0.3\times10^{21}$ m^{-3} and $T_e \approx 5$ eV at 10 μs.

The computer code ATHENE[2] has been used in an attempt to simulate the experimental observations. The code differs from the earlier version of the code[3] with respect to the treatment of the momentum equation, in which both inertial and viscous terms are included,

$$\rho \frac{d\vec{v}}{dt} = -\nabla p + \vec{j}\times\vec{B} - \nabla\cdot\vec{\vec{V}} ,$$

where ρ is the plasma density, $\vec{v}$ the fluid velocity, and $\vec{\vec{V}}$ a viscous tensor given by

$$V_{ij} = -2\mu\left[\frac{\partial v_i}{\partial x_j} - \frac{1}{3}\nabla\cdot\vec{v}\right] ,$$

where μ is the coefficient of viscosity.
This viscous tensor also provides a heating mechanism in the ion temperature equation. In order to limit the viscous heating we used $\mu = \mu_{\parallel}/(1+\omega_i^2\tau_i^2)$, where $\mu_{\parallel}$ is the Braginskii parallel viscosity.

*) Now at the Max-Planck-Institut für Plasmaphysik, Garching.
**) Guest from Culham Laboratory, England

We used a variety of initial conditions. An example of the results is shown in Fig. 3. These results were obtained for initial temperatures of $T_e = T_i$ = 1 eV and an initial density of 6×10^{20} m^{-3}(9 mtorr D_2). For higher initial temperatures, qualitative results are similar, but higher final temperatures are reached due to the larger amount of viscous heating. The figure shows T_e- and T_i-profiles at 11 μs and 36 μs, and temperatures are seen to remain peaked, while hollow density profiles persist long after the implosion phase of the pinch.

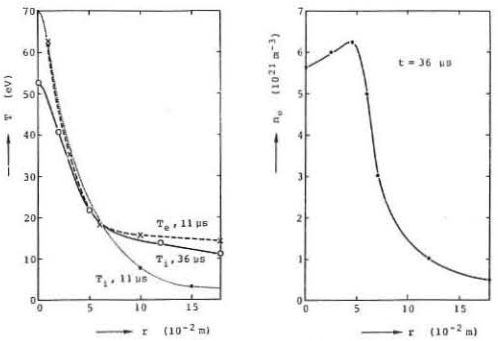

Fig. 3. T_e- and n_e-profiles computed in a cylindrical model.

Impurity radiation

To determine the nature and the density of impurities, a two-metre grazing-incidence VUV spectrometer (Hilger and Watts E580) has been installed. Both photographical and photoelectrical measurements have been done in the mid-plane, mostly in ringing discharges. Because of mechanical constraints the spectral range for photoelectrical recordings is limited to 5 nm < λ < 40 nm. From the photographical measurements the following conclusions can be drawn:
- no emission lines are found below 5 nm ($h\nu$ = 230 eV),
- all persistent O- and Si-lines between 5 and 50 nm have been identified,
- apart from O and Si also some N and probably C is present.

Unfortunately, it is not yet possible to make simultaneous recordings of different emission lines photoelectrically, which is a severe limitation in view of the poor reproducibility of the discharges. Several lines have been recorded, mostly OV-, OVI- and SiVII-lines.

The emission starts with a rapid increase in intensity between 1 and 7 μs (only slightly shifted to later times for higher ionization stages), usually followed by a ten-fold decrease in the next 10 - 15 μs, whereafter it slowly decays. Only in discharges where the interferometer does not show a decrease of line density directly after maximum compression, the OVI-lines are seen to remain at a relatively high level for several tens of microseconds (see Fig. 4). No increase in intensity of emission lines belonging to lower ionization stages is observed at later times in the discharge, indicating that density is lost before the electron temperature drops below 20 eV. The density of OVI-ions has been estimated from a measurement of the absolute intensity of the OVI 381.1 nm ($3\,s^2S - 3p^2P^0$) emission line. At maximum intensity (the intensity of emission lines belonging to OV has decreased by a factor of three then) we find $n(OVI) < 0.002\times n_e$.

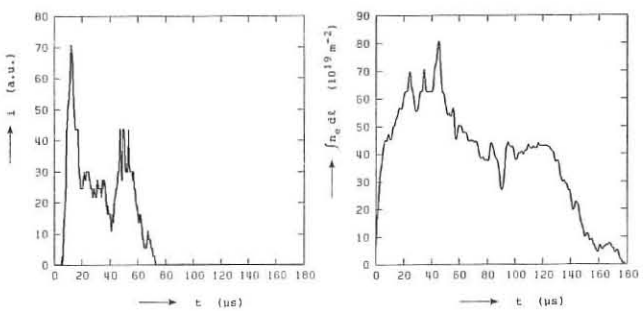

Fig. 4. Time behaviour of the intensity of the 381.1 nm OVI-line and of the electron line density.

T_i has been determined as a function of time by measuring the Doppler broadening of the NV 460.37 nm impurity line by means of a 5-channel 1-metre polychromator. The intensity of this line also displays the above-mentioned time behaviour and only between 2 and 12 μs it is high enough to allow linewidths to be measured. The derived temperatures range from 40 to 90 eV in stable discharges with 0.14 T bias field. In, as expected very unstable, discharges with $p_0 \approx 5$ mtorr and 0.035 T bias field, the ion temperature reaches 350 eV.

Conclusions

Stable screw-pinch discharges have been obtained in which the β-value of the main column remains at about 20% for at least 50 μs. The electron and ion temperature in the main column are already roughly equal at 7.5 μs. Measurements of the impurity radiation indicate that the oxygen concentration is very low (< 0.2%) and that nearly all the oxygen ions are in the OVI-state early in the discharge, so losses due to the oxygen impurity do not look very serious. Although peak values of density and temperature from both numerical computation and measurement are the same, there is a large difference in radial dependence.

Acknowledgement

The machine has been skilfully operated by P.H.M. Smeets. Further assistance was given by W. Kooijman (data handling), P.J. Busch (Thomson scattering) and W.J. Mastop (interferometer).

This work was performed under the Euratom-FOM association agreement with financial support from ZWO and Euratom.

References

1. A.A.M. Oomens et al., Proc. 8th Eur. Conf. on Contr. Fusion and Plasma Phys., Prague (1977), Vol. I, p. 73.
2. G.G. Lister and K.V. Roberts, to be published.
3. J.P. Christiansen, K.V. Roberts, CPC (1978) 14, 423.

DP10

Reversed-Field Pinch Plasma Model*

G. H. Miley and R. A. Nebel
Fusion Studies Laboratory
University of Illinois
Urbana, Illinois 61801 USA

and

R. W. Moses
Los Alamos Scientific Laboratory
Los Alamos, New Mexico 87544 USA

Introduction: The stability a Reversed-Field Pinch (RFP) is strongly dependent on the plasma profile and the confining sheared magnetic field. Magnetic diffusion and thermal transport produce changing conditions of stability. Despite the limited understanding of RFP transport, modelling is important to predict general trends and to study possible field programming options.

To study the ZT-40 experiment and to predict the performance of future RFP reactors, a one-dimensional transport code has been developed. This code includes a linear, ideal MHD stability check based on a energy principle. The transport section integrates plasma profiles forward in time while the stability section periodically checks the stability of the evolving plasma profile.

Transport Model: To accommodate fusion plasmas, the code has three fluids: electrons, ions, and alpha particles. Confined alpha particles are assumed to instantaneously thermalize in-situ, joining the background ion group. The quasi-static, quasi-neutral approximation gives seven working equations:

$$\frac{\partial n_i}{\partial t} + \vec{\nabla} \cdot \vec{\Gamma}_i = S_i - 2f(1-f) \langle \sigma v \rangle n_i^2 \tag{1}$$

$$\frac{\partial n_\alpha}{\partial t} + \vec{\nabla} \cdot \vec{\Gamma}_\alpha = f(1-f) \langle \sigma v \rangle n_i^2 \cdot F \tag{2}$$

$$\frac{3}{2} n_j \frac{dT_j}{dt} + P_j \vec{\nabla} \cdot \vec{V}_j = - \vec{\nabla} \cdot \vec{q}_j + Q_j \quad (j=i,e,\alpha) \tag{3}$$

$$\frac{\partial \vec{B}}{\partial t} = \vec{\nabla} \times (-\vec{V}_e \times \vec{B} + \frac{1}{en_e} \vec{R}_{th} + (n_\parallel J_\parallel) \hat{e}_\parallel + (n_\perp J_\perp) \hat{e}_\perp) \tag{4}$$

$$\vec{\nabla} P = \vec{J} \times \vec{B} \tag{5}$$

where i, e, alpha, denote ion, electron, and alpha particle terms respectively. S_i Q_j are particle and energy source terms, R_{th} is the thermal force, f is the tritium fraction, and F is the alpha particle confinement fraction.

The Eqns. are solved on a 1-D Lagrangian finite difference mesh using a 2-step process. First, Eqns. 1-4 are integrated forward in time. Next the mesh is rebalanced to satisfy Eq. 5 using flux conservation and ideal gas law.

Stability Model: Stability is monitored in two fashions. Suydam's criterion[1] is used to check for local modes (assumed to saturate) while a Rayleigh-Ritz type energy principle is used for global modes. Based on the 1-D form of Newcomb,[2] the energy principle is expressed as

$$\delta_W = \frac{\pi}{2} \int_0^a dr \left[f \left(\frac{d\xi}{dr}\right)^2 + g\xi^2 \right] \tag{6}$$

where

$$f = \frac{r(krB_z + m B_\theta)^2}{(k^2r^2 + m^2)} \; ; \; g = \frac{2k^2r^2}{(k^2r^2+m^2)} \frac{dp}{dr} + \frac{1}{r} (krB_z + mB_\theta)^2 \frac{(k^2r^2 + m^2 - 1)}{(k^2r^2 + m^2)}$$

$$+ \frac{2k^2r}{(k^2r^2 + m^2)^2} (k^2r^2B_t^2 - m^2B_\theta^2) \tag{7}$$

Then, using a transformation to finite functions,[3] $\psi = \sqrt{f}\,\xi$, and the integrability constraint on ξ reduces to a finite constraint of ψ. Using the Rayleigh-Ritz technique, ψ is expanded in terms of a finite sine series:

$$\psi = \sum_{i=0}^{n} C_i \sin (A_i r) \; ; \; A_i = \frac{(i+1)\pi}{a} \tag{8}$$

Here C_0 is normalized to 1 and C_i; i = 1, ...n are computed to minimize δ_W. Equation (6) is then numerically integrated. Stability is checked for m = 0, k = 1/R and m = 1, $\frac{-20}{R} < k < \frac{20}{R}$ where R is the major radius.

When Suydam eigenmodes are localized to relatively small regions, no direct effect on the global stability is observed, indicating that only local transport coefficients are affected. However, if their extent is wide, Suydam modes are observed in the Rayleigh-Ritz method. Then global stability is restricted by the δ_W minimizing eigenmode.

Results: A typical case using reactor parameters[4] is shown in Fig. 1. Off-axis ohmic heating causes the temperature and pressure to peak off axis. This is characteristic unless anomalous thermal conductivity is assumed such that the pressure initially peaks off axis and then diffuses to the center.

Off-axis pressure peaking prohibits Suydam instabilities in the central region of the plasma where shear is the weakest. However, Suydam modes do appear beyond the pressure peak at ~ 2.8 secs into the simulation. They then persist until termination by a global m = 0 instability at $r_\theta \cong 0.5$, in agreement with analytic predictions.[3] This instability correlates with Suydam instabilities reaching the m = 0 rational surface (the reversal point), e.g. note the sharp peak in the displacement eigenmode near the rational surface in Fig. 2. Simulations which allow anomalous transport in Suydam unstable regions to flatten the pressure profile have shown stability up $B_\theta \sim 0.7$.[5]

In summary, calculations using classical transport indicate that Suydam modes in the central plasma region are stable due to the off axis peak in the pressure profile. However, Suydam modes do appear outside the pressure peak and can terminate the discharge if they reach the reversal point.

References: [1] R. B. Suydam, Proc. of the Second UN Inter. Conf. Peaceful Uses of Atomic Energy, Geneva, Switzerland, 2 (31):157-159 (1968). [2] W. A. Newcomb, Anals of Physics, 10, 232-267 (1960). [3] D. C. Robinson, Plasma Physics, 13, 434-462 (1971). [4] R. Nebel and G. H. Miley, Third ANS Topical Meeting on Fusion, Santa Fe, NM (1978) pp. 15-18. [5] R. A. Nebel, G. H. Miley, and R. W. Moses, 1979 IEEE Inter. Conf. on Plasma Science, Montreal, Canada (1979) p. 146.

*This work supported by U.S. Department of Energy Contract EY-76-S-02-2218 and #W-7405-ENG-36.

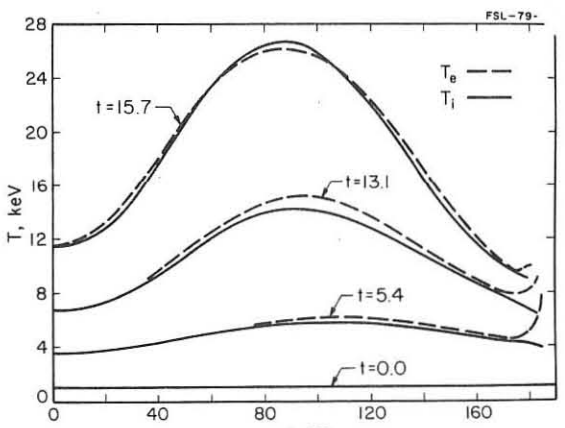

Fig. 1 Evolution of the Temperature Profile.

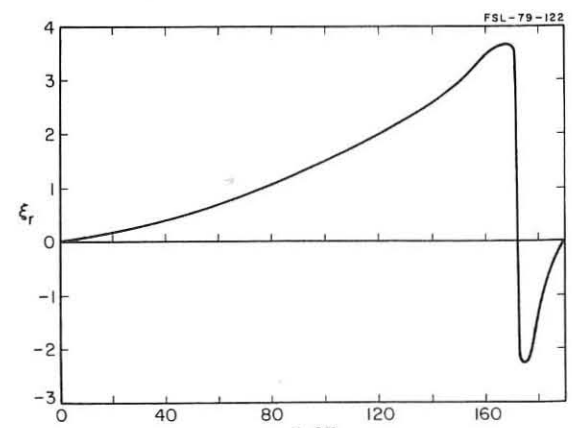

Fig. 2 Peaking of ξ_r Near Rational Surfaces.

DP11

OPTIMIZATION OF THE MATHER TYPE PF DEVICES BASED ON 2D SNOW PLOW NUMERICAL CODE AND ANALYTICAL CONSIDERATIONS

Z. Jankowicz, A. Jerzykiewicz, J. Nowikowski, B. Bartolik, A. Matusiak, M. Kabiński

Institute of Nuclear Research, Świerk, Poland

Abstract: The conclusions from 2D snow plow code and their application to the analysis of PF devices developed at INR are presented.

Several PF devices are investigated /PGN-investigations at elevated repetition rate, PF20-determination of influence of electrodes and insulation systems materials and geometry on neutron yield/ and built /PF300-investigations of energy transfer increasing possibilities, PF1000-formulation of scaling-laws, studies of Laser-Focus interaction*/ at INR Świerk. All of them were analyzed using 2D snow plow model /1/. The following conditions were taken into account: 1° The value of the current during the radial phase should be as large as possible. It is evident from scaling-laws. 2° The parameter α introduced by Imshennik /*/ should be $\alpha \geqslant 2\cdot10^{33}$. Relations resulting from 2D snow plow model analysis should be considered to fulfil the first condition

- For the axial phase: $L = 2V_Z \ln\gamma$

$$\frac{J_{max}}{J_o} = \left(1+\tau_{max}\frac{L}{\sqrt{\frac{L_o}{C_o}}}\right)^{-3/4} \qquad \tau_{max} = t_{max}/\sqrt{L_oC_o} \qquad /1/$$

where: I_{max} - the maximal value of the current in the discharge, t_{max} - the time to the I_{max} and I_o - short-circuit current. The other notation is generally adopted and units - as in the Table. This relationship is an approximation of the curve 1 in the Fig.1, if the value of τ_{max} is related to the curve 1 in the Fig.2. These both curves are results of the numerical 2D snow plow calculations. The equation /1/ is correct also when the assumption L=const. is made. Values of τ_{max} in this case should be those as on curve 1 in Fig.2. The relationship /1/ at L=const. is plotted /curve 1/ in Fig.1. From Figures 1 and 2 the good agreement is evident. The curve 2 in the Fig.1 presents ratio of the voltage V_K/τ / on condenser bank at the moment τ_{max} to V_o and the curve 2 in the Fig.2 presents the dependence $\tau_{V=o}$ on β. It is evident that the large value of β leads to the poor efficency of the energy transfer. For that reason β should be as small as possible. From analytical solution of the model, at L=const. it follows:

$$\beta \equiv L/\sqrt{\frac{L_o}{C_o}} = a\frac{\ln\gamma}{\sqrt{pR_1}}\frac{J_{max}}{J_o} = \delta\frac{J_{max}}{J_o} \qquad a = 334.9\frac{E_o}{V_oL_o} \qquad \gamma = R_2/R_1 \qquad /2/$$

- For the radial phase: The curves in Fig.3 present the dependences of the current I_{pp} at the moment of pinch formation, /the radius is assumed 1 mm/ to the value I_p - the current at the beginning of the radial phase, and the relative depth of the current singularity on the ratio of inductance rise in the radial phase ΔL_R, to the inductance of the beginning of the radial phase: L_o+L_E; $\frac{\Delta L_R}{L_o+L_E}$ should be small. ΔL_R one can estimate according to the expression $\Delta L_R \approx 2R_1 \ln 10\, R_2$ /at above mentioned radius 1 mm/. If $l_{max}=V_Z t_{max}$ would be small and $L_o+L_E^{max} < \Delta L_R$ the length of inner electrode l should be greater than l_{max}, where L_E^{max} is given by

$$L_E^{max} = d\frac{\ln\gamma\,\tau_{max}}{\sqrt{pR_1}}\frac{J_{max}}{J_o} \qquad d = 340\frac{E_o}{V_o} \qquad /3/$$

For Mather type PF devices the modyfied Imshennik's parameter is: $\alpha = b/p^3R_1^5\cdot\left(J_{max}/J_o\right)^4 = c\beta^4/pR_1\ln^4\gamma$ */

*/ will be investigated at IPP-LM Warsaw

where: $b = 3.46\cdot10^{39}E_o^2/L_o^2$; $c = 2.74\cdot10^{29}V_o^4L_o^2/E_o^2$

*/ if I_p significant differs from I_{max} then instead of I_{max}, should be I_p. Taking into account the conditions for β one can choose the range of parameters p, R_1, γ, from the condition $\alpha \geqslant 2\cdot10^{33}$. The results of above considerations concerning PF devices at INR are given in the Table:

	PGN	PF 20 nom.	PF 20 expl.	PF 300 xx	PF 1000 xx
V_o/kV/	60	50	33	50	40
E_o/kJ/	8	26	11.4	360	1150
L_o/nH/	18	75	10^x	10^x	10^x
R_1/cm/	2.5	2.5	5	15	
R_2/cm/	4	5	7.4	17.5	
l/cm/	12	20	42^x	104^x	
p/Torr/	1	2	25^x	4^x	
a	2,48	2.32	1.54	241	963
b	$6.8\ 10^{38}$	$4.2\ 10^{38}$	$8\ 10^{37}$	$4.5\ 10^{42}$	$4.6\ 10^{43}$
c	$1.8\ 10^{37}$	$1.4\ 10^{37}$		$1.3.10^{33}$	$5.3\ 10^{31}$
d	45.3	176.8	117.5	$2.45\ 10^3$	$9.8\ 10^3$
$\beta J_b/J_{max}$	0.47	0.45	0.3	3.85	5.08
$\alpha(J_b/J_{max})^4$	$7\ 10^{36}$	$5.3\ 10^{35}$	10^{35}	$9.6\ 10^{34}$	10^{36}
L_E^{max}/nH/	9.1	37.4	23	16.3^x	21^x
l_{max}/cm/	9.7	26.9	16.6	21^x	68^x
β	0.35	0.34	0.24	1.425^x	1.83^x
α	$2\ 10^{36}$	$1.7\ 10^{35}$	$4\ 10^{34}$	$1.8\ 10^{33}$	$1.75\ 10^{34}$
J_{max}/J_o	0.74	0.75	0.8	0.37^x	0.36^x
ΔL_R/nH/	18.5	19.6	19.6	43^x	155^x
$\frac{\Delta L_R}{L_o+L_E}$	0.68	0.17	0.21	1^x	1.96^x

x/ expected or calculated, xx/ cooperation with IPP LM Warsaw

The dependences $I_{max}/I_o = \delta\cdot\beta$ according to /2/ using the values given in the Table for PF20 /line 3/ and PF1000 /line 4/ are plotted in Fig.1. The points of intersection of these lines with the curve 1 give the values of I_{max}/I_o and β. The knowledge of values I_{max}/I_o or β enables to verify whether condition $\alpha \geqslant 2\cdot10^{33}$ is satisfied. From above analysis it shows that for large devices it is very difficult to fulfil simultaneously both conditions 1° and 2°. It is due mainly to the large value of $\Delta L_R/(L_o+L_E)$.

Therefore, there is necessary to find another geometry of electrodes as a Mather's type. For example, the proper guiding wall connected to outer electrode in front of the inner electrode may decrease the ΔL_R.

Literature: /1/-Z.Jankowicz - The 2D Snow Plow Calculation for the PF devices - Optimization Analysis - preprint INR-Świerk 1979

/2/-V.S.Imshennik et al.-Nuclear Fusion 13 /1973/.

Fig.1

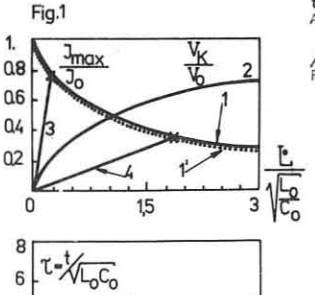

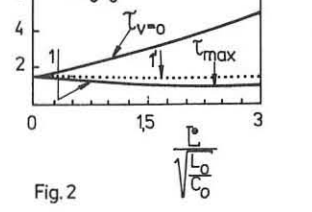

Fig.2

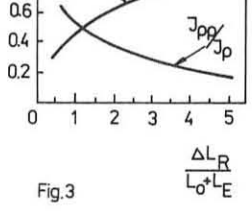

Fig.3

DP14

ENERGY DISTRIBUTION OF DEUTERONS IN THE FRASCATI 1 MJ PLASMA FOCUS FACILITY

L. Bertalot[*], *L. Bilbao*[☆], *H. Bruzzone*[⊕], *A. Gentilini*[○], *C. Gourlan*, *R.L. Gullickson*[□], *H. Kroegler*, *S. Podda*[*], *J.P. Rager*, *B.V. Robouch and K. Steinmetz*[•]

Associazione EURATOM-C.N.E.N. sulla Fusione, Centro di Frascati, C.P. 65 - 00044 Frascati, Rome, Italy

The properties of the high energy deuteron beams (hedb) produced in the Frascati 1 MJ plasma focus facility are measured as a function of the filling pressure (P_0) of each shot, for two different geometries of the electrodes (small and large diameter, see Ref.1).

Neutron energy spectra were determined by time of flight techniques (at 11 m, 34 m and 113 m simultaneously) and by nuclear plates; neutron emission anisotropy was measured by two calibrated Ag activation counters, one on axis (0°) and the other at 90°. The hedb characteristics were determined by means of the activation they induced in ^{12}C; ^{10}B and ^{14}N targets and also by detecting the high energy neutrons of the $^{7}Li(d,n)\,^{8}Be$ reaction (see Table 1), by means of the above mentioned time of flight detectors and simultaneously with a Pb activation counter.

Figures 1a and 1b show the mean neutron yield (Y_n) and the maximum hedb flux measured on axis with ^{12}C targets as functions of P_0, for both electrodes geometries at V_0 = 20 kV (250 kJ). Two neatly separated regimes can be distinguished in both situations: a *low* pressure one (lpr), where the beam intensities are maximum, with a poor Y_n and a *high* pressure regime (hpr), with maximum Y_n and beam intensities, if any, below the detection level.

Figures 2a and 2b show typical angular distributions of the hedb flux with respect to the axis the electrodes, at P_0 = 0.5 and 2.0 Torr. Strongly non-symetric angular distributions are found in just a few shots, with poor beam intensity.

The simultaneous measurement of ^{10}B and ^{14}N activation with a boron nitride target gives indication on the mean energy through the ratio of thick target yields as a function of the energy of the deuterons. The obtained values in about 20 shots range from 1 to 5 MeV. Therefore we have chosen the lower value of those mean energies (1 MeV) to unfold the number of deuterons from the activation data, in order to have an upper limit estimation of this number.

Figure 3 shows a preliminar result of the hedb energy spectrum, obtained by activation of ^{12}C foil stacks [2], unfolded according to Ref.3. Its general behaviour is similar to the ones shown in Ref.2, with the exception of the bump at high energies. Not withstanding the fact that this is the only one we have registered up to now we feel that bumps of that kind could be responsible for the reported dispersion in the mean energy of the deuteron beam.

Figures 4 and 5 show the behaviour of the anisotropy (A_c = Y (0°)/Y(90°))of the neutron flux, measured in the small and large diameter configuration, respectively, when changing the pressure from the regime of optimum beam production to the regime of optimum neutron production. The influence of the presence of an obstacle on axis (the holder for activation targets), is also shown at distances ranging from 30 to 7.5 cm from the end of the anode.

In the lpr, for both geometries the anisotropy properties can mostly be accounted for by the properties of the hedb described previously. Anisotropy is always correlated with beam intensity and hard X ray intensity. An obstacle placed on axis strongly influences the anisotropy.

In the hpr, each geometry behaves differently: (1) the small diameter gun has an anisotropy of 1.15, and the presence of an obstacle on axis diminishes substantially the neutron yield but not the anisotropy; (2) conversely, for the large diameter gun the obstacle has no effect on neutron yield but provokes a drop in anisotropy. This evidences again the particularities of the neutron production mechanism as a function of the geometry as already outlined in [1].

The measurement of the high energy neutrons from the ^{7}Li reactions were undertaken in order to check if the previous activation measurements were faulsed by partial blow-off of the targets. The results are consistent with the 1 MeV hedb flux obtained by ^{12}C activation. They also provide a measure of the time lapse of the beam, t_b = 30-50 nsec. Neutron spectra measured at 0° and 90° by nuclear plates are the same in the hpr for both geometries and different energy levels. Also, the 0° spectra peak at 2,8 MeV, irrespectively of the filling pressure, but the lpr has a higher population of faster neutrons.

An interesting property observed up to now only for the large diameter gun, is that the neutron spectrum measured side on depends very little on the pressure regime.

We want to stress the fact that, on account of the reported behaviour of neutron yield and beam production as functions of P_0, the hedb cannot be responsible of the neutron production, by means of beam-target interaction. Neutron spectra as well as anisotropy measurements give some indirect evidence of smaller energy components in the deuteron beam. Measurements reported in this paper do not alloud an evaluation of their intensity. However, to justify a 1.5×10^{11} neutron yield by beam-target interactions of 100keV deuterons with the gas blanket (30 cm at 1.5 Torr), the energy content of such a beam should be about 27% of the total energy in the system.

REFERENCES

1) Ch. Maisonnier, A. Gentilini, C. Gourlan, H. Kroegler and J.P. Rager, 7th Int.Conf. on Plasma Physics and Controlled Nuclear Fusion Research, Innsbruck (1978), U3-1.
2) R. Gullickson, W. Pickles, D. Price, H. Sahlin and T. Wainwright, Preprint UCRL-81962. (1979).
3) R. Miller, D. Straw, AFWL-TR-75-236 (April 1976).

★ CNEN Fellow; ☆ CNEN Fellow on leave from the University of Buenos Aires, Argentina; ⊕ Fellow of the CMICT (Argentina), on leave from the University of Buenos Aires; ○ Guest researcher; □ AFOSR/NP, Bolling AFB,DC; • Euratom Fellow.

TABLE I - Target Reactions for Ion Beam Diagnostics

REACTION	THRESHOLD (MeV)	HALF LIFE (min.)	PARTICLE ENERGY(MeV)
$^{12}C(d,n)^{13}N(\beta^+)^{13}C$	0.328	9.97	1.24
$^{10}B(d,n)^{11}C(\beta^+)^{11}B$	<0.200	20.40	0.98
$^{14}N(d,n)^{15}O(\beta^+)^{15}N$	0.143	2.03	1.68
$^{7}Li(d,n)\,^{8}Be$	-	-	13.3/10.8

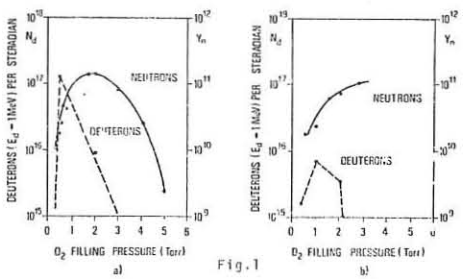

Fig.1

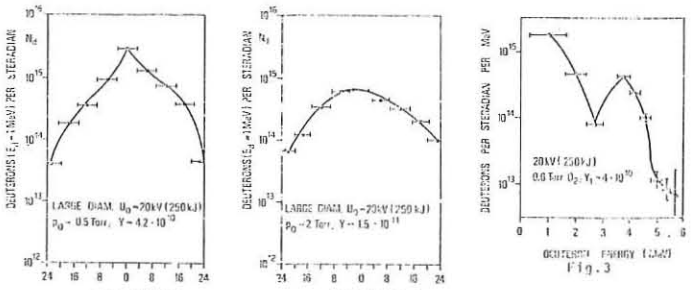

Fig.2

Fig.3

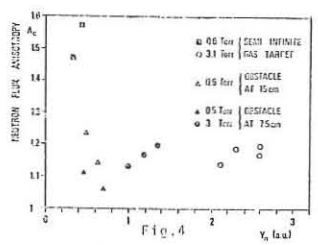

Fig.4

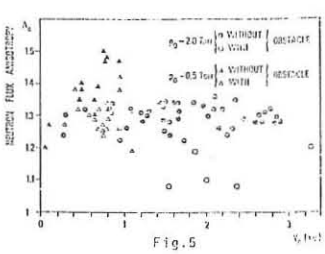

Fig.5

DP15

INVESTIGATION OF PINCHED HIGH-VELOCITY PLASMA FLUXES

A.G.Tolstolutskij, V.G.Zykov, I.M.Zolototrubov, Yu.M.Novikov

The Kharkov Physical-Technical Institute, Acad.Sci., Ukr.SSR

Kharkov, USSR

The results of plasma investigations at the output of a pulsed coaxial accelerator have been reported. In pinch operating conditions the plasma density is shown to increase up to 10^{19} cm^{-3} in 0.2mcsec at a frequency of I-5 mc/s per discharge. The average ion energy attains several kevs. Plasma oscillations are associated with an unstable state of a pinched flux.

The plasma focusing at the output of plasma accelerators has not yet been studied thoroughly enough. In papers dealing with experimental studies of physical processes in plasma fluxes /I/ the plasma parameters are shown to depend greatly on discharge conditions in the accelerator itself. The aim of the given work comprises the investigation of distinguishing features of plasma self-focusing processes at the output of a plasma accelerator (PA) at meeting optimal discharge conditions inside the accelerator.

In the experiment a standard geometry of coaxial electrodes of 7 and 3 cm in diameter, respectively, and 52 cm of length was applied. The voltage was supplied to electrodes from the 20 mcf capacitor bank in the interval U=5÷30 kv, so that discharge current J varied from 70 to 400 kA, respectively. The discharge half-period was 6mcsec and the current grew to a maximum value in 2.2mcsec under all values of U. From the side of the central electrode (cathode), at 25cm from the open edge of the coaxial system a dosed volume of the operating gas (hydrogen) V_o=0.5 ÷ 2cm^3 was injected. A gas cloud after injection spread freely in the interelectrode gap during t_d= I00-400 mcsec, then voltage was supplied to electrodes, and the breakdown took place. It is ascertained that at $t_d \leq$ I50 mcsec gas distribution inside the accelerator has steep fronts, and when a current front is moving in gas with a decreasing density, the plasma flux velocity at the PA output has great rise /I/. Besides, the plasma output from PA takes place in vacuo. Such operating conditions of PA were of particular interest in these investigations.

The plasma research at the PA output was performed by many diagnostic methods including a laser interferometer with a 230xI60 mm field of vision and the time resolution of 20 nsec. Big pinchings of a plasma flux were determined to take place at the PA output at V_o=2 cm^3, t_d=I30 mcsec, and discharge currents J > 300 kA. In this case the plasma density during 0.2 mcsec reaches the value of 10^{19} cm^{-3}, and the mean ion energy makes up several kevs /2/. The plasma density N_e at the PA output increases rapidly at U > 20 kv, as shown in fig.I. With the density growth the plasma pinch diameter d_{av} decreases so, that the number of particles per pinch length unit remains approximately the same.

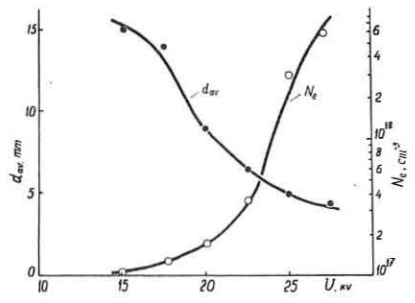

The performed current measurements at the PA output by means of magnetic probes showed that a substantial part of a discharge full current was taken outside the electrode end, and the current density grew with the U increase. It is obvious that the current taken outside at the PA output, rise at U > 20 kv not at the expense of the increase of current-carrier number, but due to the increase of current velocity of particles.

Fig.2 shows the plasma density field at the PA output at a maximum pinching moment. Solid lines determine an equal phase excess with the figures, respectively: 1 - 4π; 2 - 3π; 3 - 2π; 4 - 1π; 5 - 0.6π; 6 - 0.3π. The broken line shows the limits of measurements determined by interferometer sensitivity $(N_e \cdot L)_{min} = 10^{16}$ cm^{-2}.

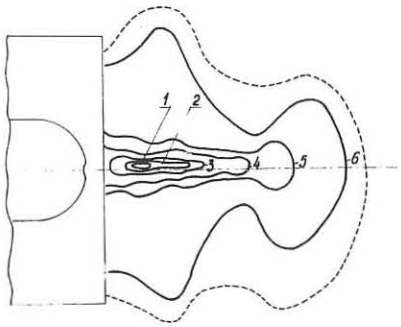

A density maximum always arises at some distance from electrodes 1 - 1.5 cm. It is possible to make a conclusion from the picture of density distribution along acceleration that a maximum density point is an obstacle for exceeding plasma flux. On the other hand, at a distance of 4 cm and more from electrodes it is observed a plasma divergence with high velocities. Substantial particle fluxes are noted in perpendicular direction relative to an acceleration axis /2/.

Spatial measurements of soft x-rays from a plasma made by means of a pinhole-camera show this radiation maximum not to coincide with a density maximum position, but to be displaced for a distance of 4 cm from PA electrodes. Availability of x-radiation determines indispensable presence of fast particles in a plasma.

Plasma compression up to densities > 10^{18} cm^{-3} does not take place regularly and lasts only 0.2 mcsec, while the plasma flux density at a level 10^{17} cm^{-3} is recorded constantly during the discharge of of 8-10 mcsec /3/. The density oscillation frequency is 1-5 mc/s. In a visible radiation range the plasma pinch oscillations are recorded by a fast photorecorder which operates in the scanning regime with time resolution of 10^{-8} sec. The plasma glow is of a discrete nature, and with removal from PA electrodes the intervals between separated plasma layers increase. Investigations by means of a spectronographic device /4/ show that the broadening of the line C IV, 4658 Å is changing with the same frequency, as the plasma density oscillations. The plasma density measured on a half-width of line C IV constitutes the value of 10^{19} cm^{-3} and higher. It is obvious that plasma flux fractionation into separate layers is associated with an unstable state of a resulting dense plasma core. During a discharge, pinchings and disruptions could repeat several times, and outwardly this shows itself in a discrete structure of the plasma flux.

The given facts attest that in our case the interaction between particles in the region of plasma flux pinching is of a collective nature.

REFERENCES

1. "Physics and Application of Plasma Accelerators". Minsk, "Nauka i Tekhnika" (USSR), 1974.
2. I.M.Zolototrubov et al., Preprint of Kharkov Phys.-Techn. Inst. 77-1, Kharkov, 1977.
3. I.M.Zolototrubov et al., Zh.Tekh.Fiz.(USSR), 44, N 8, p.1969, 1974.
4. I.M.Zolototrubov, I.P.Skoblik, A.G.Tolstolutskij. Zh.Prikl.Spektroskopii (USSR), 23, N 2, p.205, 1975.

DP16

DIRECT ENERGY CONVERSION AND CONTROL OF UNSTABLE BURN BY CYCLIC MAJOR RADIUS COMPRESSION AND DECOMPRESSION

K. Borrass, K. Lackner, E. Minardi
Association EURATOM-IPP, Garching bei München

ABSTRACT: Direct energy conversion and control of unstable burn in ignited tokamaks by cyclic major radius compression and decompression is analyzed on the basis of a general solution of the global energy and particle balance equations. With respect to direct energy conversion, cycles with arbitrary compression ratios are considered. The usual adiabatic laws are found to hold under relaxed conditions near ignition, so that compression is a promising scheme for heating devices in this regime. The cycle-averaged, converted power is given explicitly. With respect to control the energy and power required during compression are related to the compression speed and accuracy in measuring deviations from equilibrium. A lower limit for the speed of compression is derived. Unlike other non-wattless schemes, this method would have no unfavourable effect on the overall energy balance of a reactor.

BASIC EQUATIONS. We consider the equation of energy conservation including α-heating, transport and the external work p dV. The density of α-particles is neglected and the α-energy deposition is assumed to be instantaneous. Defining $n=n_i=n_e$ and assuming $T_e=T_i=T$ the global energy balance takes the form

$$\frac{d}{dt}\bar{p} = \alpha\,\bar{p}^2 - \bar{p}\left(\frac{1}{2\tau(t)} + \frac{5}{3}\,\frac{1}{V}\,\frac{d}{dt}V\right) \qquad (1)$$

where $\bar{p}=\overline{nT}$ and the bar denotes a volume average except for temperatures where $\bar{T}=\overline{nT}/\bar{n}$. The bar will be omitted from now on for convenience. The α-production has been taken to be proportional to p^2, which is a good approximation between 7 and 20 keV. α is a coefficient which includes the effect of space averaging on the α-heating and which also takes into account the possible imperfect confinement of non thermalized α-particles. $\frac{1}{\tau}=\frac{1}{\tau_e}+\frac{1}{\tau_i}$. For the total particle number it is assumed that N=const. This constraint can be realized by, for instance, a rail limiter of appropriate shape and complete recycling. Alcator scaling is considered throughout, yielding with $N=\text{const}\ \tau(V)/\tau(V_0) = (V_0/V)^{1/2}$. Equation (1) is a Riccati equation which can be integrated exactly, giving

$$p(t) = p_0\left(\frac{V_0}{V(t)}\right)^{5/3}\frac{\exp -\int_{t_0}^{t} dt/2\tau(t)}{1-\alpha\,p_0\int_{t_0}^{t} dt'\,(V_0/V)^{5/3}\exp -\int_{t_0}^{t'} dt''/2\tau} \qquad (2)$$

COMPRESSION-DECOMPRESSION CYCLE AND PLASMA-OUTER CIRCUIT COUPLING. We consider the cycle outlined on the p-V-plane in Fig. 1. The points of ignition lie on the dashed line. At the points A and D the plasma is igniting, while in B and C it is subigniting. Using the equilibrium equation for the plasma column in a tokamak one can relate the area of the cycle to the electric energy delivered to the ohmic and vertical field coils:

$$W = \sum_i \oint U_i\,I_i\,dt = -2\oint p\,dV, \qquad (3)$$

where U_i and I_i are the voltages and currents acting in the outer circuits. Ohmic losses are neglected in eq.(3). A positive area of the cycle then implies a net energy gain with the power

$$P_{av} = \frac{2\oint p\,dV}{\oint dt} \qquad (4)$$

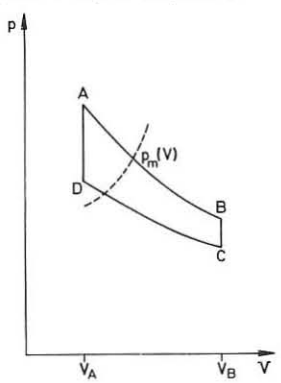

Figure 1

Cycles of this kind have already been considered earlier in pinches /1/ /2/.

DIRECT ENERGY CONVERSION. In order to study in detail the properties of the cycle we derive from eq. (2) an algebraic expression for the pressure in terms of an arbitrary change of volume ΔV in a time τ_c. We assume the approximation $\sigma \equiv \tau_c/2\tau < 1$ and moreover approximate $\tau(t)$ and $V(t)$ in the range $t_0 \le t \le t_0+\tau_c$ with an intermediate constant value $\bar{\tau}$ and $\bar{V}$. One thus obtains from eq. (2)

$$p(t_0+\tau_c) = p_0\left(\frac{V_0}{\bar{V}}\right)^{5/3}\frac{1}{1+\sigma\,[1-(1-\Delta V/\bar{V})^{5/3}]} + O(\sigma^2) + O(\sigma\cdot\eta) \qquad (5)$$

Here $\eta = (p_0-p_m)/p_m$ measures the deviation of p_0 from the ignition point p_m. Then, if

$$\frac{\tau_c}{2\bar{\tau}}\,[1-(1-\frac{\Delta V}{\bar{V}})^{5/3}] \ll 1, \quad \frac{\tau_c}{2\bar{\tau}}\,\frac{p_0-p_m}{p_m} \ll 1 \qquad (6)$$

the plasma obeys the adiabatic law. Conditions (6) for adiabaticity are much weaker than the usual one $\tau_c/\bar{\tau} \ll 1$. The physical reason is that in the plasma near ignition the non-adiabatic effects of the transport and the α-heating cancel each other in first order. Under our assumptions the following relations are derived for the temperatures of the cycle

$$\frac{T_A-T_m}{T_m} < \left(\frac{V_B}{V_A}\right)^{\frac{13}{6}} - 1, \quad \frac{T_B-T_c}{T_B} < \frac{T_A-T_m}{T_A}, \qquad (7)$$

where T_m is the ignition temperature. Moreover,

$$\frac{T_A-T_D}{T_A} = \frac{T_B-T_c}{T_B} \qquad (8)$$

Finally, the area enclosed by the cycle is given by

$$\oint p\,dV = \frac{3}{2}T_A\,n_A\,\frac{T_A-T_B}{T_A}\,\frac{T_B-T_c}{T_B} \qquad (9)$$

ENERGY AND POWER REQUIREMENTS FOR BURN CONTROL. A system being cycled as in Fig. 1 can be considered as burning controlled at the lower unstable burn point. To minimize the power requirements for control the deviations from equilibrium should be as low as possible. A lower limit is set by the accuracy with which deviations can be measured. We shall assume that the ratio $(\alpha\,p^2-p/2\tau)/\alpha\,p^2$ can be measured with accuracy ε. We now characterize the points A, B, C, D of the cycle by the following conditions:

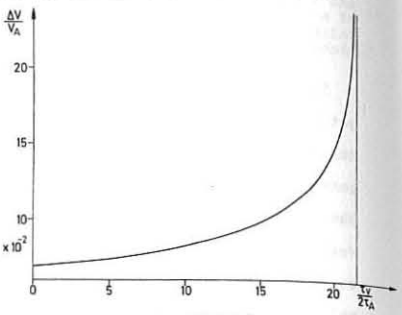

Figure 2

A) $m\varepsilon\,\alpha\,p_A^2 = \alpha\,p_A^2 - p_A/2\tau_A$, (9) C) $-m'\varepsilon\,\alpha\,p_C^2 = \alpha p_C^2 - p_C/2\tau_C$, (11)

B) $-\varepsilon\,\alpha p_B^2 = \alpha\,p_B^2 - p_B/2\tau_B$, (10) D) $\varepsilon\,\alpha\,p_D^2 = \alpha p_D^2 - p_D/2\tau_D$,

where $m > 1$ is arbitrary and m' has to be chosen such that the cycle is closed. The optimum value of m will strongly depend on the specific design of the power supply (switches, sources etc.). Our conclusions do not qualitatively depend on the choice of m.

We shall assume $\frac{d}{dt}V = \text{const}$ (13) during compression and decompression. This choice, corresponding to switching of and on constant voltages in the outer circuits, is not unreasonable from a technical point of view. Introducing $\tau_V = V_A/\dot{V}$ and $\Delta V = V_B - V_A$, we have $V_B = V_A\,(1+\Delta V/V_A) = V_A\,(1+\tau_c/\tau_V)$.

Studying the control problem the ordering

$$\varepsilon;\ \frac{\Delta V}{V_A} = \frac{\tau_c}{\tau_V} \ll 1 \qquad (14)$$

is adequate. Applying eq. (13) and (14) to eq. (2) gives to first order in ε and τ_c/τ_V

$$p_B = p_A\,(1+m\varepsilon\,\tau_c/2\tau_A\,g(\tau_c/2\tau_A) - \frac{5}{3}\frac{\tau_c}{\tau_V} + \frac{13}{6}\,(1-g\,(\tau_c/2\tau_A))\frac{\tau_c}{\tau_V}), \qquad (15)$$

(where $g(x) = (e^x-1)/x \ge 1$. From eqs. (9), (10), (15) one gets in the same approximation

$$(m+1)\varepsilon\,\frac{V_A}{\Delta V} + m\varepsilon\ \tau_V/2\tau_A\,g\,(\frac{\tau_V}{2\tau_A}\frac{\Delta V}{V_A}) = \frac{13}{6}\,g\,(\frac{\tau_V}{2\tau_A}\frac{\Delta V}{V_A}). \qquad (16)$$

Equation (16) holds for arbitrary values of $\frac{\tau_c}{2\tau_A} = \frac{\tau_V}{2\tau_A}\frac{\Delta V}{V_A}$. All terms being positive in eq. (16), it follows that

$$\tau_V/2\tau_A \ge \frac{13}{6\,m\,\varepsilon} \qquad (17)$$

must hold, giving a lower limit for the speed of decompression in segment A-B. In the limit $\tau_V/2\tau_A \to 0$ (fast compression and decompression) eq. (16) gives

$$\frac{\Delta V}{V_A} \to \frac{\Delta V}{V_A}\Big|_{min} = \frac{6}{13}\,(m+1)\,\varepsilon. \qquad (18)$$

Figure 2 gives $\Delta V/V_A$ as a function of $\tau_V/2\tau_A$ according to eq. (16) for m=2 and ε=0.05. $\Delta V/V_A$ increases only slightly over its minimum value except in the very vicinity of the limit set by eq. (17). This behaviour is, of course, independent of the specific choice of m and ε.

For the power that has to be applied in segment A-B one gets with eq.(3)

$$|P_c| \ge \frac{4}{13}\,m\,\varepsilon\,P_A^{\alpha}, \qquad (19)$$

where $P^{\alpha} = 3\,V\,\alpha\,p^2$ is the total α-power. The energy that is transferred in this phase is given by

$$|E_c| = p_A\ \Delta V \ge (m+1)\,\varepsilon\,\frac{4}{13}\,E_p. \qquad (20)$$

where $E_p = 3\,p_A\,V_A$. Deviations from equality are small in eq. (20) except near the limit set by eq. (17).

It is easy to verify that the same conclusions result from considering the compression phase C-D. In addition, we note that, as is already indicated by eq. (9), P_{av} is of the order ε^2, so that unlike from other control schemes, P_{av} would only be a negligible fraction of the recycling power in a reactor /3/.

The results given here agree well with numerical solutions of the general particle and energy balance equations /3/.

REFERENCES

/1/ R.J. Bickerton and J.D. Jukes, J.Nucl. Energy, 8 206 (1959).
/2/ G.H. Miley, Fusion Energy Conversion (American Nuclear Society, 1975).
/3/ K. Borrass, R. Buende, Max-Planck-Institut für Plasmaphysik Report IPP 4/178 (1979)

THE INFLUENCE OF PLASMA EDGE EFFECTS AND OF IMPURITIES ON THE THERMAL STABILITY OF A TOKAMAK REACTOR

B. K. Bein
Uni-Center P.O. Box 250149
D-4630 Bochum, Federal Republic of Germany

Introduction: In future Tokamak reactors and in the near future ignition experiments, the stability of the burning D-T plasma against temperature/density perturbations is one of the fundamental problems. It is also obvious that a fusion plasma, surrounded by material walls of a technical device, contains light and heavy impurities (due to desorption and sputtering) and, even in a well prepared ignition experiment, the plasma is contaminated by discharge induced arcs. On the other hand, the simple existence of final dimensions of any fusion device imposes edge effects, such as reduced α-particle heating efficiency, special diffusion coefficients, edge temperatures, density of neutrals at the edge, etc. Consequently, the stability problem of the burning plasma should be treated taking into account edge effects and impurities.

Plasma model: With the assumption $\tau_E<\tau<\tau_p$ (τ_E, τ_p energy and particle confinement time, τ time of stable or quasi-stable burning of the plasma), the temperature/density perturbations decouple: The faster thermal instabilities can be studied separately[1], the density profile is a free parameter, and particle loss and fuel injection are excluded from treatment. The core temperature may be limited by 5 keV$<T_c<$20 keV. Consequently, ohmic heating, injection heating, and synchrotron radiation loss are less important. The α-particle heating, impurity radiation loss (based on the average ion model[2] for iron and on n_I/n_e=const), and plasma bremsstrahlung are dominant terms in the space-time dependent energy balance of the isothermal plasma,

$$\partial(3nT)/\partial t=\nabla(K\nabla T) + E_\alpha(r)\, P_\alpha(n,T) - P_I(Z_{eff},n,T) - c_b n^2 T^{1/2}$$

The α-particle heating efficiency, $E_\alpha(r)$, is a free parameter in the above equation and takes account of α-particle loss during slowing down[3]. The heat conduction coefficient is given in functional form, $K_\perp=K_{\perp o} n^\beta T^\gamma B^\delta$, where the constant $K_{\perp o}$ remains undefined throughout this work.

Stability analysis: A linear stability analysis with

$$T(r,t)=\bar{T}(r) + R(r)\exp i(\omega t + k\theta + m\phi) ,$$

with the boundary conditions $R(0)=R_c$, $dR(0)/dr=0$, $R(a)=0$, $T(0)=T_c$, $dT(0)/dr=0$, $T(a)=T_a$, $T_a/T_c\ll 1$, and with some obvious further simplifications ($m=k=0$, $a/R_o\ll 1$) transforms the above space-time dependent energy balance into two two boundary value problems (the first, non-linear, for the temperature profile, $\bar{T}(r)$, the second, linear, for the perturbation profile, R(r)) with two eigenvalues

$$\Pi_a=K_{\perp o} n_c^{\beta-2}\, T_c^{\gamma+1/2}\, a^{\delta}/c_b\, a^2 \quad \text{and} \quad \Lambda = 3\, T_c^{1/2}\lambda/Z_{eff} c_b n_c .$$

(If the constant $K_{\perp o}$ is defined, the eigenvalue Π_a can serve for the scaling of the minor radius a: this is not intended in this work.) The second eigenvalue, Λ, serves to determine the burning performance: $\Lambda > 0$: stable burning,

$\Lambda < 0$, $|\lambda|\tau \lesssim 1$: quasi-stable burning

with an upper limitation for the product of axial ion density and burning time, $n_c\tau$, by the relation

$$n_c\tau \lesssim 3\, T_c^{1/2}/Z_{eff}|\Lambda|\, c_b$$

(It should be mentioned that the constant $K_{\perp o}$ has no influence on the stability/instability problem.)

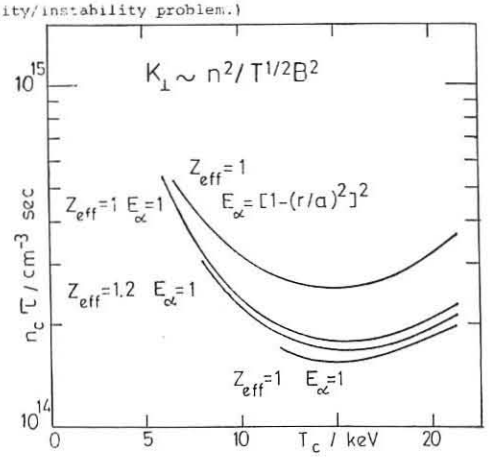

Fig. 1 Reduced α-heating efficiency
Effect of impurities

Main results: 1) There are two regions for steady reactor operation: The first, above 6 keV, quasi-stable with $n_c\tau\lesssim 5\cdot10^{14}$ s/cm^3, very low Z_{eff}, and with a heat conduction coefficient of classical type, $K_\perp\sim n^2/T^{1/2}B^2$ (Fig.1); the second region below 20 keV, stable, without limitation of $n_c\tau$, and with a Bohm-like heat conduction coefficient, $K_\perp\sim n\,T/B$ (fig.2).

2) In the case of classical-type heat conduction, impurities do not affect the limitation for $n_c\tau$ very much (Fig.1); but in the case of Bohm-like heat conduction, the region of stable burning is shifted to higher core temperatures with increasing Z_{eff} (Fig.2).

3) The reduced α-heating efficiency, $E_\alpha<1$, raises the upper limit for the product $n_c\tau$ (Fig.1 and Fig.2).

4) Under the combined effect of reduced α-heating efficiency and of a higher impurity concentration, $Z_{eff}=2$, there is only one region of quasi-stable burning near 20 keV, for both types of heat conduction coefficients (Fig.3 and Fig.4).

5) The results of Fig.1,2,3 a.4 were calculated with a density profile $n=n_c(T/T_c)^\eta$, η=1. They are not very different with a variation of η in the interval $1/2 \lesssim \eta \lesssim 2$.

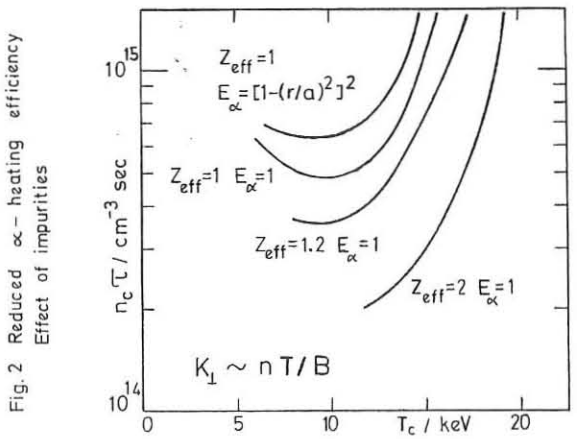

Fig. 2 Reduced α-heating efficiency
Effect of impurities

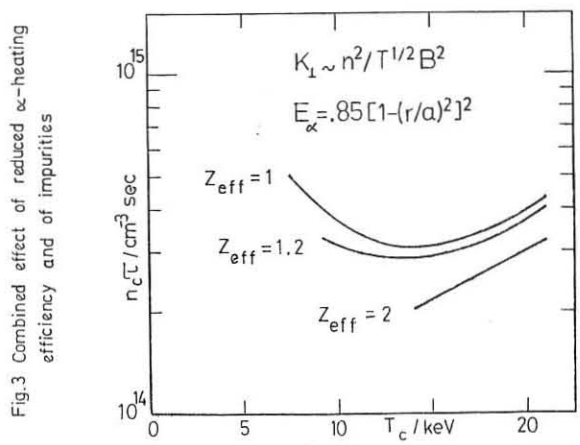

Fig.3 Combined effect of reduced α-heating efficiency and of impurities

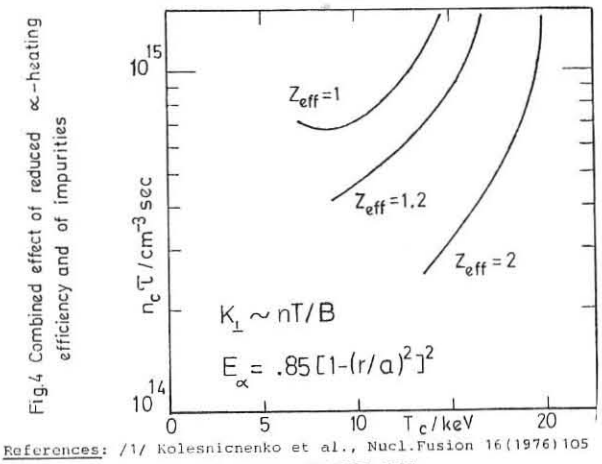

Fig.4 Combined effect of reduced α-heating efficiency and of impurities

References: /1/ Kolesnichenko et al., Nucl.Fusion 16(1976)105
/2/ Jensen et al., Nucl.Fusion 17(1977)1187
/3/ Ohnishi et al., Nucl.Fusion 18(1978)859

DP18

KINETIC THEORY OF NEUTRALS IN A BOUNDED PLASMA SLAB WITH INHOMOGENOUS ION TEMPERATURE AND DENSITY

M. Tendler, Institute of Technology, Uppsala University, Sweden

Abstract: The analytical solution of the kinetic equation for the neutrals in a plasma is proposed taking into account, besides previously considered charge-exchange, impact ionisation and gas feed, inhomogenous temperature profile and photorecombination. Steady-state neutral profiles and neutral particle fluxes are obtained showing the effect of non-uniform temperature.

The appearance of neutrals in the fusion reactor is a desirable fact provided that cold gas mantel system [1] being established near the wall. The full problem contains the simultaneous solution of the coupled kinetic equations for the ion and neutral distribution functions. Here, we assume ion parameters to be given and treat the kinetic equation for neutral distribution function. For a plasma with optical thickness, exceeding impermeability criteria [1], a slab model is sufficient. The equation for neutral distribution function reads:

$$v\frac{\partial F_n}{\partial X} = F_i(v)\int|V-V'|\sigma_c(|V-V'|)F_n(V')dV' - F_n(v)\int|V-V'|\sigma_c(|V-V'|)F_i(V')dV' - F_n(v)\int|V-V'|(\sigma_i^e|V-V'|F_e(V') + \sigma_i^i|V-V'|F_i(V')|dV' + F_i(v)\int|V-V'|F_e(V')\sigma_{rec}^{ph}(V')dV' \quad (1)$$

Here, F_n, F_i, F_e- distribution functions of neutrals, ions and electrons, respectively, σ_c, σ_i^e, σ_i^i, σ_{rec}^{ph} - cross-sections for resonance charge-exchange, ionization by electron and ion impact and photo-recombination.

By doing two conventional assumptions that σv_c-const, $v_e \gg v_n$ and $N_e=N_i$ equation (1) can be simplified as:

$$v\frac{\partial F_n}{\partial X} = -(\sigma_c v+\langle v\sigma_i\rangle)N_i F_n + \langle v\sigma_c\rangle N_n F_i + N_i\langle v\sigma_{rec}^{(ph)}\rangle F_i \quad (2)$$

Here, N_n and N_i - neutral and ion density.

Further, we assume the local ion distribution function

$$F_i = \frac{N_i(X)}{v_i(X)}\varphi_i\left(\frac{v}{v_i(X)}\right)$$

Introducing the new variables $\xi = \int_0^X \frac{dX'N_i(X')}{v_i(X')(\sigma_c v+\langle v\sigma_i\rangle)}$

$w = \frac{v}{v_i(X)}$ and $f_n = v_i(X)F_n(v,X)$ equation (2) takes the form

$$w\frac{\partial f_n}{\partial\xi} + f_n - \frac{1}{L}w\frac{\partial(f_n w)}{\partial w} = \beta N_n\varphi_i + \gamma N_i\varphi_i \quad (3)$$

Here $\beta = \frac{\langle v\sigma_c\rangle}{\sigma_c v+\langle v\sigma_i\rangle}$; $\gamma = \frac{\langle v\sigma_{rec}^{(ph)}\rangle}{\sigma_c v+\langle\sigma_i v\rangle}$; $\frac{1}{L} = \frac{dv_i}{v_i(\xi)d\xi}$ -

- the temperature gradient scale

$$N_n = \int_{-\infty}^{+\infty} f_n dw \quad (4)$$

We assume, that the plasma is located in a layer ($0\le\xi\le a$) and that the density and velocity of neutrals issued from the wall is N_0 and V_0, respectively. We start from a formal solution of the equation (3) considering the source function (r.h.s. of equation (3)) being given. Introducing the new variables $\psi = wf_n \exp\frac{L}{w}$, $t = L\ln w$ we get

$$\frac{\partial\psi}{\partial\xi} - \frac{\partial\psi}{\partial t} = \beta N(\xi)\varphi_i(t)\exp\frac{L}{w(t)} + \gamma N_i(\xi)\varphi_i(t)\exp\frac{L}{w(t)} \quad (5)$$

The quasilinear equation (5) can be reduced to the first order differential equation along their characteristics defined as $\bar{X}=-\xi-t$, $\bar{\xi}=\xi$ and $\zeta(\bar{X},\bar{\xi})=\psi(\xi,t)$ The formal solution of equation (5) with taken into account boundary conditions can be written as:

$$\psi^+(\xi,t) = \zeta^+(\bar{X},\bar{\xi}) = \zeta_0(\bar{X}) + \int_0^{\bar{\xi}}\varphi_i(-\bar{\xi}'-\bar{X})\exp\frac{L}{w(-\bar{\xi}'-\bar{X}')}\left[\beta N(\bar{\xi}')+\gamma N_i(\bar{\xi}')\right]d\bar{\xi}' \quad \text{for } w>0 \quad (6a)$$

$$\psi^-(\xi,t) = \zeta(\bar{X},\bar{\xi}) = \zeta_0(a-\bar{X}) - \int_{\bar{\xi}}^{a}\varphi_i(-\bar{\xi}'-\bar{X})\exp\frac{L}{w(-\bar{\xi}'-\bar{X}')}\left[\beta N(\bar{\xi}')+\gamma N_i(\bar{\xi}')\right]d\bar{\xi}' \quad \text{for } w<0 \quad (6b)$$

where $\zeta_0(\bar{X})$ was defined above.

Further, using the relation (4) and the simplifying assumption $\varphi_i = \frac{1}{2}[\delta(w-1)+\delta(w+1)]$ we will get the integral equation for the neutral density and solve it, then return back to 6(a-b) and determine the distribution function of that because neutral density appears in (6) within the integral, the neutral distribution is only slightly sensitive to the fine details of the neutral density profile. Integrating equation (6) with respect to velocity, an integral equation for the neutral density is easily obtained:

$$N(\xi) = N^0(\xi) + \frac{1}{2}\int_0^a K(\xi-\xi')[\beta N(\xi')+\gamma N_i(\xi')]d\xi' \quad (7)$$

where

$$K(\xi-\xi') = \exp\left[-\frac{\xi'-\xi}{L} - L\,\mathrm{sign}(\xi-\xi')\exp\frac{\xi-\xi'}{L} + L\,\mathrm{sign}(\xi-\xi')\right] \quad (8)$$

$$N_c(\xi) = N_0 e^{-\frac{a}{2w_0}}\,\mathrm{ch}\,\frac{\xi-\frac{a}{2}}{w_0} \quad (9)$$

Here $N_0(\xi)$ means the neutral density with multiple charge-exchange, recombination and temperature gradient neglected. After differentiating twice equation (7) and taking into account that $\frac{1}{L} < 1$, we get a second-order ordinary differential equation with the constant coefficients:

$$\frac{d^2N}{d\xi^2} - \frac{1}{L}\frac{dN}{d\xi} - (1-\beta)N - \frac{2}{L^2}N = \frac{d^2N_0}{d\xi^2} - N_0(\xi) - \gamma N_i(\xi) \quad (10)$$

The full solution of the equation (10) consists of the general solution of the homogenous equation (r.h.s. of (10) equal to zero) and arbitrary solution of the inhomogenous equation. The both parts of the solution are coupled through boundary conditions, which can be obtained from the integral equation (7). So, we get

$$N(\xi) = \varphi_2\int\frac{\varphi_1 h}{w}d\xi' - \varphi_1\int\frac{\varphi_2 h}{w}d\xi' + C_1\varphi_1 + C_2\varphi_2 \quad (11)$$

where $\varphi_{1,2} = e^{-\chi_{1,2}\xi}$, $\chi_{1,2} = -\frac{1}{2L} \pm \sqrt{\frac{9}{4L^2}+(1-\beta)}$ (12)

$$h = \left(\frac{1}{w_0^2}-1\right)N_0 - \gamma N_i \quad (13)$$

$$W = \varphi_1\varphi_2' - \varphi_2\varphi_1' \quad (14)$$

Note that in case of the homogenous temperature profile $\left(\frac{1}{L}\to\infty\right)$, our results coincides with the well-known Lehnert estimate for the thickness of the cold-gas mantle systems $\delta = \sqrt{2}\lambda_i$ [1]. The conclusion, which can be drawn from formula (12), is that the temperature gradient hinders the neutrals on their way toward the plasma core and their penetration length can be significantly decreased due to the high temperature gradient. The solution (10) can be written as follows:

$$N(\xi) = N^0(\xi) \times \frac{\left(\frac{1}{w_0^2}-1\right)}{\left(\frac{1}{w_0^2}+\beta-1\right)} + N_i(\xi)\frac{\gamma}{\left(\frac{1}{w_0^2}+\beta-1\right)} + C_1 e^{-\chi_1\xi} + C_1 e^{-\frac{\chi_1-\chi_2}{2}a^* - \chi_2\xi} \quad (15)$$

where $C_1 = w_0 + O(a)$, $O(a)\to 0$ for $a\to\infty$

The first term in fomula (15) represents the density of the primary atoms, injected from the wall, the second term describes the density arising due to photo-recombination, the last two terms result from the multiple recharging. Since under experimental conditions $\frac{1}{w_0} \gg 1$ the first term is attenuated very fast, then the main contribution is coming from the multiple recharging, finally in the inner parts of the discharge the recombination effects became important. The amplitude of the recharged density scales in accordance with (15) as w_c. (In the initial coordinates it means as the ratio of the velocity of the injected atoms to the ion mean velocity.) The spectra of neutrals ejected by the plasma can be calculated from formulae (6) and (8) as:

$$j(V) = \int_0^a d\xi wf(w,\xi) = \int_0^a d\xi\psi(\xi,t)\exp+\frac{L}{w}$$

The non-trivial part of the flux, which is responsible for the flux due to the temperature gradient is given by:

$$j = \frac{C_1 F_2(w)}{\chi_2}, \text{ where } F_2(w) = \frac{L\exp\frac{L}{w}}{w^{\chi_2 L}}\int_0^w\frac{w\,\varphi_i(w')\exp-\frac{L}{w'}}{w'^{1-\chi_2 L}}dw$$

The explicit calculations will be published elsewhere [5].

Acknowledgements: We thank Prof E.T. Karlson, Uppsala University, Prof. F. Engelmann, FOAM Institute for Plasma Physics and Prof. U. Daybelge, Ruhr-University, for valuable discussions.
Part of this work was done during the author's stay at Ruhr-University.

References:

[1] B. Lehnert, Phys Ser. 12.327. (1975)
[2] Perel V.I. Konstantinod O.V. Sod. Phys. - Tech. Phys 5. 1403 (1961)
[3] Yu. N. Dnestrovskij, S.E. Lysenko, A.I. Kislyakov, Nucl.Fus. 19.293 (1979)
[4] K. Burrell, Phys Fl. 21.2202. 1978
[5] M. Tendler to be published in Physics of Fluids

DP19

FUSION REACTORS THROUGH EFFICIENT ENERGY CONVERSION

A. Hertzberg
Aerospace and Energetics Research Program, University of Washington
Seattle, WA 98195 U.S.A.

J. Dawson
Department of Physics, University of California
Los Angeles, CA 90024, U.S.A.

P. Rose
Mathematical Sciences Northwest
Seattle, WA 98195, U.S.A.

Recent experimental results have demonstrated that Q's > 2 will soon be available. Therefore, a high efficiency thermal system which can effectively exploit the high temperature potential of fusion reactors may expedite the establishment of economically viable fusion power. These high efficiency thermal energy conversion systems require the development of high temperature (1500°K to 2500°K) components for neutron absorption and power extraction.

Efficient energy recovery also provides other important benefits. At values of Q > 10, the sensitivity to energy conversion efficiency does not appear important to the circulating power fraction of a fusion power plant. However, collateral gains of equal value are achieved, such as large reductions in neutron wall loading for a given output power, and reductions in waste heat and in the production of radioactive products in the machine walls. In addition, relaxed engineering design constraints are possible, leading to options in terms of the types of machines which may prove economical energy producers. Thus, the advantages of high thermal efficiency are not restricted to early, low Q concepts.

It is also possible that through the use of efficient energy recovery methods, fusion reactions other than that of DT can be made practical. These could eliminate the necessity for breeding tritium. If low neutron producing fuels can be harnessed, a great reduction in radiological problems might be achieved.[1]

Modest extrapolations of recent experimental results indicate that the next generation of fusion devices, such as TFTR, JET, JT60, T20 and Doublet III, should produce fusion plasmas capable of Q's greater than one. The Princeton Large Torus (PLT) recently demonstrated ion temperatures greater than 6.5 kilovolts. At the Massachusetts Institute of Technology, the Alcator has achieved a confinement time, $n\tau$, of 3×10^{13} at temperatures of about 1 kilovolt.[2]

Important results have also been attained in the magnetic mirror program, where temperatures of over 20 kilovolts and beta values close to 1 have been achieved.[3] If new mirror concepts such as the tandem mirror[4] and the reversed field mirror[5] succeed, losses will be significantly reduced, paving the way for the development of mirror fusion machines with Q's greater than 1.

As indicated in the preceding paragraphs, the physics of near-term fusion devices with Q's in the range of 1 to 5 is now nearly established. These devices, which are beam driven[6,7,8] and do not necessarily reach ignition, have engineering demands which are consistent with current practice. However, economic viability requires more than just a successful low Q fusion device; a high efficiency thermodynamic power cycle is also needed.

The importance of high thermal conversion efficiencies is illustrated in Figure 1, in which a neutral beam driven fusion power plant is used as an example. A conventional steam plant has a thermal conversion efficiency of about 40%. If such an energy conversion system is coupled to a fusion device with Q = 2, the resulting system will not produce adequate circulating power to sustain the fusion reaction, and essentially no power will be available for distribution. However, if this same fusion device is coupled to an engine with a thermal efficiency of between 50% and 70%, then the amount of circulating power will be reduced to manageable levels and power will be available for commercial use. Thus, only if high efficiency thermal cycles are employed can low Q fusion power plants be utilized to deliver commercially competitive electrical power.

In order to construct the components of a thermal cycle with energy conversion efficiencies in the 50-70% range, the components of the energy conversion system must be able to sustain continuous exposure to high temperatures. In the past, materials limitations have restricted the peak operating temperature of conventional systems to less than 1000°K. The thermal engine therefore requires both a direct high temperature heater for the working fluid and a high temperature energy conversion device to produce an efficient cycle.

The next section will review the engineering requirements of these key components. In all fusion reactors, the neutrons pass through a first wall which is nearly transparent to the high energy neutrons. Normally, the neutrons are absorbed in a lithium bearing blanket which transfers energy through a heat exchanger at modest temperatures to a conventional heat engine. For a high efficiency system, the secondary heat exchanger must be eliminated. The neutrons therefore are absorbed in a high temperature refractory blanket through which the working fluid of the heat engine is directly circulated. Several promising approaches to such boiler schemes are currently under study at Mathematical Sciences Northwest, Inc. (MSNW) and it appears that working fluids with temperatures of 2500°K can be obtained while still retaining the capability of tritium breeding. The key element of such a system is the elimination of the secondary heat exchanger and therefore great care will have to be taken to prevent the contamination of the working fluid with radioactive products from the blanket.[9]

The high temperature capability of such a radiation boiler can only be used by advanced energy conversion systems which are still under development. At the present time, significant work is in progress leading to the development of turbo-expander technology with inlet temperatures approaching 2000°K.[10] Other approaches also being developed are even more suitable at the high temperatures required. In particular, a device called the "energy exchanger," which has an operating temperature potential of up to 2500°K, is under development at MSNW.[11] Finally, the high temperatures of the working fluid may allow the effective employment of magnetohydrodynamic energy conversion. The development of these devices is now being spurred by the need for higher energy conversion efficiencies created by the ever-increasing energy shortage. Unfortunately, due to space limitations it is not possible to discuss in detail the various advantages of each of these design approaches and the techniques of exploiting these expanders using either combined cycles (Brayton-Rankine) or binary cycles (Rankine).[10,12]

In combining low Q fusion devices with high efficiency cycles, one unknown must not be traded for another. We have concentrated on fusion devices with physics that is relatively well known. While several approaches to increasing thermal efficiency are currently under development, they all involve varying degrees of engineering complexity and risk, balanced by the potential for cycle improvement. Indeed, if any improvement can be made in the efficiency of thermal conversion systems for fusion, it reflects favorably on all approaches to fusion.

While none of the components place unreasonable demands on existing engineering practice, the proposed approach involves a significant development program. However, no technology is introduced in which the physics and engineering are not understood and the key lies in the economical combination of these various components into a power reactor. Thus, the capability of fully exploiting the high temperature potential of fusion neutrons in high efficiency thermal conversion systems will serve to accelerate the introduction of fusion power.

References

1. Mathematical Sciences Northwest, Inc., High Thermal Efficiency, Radiation Based Advanced Fusion Reactors, EPRI Report, EPRI ER-544, April 1977.
2. M. Murakami and H.P. Eubank, Physics Today 32, 25 (1979).
3. T.K. Fowler, Bull. APS 22, 1183 (1977).
4. G.I. Dimov, V.V. Zakaidakov and M.E. Kismevskii, Fitika Plasma 2, 597 (1976); T.K. Fowler and B.G. Logan, Comments on Plasma Physics and Controlled Fusion Research, Vol. II, No. 6, 167 (1977).
5. W.C. Turner, Bull. APS 22, 1183 (1977).
6. J.M. Dawson, H.P. Furth and F.H. Tenney, Phys. Rev. Lett. 26, 1156 (1971).
7. D.L. Jassby, Nucl. Fusion 12, 328 (1977).
8. J.M. Dawson and A.T. Lin, UCLA PPG #218, "Some New Ideas on Wet Wood Burners;" Proceedings of the Review Meeting on Advanced Fuel Fusion, EPRI Report, EPRI ER-536-5R. (377) Sept. 1977.
9. A. Hertzberg, J. Dawson and P. Rose, Near-Term Fusion Reactors Through Efficient Energy Conversion, Mathematical Sciences Northwest, Inc., Preliminary Report, July 1978.
10. National Aeronautics and Space Administration, Energy Conversion Alternatives Study (ECAS), NASA TM-73871, Sept. 1977.
11. P. Rose, "Potential Applications of Wave Machinery to Energy and Chemical Processes, to be presented at the XII International Symposium on Shock Tubes and Waves, Jerusalem, Israel, July 16-19, 1979.
12. A.T. Mattick, A. Hertzberg, R. Decher and C.V. Lau, "High-Temperature Solar Photon Engines," J. Energy 3, 30 (1979).

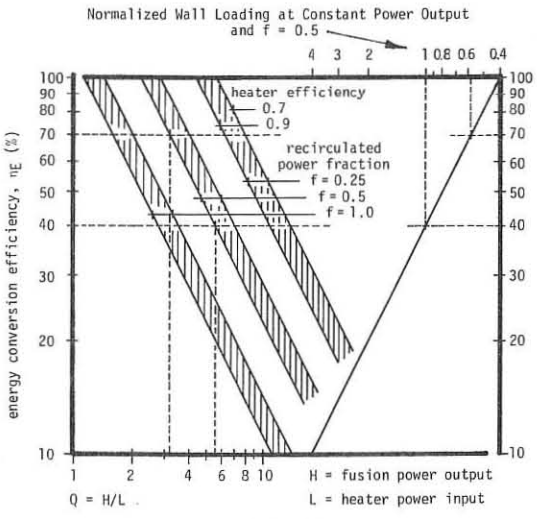

Figure 1

DP20

THERMAL FLUCTUATIONS AND LEAKING RADIATION FROM LASER-PRODUCED PLASMA

Yu.M. Aliev, S. Vuković*, O.M. Gradov, A.Yu. Kyrie and A.A.Frolov

Lebedev Physical Institute, USSR Academy of Sciences, Moscow
and
*Institute of Physics, Belgrade, Yugoslavia

The theory of thermal radiation of electromagnetic waves has been sufficiently well developed for plasmas with sharp boundary[1]. However, in laser-produced plasmas the existence of corona region makes the sharp boundary model inadequate. Theoretical[2] and numerical[3] calculations, as well as, experimental measurements[4] revealed a steepening of plasma density profile near the resonant point, induced by ponderomotive force of a longitudinal high-frequency field. One of the important characteristics of such a density profile is the appearance of leaky surface waves as eigenmodes of the system. These modes are quasi-localised in the vicinity of plasma resonance and are propagating with the wave vector $\vec{K}_{\parallel}$ along the plane, which is orthogonal to the direction of density gradient (z-axis). Their frequency is given by[5]:

$$\omega^2 \simeq \frac{1}{2}\left\{\omega_{Le}^2(a)+\omega_{Le}^2(0)+2K_{\parallel}^2c^2-\sqrt{\left[\omega_{Le}^2(a)-\omega_{Le}^2(0)\right]^2+4K_{\parallel}^4c^4}\right\} \quad (1)$$

where $\omega_{Le}(0)$ and $\omega_{Le}(a)$ are the electron plasma frequencies at the bottom and the top of the steepened density region. Outside this strongly ingomogenous region of the length a ($K_{\parallel}a \ll 1$). Besides the standard dissipation processes, like the linear wave transformation, collisions, etc., surface waves with $\omega \gg K_{\parallel}c$ are damped by energy loss due to radiation (leaking) into the transparent region $\mathcal{K}^2(z) < 0$, where

$$\mathcal{K}(z) = \sqrt{K_{\parallel}^2 - \frac{\omega^2}{c^2}\varepsilon(\omega,z)} \; ; \quad \varepsilon(\omega,z) = 1 - \frac{\omega_{Le}^2(z)}{\omega^2}$$

Being interested in the radiation due to thermal fluctuations of leaky surface waves, we suppose that plasma is stationary but not in equilibrium, assuming the damping time of surface waves much less than the characteristic time of density profile modification. The energy flux density of the radiation leaking to vacuum can be expressed through the Fourier-components of random electric $\vec{E}$ and magnetic $\vec{B}$ fields as:

$$\vec{S}(\omega,\vec{K}_{\parallel}) = \frac{c}{8\pi}\left[\overline{\vec{E}(\omega,\vec{K}_{\parallel},z)\times\vec{B}^{*}(\omega,\vec{K}_{\parallel},z)}+c.c.\right] \quad (2)$$

where the line above means the ensemble-averaged. Only z-component of this quantity is different from zero, since plasma is supposed to be isotropic in xy-plane, The related spectral intensity $I_{\omega} = dI/d\omega d\Omega$ where $d\Omega$ is the elementary solid angle, is defined as:

$$I_{\omega} = \frac{\omega^2}{8\pi^3c^2}\, S_z(\omega,\vec{K}_{\parallel})$$

and can be calculated using the method of phase micro-densities[6,7] to determine the correlation functions of electromagnetic field fluctuations introduced in eq. (2). As shown in [6] all relevant correlation functions can be expressed by means of the the longitudinal electric field correlator $G_{\parallel}(\omega,K_{\parallel},z,z')$:

$$(2\pi)^2\delta(\vec{K}_{\parallel}-\vec{K}_{\parallel}')\,G_{\parallel}(\omega,K_{\parallel},z,z') = \lim_{\Delta\to 0} 2\Delta\, \overline{E_{\parallel}(\omega+i\Delta,K_{\parallel},z)\,E_{\parallel}^{*}(\omega+i\Delta,K_{\parallel},z)} \quad (3)$$

Also, the correlation functions for various z, can be expressed through $G_{\parallel}(\omega,K_{\parallel},z=0,z'=0)$. As a result for spectral intensity we get

$$I_{\omega} = \frac{\omega^3}{32\pi^3c^2}\,\frac{\varepsilon(\omega,z=0)}{\mathcal{K}'(z=0)}\exp\left\{-\int_{z_l}^{0}\mathcal{K}(z)\,dz\right\}G_{\parallel}(\omega,K_{\parallel},z=0,z'=0) \quad (4)$$

$$G_{\parallel}(\omega,K_{\parallel},z=0,z'=0) = \frac{4\pi^2K_{\parallel}^2\,\mathrm{sign}\,\omega}{\omega\left|\mathcal{D}(\omega,\vec{K}_{\parallel})\right|^2}\,\frac{T(z_0)}{\left|\frac{\partial\varepsilon}{\partial z}\right|_{z=z_0}}$$

Here $\mathcal{D}(\omega,\vec{K}_{\parallel})$ is the dispersion function of leaky surface waves, z_l is the leaking point $\mathcal{K}(z_l)=0$, z_0 the resonant point $\varepsilon(\omega,z_0)=0$ and $T(z_0)$ electron temperature at the resonant point. In the case of part-by part linear density profile:

$$n_{oe}(z) = n_{oe}(0)\left(1+\frac{z}{L}\right) \; ; \quad z<0$$

$$n_{oe}(z) = n_{oe}(0) + \frac{n_{oe}(a)-n_{oe}(0)}{a}z \; ; \quad 0<z<a$$

$$n_{oe}(z) = n_{oe}(a)\left(1+\frac{z}{L}\right) \; ; \quad z>a$$

we obtain the following expression for spectral intensity (4)

$$I_{\omega} = \frac{\omega^2T(z_0)}{8\pi^3c^2}\,\frac{2d_r''d_i''}{(1-d')^2+\left[d_r''+d_i''(1+d')\right]^2}$$

where

$$d' = \frac{x-1}{\alpha-x}\left(\frac{\alpha-x\cos^2\theta}{1-x\cos^2\theta}\right)^{1/2}$$

$$d_r'' = \frac{\pi\beta}{\alpha-1}\sin^2\theta\; x(x-1)(1-x\cos^2\theta)^{-1/2}$$

$$d_i'' = \frac{1}{2}\exp\left\{-\frac{4}{3}\delta\cdot(1-x\cos^2\theta)^{3/2}\right\}$$

and nondimensional parameters

$$x = \frac{\omega^2}{\omega_{Le}^2(0)} \; ; \quad \alpha = \frac{\omega_{Le}^2(a)}{\omega_{Le}^2(0)} \; ; \quad \beta = \frac{a\,\omega_{Le}(0)}{c} \; ; \quad \delta = \frac{L\,\omega_{Le}(0)}{c}$$

have been introduced. θ is the angle between z - axis and the direction of observation defined by: θ = arc sin Investigating this spectrum one can determine important plasma parameters L, a, $\omega_{Le}(0)$, $\omega_{Le}(a)$ and $T(z_0)$. An example of such a procedure will be presented on the conference.

Throughout the paper we have neglected the contribution of electron-ion collisions to the correlation function $G_{\parallel}(\omega,K_{\parallel},z,z')$ For characteristic parameters of laser-produced plasmas: $\omega = 10^{15}$ sec^{-1}, $L = 10^{-2}$cm, $a = 10^{-4}$cm, $T(z_0) = 1 \div 10$ KeV this contribution will be small if

$$0.2 \gg x - 1 \gg 0.001$$

Taking into account that the rate of the density profile deformation is determined by the ion-sound velocity, the quasistationarity condition gives the following limitation to the angle θ:

$$\theta^4 > (\alpha-1)\,\frac{\omega_{Li}(0)}{\omega_{Le}(0)}\,\frac{r_{De}(0)}{a}$$

where r_{De} is electron Debuye radius.

The estimated peak value of the radiated energy flux is 10^5-10^6 W/cm^2.

In conclusion we want to underline that the results of this paper could be used as a base for a new method of laser-produsedplasma diagnostics.

References

[1] I.P.Yakimenko, Fluctuations and correlations in bounded systems of charged particles, Preprint ITP 75-143E, Kiev (1975).

[2] V.M.Gildenburg and G.M.Fraiman, Zh.Eksp.Teor.Fiz. 69, 1601 (1975).

[3] D.V.Forslund, J.M.Kindel, K.Lee, E.L.Lindman and R.L. Morse, Phys. Rev. A 11, 679 (1975).

[4] D.T.Attwood, D.W.Sweeney, J.M.Auerbach and P.H.Y.Lee, Phys. Rev. Letters 40, 184 (1978).

[5] Yu.A.Romanov, Izv. Vyssh. Uchebn, Zaved.Radiofiz. 7,242 (1964).

[6] Yu.M.Aliev, S.Vuković, O.M.Gradov and A.Yu.Kyrie, J.Plasma Phys. 13, 273 (1975).

[7] Yu.L.Klimontovich, Statistical theory of non-equilibrium processes in plasma, MGU, Moscow (1964).

The Wavelength Dependence of Energy Absorption in Laser-Plasmas.

Helmut Schwarz
Rensselaer Polytechnic Institute, Troy, New York 12181, USA, and Departamento de Física, Universidade de Brasília, 70.910 Brasília, D.F., Brazil

The initial heating of a plasma by radiation in the optical region aiming at laser-driven fusion[1] is almost entirely due to the transfer of electromagnetic energy to the electrons. Electrons acquire oscillations within the electric field of the radiation, which, at high laser intensities, can reach relativistic velocities. The electrons transfer their energy mainly by electron-ion collisions to the whole plasma. The duration of this thermalization should be shorter than the pulse duration of the laser radiation which leads to a modified "Lawson condition" for laser fusion. The radiation absorption mechanism is of greatest importance for laser fusion where intensities are applied that produce electric fields several ten to hundreds of billions of volts per cm. Such fields will lead to electron oscillation energies exceeding the rest mass energy of the electron, so that the refractive index of the plasma will become a nonlinear function of the radiation power[2-5]. The resulting mass variation will induce relativistic self-focusing[2,3,6,7] of the intense laser beam, especially when the plasma to be irradiated has a density near or above the critical density $N_{ocr}=\varepsilon_o m_o \omega^2/e^2$ (ε_o = 8.85×10^{-12} F/m; m_o = 9.11×10^{-31} kg; e = 1.6×10^{-19} C; ω - radial frequency of radiation)+. Under such conditions the laser beam can be focused to a diameter equal to its vacuum wavelength[8] λ_o, so that for laser powers P exhibiting self-focusing, the radiation intensity I is approximately equal to:

$$I \approx P/\lambda_o^2 \qquad (1)$$

The kinetic engergy of the electron is a function of the field strength parameter[9]

$$\alpha = eE_o/(cm_o\omega) \qquad (2)$$

(E_o - peak electric field within focus of laser beam; c = 3×10^8 m/s), which will become independent of $\lambda_o = 2\pi c/\omega$ as follows from Eqs. (1) and (6). The kinetic energy is given by

$$T = m_o c^2(\gamma - 1) \qquad (3)$$

[$\gamma = (1 - \frac{v^2}{c^2})^{-1/2}$; v - electron velocity]

and determined by:

$$\gamma = \sqrt{1+\alpha^2} \qquad (4)$$

for circularly polarized light, or

$$\gamma = \alpha\,(1 - n\sqrt{1 - v_o^2\kappa^2})/(\kappa\sqrt{1 - n^2}) \qquad (5)$$

for linearly polarized laser light.
Hereby are:

$$\alpha^2 = \frac{2e^2 I}{\varepsilon_o \omega^2 m_o^2 c^3 n} \qquad (6)$$

n - refractive index; $v_o^2 = 1 + 1/\alpha^2$, and κ -the solution of the following complete elliptic integral of the first kind (see Eqs. 51 and 52 of Ref. 9):
$K(\kappa) = \pi n\left[2(1 - v_o^2\kappa^2)\right]^{-1/2}$. α turns out to be simply a function of the laser power P and the refractive index n:

$$\alpha^2 = b_o P/n \qquad (7)$$

with $b_o = e^2/(2\pi^2\varepsilon_o c^5 m_o^2) = 7.31\times10^{-11}$ [W^{-1}] (7a)

a constant, which means that the kinetic energy in this case of self-focusing is independent of the wavelength of the applied laser radiation, except for the wavelength dependence of the refractive index n. The refractive index, neglecting collisions, is given by[5]:

$$n^2 = 1 - \omega_p^2/(\omega^2\gamma) = 1 - \nu^2/\gamma \qquad (8)$$

where ω_p - plasma frequency and

$$\nu = N_o/N_{ocr}, \qquad (9)$$

N_o being the plasma density.
It turns out that the kinetic energy is indeed completely independent of the wavelength of the radiation as long as the plasma density adjusts itself or is being adjusted such that ν remains the same for the different wavelengths of the applied radiation.
This statement does not only hold for the self-focusing case as inferred by H. Hora et al[8], but also for the case where a focusing system is used to its maximum focusing power, esp. where lower laser energies are applied with lower density plasmas (n=1, independent of laser wavelength). The actual irradiance of any focusing system of a given focal ratio $f = n_\ell \ell_f/d$ (n_ℓ - refractive index of lens, ℓ_f - focal length, d - lens diameter) at the spot center is given by[10]:

$$I_{center} = \pi^2 P/\lambda_o^2 f^2 \qquad (10)$$

so that one arrives almost at the same values for α^2 (Eq.7), if one assumes f = 3.14:

$$\alpha^2 = b_1 P/n \qquad (11)$$

$b_1 = e^2(1/f^2)/(2\varepsilon_o c^5 m_o^2) = 7.21\times10^{-10}/f^2$ [W^{-1}] a constant (11a)

Applying an optimally focused laser beam, initial energy absorption depends directly only on the laser power and weakly on the refractive index, regardless whether relativistic self-focusing occurs or not.
Figures 1 and 2 represent this dependence for different plasma densities given in terms of the parameter $\nu = N_o/N_{ocr}$. The kinetic energy is plotted in units of the electron rest mass energy $m_o c^2$ as a function of laser power P for circularly polarized light focused with an optical system of focal ratio f = 10. The points were calculated from Eqs. (4) and (11) combined with Eq. (8). Hereby the resulting equations:

$$(1 + n)^2(1 - n)^2(1 + b_{1,o}P/n) - \nu^2 = 0 \qquad (12,13)$$

were solved for n at different P and ν. Equations (4) and (3) were then used to determine the kinetic energy $T/m_o c^2$.

Equation (12) with the constant b_1 (Eq.11a) and lower powers P served for Fig. 1, whereas Eq.[1](13) with the constant b_o (Eq. 7a) served for Fig. 2. Values for linearly polarized light should also show a similar wavelength independence. Our results seem to be experimentally confirmed by McCall et al[11] when they compared their measurments of high-energy charged particles originating from plasmas produced by an Nd doped glass laser (λ_o = 1.06μm) and by a CO_2 laser (λ_o = 10.6μm). No appreciable wavelength dependence was found in agreement with our theoretical results.

References:

1. K. H. Brueckner and S. Jorna, Rev.Mod.Phys. 46,325 (1974).
2. C. E. Max, J. Arons, and A. B. Langdon, Phys.Rev.Lett. 33, 209(1974).
3. K. H. Spatschek, J.Plasma Phys.(GB) 18, 293(1977).
4. ....., "Fortschritte d.Phys." 24, 687(1976) (GDR).
5. H. Schwarz and Y. S. Liu, Opt. and Quantum Electronics (London) 10, 515 (1978).
6. H. Hora, J.Opt.Soc.Am. 65, 882 (1975).
7. E. L. Kane and H. Hora, in Laser Interaction and Related Plasma Phenomena. Editors: H. Schwarz and H. Hora (Plenum Press, New York 1977) Vol. 4B, pp.913.
8. H. Hora, E.L. Kane, and J.L. Hughes, J.Appl.Phys.49,923 (1978).
9. H. Schwarz and R. Tabensky, in Laser Interaction and Related Plasma Phenomena. Editors: H.Schwarz and H. Hora (Plenum Press, New York 1977) Vol. 4B, pp. 961.
10. A. F. Harvey, Coherent Light. (Wiley-Interscience, London 1970) p. 620.
11. T. H. Tan, G. H. McCall, A. Williams, and D. Giovanielli, in Laser Interaction and Related Plasma Phenomena. Ed.: H. Schwarz and H. Hora (Plenum Press, New York 1977) Vol. 4B, pp. 677.

+ All formulae in this paper are written in such a way that the SI system of units (Système Internationale) can be used which is identical with the rationalized MKSA system.

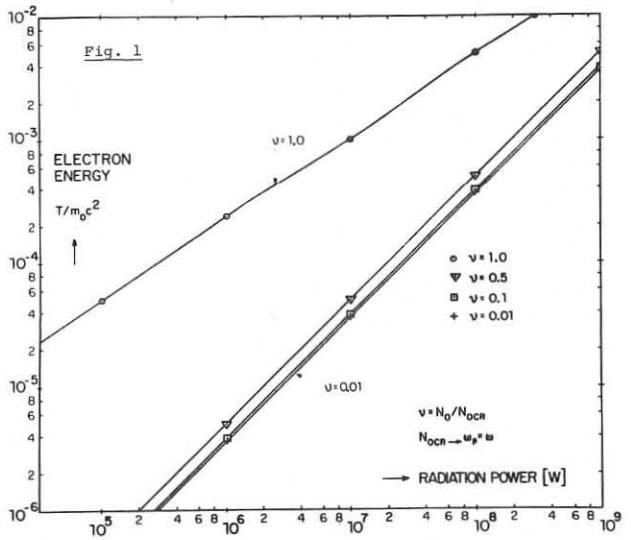

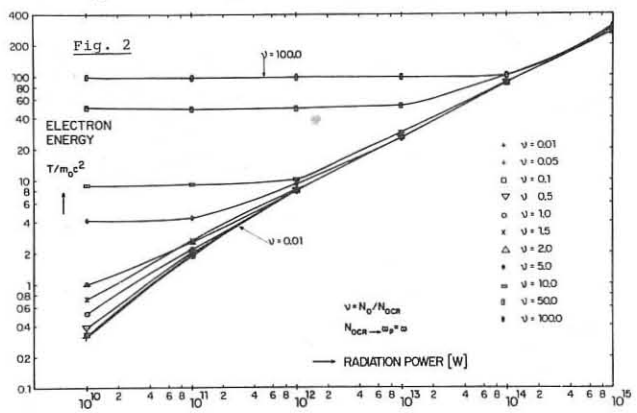

DP22

INVESTIGATION OF LASER-PRODUCED PLASMA IN SM MAGNETIC TRAP

J. Baranowski, S. Chyrczakowski, K. Czaus, K. Melzacki, M. Sadowski, E. Składnik-Sadowska, A. S. Slavnyj*, S. Ugniewski
Institute of Nuclear Research, 05-400 Otwock-Świerk, Poland

Abstract: The paper presents the results of recent experimental studies on the behaviour of a laser-produced plasma in the spherical multipole /SM/ magnetic trap. The plasma containment time and the particle loss aperture are estimated.

The concept of plasma containment within the nearly-zero magnetic field region surrounded by the spherical multipole /SM/magnetic surface was developed in the mid sixties [1]. Later experiments with plasma injection into the SM trap [2] demonstrated that the particle losses through the point cusps, although smaller than those in a comparable spindle-cusped configuration, are inherently connected with the interaction of the injected plasma streams. Other measurements [3] proved that the trapping and randominization of the injected plasma are strongly affected by the polarization phenomena. At the same time the concept of symmetrical arrangement of magnetic dipoles over the surface of the vacuum vessel was also adopted by other investigators [4,5] to build large cylindrical machines.

In order to improve the conditions of the plasma generation and containment within the orginal SM configuration a new experimental facility Kaktus II was constructed [6,7]. To eliminate all the problems connected with the plasma injection, a laser method of plasma production in the SM trap has been applied. Some preliminary results of experimental research on the laser-produced plasma behaviour in the SM geometry were presented at the previous Conference [8]. Recently some new and more detailed results have been obtained. To get these data use was made of the same experimental setup as described in Ref. [8].

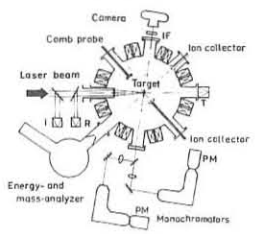

Fig.1.

Plasma was produced by 1J, 40 ns, ruby laser pulses focused onto a thin polyethylene foil located at the center of the experimental chamber /see Fig.1/. All the optical measurements were performed at the pressure of 10^{-3} Pa and without any external magnetic field since its influence could be neglected for the initial stage of the discharge. To measure the incident laser beam as well as the transmitted- and reflected-radiation use was made of BPYP-49 photodiodes calibrated by means of a laser calorimeter of the "rat's nest" type [9]. As a compromise between assymetry of the integral visible radiation and the amount of energy absorbed by plasma, a 250- μm polyethylene foil target has been selected. Although the laser pulses were very reproducible, the transmitted radiation varried from 15 to 95 percent of the incident beam [10]. The reflected radiation reached only 0.4 percent and was slightly affected by plasma /see Fig. 2/. From the analysis of laser craters in the target foil one could estimate that the average number of hydrogen atoms vaporized by one shot amounted to 2×10^{17}. It was also shown that the region surrounding the laser crater in the foil was not transparent for the light because of changes in the structure of the material, and not of the carbon deposition. To determine initial plasma parameters detailed observations of time-resolved spectral lines of various ion species were performed. The lines observed revealed a distinct spike structure [10]. Under typical experimental conditions the electron temperature was found to be 10 eV at the laser focus and 3 eV at the distance of 1 mm from the target.

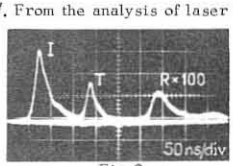

Fig.2.

The temperatures of C^+ and H^o species at r = 1 mm were equal to 1.3 eV and 1.0 eV, respectively. The electron concentration, as determined on the basis of the spectroscopic measurements /also at r = 1 mm/, was found to be 5×10^{17} cm^{-3} at t = 20 ns, and 2×10^{16} cm^{-3} at t = 100 ns. These values were consistent with the interferometric measurements performed with a laser interferometer of the Mach-Zehnder type similar as in Ref. [3]. Since the spectroscopic observations have also demonstrated C^+ ions of energy of 20 - 100 eV, and C^{++} ions of energy of 100-500 eV, as well as C^{3+} ions, the low degree of ionization /estimated to be 1 percent/was probably due to a large amount of neutrals /some 10^{17}/. Since the thermal velocities of H^o and C^o neutrals were, respectively, equal to 1.4×10^6 cm/s and 4.0×10^5 cm/s, those neutrals could reach the cusped regions in 5-20 μs and reduce the confinement time of ions by charge-exchange processes.

In order to study the interaction of the laser-produced plasma with the investigated SM magnetic surface use was made of Langmuir probes, an electrostatic energy analyzer, and a multi-pin comb probe. The electron temperature of the expanding plasma, as measured with the probes at the distance r = 10 cm /i.e., in the point cusp region/, was almost the same as determined by means of spestroscopy at the distance r = 0.1 cm. To investigate the plasma expansion and containment various ion species were analyzed. No ions of energy below 20 eV were observed, what could be explained as a result of recombination processes. Energy spectrum of H^+ ions measured without magnetic field /see Fig.3/ was narrower than that of carbon ions, since the C^+ ions /as well as neutrals/ of energy up to 1 keV were observed. Those could be generated by the known acceleration mechanism [11]. Since such fast ions could not be confined within the investigated trap because of a limited value of magnetic field, attention was paid to low-energy ions and in particular to 100-eV protons. With the SM field of the order of 3 T at the chamber wall and 0.1 T at the point cusps, all the protons and highly-ionized carbon ions were trapped, and only C^+ ions were registered with the energy analyzer placed approx. 70 cm from the trap center.

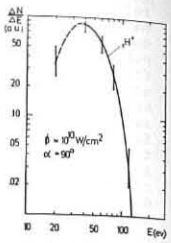

Fig.3.

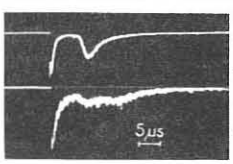

Fig.4.

To study the plasma containment detailed measurements of neutrals flux were carried out with a setup consisted of ion deflecting plates and a neutrals detector. With the SM field the neutrals signals were considerably longer than those obtained without the SM field /see Fig.4/. Under the experimental conditions considered, the containment time, as determined from the neutrals measurements, was approx. 30 μs only. It was limited probably by too large amount of neutral atoms vaporized from the target. In order to determine the effective loss-cone aperure for ions, similar to the preliminary studies [8], detailed measurements with a 6-pin comb probe were performed in the point cusp regions. With the SM field the signals from the side pins were considerably smaller than the signal from the center pin /see Fig.5/. The measurements proved that the particle leakage aperture depends on the SM field strength, and for the ions investigated it is comparable to the local value of the electron-ion hybrid gyroradius, in compliance with the results of the preliminary studies [8]. Since those measurements were performed for a relatively low-beta plasma it is required to check whether a dense energetic plasma of fusion interest can be confined in the SM geometry without unacceptable losses. In order to generate a high-beta, nearly fully ionized plasma, it is necessary to increase laser energy and optimize the target or to use another method of the plasma production. In any case, in order to obtain plasmas as nearly isotropic as possible, some special measures are required. Such studies would be of particular interest for fusion research because the SM magnetic surface concept offers some important advantages, e.g., the mhd stability, the possibility of confining a plasma within a region of low magnetic field, and the reduction of cyclotron radiation losses.

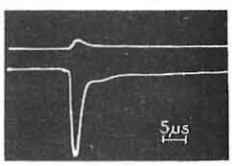

Fig.5.

* On leave from the Physico-Technical Institute, Kharkov, USSR.

1. M. Sadowski, Phys. Lett. 25A, 695/1967/; J. Plasma Phys. 4, 1/1970/.
2. M. Sadowski et al., Proc. 5th ECPP, Grenoble 1972, p. 102.
3. M. Sadowski et al., Proc. 6th ECPP, Moscow 1973, p. 393.
4. R. Limpaecher, R. K. MacKenzie, Rev. Sci. Instrum. 44, 726/1973/.
5. J. R. Roth, IEEE Trans. Plasma Sci. PS-6, 270/1978/.
6. World Survey of Major Fac. in CFR, Nucl. Fusion Suppl. 1976.
7. K. Czaus, M. Sadowski, Proc. 6th ICMT, Bratislava 1977, p. 123.
8. J. Baranowski et al., Proc. 8th ECPP, Prague 1977, p. 106.
9. J. Appelt, INR Intern. Report No. 0-96/SLFPG/72.
10. S. Chyrczakowski et al., Proc. ICPIG-14, Grenoble 1979.
11. Yu. A. Bykovskij et al., Kvant. Elektronika 2, 989/1975/.

DP23

INTERACTION OF SHORT 1.06 μm LASER PULSES WITH LOW-Z PLASMA

J.E. Balmer, P. Lädrach, A.P. Schwarzenbach, T.P. Donaldson, H.P. Weber

Institute of Applied Physics, University of Berne,
CH-3012 Berne / Switzerland

Abstract Resonance absorption effects in laser generated plasma have been investigated by focussing short neodymium laser pulses (35 psec, 1.06 μm) onto plane perspex slab targets. The experimental results are interpreted with the aid of a numerical simulation code that calculates the time dependent behaviour of the electric field in the critical density region.

Introduction Resonance absorption of short laser pulses in plasma has been demonstrated experimentally by several authors [1,2]. Theoretical and numerical treatments of the problem show the existence of a resonantly excited electric field spike in the region of the critical density [3,4]. In a warm plasma, the height and width of the resonance peak are determined either by collisional damping or by plasma wave convection [5]. The common feature of these models is the standing-wave nature of the electric field in the plasma. Here we report on a numerical calculation of the time dependent electric field including collisional absorption. It is shown that for $n_e < n_{ec}$ the resulting electric field behaves as a travelling wave moving inwards, whereas in the vicinity of the critical density it appears as a sequence of positive and negative "pulses" growing up on the high-density end of the resonance peak and moving towards its lower-density end in one oscillation period. A similar result has previously been obtained for the collisionless regime [6]. The propagating pulses affect the electron velocity distribution in that they preferentially accelerate electrons that initially move in the direction of lower density. A simple model was used to calculate this effect and the results are shown to be consistent with hard X-ray and ion measurements[7].

Equations The one-dimensional inhomogeneous plasma is assumed to have a stationary density profile of the form $n_e(x)=n_{ec}x/L$. The laser light electric field vector is laid in the xy-plane as is its wave vector k_o. Starting from Maxwell's equations and the generalized Ohm's law the wave equation for the E_x-component of the electric field reads [3]:

$$\left(\frac{\delta^2}{\delta x^2}+\frac{\delta^2}{\delta y^2}\right)E_x + 2\,\frac{\delta E_x}{\delta x}\,\frac{\delta(\ln n)}{\delta x} + \left[\frac{\omega^2}{c^2}n^2 + 2\,\frac{\delta^2(\ln n)}{\delta x^2}\right]E_x = 0 \qquad (1)$$

where $n^2(x) = \varepsilon(x) = 1 - \dfrac{\omega_p^2(x)}{\omega^2(1 + i\nu(x)/\omega)}$ (2) is the complex dielectric constant for a cold plasma, $\omega_p^2(x) = 4\pi e^2 n_e(x)/m_e$ is the electron plasma frequency and $\nu(x) \sim n_e(x)/T_e^{3/2}$ the electron-ion collision frequency.

By separating $E_x(x,y) = e_{xx}(x)\, e_{xy}(y)$
and substituting $u(x) = e_{xx}(x)\, n(x)$
a linear 2nd-order differential equation for u(x) is obtained:

$$\frac{\delta^2}{\delta x^2}u(x) + K^2(x)\,u(x) = 0 \qquad (3)$$

where $K^2(x) = \dfrac{\omega^2}{c^2}[n^2(x) - \sin^2\theta_o] - 2\left[\dfrac{n'(x)}{n(x)}\right]^2 + \dfrac{n''(x)}{n(x)}$ (4)

is the square of a complex x-dependent wave number with its real and imaginary parts plotted in Fig.1. The dashed lines represent the collisionless case. Note that in equation (5) the first and second order derivatives of the complex refractive index, n'(x) and n"(x) respectively, have to be kept in the calculations, since the changes in n(x) are biggest in the region of the resonance where n(x) approaches zero.

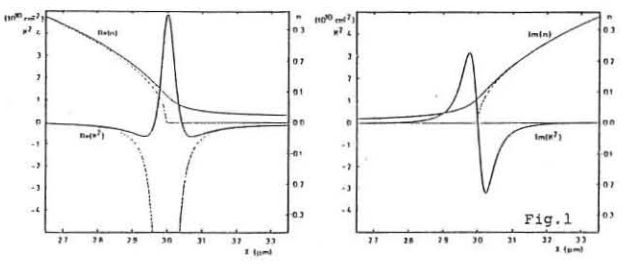

Fig.1

Calculations and discussion Equation (3) was solved numerically using a 4th-order Runge-Kutta method. The calculation has been performed for a range of realistic values of electron temperatures and density scale lengths obtained from previous experiments [2,8]. An example is shown in Fig.2. Here the real part of the electric field (which is the physically significant quantity) is plotted as a function of x for three different instants of the oscillation period (thick line). The thin line represents the absolute value of the electric field (which is usually discussed in the works referred to in the introduction). It constitutes the (time independent) envelope of the real part of the field which appears as a positive pulse followed by a negative pulse, both crossing the resonance peak from supercritical towards subcritical density in one oscillation period. The propagation velocity of these pulses was calculated numerically and was found to be temperature dependent and $\simeq 4\times10^9$cm/s. This behaviour very strongly suggests a possible acceleration mechanism for electrons entering the resonance region at its high-density end. Qualitatively it is obvious that electrons within a certain range of v_x-components matched to the propagation velocity of the field spike and arriving in phase with it should be accelerated optimally while crossing the enhanced field region. From the value of the pulse propagation velocity an electron energy of $\simeq 4$ keV can be estimated for optimum acceleration.

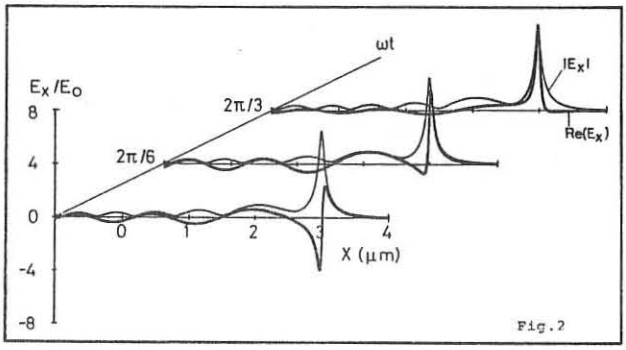

Fig.2

In order to more quantitatively determine how this mechanism affects the electron velocity distribution the total acceleration was calculated for electrons entering the resonance peak region with different initial velocities and phases. A Maxwellian velocity distribution was assumed at the beginning. A typical result of this calculation is shown in Fig.3 where the undisturbed (dashed line) and the disturbed (solid line) electron distributions are plotted as a function of the electron energy E for a cold electron temperature of 400 eV. It is clearly seen that electrons with initial energies $E \gtrsim 4$ keV are strongly accelerated to form a high-energy tail on the Maxwellian. This result is in good agreement with hard X-ray measurements in which a signal depletion has been found at foil cut-off energies of 10 and 17 keV for p-polarized laser light [7].

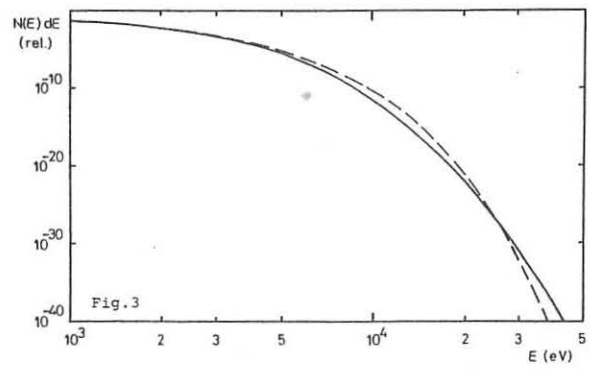

Fig.3

References
[1] P. Kolodner and E. Yablonovitch, Phys.Rev.Lett. 37,1754(1976); K.R. Manes et al., Phys.Rev.Lett. 39,281(1977)
[2] J.E. Balmer and T.P. Donaldson, Phys.Rev.Lett. 39,1084(1977)
[3] V.L. Ginzburg, "The Propagation of Electromagnetic Waves in Plasmas", (Pergamon, Oxford, 1970)
[4] J.S. DeGroot and J.E. Tull, Phys.Fluids 18,672(1975); K.G. Estabrook et al.,Phys Fluids 18,1151(1975)
[5] T.J.M. Boyd and W.T. Hewitt, J.Phys.D 10,247(1977)
[6] J.P. Freidberg et al.,Phys.Rev.Lett. 28,795(1972)
[7] T.P. Donaldson et al.,to be published in Opt.Commun.
[8] T.P. Donaldson et al.,to be published in J.Phys.D

DP24

A Time-dependent Study of Linear Collective Ion Acceleration

A. Sternlieb

Department of Physics and Astronomy
University of Maryland
College Park, Maryland 20742

Recently heavy ion beams (HIB) have been considered as possible drivers in an inertial confinement fusion scheme [1]. The first major objective is to produce, transport and focus 100 TW, 1 MJ beams of particles with a short range in a millimetric-size target. HIB became attractive because of the existence of advanced accelerator technology, capable of high repetition rates. A promising and possibly cheaper approach is the use of collective ion acceleration (CIA) as a source for HIB. In a typical CIA experiment a relativistic electron beam is injected into a drift tube in which an ion source is present. The ions which initially have negligible kinetic energy are eventually accelerated by the collective electrostatic fields generated by the incoming electron beam. Basically, in CIA long e-beam pulses are transformed into short energetic ion pulses. Ion energies many times higher than the injected electron beam energy have been detected in several experiments [2-5]. CIA in vacuum drift tubes has not been well understood until now. Some basic steady-state theories exist, but they either do not include ions self-consistently, or cannot account for the high ion energies obtained with linear electron beams in vacuum drift tubes [3]. All models are based on the assumption that a virtual cathode is formed inside the drift tube, when the injected current exceeds the limiting current. In spite of the advantages of the steady-state theories in giving some crude evaluation of the achievable ion energies, there is a critical need for a time-dependent model, in which electrons and ions are included in a self-consistent manner. At present, this goal can be achieved only by a particle computer simulation model. For this purpose, a 1-d relativistic PIC code is used in order to simulate the processes following the injection of an intense, relativistic electron beam into a vacuum drift tube, when a plasma source is available at the site of injection, inside the tube [Fig. 1]. Space-charge limited emission from the plasma source is assumed.

Preliminary results indicate that an irregular space and time-varying virtual cathode is formed, whose left wall is nearly stationary [Fig. 2a]. This suggests that part of the ion acceleration occurs within a finite distance adjacent to the injection boundary.

An unexpected feature in our simulations is the periodical formation of short-lived regions of positive electrostatic potential ("virtual anodes") inside the drift tube [Fig. 2b]. The upstream sides of these regions accelerate the incoming electrons and the downstream sides further accelerate the ions. Thus one should expect the presence of spikes of energetic ion currents inside the drift tube. Our conclusion is that both accelerated electrons and the bulk of slow ions are responsible for the high acceleration of the fastest ions. In Fig. 3 one can see the gradual transfer of energy from slow ions to faster ions (marked by successive arrows).

In agreement with experiments, we find good propagation of the electron beam, when ions are present. A strong coupling exists between electrons and fast ions during propagation, which is also corroborated by experiments.

Finally, the total ion current is a few percent of the injected electron current (10 KA/cm^2) and the maximum ion energy is 4 times the injected beam energy (1 Mev). The various current components are presented in Fig. 4. The notations are: e = electron, i = ion, em = emitted, abs = absorbed, A1 = left anode, A2 = right (downstream) anode. Figure 5 gives the time variation of the virtual cathode ($\phi^{min}(t)$) and virtual anode ($\phi^{max}(t)$).

In summary, the computer simulation model seems to be an indispensable tool for explaining and guiding present and future linear collective ion acceleration experiments.

References

1. Proceedings of the Heavy Ion Fusion Workshop, Brookhaven Nat. Lab., Upton, New York, October 17-21, 1977.
2. S.E. Graybill and J.R. Uglum, J. Appl. Phys. 41, 2361 (1970).
3. C.L. Olson, Ph. Fl. 18, 585 (1975).
4. W.W. Destler and H. Kim, Proc. 2nd Int. Topical Conf. on High-Power Electron and Ion Beams Res. and Tech. (Ithaca, N.Y., Oct. 1977, p. 521).
5. J. Luce: Ann. N.Y. Acad. Sci. 25, 217 (1975).
6. H.S. Uhm and H. Kim, "High Intensity Electron Beam Propagation between Two Plane Conductors, and Its Implications for Collective Ion Acceleration," Univ. of Maryland Tech. Rep. No. 79-012.
7. J.W. Powkey and N. Rostoker, Plasma Phys. 13, 897 (1971).

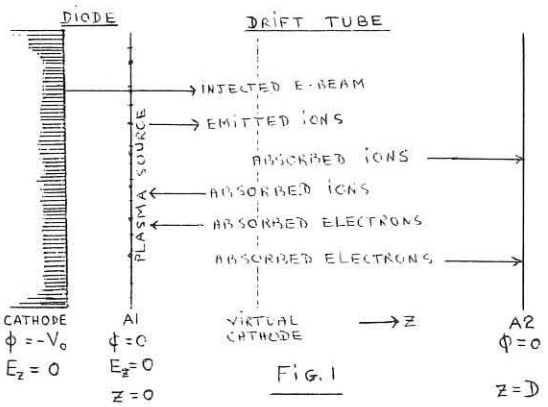

Fig. 1

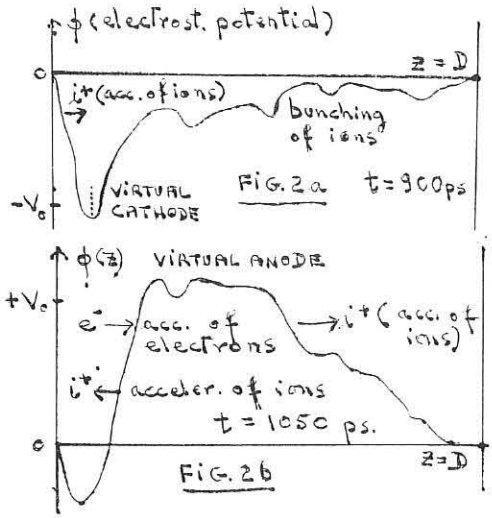

Fig. 2a

Fig. 2b

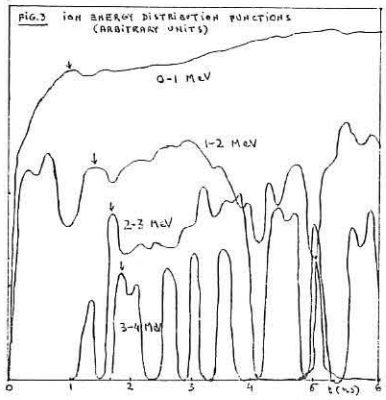

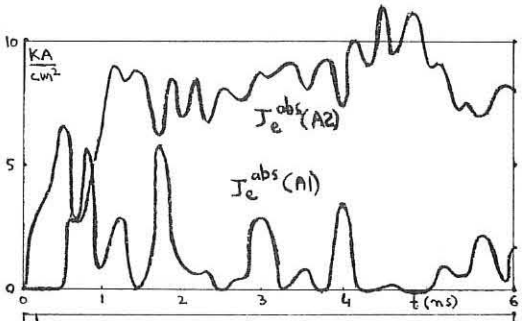

Fig. 4

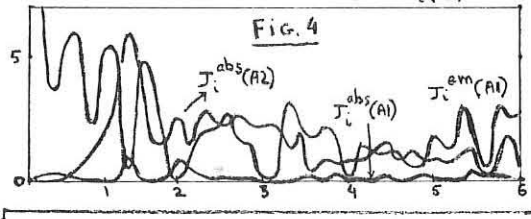

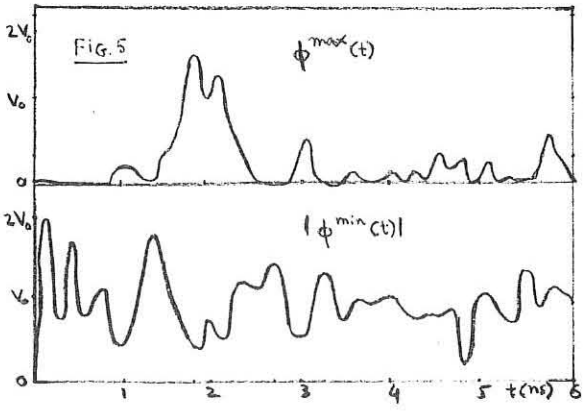

Fig. 5

X-RAY SPECTROMETRY OF LASER COMPRESSED MICROBALLOONS

J G Lunney, C L S Lewis, A Moore — Dept. of Pure & Applied Physics, Queen's University, Belfast

M H Key*, — Rutherford Laboratory, Oxon

J D Kilkenny, R W Lee, — Imperial College, London

Thin-walled glass microballoons irradiated at high laser intensity (2×10^{15} W cm^{-2}) exhibit an implosion behaviour that has been termed "exploding pusher" since the glass wall is heated throughout by supra-thermal electrons, generated by the laser absorption process at the target surface, and the resulting explosion of the glass wall compresses the gas filling the microballoon leading to an implosion core of high temperature but low density . Space resolved X-ray spectroscopy has been used to diagnose the plasma parameters in the implosion core (1-6).

Glass microballoons of $\sim$ 70 μm diameter, $\sim$ 1 μm wall thickness filled with various gases (Neon, Argon, Deuterium + 5% Neon, or Deuterium + Tritium + 5% Neon) were irradiated at a laser intensity of $\sim 3 \times 10^{15}$ W cm^{-2}, in a 100 ps pulse, using a two beam Neodymium laser. A space resolving crystal spectrometer was used to record, separately, the X-ray emission spectra of the implosion core and the two regions of ablation plasma centred on the laser heated poles of the microballoon wall. Space resolution, down to 7 μm, was obtained by a narrow slit (6 μm) in the plane of dispersion (4).

Our analysis of the implosion core spectra is discussed in detail elsewhere (2 to 6). The transverse dimension of the core spectrum gave the core size. The electron temperature was deduced from the slope of the recombination continuum and the state of ionisation from the intensity ratio of high series member, optically thin, Hydrogen-like and Helium-like emission lines. At the densities encountered here Stark broadening predominates and this was calculated using the theory outlined in Reference 5.

An improved method of using the line profiles as a diagnostic has been developed. In general the spectral profiles depend on electron density N_e, optical opacity due to $N_1 L$ (ground state density x line of sight depth) and electron temperature T_e.

The dependence on T_e is weak and the temperature measured from the continuum slope has been used in the computation of the intrinsic Stark profiles. Experimental He-like and H-like line profiles are then compared with the line profiles calculated for a homogeneous plasma slab of variable Ne and $N_1 L$ to plot contours of quality of line shape fit in the plane defined by the axes Ne and $N_1 L$. The unique values of N_e and $N_1 L$ that give a fit to all the lines are then sought; thus determining the density (ρ) and the density x length product (ρR) in the implosion core. The plasma parameters of the compressed gas and the imploded glass have thus been measured by using the line broadening of He-like and H-like emission lines of Neon and Silicon respectively.

We report the first observations of the Stark broadening of the He-like Argon line, Ar XVIII $1^1S_o - 3^1P_1$ from the implosion core of an Argon filled microballoon. The line width implies (see figure 1) an electron density of 1.5×10^{23} cm^{-3} which is the same as that derived from an analysis of silicon emission from the imploded glass. The shorter wavelength of the Ar XVIII emission, relative to Ne IX and Ne X, is more suitable for the diagnosis of denser implosions.

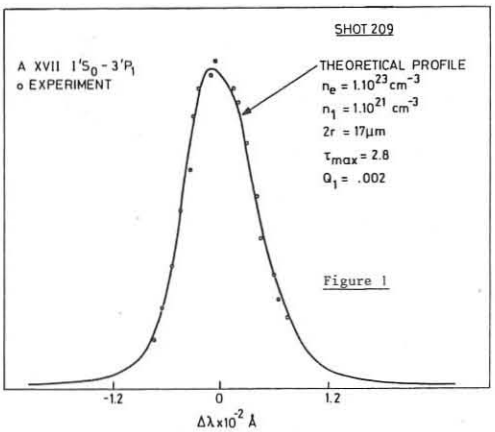

Figure 1

We also report the first observations of the time variation of the spectral profiles of Stark broadened x-ray emission lines from laser imploded, Neon filled microballoons. The spectrum was dispersed using Bragg reflection on to a very sensitive, low density Caesium Iodide photocathode of an X-ray streak camera. A short section of the spectrum in the region of NeX Lyβ was time resolved and is shown in figure 2(b). Here it was observed that the NeX Lyβ line emission was delayed with respect to the NaXI Lyα line from the ablation plasma and this delay (the implosion time) was dependent on the balloon size. The Stark broadening of the NeX Lyβ line was well resolved and the duration of emission was $\sim$ 250 ps. In a time resolved recording of the Si XIII $1^1S_o - 3^1P_1$ line from the ablation plasma (figure 2(a)) the linewidth was observed to change with time by a factor of $\sim$2 and the duration of emission was 500 ps. The continuum emission lasted for only 150 ps. These measurements can be used to check the validity of using time-integrated X-ray spectra to diagnose the plasma parameters in the ablation plasma and in the core of laser imploded microballoons.

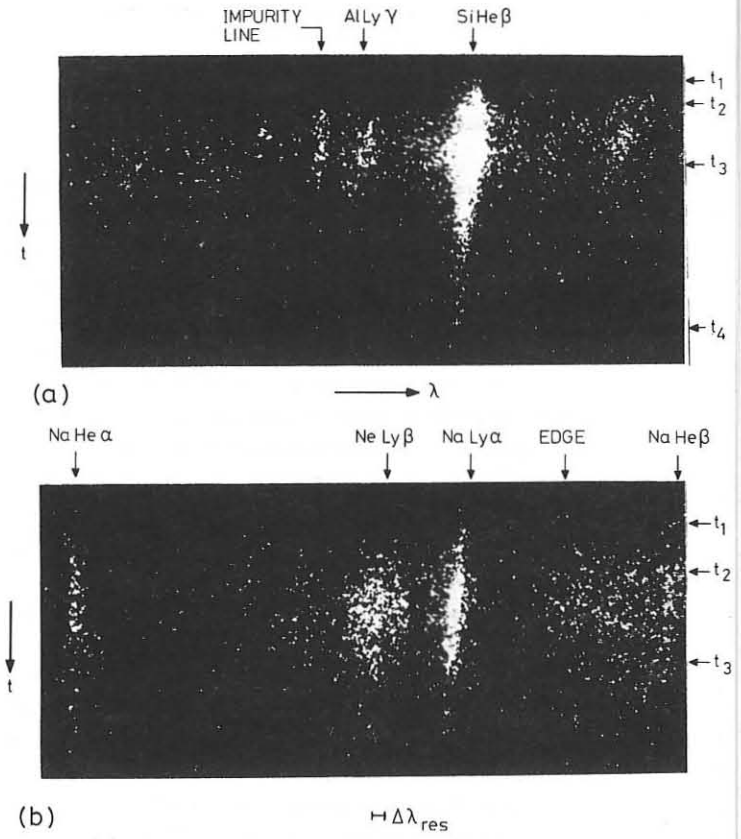

Figure 2
Streaked X-ray Spectra

(a) 0.2 μm Al coated microballoon with .64 μm thick glass wall and 52 μm diameter imploded with a 22 J 100 ps laser pulse.

(b) 64 μm diameter .72 μm wall thickness neon filled glass microballoon imploded with a 17 J 100 ps laser pulse.

Time scale: t_1 to t_3 in (b) is 320 ps.

* On leave from Queen's University, Belfast.

References

1. B Yaakobi et al, Phys Rev Letts Vol 39 No 24 1526 (1977)

2. M H Key et al, Rutherford Laboratory Report RL-77-122/B (1977)

3. R G Evans et al, J Phys B Letts 12 L213 (1979)

4. K B Mitchell et al, Phys Rev Letts Vol 42 No 4 232 (1979)

5. Rutherford Laboratory Laser Division Annual Report RL-780039 (1978) and RL-79-036 (1979)

6. M H Key et al, Rutherford Laboratory Report RL-79-014 (1979)

DP26

TRANSITION FROM ISENTROPIC TO ISOTHERMAL EXPANSION IN LASER-PRODUCED PLASMAS

A. Barrero and J.R. Sanmartín
E.T.S.Ingenieros Aeronáuticos
Universidad Politécnica de Madrid, Madrid-3, Spain

The expansion flow of plasmas produced by irradiating solid targets with laser light, changes non trivially as one moves from long, low intensity pulses to short, intense ones. In the first limit the neighbourhood of the plasma-vacuum boundary, which lies at a finite distance at any given time, behaves isentropically, and the electron temperature T_e vanishes there; in the opposite limit, and assuming quasineutrality and a short enough mean-free-path, the flow extends to infinity at any time, and T_e is non-zero and uniform in the rarefied plasma [1]. This transition has important consequences: in an isothermal expansion the above mentioned assumptions may break down, leading to phenomena such as significant ion acceleration or non-thermal electrons [2], undesirable for laser fusion.

We have found that the transition occurs, in a sense, discontinuosly. In a rising pulse, the rate of entropy generation in the absorption process increases with the laser irradiation $\phi(t)$. If the increase is slow enough, the plasma is able to convey away all the entropy produced, conduction been negligible outside the absorption region. The convection is less efficient if the increase is faster. There is a finite value of $\frac{d\phi}{dt}$, for a given plasma and a given laser frequency, above which conduction is important throughout the expansion, and the rarefied plasma is isothermal.

Consider, first, planar geometry, large ion number Z_i (to neglect ion pressure and thermal energy), absorption at the critical density n_c, and a pulse reasonably described by a rise time τ and a peak intensity ϕ_o ($\phi=t\phi_o/\tau=td\phi/dt$). The equations of motion for the ion-electron fluid are then

$$\frac{Dn}{Dt}=-n\frac{\partial v}{\partial x}\ , \qquad \frac{Dv}{Dt}=-\frac{Z_i k}{m_i n}\frac{\partial}{\partial x}n T_e\ ,$$

$$n T_e \frac{D}{Dt} k \ln\frac{T_e^{3/2}}{n}=\frac{\partial}{\partial x}\left(\bar{K} T_e^{5/2}\frac{\partial T_e}{\partial x}\right)+t\frac{d\phi}{dt}\delta(x-x_c)\ ;$$

$\bar{K}$ is Spitzer's conductivity coefficient, and other symbols have their usual meaning. Light is incident from $x=-\infty$ on the solid half-space $x>0$; since n_c is much less than the solid density we may analize the expansion assuming the ablation surface at $x=0$ at all times.

We have found that, for $d\phi/dt$ low, the (isentropic) plasma behaviour near the plasma-vacuum front ($x_{vac}\sim t^{4/3}$) is

$$n=C(1-x/x_{vac})^{3/7}, \quad v/\dot{x}_{vac}=1-(3/10)(1-x/x_{vac})\ ,$$
$$Z_i k T_e/m_i\dot{x}_{vac}^2=(7/40)(1-x/x_{vac})\ . \qquad (1)$$

The constant C decreases with increasing $d\phi/dt$, and vanishes at a finite value

$$(d\phi/dt)^*=0.14(27/8)k^{7/2}Z_i^{3/2}n_c^2/m_i^{3/2}\bar{K}\ . \qquad (2)$$

For $d\phi/dt$ slightly below $(d\phi/dt)^*$, i.e. C small, the approximation (1) fails very close to the front [$1-x/x_{vac}=O(C^{14})$] where the flow takes smoothly the form

$$n=\left(\frac{2}{3}\right)^{11/2}10\frac{\bar{K}m_i^{5/2}}{k^{7/2}Z_i^{5/2}}\left(\frac{x_{vac}}{t^{4/3}}\right)^3\left(1-\frac{x}{x_{vac}}\right)^{1/2},$$
$$\frac{v}{\dot{x}_{vac}}=1-\frac{1}{3}\left(1-\frac{x}{x_{vac}}\right), \quad \frac{Z_i k T_e}{m_i\dot{x}_{vac}^2}=\frac{1}{6}\left(1-\frac{x}{x_{vac}}\right). \qquad (3)$$

As $d\phi/dt$ approaches $(d\phi/dt)^*$ from below (C→0), the thickness of the isentropic region (1) adjoining the front collapses to zero, so that, at the value $(d\phi/dt)^*$ the behaviour at the front is the (non-isentropic) limiting one given by (3). For $d\phi/dt>(d\phi/dt)^*$ there is no solution with finite x_{vac}; n decays exponentially to zero at $x=-\infty$ where T_e takes a finite value shown in Fig 1 for values close to $(d\phi/dt)^*$. Figure 2 shows schematically n and T_e versus x.

The ratio of heat flow to internal energy convection flow

$$r\equiv\frac{\bar{K}T_e^{5/2}\partial T_e/\partial x}{(3/2)n k T_e(dx/dt|_n-v)}\ ,$$

[convection measured in a frame where the local density is constant: $dx/dt|_n\equiv-(\partial n/\partial t)/(\partial n/\partial x)$] is an index of the non-isentropic character of the flow. For $d\phi/dt<(d\phi/dt)^*$ (C given) we have $r\to 0$ as $x\to x_{vac}$; on the other hand, $r\to\infty$ as $C\to 0$, for any given, small $(1-x/x_{vac})$. At the transition (C=0), $r\to 1/30$ at the front. For $d\phi/dt>(d\phi/dt)^*$, we have $r\to 35/30$ as $n\to 0$.

We found the preceding results valid for finite Z_i, though the numerical value 0.14 in (2) may change. A similar conclussion should follow from an analysis allowing absorption at densities below critical. We found that in spherical geometry the characteristic radius leads to an effect similar to the present one, even in steady conditions. For a structured pulse $d\phi/dt$ may change dramatically in time; condition $d\phi/dt=(d\phi/dt)^*$ should mark the time of transition from isentropic to isothermal flow. Notice finally that short-wavelength lasers and high Z_i plasmas ($\bar{K}\sim Z_i^{-1}$) allow fast-rising pulses below transition.

REFERENCES

[1] J.R. Sanmartín and A. Barrero, Phys. Fluids 21, 1957 (1978); 21, 1967 (1978).

[2] J.E. Crow, P.L. Auer, and J.E. Allen, J. Plasma Phys. 14, 65 (1975); J.S. Pearlman and R.L. Morse, Phys. Rev. Lett. 40, 1652 (1978); R. Decoste, N.R.L. Mem. Report 3774 (April 1978).

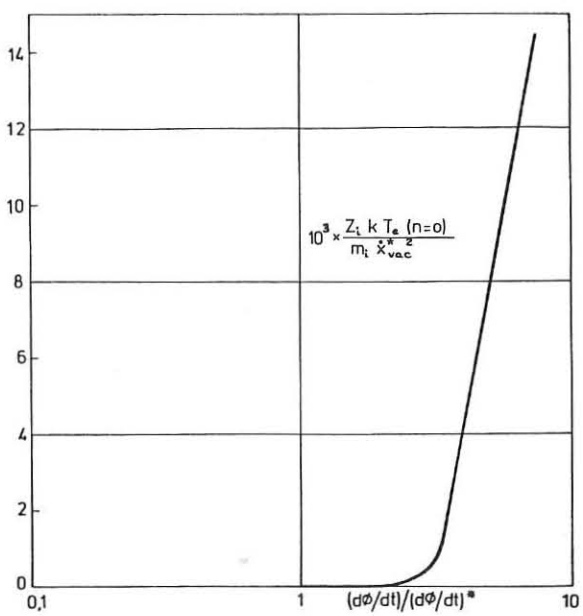

Fig. 1. T_e at vanishing density above transition; $\dot{x}_{vac}^*=\dot{x}_{vac}$ at transition.

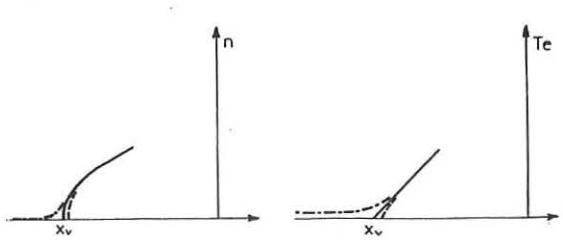

Fig. 2. Schematics of n and T_e for $d\phi/dt$ just below (----), at (——), and just above (-·-·-) transition.

CHARACTERIZATION TECHNIQUES FOR HIGH QUALITY ICF TARGETS*

B. W. Weinstein and C. D. Hendricks

University of California
Lawrence Livermore Laboratory
Livermore, California 94550 U.S.A.

To obtain fusion targets which have the required symmetry and surface quality for inertial confinement fusion, it is necessary to develop adequate target measurement techniques. These techniques are necessary both to provide feedback during development of the fabrication procedures, and to inspect the final product. In this paper we outline the resolution and speed which must be met and review the capabilities of techniques currently in use and under active development. We also suggest some possibilities for future research and implications for power plant production processes.

Consider a simple target (Fig. 1) consisting of an inner fuel region surrounded by a hollow shell of high density "pusher" and an outer layer of "ablator". If one part of the pusher or ablator wall is initially thicker than the other, then as the pellet is imploded, the thick side will lag behind the other and the implosion will not converge symmetrically. Also, the imploding pellet is subject to fluid instabilities. Small perturbations on the surface grow exponentially in amplitude as the pellet is compressed and can cause breakup of the imploding shell.

The growth rate of the perturbation is dependent on its initial lateral dimensions or "wavelength." From computational analysis of fusion implosions, one can generate a plot of the maximum allowable initial amplitude for a perturbation as a function of perturbation wavelength. Figure 2 shows such curves for two different target sizes. The smaller size is appropriate for current lasers (10 kJ), while the larger target would be appropriate for more powerful lasers (100 kJ). While the actual allowable defect amplitudes depend on the specifics of the pellet construction and the implosion process, the general shape of the curve will apply to all targets of roughly the same size.

Curves such as those shown in Fig. 2 are very useful in deciding which characterization techniques should be pursued for fusion targets. Generally when one considers the "resolution" of a measurement technique, one thinks only of the spatial resolution. In evaluating techniques for fusion targets, however, a more important parameter is the sensitivity of the technique for defects with a very low amplitude and a relatively long wavelength. The basic task in characterizing fusion targets is to develop a set of techniques with a combination of spatial and amplitude resolution which covers the entire "defect space" shown in Fig. 2.

Currently the three primary techniques for measuring the uniformity of inertial fusion targets are optical interference microscopy, microradiography, and scanning electron microscopy. Figure 3 shows the approximate resolution limits which can be achieved with these three measurement techniques if they are fully developed. With the combined coverage of all three techniques, most of the relevant defects can be detected. Other techniques which can be used to supplement the above methods are acoustic microscopy, mechanical stylus measurements, air balancing, and destructive sectioning.

In addition to the resolution requirements, the techniques should be nondestructive and must be fast enough to allow complete characterization of a target sphere in an acceptable length of time. The speed constraint becomes particularly important when the techniques are used for sorting pellets as well as for final measurements.

We have underway a program to develop all of the above techniques to the maximum achieveable resolution and to automate the measurement procedures in order to provide the necessary speed. The first fully automated system for mapping a sphere with transmission interferometry was completed recently. A schematic of the system is shown in Fig. 4. This system employs computer control of both the manipulation and the phase measurement to map the wall thickness variations of a target microsphere. The data is stored on a flexible disc cartridge and can be displayed immediately or saved for later analysis. The entire time to map a 200 μm diameter sphere with 2 μm spatial resolution and 10 nm thickness resolution is less than one minute. We have also completed an automated scanning electron microscope and automation of radiographic measurements is under intensive development.

An important future issue is what type of characterization techniques might be incorporated into a power plant. It has been our experience that most types of defects, once they have been identified, can be eliminated by careful control of the production process. Some defects are more difficult to control than others, however, and it may be that for some fabrication processes, elimination of specific types of defects may be too difficult or expensive.

Our general approach is twofold: For the near term, while inertial fusion is in an experimental stage, we are pursuing measurement techniques which are capable of locating and measuring all possible defects but which are not fast enough to be used for sorting large numbers of targets. For the long term, we plan to determine which types of defects cannot be eliminated by fabrication process control and then build highly specialized, rapid sorting systems which do not detect all possible defects but which can discriminate against pellets with a specific type of defect. Such systems could be fast enough and inexpensive enough to be included in the target production sequence for a reactor.

*Work performed under the auspices of the U.S. Department of Energy by the Lawrence Livermore Laboratory under contract number W-7405-ENG-48.

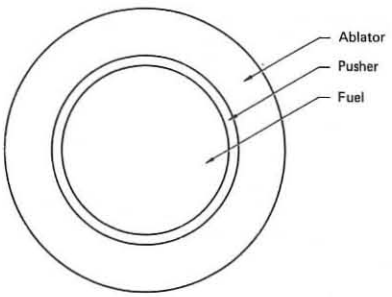

FIGURE 1. Basic structure of an inertial fusion target. To obtain high density compression of the fuel, the pusher and ablator layers must be extremely uniform.

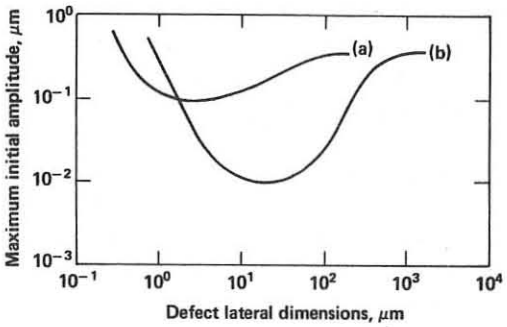

FIGURE 2. Pellet wall uniformity requirements. Curve (a) is for a target approximately 200 μm in diameter with a 20 μm thick wall. Curve (b) is for one 600 μm in diameter and 50 μm thick. The smaller size pellet is appropriate for current 10 kJ lasers, while the larger pellet would be appropriate for a 100 kJ laser.

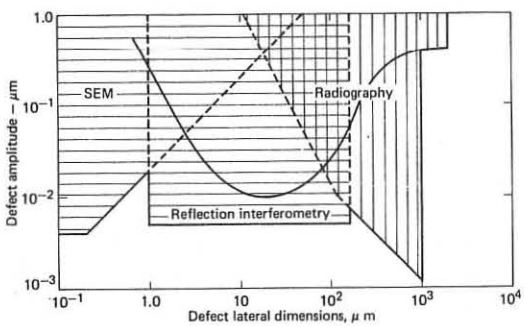

FIGURE 3. Resolution limits attainable with three common target measurement techniques. The horizontal hatching indicates a surface contour measurement while the vertical hatching indicates a wall thickness measurement. Ideally, one should be able to make both measurements over the entire defect space which is of interest.

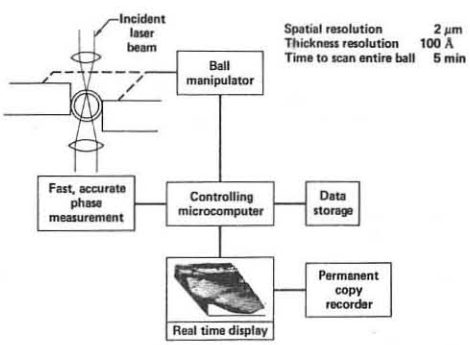

FIGURE 4. Block diagram of TOPO-II, an automated interferometric mapping system currently used to measure fusion pellets. This is one of several automated characterization techniques being developed at Lawrence Livermore Laboratory.

DP28

AXIAL VARIATION OF THE ENERGY TRANSFER FROM AN INTENSE RELATIVISTIC ELECTRON BEAM TO A PLASMA

A.E.Dangor, A.K.L.Dymoke-Bradshaw, G.S.Kerslick, P.Šunka*
Blackett Laboratory, Imperial College, London, U.K.
*Institute of Plasma Physics, Czechoslovk Acad.Sci.,Prague 9.

Experiments investigating the interaction of intense relativistic electron beams and plasmas indicate that appreciable plasma heating is possible under certain conditions. At Imperial College a 350kV, 15kA cm^{-2} and 100ns duration beam ($^{v}/_{\gamma}$ ∿2.4) is injected into a chamber containing neutral hydrogen, at pressures from 0.05 to 1 Torr, immersed in an axial magnetic field of ∿ 1.5T.

Diagnostics used have been ruby laser scattering ($\alpha<<1$) for n_e and T_e, Stark and Doppler broadening of the H_α and H_β lines for T_i and a check on n_e, beam and net currents for the return current dissipation ($= \int \underline{j}_p.\underline{E}_z\, dt$) in the plasma and the plasma diamagnetism for the total perpendicular plasma energy density.

Previously reported results[1] indicate that the return current dissipation and plasma diamagnetism is strongly dependent, especially at lower fill pressures, on both the input beam angular scatter and the beam rise time. The deposition is higher for fast rising beams and aluminised Mylar anode foils. In addition under these conditions the return current deposition rate peaks later at 30ns from the start of beam injection, compared with 20ns under other conditions. The return current deposition makes a significant contribution to the total plasma energy density under these conditions. In addition the measured resistivity falls far slower and is anomolous under these conditions.

The dependence of the return current dissipation on the beam angular scatter introduced by the foil implies a non-linear interaction, (Thode[2] and Papadopolous[3]). According to this theory Langmuir turbulence generated directly by the beam, decays parametrically to produce a high level of ion acoustic turbulence and hence an enhanced resistive dissipation of the return current. A "cold" unscattered beam will produce a high level of Langmuir turbulence.

In this paper we report results of the axial dependence of the plasma diamagnetism and laser scattering results and also some work on fast ion production. Fast ions are important because they are responsible for ionization in the early stages of the interaction and control the overall temporal history of the plasma number density.

Results of the plasma diamagnetism at two axial positions and for two types of anode foil are shown in Fig.1. It is apparent that for aluminised Mylar anodes, over the whole pressure range investigated, the total plasma energy density is some 2-3 times higher at position 1 (2cm from the foil) than at position 2 (13cm from the foil). Plasma diamagnetism is always small with the 25μm thick aluminium anode foil. This is consistent with the non-linear description of the interaction according to which the plasma turbulence acts back on the beam increasing its mean scatter angle and reducing the growth rate of Langmuir waves downstream. Some diamagnetism waveforms are shown in Fig.2. The signal has a period of either ∿ 250ns or ∿ 500ns, the longer period being observed at position 1 and with aluminised Mylar foils.

Whilst the diamagnetic results indicate significantly different plasma conditions near the anode, the laser scattering results do not. Typical densities and electron temperatures are ∿ $5.10^{15} cm^{-3}$ and 5eV respectively near the foil. Somewhat higher temperatures, 5-10eV, but the same densities have been observed downstream. It should be noted that the laser scattering results are only available at times later than ∿ 80ns, which is about 50ns later than the peak return current dissipation rate.

Measurements of fast ions produced have been observed with a Faraday cup, screened from the applied magnetic field and with a localized transverse magnetic field to reject electrons. Observations show that with aluminium foils a short burst of energetic ions ∿ 200keV is generated at the time of beam injection. At very low pressures some ions were detected from shots with aluminised Mylar foils. The number of ions produced decreases with increasing fill pressure. This could be due in part to charge exchange losses. The implications here are that the ionization rate with aluminised Mylar foils will be lower and that the ratio n_b/n_p will remain higher longer permitting a fast growth of the Langmuir waves. It is not clear which effect is dominant, beam scatter in the foil or changes in the ionization rate. More work is required to independently vary the beam scatter and ion production.

REFERENCES

(1) A.K.L. Dymoke-Bradshaw et al. Plasma Physics and Controlled Nuclear Fusion. Vol II, 555 (IAEA, 1977).
A.K.L. Dymoke-Bradshaw et al 2nd International Topical Conference on Electron and Ion Beam Research and Technology, Cornell. 1977.
(2) L.E. Thode and R.N. Sudan. Phys.Fluids 18, 1552 (1975)
(3) K. Papadopolous. Phys.Fluids 18, 1769 (1975).

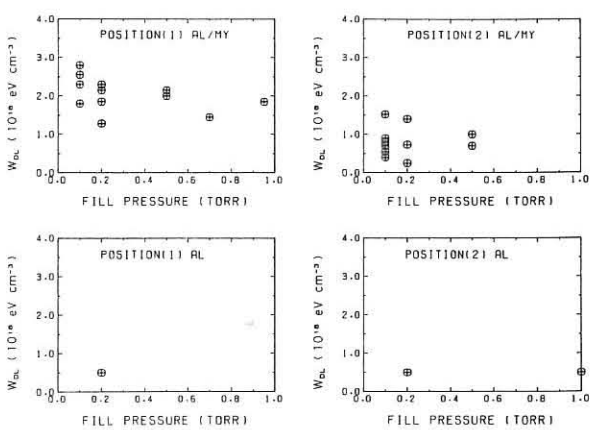

Fig.1 Diamagnetism v. pressure for 4 conditions.

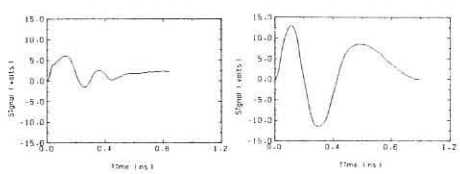

Fig.2 Diamagnetic Traces showing change of period.

DP29

APPLICATION OF INTENSE RELATIVISTIC ELECTRON BEAMS TO STEADY STATE TOKAMAKS

V. Bailey, J. Benford, and H. Helava
Physics International Company
San Leandro, California 94577

Use of intense relativistic electron beams (REBs) has been proposed for (1) starting up or maintaining the toroidal current in an essentially steady-state tokamak reactor[1-2]; (2) producing the confining magnetic fields for the plasma[3-6]; (3) rapidly heating the plasma to ignition conditions[7]; and (4) providing start-up plasma heating and current maintenance for a steady-state, compact, high β tokamak[8-9]. This paper discusses the periodic injection of an intense REB to maintain the toroidal current in a tokamak reactor and thus permit a steady-state mode of operation.

Prior to REB injection the toroidal plasma currents are decaying due to resistive dissipation. The REB is injected parallel to the toroidal magnetic field and trapped in the toroidal plasma column by drift-injection, energy-loss trapping[10-13]. When the REB is injected in the same direction as the original plasma electron drift, the REB induces a back emf which reduces the plasma electron drift velocity so as to maintain the net current (the plasma current plus the REB current) approximately constant.

Since the injection time of the REB is much longer than the transit time of a relativistic electron around the torus, the REB wraps up on itself and as a consequence the circulating REB current can be much larger than the injected REB current. At the end of beam injection, the counterstreaming plasma electron current cancels a portion of the beam current and the net current is approximately equal to the intial net current. As the counterstreaming plasma current is dissipated by the frictional force between the plasma electrons and ions, the absolute magnitude of the plasma electron current decreases, and the counterstreaming plasma current cancels less and less of the beam current. This effect causes an increase in the magnitude of the net toroidal current. The rising net toroidal current induces a toroidal electric field, which takes kinetic energy out of the REB and drives the plasma current. Thus, a portion of the beam kinetic energy is dissipated in increasing the poloidal magnetic fields, and a portion is dissipated in plasma heating by maintaining the decaying currents.

After the REB energy has been significantly degraded the relativisitc electrons give up their momentum to the background plasma electrons by coulomb collisions. Because of the strong inductive coupling of the beam-plasma system the net current will remain constant during this momentum transfer. The extension of this scenario to the case in which there is no initial plasma current (i.e., start-up) is straightforward and is not discussed here.

Simple formulas for calculating the increase in the net toroidal current per injected REB pulse, the time scale for this increase, and the fraction of the injected beam energy which appears as increased poloidal magnetic field energy are presented. The increase in the net toroidal current is a linearly increasing function of the kinetic energy of the injected REB and is inversely proportional to the inductance per unit length of the beam-plasma system. For example, in a reactor geometry, injection and trapping of a single pulse of a 15-MeV intense REB will increase the net toroidal current by 1 MA, while four pulses of the same beam will produce an increase of $\sim$ 4 MA. The time scale for this increase in net toroidal current is shown to be significantly shorter than the normal L/R decay time of of the plasma. The fraction of the injected REB energy that is initially converted to poloidal magnetic field energy or plasma heating can be adjusted by changing the parameters of the injected REB.

For the application of REB current drive to a tokamak reactor, the UWMAK III reactor was considered. The average power of the injected REB required to maintain the 15.6 MA toroidal current in the reactor was found to scale inversely with the kinetic energy of the injected REB. The periodic injection of a 6.6-MV REB with an average power of 1.5 MW could maintain the 15.6 MA of toroidal current in UWMAK III. In this example approximately 80% of the injected beam energy is converted to increased poloidal magnetic field energy.

The technology of REB generators is such that significant experiments can be carried out immediately. Overall electrical efficiency from energy store to beam of > 50% has been demonstrated. The key factor for the future is repetitive beam generation and injection, which will be accomplished first in a burst of a few pulses. High frequency burst mode pulses are produced by charging lines from separate Marx generators. The lines are connected by triggerable gas switches so that the pulses can be fired in succession down a transmission line. To date this method has produced three pulses of 1.5 MV, 80 kA and 40 ns with pulse separation of 10^{-7}-10^{-3} sec.[14] Therefore, considerable flexibility in the injection sequence can be obtained.

Energy is brought through the field coils of the tokamak by a magnetically insulted transmission line at > 10^{10} W/cm^2. Experiments have shown $\sim$ 90% efficient energy transmission over distances of several meters. A plasma diode is used to avoid anode foil rupture and contamination from impurities. A low density plasma at ground potential is in contact with the cathode. As the pulsed current depletes ions from the plasma immediately in front of the cathode, the diode gap grows and an REB is emitted. This scheme allows repetitive REB injection at high frequencies. Repetitive CW systems are now under development and have achieved kHz operation[15].

The major technical areas requiring further research are outlined and suggestions are made for experiments directed toward a steady-state reactor.

REFERENCES

1. K. Ikuta, Jap. J. Appl. Phys., II, 1684 (1972).

2. V. Bailey, Steady-State Current Drive In Tokamaks Workshop Summary, DOE/ET-0077, National Technical Information Service (NTIS), Springfield, Virginia (February 1979).

3. S. Yoshikawa, Phys. Rev. Letters, 26, 295 (1971).

4. S. Yoshikawa and N. Christofilos, Proceedings of the Fourth International Conference on Plasma Physics and Controlled Nuclear Fusion Research, Vol. 2, p. 357, held in Madision, Wisconsin (1971); published by International Atomic Energy Agency, Vienna, Austria (1972).

5. C. W. Hartman, Phys. Rev. Letters, 267, 14, 826 (1971).

6. S. Yoshikawa, Bull. Am. Phys. Soc., p. 996, (November 1971).

7. D. Hammer and K. Papadopoulos, Nuclear Fusion, 15, 977 (1975).

8. V. Bailey, R. Cooper, and T. S. T. Young, Third International Topical Conference on High Power Electron and Ion Beam Research and Technology, July 3-6, 1979, Novosibirsk, USSR.

9. Y-K. M. Peng and R. A. Dory, Oak Ridge National Laboratory Report, ORNL/TM-6535 (October 1978).

10. J. Benford, B. Ecker, and V. Bailey, Phys. Rev. Letters, 33, 574 (1974).

11. M. Masuzaki, et al., Jap. J. Appl. Phys., 14, 1413 (1975).

12. V. Bailey, Proceedings of the International Conference on Synchrotron Radiation and Runaway Electrons in Tokamaks, held in College Park, Maryland (1977).

13. A. Mohri, et al., Proceedings of the Fifth International Conference on Plasma Physics and Controlled Fusion Research, IAEA-CN-37-X-5, held in Innsbruck, Austria (1978).

14. D. Cummings and H. Hammon, Proceedings of the Second IEEE International Pulsed Power Conference, Lubbock, Texas (June 1979).

15. R. Sojka, G. Simcox, and D. Cummings, Proceedings of the Second IEEE International Pulsed Power Conference, Lubbock, Texas (June, 1979).

DP30

A NUMERICAL STUDY ON WAVE SHAPING IN REB DIODES

S.SINMAN

Middle East Technical University
Electrical Engineering Department
Plasma Engineering Laboratory, Ankara - TURKEY

A.SINMAN

Ankara Nuclear Research and Training Center
Electron Physics Laboratory, Ankara - TURKEY

Abstract: In this study, using a numerical method and bearing in mind Child-Langmuir and parapotential models with low and high I_B/I_A ratios the electrical characteristics of foil and foilless diodes driven by a charged line, have been investigated. The simulation algorithm is based on the theory of transmission line, the dynamics of cathode plasma and formulation of De Packh.

Introduction: In REB machines, in the case of inertial confinement short termed (FWHM=10 nsec.), but on the other side in magnetically confinement at the order of μsec. beam pulses are required. The problem of beam shaping also rises at inductive effects of collective ion acceleration /1/ and TEA lasers schemes /2/. Showing a time varying and non-linear properties, the REB diodes make difficult to control the current pulse shaping. It is clear that, for a constant storage energy in the system consisting of Marx or Tesla resonant transformer, for a solution with a best efficiency an convenient to an aim of research problem, it is necessary to know the characteristics of REB diodes. In other words, it can also be called as the optimization of REB diodes. Among the results obtained, depending on above consideration, determination of the condition to obtain the square wave current pulse and other characteristics of the REB diodes are present. Consequently, these computational finding, taking into account the different application fields of REB have been discussed.

Numerical Scheme: The parameters of actual REB system is in time-varying and non-linear features. For this reason, the mathematical model would be dynamical. In simulation algorithm, the general system parameters or its identity should be described with $X_y(t_j)$ or with X_y^j.

Here, y is generally symbolizing a component of the REB system. The sampling time dt, is equal to $t_{j+1} - t_j$ or to its foldings $t_{j+1}/(j+1)$ depending on j, where $j=0, 1, \ldots, n$. In some situation it has been used the symbol of $j+1=k$. The results of the analytical solution have been written in time-domain based on above concepts. The expression used are as follows:

The diode impedance; $$R_d^{j+1} = 136(d_{ac} - v_p t_{j+1})^2/(v_L^k)^{1/2} R_c^2 \qquad (1)$$

The line voltage; $$V_L^{j+1} = V_L^j R_d^j (R_d^j + Z_o) e^{-A^j}, \quad A_j = t_j (\mathrm{Log}_e \Gamma_j^{-1}) t_L^{-1} \qquad (2)$$

The diode voltage; $$V_d^{j+1} = 2V_L^k (a^k/b^k) \exp[-a^k t^k \sinh(b)^k t^k] \qquad (3)$$

where, $a^{j+1} = R_d^{j+1}/2L_c$ and $b^{j+1} = (1/2L_c)[(R_d^k)^2 - 4L_c/C_o]^{1/2}$.

According to Child-Langmuir model, the diodecurrent may be calculate from equations (1) and (3). As to parapotential model /3/, the current passed in high I_B/I_A diodes is, $I_d^k = 8500(R_c/d_{ac})(V_b/c)^k \mathrm{Ln}[\gamma^k + (\gamma^2-1)^{1/2}]\gamma_k^2$ where; $\gamma^k = 1 + 1.96\times10^{-6} V_L^k$ and $(v_b/c)^k = [1-(1/\gamma_k^2)]^{1/2}$. (4)

The symbols used above expression are: diode impedance R_d; anode cathode gap d_{ac}; velocity of cathode plasma v_p; line voltage V_L; cathode radius R_c; characteristic impedance of line Z_o; reflection factor Γ; diode voltage V_d; cathode inductance L_c; capacitance of line C_o; diode current I_d; beam velocity v_b; velocity of light c; relativistic mass factor γ; time constant of line t_L.

Results of Computational Experiments: Two fundamental construction, being foil and foilless diodes, have been taken into attention. As a dielectric medium deionized water (K=82) is accepted. Because of a few alternative given values of Z_o (2, 5 and 7 ohms) and C_o(5400, 7200 and 18000 pFs), two-way travelling time of transmission line (TWTT = t_L) have changed between the highest and lowest values of 181 nsec. and 21.62 nsec. The values of R_d are generally being greater than Z_o. At such construction, taking into account the dynamic of the cathode plasma too, it has been convenient to carry out the computational experiment, using low sampling times ($t_L/16$). Serial cathode inductances (5 nH - 100 nH) have not influenced the wave shaping but it has only changed the rise time of current pulse (2 - 10 nsec.). Wave shaping are being affected by V_L and R_c for constant d_{ac}. Normalized beam currents versus time are seen in Fig.1

and Fig.2. In the model of De Packh, using a transmission line at the same specification (Z_o=5 ohms, C_o=18000 pF, t_L=181 nsec.), keeping constant the line voltage [$V_L(o)=10^6$v] and cathode radius (R_c=1.0 cm), beam currents of 69.7 kA and 78.1 kA, corresponding to cathode inductances of 30 nH and 10 nH have respectively been found. For these conditions, diode efficiencies and diode impedances are 77 %, 84 % and 7.84 ohms, 7.80 ohms respectively. At the end of the first TWTT, very close voltage values such as 31.7 kV [$0.032V_L(o)$] for L_c=30 nH and 27.5 kV[$0.028V_L(o)$] for L_c=10 nH have been obtained. Thus guarding the value of cathode inductance in reasonable limits, the waveform and the performance of a REB system for high I_B/I_A are not considerably effected even if for instance its value rises three times. Computational results without changing all of the parameters except the capacitance of transmission line are given in Table 1. In both cases (C_o=5400 pF and C_o=18kpF), while the cathode radius to be increased, the diode current and the efficiency are also increased. Very close beam current values such as 117 kA (C_o=5400 pF) and 128 kA (C_o=18kpF) for R_c=1.50 cm are intresting. But here it must never be forgotten that TWTT's are 21.62 nsec. and 72.02 nsec. (for the case of Z_o=2 ohms). Beyond of this, at the end of the first TWTT, the voltage across the transmission line is dropped to 184 kV for C_o=5400 pF and to 138 kV for C_o=18kpF. These values are 18% and 14% of initial value of line voltage respectively. On the other hand, at the end of second TWTT, these ratios are found as 2.8 % and 1.6 %. Thus in return to be high of beam current, in wave-shaping there exist an important second voltage step with a level of 14 - 18 %. At above given example for Z_o=5 ohms, Γ reflection coefficient is 0.183 whereas at last example it is 0.414. Consequently, it could be noted that the mismatch is more effective on wave-shaping than all of other parameters. Beside the expected effect on t_r rise time of cathode inductance, the increase of t_r as the cathode radius increasing, is an other intresting feature demonstrated by the numerical study.

Conclusion: (i) Using the model of Child-Langmuir in the diodes with low I_B/I_A ratio; selecting convenient cathode radius, line voltage, and TWTT, it would be possible to control the wave-shaping although there exist mismatch; (ii) In the diodes of high I_B/I_A, it has been understood that the cathode inductance (provided that it remains in definite limits) is not so important as expected. At ungated beam mode of operation, from this way constructional facility could be supplied; (iii) In the case of cullective ion acceleration, controlling both of the limiting current of diode to be used and wave-shaping, the optimum operational conditions may be determined; (iv) For TEA lasers, optimizing the interface between REB diode and laser cavity, higher electrical efficiency can be obtained. The same procedure is applicable for microwave generation.

Table 1

L_c=10nH, Z_o=2 ohms, C_o=5.4kpF			L_c=10nH, Z_o=2 ohms, C_o=18kpF		
R_c=0.50 cm.	1.0 cm.	1.50 cm.	R_c=0.50 cm.	1.0 cm.	1.5 cm.
38.5 %	* 53.2 %	57 %	40.7 %	* 60.4 %	67.0 %
I_d=56.9 kA	93.3 kA	117 kA	I_d=58.6 kA	100 kA	128 kA

* Efficiency

References: /1/ Olson, C.L., IEEE Trans.Nucl. Sci. NS-22 No.3 962 (1975); /2/ Harris, N.W., et al., Rev.Sci.Instrum., Vol.48 No.8 1042 (1977); /3/ De Packh, D., Naval Research Lab., Radiation Proj. Int. Rep. 7 (1968).

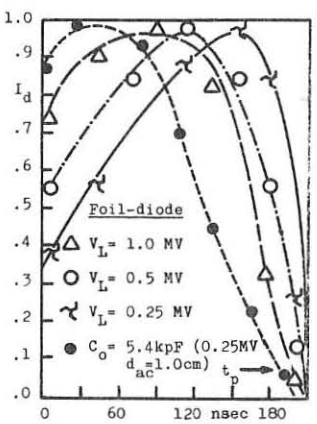

Fig.1 (C_o= 18kpF, t_L= 181 nsec., dt = 22.6 nsec., L_c= 100nH, Z_o= 5 ohms, R_c= 1.0 cm., d_{ac}= 1.0cm.

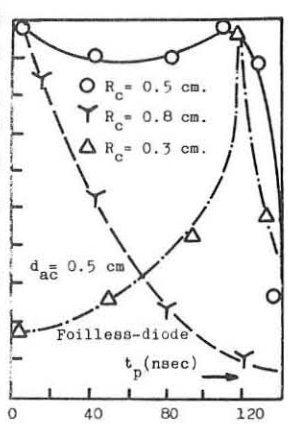

Fig.2 (C_o= 5400 pF, V_L= 0.5 MV, L_c= 50nH, t_L = 54.2 nsec., Z_o= 5 ohms, dt = 13.6 nsec.

DP31

FORMATION OF A REVERSED-FIELD PLASMA CONFIGURATION WITH A ROTATING RELATIVISTIC ELECTRON BEAM

by

J.D. Sethian, K.A. Gerber, D.N. Spector & A.E. Robson

Naval Research Laboratory, Washington, D.C. 20375 USA

Introduction

The use of relativistic beams to create field-reversed configurations was first proposed by Christofilos.[1] In his Astron concept, the field-reversing currents were carried by the relativistic electrons. This paper describes a different application, in which the relativistic electron beam is used to induce plasma currents, which maintain a field-reversed configuration after the beam has passed out of the system.

Modern pulse generators, coupled to field-emission diodes, can readily produce electron beams that will reverse an applied magnetic field.[2,3,4] Rotating beams can also propagate in a closed metal tube in the absence of an applied magnetic field.[5] When injected into neutral hydrogen at a pressure of about 150 mTorr, the beam produces enough plasma to neutralize its charge but not enough to neutralize its current. The radial equilibrium of the beam is then determined by a balance between the centrifugal forces and the interaction of the beam with its self-field. This arrangement automatically produces a field-reversed configuration. The passage of the beam increases the electron temperature, so that when the beam leaves the system its magnetic field is frozen into the plasma, and persists for a time determined by resistive dissipation of the induced plasma currents.

Beam Propagation

Studies of beam propagation have been carried out in the apparatus shown in Fig. 1. The rotating beam is produced by first forming a hollow

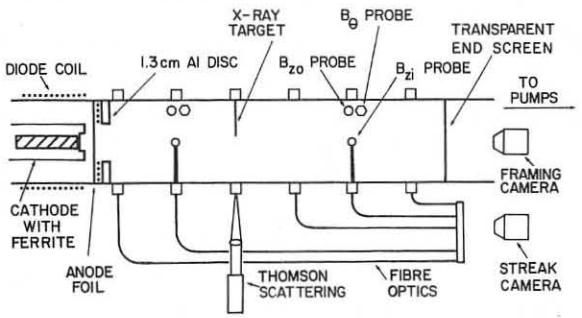

Fig. 1. Experimental Apparatus

cylindrical beam (V_o = 900 kV, I = 100 kA, τ = 100 nsec) with an annular diode immersed in a uniform axial magnetic field, and passing it through a half-cusp in which the field is brought to zero in a short distance. The half-cusp is created by a pulsed coil and a flux-excluding aluminum disc. The rotation of the beam arises from the interaction of the axial velocity with the radial field of the half-cusp.

A simple model has been developed[6] to describe the radial equilibrium of a thin, hollow beam as it propagates down the tube. The model takes into account the balance between the centrifugal and magnetic forces and uses conservation of flux, Ampere's Law and conservation of canonical angular momentum to give the following relations:

$$r_b/r_w = \left(\frac{1 - \cot^2\alpha + \gamma/\nu}{2}\right)^{1/2} \qquad (1)$$

$$r_b^2 B_{zi} = r_c^2 B_c \left(\frac{1 + \cot^2\alpha - \gamma/\nu}{1 + \cot^2\alpha + \gamma/\nu}\right) \qquad (2)$$

$$cr_c^2 B_c/2Ir_w = \left(\frac{\tan^2\alpha(\gamma/\nu + 1) - 1}{2}\right)^{1/2}\left(\frac{1 + \cot^2\alpha + \gamma/\nu}{2}\right) \qquad (3)$$

where r_c, r_b, r_w are respectively the radii of the cathode, the beam and the tube, I is the beam current, B_c is the field at the cathode, B_{zi} is the axial field inside the beam, α is the pitch angle of the beam current and $\gamma/\nu = \gamma m_o c^2/Ne^2$, where N is the line density of electrons in the beam. Equation (3) shows that for dense beams ($\gamma/\nu \ll 1$) the pitch angle is determined by I/B_c and the geometry, and the beam radius is then determined by Equation (1). For dense beams the beam current takes up a nearly force-free configuration.[7] Equation (2) shows that the axial flux inside the beam is equal to the flux in the cathode to $O(\gamma/\nu)$. The beam may thus be regarded as stretching out the field lines from the half-cusp, as shown schematically in Fig. 2.

The velocity of propagation of the beam, v_b, is determined by the balance between the injected power and the power required to create new beam. This leads to[6]

$$v_b \approx V_o/LI \qquad (4)$$

where L is the inductance per unit length, which in turn depends on α.

In the experiments, $v_b \sim 0.05 - 0.1c$, that is, the beam propagates much slower than the velocity of the injected electrons (0.94c). This is not simply on account of the spiral current path, since α is, typically, 50°-60°. The fast electrons from the diode are reflected by the radial magnetic field B_r at the beam head (Fig. 2). They return to the diode, and are re-injected into the beam. The electrons lose energy in their successive collisions with the moving beam front, and this energy goes into creating new magnetic field. The beam density is enhanced by this reflexing process, and the condition $\gamma/\nu \ll 1$ is easily satisfied. By making the length of the beam, $v_b\tau$, equal to the length of the experimental tube, the energy of the beam may be converted into magnetic field energy with efficiency $\geq$ 50%. Equations 1 through 4, which have been verified experimentally,[6] provide a prescription for setting up a magnetic configuration inside a conducting tube with azimuthal and reversed axial fields, that is to say a linear reversed-field pinch.

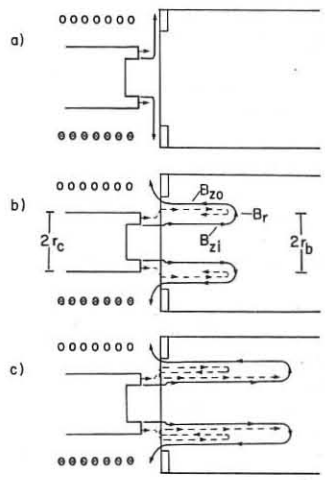

Fig. 2. Stages in the Propagation of the Rotating Beam

a) Beam injected through half-cusp.

b) Field lines stretched out into tube.

c) Electrons execute multiple reflections between beam front and diode. Electron energy → magnetic energy.

Solid lines: magnetic field lines.

Dotted lines: electron trajectories.

(B_θ field not shown)

Plasma Behavior

The beam breaks down the gas and produces a partially-ionized plasma in which the electrons are heated by beam-plasma interaction. Shortly after the passage of the 100 ns duration beam, the ionization is complete and the electron temperature is, typically, ~ 5 eV[8]: the magnetic configuration, maintained now by plasma currents, decays over a period of 20 μsec. The history of the configuration can be seen in Fig. 3, which shows traces from three pairs of magnetic probes at 20, 40 and 60 cm respectively from the diode. The beam creates an azimuthal magnetic field B_θ = 2.5 kG and an external axial field B_{zo} = 1.0 kG at each position. Over a period of 5 μsec, a rearrangement of the configuration occurs, in which B_{zo} increases by a factor of two at the end furthest from the diode, and B_θ decreases by about the same factor along the entire length. The axial current is still continuous, but its pitch angle now varies with axial position. This re-arrangement is analogous to the motion of a coil tending to maximize its inductance: in this case the process is probably limited by axial pressure gradients. After the re-arrangement, the entire configuration decays uniformly with a time constant of about 8 μsec, which is consistent with classical resistive dissipation of the plasma currents, at the electron temperatures of ~ 7 eV measured by Thomson scattering. The dissipation of the currents tends to heat the electrons, and in similar experiments[4] an increase in electron temperature was observed several microseconds after the beam had left the system.

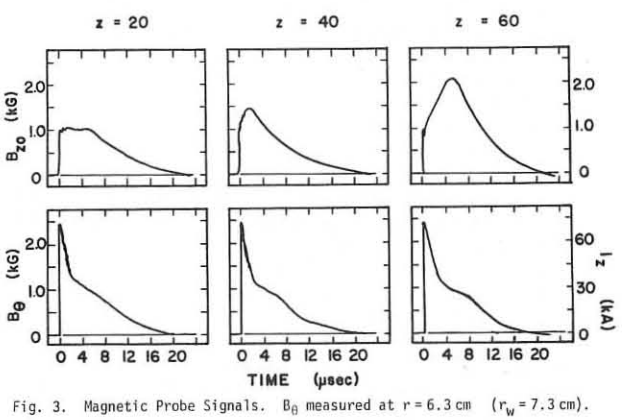

Fig. 3. Magnetic Probe Signals. B_θ measured at r = 6.3 cm (r_w = 7.3 cm).

Further Applications

These experiments have demonstrated a method of creating a plasma and its associated confining magnetic field inside a closed metal tube. The immediate application is to make the initial plasma for imploding-liner experiments;[9] for this purpose it is desirable that the field lines should be closed, which is not the case in the experiments described here. However, if a second, hollow, rotating electron beam were injected between the first beam and the tube wall, but in the opposite direction, the net axial current could be brought to zero. Natural reconnection of the axial field lines at the ends would produce the configuration of a reversed-field theta pinch with internal B_θ or, if the geometry were appropriate, a Spheromak.[9] Experiments to test this concept are in preparation.

References

1. N.C. Christofilos, Proc. 2nd Int. Conf. on Peaceful Uses of Atomic Energy (United Nations, Geneva 1958) Vol. 32, p. 279.
2. M.L. Andrews et al. Phys. Rev. Lett. 27, 1428 (1971).
3. C.A. Kapetanakos, W.M. Black and C.D. Striffler, Appl. Phys. Lett 26, 368 (1975).
4. J.D. Sethian et al. Phys. Fluids 21, 1227 (1978).
5. J.D. Sethian, K.A. Gerber, D.N. Spector and A.E. Robson, Phys. Rev. Lett. 41, 798 (1978).
6. J.D. Sethian, K.A. Gerber, D.N. Spector and A.E. Robson, Submitted to Phys. Fluids.
7. S. Yoshikawa, Phys. Rev. Lett 26, 295 (1971).
8. D.L. Book et al. Plasma Physics and Controlled Nuclear Fusion Research 1976 (IAEA Vienna, 1977) Vol. III, p. 507.
9. M.N. Bussac et al., 7th Int. Conf. on Plasma Physics and Controlled Nuclear Fusion Research, Innsbruck, Austria, 23-30 Aug. 1978, Paper X-1.

DP32

VELOCITY ANGLE SCATTERING OF A RELATIVISTIC ELECTRON BEAM DURING TRANSPORT THROUGH A PLASMA

P.H. de Haan, H.J. Hopman, G.C.A.M. Janssen, E.H.A. Granneman, R. Jayakumar*, P.S. Strelkov**, B. Jurgens***

FOM-Institute for Atomic and Molecular Physics, Amsterdam, The Netherlands
Association Euratom-FOM.

ABSTRACT. Measurements on the propagation of a relativistic electron beam indicate good beam transport through a weakly ionized hydrogen gas with an electron temperature $T_e \approx 18$ eV, degree of ionization $\approx 2 \times 10^{-3}$ and beam to plasma density ratio $\approx 10^{-3}$.

INTRODUCTION. In this paper are presented experimental results on the propagation of a relativistic electron beam through hydrogen gas. Beam parameters are 0.83 MV, 6.2 kA, 3 cm diam. and a pulselength of 100 to 150 ns. The beam is drawn from a spherical carbon cathode and is injected along a 0.21 T guide magnetic field into a metallic chamber of 2.5 m length and 12 cm diam. Fill pressures were varied between 10^{-6} and 1.4 Torr.
Diagnostics include an energy analyzer measuring the energy distribution of beam electrons with the velocity vector within a cone of 2^o about the magnetic field axis; an angle analyzer measuring the angular distribution of beam electron velocities up to 60^o; optical spectroscopy giving H_α and H_β line profiles. All diagnostics are time resolved and results are integrated over 8 ns time intervals.

MAIN FEATURES. *VACUUM CURRENT.* The full beam current $I_b = 6.2$ kA is transported in vacuum, $10^{-6} \leq p \leq 10^{-3}$ Torr. Angle scattering is negligibly small. The Bogdankevich-Rukhadze [1] limiting current in vacuum under our conditions is 3.8 kA. The fact that we measure a larger vacuum current lends support to the calculations of Thode et al. [2], indicating larger limiting currents in weak guide fields. The essential parameter is the ratio of electron cyclotron frequency over beam plasma frequency ω_{ce}/ω_{pb}. In our case $\omega_{ce}/\omega_{pb} = 1.4$, for which value a factor 1.3 increase in limiting current is found by Thode et al.
BEAM CURRENT DISRUPTION. The pressure interval $10^{-2} < p < 5 \times 10^{-2}$ Torr revealed two phenomena. It was found with the energy analyzer that the whole beam loses ≈ 100 keV, in some shots without a distinct broadening of the distribution function. This can tentatively be explained by the reduction of beam space charge fields by ionization of the background gas. Transit time considerations then suggest that these space charge fields occupy a larger area (length ≈ 1 m) than discussed in most theories (length 0.1 m) [2,3]. The filling up of the space charge well takes ≈ 30 ns [4]. When approximate charge neutrality has been attained a strong instability sets in. The beam is driven across the guide field and hits the drift chamber wall at 50 cm distance from the diode. Beyond this distance the beam current is found to drop to $\approx 10\%$ of the vacuum value.
ANGLE SCATTERING. The angle analyzer [5] consists of four concentric ring electrodes. The electrodes are placed behind a 0.1 cm diam. entrance hole and collect beam electrons within the intervals $0 - 18^o$, $18^o - 36^o$, $36^o - 54^o$ and $54^o - 60^o$ respectively. In the present measurements the analyzer is placed on axis. The measured data are fitted with a Gaussian distribution,

$$f(\theta) \alpha \exp\{2 \cos\theta / \langle\theta\rangle^2\}. \qquad (1)$$

With the analyzer placed in front of the diode the measured distribution agrees with a calculated one [6]. In case of the use of a 30 μm thick anode foil we have $\langle\theta\rangle = 18^o$. Injecting the beam in hydrogen gas of 1.4 Torr it is found that the mean angle rises with a characteristic time of ≈ 13 ns to $\approx 90^o$. Fig. 1 gives $\langle\theta\rangle$ as function of time for three different shots. In this case the analyzer was placed at 150 cm distance to the diode. At 100 cm the results are similar. At 50 cm $\langle\theta\rangle$ remains small at all times.
The energy analyzer indicates an energy loss at the moment of strong beam scattering of $\approx 10\%$. Spectroscopic measurements give an ion temperature $T_i = 3.5$ eV and a density $n_e = 8 \times 10^{19}$ m^{-3} at t = 50 ns. At later times the energy loss decreases to $\approx 3\%$ and the density rises slowly to a final 2×10^{20} m^{-3}. Rogowski coil measurements show a rapid decay of the return current, from which a collision frequency $\nu_{eff} = 3 \times 10^9$ s^{-1} is deduced.
The slow rate of ionization at t = 50 ns suggests a small plasma electron temperature. An upper estimate is obtained by assuming that the beam energy loss is used to maintain T_e against energy loss of the plasma electrons due to ionization of the gas. The beam energy loss of 10% represents a power deposition of 5×10^8 W in the plasma volume. Equalizing this to the ionization losses one obtaines

$$\langle\sigma_i v_e\rangle n_n n_e E_i \times \text{plasma volume} = 5 \times 10^8, \qquad (2)$$

where n_n is the density of the neutral gas and E_i is the energy lost by a primary electron in an ionizing collision. Taking $E_i = 20$ eV, Eq. (2) gives $\langle\sigma_i v_e\rangle = 1.2 \times 10^{-14}$ m^{3}s^{-1}, which leads to $T_e = 18$ eV, if a Maxwellian plasma electron distribution is assumed. At $n_e = 8 \times 10^{19}$ m^{-3} we have $\omega_{pi} = 1.15 \times 10^{10}$ s^{-1} > $\nu_{eff} = 3 \times 10^9$ s^{-1} > $n_n \langle\sigma_i v_e\rangle = 6 \times 10^8$ s^{-1}. It therefore seems reasonable to assume that turbulence is the main cause of the friction felt by plasma electrons. It follows from $T_e = 18$ eV and from a return current $I_p = 0.5\, I_b$ that the ratio of electron drift velocity over sound speed $v_d/c_s \approx 5$. Furthermore $T_e > T_i$ and turbulence must be excited under these conditions. A turbulent collision frequency is obtained from [7]

$$\nu_{eff} = 10^{-2}\, \omega_{pi} (v_d/c_s)\, (T_e/T_i), \qquad (3)$$

yielding $\nu_{eff} = 3.7 \times 10^9$ s^{-1}. This value is in fair agreement with the experimental result. The maximum level of turbulence is obtained from [7]

$$\nu_{eff} = \omega_{pe}\, (W/nk\, T_e), \qquad (4)$$

from which $(W/nk\, T_e) = 6 \times 10^{-3}$. Plugging this number in the formula for beam angle scattering [8] we find,

$$\nu_D = \omega_{pe}\, (W/nk\, T_e)\, (T_e/mc^2)^{3/2} = 600 \text{ s}^{-1}, \qquad (5)$$

where ν_D is the time required by a beam electron to scatter over one radian. Compared to a transit time less than 10 ns this scatter frequency ν_D is rediculously small. We note that the beam electron angular distribution fairly well approximates a Gaussian shape, which suggests scattering caused by turbulence. Because $\langle\theta\rangle$ increases by ≈ 1 radian when the beam electron has travelled a distance of ≈ 1 m, the experiment indicates a value $\nu_D \approx 3 \times 10^8$ s^{-1}. Taking this value into Eq. (5) one finds $T_e = 100$ keV. A way out of the dilemma of two electron temperatures might be the assumption of a two temperature distribution. A high energy fraction accelerated in the strong fields at a lower plasma density earlier during the shot and a cold fraction originating from a later time.
Once the strong angular scattering has decayed, data suggest a fairly efficient beam transport $\langle\theta\rangle \approx 25^o$, see Fig. 1, and the energy loss over a path length of 2.5 m amounts to 3%.

LINEAR REACTOR CALCULATIONS. REB's have the potential to heat the plasma in linear magnetic fusion devices to ignition temperatures. Therefore computer studies of the properties of the plasma in these devices were performed to obtain information on the requirements REB's have to fulfil. A one-dimensional (radial) MHD code has been used to study the nuclear burn phase of a high beta (0.85), high density (10^{23} m^{-3}), 5 keV plasma of radius $r_p = 0.03$ m [9]. The vacuum magnetic field is $B_o = 20$ T. Radial heat conduction is reduced by application of low density (10^{21} m^{-3}) cold plasma blanket between the hot burning core plasma and the wall. A finite length L is simulated in the code by extracting energy from the plasma at a rate corresponding to multiple mirror end losses. The calculations suggest a 450 m long plasma column can reach a scientific Q equal to two. For this particular length the radial and axial energy losses are equal. The wall loading integrated over the burn cycle amounts to 0.73 MJ m^{-2} on a wall of radius 0.1 m. The total plasma heating power required is 320 MJ. Following the plasma during complete cycle for several plasma lengths, it was verified that Q scales proportional to L^2. If $L \geq 2000$ m a self sustained burning plasma column becomes possible.

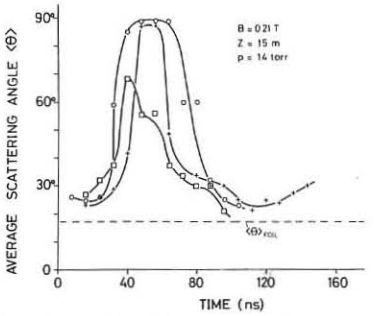

Fig. 1

* Cornell University, Ithaca N.Y., USA

** Lebedev Physical Institute, Moscou, USSR

*** Philips Data Systems, Apeldoorn, Netherlands

REFERENCES

[1] Bogdankevich L.S., Rukhadze A.A., Sov.Phys. Uspekhi 14 (1971) 163
[2] Thode L.E., Godfrey B.B., Shanahan W.R., Phys.Fluids 22 (1979) 747
[3] Olson C.L., Phys.Fluids 18 (1975) 598
[4] Olson C.L., Phys.Rev.A. 11 (1975) 288
[5] This device was originally proposed by Dr. A.G. Shkvarunets of the Lebedev Institute, Moscou, USSR
[6] Bethe H.A., Ashkin J., in "Experimental Nuclear Physics", E. Segrè ed., John Wiley, New York (1953)
[7] Sagdeev R.Z., Rev.Modern Phys. 51 (1979) 1
[8] Sudan R.N., NRL Memorandum Report 3073, Washington, D.C. (1975)
[9] Jurgens B., Hopman H.J., submitted to Plasma Physics.

MODEL INVESTIGATION OF QUASISPHERICAL LINER COMPRESSION OF TOROIDAL PLASMA

V.M. Goloviznin, R. Kh. Kurtmullaev, V.N. Semenov,
I.V. Kurchatov Institute of Atomic Energy, Moscow, USSR

V.A. Gasilov, A.P. Favorsky, M. Lu.Shaskov
M.V. Keldysh Institute of Applied Mathematics, Ac.Sci., Moscow, USSR

N.V. Sosnin
M.V. Lomonosov Moscow State University, Moscow, USSR.

The results of the numerical simulation process of the plasma adiabatic compression in the thermonuclear system with the closed configuration toroidal plasma compression by the quasispherical liner are discussed in this paper.

Plasma toroid, with poloidal field is created in the cylindrical forming camera and injected into the liner camera. The envelope compression quasispherical regime is obtained by butt-ends outstripping motion of the initially cylindrical liner with the profiled wall thickness.

The distribution of the initial envelope thickness and the initial motion velocity were set beforehand according to the assessment of the energy minimization (the energy was wasting during the process of envelope butt-ends slamming) in preliminary and simplified calculations /I/.

The calculation of liner motion was based on the two-dimensional model of the incompressible ideally conducting fluid /I/. The variational principle of calculation of the equilibrium plasma state in the closed magnetic field was used.

The minimization of the energy functional $W = \int_V \left(\frac{B^2}{8\pi} + \frac{1}{\gamma-1} nT\right) dV$ /2/ was accomplished by the local variation method /3/.

At the first moment both the radial velocity distribution over liner length and the magnetic flux dependence on the plasma pressure, which defined the configuration of equilibrium, were set. At some moment after slamming the envelope form and the configuration of magnetic force lines for two cases, differed by initial velocity distribution, are shown in the Figure 1. The initial profiles both of the liner thickness and $P(\Psi)$ plasma dependence were the same. It is at once apparent that in the first case (a) the envelope takes practically quasispherical form; in the second case the closed cavity is strongly stretched out.

In the first case (quasispherical compression regime) the maximum plasma pressure Pm dependence on the closed cavity volume V to the compression coefficient $K \sim 10$ satisfies to a law $Pm \cdot V^{\gamma_{ef}} = \text{const}$, where γ_{ef} value is equal to 1.3 (Plasma specific-heat ratio is equal to $\gamma = \frac{5}{3} \approx 1.67$). The evolution of the ratio of the plasma heat energy to the magnetic energy with the closed cavity volume change is shown in the Figure 2a.

The grouth of the relative plasma energy takes place in the quasispherical regime during the compression process (Figure 2a). In the second case (cylindrical regime) the ratio of the maximum pressure to the cavity volume is not satisfy to the law $Pm\, V^{\gamma_{ef}} = \text{const}$.

In order to use this formula γ_{ef} is set as a variable value which may grow from 1.6 to 1.8 during the compression process. So, in this case the maximum plasma pressure grows more quickly then in the previous one, but the ratio of the full plasma energy to the magnetic energy changes more slowly then in the quasispherical regime (Fig. 2b).

It depends on the $P(\Psi)$ ratio change, leading to the plasma volume relative decrease to the volume of the magnetic field during the comression process.

The preference of quasispherical compression regime for almost cilindrical compression case is shown by these results. The creation of the cumulative jets during the liner butt-ends slamming (Figure Ia). were observed in the examined versions; the compression coefficient was limited by the moment of the meeting jets collision in the camera centre.

The initial velocity profile was specially chosen to get large compression coefficients; so,the penetrating of the cumulative jets into the camera was loosened /I/.

The high comression degree can be achieved in the opened magnetic flow regime, where the compact toroid is covered by the magnetic flow. In this case the envelope is not completely closed; the converging butt-ends cavity is created by the central part of it; the opened flux gets out through these butt-ends.

REFERENCES

1. V.M. Goloviznin, R.Kh. Kurtmullaev, V.N. Semenov, V.A. Gasilov, A.P. Favorsky, M.Lu. Shashkov.
The International Conference of Megagauss Fields Generation. Washington, 1979.
2. В.Д. Шафранов. Равновесие плазмы в магнитном поле. В кн. "Вопросы теории плазмы", вып. 2, стр. 92-I3I.
3. Ф.Л. Черноусько, Н.В. Баничук. Вариационные задачи механики и управления. "Наука", М., I973.

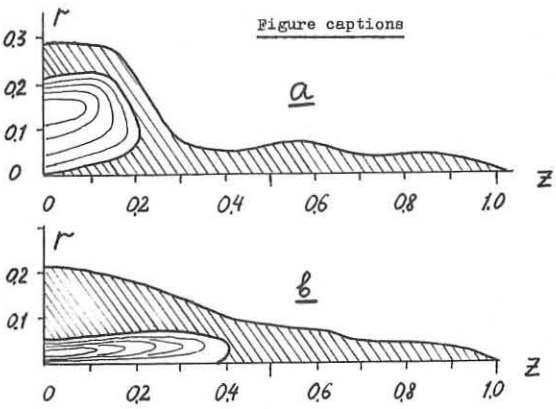

Figure 1.

The envelope form and the force lines configuration of the poloidal field (solid lines insude the cavity) for the diffirent initial envelope velocity distributions:
a) bell-type velocity distribution along the length;
b) parabolic distribution.

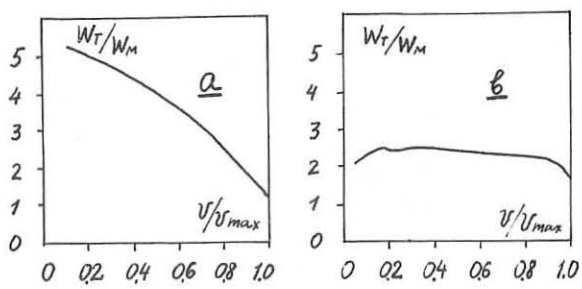

Fugure 2.

The ratio of the total heat plasma energy W_T to the magnetic field energy W_M dependence on the closed cavity volume respectively for the cases a) and b) of Figure 1.

DP35

BUILD-UP OF ANTIPARALLEL STRUCTURE AND ITS STABILITY IN SYSTEMS WITH MAGNETIC BARRIER

A.G. Es'kov, A.G. Kalygin, R.Kh. Kurtmullaev, A.I. Malutin
A.P. Proshletsov, V.N. Semenov

A method of pulsed formation of a compact antiparallel magnetic structure in plasma suggested in /1/ is developed. The process is realized by a programmed capacitor storage discharge on a cylinder shock coil when a multipole magnetic barrier, controlling coils and quasistationary mirrors are involved /2/. In optimizing the scheme a method of pulsed trapping of an initial magnetic flux Φ_{tr} in plasma was investigated. The magnetic pulse with independently variable parameters (amplitude $B_z \sim 4$+ 15 kGs, half-period T/2 = 9 μs) was used. In Fig. 1 the value of the trapped field $B_{tr} = \Phi_{tr}/\pi R^2$ versus shock pulse amplitude is shown. Among other factors which determine the trapped field strength is the barrier field, the influence of which is very efficient and can be used at different stages of the process. a) Firing of the pulsed barrier field just before reversal (after comletion of B_z diffusion into plasma) is the main mode of operation. In this case the function of the barrier field is to couserve the frozen flux by preventing plasma from counteraction with walls (compare the curves a and b, Fig 1). Fig. 2 clearly shows, that losses of the trapped flux, which are of 50% without barrier field, reduce practically to zero with barrier field. The reversal phase with wall (a) and barrier (b) confinement is shown in Fig. 3 (pictures are taken by an electron image converter at an angle of 3° to axis). A very strong reduction of the plasma flow to walls in the second case (b) of barrier confinement can be clearly seen. b) It is fround, that when using a quasi - D.C. barrier field at the phase of pulsed trapping of Φ_{tr} , the trapped flux considerably increases. This interesting result can be seen in Fig. 4 where the value of the trapped field (before reversal) versus B_δ is shown. A probable explanation is that the barrier field, frozen in outer region of plasma prevents from strong radial compression, which results in increasing $\Phi_{tr} = B_t \cdot \pi r_{min}^2$. Effects mentioned above lead to important qualitative consequencies. Reversal with wall plasma support $(B_\delta = 0)$ results in a strong change of the radial distribution of plasma parameters: density in the neutral layer increases, while temperature remains low. In this mode of operation a considerable amount of total plasma concentrates in the neutral layer. On the other hand the miltipole magnetic barrier and mirrors provide an efficient control of plasma and energy flow to the walls and ends of the system and, as a result, a depression of main losses characteristic for conventional reversed field θ - pinch. A clear demonstration of this effect is a depression of an inertial outburst on diamagnetic signals just after reversal by means of barrier field (Fig.5) Simultaneously one more important result is achieved - possibility to control the parameters of the neutral layer ($\delta \sim 0{,}2$ + 2 cm, $n \sim 10^{14}$+10^{16} cm^{-3}) and of the whole toroidal formation (B_{tr} = 1 + 4 kGs, r_s = 5+15 cm). The parameters mentioned, in their turn, predetermine the main physical processes: axial shock wave generation, evolution of microturbulence, equilibrium, stability and energy content of the whole torus. Notable in this respect is the dependence of the compact torus radius r_s (in the final state) on the trapped field B_{tr} (Fig.6). Here main effects, connected with heating and losses are presented in an accumulative way. From Fig. 6 a principally important conclusion follows about a possibility to control a rate of closed magnetic flux losses. Large difference between curves a and b demonstrates effect of operational regime on occurence and disappearance of microturbulence in the neutral layer. Equally, a correlation is determined between MHD plasma instability, and conditions under which sharp gradients of main parameters (n, B) in the neutral layer are observed.

References

1. Es'kov A.G. et al - 6th Europ. Conf. on Controlled Fus. and Plasma Phys. Moscow, 1973, p. 595, 599.
Es'kov A.G. et al - 7th Europ. Conf. on Controlled Fus. and Plasma Phys. Lousanue, 1975, v. 1, p. 55.
2. Es'kov A.G. et al - 7th Intern. Conf. on Plasma Phys. and Controlled Nucl. Fus. Res. Insbruk, 1978.

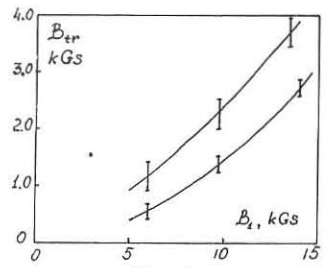

Fig. 1

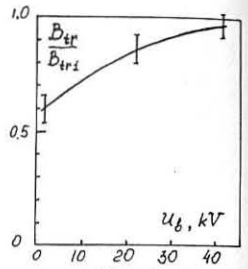

Fig. 2

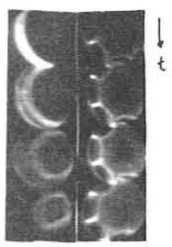

Fig.3.

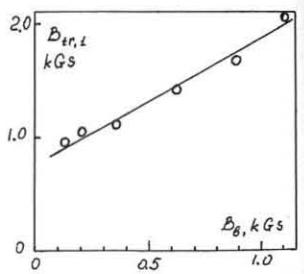

Fig. 4.

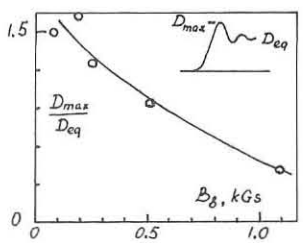

Fig. 5

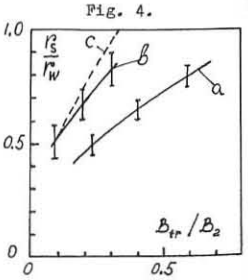

Fig. 6

Fig. 1 Trapped field B_{tr} dependence on shock field B_t . a) Without barrier field, b) barrier bank voltage U_b = 40 kv. Shock coil radius R= 10,7 cm

Fig.2 Magnetic barrier influence on losses of trapped field. $B_{tr\,i}$- before reversal, B_{tr} - after reversal.

Fig. 3 Reversal phase. a) without barrier field and b) with pulsed barrier field (Ub =40kV), Δt = 0,3 μs , $n_o = 3.10^{14} cm^{-3}$, R= 10,7 cm.

Fig. 4 Trapped field (before reversal) versus quasi - D.C. barrier field $n_o = 3.10^{14} cm^{-3}$, R=21 cm.

Fig. 5 Depression of the inertial outburst on diamagnetic signal by means of barrier field.

Fig. 6 Dependence of compact torus radius on trapped field. a) without controlling coils, b) controlling coils are energized, c) calculation assuming conservation of trapped flux.

PARAMAGNETIC SPHEROMAK FORMATION IN A COMBINED ZEE AND THETA PINCH

by
G.C. Goldenbaum, J.H. Irby, Y.P. Chong, and G. Hart
Department of Physics and Astronomy
University of Maryland
College Park, Maryland 20742

We report here our first results on the formation of a new type of configuration with the generic name of spheromak.[1] Our experiment, called Paramagnetic Spheromak (PS-1), uses theta and zee pinches to produce the poloidal (B_z) and toroidal (B_θ) fields. Our results show that a toroidal plasma is formed and that the necessary currents are set up within the plasma to produce the toroidal field.

A key feature of the spheromak is that both the toroidal and poloidal fields are produced by plasma currents induced by external coils which do not pass through the toroidal hole on the symmetry axis. Our experiment has this property and combines the good heating characteristics of the theta pinch and the favorable stability properties of a paramagnetic toroidal field. Theoretical stability investigations[2] using a force-free current model point out the possibility of a tilting mode being unstable in prolate and classical spheroids but not in oblate spheroids.

The present version of our experiment (PS-1) is designed to investigate a method of producing the configuration. Future electrical modifications will allow stability and transport effects to be investigated. Our method for producing the configuration is shown in the figure on the right. Initially we start with an 11.4 cm radius cylindrical deuterium gas column (p = 20 mTorr). The column contains an axial bias field ($-B_z$) produced by I_θ currents in a 30 cm long single turn mirror coil with a mirror ratio of 1.1 (see Figure a). Typically fields of 4 kG are used. Next (b) a zee directed current shell is produced by discharging a second capacitor bank between two annular electrodes with a radius of 7.6 cm located at the mirror points. The I_z current rises to about 200 kA in 4 μsec. The I_z current creates an annular shell of plasma and a slight pinching of the column with compression of initial B_z flux. Finally the last capacitor bank is discharged into the I_θ mirror coil creating a reversed ($+B_z$) field on the outer edge of the column (c). The fast B_z bank produces a 10 kG field rising in 1.5 μsec. This further compresses and heats the plasma annulis. During this time it is expected that field line reconnection will take place at the ends[3] allowing some current to circulate within the plasma on closed flux surfaces.

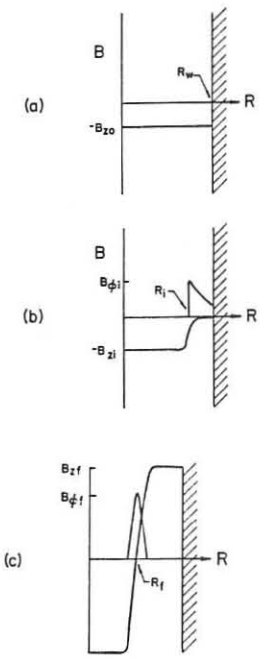

Presently both the I_z and fast B_z circuits oscillate. Our initial investigations are therefore limited to the formation phase (≲ 3 μsec). We will shortly install crowbar and clamp circuits to prolong the currents and allow longer term stability investigations.

Framing camera photographs show an imploding shell of plasma which is axisymmetric and free of gross instability for a useful range of parameters. The shell reaches its equilibrium position, approximately 4.5 cm radius, at about 2 to 3 μsec after the start of the fast B_z field. Since this is after the time of maximum applied field it is apparent that the field accelerates the plasma ring which then coasts inward compressing the bias flux until the poloidal magnetic pressure on axis is sufficient to stop the motion. Presumably this kinetic energy is available for conversion to thermal energy.

Magnetic probes were used to measure the toroidal (B_θ) and poloidal (B_z) fields in the midplane of the mirror coil. The probes were moved to different radii on a shot to shot basis so that radial profiles of the field can be constructed for different times. The toroidal field component is shown in the figure below for t = 2 μsec after the start of the fast B_z bank. From the field structures one can calculate the poloidal current density , j_z. This is also shown in the figure. In this figure positive current density corresponds to the direction of the current from the I_z capacitor bank. The negative current density at large radii indicates that current is returning in the plasma signifying closed surfaces within the plasma. The peak net I_z in the plasma is 240 kA while the net current on the outer wall is only 170 kA. We plan to optimize the amount of internally circulating current and then damp out the external current.

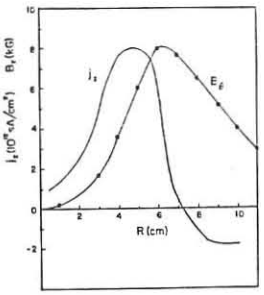

Using both the B_z and B_θ field profiles and assuming static MHD equilibrium we have calculated the radial pressure profile. We find a peak pressure of 3.5×10^{18} eV/cm^3 at approximately the center of the bright annulis seen in the image converter photographs ($r \gtrsim 4.5$ cm). We have obtained some indication of the ion temperature by observing the shape of the Balmer lines (D_β is shown below) and carbon impurity lines. From the width of the Balmer lines assuming only Doppler broadening we find a temperature of 230 eV. Carbon lines give temperatures of about 160 eV at the same time. At this time we do not understand the difference between the line widths. For an electron and ion temperature of 230 eV at the peak of the pressure profile this corresponds to a density of 8×10^{15} cm^{-3}. This corresponds to a total compression (axial plus radial) of about 7, which is not unreasonable.

In summary we have observed the formation phase of a pulsed, compact torus configuration with toroidal and poloidal fields. From magnetic fields measurements the aspect ratio has been found to be 1.8, the elongation (length to width ratio) is about 3. This means the configuration, at present, is a prolate spheroid. The paramagnetic toroidal field is partly due to internally circulating currents indicating some closed surfaces. Measurements are underway to map out flux surfaces as are modifications to extend the pulse lifetime to study stability properties.

This work is supported by the U.S. Department of Energy.

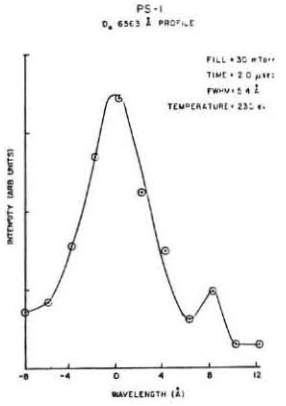

References

1. M.N. Bussac, H.P. Furth, M. Okabayashi, M.N. Rosenbluth and A.M. Todd in Plasma Physics and Controlled Nuclear Fusion Research (Proc. 7th Int. Conf. Innsbruck, 1978) Vol. 3, to appear (also available as PPPL Report 1972).
2. M.N. Rosenbluth and M.N. Bussac, Nuclear Fusion 19 (1979) 489.
3. J.H. Irby, J.F. Drake and Hans R. Griem Phys. Rev. Letters 42 (1979) 228.

E1.1

COMPUTATIONAL STUDY OF LASER IMPLOSION AND COMPARISON WITH EXPERIMENTAL RESULTS AT ILE OSAKA

T.YABE, K.NISHIHARA, K.MIMA, N.MIYANAGA, Y.KATO, C.YAMANAKA
INSTIUTE OF LASER ENGNEERING, OSAKA UNIVERSITY
SUITA, OSAKA, 565 JAPAN

INTRODUCTION

We are studying implosion process of double layer spherical target irradiated by 1.06μm glass laser light using GEKKO IV glass laser system. Our major interest in this work is to investigate transition from exploding pusher type compression to ablative mode compression by variyng the thickness of coating material on a spherical glass microballoon target. Comparison of experimental results with simulation calculation of implosion process is expected to provide transport properties of hot electrons.

CODE DEVELOPEMENTS

We have developed 1-dimensional Lagrangian hydrodynamic code which includes transport of hot electron by multi-group flux-limited diffusion model[1]. Ionization process are calculated by use of Saha equation. We also developed codes solving the rate equation and calculating X-ray line shapes. Reliabilities of the multi-group code has been checked by comparison with the analytical results obtained by one of authors . Detailed investigations of transport characteristics were performed. Among those results we present here two interesting examples.

If electron distribution has trancation at the velocity $v=v_{cut}$ [2], diffusion depth of hot electron strongly depends on the ratio v_{cut}/v_{Th} , v_{Th} being thermal velocity of hot electron , as shown in Fig.1.

In weak collisional region where density is lower than the critical density, the multi-group formalism is not correct. We are now developing new code in which distribution function of hot electron is expanded into Legendre series in angular velocity space. Figure 2 shows preliminary results from new code and multi-group code. In this case, background density, hot electron temperature and effective Z are fixed to 10^{19} cm^{-3}, 10 keV and 1, respectively, and constant E field is imposed, maximum potential being 20 keV. In the figure, solid line shows spatial distribution of hot electron density obtained from our new code, dashed line and dash-dot line represent ones from multi-group code and collisionless B.G.K. solution, respectively. Comparing results we may conclude that hot electron in the multi-group code quickly approaches equilibrium state and feels less E field due to the free-streaming limit.

IMPLOSION STUDY OF DOUBLE LAYER SPHERICAL TARGET

We simulated implosion processes of glass microballoon (80μm diameter and 1.1μm thickness) filled with Neon at 26 atm, coated by polyethylene. Total laser input power was 2.5 TW in 100 psec. Absorption rate due to classical inverse bremsstrahlung was a few percent and absorption due to resonant effect were assumed to be 10 %, whose energy was converted to hot electrons. Temperature of hot electrons was determined by using the formula by Estabrook and Kruer [3].

Figure 3 shows calculated flow lines for various coating thickness. The transition from exploding pusher mode to ablative mode with increasing coating thickness is clearly seen form the figure. This is also confirmed by viewing radial distribution of hot electron, which is completely stopped at 10μm polyethylene. In Fig.4, some of plasma parameters are plotted as a function of coating thickness. Peak density of compressed core exponentially increases with thickness whereas peak electron temperature decreases. Experimentally obseved density of Neon core are also plotted by circles. Within a factor of 2, both results are in quite an agreement with each other.

X-ray spectroscopy is one of the useful diagnostic tools to measure ρ , ρR and T_e in compressed fuel and pusher. In order to know the stage of the implosion process when X-ray line emission mostly occurs in the experiments, we have solved both rate equations for the fuel and pusher and transport equations for line x-ray from them. The number of the states in the code are 20 for Neon, 41 for silicon and 16 for oxygen. For the case of the exploding pusher type compression, line emission occurs in the expanding phase after peak compression. As shown in Fig.5, the line emission however occures near the peak compression.

References

1) G.Zimmermann : Lawrence Livermore Lab. UCRL-74811,1973.
2) C.P.DeNeef, J.S.DeGroot : Phys. Fluids 20(1977)1074.
J.S.Pearlman,R.L.Morse : Phys.Rev.Lett. 40(1978)1652.
3) K.Estabrook,W.L.Kruer : Phys.Rev.Lett. 40(1978)42.

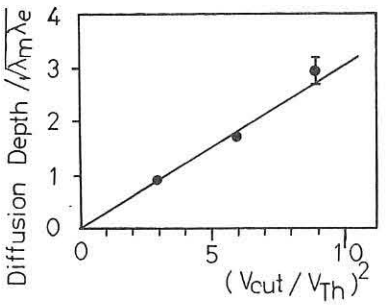

Fig.1: Diffusion depth estimated by spatial distribution of hot electron. λ_m,λ_e mean momentum, energy mean free path..

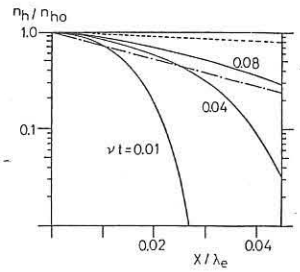

Fig.2: Spatial distribution of hot electron calculated by Legendre expansion (solid), B.G.K. (dash dot) and multi-group code (dash) whose profile reaches steady state $\upsilon t > 0.01$, υ being the collision frequency.

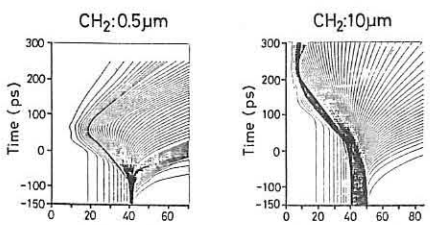

Fig.3

Fig.4

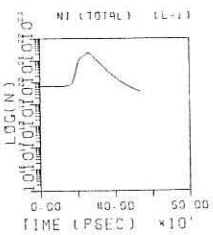

Fig.5

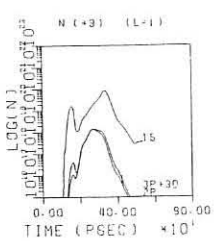

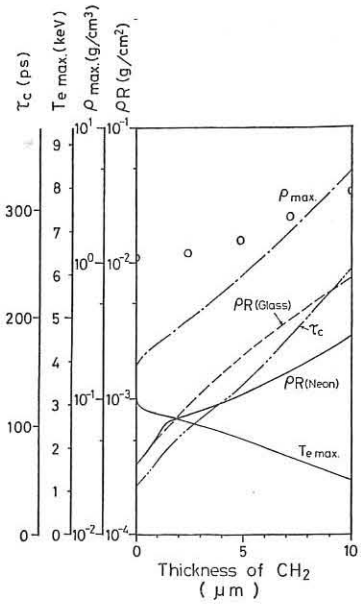

LASER FUSION EXPERIMENTS AT KMSF*

Roy R. Johnson, R.L. Berger, P.M. Campbell, G. Charatis, J.G. Downward, T.M. Henderson, F.J. Mayer, N.K. Moncur, D.L. Musinski, L.V. Powers, S.B. Segall, L.D. Siebert, D.C. Slater, D.E. Solomon, J.A. Tarvin, and C.E. Thomas

KMS Fusion, Inc.
Ann Arbor, Michigan 48106
U.S.A.

The KMSF laser fusion program has been directed at investigations of a wide spectrum of physics issues, with our primary effort focused on the spherical illumination and implosion of spherical shell targets. We have done experiments to quantify the conditions of the imploded target core, to measure the amount of laser energy absorbed, to examine the partitioning of this energy into its various components, and to examine the transport of the absorbed energy. Theoretical investigations have been directed toward achieving an understanding of the physical mechanisms relevant to these experiments.

The implosion process has been investigated by measuring the neutron yield, alpha-particle spectra, and x-ray pinhole photographs from the compressed targets. Using targets of varied size, fuel-gas pressure and fuel distribution, we have attempted to determine the final compressed-fuel densities and temperatures at laser powers up to 0.7 TW. Typical neutron yields of a few times 10^7 and fuel-ion temperatures of 2.2 keV are obtained from the implosion of 60-μm-diameter (10 atm) targets at 0.4TW. These values are consistent with peak compressed-fuel densities of ∿1 to 2 g/cm^3. With somewhat larger, 80-μm-diameter (30 atm) targets, x-ray pinhole photographs directly show a compressed-fuel volume which represents a fuel density of ∿0.5 g/cm^3. In implosion experiments with cryogenic fuel layers, x-ray pinhole photographs show that the fuel has been compressed to densities as high as 7 g/cm^3. In these experiments slowing of alpha particles (expected with the higher density) was observed for the first time at KMSF when the loss in energy was determined from the alpha-particle spectrum. The experimental data on compression and alpha particle energy loss were found to be consistent with the neutron yield. The relatively high densities achieved at modest absorbed energies are believed to be due to the symmetric target illumination afforded by the ellipsoidal-mirror system. A maximum neutron yield of 10^8 was obtained from an 80-μm-diameter gas-filled glass shell with 0.7 TW on target.

The effects on absorption of laser wavelength and bandwidth have been investigated at KMSF using frequency-doubling crystals to obtain 0.53 μm light and a plasma spatial filter device to increase the laser bandwidth. In experiments at 0.1 TW on target, absorption at 0.53 μm is substantially greater than equivalent experiments at 1.06 μm only when the plasma spatial filter is included in the laser system. Although there are insufficient compression data at these low laser intensities, the neutron yields at the level of 10^6 are an order of magnitude greater than the yields of similar experiments at 1.06 μm. The neutron results are also consistent with smaller energy loss to fast ions and the increased absorption. The KMSF simulation code incorporating ion turbulence has shown that the fast-ion component decreases and total energy absorbed increases at the lower wavelength with a resulting increase in neutron yield.

In absorption experiments at 1.06 μm typically 20% to 30% of the laser light is absorbed. The relative contributions of various absorption mechanisms have still to be established experimentally. Simulation studies indicate that approximately 40% of the absorbed energy is due to resonance absorption. This energy is coupled into a fast electron tail on the thermal distribution and has an important effect on energy transport in the pellet.

Time-resolved laser-harmonic-emission measurements have been made to study the evolution of the spherical target's critical-density surface during laser irradiation. These measurements have shown an interesting intensity-dependent evolution of the critical surface, and strong spatial and temporal structure, possibly associated with ponderomotive force effects. Ponderomotive force, when included in the simulation code, has a significant effect on absorption, heating, and maximum compression in addition to the expected steepening of the density profile. The form of the density profile controls the relative mix of the possible absorption and scattering processes.

We have performed a variety of experiments to investigate the production and dynamics of fast ions. Fast ions constitute a small fraction (∿8%) of the mass of the target but carry off a sizable amount (∿40%) of the absorbed laser energy. Experiments have shown that (1) these fast ions originate from a very thin (∿500 Å) layer at the outer surface of the target, (2) they have a velocity distribution characteristic of an isothermal rarefaction with electron temperature that depends on the laser intensity, (3) they are accelerated outward with a broad, laser-intensity-dependent angular distribution, and (4) some of the ions from the outer shell surface can mix with the fuel during the implosion. Most of the observed properties of fast ions can be obtained from the simulation codes assuming they are produced by a combination of reduced thermal conductivity in the laser deposition region and fast electrons originating from resonance absorption.

Computer simulations generally agree with the experimental results in the 0.3 TW to 0.7 TW range, including the inferred fuel-density values. Other measured quantities which are compared to the simulation runs are neutron yield, fuel-ion temperature, absorbed energy (including the partitioning between slow- and fast-ion expansion energy and x-ray emission), ion velocity spectra, x-ray spectra, and alpha-particle energies.

Significant improvements have been made in the KMSF laser system. As a result of cleaning and restaging, the focusable laser power from two beams was increased from an average of 240 GW to an average of 440 GW on target. The beam fill-factor was also increased from about 70% to 90%, raising the average power to 502 GW, with a maximum of 758 GW on target. The focal-spot size of the laser was reduced by a factor of about 5. Despite the improved cleanliness of the laser, previous damage tracks inside the used laser glass generated low-frequency spatial ripple at the output of the laser. This low-frequency noise, which could not be removed by spatial filters, damaged the output dielectric coatings. We therefore installed the plasma spatial filter, which time-averages spatial ripple by partially degrading laser coherence. The average focusable power decreased from about 500 GW to 400 GW, but further component damage has been eliminated.

*This work was supported by the United States Department of Energy under Contract ED-AC08-78DP40030.

E1.3

ENERGY TRANSPORT FROM 1.06μm AND 0.53μm LASER PLASMAS INTERACTIONS AT 10^{15}W cm^{-2}

J.D.Kilkenny, D.J.Bond, D.R.Gray, J.D. Hares,
Blackett Laboratory, Imperial College, London.
R.G. Evans, M.Key, W.Toner, Rutherford Laboratory.
J.G. Lunney, Queens University Belfast.

Two types of experiments measuring the transport of energy by thermal and fast electrons for 1.06μm laser plasma interactions at intensities around 10^{15}W cm^{-2} are presented. Heat flux inhibition at 3% of the free streaming value and a low absorption are measured for thermal electrons. In contrast the fast electrons carry most of the absorbed energy many microns into solid density targets. However a low density target material is shown to inhibit these fast electrons by a resistive electric field.

(i) Inhibited transport by thermal electrons

It is well known that the penetration depth of the high temperature ablation front in high intensity laser interaction with solid targets is much less than is consistent with classical thermal conductivity. Other experiments (1,2) have measured the penertration depth on plane targets where there is the possibility of magnetic field heat flux inhibition. Here we have used plane targets and microballoons for which the measured magnetic field is less than 100 kG.(3).

A uniform layer of Aℓ was coated onto 70μm diameter glass microballoons, or plane SiO substrates. Targets were irradiated with 100ps laser pulses using the Rutherford Laboratory C.L.F. Experiments were done at 1.06μm and 0.53μm by frequency doubling the 1.06μm laser output. For microballoon illumination the intensities were 2 10^{15}W cm^{-2} and 5 10^{14}W cm^{-2} for λ= 1.06μm and 0.53μm respectively. Xray emission was recorded using a space resolving P.E.T. crystal spectrometer. This allowed measurements of the electron temperature from the slope of the Aℓ XII and Aℓ XIII recombination continuum, the electron density from line broadening and the ablation plasma burn depth from the ratio of helium like Si to Aℓ lines.

For microballoons the electron temperatures were 500±50 eV for both wavelengths. The electron densities (and opacity) obtained by fitting AℓXIII L_α, L_β, L_γ and L_δ lines self consistently (3).were n_e= 1.± .3 10^{22} cm^{-3} for both wavelengths. This implies that the ablation pressures were similar for both wavelengths. The burn depths, for both wavelengths are shown in Fig.1. Here there is a significant difference, the burn depth being two to three times larger for 0.53μm than for 1.06μm. For 1.06μm radiation on plane targets the temperature was measured over a range of intensities I and was found to scale $T_e \alpha I^{0.18\pm.04}$

Modelling with a 1D Langrangian code has assumed that the fast electrons have a negligeable effect on the heat front as the temperature rise they cause a small c.f. 500eV. (see below) Two parameters were used to fit the observations to the code, namely the fraction of the incident energy 'ε' deposited into the ablation plasma at the critical density surface and the heat flux inhibition factor 'f' applied to the free streaming limit and the Spitzer thermal conductivity. For λ= 1.06μm a unique fit for f and ε to the experimental observables was obtained with ε = 3 ± 1% and f = 30 ± 20. For λ= 0.53μm a tentative analysis indicates a fit with f=30 but with ε = 6% as would be expected with the larger critical density.

(ii) Transport by fast electrons

Fast electrons are usually diagnosed either by the continuum Xray spectrum they produce or by fast ion-production A more accurate measurement is obtained by layers of K_α fluors buried at known depths within targets (4). Recently we demonstrated how such targets can measure the electron energy distribution function and thus the total energy in fast electrons. By varying the laser intensity the scaling of the hot electron temperature T_H and the energy in the hot electrons has been measured for 1.06μm irradiation. The fraction of incident energy measured as preheat is shown in Fig.2; assuming that the absorption is 30-40%, the fraction of the absorbed energy going into preheat is about 50%. The measured scaling of T_H was $T_H = 11(I/10^{15})^{0.48}$ for 4 10^{14}Wcm^{-2} < I < 6 10^{15}W cm^{-2}, which is consistent with hard Xray continuum measurements.

With solid density targets there was no evidence of inhibition of fast electrons. However the resistive electric field set up to drive the return current that cancels the current density of the fast electrons can inhibit the fast electrons. This inhibition will be largest for materials of low density and high resistivity when the electron energy is deposited. A Monte Carlo electron deposition code predicts that at 10^{15}W cm^{-2} high density gold targets will not inhibit fast electrons, whereas low density (1% solid) gold targets will appreciably decrease the effective range. This was demonstrated experimentally, by detecting the electron flux through 1 mgm cm^{-2} of gold. The flux of fast electron through solid density gold was consistent with the previously measured T_H. However for 1% solid density gold the electron flux was reduced by at least a factor of 6.

(1) B.Yaakobi and T.C. Bristow, Phys.Rev.Lett., 38, 350 (1977).
(2) F.C.Young et.al., Appl.Phys.Lett., 30, 45 (1977).
(3) 1979 Rutherford Lab.Annual Progress Report, RL-79-036.
(4) J.D.Hares et.al., Phys.Rev.Lett., 42, 1216 (1979).

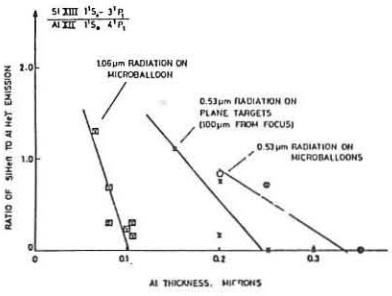

FIG 1 BURN DEPTH FOR 0.53μm AND 1.06μm BEAMS

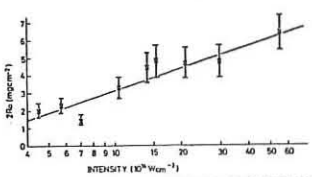

MEASURED RANGE OF PREHEATING AS A FUNCTION OF INTENSITY.

FIG 2

E1.4

ACCELERATION OF THIN FOIL TARGETS UNDER INTENSE LASER IRRADIATION

G. Brederlow, R. Brodmann, K. Eidmann, P. Mulser, R. Petsch, R. Sigel, G. Spindler, G. Tsakiris, R. Volk, S. Witkowski,
Projektgruppe für Laserforschung der Max-Planck-Gesellschaft zur Förderung der Wissenschaften e.V., D-8046 Garching/FRG

1. The laser fusion concept relies basically on the efficient and stable acceleration of a thin, fuel containing shell to a large implosion velocity. In this investigation we have attempted to study several aspects of this acceleration process, namely mass ablation rate and efficiency of energy transfer, in planar geometry using thin foil targets of variable thickness. In this manner it is hoped to gain insight into the underlying physical mechanisms which govern the interaction of the laser radiation with the target material.

2. The basic idea is best illustrated by assuming a stationary situation where the laser-irradiated foil is accelerated by the ablating plasma like a rocket by its burning fuel. From integration of the well-known rocket equation (see poster) it becomes clear that the efficiency of energy transfer to the cold material depends only on the ratio of ablated and initial mass of the foil, regardless of the ablation mechanism. The optimum energy transfer is achieved for $m_a = 0.8\, m_0$ with $\eta = 0.65$. The absolute value of the ablated mass is most directly determined by a measurement of the foil kinetic energy as a function of initial foil thickness. In a nonstationary situation recourse has to be made to a numerical simulation.

3. Experiments were carried out by irradiating plastic $(C_6H_7O_{11}N_3)_n$ foils in the thickness range 0.1-10 µm with 0.3 TW pulses from the iodine laser Asterix III ($\lambda = 1{,}3$ µm). To ensure a planar interaction a large focal spot diameter (400 µm diam.) with a corresponding intensity of $2 \times 10^{14}\,W\,cm^{-2}$ was used. The kinetic energy of the accelerated foil material was measured with a large graphite cone calorimeter. In separate series we measured also transmission and total absorption of the foils; the latter by an Ulbricht spherical photometer. Additional diagnostics included ion time-of-flight probes in the front and rear space, a Thomson parabola mass spectrometer, x-ray pinhole camera and a 6-channel absorber foil spectrometer (1.3-50 KeV).

4. The experimental results (see poster) are consistent with a stationary ablation (rocket equation). From the kinetic energy measurements an ablated layer thickness of only $d_a = 0.06$ µm is obtained; the transmission measurements give a somewhat larger value ($d_a = 0.15$ µm). Thus efficient acceleration is achieved only for very thin foils.

5. The results have been analyzed with the help of a 1-D, single fluid hydrodynamic code. The following points should be emphasized:

   (i) Unlimited (f = 1) Spitzer heat conductivity predicts symmetric foil expansion up to a thickness of 2 µm. This is clearly not observed.

   (ii) Reasonable agreement with the experiments can be obtained if strong heat flux limitation is assumed in the code (f = 0.003 is shown in the poster). The calculations show that the foil acceleration then is well described by the stationary rocket model. Possible causes for heat flux limitation cannot be inferred from this work.

   (iii) An alternate interaction model ("exploding pusher") assumes that the absorbed laser energy is deposited by superthermal electrons in the target. From our x-ray measurements in the range $h\nu$= 4-15 keV a temperature of the superthermal electrons of $T_H \simeq 3$ keV is found. One-sided ablation as observed in the experiment is consistent with dominant superthermal energy transport only if the range R of these electrons does not exceed the ablated layer thickness: $R \simeq d_a$. The measured $d_a \simeq 0.1$ µm corresponds to a range of $\simeq 1$ keV electrons in cold plastic. This energy is less than the measured x-ray hot electron temperature $T_h \simeq 3$ keV. Note however that T_h values derived from x-ray spectra depend on the photon energies of the measurement and give only a rough figure for the characteristic electron energy. We must admit therefore that superthermal electrons may be important in the ablation process; quantitatively their contribution can be assessed only by a more detailed model for energy transport.

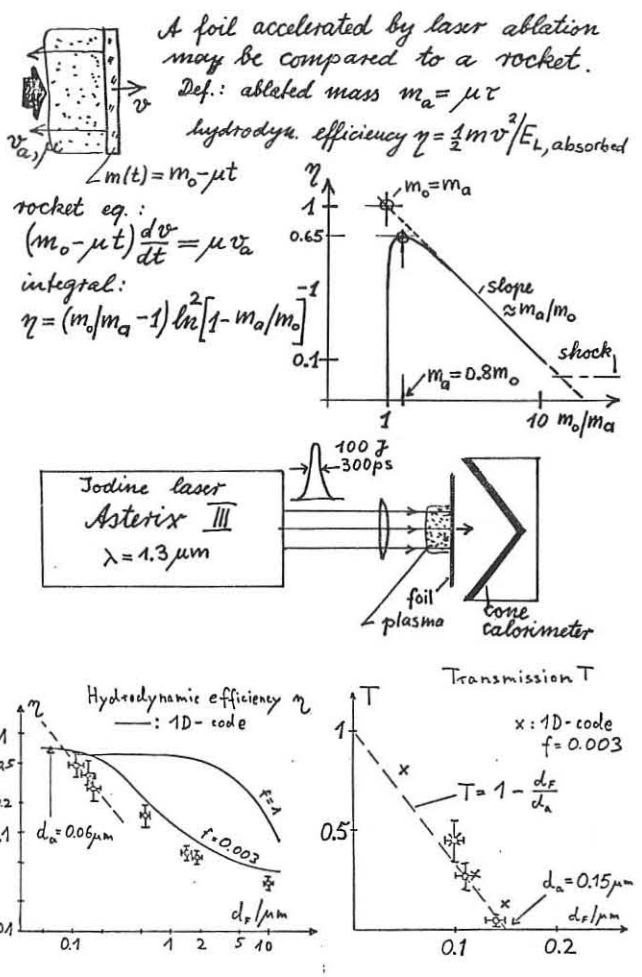

E1.5

STUDIES OF LASER DRIVEN IMPLOSIONS BY TIME-RESOLVED SHADOWGRAPHY

C L S Lewis, L Cooke, J G Lunney, A Moore, J M Ward - The Queen's University of Belfast

R G Evans, M H Key* - Rutherford Laboratory, Oxon

T A Hall - Essex University, Colchester

* On leave from Queen's University, Belfast

X-ray shadowgraphy techniques have been developed to diagnose dense laser imploded plasmas which are too cold to characterise themselves by self emission of XUV radiation. Experiments we have carried out to date can be grouped under two categories.

1. Pulsed X-ray shadowgraphy of microballoons irradiated in the exploding pusher mode. Here 65 μm diameter 1.3 μm wall thickness glass microballoon targets were irradiated at 5 x 10^{14} w cm^{-2} with 100 ps, 1.06 μm pulses and the imploding plasma probed with ∿ 100 psec duration, 1.8 keV X-rays from an auxilliary laser produced plasma. By imaging the backlighting plasma through the balloon with a pinhole camera and varying the arrival time of the auxilliary pulse, "time frozen" images of the plasma were obtained which show the spatial and temporal development of the absorption zone. Experimental data were found to be in general agreement with predictions from the 1-D fluid code MEDUSA and early experiments with 87 Bar Ne filled balloons indicated a peak core density of 4 ± 2 g cm^{-3}(1). Improved experimental conditions have corroborated this observation and yielded better quality images (Fig. 1).

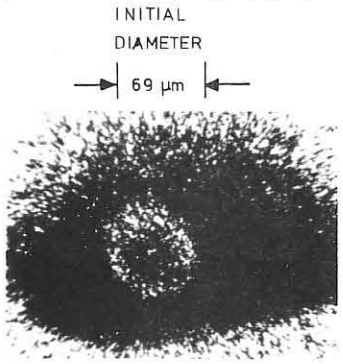

Figure 1
Pulsed X-ray shadowgraph 250 ps after irradiation showing imploding shell.

2. Streaked shadwography of microballoons irradiated in the ablative mode. These experiments used 1.6 ns laser pulses with incident power densities, I ∿ 3 x 10^{13} w cm^{-2} on 240 μm diameter 1.4 μm glass wall thickness microballoons coated with 1 to 6 μm of polymer. The hot electron preheating range λ_H was small relative to the shell thickness ($\lambda_H/\Delta r \sim 0.1$ to 0.5) ensuring ablatively driven implosions. As above a backlighting source was imaged through the balloon with a pinhole camera but the image was sampled with a slit before detection on the photocathode of an X-ray streak camera. Streaked images provided ∿ 10 μ spatial resolution in one dimension and ∿ 250 psec temporal resolution and showed the implosion dynamics directly in a single shot. Figure 2 shows a streak photograph in which the irradiation of the X-ray backlighting target was 1.8 ns delayed relative to the microballoon target irradiation. Peak compression is seen as a minimum (∿ 100 μm) width of the absorbing zone.

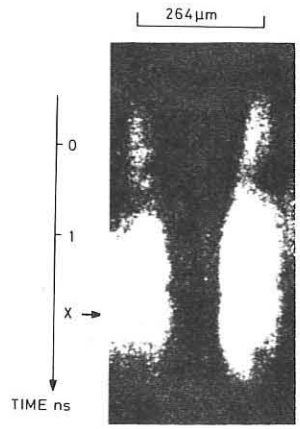

Figure 2
Streaked X-ray shadowgraph microballoon irradiation centred at t = 0

This and other data show anomalous features which suggest the development of significant Rayleigh-Taylor instabilities in the imploding shell. The anomalies are: (a) The intensity of the X-ray emission from the target (preceding the intense backlighting intensity in figure 2) which is much larger than in pure polymer targets and is evidence of SiO_2 in the ablation plasma. The simple burn depth of the ablation is insufficient to explain this and unstable mixing may be occurring. (b) The boundary of the zone of absorption in figure 2 is diffuse on a scale ∿ 30 μm while calculations with the 2-D MEDUSA hydrodynamic code suggest it should be at the instrumental limit of sharpness (∿ 10 μm). This could be explained by SiO_2 mixing with the polymer.

(c) The transmission of backlighting X-rays seen in the early stage of the implosion (with zero time delay backlighting) is anomalously large (compared to computed values and shadowgraphs of unirradiated targets). This could be explained by breakup of the high Z glass shell.

Estimates of the growth exponent for surface ripples on a scale equal to the shell thickness (present with amplitudes of 0.1 to 0.3 μm in the polymer coating), using classical Rayleigh Taylor growth rate and the observed shell acceleration, indicate growth exponents $\int \gamma dt$ reaching 10 before the shell has imploded by more than 20% of its initial radius (see figure 3).

Figure 3

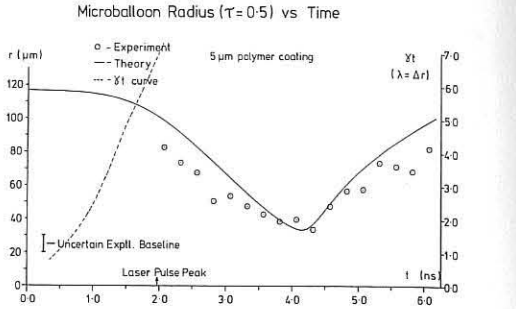

The time to implosion peak and radius time characteristic of the absorption zone boundary are otherwise consistent with MEDUSA calculations which predict ∿ 10 g cm^{-3} in the imploded glass.

New experiments to study ablative implosions of shells will be reported. These will use symmetric target irradiation with 6 beams and a streak shadowgraphy system incorporating an X-ray microscope as shown in figure 4. One aim of the experiments is to use a combination of shell material, gas fill and X-ray backlighting energy which will give measurable X-ray transmission through the compressed core, dominant absorption from the gas fill, and thus a direct measure of the compressed gas density.

Analytic modelling of ablatively driven implosions is being used to give a broader view of parameter dependences than is afforded by hydrodynamic code calculations. These models are discussed elsewhere (2) and suggest for example that for unshaped laser pulses (constant applied ablation pressure) the mass ablation fraction α, for α << 1 is given by,

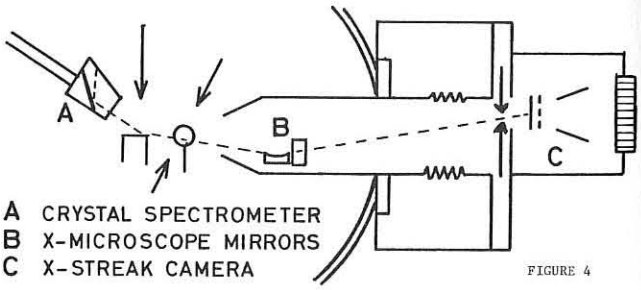

FIGURE 4

$\alpha = \left(\frac{2r}{\Delta r}\frac{\rho_a}{\rho_s}\right)^{\frac{1}{2}}$ where ρ_a is the ablation front density and ρ_s the shell density; and that the compressed core density ρ_c is

$$\rho_c \sim 2.2\, \rho_g^{2/5}\, \rho_s^{3/5}\, (r/\Delta r)^{3/5}$$

where ρ_g is the fill gas density.

Increasing ρ_c by increasing $r/\Delta r$ is limited since there is a practical limit to α and also because Rayleigh-Taylor instability growth is expected to scale as $\exp\left|(r/\Delta r)^{\frac{1}{2}}\right|$. The analysis suggests that if the ablation density is proportional to the critical density and if the optimum irradiation intensity is given by constant $I\lambda^2$ for constant hot electron effects, then for a given α the attainable implosion velocity is wavelength independent but the necessary $r/\Delta r$ scales as ρ_a^{-1} or λ^2.

Stability and scaling behaviour of ablative implosions can be investigated directly with the shadowgraphy techniques discussed above.

We should like to acknowledge the valuable contribution of B Ahlborn to the development of our understanding of the implosion hydrodynamics.

(1) Key M H, Lewis C L S, Lunney J G, Moore A, Hall T A, Evans R G Phys Rev Letts 41 1467 (1978)

(2) Ahlborn B, Key M H (to be published)

LASER MATTER INTERACTION AND IMPLOSION STUDIES IN LIMEIL RESEARCH CENTRE

A. BEKIARIAN - A. BERNARD - E. BURESI - R. DAUTRAY - M. DECROISETTE
F. DELOBEAU - P. GUILLANEUX - J.M. REISSE - B. SITT - J.M. VEDEL
J.P. WATTEAU

CENTRE D'ETUDES DE LIMEIL - B.P. 27 - VILLENEUVE SAINT GEORGES - FRANCE

I. INTERACTION EXPERIMENTS AT 1,06 µm

During the last year, Limeil laboratory placed emphasis in that field on a better knowledge of absorption and transport processes in 80 ps pulse experiments at λ = 1,06 µm.

Results dealing with absorption have been recorded with our solid D_2 plane target experiment /1/. Energy balance was performed using twenty five photon glass calorimeters, and an equal number of faraday cups or ion calorimeters isotropically set around the target ; the advantage of such an arrangement is an easy recording of energy lobes, for ions as well as for specular or scattered light. The normal to the target surface could be rotated in the horizontal plane, and a quartz plate allowed P or S polarization irradiations. Moreover, scattering spectra near 1,06 or 0,53 µm have been studied with a photodiode array system. Near 4.10^{15} W.cm^{-2} and for rotated angle of 15°, an absorption efficiency of 37 ± 2 % have been obtained for S polarization, and 60 ± 3 % for P polarization. Ion calorimetry was found in agreement with the photon energy balance. It was observed that P polarization increased ion acceleration along the normal to the target. Concerning the spectral studies, the Doppler shift of 2 ω0 harmonic was found to decrease and pass from the blue to the red side for increasing laser intensities around 10^{15} W.cm^2, while spectral width increased from 8 Å to ≃ 30 Å. Ion acoustic instability is able to explain such results, but to confirm this interpretation we still need further investigations which are now in progress.

Axial energy transport have been investigated in similar irradiation conditions (1,06 µm 80 ps) using layered targets /2/. The main diagnostic was here X-ray spectrography ; spatial profiles, energies and ratios of X-ray lines have been measured and compared to those deduced from a one dimensional hydrodynamic lagrangian code including thermal flux inhibition and preheating, X-ray emission being calculated with a corona model taking into account spectral opacities. Targets were composed of a glass substrate, coated with various thicknesses of aluminium between 160 and 4000 Å. In the case of single laser pulse, the ablation depth (deduced from the resonance Si-Lines cut off) and the dependence on Al thickness of the main lines intensity ratios, allowed to infer the thermal flux limitation factor for a given absorbed flux. Then, a double laser pulse technique (time delay 1-2 ns) producing two well separated-in-space X-ray emitting plasmas, gave access to parameters relative to the preheating due to fast electrons occurrence, as hydrodynamic strongly depends on the preheating depth and ratio. Typical values at ≃ 10^{15} W.cm^{-2} are : a few per cent for the thermal flux limitation factor, around 10 % for the preheating ratio, and 10 to 30 µm for the preheating depth.

II. IMPLOSION EXPERIMENTS

We reported at the Innsbruck conference (1978) the first results obtained with our implosion experiment Camelia /3/. It is performed with our eight beams laser facility Octal, currently delivering on target 1 TW in 50 ps. We proceeded with a series of implosion experiments in the exploding pusher regime /4/. Targets were microballoons typically less than 1 µm in wall thickness, 60 - 120 µm in diameter. The irradiation geometry was that previously described, i-e with the laser beams incoming along the directions of the diagonals of a cube, such a situation insuring a nearly isotropic energy deposition.

Besides usual corona and core diagnostics such as time integrated X-ray pinhole photographs or space resolved spectroscopy, particular interest has been given to neutron yield and evolution in time of X-ray emission. Implosion dynamics was obtained with a fast X-ray streak camera, the spatial resolution being given by a second slit perpendicular to that of the photocathode. A typical result is shown on the fig. 1 ; it has been obtained with a standard 80 µm diameter microballoon filled with ≃ 30 bars of DT. The collapse time, identified as the delay between corona and core emission, was 100 ps. On fig. 2 is reported the neutron yield versus the absorbed specific energy εa. If taking into account the fast ion energy, the neutron variation versus the useful specific energy is in good agreement with numerical predictions from the LLL analytical model /5/. At last the effect of a prepulse (in the contrast ratio range 10^4 - 10^6) on the implosion characteristics has been studied, which provided useful informations for exploding pusher regime understanding.

III. THEORY AND NUMERICAL SIMULATION

In relation with experimental studies, the following theoretical and numerical studies are pursued. A self similar expansion of a spherical plasma into vacuum, without any assumption about the electron states equation, has been developed /6/. In order to model fluid behaviour far away from quasi equilibrium when high gradients and thermal flux are existing an equation system giving the fourteen moments of a kinetic equation has been set, which describes as well adiabatic collisionless flow as collisionnal equilibrium. Thermal flux limitation by ion acoustic instability and the kinetic theory of magnetic fiel generation in resonant absorption of laser light /7/ have been also studied. In order to interpret X-ray spectra, a non LTE plasma ionisation model has been obtained by solving the rate equation for radiative and collisionnal transitions. Using a Monte Carlo simulation, penetration length of suprathermal electrons has been evaluated /8/.

Studies on the fluid dynamic stability of target implosions have been continued. In particular, theoretical model for the description of small perturbations of a plane or spherical implosion has been extended to include the effect of viscosity and of self-generated magnetic fields (which might reach the megagauss range in the overdense region) /9/. Besides, our spherical perturbation code PERTUS has been used to investigate more thoroughly the instability of the converging shock front and of the ablation layer /9/ /10/. At last, special emphasis has been put on the development of a two dimensional code to allow a better simulation of laser light absorption and thermal conduction.

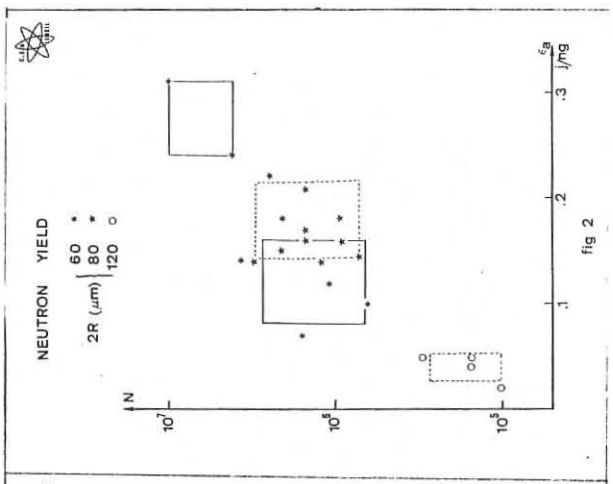

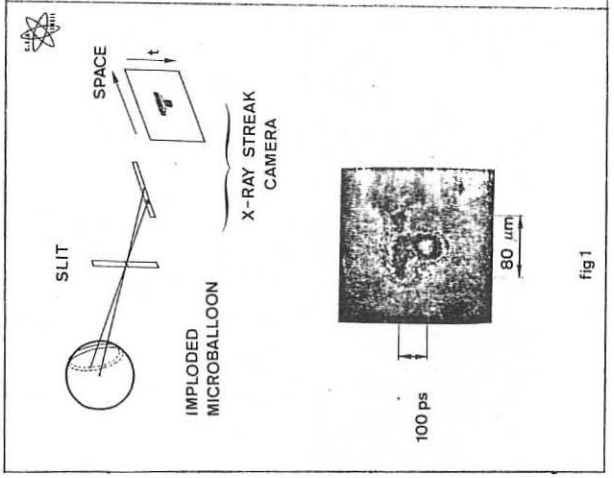

REFERENCES

/1/ C. GOUEDARD - A. SALERES
Experimental observation of non linear effects in a laser created plasma with S or P polarization
9th annual conference on anomalous absorption of electromagnetic waves. ROCHESTER 1979

/2/ J.C. COUTURAUD and al
Experimental and numerical energy transport studies with 80 ps ; 1,06 µm laser pulses
9th annual conference on anomalous absorption of electromagnetic waves - ROCHESTER 1979

/3/ A.BEKIARIAN and al
Travaux sur l'interaction et l'implosion laser au Centre d'Etudes de Limeil
7th conférence internationale sur la Physique des Plasmas - INNSBRUCK 1978

/4/ D. BILLON and al
Eight beams implosion experiments at Limeil
XIIth European conference on laser interaction with matter and laser thermonuclear fusion - MOSCOU 1978

/5/ E.K. STORM and al., P.R.L. 40, 24 (1978) 1570

/6/ P. MORA - R. PELLAT
Boltzmann equilibrium and energy conservation in the self similar expansion of a plasma into a vacuum
To be published in Physics of fluids

/7/ P. MORA, R. PELLAT - Journal de Physique lettres 40, 245 (1979)

/8/ J.P. NICOLLE
Etude du ralentissemrnt d'électrons suprathermiques dans un plasma créé par laser
rapport CEA - R - 4898

/9/ B. SITT
Analytical and Numerical studies of the Linear stability of Inertial Confinement Fusion target implosions,
Bull of the APS 24 (4) 721 (1979)

/10/ N.WILKE - B. SITT -
Stability of a spherical shock wave in the implosion of an ICF target, ibid

E1.7

RECENT HIGH DENSITY INERTIAL FUSION RESULTS FROM THE SHIVA FACILITY

E. K. Storm, H. G. Ahlstrom, J. A. Glaze, K. R. Manes, J. H. Nuckolls

University of California Lawrence Livermore Laboratory
Livermore, California 94550

One of the near team goals of the inertial confinement fusion program at the Lawrence Livermore Laboratory, is to demonstrate scientific breakeven with the Nova laser system in the mid-1980's. The conditions required for this goal are several thousand times liquid DT densities at fusion ignition temperatures. The Shiva laser system, capable of focusing up to 15 kJ at 1 nsec and 30 TW at 100 psec, was developed to study the physics of laser driven inertial confinement fusion (ICF) and attain intermediate milestones for the U.S. ICF program. In recent experiments we have achieved compressed DT fuel densities in excess of 15 9/cm^3, or greater than 75 times the liquid density of DT. Although the DT burn temperatures obtained were rather low, ~0.5 keV, neutron yields of 10^7 imply that confinement-time product values ($n\tau$) in excess of 10^{14} cm^{-3} sec were achieved.

Extensive target diagnostics have been developed for Shiva. These diagnostics are routinely used to measure neutron yield and spectrum, energy balance, alpha, beta, X-ray, optical, ion and proton spectra and temporally, spatially and spectrally resolved X-ray and alpha particle emissions of the imploding target. Some of the more recent additions to our target diagnostics capability are listed in Table I. Four new instruments have been developed to investigate implosion dynamics and to determine the fuel density of the imploded fusion pellet. The first, neutron interval timing, is used to measure the time interval between the peak of the laser pulse and the later neutron emission from the imploded fuel. An example of data from this diagnostic, in the form of average implosion velocities for 3 generic target types, is shown in Figure 4. The second utilizes an imaging X-ray spectrometer to measure the spatial extent of Argon tracer seed gas introduced into the DT fuel. An example of data from this technique for an exploding pusher target is shown in Figure 2. Figure 3 shows the compressed fuel as determined from our α zone plate coded imaging technique for the same experiment, indicating good agreement between the two methods. The Argon imaging spectrograph will be used in the intermediate density regime when the α-particle range prohibits the use of the zone plate coded imaging technique. The third utilizes radiochemistry techniques to obtain a direct measurement of the average density-radius product ($\rho\Delta r$) of the various target elements at peak neutron production. A generic target with several possibilities for this technique is shown in Figure 4. From measurements such as these, the final DT fuel density can be inferred. The fourth technique involves X-ray backlighting. By creating an intense X-ray source and spatially and temporally resolving the transmission of these X-rays through the target, detailed information about the target dynamics can be obtained. We have recently carried out the preliminary experiments shown in Figure 5. For this experiment, no time resolution was attempted, and the target itself was not irradiated. A Fresnel zone plate coded aperture was used to image the transmission of Sn L line emissions through a 143 μm by 5 μm thick SiO_2 microsphere coated with 50 um of CH.

During the past year we have irradiated both exploding pusher and ablatively driven targets with simple pulse shapes, producing higher neutron yields than previously attained from both types of targets. A series of target irradiations with exploding pusher designs at 15 to 20 TW in a 90 ps pulse resulted in a maximum neutron yield of 3 X 10^{10}. In addition the experiments further extended our confidence in our simple exploding pusher model. Figure 6 shows a comparison with predicted and measured neutron yields as a function of specific energy absorbed by the target. The exploding pusher targets were also used to correlate fuel densities as inferred from radiochemistry neutron activation techniques and α zone plate imaging. The exploding pusher high neutron yields produced easily detectable quantities of Al^{28} by neutron activation of silicon in the target shell, and made possible the determination of the $\rho\Delta r$ of the imploded shell. The inferred fuel density from this experiment, was then compared with data from the α zone plate camera on the same shot. A simple isobaric-isothermal model has been developed which relates pusher $\rho\Delta r$ values to final fuel densities both for exploding pusher targets and for targets such as the one indicated in Figure 7. This model and the exploding pusher scaling regime, is compared to detailed 1-D simulations in Figure 8. To date, neutron yields in excess of 10^7 have been obtained from the exploding outer shell high density targets shown in Figure 7. Irradiation of ablatively driven targets designed for high compression at 7 to 10 kJ with pulses from 0.7 to 1 ns duration have produced a maximum neutron yield of 1 x 10^8. Peak DT densities in excess of 15 9/cm^3 have been observed. The total range of DT densities and neutron yields available with the 10 kJ/1 ns to 25 TW/100 ps Shiva facility are summarized in Figure 9. Results of these, and other experiments, will be reviewed.

NEW TARGET DIAGNOSTICS

- Pb Activation detector ~ hi sensitivity, noise immune neutron yield
- S-20 streak camera with orange and blue energy channels ~ 0.3 - 80 eV preheat temperature measurements
- Dante, windowless x-ray diodes and filters ~ x-ray spectrum $h\nu$ = 100 eV - 1.5 keV
- Dante 5-2 ~ 20 - 100 eV preheat temperature measurements
- Carbon window x-ray streak camera with mirror reflectors and filters ~ 15 ps time resolved x-rays $h\nu$ = 200 - 700 eV
- Fast flat colorimeter, windowless x-ray diode with composite filter ~ 200 ps time resolved x-rays $E(T) = \int_0^{1.5\,keV} E(h\nu)\,dh\nu$
- Filter fluorescer experiment ~ x-ray spectrum 5 keV - 300 keV
- Pusher tracer radio chemistry ~ Si pusher $\rho\Delta r$
- Fuel tracer radio chemistry ~ fuel ρr
- Argon Line Imaging Spectragraph ~ fuel radius
- Fast neutron detector, microchannel pluto ~ laser pulse to neutron pulse interval time
- X-ray backlighting ~ implosion history and symmetry

Table 1

Work performed under the auspices of the U.S. Department of Energy by the Lawrence Livermore Laboratory under contract number W-7405-Eng-48.

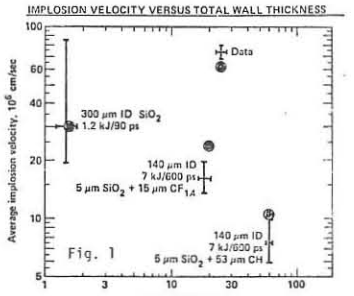

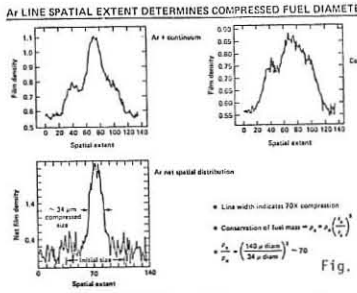

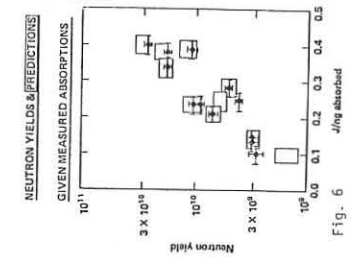

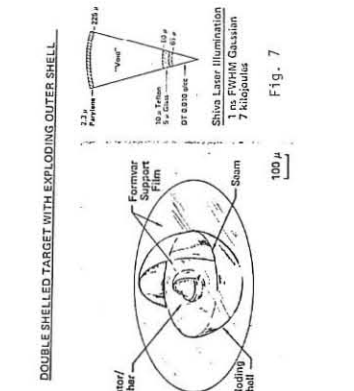

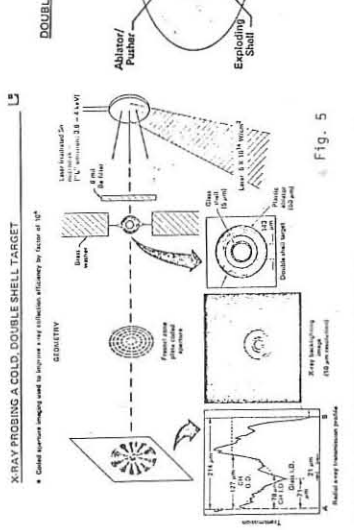

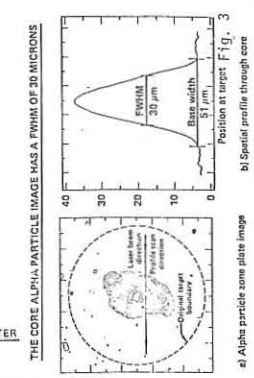

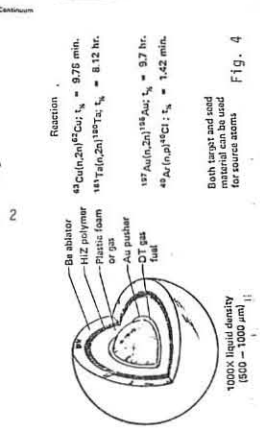

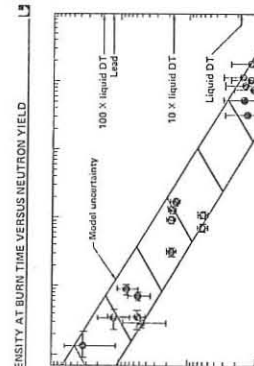

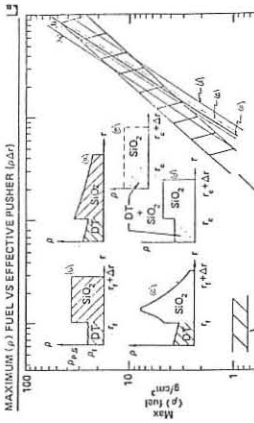

PLASMA HEATING BY THE AMPLIFIER MODULE RADIATION IN THERMONUCLEAR INSTALLATION "DELFIN"

N.G.Basov, Yu.A.Mikhailov, G.V.Sklizkov, S.I.Fedotov

P.N.Lebedev Physical Institute of Academy of Sciences of the USSR, Leninsky prospect 53, Moscow, USSR

The laser amplifier module under consideration is a basic unit of a multi-beam fusion installation "DELFIN". This installation is intended for spherical heating of plasma at the light energy level $E_L \simeq 10^4$ J [1,2]. Laser installations for such experiments must comply with a number of specific demads, such as high degree of energy contrast ratio $K_E \simeq 10^7$-10^8, small divergence of laser radiation $\alpha \simeq 10^{-4}$-10^{-3}, precise time and space synchronization of a great number of optical beams, and a possibility of pulse shaping in time interval $\tau_L \simeq 0.1$-10 ns [2,3]. Noted requirements have been taken into account in the creation of the amplifier module.

Laser radiation from the output of the linear preliminary stages of amplification with energy $E_{LPSA} \simeq (30\text{-}40)$J and beam diameter ϕ 45 mm is directed into amplifier module. Construction was based on successive-parallel disposition of active elements with splitting coefficients from stage to stage : n=3,2,3,3. Mentioned above parameters of laser radiation have been measured along the optical beam, and the corresponding correction of beam quality has been performed by means of optimization and alignment of the optical elements. In Fig. 1 is presented far field transformation distribution, which is connected with a divergence of laser radiation.

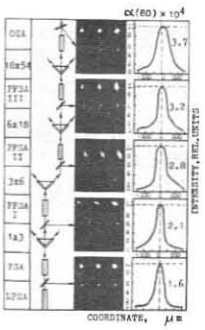

Fig.1. Far field zone of laser radiation at different stages of amplifier module. α - radiation divergence.

At the amplifier module output 54 light beams 45 mm in diameter are summed into 3 composed beams containing 18 small beams each. These 3 composed beams correspond to the three out of twelve directions of the target illumination in the vacuum chamber.

Fig.2 presents far and near field distributions pictures for one of the composed beams. Laser radiation parameters for pumping Nd-glass active rods by light pulses with energy $E_p \simeq 25$ kJ per amplifier in the time interval τ_p =800 μs are listed in Table 1.

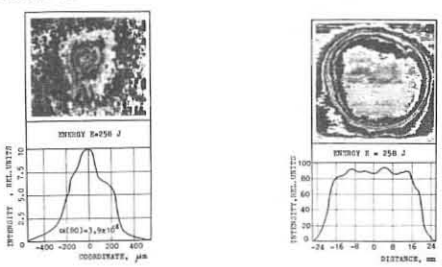

Fig. 2. Typical structure of a composed beam in far field (A) and in the near field (B)(B - for one of 18 small beams).

Table 1.

CROSS SECTION cm^2	NUMBER OF BEAMS ϕ45 mm	ENERGY J	DIVERGENCE rad	FLUX DENSITY W/cm^2	BRIGHTNESS W/cm^2ster
810	3x18=54	10^3	$3.9.10^{-4}$	5.10^8	10^{15}

Radiation of each of the composed beams (285 mm in aperture) was directed by means of prisms and lenses into a vacuum chamber and was focused by two-component objectives with equivalent focal length f_s=780 mm onto the target. In our experiment Al foils 0.5-10 μm thick, and both glass and plastic spherical microshells were used as targets. The main goals of the experiments with one and three composed beams was to study optical communication in laser-target system, and the efficiency of laser light absorption in thin-shell targets. Investigations of the energy balance in laser-target system and the composed beams parameters during interaction with plasma showed good optical isolation of the amplifier stages from plasma reflected radiation. The latter was about 3 % of the radiation incident onto the plasma (in focusing optics aperture). Measurements of plasma parameters carried out by X-ray spectroscopy of both Bremstrallung [4] and linear [5] radiation from plasma allowed us to make a conclusion about possible heating of thin shells up to the kilovolt temperatures. Flux densities of laser radiation on the target surface were $q \simeq 10^{14}$ W/cm^2. Figure 3 presents pin-hole photographs of a plasma target in its X-ray radiation in the wavelength region $\lambda = (3.5 - 5.5)$Å . X-ray radiation spectra of multiply charged ions in laser plasma are used for space resolved measurements of the electron temperature and electron density profiles.

Fig.3. Pin-hole image of thin foil plasma in 3 frames.

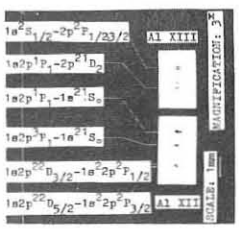

Fig.4. Typical spectrogram of [H]- and [He]-like AlXIII and AlXII ions from foil plasma.

References

1. N.G.Basov, O.N.Krokhin, Yu.A.Mikhailov, G.V.Sklizkov, S.I. Fedotov. In: Proc. of the VIII European Conf. on Controlled Fusion and Plasma Physics, p.53, Prague, 1977.
2. N.G.Basov et al. Trudy FIAN, 103, p.3, 1978.
3. O.N.Krokhin, Yu.A.Mikhailov, G.V.Sklizkov, S.I.Fedotov. Sov.J.Quant.Electron., 6, 3, p.347, 1976.
4. O.N.Krokhin, Yu.A.Mikhailov, A.A.Rupasov, G.V.Sklizkov, A.S.Shikanov, Yu.A.Zakharenkov, N.N.Zorev. In: Proc. of XII Internat.Conf. on Phenomena in Ionized Gases, p.349, Eindhoven, 1975.
5. Yu.A.Mikhailov, S.A.Pikuz, G.V.Sklizkov, A.Ya.Faenov, S.I.Fedotov. Sov.J.Optics and Spectroscopy, 42, 5, p.811, 1977.

E2.1

NONRESONANT DECAY OF LOWER HYBRID WAVES

M. BRAMBILLA, B. LIBERMAN*, S.S. PESIC, D. MOREAU

ASSOCIATION EURATOM-CEA
DPh-PFC - Centre d'Etudes Nucléaires
85 X - 38041 GRENOBLE CEDEX (France)

Parametric decay of Lower Hybrid waves has been extensively studied since a few years[1]. To derive the dispersion relation of the decay waves, two different approaches have been used in the literature. In the first[2] the pump electric field is assumed to be homogeneous in space (dipole approximation) and Vlasov Equation is integrated in the Oscillating Center Coordinates (OCC). In the second approach[3] the parametric decay process is considered as the linear stage of a three wave interaction (pump, sideband and beat wave) and the dispersion relation is obtained from a recursive solution of Vlasov equation.

To second order in the amplitude of the pump, one would expect agreement between the two approaches in the limit in which the wavelength of the decay wave is short compared with the wavelength of the pump, $|\vec{k}| >> |\vec{k}_o|$. In this limit, the dispersion relation obtained in[3] (neglecting for simplicity the upper sideband and terms small in the electron to ion mass ratio) becomes

$$\varepsilon\ (\omega,\ \vec{k}) = \frac{|\mu_e|^2}{4}\ \frac{\left[\chi_e(\omega,\ \vec{k}) - \chi_e(\omega-\omega_o,\ \vec{k})\right]^2}{\varepsilon(\omega-\omega_o,\vec{k})} \qquad (1)$$

where

$$\mu_e = \frac{e}{m_e}\left[\frac{(\vec{E}_o \times \vec{k})\cdot\vec{b}}{\omega_o\ \Omega_{ce}} + i\ \left(\frac{\vec{E}_{ok}\vec{k}_\perp}{\Omega^2_{ce}} - \frac{E_{//o}k_{//}}{\omega^2_o}\right)\right]$$

($\vec{b}$ is a unit vector in the direction of the static magnetic field ; other notations are standard). Eq. (1) has to be compared with the dispersion relation obtained with the OCC method but under otherwise identical assumptions,[2]

$$1 = -\frac{|\mu_e|^2}{4}\left\{\frac{\chi_i(\omega-\omega_o,\ \vec{k})\ \chi_e(\omega-\omega_o,\ \vec{k})}{\varepsilon(\omega-\omega_o,\vec{k})} + \right.$$
$$\left. + \frac{\left[\chi_i\ (\omega-\omega_o\ ,\ \vec{k}) - \chi_i\ (\omega,\ \vec{k})\right]\left[\chi_e(\omega-\omega_o,\ \vec{k}) - \chi_e\ (\omega,\ \vec{k})\right]}{\varepsilon(\omega,\ \vec{k})\ \varepsilon(\omega-\omega_o\ \vec{k})}\right\} \qquad (2)$$

If both the sideband and the beat waves are resonant,

$$\varepsilon_{Re}\ (\omega,\ \vec{k}) = 0 \quad (\omega_1 = \omega,\ \ \omega_2 = \omega - \omega_o) \qquad (3)$$

Eq.(2) becomes identical with Eq.(1). However Eqs.(1) and (2) admit unstable solutions for which (3) are not valid, the beat wave being heavily damped or evanescent in the absence of the pump. For such "quasimodes" Eqs. (1) and (2) are quantitatively different, as illustrated by the example of Fig. 1 (these curves are obtained from the complete dispersion relations of[3] and[2] respectively ; the curves cross at a point which happens to satisfy Eqs.(3) exactly). The discrepancy between the two approaches had been previously noted for unmagnetized plasmas[4].

To understand the origin of the discrepancy, we recall how Vlasov Equation is solved in the two cases. The steady state distribution function in the OCC method is assumed to be

$$F^{OC}\ (\vec{v},\ t) = F_M(|\vec{v} - \vec{u}_E|^2) \qquad (4)$$

where F_M is usually a Maxwellian, and $\vec{u}_E(t)$ is the oscillating velocity of the particles in the pump field. To solve the perturbed Vlasov Equation one then looks for a solution of the form

$$\delta f^{OC}(\vec{r},\ \vec{v},\ t) = \tilde{f}\ (\vec{v}-\vec{u}_E(t))e^{\,i\left[\vec{k}\cdot(\vec{r} - \int^t \vec{u}_E(t')dt') - \omega t\right]} \qquad (5)$$

$\tilde{f}(\vec{w})$ then satisfies a linear Vlasov Equation from which $\vec{E}_o(t)$ has been eliminated and whose integration is straightforward. The dispersion relation (2) is then found by applying Floquet theorem and developing Poisson Equation to 2^d order in $|\mu_e|$.

However (5) is not the solution one would obtain by integrating the perturbed Vlasov equation along its characteristics (the later has an unmanageable secular term in the phase factor). The difference has a non-vanishing component at the pump frequency, implying the need of a "renormalization" if (4) has to represent the steady state to all orders. However, since the choice of F_M is arbitrary, while the dispersion relation of quasimodes is critically sensitive to corrections of order $|\mu_e|^2$, it appears difficult to reach unambiguous conclusions within the OCC method.

On the other hand in the iterative approach

$$F(\vec{v},\ t) = F_M(v^2) - \vec{u}_E(t)\ \cdot \frac{\partial F_M}{\partial \vec{u}} \qquad (6)$$

This is not just an approximation to Eq. (4), but corresponds to the assumption that to order $|\mu_e|$ the pump propagates linearly, the "exact" integrals of motion in the pump field being destroyed in less than a bounce time. A sufficient condition for this is $|\Delta(\omega_o/k_{//o})| \simeq (\omega_o/k^2_{//o})|\Delta k_{//o}| >> (2eE_o/m_e k_{//o})^{1/2}$, always satisfied by LH waves excited by a finite length antenna.

To next order $F_M(\vec{v})$ will vary slowly with time because of quasi-linear diffusion in velocity space due to interaction with the pump. For electrons[5] :

$$\frac{\partial F_e}{\partial t} = -\frac{\pi^2 e^2}{2m_e^2}\int dk_{//o}\ \frac{|E_o(k_{//o})|^2}{k_{//o}}\ \frac{\partial}{\partial v_{//}}\ \delta(v_{//} - \frac{\omega_o}{k_{//o}})\ \frac{\partial F_e}{\partial v_{//}} \qquad (7)$$

This equation has within the iterative approach just the same role as renormalization within the OCC method ; however here the arbitrariness of the steady state distribution function has been eliminated using simple and justified physical assymption.

The dispersion relation of Ref.[3] is then obtained by iterating twice the perturbed Vlasov Equation and substituting into Poisson equation. In so doing, terms of order $|\mu_e|$ drop out, and the usual coupling coefficient of order $|\mu_e|^2$ is obtained. It turns out however that terms of this order are contributed also by the next iteration, in the form of nonlinear modification of the susceptibilities, e.g.

$$\delta\varepsilon(\omega_\pm,\ \vec{k}_\pm) = \sum_{sp}\ \frac{e^2|\phi^+_{ko}|^2}{16m^2v^4_{th}}\ \frac{\omega_p^2}{k^2_\pm\ v^2_{th}}\ v^5_{th}\ d_3\vec{v}\int_0^\infty d\tau' G'_{k_\pm}\ (\pm i\vec{k}_o\ \cdot \frac{\partial}{\partial\vec{v}'}) \cdot$$
$$\cdot\int_0^\infty d\tau'' G^+_{\vec{k}}(r'')\left\{ i\vec{k}_\pm \frac{\partial}{\partial\vec{v}''}\int_0^\infty d\tau'''\ G'''_{k_o}\cdot(\mp i\vec{k}_o\cdot\frac{\partial F_M}{\partial\vec{v}'''}) + (\mp\vec{k}_o \neq \vec{k}_\pm)\right\} \qquad (8)$$

where $G^+_{k_\alpha}$ represent the usual propagators. For nonresonant decays, $\varepsilon(\omega,\vec{k})=O(1)$ implies $\varepsilon(\omega_\pm,\vec{k}_\pm) = 0\ (|\mu_e|^2)$ for one of the sidebands ; hence the corresponding $\delta\varepsilon_\pm$ cannot be neglected.

In conclusion, the iterative approach correctly describes in principle the nonresonant decay of LH waves in Tokamaks ; the dispersion relation quoted in /3/ is however incomplete. Work to evaluate (8) explicitly and to include it in the numerical code which solves the dispersion relation is actively in progress.

* Permanent adress : Institut de Fisica, UFRGS 90.000, Porto Alegre-RS-Brazil.

1 - M. PORKOLAB, Nucl. Fusion 18, 367, 1978 and references therein.
2 - M. PORKOLAB, Phys. Fluids 20, 2058, 1977 ; S.S. PESIC Phys. Lett. A65, 124, 1978.
3 - V.K. TRIPATHI; C. GREBOGI, C.S. LIU, Phys. Fluids 20, 1525, 1977 ; D.C. WATSON, A. BERS, Phys. Fluids 20, 1074, 1977.
4 - NGUYEN THE HUNG, J.M. WERSINGER, Helvetica Phys. Acta 48, 465, 1975.
5 - N.J. FISH, Phys. Rev. Letters 41, 873, 1978.

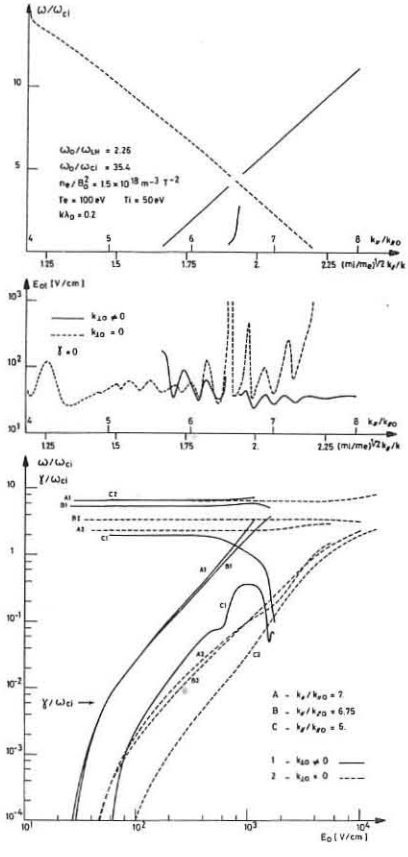

Fig. 1 - Decay spectrum for $\omega_o/\omega_{LH} = 2.26$ (—— iterative method ; ---- OCC method).

THE DISTORTION OF THE THERMAL ION DISTRIBUTION BY NEUTRAL INJECTION HEATING

E Bittoni*, J G Cordey and M Cox
Culham Laboratory, Abingdon, Oxon, OX14 3DB, UK.
(Euratom/UKAEA Fusion Association)

*Permanent address: CNEN, Centro Calcolo (Bologna)

ABSTRACT It is shown that the heating of a plasma by neutral injection leads to the formation of a high energy tail on the background ion distribution. The temperature of this tail is found to vary rapidly with the ratio of fast ion to thermal ion energy density. The case of particle loss by charge exchange is given particular attention.

INTRODUCTION In many experiments, including recent neutral injection experiments on PLT[1], the energy spectrum of the charge-exchange atom flux has a two temperature form. At low energies the spectrum is approximately Maxwellian with a low temperature, usually much less than 1 keV, while at higher energies the spectrum corresponds to a Maxwellian of much higher temperature. One explanation[2] of this is that the low temperature component is a measure of the temperature near the edge, whereas the high energy tail is a measure of the central plasma temperature. It was then shown by Cordey[3] that neutral injection heating could lead to a strong distortion of the thermal ion distribution. We examine this distortion mechanism in more detail by solving the linearised Fokker-Planck equation analytically. These analytical results have been checked by numerical solution of the full equation and a comparison is given for the case of particle loss by charge-exchange.

SOLUTION OF THE FOKKER PLANCK EQUATION We consider an equilibrium Fokker-Planck equation for the zeroth term, f_o, in the Legendre polynomial expansion of the distribution function[4]. Particles are lost by either diffusion or charge-exchange (containment time τ_c) and energy is lost by thermal conduction (containment time τ_ε). Constant density is maintained by ionising the background gas (assumed to be monoenergetic for convenience) at the same rate as particles are lost. The resulting equation is

$$\Gamma\left[(2v^2)^{-1}\frac{\partial^2}{\partial v^2}\left(v^2\frac{\partial^2 g}{\partial v^2}f_o\right) - v^{-2}\frac{\partial}{\partial v}\left\{(v^2\frac{\partial h}{\partial v}+\frac{\partial g}{\partial v})f_o\right\}\right]$$

$$-\frac{f_o}{\tau_c}+\left(\int_o^\infty\frac{f_o v^2 dv}{\tau_c}\right)\frac{\delta(v-v_{neut})}{v^2}+\frac{1}{2v^2}\frac{\partial}{\partial v}\left(\frac{f_o v^3}{\tau_\varepsilon}\right)=0 \qquad (1)$$

where $\Gamma=4\pi e^4 Z_i^2 \log n/m_i$. The functions h and g, the Rosenbluth potentials, are summed over the species present to take account of thermal-thermal, thermal-fast ion collisions and thermal ion-electron collisions. Integrating eq(1) with respect to v and after taking the electron distribution as Maxwellian one obtains

$$\frac{1}{f_o}\frac{\partial f_o}{\partial v^2}=-\Bigg[\frac{\kappa}{v_c^3 f_o}\int_v^\infty\frac{f_o v^2 dv}{\tau_c}+\frac{\kappa}{v_c^3 f_o}(H(v-v_{neut})-1)\int_o^v\frac{f_o v^2 dv}{\tau_c}+\frac{\kappa v^3}{2\tau_\varepsilon v_c^3}$$

$$+\frac{n_e v^3}{v_c^3}+\frac{Z_f^2 m_i}{3m_f}\int_o^v f_f v^2 dv+Z_i^2\int_o^v dv v^2 f_o\Bigg]\Bigg/$$

$$\left[\frac{n_e m_e v_e^2 v^3}{m_i v_c^3}+\frac{2}{3}Z_f^2\left(\int_o^v dv v^4 f_f+v^3\int_v^\infty dv v f_f\right)+\frac{2}{3}Z_i^2\left(\int_o^v dv v^4 f_o+v^3\int_v^\infty dv v f_o\right)\right] \qquad (2)$$

where $\kappa=n_e\tau_s=10^{12}A_i T_e^{3/2}/Z_i^2$, $v_c^3=0.75\pi^{\frac{1}{2}}m_e v_e^3/m_i$, f_f is the fast ion distribution and v_{neut} is the speed of the background gas atoms. The subscripts e, i, f refer to the electrons, background ions and fast ions respectively. When $v>>v_i$ eq(2) may be linearised by replacing $\int_o^v f_o v^2 dv$ by n_i then solved by substituting the eikonal form

$$f_o \sim \exp\left\{-\frac{m}{2}\int_o^{v^2}\frac{dv^2}{T(v^2)}\right\} \qquad (3)$$

This gives

$$\frac{m_i}{2T(v^2)}=\left[n_i Z_i^2+\frac{\kappa v^3}{2v_c^3}\left(\frac{m_i}{2\tau_c\ln v^2}+\frac{v^2}{\tau_\varepsilon}\right)+n_e v^3/v_c^3+\frac{Z_f^2 m_i}{3m_f}S\tau_{sf}\,2n(v^3/v_c^3+1)\right]\Bigg/$$

$$\left[2Z_i^2 n_i T_{act}/m_i+n_e v^3 v_e^2 m_e/m_i v_c^3+\frac{2}{3}Z_f^2 S\tau_{sf}\left\{\int dv v^4/(v^3+v_c^3)\right.\right.$$

$$\left.\left.+v^3\int_v^{v_{inj}} dv v/(v^3+v_c^3)\right\}\right] \qquad (4)$$

where $T_{act}=\frac{m_i}{3n_i}\int_o^\infty dv v^4 f_o$ and the fast ion distribution has been assumed to be[5]

$$f_f = S\tau_{sf}/(v^3+v_c^3) \qquad v \le v_{inj}$$
$$= 0 \qquad v > v_{inj}$$

with $\tau_{sf}=10^{12}A_f T_e^{3/2}/Z_f^2 n_e$. We now investigate two specific examples.

(a) Good High Energy Containment We consider the case where the energy and particle confinement is very good at high energies, all the energy being lost by the low energy ions. Assuming $v^3/v_c^3 \ll 1$, eq(4) gives for $v \ll v_{inj}$ $T = T_{act}$, and for $v > v_{inj}$

$$T=\left(\frac{n_i}{m_i}T_{act}+\frac{2}{3}\frac{n_f}{m_f}\bar{\varepsilon}_f\right)\Big/(n_f/m_f+n_i/m_i)$$

Thus the ratio of tail temperature, T_{tail}, to T_{act} is

$$\frac{T_{tail}}{T_{act}}=\frac{1+\frac{2}{3}\frac{\bar{\varepsilon}_f}{T_{act}}\frac{n_f}{n_i}\frac{m_i}{m_f}}{1+\frac{n_f}{n_i}\frac{m_i}{m_f}}$$

Since the mean energy of the fast ions $\bar{\varepsilon}_f$ is always much greater than $\frac{3}{2}T_{act}$, T_{tail} is always larger than T_{act} and is a measure of the mean energy of the total ion population (fast plus thermal) rather than the temperature of the thermal ions.

(b) Loss of Particles by Charge Exchange We assume τ_c to be constant and τ_ε to be infinite. Again using eq(4) we obtain

$$\frac{T_{tail}}{T_{act}}=\frac{1+\frac{2}{3}\frac{m_i}{m_f}\frac{n_f}{n_i}\frac{\bar{\varepsilon}_f}{T_{act}}+\left(\frac{v_{inj}}{v_c}\right)^3\frac{n_e T_e}{n_i T_{act}}}{1+\frac{m_i}{m_f}\frac{n_f}{n_i}+\frac{n_e}{2}\frac{\tau_s}{v_c^3}\frac{v_{inj}}{\tau_c}\frac{2T_{tail}}{m_i n_i}+\left(\frac{v_{inj}}{v_c}\right)^3\frac{n_e}{n_i}} \qquad (5)$$

Where, in this case, T_{tail} is the value of $T(v^2)$ at $v = v_{inj}$. This expression may be used to determine T_{act} from experimentally measured values of T_{tail} if τ_s and τ_c are known. To proceed with the analytic solution the thermal ion containment time, τ_c, must be expressed in terms of the other parameters. This may be achieved by using the ion power balance equation which is

$$\frac{n_f(\bar{\varepsilon}_f-\frac{3}{2}T_{act})}{\tau_{fi}}=\frac{n_i}{\tau_c}\left(\frac{3}{2}T_{act}-E_{neut}\right)+\frac{3}{2}\frac{n_i(T_{act}-T_e)}{\tau_{ie}} \qquad (6)$$

where τ_{fi} and τ_{ie} are the relevant average energy transfer times. For simplicity we have assumed that both τ_{fi} and τ_{ie} are equal to the energy transfer times for the case when the distribution functions are Maxwellian[5]. The results of substituting for τ_c from eq(6) into eq(5) are shown in Fig.1 for various n_f/n_i with the other parameters fixed. One sees that, as expected, the ratio T_{tail}/T_{actual} increases with increasing n_f/n_i at constant T_{tail} and that it is largest for small values of T_{tail}. Note also that the curves drop below $T_{tail}/T_{actual} = 1$ at higher temperatures. In Fig.2 the $n_f/n_i = \frac{1}{4}$ curve from Fig.1 is compared with the numerical results for the same parameters. It can be seen that the agreement between the two is good, particularly for small T_{tail}.

CONCLUSION We have found that neutral injection gives rise to a distortion of the ion distribution which is strongly dependent on the form of the loss mechanism and also the ratio of fast ion to thermal ion energy density.

For loss by charge-exchange, the distortion is small at the high tail temperatures (≤ 6 keV) seen in PLT.

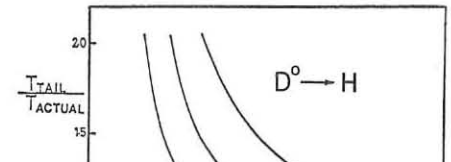

Fig.1 $n_i = 3 \times 10^{13} cm^{-3}$, $T_e = 3$ keV, $E_{neut} = 0$. Injection energy = 40 keV. $n_f/n_i = \frac{1}{4}$.

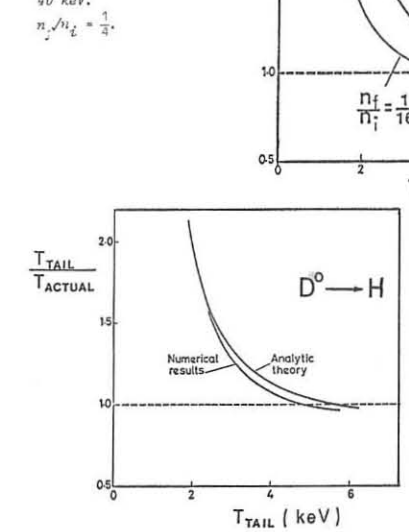

Fig. 2 Comparison between numerical and analytical results for parameters given in Fig.1 with $n_f/n_i = \frac{1}{4}$.

REFERENCES
[1] Eubank H et al, IAEA VII Conf. on Plasma Physics and Controlled Nuclear Fusion Research, Innsbruck (1978), paper IAEA-CN-37-C3
[2] Parsons C R and Medley S S, Plasma Physics, Vol 16, 267 (1974)
[3] Cordey J G, Plasma Physics and Controlled Nuclear Fusion Research, IAEA-CN-33/A16-1 623 (1975)
[4] Rosenbluth M N, McDonald W M and Judd D L, Phys. Rev. 107, 1 (1957)
[5] Book D L, NRL Plasma Formulary

ACKNOWLEDGEMENT The authors acknowledge with pleasure several discussions on this work with Dr R J Goldston.

E2.3

ION-ION HYBRID RESONANCE DAMPING AND HEATING IN THE ERASMUS TOKAMAK.

V.P. BHATNAGAR, G. BOSIA, M. CALDERON, I. DARIUS, E. DESOPPERE, R. KOCH, A.M. MESSIAEN, D. PEARSON, Cl. PIRET, G. TELESCA, P.E. VANDENPLAS, G. VAN OOST, R.R. WEYNANTS

Laboratoire de Physique des Plasmas - Laboratorium voor Plasmafysica
Association "Euratom-Etat belge" - Associatie "Euratom-Belgische Staat"
Ecole Royale Militaire - 1040 Brussels - Koninklijke Militaire School

Significant theoretical and experimental progress (TFR, PLT, DIVA) is presently being made in the understanding of ICRF heating. Prominent in this respect is the insight in the role played by the ion-ion hybrid resonance in two-component plasmas. Recent experiments on ERASMUS confirm important details of this process and enlarge significantly the experimental data base concerning these phenomena.

(i) The damping of the magneto-acoustic eigenmodes, excited in the toroidal cavity, and as inferred from their Q values, is shown to be attributable to the mode conversion that results from the ion-ion hybrid resonance.

(ii) The spatial localization of the heat deposition resulting from the mode conversion mechanism is consistent with the heating results at power levels up to 50 kW, and where ion temperature increases up to 40 % are observed.

The characteristics of the coil loading are such that the coupling to magnetosonic waves does not appear to be the only contribution to the loading resistance. This might have an important bearing on the overall heating efficiency, for which only very preliminary estimates are at present available.

1. Description of the RF setup.

The launching half loop antenna is "all metal" and of the strip line type with an electrostatic shield made of stainless steel strips (see Fig. 1). Penetration of the plasma into the antenna is prevented by a second row of radial strips and by the closeness of the Mo limiter (ϕ = 39 cm). The antenna is fed through an impedance matching network,consisting of a transmission line of length $l \lesssim \lambda/4$ having a characteristic impedance of 16.7 Ω and of a tunable condensor C_A,by a Colpitts oscillator capable of delivering up to 150 kW into its tank circuit at 4.85 MHz.The power delivered by the generator can be written as $P_T = \frac{1}{2} I_A^2 (R_C + R_S)$ where R_C (≈ 0.38 Ω) is an equivalent series resistor accounting for all the losses in the absence of plasma (tank, coupling system and antenna) and R_S is the loading resistance due to the plasma. I_p is measured by a current transformer and $P_{HF} = \frac{1}{2} I_A^2 R_S$ is obtained from VI cos ϕ as indicated in Fig. 1.

2. Wave damping.

The quality factor Q of the toroidal eigenmodes is a direct measure of the amount of wave damping and ion-ion hybrid mode conversion is identified in ERASMUS as the dominant damping mechanism[1]. We summarize these findings in view of their connection to the heating results reported further on.

(a) A simplified analysis [1], based on the Budden model [2], leads to $Q = \frac{1}{2} \frac{a}{\bar{w}} \frac{a}{h} G$, where a is the plasma radius,$\bar{w}$ the distance between cut-off and confluence in the cold plasma approximation and averaged over the plasma cross section and h is the half length of the chord along which $\omega = 2\omega_{CD} = \omega_{CH}$. G is the average ratio of the perpendicular phase and group velocities.

(b) Agreement within a factor of two is obtained between the above formula and the measured Q, when the plasma composition is changed from 95 % of deuterium to 95 % of hydrogen and when the conversion layer is moved from the plasma center to the boundary. Figure 2 shows an example of the comparison between theory and experiment. The experimental error is about 20 % .

(c) At high power excitation, the resonances often become less defined because of the interaction of the RF with the background plasma resulting in density modification, MHD activity and increased fluctuation level.

3. Heating results.

(i) Overall plasma response.

The sequence shown in Fig. 3 is an average over about 15 shots, necessitated by the one pulse-per-shot limitation of the laser scattering, the rather large error bars on the ion temperature measurements and the low reproducibility of the discharge in the presence of RF.

Figure 3a shows the power input. Trace 1 is a typical record for one shot showing the individual resonances on top of a non-resonant background loading. The resonances account for at most 30 % of the power input. The time of occurrence of the resonances shifts from shot to shot yielding a rather smooth average power deposition (curve 2).

The plasmas reacts by an increase of the loop voltage together with an increase of MHD activity which, however, does not result in a disruptive instability (3b), a decrease of the plasma current (3b) and an increase of the ohmic heating power (3c). The central density increase (3d) amounts to about 20 % with an average of about $2.0 \times 10^{12} cm^{-3}$ per 40 kW injected. The density build up starts at the edge and gradually pervades the interior. The central electron temperature (3e) is not affected within the 25 % error bars of the laser scattering, whereas the ion temperature (3f) as measured by the Doppler broadening of an OV impurity line increases distinctly. The ion heating is not due to the density increase as borne out by gas puffing simulation. An influx of impurities is apparent from the enhancement of the OV light output, as well as CV, and NIV, and from the increase of Z_{eff} (resistivity) from 4 to 5 (3g). The latter effect also accounts for the overall increase of P_{OH}.

(ii) Ion heating.

The dependence of the ion heating efficiency, defined as $1.5 \int N\Delta T_i dV / P_{HF,o}$, on the hydrogen concentration (Fig. 4a) has been studied at fixed frequency and magnetic field. In spite of the low reproducibility, the trend implied by the average dotted line is clear : heating occurs over a rather broad concentration range but decreases distinctly towards high $X_H = N_H/(N_H + N_D)$. Figure 4b shows the radial localization, along the major axis, of the confluence zone (cut-off infinity pair) as the concentration is changed. This location is thought to be a rather good first approximation of the energy deposition zone : although the energy absorption occurs to the right of this zone and hence towards the center, the actual localization of this zone off the major radius occurs more to the outside as seen in Fig. 4c. We believe that Fig. 4a reflects the gradual shifting of the heat deposition over the plasma cross section.

No high energy tail has been found when scanning the CX analyser up to energies of 60 times T_i, even at the lowest proton concentrations. The lower limit for X_H as found from spectroscopy was 5 % ± 2 %. The detection of an high energy component is however rendered difficult by the fact that the background ions are non-Maxwellian in ERASMUS, as already observed in the TM-3 [3] and TOI [4] experiments.

4. Loading resistance.

Figure 3a shows that the resistance corresponding to the power absorbed by the plasma can be subdivided into a contribution from the M.A. resonances and a mean loading $\bar{R}_S$. This $\bar{R}_S$ has the following behaviour :

(a) $\bar{R}_S$ decreases with the antenna current I_A for a given density N (see Fig. 5 and [5]).

(b) At I_A < 300 A, $\bar{R}_S$ is higher for the all metal antenna than for one covered with a glass insulator [6].

(c) $\bar{R}_S$ increases with N for a given I_A ([6, 7]).

The linear increase with I_A of the $\tilde{B}_Z$ signal (Fig. 5) picked up, both at resonance and off resonance, by probes distributed along the torus suggests constant magnetosonic R_S . From the decrease of $\bar{R}_S$ we conclude that the mean loading is only partly due to magneto-acoustic loading. Decreasing the non-magneto-acoustic contribution by better electrostatic shielding, by increasing the value of the toroidal field [5] or by the use of multiple antennae might have an important bearing on the overall heating efficiency.

References.

1. A.M. MESSIAEN, R.R. WEYNANTS, V.P. BHATNAGAR and P.E. VANDENPLAS, Phys. Lett. 71A , p. 431 (1979).
2. K.G. BUDDEN, Radio Waves in the Ionosphere, Cambridge Univ. Press (1961), p. 476.
3. G.A. BOBROVSKY, E.I. KUZNETSOV, and K.A. RAZUMOVA , Journ. Exp. Theor. Phys. 59, p. 1103 (1970).
4. N.V. IVANOV, and I.A. KOVAN, Proc. 5th Int. Conf. Plasma Phys. and Cont. Nucl. Fusion Research, Tokyo 1974, Vol. III, p. 41.
5. V.V. BUZANKIN et al. , Proc. 6th Conf. Plasma Phys. and Cont. Nucl. Fusion Research, Berchtesgaden 1976, Vol. III, p. 75.
6. V.P. BHATNAGAR et al., Proc. Joint Varenna-Grenoble Int. Symp. on Heating in Toroidal Plasmas, Grenoble 1978, Vol. I, p. 133.
7. G.J. MORALES, and R.J. TAYLOR, ibidem, Vol. II, p. 241.

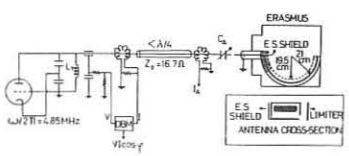

Fig. 1. RF setup schematic.

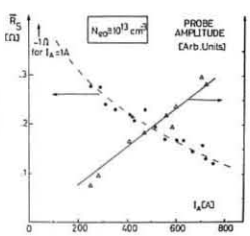

Fig. 5. $\bar{R}_S$ and $\tilde{B}_Z$ vs. I_A

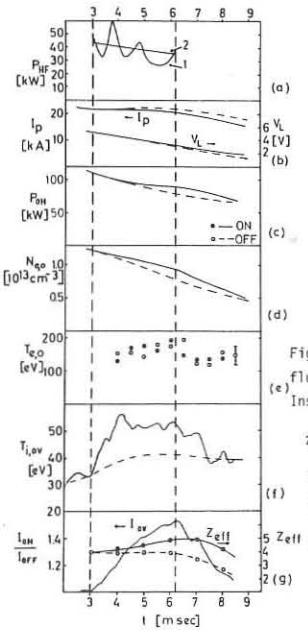

Fig. 3. Time evolution of plasma parameters.

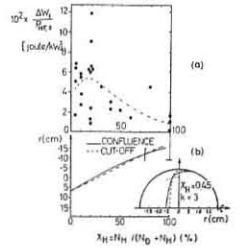

Fig. 4. (a) $\Delta W_i / P_{HF,o}$ vs. X_H . (b) Confluence /cut off location vs. X_H . Inset : same in the cross section.

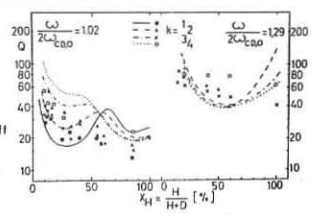

Fig. 2. Q vs. X_H. Theoretical : lines, Experimental : points, $k = k_{//} R$

THE ACCESSIBILITY OF THE RESONANT SURFACES AND THE ROLE OF SURFACE WAVES IN RF PLASMA HEATING

Ernesto Canobbio

Department of Physics, University of California
Los Angeles, California 90024, USA*

and

Association EURATOM-CEA, Departement de Physique du Plasma
et de la Fusion Contrôlée,
Centre D'Etudes Nucleaires, Grenoble, 38041, FRANCE**

Abstract. Resonant surfaces, mode conversion layers, resonance cones, surface waves and caustics are briefly discussed in four frequency ranges.

Introduction. The primary requirement any efficient heating scheme should fulfill is that most of the launched energy be dissipated well within the confined plasma volume. EM-power is absorbed mainly in places where the field amplitude becomes large and preferentially in the neighborhood of the wave resonance surfaces which occur in four frequency ranges: 1. $\omega < \omega_{ci}$ (Low Resonance Frequency Heating, LRFR), 2. $\omega \approx \omega_{ci}$ (Ion Cyclotron Resonance Heating, ICRH), 3. $\omega \approx \omega_{pi}$ (Lower Hybrid Resonance Heating, LHRH), and 4. $\omega \approx (\omega_{pe}^2 + \omega_{ce}^2)$ (Upper Hybrid Resonance Heating, UHRH). Unfortunately, such surfaces may cross the plasma periphery and, in addition, if sufficiently high mode numbers are excited, resonance cones from localized antennas, surface waves, and caustics, may substantially enhance the field amplitude at the plasma surface. We shall discuss these matters with emphasis on frequency range (1) and other areas requiring further study.

Resonant Surfaces and Mode Conversion Layers. In non-uniform cold plasmas, resonances appear at surfaces where the wave frequency equals the eigenfrequency of the local collective oscillations. When the wave crosses the $\vec{B}_o$-lines, the resonance frequencies do not coincide with any of the frequencies of the unperturbed single particle motion. The collective oscillations involve a frozen-in field which at all hybrid frequencies is purely electrostatic, and at the resonance in range (1) is magnetic, with an electrostatic component of $\omega/\omega_{ci} \neq 0$. In all cases, the limit of the uniform-plasma eigenfrequencies for $k_\perp \to \infty$ must exist ($\vec{k}_\perp$ is the wave number across the considered surface).

In hot plasmas, the cold resonances are replaced by neighboring mode conversion layers where the group velocity either vanishes or is very small. But in addition, all wave branches now have resonances ($k_\perp \to \infty$) and cutoffs ($k_\perp \to 0$), with zero group velocity, exactly at $\omega = n\omega_{c\alpha}$ ($n = 1, 2, \ldots$; $\alpha = i,e$). There, for such k-values, no net energy flow can exist between a wave and a uniform thermal (collisionless) plasma even though all particles are in resonance with the wave. New mode conversion layers with vanishing group velocity appear near $\omega = n\omega_{c\alpha}$. Between two adjacent harmonics the behavior of the various hot plasma modes (a full electromagnetic generalization of the Gross-Bernstein modes) depends strongly upon the field polarization and the wave number along B. In a toroidal system, where the equi-density surfaces and the equi-B surfaces have entirely different geometries, the wave propagation characteristics may be difficult to visualize even within the WKB approximation. Although some of these modes are expected to play an important role in rf-heating in the four frequency ranges cited above, as yet no direct check of these modes on any toroidal experiment has been made.

At low frequencies the wave properties, although relatively simple, have been worked out only partially even within the WKB approximation. Assuming $k_\parallel v_i < \omega << (k_\parallel v_e, \omega_{pi}) << \omega_{ce}$; $k_\parallel v_i << |\omega - \omega_{ci}|, \omega_{ci} << \omega_{pi}$; $\beta \equiv (v_i/v_A)^2 << 1$, where $v_i = 2T_i/m_i$ and v_A is the Alfvén speed, and keeping terms up to $\rho_i^2 = v_i^2/2\omega_{ci}^2$, the dispersion relation can be written

$$\tfrac{1}{2}\beta(A-1)(1+X_\parallel T_e/T_i)X_\perp^2 + (X_\parallel - A)X_\perp + \{A - 2AX_\parallel + X_\parallel^2 - \tfrac{1}{2}\beta(T_e/T_i)X_\parallel\} = 0 \qquad (1)$$

where $A \equiv (1 - (\omega/\omega_{ci})^2)^{-1}$ and $X_{\perp,\parallel} \equiv (k_{\perp,\parallel} v_A/\omega)^2$. Qualitative plots of $X_\perp(X_\parallel)$ are shown on Fig. 1. (Notice that in order to apply Eq. (1) to toroidal situations, $X_\parallel$ has to be considered as a function of the minor radius, which vanishes at the MHD singular surfaces). When $\omega < \omega_{ci}$, the vertical cold plasma asymptote (1) at $X_\parallel = 1 + (k_\parallel c/\omega_{pi})^2$ is rotated and bends into the hot plasma asymptote (2) described by Eq. (1) when the terms in the curly brackets are neglected. This corrects and generalizes previous estimates /1/ . Asymptote (3) is the vacuum dispersion relation in the absence of displacement currents. Wave penetration into the plasma is possible by tunnelling through the evanescence peripheral zone and mode conversion into the very slow hot-plasma mode with little reflection and negligible transmission to the fast mode. (When the $X_\perp$ component tangent to the magnetic surfaces is considered as given, and the full wave equation is used, the two adjacent cutoffs would be less closely spaced.) The wave branch tending to the electrostatic asymptote (4) has been considered in /2/ in relation to resonance cone formations (See next section). When $\omega > \omega_{ci}$ the only notable aspect is a new mode conversion layer at short wave lengths, whose role in the ICRH problem remains to be investigated.

Resonant Cones. These are constructive interference patterns of waves launched by a finite length antenna which occur when the ray trajectories are independent of the wavelength, as in the case of asymptote (4) in Fig. 1. The large electrostatic fields which develop along such cones are the result of the presence of very high mode-number waves. (Mathematically resonance cones are a consequence of the hyperbolic character of the spatial differential operator of the electrostatic wave equation). Resonance cones can be at the origin of unwanted effects inhibiting rf-power penetration into the plasma, producing runaway particle populations at the surface or even deteriorating plasma confinement. Resonance cones are an important and unavoidable aspect of LHRH, where the electrostatic approximation is remarkably accurate even fairly close to the slow wave launching structure /3/, at least for the high-$n_\parallel$ wave components. Their role may be non-negligible in some of the LRFH and ICRH experiments, while it should be immaterial for UHRH where slow wave structures are not used.

Free Surface, "Whispering Gallery" and "Bouncing Ball" Modes. Large field amplitudes can also be found localized along "discontinuity" surfaces - actually zones of sharp transition between adjacent uniformly refracting regions-like free surfaces and reflecting fixed walls. This occurs when the wave numbers parallel to the discontinuity surface are sufficiently high to make the first nonvanishing zero of the eigenfunctions (more generally of same appropriate combination of eigenfunctions and their radial derivatives) essentially to coincide with the discontinuity surface. Only few cases of free-surface waves having at least partial bearing on rf-heating in toroidal systems is found treated in the literature /4/ although more general cases could easily be worked out (even including a toroidal B-field which falls off inversely as the major radius /5/). But even the simplest case of a cylindrical cold plasma with uniform axial B-field is instructive. By using Eq. (24) Sect. IV of Ref. /6/, high azimuthal mode number surface waves are found when $(k_\parallel c/\omega_{pi})^2 \approx (\omega/\omega_{ci})^2(1 - \omega/\omega_{ci})$ or when $2(k_\parallel c/\omega_{pi})^2 \approx (\omega/\omega_{ci})^2(1 + \omega/\omega_{ci})$.

We call "whispering gallery"modes, waves localized near a fixed reflecting concave wall. They correspond to the Rayleigh explanation of the well known acoustic phenomenon /7/. These modes may occur at the short wave lengths that are required for UHRH. Here the rays which escape the narrow solid angle leading to the absorption zones within the plasma, have the undesirable tendency to fill out a thin layer next to the wall and bounded internally by a caustic. Mechanically this describes a particle sliding or bouncing along a wall, but staying close to it. Whispering gallery modes are also excited by LHRL launching structures, but their significance should be secondary compared to the resonance cone amplification /8/.

Another set of eigenmodes can be found in convex non-circular 2D domains /7/. We call them "bouncing ball" modes since, mechanically, they describe a particle bouncing back and forth between opposite wall points along a diameter. In order that such a motion be stable, the diameter must be the minimum diameter of the domain. These modes differ essentially from zero only in a thin strip around this diameter, and the strip is bounded by two caustics. They may occur during UHRH especially when the plasma and the wall have non-circular cross-sections.

*Partially supported by USDOE
**Permanent address

References.

1. Mikhailovskii, A. B. and Rudakov, L. I., Sov. Phys. JETP, 17 (1963) 621; Hasegawa, A. and Chen, L., Phys. Fluids 19 (1976) 1924.
2. Kuehl, H. H., Phys. Fluids, 17 (1974) 1636.
3. Brambilla, M., Heating in Toroidal Plasmas, Grenoble, July 3-7, 1978, Vol. II, p. 251.
4. Demirkhanov, R. A. et al., VII European Conference on CFPP, Lausanne (1975), Vol. I, p. 148.
5. Swanson, D. G., Phys. Fluids, 17 (1974) 2241.
6. Bernstein, I. B. and Trehan, S. K., Nuclear Fusion 1 (1960) 3.
7. Keller, J. B. and Rabinow, S. I., Ann. of Phys. 9 (1960) 24.
8. Brambilla, M., paper submitted to Nuclear Fusion; See also Report EUR-CEA-FC-906 (1977).

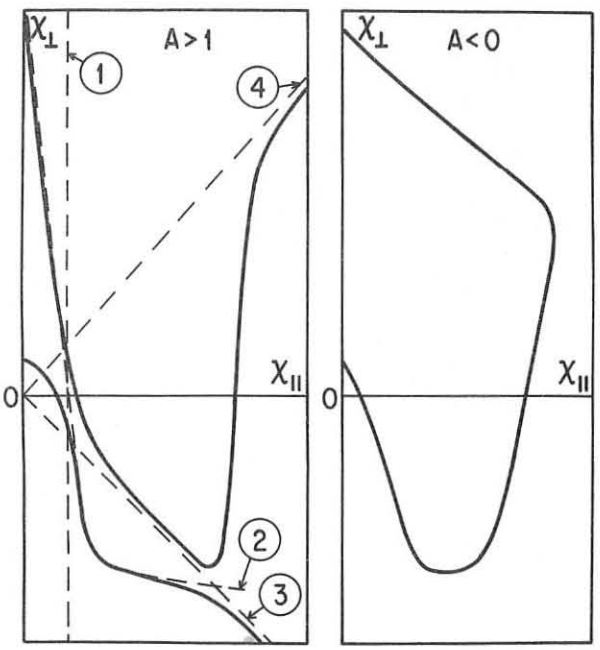

E2.5

CHARACTERIZATION OF HIGH POWER NEUTRAL BEAMS BY OPTICAL DIAGNOSTICS

J.F. BONNAL, G. BRACCO, C. BRETON, J.P. BUSSAC, C. DE MICHELIS, J. DRUAUX
M. MATTIOLI, R. OBERSON, J. RAMETTE

ASSOCIATION EURATOM-CEA SUR LA FUSION
Département de Physique du Plasma et de la Fusion Contrôlée
Centre d'Etudes Nucléaires
Boîte Postale n° 6, 92260 FONTENAY-AUX-ROSES (FRANCE)

Abstract : The light emitted by a high power hydrogen neutral beam has been spectrally analized. This measurement allows the relative proportions of beam neutrals and ions at different energies to be directly estimated.

High power neutral beams used for additional heating in fusion oriented devices must be reliably diagnosed. At the high powers now available, this is an increasingly difficult task since conventional electrical and calorimetric techniques eventually suffer from severe destruction of the measuring devices. We shall describe a non-destructive diagnostic based on the study of the optical emission arising from the interaction of the beam particles with the hydrogen molecular residual gas.

In a recent paper /1/, we have shown that space-resolved measurements of the total H_β light emitted at 90° to the beam yield the same profiles as these obtained with conventional electrical techniques. Now, a new step has been done and a more complete diagnostic of the beam is available:spatial profiles and relative proportion of each neutral species have been obtained.

Neutral hydrogen beams are mainly composed of atomic neutrals with energy E_B, $E_{B/2}$ and $E_{B/3}$ originating from charge-exchange and dissociation of H^+, H_2^+, H_3^+ issued from the plasma source. E_B is the energy corresponding to the applied accelerating voltage. Taking advantage of the Doppler effect due to the large directed velocity of the neutrals it is then possible to separate the emission (H_α or H_β) of each neutral species.

Figure 1 shows schematically the experimental set-up. The neutral hydrogen beam (20-40 keV, 10-25 Amp.) is produced by a "periplasmatron source" /2/. The light emitted at 60° to the beam direction is imaged by a 20 cm focal length lens on the entrance slit of a monochromator (50 cm Czerny-Turner with 2160 grooves/mm grating). The monochromator exit slit is imaged by a 12 cm focal length lens on a vertical array of optical guides, having an entrance section of 2×4 mm^2 each. These optical guides are coupled to /56T.V.P/ photomultipliers. This system results in a spatial resolution of approximately 9 mm across the beam.

Figure 2 shows the spectral profiles of the H_α (6563 Å) and the H_β (4861 Å) emission lines, obtained shot by shot, using the optical guide looking along the central chord. The observed spectra (H_α or H_β) consists of one unshifted component originating from the dissociative excitation of the residual molecular hydrogen, and three Doppler-shifted components corresponding to the three moving neutral species with kinetic energy E_B, $E_{B/2}$ and $E_{B/3}$; between the unshifted and the $E_{B/3}$ peaks a fourth shifted component is seen, the displacement of which corresponds to a moving neutral with a kinetic energy of $(E_{B/18 \pm 2})$; the uncertainty comes from the spectral resolution used in this work and the low value of the signal to noise ratio. This peak is probably due to the hydrogen atoms coming from the dissociation of water ions (H_2O^+) extracted from the plasma source (or other "hydrogen-oxygen" compounds like $(HO)^+$ or $(H_3O)^+$).

By using the vertical array of optical guides it is possible to obtain, at the same time, the spatial profile of each beam component. Figure 3 compares the "electrical profile" with the half-normalized profile of the H_α radiance for the unshifted component and the full-shifted one (i.e. corresponding to the fastest moving neutral). Except in the far wing, where they present a little bump, the two optical profiles are very close to the electrical one in the central part, (+ 6 to - 6 cm). These profiles are almost gaussian, hence the Abel-inverted profiles are not presented. Within the experimental error, mainly due to poor resolution of the $E_{B/2}$ and $E_{B/3}$ peaks, the three main species have the same profile.

Taking advantage of the fact that the neutralization conditions are such as to assure equilibrium between charge-exchange and ionization, and that the spatial profiles of all species are identical and therefore we can use the radiance values rather than the Abel-inverted intensity, it is then possible to write

$$I_v = n_g \left| \sigma_v^+ \frac{\sigma_v^{ion}}{\sigma_v^{c-ex}} + \sigma_v^\circ \right| \underline{n}_v^\circ \, v \quad (1) \; ; \text{ with } \underline{n}_v^+ = \frac{\sigma_v^{ion}}{\sigma_v^{c-ex}} \underline{n}_v^\circ \; .$$

I_v is the emitted intensity by the neutral species moving with velocity v, σ_v° and σ_v^+ are the cross-section of the reactions:

$$\underline{H}^\circ + H_2 \rightarrow H^{\hat{\ }} + \ldots$$

$$\underline{H}^+ + H_2 \rightarrow H^{\hat{\ }} + \ldots$$ (the asterisk indicates an excited state, the underlining a fast particle) ; $\underline{n}_v^\circ$ and $\underline{n}_v^+$ are the densities of fast atoms and ions with velocity v, and n_g the density of residual gas. The relative proportions of the different populations have been calculated from equation 1. The results are shown in table 1. With the same hypothesis on neutralization equilibrium, it is also possible to obtain the relative proportions of extracted currents. Disregarding water impurities we obtain : $I_{ext}(H_1^+) = 50$ % ; $I_{ext}(H_2^+) = 29$ % and $I_{ext}(H_3^+) = 21$ %. The calculated extracted current proportions agree with what is expected for a "periplasmatron source" like ours in the first beginning of the experiment, having a current density of approximately 100 mA/cm^2. The evaluate contribution of water impurities to the extracted current is small:only a few percent (1 to 2 %).

Reference :

/1/ J.F. BONNAL et al., Phys. Lett. A 69, 116, (1978).

/2/ J.F. BONNAL et al., "Circular Periplasmatron for T.F.R. 604" 10th Symposium on Fusion Technology, Padova, Italy, Sept. 1978, paper C4.

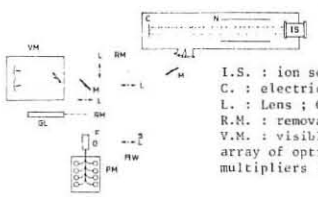

Fig. 1 : Experimental Set-up

I.S. : ion source ; N. : neutralizer ; C. : electrical target ; M. : mirror ; L. : Lens ; G.L. : glas laser ; S. : shutter ; R.M. : removable mirror ; F. : vertical slit ; V.M. : visible monochromator ; O. : vertical array of optical guides ; P.M. : Photomultipliers ; W. : tungsten ribbon lamp.

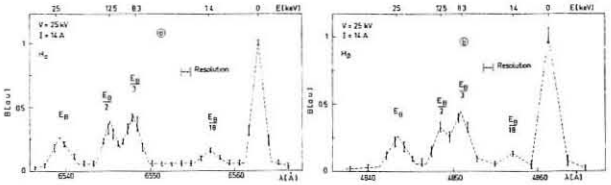

Fig. 2 : Measured radiances along the central chord, normalized to the unshifted peak, as a function of wavelength. a) H_α ; b) H_β.

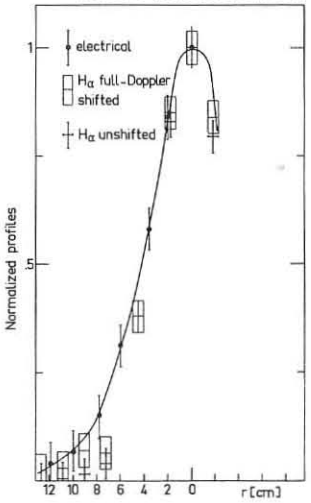

Fig. 3 : Half-beam normalized profiles.

Continuous line : electrical profile
Discrete values : H_α radiances for the unshifted and the full-shifted lines.

E	Density		Current	
	$\underline{n}^\circ$	$\underline{n}^+$	i°	i^+
E_B	13	4	21.0	6.4
$E_{B/2}$	25	3	28.5	3.4
$E_{B/3}$	33	3	30.8	2.8
$E_{B/18}$	18	1	6.8	0.3

Table 1

Proportions (%) of hydrogen neutrals and ions.

MICROTEARING MODES AND ANOMALOUS TRANSPORT IN TOKAMAKS

J. F. Drake, N. T. Gladd, C. S. Liu, and C. L. Chang
Department of Physics and Astronomy
University of Maryland
College Park, Maryland 20742

The anomaly in the electron thermal transport has been widely observed in tokamak discharges.[1] Recently the importance of magnetic fluctuations in producing stochastic magnetic fields and enhanced thermal transport has been recognized. Radial magnetic fluctuations allow electrons to move along $\tilde{B}$ in the radial direction; thereby effectively coupling the parallel thermal conductivity $\chi_{e\parallel}$ to $\chi_{e\perp}$. A self-consistent investigation of the source of these magnetic perturbations and the resultant transport in a real experiment must be carried out.

In this paper, we investigate the stability of microtearing (high m) modes[2] and the associated electron thermal transport. Linearly, we demonstrate that microtearing modes are driven unstable by the electron temperature gradient in present tokamaks, even in the absence of toroidal and trapped particle effects. Nonlinearly, these tearing modes produce overlappping magnetic islands which saturate when $|\tilde{B}|/B \simeq \rho_e/L_T$ (the ratio of electron gyroradius to the temperature gradient scale length). The resulting perpendicular thermal conductivity $\chi_{e\perp}$ scales inversely with density, consistent with empirical Alcator scaling, and is comparable in magnitude with experimental measurements of energy confinement time.

We consider a slab plasma with density and temperature gradients (scale lengths L_n and L_T, respectively) immersed in a sheared magnetic field $B = B_0[\hat{z} + (x/L_s)\hat{y}]$. In a low β system the electric and magnetic perturbations of the tearing mode can be represented by the parallel vector potential $\tilde{A}_\parallel$ and the scaler potential $\tilde{\phi}$. From Ampere's law and the quasi-neutrality condition, we obtain the following coupled equations for $\tilde{A}_\parallel$ and $\tilde{\phi}$:

$$(\partial^2/\partial x^2 - k_y^2)\tilde{A}_\parallel = -(4\pi/c)\sigma_{\parallel e}\tilde{E}_\parallel = -(4\pi/c)\sigma_{\parallel e}(i\omega\tilde{A}_\parallel/c - ik_\parallel\tilde{\phi}) \tag{1}$$

$$(c^2/c_A^2)(\omega+\omega_{*i})[\partial^2/\partial x^2 - k_y^2]\tilde{\phi} = -4\pi k_\parallel\tilde{E}_\parallel\sigma_{\parallel e} , \tag{2}$$

when the parallel electron conductively,

$$\sigma_{\parallel e} = (2i/3\pi^{3/2})\,\omega_{pe}^2\int_0^\infty ds\, s^4\exp(-s^2)[\omega-\omega_*(s)] \times [i\omega(\nu-i\omega)\alpha_1 - k_\parallel^2 v_e^2 s^2/3]^{-1} , \tag{3}$$

is calculated from the drift-kinetic equation with a velocity-dependent, Lorentz collision-operator. We have defined $\nu(v) = 4\pi n_o Z^2 e^4 \ln\Lambda/m^2 s^3 v_e^3$, $s = v/v_e$, $\omega_* = \omega_{*n}[1+\eta_e(s^2-3/2)]$, $\omega_{*n} = (c\,T_e/eB)\,d\ln n/dx$, $\eta_e = d\ln T_e/d\ln n$, $k_\parallel = k_y x/L_s$ and α_1 is given by the continued fraction

$$\alpha_n = 1 + k_\parallel^2 v^2 (n+1)^2/(2n+1)(2n+3)[i\omega - \tfrac{\nu}{2}(n+1)(n+2)][i\omega - \tfrac{\nu}{2}n(n+1)]\alpha_{n+1} .$$

For $|k_\parallel v/(\nu-i\omega)| \ll 1$, $\alpha_1 \simeq 1$ and $\sigma_{\parallel e}$ reduces to that derived by Drake and Lee,[3] where the physical mechanisms leading to (2) and (3) have been discussed.

The tearing branch of Eq. (2) and (3) correspond to modes with even $\tilde{A}_\parallel(x)$ and odd $\tilde{\phi}(x)$, i.e., $\tilde{B}_x(0) = ik_y\tilde{A}_\parallel \neq 0$ with $\tilde{\phi}(0)=0$, and $\tilde{E}_\parallel \neq 0$ at large x. The usual (macro) tearing modes, with $k_y L_n \simeq 1$, are global modes driven by the magnetic field energy. Microtearing modes, on the other hand, are short wavelength modes, with $k_y L_n \gg 1$, which are localized near the rational surface ($x=0$). At large $|x|$, $\tilde{A}_\parallel \sim \exp(-k_y|x|)$, corresponding to a negative Δ' in the usual tearing mode terminology. The magnetic field perturbation, therefore, increases the magnetic energy and is stabilizing. The electron temperature gradient η_e can overcome the stabilizing magnetic forces and produce instability provided the realistic velocity dependence of electron-ion collisions is included.[3,4] These modes are stable in the collisionless regime.[2,5]

The coupled equations for $\tilde{A}_\parallel$ and $\tilde{\phi}$ have been solved numerically using standard shooting techniques to find the eigenfrequency ω. The real frequency of the mode is approximately $\omega_r = \omega_{*n}(1+1.5\eta_e)$. The growth rate γ/ν_{ei} is shown as a function of $k_y \propto \omega_{*n}/\nu_{ei}$ in Fig. 1 for $\eta_e = 0, 1, 2, 3$. Without a temperature gradient the modes are stable. A positive temperature gradient $\eta_e > 0$ is destabilizing at intermediate wavelengths $\omega_{*n}/\nu_{ei} \sim .1$ and is stabilizing in both the short and long wavelength regimes, a result which differs from previous analytic theory where $\eta_e > 0$ was always destabilizing.[2] In the analytic treatment $\tilde{\phi}$ and the spatial variation of $\tilde{A}_\parallel$ (constant ψ approximation) were neglected on the right side of Eq.(1).[2] Neither of these approximations can be justified for present tokamak parameters. In particular, the rapid spatial variation of $\tilde{A}_\parallel$ in the vicinity of the rational surface (corresponding to strong bending of the magnetic field lines) has a strong stabilizing influence on the tearing mode when $n_e^2\beta L_s^2/L_n^2 > 1$. In contrast the potential $\tilde{\phi}$ has a destabilizing influence and is typically necessary for instability. The competition between these two effects can lead either to instability or stability as shown in Fig. 1.

The nonlinear saturation of microtearing instability has been investigated by solving the drift kinetic equation to the third order in the perturbed field $\tilde{B}$. The dominant nonlinearity arises from the electron motion along the flucuating magnetic field lines. We consider the case of zero shear and $|\omega| \ll \nu_{ei}$ for simplicity, although both of these restrictions can be relaxed. The nonlinear dispersion relation is

$$\omega = \omega_k + i[3\Gamma(9/2)/4]\omega_k\omega_{*n}\eta_e/\nu(v_e) - i(3\sqrt{\pi}/8)k^2c^2\nu(v_e)\omega_{pe}^2 - i[5\Gamma(11/2)/12]\frac{v_e^2}{\nu(v_e)}\,k^2\sum_{k'}(|\tilde{B}_{k-\omega}'|^2/B^2)\frac{(\omega_k\omega_{*n}+\omega_k'\omega_{*n}')}{(\omega_k^2-\omega_{k'}^2)}\eta_e \tag{4}$$

where $\omega_k \simeq \omega_{*n}(1+2.5\eta_e)$. The first imaginary term in (4) represents the destabilizing influence of η_e and the second arises from field line bending. The nonlinear term in Eq. (4) scales as $k^2 D_\perp$, where $D_\perp = (v_e^2/\nu_e)|\tilde{B}_\omega|^2/B^2$ is the perpendicular electron diffusion coefficient, and is destabilizing for $\omega_k < \omega_k'$ and stabilizing for $\omega_k > \omega_k'$. Thus, the nonlinearity leads to an energy flow from short to long wavelength. Since the long wavelength modes are stable, this energy cascade saturates the instability when the growth and damping rates balance or

$$|\tilde{B}|/B \simeq \rho_e/L_T . \tag{5}$$

For typical tokamak discharges $|\tilde{B}|/B \sim 10^{-4}$. With $|\tilde{B}|/B = \rho_e/L_T$, the anomalous crossfield transport coefficient is $D_\perp = v_e^2\rho_e^2/\nu_e L_T^2$. The temperature gradient scale length L_T is determined self-consistently by balancing the ohmic heating and thermal loss rate, $\eta J^2 = D_\perp n T_e/L_T^2$. After solving this equation for L_T, we find

$$D_\perp \simeq (c^2/\omega_{pe}^2)(T_e/m)^{1/2}/qR , \tag{6}$$

where $q = rB_z/RB_\theta$. Remarkably, this is the scaling obtained previously by Ohkawa from a dimensional argument.[6] The magnitude of the diffusion coefficient is of order $10^4 cm^2/sec$ for typical tokamak parameters ($n=10^{14}/cm^3$ and $T_e=1$ Kev) which is of the same order as inferred from experimental measurements of the energy confinement time.

Recent probe measurements of the magnetic fluctuations on the macrotor tokamak revealed a broad spectrum of waves peaked at 25 kHz and extending up to 100 kHz.[7] This spectrum was relatively insensitive to the lower frequency MHD oscillations at 7 kHz. For the parameters of their experiment the maximum linear growth rate of the microtearing mode corresponds to 50 kHz, which is in reasonable agreement with the observations.

This work was supported by USDOE.

REFERENCES

1. A. Gondhalekar, D. Overskei, R. Parker and J. West, MIT Report PFC/RR-78-15 (1978).
2. D. A. D'Ippolito, J. F. Drake, and Y. C. Lee, Bull. Amer. Phys. Soc. 23, 867 (1978).
3. J. F. Drake and Y. C. Lee, Phys. Fluids 20, 1347 (1977).
4. R. D. Hazeltine, D. Dobrott and T. S. Wang, Phys. Fluids 18, 1778 (1975).
5. K. T. Tsang, et al., Phys. Rev. Lett. 41, 557 (1978).
6. T. Ohkawa, Phys. Lett. 67A, 35 (1978).
7. S. J. Zweben, C. R. Menyuk, and R. J. Taylor, Phys. Rev. Lett. 42, (1979).

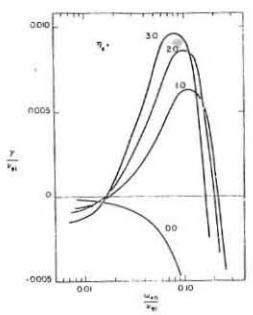

Fig. 1: The growth rate γ/ν_e is shown as a function of $k_y \propto \omega_{*n}/\nu_{ei}$ for $\eta_e = 0$, 1,2,3 with $L_n/L_s = .05$, $\beta = .01$, $T_e = T_i$ and ν_{ei} chosen so that $\nu_{ei} = \omega_{*n}$ when $k\rho_s = 1$.

EP3

Experiments on High Beta Tokamak Stability*

P.G. Weber, T.C. Marshall and R.A. Gross
Columbia University, New York, NY 10027

Experimental research on high beta pinch tokamak plasmas suggests that stable configurations can be achieved.[1,2] There are also recent theoretical predictions of a region of tokamak stability at high beta.[3,4] In this paper we report on experiments using Columbia Torus 2 in which a high beta (~10%), hot (~100 eV), dense ($\sim 10^{21} m^{-3}$) tokamak plasma is produced and held in macroscopic equilibrium for many (~30) MHD instability growth times.

Torus 2 has a glass vacuum vessel of major radius 0.225 m, width of 0.125 m and height 0.25 m. After preionization a toroidal Z-Pinch is formed for purposes of preheating to 5-10 eV at a density of $10^{21} m^{-3}$. The Z-Pinch plasma carries a toroidal current of 40 kA, toroidal magnetic field $B_T(R_0)$ = 0.2 T, and is held in radial equilibrium by an appropriate vertical field. After several microseconds, the toroidal magnetic field is very rapidly (τ_R = 1.7 μs) reversed to 0.4-1.0 T, and the vertical field is also increased. Up to 50 GW of power is employed in this fast heating technique. At low heating power (12 GW) we have used magnetic field probes to observe the transition during the rapid heating from a Z-Pinch to a tokamak configuration. Fig. 1(a) shows the Z-Pinch toroidal magnetic field at the time of application of the heating pulse. Fig. 1(b) shows the gradients induced in the toroidal field as the strong poloidal heating current penetrates to the centre of the plasma. The resistivity in this layer is anomalously high due to microturbulence in the strong (~50 kV/m) poloidal electric field, leading to very efficient plasma heating.[5] The final tokamak configuration evolves in about four microseconds with the dissipation of the skin current. Careful control of the vertical and radial magnetic fields allows us to maintain an equilibrium for at least

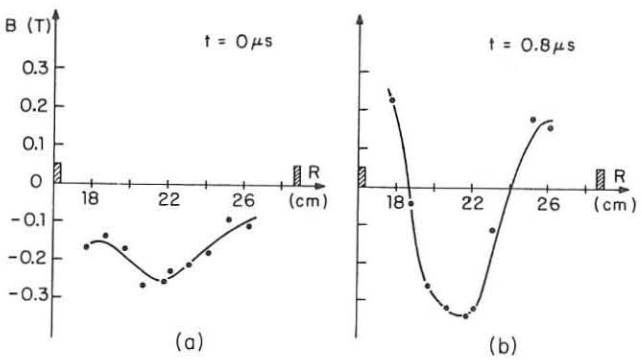

Fig. 1: Toroidal Magnetic Field as a function of radius during heating.

the following 30 μs. (The capacitor banks are crow-barred at the peak of the heating pulse, and their L/R decay time is 50-60 μs.)

As an example of the equilibrium configuration at t = 15 μs after a 12 GW heating pulse, Fig. 2 shows plots of constant toroidal current density derived from the magnetic field data. Note that the plasma is elongated, albeit with some concentration of current at the centre, attributable to the considerable distance between the plasma and the external conductors.[6] The apparent radial shifts in the vertical direction are probably due to experimental errors. For this case the total plasma current is ~25 kA and q(a) ~ 2. Electron temperatures were estimated here by the spectral line-to-continuum method; the central value is 30 ± 10 eV. Ion temperatures were measured by Doppler line broadening of He II (4686 Å) and are approximately equal to the electron temperature. Combined with an electron density of $10^{21} m^{-3}$, this gives a peak β of ~30% for this typical equilibrium. We estimate $\langle\beta\rangle$ to be of order 10%; more diagnostics are being added to determine this value more precisely.

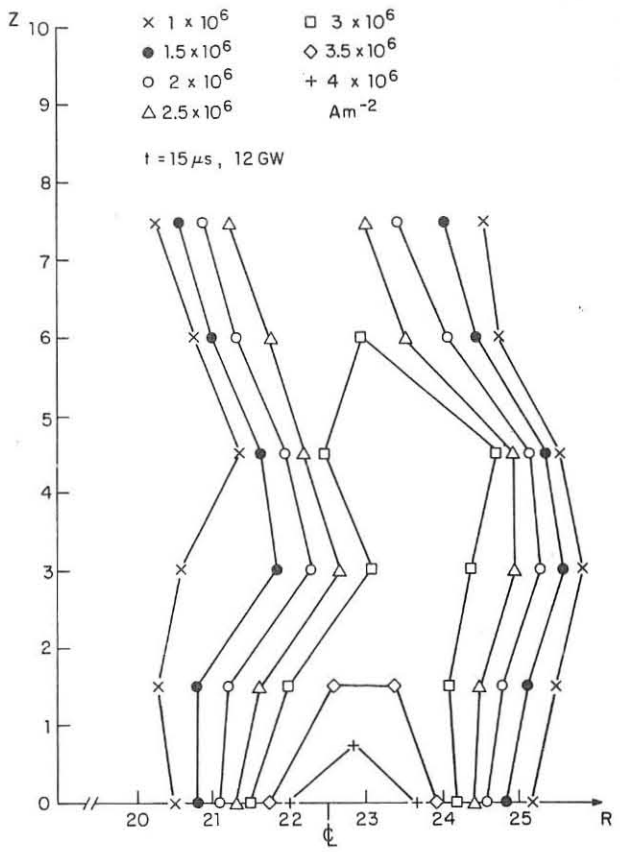

Fig. 2: Contours of Constant Toroidal Current Density at t = 15 μs after 12 GW heating pulse. Z denotes the distance from the torus midplane; R is the major radius (in cms).

It is our observation that under these high beta conditions the shot-to-shot reproducibility of the data is good; there are no rapid changes in the equilibrium and the magnetic field probes do not detect any significant fluctuations. The operating conditions described place most of the plasma in the second (high beta) region of tokamak staiblity predicted by theory,[3,4] and our preliminary results show that macroscopic high beta tokamak stability may indeed be achieved.

Recent experiments have explored operation at higher heating powers, in particular 25 GW. Soft X-ray diagnostics indicate electron temperatures of 200 eV at early times, and the ion temperature also reaches this value before the plasma cools to ≲100 eV in its equilibrium phase. Again streak photography and reproducibility of the diagnostics indicate the absence of macroscopic instabilities. More detailed studies of this and other conditions, employing Thomson and CO_2 scattering are planned.

In conclusion, we have succeeded in producing a tokamak plasma at elevated values of beta with a gross equilibrium maintained for many MHD instability growth times. We believe that our fast initial heating is responsible for allowing us to operate in this regime, which may not be accessible with conventional low beta tokamak start-up methods.

* Research supported by DOE contract EY-76-S-02-2456.

References

1. G. Becker, et al., Nucl. Fusion 18, 1653 (1978).
2. R.A. Gross, Comments Plasma Phys. and Contr. Fusion 3, 103 (1977).
2a. C.K. Chu and R.A. Gross, Proc. Finite Beta Theory Workshop, Varenna, Italy (1977).
3. B. Coppi, et al., Nuclear Fusion 19, 715 (1979).
4. H.R. Strauss, et al., Princeton Plasma Physics Lab Report 1535 (1979).
5. T.C. Marshall and H.C. Lui, Phys. Fluids 19, 1417 (1976).
6. K.U. Von Hagenow and K. Lackner, Proc. 3rd Symp. Toroidal Plasma Confinement, F-7 (1973).

EP4

Influence of q on Confinement and Stability in the Garching Belt-Pinch IIa

G. Becker, O. Gruber
Max-Planck-Institut für Plasmaphysik, D-8046 Garching
EURATOM - Association

Abstract: In the new version of Belt-Pinch IIa equilibria with reduced half-axis ratios $b/a \lesssim 6$ and poloidal beta values above the aspect ratio ($\beta_p \lesssim 7$) have been achieved. For higher q-values ($q_o \approx 3$, $q_b \gtrsim 8$) the energy decay is dominated by impurity radiation cooling and classical transport is found. For lower q-values ($q_o \approx 1.5$, $q_b \approx 6$), however, additional particle and energy losses and enhanced field diffusion occur which indicate the existence of MHD mode activity.

1. Introduction: Toroidal high-beta plasmas in belt-pinches produced by shock heating are able to provide valuable information on MHD stability and confinement of future high-beta tokamaks. In order to achieve moderately elongated equilibria (half-axis ratio $b/a \leq 6$) with high poloidal beta values $\beta_p \geq A$ (aspect ratio), a Belt-Pinch IIa version with a smaller coil height (130 cm) has been built up. With this device a stronger shock heating results and the temperature sum $T_e + T_i$ is nearly doubled compared with earlier experiments /1/. In order to study the influence of q on stability and confinement an improved poloidal field system has been installed which allows a variation of q.

2. Plasma Parameters: With the changed coil system equilibria with $b/a \approx 6$ at a radial compression ratio ≈ 2.5 could be achieved. Higher multipole currents near the coil ends resulted in a clear separation of the plasma from the end plates of the vacuum vessel walls and suppressed vertical displacement instabilities at least for the experimental time scale. Series of discharges with two different q-values at the plasma boundary have been investigated. Measured and calculated plasma parameters at 11 μs when the compressional oscillations are damped out, and at the end of the high β_p-phase are given in the following table. Standard data are: filling pressure 2 mTorr deuterium and a toroidal magnetic field $B_t = 1.4$ kG at the plasma axis ($R_p \approx 50$ cm).

	higher q-case			lower q-case	
t [μs]	11	50	90	11	50
q_b	10	10	7.5	6	5.5
q_o	3.0	2.5	3.0	1.5	2.6
$\langle\beta_p\rangle$	7.0	3.8	1.6	5.0	1.5
$(\beta_t)_o$	0.80	0.40	0.03	0.85	0.05
b [cm]	60	60	40	60	52.5
a [cm]	10.5	12	16	10.5	12
n_{eo} [cm^{-3}]	$3.8\cdot10^{14}$	$4.5\cdot10^{14}$		$4.5\cdot10^{14}$	$3.0\cdot10^{14}$
N/N_o	0.50	0.65		0.75	0.40
α_t, α_C, α_N [%]	1.4, 1.4, 0.2			1.0, 1.0, 0.1	
$I_{t,plasma}$ [kA]	60	47	35	76	71
$\tau_{1/e}$ [μs]		45		30	

Toroidal and poloidal beta and q-values are defined as follows

$$\beta_t = 1 - \langle\psi\rangle / F_{vac}\bar{b}^2 \; ; \; \beta_p = 8\pi\langle p\rangle / \bar{B}_p^2 \; ; \; q = \oint (B_t\, dl_r)/(B_p 2\pi R)$$

The averages denoted by $\langle\rangle$ and $\bar{}$ are taken over the plasma cross-section and the poloidal circumference l_p on the plasma surface, respectively. Width and height of the basis of the pressure profile are 2a and 2b. Subscripts o and b refer to the magnetic axis and the plasma boundary, respectively. The ß and q-values and the 1/e decay time of the plasma energy $\tau_{1/e}$ are taken from measurements of the toroidal diamagnetic flux, of the radial magnetic field profiles (B_t, B_p) and of the axial B_z-profiles outside the discharge vessel and from calculations using an equilibrium code /2/ and the Garching high-beta transport code /3/. The electron density n_e and the total particle number N were measured by end-on 3.4 μm Ashby interferometry /1/. N_o is the particle number filled in. From the pressure balance a temperature sum $T_e + T_i \approx 150$ eV at 11 μs has been derived. As the shock wave mainly heats the ions, $T_i \gg T_e \approx 20$ eV results. The impurity degrees of oxygen (α_O), carbon (α_C) and nitrogen (α_N) normalized to the electron density were determined spectroscopically by adding small amounts of impurities.

3. Plasma Confinement: The equilibria are studied by means of a free-boundary equilibrium code which matches measured plasma thickness (2a), $\langle ß\rangle$, $\langle\beta_p\rangle$ - values and axial B_z-profiles. As in the former extremely elongated equilibria ($b/a \approx 11$) /1/ the toroidal current density j_t remains roughly constant over z throughout the discharge. For the higher q-case consistent equilibrium solutions and q (ψ) - profiles are shown in Figs. 1 and 2 (ψ poloidal flux function). For large $\langle\beta_p\rangle$ - values the exact radial dependence of j_t and thus of q (ψ) in the plasma centre cannot be simulated by the equilibrium code used. The shown initial q-values on axis have been derived from local measurements of B_t and B_p. Although the plasma changes its shape in the course of the discharge and suffers a strong energy decay, toroidal and poloidal fluxes and q are roughly conserved except in the colder boundary regions. In contrast to that the lower q-case exhibits a rapid change of q(ψ) (see Fig. 2) suggesting that flux conservation is violated over a considerable plasma region.

Differences in the two cases are also observed in the transport behaviour. The higher q-case is fully consistent in stability and confinement with the earlier $b/a \approx 11$ Belt-Pinch IIa plasmas. Again the dominant loss is caused by radiation of oxygen and carbon impurities. The observed increase of plasma density on axis due to strong radiation losses and subsequent plasma compression, the development of side maxima on the n_e-profile, the time behaviour of line density and plasma energy are in good agreement with computer simulations with the Garching high-beta transport code.

All computations have been carried out with classical coefficients, since neoclassical corrections in the Pfirsch-Schlüter regime due to elongation and high-beta effects may still be neglected for $b/a \approx 6$ /4/.

In the lower q-case, however, a two times smaller $\tau_{1/e}$ than calculated with the data given in the table and a decrease of axial plasma density and line density have been found (see Fig. 3) which cannot be explained by classical processes alone. There exist additional energy and particle losses which can be simulated by an ambipolar diffusion model with a variable length of magnetic field lines

$$L\,(cm) = 600\ \exp\left[-R\text{-}R_p^2/36\right]+120 \text{ (see Fig. 3).}$$

This model tries to describe losses parallel to ergodic $\vec{B}$-lines present in magnetic islands.

Thus, MHD mode activity in the lower q-case is both suggested by the observed enhancement of particle and energy losses and by the change of q(ψ)-profiles. The modes seem to grow unstable in the lower q-case with $q_o \approx 1.5$ and $q_b/q_o \approx 4$. The stable behaviour in the higher q-case with $q_o \approx 3$ and $q_b/q_o \approx 2.5$ to 3 has been found also in the experiments with $b/a \approx 11$. The fact that the lower q-case becomes unstable in spite of the larger shear indicates that the instability results from a too small q_o-value and represents an internal mode, e.g. of ballooning type /5/.

References

/1/ G. Becker et al., Nucl. Fusion 18, 1653 (1978) and IAEA-CN-37/U-2, Innsbruck 1978
/2/ G. Becker, K. Lackner, Nucl. Fusion 17, 903 (1977)
/3/ G. Becker, D.F. Düchs, Nucl. Fusion 16, 763 (1976)
/4/ E.K. Maschke, Plasma Physics 13, 905 (1971) and 14, 141 (1972)
/5/ D. Berger, Numerical Computations of the Ideal MHD Stability of Small-Aspect-Ratio Tokamak, Thesis at Ecole Polytechnique Fédérale de Lausanne (1977)

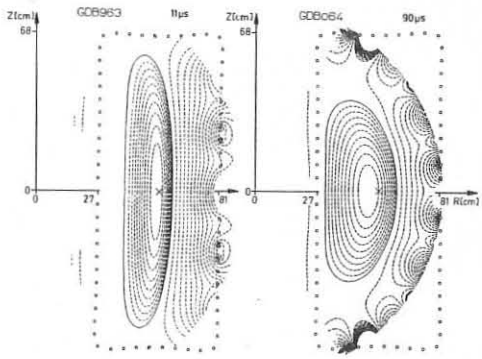

Fig. 1 Equilibrium solutions for the higher q-case

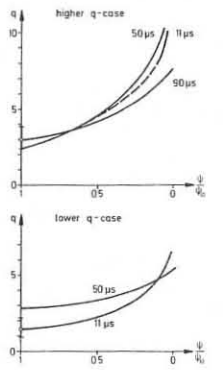

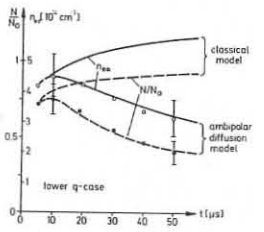

Fig. 3 Time behaviour of the total particle number N and of the electron density on axis n_{eo} for the lower q-case

Fig. 2 Time behaviour of the q(ψ)-profiles

EP5

LIMITATION OF THE ELECTRON DENSITY IN THE PULSATOR TOKAMAK

G.Fußmann, O.Klüber, W.Engelhardt, F.Karger, J.Gernhardt, E.Glock, S.von Goeler[+], N.Gottardi, K.Lackner, G.Lisitano, H.M.Mayer, D.Meisel, H.Murmann, S.Sesnic, F.Wagner, H.P.Zehrfeld.
Max-Planck-Institut für Plasmaphysik, EURATOM-IPP Assoc.
8046 Garching, F.R.G.

The density of tokamak plasmas cannot be increased arbitrarily since the occurrence of the disruptive instability constitutes an upper limit. In the Pulsator tokamak at fixed toroidal magnetic field of 27 kG this density limit is surprisingly sharp: The line averaged electron density determined by 2 mm microwave interferometer does not exceed $1.15 \times 10^{14} cm^{-3}$ corresponding to 27 fringes /1/. Only in low q-discharges ($I_p > 80$ kA) 36 fringes ($\bar{n}_e = 1.4 \times 10^{14} cm^{-3}$) have been achieved, when weak resonant helical fields were applied /2/.

In all discharges the density increases continuously. The density limit was reached for different functions of $n_e(t)$ (e.g. $n_e(t) = \text{const.} \cdot t$ or $n_e(t) \propto 1 - \exp(-t/t_o)$) and different currents between 90 kA and 45 kA corresponding to $2.6 \leq q_a \leq 5.2$. The β_p values at n_{max} varied between 0.9 and 1.8 in such a way that in all cases $\beta_p/q_a = \text{const.} = 0.36$ was found with an accuracy better than 10 %.

Pulsator discharges in the high density regime exhibit particular properties. In the regime $\bar{n}_{max}/2 \leq \bar{n}_e \leq \bar{n}_{max}$ two types of discharges can be distinguished. The difference between them is most distinctly manifested in the temporal behaviour of the signal from the central X-ray diode (cf.Fig.1). In the S-type discharges the sawtooth oscillation continues up to the disruptive end of the discharge. The amplitude modulation $\Delta\bar{A}/A$ is 20 % -40 %, the repetition time $\tau_r = 3 - 5$ ms. The A-type discharge is characterized by a sudden increase of the diode signal towards the end of the discharge which is ascribed to an accumulation of impurities /1,3/. Before the onset of this phenomenon $\Delta\bar{A}/A$ and τ_r can attain the same values as in S-type discharges. During the signal rise, however, $\Delta\bar{A}/A$ decreases drastically; in many cases, there is no sawtooth relaxation during the last 10 ms before the disruption. Enhancement of the gas flow rate postpones this effect to higher density until $\bar{n}_e = 1 \times 10^{14} cm^{-3}$. The actual density limit, however, is reached only in S-type discharges.

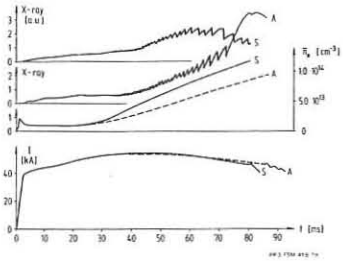

Fig.1: Traces of the soft X-ray intensity, electron density, and plasma current for A-type (accumulation) and S-type (sawtooth) discharges.

For both types, the m=2/n=1 tearing mode exists in a quasi-stationary saturated state leading to a modulation $\tilde{B}_\theta$ of the Mirnov probe signal with $\tilde{B}_\theta/B_\theta \leq 0.2$ % and $\nu = 20 - 25$ kHz ($q_a = 3.4$). The measured amplitude of the modulation is roughly in agreement with the values obtained from tearing mode calculations /4/ referring to Pulsator current density profiles. According to these calculations the only unstable mode is m=2/n=1 which saturates at island widths of 1.7 - 2.6 cm and $0.05\ \% \leq \tilde{B}_\theta/B_\theta \leq 0.15$ % with respect to $5.2 \geq q_a \geq 2.6$. In the experiments the unstable growth of the mode preceding the external disruption occurs on different time scales: the e-folding time is 0.25 ms for S-type discharges and $\gtrsim 1$ ms for A-type discharges. The amount by which the frequency decreases is also different: for A-type discharges a factor of 1.5 is typical whereas in S-type discharges a decrease by a factor $\gtrsim 3$ is observed. The $\tilde{B}_\theta/B_\theta$ value which is attained just before the negative voltage spike ranges from 0.5 to 2 % for both types of discharges. Another common feature is the increase of the hard X-ray signal arising from the limiter during the growth of the mode. It indicates the rapid loss of runaways in this phase. During this time the hard X-ray intensity is modulated by the frequency of the 2/1 mode.

In the S-type discharges the mode starts to grow immediately after the last sawtooth relaxation. The time difference between this event and the negative voltage spike is therefore $\lesssim 1$ ms in 3/4 of the cases. Another characteristic feature of the S-type discharges is the sawtooth modulation of the hard X-ray intensity /5/. There is a threshold for the occurrence of this effect: it is observed only for $\Delta\bar{A}/A > 25$ %. A-type discharges do not exhibit this modulation even if $\Delta\bar{A}/A$ reaches 40 %.

Some of these findings agree fairly well with the basic results of tearing mode theory /6/. The transition from a peaked to a more rectangular current density profile is expected to deteriorate the stability. Such a transition occurs at every sawtooth relaxation and can explain to some extent the temporal correlation between the relaxation and the onset of the external disruption in the S-type discharges. In the case of the A-type discharges the cessation of the sawteeth indicates that q(o) stays > 1. The accumulation of impurities is likely to be accompanied by a continuous flattening of the current density in the plasma centre, thereby producing profiles leading inevitably to disruption.

The existence of the sharp density limit, however, is difficult to understand in this context. The T_e profiles do not change towards a rectangular shape during the last 30 ms before the disruption. Within the experimental error of $\pm$ 10 % they stay constant. The plasma survives many sawteeth with statistically varying relaxation amplitudes before a disruption (Fig.1). Furthermore, shaping of the current profile by induced currents does not trigger the disruption unless the density is close to the limit /8/. All these observations lead to the conclusion that there must be an additional cause for the disruption in S-type discharges which is directly connected with the density (or the pressure).

In search of a different mechanism that could explain our observations, the influence of finite β_{pol} on the magnetic topology has already been briefly discussed in a previous paper /7/. With increasing β_{pol} the magnetic surfaces are compressed at the outside of the torus. This compression leads to a deformation of the magnetic islands and, more importantly, increases the degree of ergodization. To demonstrate the relevance of this effect code calculations on magnetic field lines are performed where the tokamak equlibrium field (in the large aspect ratio approximation) is perturbed by the m=2/n=1 winding available on Pulsator. The following current and pressure profiles have been used

$$I(r) = I_o\left[1-(1-r^2/a^2)^{\mu+1}\right], \quad p(r) = p_o(1-r^2/a^2)^{\mu}, \quad \mu + 1 = q_a/q(o).$$

a = 11 cm is the limiter radius and r is the radius of a toroidal magnetic surface displaced to the outside of the torus by $\Delta = \Delta(r, \beta_{pol}, \mu, R_o/a)$. The surface coinciding with the limiter is assumed fixed: $\Delta(a) = 0$. The above profiles fit well to measured ones in the range $2.6 \leq q_a \leq 5.2$ when $q(o) = 0.85$ is assumed. Computational results are shown in the Figs. 2a - 2c for varying β_{pol} and the following set of data: $q_a = 5.1$, $I_o = 45.8$ kA, $I_{hel} = 1.2$ kA, $r_{hel} = 18$ cm, $R_o = 70$ cm. In each case a field line is followed for 120 toroidal revolutions with the starting point at the X-point of the m=2/n=1 island. As it is to be seen, the island structure is well conserved up to $\beta_{pol} = 1.5$. Above this value, however, a tremendous increase of the ergodization is observed and for $\beta_{pol} = 1.6$ a large scattering of the intersection points is found (Fig.2c). Calculations for smaller values of q_a show the same effect but lead easily to ergodized regions extending beyond the limiter.

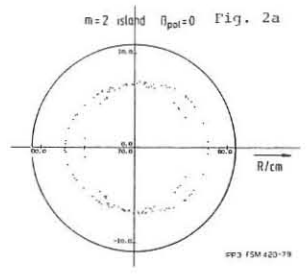

Fig. 2a

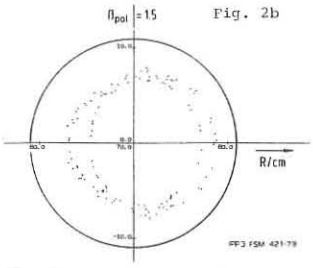

Fig. 2b

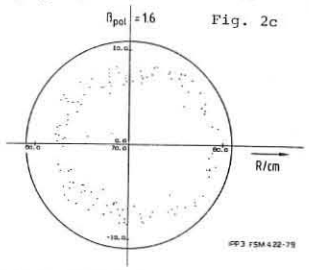

Fig. 2c

Fig. 2: Intersection points of magnetic field lines with a poloidal plane.

Preliminary experimental results are in rough agreement with these calculations: By means of the cited helical winding disruptions are triggered at various densities. The critical helical currents at which the disruptions occur are found to decrease with increasing density. Also, the absolute values of the currents are nearly the same as those needed in the calculations to produce strong ergodization.

Similar ergodization effects may play a crucial role also for the spontaneous disruptions defining the density limit. It is conceivable that in these cases a sudden rise of ergodization due to increasing β_{pol} can trigger the rapid growth of the m=2/n=1 and possibly other modes. The enhanced runaway losses observed during the growing phase of the 2/1 mode support the assumption that ergodization is of importance during this growth. Furthermore, the inverted sawteeth in the hard X-rays appearing ~25 ms before the density limit is reached may also indicate a strong but less severe ergodization correlated with the internal disruptions.

Conclusion: The experimental observations indicate that the disruption at the high density limit is not entirely due to changes of the current density profile. Rather, some evidence has been found that ergodization induced by the increase of β_{pol} is responsible for the onset of the disruption.

References:

/1/ W.Engelhardt, O.Klüber et al. in Plasma Physics and Controlled Nuclear Fusion Research (Proc.7th Int.Conf. Innsbruck(1978) I, 123
/2/ F.Karger et al., Proc.of Symposium on Disruptive Instabilities in Toroidal Devices, Garching (1979) (to be published by IAEA)
/3/ W.Engelhardt, S.Sesnic et al. this conference
/4/ A code developped by K.Lackner, H.Wobig and R.Jaenicke
/5/ G.Fussmann, W.Engelhardt et al. in Plasma Physics and Controlled Nuclear Fusion Research (Proc. 7th Int.Conf. Innsbruck (1978) I, 401
/6/ B.V.Waddel, B.Carreras, H.R.Hicks and J.A.Holmes; Phys. Fluids 22 (5), 1979
/7/ G.Fussmann and H.P.Zehrfeld; Proc.of Symposium on Disruptive Instabilities in Toroidal Devices, Garching (1979) (to be published by IAEA)
/8/ S.v.Goeler, O.Klüber et al. (this conference)

[+] On leave from the Plasma Physics Laboratory of Princeton University

Tokamak Discharges with AC Modulation

S.von Goeler [x]), J.Gernhardt, F.Pohl, W.Engelhardt, H.Murmann
Max-Planck-Institut für Plasmaphysik, EURATOM-Assoc.
8046 Garching

An experiment has been performed on the Pulsator tokamak in which the plasma current was modulated in the frequency range 100 Hz $\leq f \leq$ 2000 Hz /1/. The aim of these investigations was to study the stability of tokamak discharges against tearing modes - more specifically, to drastically change the radial distribution of the plasma current density which, according to theory /2,3/, is the most important factor determining stability. Originally, another aim was to heat the plasma with the ac-currents. However, since only very little heating was observed with the x-ray diodes, this aspect of the experiment has remained in the background. The main results can be summarized as follows:

1) Small modulation of the plasma current ($\Delta I_{pl} <$ 10 kA) has practically no effect on 50 kA discharges with reasonably high safety factor (q (a) $\geq$ 4) and moderate densities. The amplitude of the Mirnov oscillations is sometimes slightly modulated. The level of the Mirnov oscillations is, however, comparable to the level without ac-modulation. This is a remarkable result because even 10 kA-modulations are expected to produce quite substantial changes in the current distribution. At low q and close to the high density limit the discharge is sensitve to any perturbation and small ac-modulations lead to disruptions.

2) When large current modulations (10 kA$< \Delta I_{pl} <$ 40 kA) are applied, growth of m=2 oscillations is observed on the Mirnov coils. This growth leads to minor and major disruptions. (In some cases, when the safety factor q(a) reaches 3.5 in the course of the modulation, m=3 oscillations seem to be excited /4/.) The level of these oscillations is comparable to the fluctuation level before a major disruption . Often the growth is phase correlated with the ac-modulation. At the same time the level of the Mirnov oscillations averaged over one ac period increases.

3) In order to compare the experimental results with predictions of the tearing mode theory, we have computed the instability parameter Δ'/2/ for the modulated current profiles, taking into account the skin effect. The same code also predicts a "nonlinear saturated island width W", which is obtained by determining the distance W/2, where the derivative $\left[\Psi\left(r_s+\frac{w}{2}\right)-\Psi\left(r_s-\frac{w}{2}\right)\right]'$ becomes zero /5,6/. These computer codes calculations can be summarized as follows: The instability parameter $\Delta'(t)$ oscillates sinusoidally around its dc-value for small ac-currents. For large ac-currents $\Delta'(t)$ becomes nonsinusoidal and $\langle\Delta'\rangle$ the average over an ac-period, becomes much larger than the dc-value. The dc-current profile which has been deduced from laser-temperature profiles, seems to be marginally unstable against the m/n=2/1 mode. Depending on the exact shape of the current distribution the dc-profile then has already an island or has none. Once Δ' becomes greater than zero an island is formed. The island size is usually relatively large even for small values of Δ' and does not depend strongly on Δ'. Therefore, when we increase the amplitude of the ac-modulation, the Δ' becomes very large but the island width increases only very slightly. During the modulation the distance between the 2/1 and 3/2 resonant surfaces periodically increases and decreases. For large modulations the decrease of the distance between resonant surfaces coupled with the earlier mentioned slight increase of the island width leads to the overlap of the 2/1 and 3/2 islands.

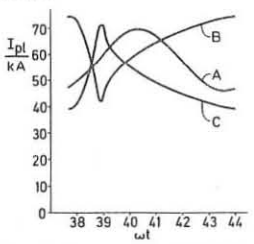

Fig. 1 Plasma current waveforms for sinusoidal (A) sawtooth (B) and inverted sawtooth modulation (C).

An ac-modulation will periodically alter the current profile and therefore worsen and improve the stability of the plasma column at different times. With a nonsinusoidal modulation it might be possible to minimize the adverse effects on the stability behaviour, at least in the time average. We have therefore compared a sinusoidal modulation with a sawtooth and an inverted sawtooth modulation. The current waveforms for the three cases, labelled A,B,C are shown in Fig. 1. Since our computer code calculates the onset of the oscillations, we plot the results for the 6th period where the oscillation has approximately reached a stationary state. The instability parameter $\Delta'(t)$ for the three cases is shown in Fig. 2a, 3a and 4a, respectively. The radial location of the resonant surfaces and the saturation width of the islands is shown in Fig. 2b, 3b and 4b. For the sinusoidal modulation (Fig. 2) we find a strong increase of $\langle\Delta'\rangle$ and a severe overlap of the m/n=2/1 and the m/n=3/2 islands. For the sawtooth modulation (Fig. 3) $\langle\Delta'\rangle$ is comparable with the dc-value of 4.4, a favourable result. However, Δ' becomes relatively large simultaneously for the 2/1 and the 3/2 mode during the sharp decrease of the current. In addition the resonant q-surfaces move very closely together during this instable period so that a severe overlap of islands occurs (Fig. 3b). In the case of the inverted sawtooth modulation (Fig. 4) the situation looks unfavourable as far as Δ' is concerned. The 2/1, the 3/2 and the 3/1 mode become unstable, $\langle\Delta'\rangle$ for the 2/1 mode being very large. However, since this kind of modulation tends to move resonant surfaces apart, (see Fig. 4b), we do not encounter a large overlap of magnetic islands. These calculations then demonstrate that appropriate nonsinusoidal modulation should theoretically offer appreciable improvements over sinusoidal modulation. We remark that these calculations depend sensitively on the exact shape of the current profile.

Acknowledgements: We thank J. Stadelbauer, J. Ernesti and E. Denz for their technical assistance. We are grateful to Drs.D. Biskamp, K. Lackner and H. Wobig and the Pulsator Team for many discussions and valuable suggestions.

References:

/1/ S.von Goeler, J.Gernhardt et al.: Proc.of Symposium on Disruptive Instabilities in Toroidal Devices, Garching (1979) (to be published by IAEA)
/2/ H.P.Furth, P.Rutherford, H.Sellberg: Phys.Fluids 16, 1054 (1974)
/3/ A.Glasser, J.Greene, J.L.Johnson: Phys.Fluids 19, 567 (1976)
/4/ K.Toi, S.Itoh, K.Kadota et al.: Proc.Symp.on Disrupt.Instability in Tor.Devices, Garching (1979) to be published by IAEA)
/5/ This code is an adaption of a computer code developed by Dr. Wobig and Dr. Lackner for W VII. See R.Jaenicke, H.Wobig: this conference
/6/ R.White, D.Monticello, M.N.Rosenbluth and B.V.Waddell: Phys. Fluids 20, 800 (1977)

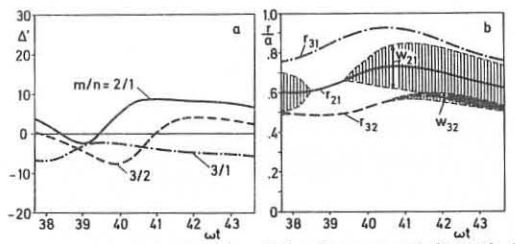

Fig.2 Sinusoidal modulation of the plasma current (case A). Subfigure (a): the instability parameter $\Delta'(t)$ vs. time during one period, for the m/n=2/1, 3/1 and 3/2 tearing mode. Subfigure (b): the radius of the resonant surface and the island width vs. time. The frequency of the ac-modulation was 200 Hz. The conductivity has the radial dependence $\sigma(r) = 1.4 \cdot 10^7\ (\Omega m)^{-1}\ (1 - .72(r/a)^2)^{5.76}$

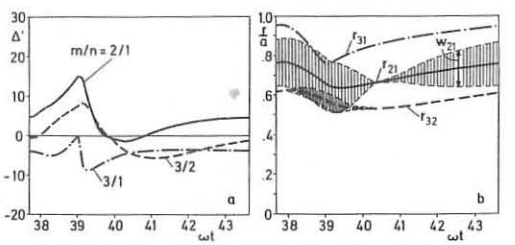

Fig.3 Sawtooth modulation of the plasma current (case B). Otherwise the same as Fig. 2.

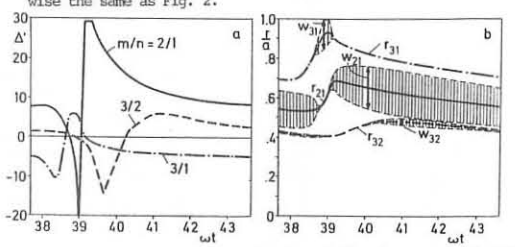

Fig.4 Inverted sawtooth modulation of the plasma current (case C). Otherwise the same as Fig. 3.

[x]) On leave from the Plasma Physics Laboratory of Princeton University.

EP7

Schlieren Measurements of Plasma Cinematics during Current Disruptions in Tokamaks

G.Lisitano
Max-Planck-Institut für Plasmaphysik, EURATOM-IPP Assoc.
8046 Garching, F.R.G.

Abstract: A new "schlieren" diagnostic applied to the Pulsator tokamak using several $\lambda = 2$ mm vertical probing chords, gives a fairly localized picture of the variation of the density gradient at about the equatorial plane of the torus. One feature of the schlieren signals reported here is the observation of a localized, rapid deformation of the density distribution during a major disruption.

Introduction: As is well known, the schlieren technique depends on light-ray deviations which are roughly proportional to the transverse electron density gradient. These techniques have hitherto been applied to high density pinch discharges. For the relatively low density values in tokamak plasmas, i.e. $N_e \simeq 10^{14}$ cm^{-3}, a finite angular deviation of the exploring ray is encountered in the millimetre wavelength range. The x-component of the total angular deviation of the exploring millimetre wave ray is related to the x-component of the gradient of the refractive index by the expression /1/:

$$\Theta_x = \int_0^L (1/n)\,(\delta n/\delta x)\,dz,$$

where n is the refractive index and the integral is taken over the length L of the plasma in the beam direction z.

In the Pulsator tokamak seven $\lambda = 2$ mm wave beams explore the plasma along vertical chords. The amplitude-independent phase variation of the beam interferometric signals is used to derive the average density distribution of the plasma. All channels are decoupled from each other by interferometric frequency selection. The amplitude decrement ΔA of the deviating beam and the signal amplitude A of the undeviated beam are related to the angular pattern of the radiators used in the Pulsator tokamak by the expression $\Delta A/A \simeq (\Theta_x/\Theta_o)^{1.2}$, where Θ_o is the first zero of the antenna radiation pattern. Combining the above equation with the refractive index $n^2 = 1 - N_e/N_c$, where N_c is the cut-off density corresponding to the $\lambda = 2$ mm wave, we have:

$$\Delta A/A \simeq (1/2N_c\Theta_o) \int_0^L [1/(1-N_e/N_c)]\,(\delta N_e/\delta x)\,dz$$

Thus, the electron density gradient may be very sensitively measured by choosing the exploring wavelength such that the density cut-off value N_c is close to N_e; i.e. $N_e/N_c \lesssim 1$.

Schlieren signals: The amplitude variation of the five $\lambda = 2$ mm probing beams shown in Fig.1a, represents the first demonstration of the applicability of schlieren techniques, in the millimetre wave range, on a tokamak plasma.

The amplitude decrement ΔA, representing the refraction losses of the various beams, is most sensitive to density gradients transverse to the radiation path of the waves. Thus, the density gradient variations deduced from the amplitude variations of the millimetre wave beams, which are arranged vertically, are fairly localized in a region about the equatorial plane of the torus, where the most important current redistribution phenomena occur.

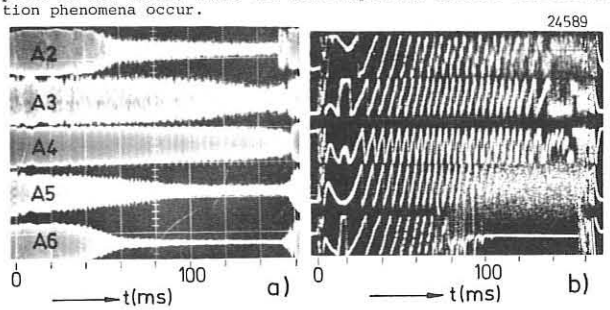

Fig.1a: Schlieren signals of five vertical probing chords at $\lambda = 2$ mm. A4 is the central channel at r = 0. A3 and A5 are positioned at $r = \mp 2.8$ cm; A2 and A6 at $r = \mp 5.6$ cm. Minus sign refers to inside channels.

Fig.1b: Phase-shift of the 5 channels. One fringe (2π phase-shift) of ch. 4 represents an average density of 5×10^{12} cm^{-3} within a limiter diameter of 22 cm. For ch. 3, 5 and 2,6 one fringe represents an average density of respectively 5.2×10^{12} cm^{-3} and 6.0×10^{12} cm^{-3}. The standard set of parameters for the shot of Fig.1 is: I = 75 kA; B = 27 kG; $q(a_L) = 3.1$.

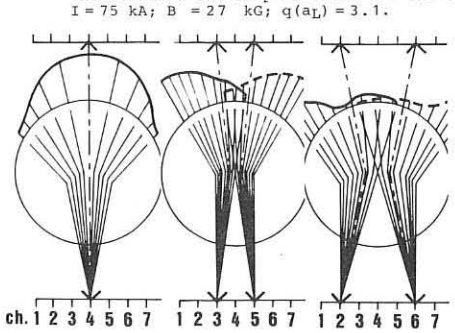

Fig.2: Sketch of the ray-path deflection-angle and of the corresponding schlieren amplitude variation of 5 probing beams for a parabolic density profile with $N_{max} = 10^{14}$cm^{-3}

Using the calculation of Shmoys/2/ for a parabolic density distribution Fig.2 shows the correspondence between the ray-deviation angles and the amplitude variation of the millimetre wave signal intercepted by the receiving antennas for a maximum density of $N_e = 10^{14}$cm^{-3}.

In Figure 2 each deviated ray has been extended over the circle, representing the limiter, by a segment corresponding to the measured amplitude of each undeviated ray. The resulting deformation of the ray pattern gives a picture of the decrease of the millimetre wave signal intercepted by the receiver antennas. The fan-like deformation of the ray pattern of ch. 4 produces an attenuation of the ray density intercepting the antenna. Calculations have shown that for a parabolic density profile having a maximum density $N_e = 10^{14}$ cm^{-3} such attenuation of the ch. 4 can be more than 50 % of that corresponding to the undeviated signal.

Non-symmetric, flat density profile: A comparison between the calculations shown in Fig.2 and the schlieren and phase-shift signals of Fig.1 illustrates two main features of the discharge shot of Fig.1.

First, the non-symmetric amplitude of the schlieren signals indicate a slightly inward off-centering of the discharge. Second, at t = 110 ms the average density for ch.4 (after gas puffing of t = 20 ms) is 10^{14} cm^{-3}. However, as seen in Fig.1a, the amplitude of the schlieren signal of ch.4 is not affected by this high value of density, whereas it should have been reduced as mentioned earlier by more than 50 %. This indicates that instead of being parabolic, the density profile must be very flat. This is in fact confirmed by the densities measured by all five channels shown in Fig.1b, from which the same density value can be derived, in so far the strong attenuation of of the schlieren signals allows a phase-shift measurement.

Schlieren cinematics of a current disruption: Figure 3 shows in an enlarged time-scale the variation of the schlieren signals of ch. 2 to 5 during a major disruption. As shown by the current position signal the discharge is centered slightly outwards. The position signal does not give, however, any detailed informations about the spatial resolution of the discharge current during the disruption.

On the other hand, the schlieren signals of Fig.3 show a very rapid (within a few microseconds) and localized redistribution of the density. At this time the density has an average value well above 10^{14}cm^{-3}. At the onset of the negative voltage spike, a significant part of the density first moves inwards from the inside part of the discharge closest to the center. This is deduced in Fig.3 by the rapid enlargement of the schlieren signal of channel 3.

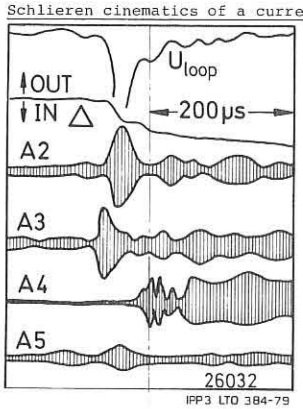

Fig.3: Enlarged time-scale view of the schlieren signals of channels A2 to A5 during a major disruption. The current position signal (second trace) has been delivered by magnetic pick-up coils.

Subsequently, with a time delay of about 10 us, this inward shift of density is observed by the ch. 2, positioned 2.8 cm inwards from channel 3. This first rapid shift of density occurs simultaneously with the first inward step observed in the position signal .

Immediately after this first deformation of the density distribution, the density profile is rapidly flattened by a second step-like inward shift of density from the center of the discharge. This is deduced in Fig.3 from the rapid increase of the schlieren signal of ch. 4. From now on the density profile is flattened and shifted inwards, as it can be deduced from the enlargement of the schlieren signal of ch. 4 and (to a smaller extent) from that of ch.3 and ch.2.

Depending on the discharge conditions prior to disruption, the cinematics of the schlieren signals presents a rich variety of supplementary features; but in all cases one can observe a localized, rapid density redistribution followed by an inward shift and flattening of the density profile.

In order to investigate the more important part of the discharge immediately preceeding the onset of the disruption a refined schlieren system is under development.

Acknowledgement

The author wishes to thank Dr.G.v.Gierke for his interest in this diagnostic from the very beginning of the development. He is very grateful to the whole Pulsator-crew and microwave group for their support.

References

/1/ see, for example, Leonard L. Stanley in Plasma Diagnostic Techniques (Richard H. Huddlestone and Stanley L. Leonard eds.) p.46,47, Academic Press, New York, London (1965)

/2/ Shmoys, J., J.Appl.Phys. 32 (1961) 689

RESULTS FROM THE DITE BUNDLE DIVERTOR

S.J. Fielding, J.W.M. Paul and A.J. Wootton
Culham Laboratory, Abingdon, Oxon, OX14 3DB, UK
(Euratom/UKAEA Fusion Association)

ABSTRACT

The DITE bundle divertor has been operated in conjunction with a titanium gettered torus wall and results compared with those without gettering. Higher densities have been achieved with gettering and diversion. Preliminary observations with injection and diversion are reported.

INTRODUCTION

Both the bundle divertor[1] and gettering of the torus wall[2] have been used, previously separately and now together, to reduce impurities in DITE. The bundle divertor acts by producing a separatrix, outside of which a scrape-off layer exists. Particles and energy are exhausted via this layer onto a target in a chamber outside the main torus, thus reducing the plasma-wall interaction. Impurities produced at the wall are ionised and removed to the target. Typically, low Z impurities are reduced to ~ 0.25 and high Z impurities to $\lesssim$ 0.1, of their previous concentrations in the main discharge.

Gettering operates by chemically trapping particles on the wall. This reduces the low Z impurities to ~ 0.12 of their previous values. Because the working gas is trapped, additional gas feed is required to maintain the density. The high Z impurities concentration is reduced to ~ 0.2 at high densities.

LOW DENSITIES

Preliminary results with and without the divertor, for both non-gettered and gettered walls, are compared in Figs. 1 and 2. The divertor is switched on in the middle of the tokamak pulse for a duration of about 150 ms. Other parameters are R_p = 1.17 m, a_{lim} ~ 0.26 m, a_{sep} ~ 0.16 - 0.19 m, B_{To} ~ 0.9 T, I_p ~ 50 kA, q_{lim} ~ 5.2, q_{sep} ~ 2.0 - 2.8, T_{eo} ~ 300 eV. The limiter material is Mo. The gettering, between each discharge, covers about 50% of the torus walls with two monolayers of Ti. The data presented here is derived from a few short periods of operation and is not always consistent.

In a non-gettered torus, operation of the divertor increases the plasma current and decreases the volts. The opposite effect occurs in a gettered torus, where the decrease in current may be caused by the expulsion of a component of runaway electrons. The effect does not occur when low initial density is avoided.

After the initial gas filling there is a steady gas feed during the discharge. In a non-gettered torus, diversion reduces the steady density to 0.35 of its initial value. In a gettered torus there is a smaller reduction to 0.7, although a steady state is difficult to obtain. With ungettered walls, refueling is mainly from the walls with the gas feed constituting a small component of the total hydrogen flux into the plasma. Diversion approximately halves the flux of ions to the wall thereby reducing the recycling and hence the density. With gettered walls this wall recycling is reduced before diversion and the gas feed is increased to compensate. The hydrogen flux into the plasma is now dominated by the gas feed, which is not greatly affected by the divertor because at these densities the screening efficiency for hydrogen is low (< 0.2). This explains the lower density drop with gettered walls.

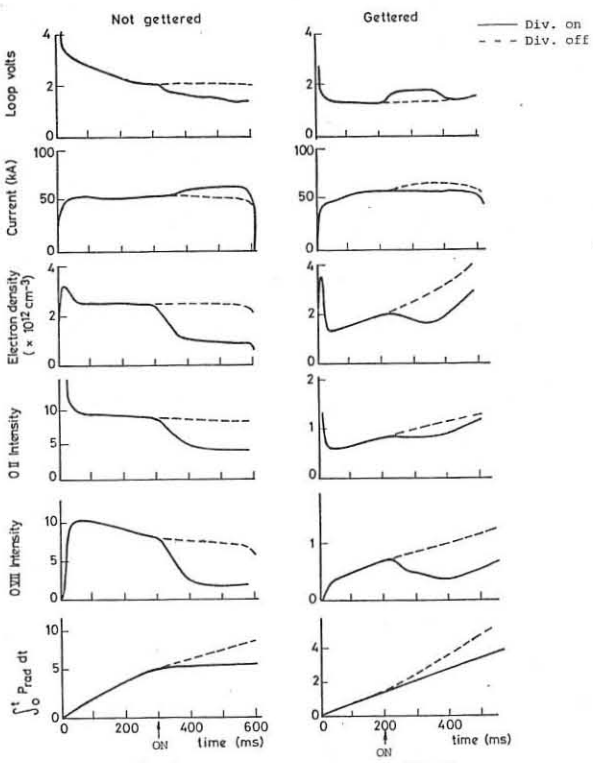

Fig. 1

Fig. 2.

TABLE I: Normalised Intensities of Oxygen Lines

	Divertor off		Divertor on		ξ_{SO}
	O II	O VII	O II	O VII	
Ungettered	1	1	0.5	0.25	50%
Gettered	0.12	0.13	0.1	0.05	46%

The intensity of the O II (4414 Å) line is assumed to represent the influx of oxygen at the edge. Operation of the divertor reduces this influx less in a gettered than in an ungettered torus (Table I) probably because of a smaller change in the particle flux to the wall. The intensities of the O VI (1031 Å) and O VII (1623 Å) lines, which arise inside the separatrix, are assumed to represent the influx of oxygen inside the separatrix. The decrease in these lines on diversion (Figs. 1 and 2; Table I) results from both the decreased source at the wall and the screening effect. Thus the screening efficiency (ξ_{SO}) can be calculated (Table I). For both lines gettering reduces the intensities to 0.12.

The total radiated power from r < 0.1 m drops dramatically when the divertor is switched on with an ungettered torus, but hardly changes with a gettered torus (Figs. 1 and 2; Table IIa). However, it changes during the pulse even without diversion (Table IIb) so that the effect should be measured by the ratio divertor on to off at the same time (Table IIc). The total radiation before diversion with gettering is about half that without gettering and so the absolute value after diversion is about the same in both cases.

The measured X-ray anomaly factors (ζ), (Table III) demonstrate the reduction of heavy metals and the production of pure plasma ($\zeta \sim 1$). An understanding of the behaviour of the radiated power and X-ray anomaly factor requires clearly consistent sets of data including profiles of both and the impurity species.

HIGH DENSITY OPERATION

In preliminary experiments, gettering without diversion did not extend the operating range of density, but when combined with diversion the range was extended by a factor of about two (Fig. 3). Diverted discharges recover more readily from soft disruptions during gas feed probably because of the weaker interaction with the wall. More perseverence might also allow higher density operation with gettering alone. Parameters have been increased to $n_{eo} \sim 6 \times 10^{19}$ m^{-3}, $\bar{n}_e \sim 2 \times 10^{19}$ m^{-3}, $\tau_E \sim 11$ ms, $\beta_p \sim 0.75$ and (β_T) inside the separatrix $\lesssim$ 0.3%.

INJECTION AND DIVERSION

Preliminary experiments with the divertor and 0.2 MW (100 ms) of injection power into an ungettered torus have shown beam trapping of up to 50%. The density increase on injection corresponds roughly with the trapped beam and is unaffected by diversion. There is a large influx of impurities (O, C, Fe) resulting from the absorbed and not the transmitted power. The divertor is not as effective at controlling the beam induced impurities and radiative loss as it is for the comparable ohmic power input. The beam appears to be lost by charge-exchange, because of the low density, and by orbit effects, because of the low current. These effects will be reduced in the near future by operating at higher density and current (lower q) and after that by a new full field divertor.

ACKNOWLEDGEMENTS

We thank Drs J. Hugill, P.E. Stott and P.J. Lomas and Messrs K.B. Axon, B.A. Powell and R. Prentice for advice and assistance and the DITE operation team.

REFERENCES

(1) S.J. Fielding et al, Proc. 8th Europ. Conf. on Controlled Fusion and Plasma Physics, Prague (1977) 1, 36.
(2) S.J. Fielding et al, Nuclear Fusion 17 (1977) 1383.
(3) J.W.M. Paul et al, Proc. 8th Europ. Conf. on Controlled Fusion and Plasma Physics, Prague (1977) 2, 49.

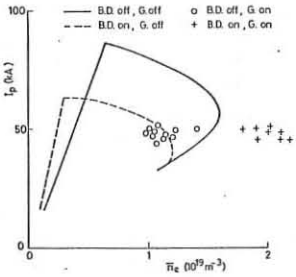

Fig. 3.

TABLE II: Ratios of radiated power

	After/Before BD on (a)	After/Before BD off (b)	On/off same t (c)
Ungettered	0.19	0.67	0.28
Gettered	1.0	1.5	0.67

TABLE III: X-ray Anomaly Factors

Divertor	Ungettered[3]	Gettered
Off	400	4.2
On	80	1.0

EP9

NEUTRAL INJECTION HEATING IN DITE

R.D. Gill, K.B. Axon, G.A. Baxter, W.H.M. Clark, R.S. Hemsworth, J. Hugill, J.W.M. Paul, J.B.B. Percival, R. Prentice, B.A. Powell and A.A. Mirin*

Culham Laboratory, Abingdon, Oxon, OX14 3DB, UK
(Euratom/UKAEA Fusion Association)

*Lawrence Livermore Laboratory, U.S.A.

We have recently operated DITE tokamak[1] (R = 117 cm, a = 26 cm, $B_\phi \leq 2.8$ T) with the 1.2 MW, 50 ms, 30 keV hydrogen neutral injection system[2]. Four injectors with McKenzie bucket design are fitted to two tangential beam lines directed with the plasma current (co-injection). The measured ion species extracted from the sources are $I(H^+):I(H_2^+):I(H_3^+)$ = 77:18:5. The tokamak plasma was H^+.

The main experiments were carried out with molybdenum limiters and titanium gettered torus walls. Typical parameters with and without injection are shown in the table. The considerable drop in loop volts (V_ℓ) with no electron temperature change is suggestive of the presence of a beam driven Ohkawa current although this is difficult to prove. Standard diagnostics were used to measure most of the main plasma parameters and a mass selective neutral particle analyser measured the ion temperature (T_i) profiles. The ion temperature increases linearly with neutral injection power per unit particle ($P/\bar{n}_e$) at first (Fig. 1) but saturates at a value approaching 900 eV. The electron temperature (T_e) did not rise but there was usually a considerable rise in electron density (n_e) during injection. One feature of our experiment which is not well illustrated by this data was the observation on many discharges of plasma disruptions when injecting more than 600 kW.

We have used these injection results to determine values for the ion thermal conductivity (K_i) in the absence of disruption. The energy balance equation for the ions at minor radius r can be written[3] in the steady state as

$$-\frac{1}{r}\frac{\partial(rQ_i)}{\partial r} + n_i e v E_r + Q_{ei} + Q_{NI} + \frac{3}{2} n_e n_o \langle\sigma v\rangle_i T_o - \frac{3}{2} n_i n_o \langle\sigma v\rangle_x (T_i - T_o) = 0$$

where the radial heat flux (Q_i) and the radial velocity (v) are determined by

$$-\frac{1}{r}\frac{\partial}{\partial r}(r n_i v) + n_e n_o \langle\sigma v\rangle_i = 0$$

$$Q_i = -K_i n_i \frac{\partial T_i}{\partial r} + \gamma n_i T_i v$$

where n_o and T_o are the neutral density and temperature. Q_{ei} and Q_{NI} are the heat input terms due to electron-ion collisions and neutral injection and are calculated in the standard way[4]. The terms involving $\langle\sigma v\rangle_i$ and $\langle\sigma v\rangle_x$ are the source terms due to ionisation and charge-exchange of neutrals in the plasma. γ is a coefficient which is approximately 2.5 for DITE and we have assumed that the radial electric field $E_r = 0$, although our values of K_i are insensitive to this assumption.

In order to solve these equations for K_i we must know n_o and T_o. The former was determined from the intensity of the neutral particle analyser signals and the latter by assuming $T_o(r) = T_i(r + \lambda/2)$ where λ is the neutrals mean free path. This assumption is justified because the strong inward gradient of n_o in a tokamak plasma implies that neutrals at r have originated, on average, at $(r + \lambda/2)$. The ion heat fluxes determined by this procedure are shown in Fig. 2 and the values of K_i deduced are shown in Fig. 3 as a function of radius. The theoretical neoclassical[5] values are also shown and are less than the experimental values by a factor of about 5 both with and without neutral injection. The other main result of these calculations was to show that at the highest ion temperatures the heat loss to the cooler electrons was a dominant process and that this caused the observed saturation in T_i as a function of injection power. The plot of $\nu = qR/v_i T_i$ as a function of radius (Fig. 4) shows that the ions are in the plateau region during ohmic heating but move into the banana regime during strong neutral injection heating.

We have also compared our results with the predictions of a Fokker-Planck/transport code developed by Mirin et al[6]. The code uses empirical values for the transport coefficients, the Hughes-Post method for treating neutrals and a two regime Fokker-Planck method for determining the heating effects of the neutral injection. Specifically we assume that $K_e = 5 \times 10^{17}/n_e$ cm^2 s^{-1}, $K_i = 10^4$ cm^2 s^{-1} and $D(r) = [10^3 + 9 \times 10^3 (r/a)^2]$ cm^2 s^{-1}, since these values give good agreement with our discharges without neutral injection. The code was used to compute the results shown in Fig. 1 and agreement with experiment is good except at the highest power levels. This difference appears because the code does not correctly model the impurity radiation losses and hence predicts substantial electron heating which is not observed experimentally.

We have also carried out an overall electron energy balance (Fig. 5) both with and without 1.0 MW of neutral injection. The radiated power determined from a radially scanned thermopile showed a very striking increase on injection, but the energy lost due to conduction and convention remained approximately constant. The large radiation losses implies the presence of high Z atoms in the discharge (probably Mo) and it was for this reason it was decided to change the fixed limiters to titanium together with a pair of adjustable carbon limiters.

Preliminary experiments with no Mo in the torus showed a dramatic reduction in the total radiated power by a factor of ~ 5 and electron heating was observed during injection into higher density discharges. The occurrence of disruptions was very much reduced and with injection of ~ 1.0 MW of H into a D^+ plasma it was possible to reach peak plasma $\hat{\beta}_T = 1.5\%$ and $\beta_\theta = 0.65$. It was also found that the ion temperature increased linearly with $(P/\bar{n}_e)$ up to P = 1.0 MW.

REFERENCES

(1) PAUL, J.W.M. et al, Proc. 6th Int. Conf. on Plasma Physics and Contr. Nuclear Fusion, Berchtesgaden 1976, (IAEA Vienna 1977) 2, 269.
(2) HEMSWORTH, R.S. et al, Joint Varenna-Grenoble Int. Symp. on Heating in Toroidal Plasmas, Grenoble, 3-7 July 1978.
(3) HINTON, F.L., et al, Phys. Rev. Lett. 29 (1972) 698.
(4) AXON, K.B. et al, Nuclear Fusion 18 (1978) 981.
(5) Equipe TFR, Proc. 8th Europ. Conf. on Controlled Fusion and Plasma Phys. 2 (Prague 1977) 1.
(6) MIRIN, A.A. et al, J. Comput. Phys. 23 (1977) 23.

Injection		off	on		off	on
B_ϕ	(T)	2.0	2.0	q(limiter)	4.04	4.04
I_G	(kA)	150	150	q(centre)	1.54	2.18
V_ℓ	(v)	3.01	1.95	$\bar{n}_e$ (cm^{-3})	1.2×10^{13}	1.6×10^{13}
Z_e		4.92	3.19	$\hat{T}_e$ (eV)	520	520
P_Ω	(kW)	451	290	T_i (eV)	290	900
P	(kW)	0	800			

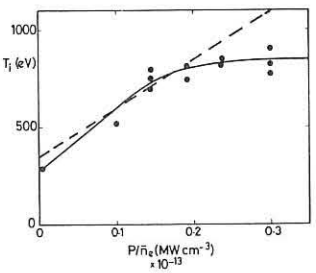

Fig. 1 Ion temperature as a function of $P/\bar{n}_e$. The broken line shows the transport calculation.

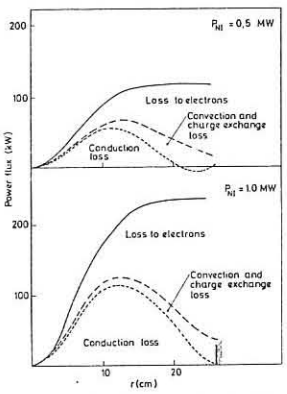

Fig. 2 Total power flux integrated over a toroidal surface as a function of minor radius.

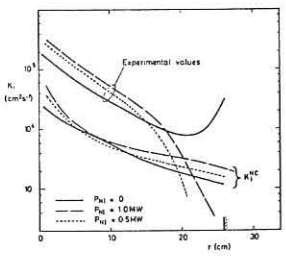

Fig. 3 Experimental and theoretical ion thermal conductivity as a function of minor radius.

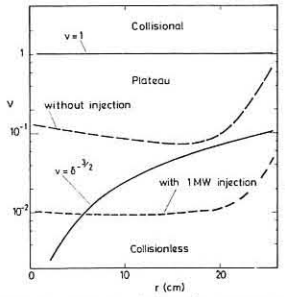

Fig. 4 The collisionality parameter ν as a function of minor radius. The injection takes the plasma from the plateau to the collisionless regime.

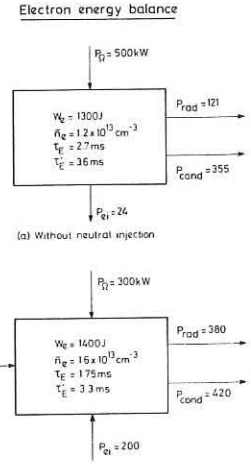

Fig. 5 Electron heat balance (a) without and (b) with neutral injection.

LOW-Q DISCHARGES IN DITE TOKAMAK

J. Hugill, A.J. Wootton, K.B. Axon, B.A. Powell, R. Prentice, D.D.R. Summers and C.M. Wilson

Culham Laboratory, Abingdon, Oxon, OX14 3DB, UK
(Euratom/UKAEA Fusion Association)

ABSTRACT Reproducible, grossly stable discharges with $2.4 > q_L > 2.2$ for up to 100 ms are produced in DITE tokamak by careful attention to operating procedures. The m.h.d. behaviour is described and an energy balance given. The confinement properties are not inferior to those at higher toroidal field.

- - - - - - - - - - - - -

The main parameters of the DITE Tokamak during these experiments are $R = 1.17$ m, $a_L = 0.26$ m, $B_T = 1.35$ T, $I = 160 - 175$ kA, giving $q_L = 2.2 - 2.5$. Two limiters, each consisting of two semi-circular arcs, spaced at least 30 mm from the vacuum vessel, are of either Mo or Ti. The bundle divertor is not used. Feedback control keeps the plasma centre at $R = 1.16$-1.17 m. The eight box-shaped sections of the vacuum vessel are connected toroidally by bellows and copper straps and have a time constant for vertical field penetration of ~ 4 ms. The torus is gettered with titanium for one hour before operation and between discharges (10 mins) using between one and three Varian Ti balls spaced around the vacuum vessel. Cold gas feed via piezoelectric valves maintains or increases the density during a discharge.

The discharge current is first raised to ~ 100 kA ($q_L = 4$) in 3 ms and is then ramped more slowly to 160 - 175 kA in 40 - 50 ms, either immediately or after a 100 ms plateau at the lower current level. The gas feed rate is usually held constant during the second current ramp, at a low level giving constant $\bar{n}_e \sim 10^{19}$ m^{-3}, or sufficient to increase $\bar{n}_e$ at a rate up to about 3×10^{20} m^{-3} s^{-1}. The general behaviour of the discharge does not seem to depend critically on the gas feed rate. Fig. 1 shows the various paths followed in I v n space. The highest density was reached with a 50 ms 0.3 MW pulse of neutral beam injection at 22 kV.

Operation at low q in DITE depends mainly on the following conditions

a) Cleanliness of the vacuum wall, provided in this case by gettering.

b) Absence of mhd modes with m = 2, measured by coils outside the plasma column.

c) Removal of heavy metals from the vacuum system. Although low-q operation is possible with Mo limiters, it is much easier with limiters of Ti.

d) Conditioning of the vacuum vessel and/or limiters and the patience of the experimentalist. The first discharges usually disrupt even at high q but the behaviour gradually improves. Violent disruptions can themselves cause deconditioning and affect the subsequent discharge but in a well conditioned vacuum vessel the discharge recovers from minor disruptions even during the low-q plateau.

Sixteen coils positioned at r = 0.29 m around the minor aximuth measure the amplitude and poloidal mode number of magnetic fluctuations in B_p. Soft X-ray diodes are used to detect sawtooth oscillations and measure the radius of phase inversion. Sawtooth oscilations are also seen on the 2 mm microwave interferometer.

Figure 2 shows the time behaviour of the main discharge parameters and the mhd behaviour, for a low-q D_2 discharge with Ti limiters. As the current passes through the levels where $3.1 > q_L > 2.7$ a rapidly growing m = 3 mode is seen associated with a small + ve spike on the loop voltage. Because of its rapid growth rate and its persistence to $q_L < 3$, this is thought to be a kink mode. At the same time a more slowly growing m = 2 mode is seen which may persist at low-q and, in a badly conditioned vacuum vessel, leads to disruption. This is probably a tearing mode centred at the q = 2 surface. During the low-q current plateau, strong sawtooth oscillations are seen with a period of 2.5 ms. The radius of the q = 1 surface obtained from the T_e profile is 0.14 m, with or without neoclassical corrections to the resistivity. After Abel inversion, the profiles of sawtooth oscillations in soft X-ray signals and in the line of sight density show that the inversion point lies between r = 0.11 m and r = 0.13 m. The amplitude of the density fluctuations at r = 0 is $\sim 5\%$.

Figure 3 gives the profiles of T_e, n_e, T_i and total radiation for the discharge shown in Fig. 2. The profiles of T_i were made with a neutral particle analyser scanned across the minor radius, observing at an angle of 7.5° to the major radius. All the profiles are quite flat inside the q = 1 surface. With neoclassical corrections, there is no resistance anomaly, indicating low impurity content. Total radiation, including charge-exchange neutrals, accounts for only $(32^{+15}_{-5})\%$ of the ohmic input. The main impurity is probably Ti from the walls and limiters. Table I lists the parameters derived from these profiles and an energy balance at r = 0.2 m is given in Fig. 4.

Comparison with discharges at similar current and density at higher q, shows that the confinement properties of the low-q discharge are similar to those at higher B_T, the profiles being somewhat broader and T_{eo} and n_{eo} lower.

Preliminary attempts to raise the current rapidly to achieve $q_L < 2$ were unsuccessful. A major disruption occurs, preceded by very rapidly growing mhd modes with undetermined mode number. A more systematic attempt to reach $q_L < 2$ will be made in due course. The effect of using the DITE bundle divertor will also be studied.

ACKNOWLEDGEMENTS

We are indebted to Mr G.W. Reid and the DITE operating team and to Dr J.W.M. Paul for supporting this work. Drs J.A. Wesson and F. Alladio provided computations of mhd stability, with the assistance of Mrs M. Turner. Mr J.B.B. Percival provided the data from the neutral particle analyser.

REFERENCES

(1) S.J. Fielding et al, Nuclear Fusion 17 (1977) 1382.

(2) J.A. Wesson, Nuclear Fusion 18 (1978) 87.

Fig. 4. The energy balance inside r = 0.2 m at t = 150 ms.

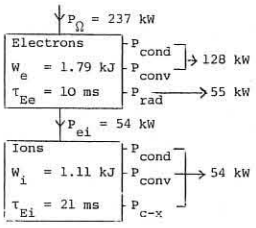

Table I - Main discharge parameters

R	= 1.17 m	N	= 3.4 x 10^{18} m^{-1}
a	= 0.26 m	$\langle T_e \rangle$	= 312 eV
B_T	= 1.35 T	$\langle T_i \rangle$	= 239 eV
I	= 170 kA	Z_{eff}	from resistance
V_R	= 1.5 V	a) $j \sim T_e^{3/2}$	1.4
q_L	= 2.3	b) N-C corrections	1.0
τ_E	= 12 ms	$\nu^*_{e(min)}$	= 0.6 at r = 0.1 m
β_p	= 0.20	ν^*_i	= 0.8 at r = 0.2 m
P_{rad}/P_{OH}	= 0.32		

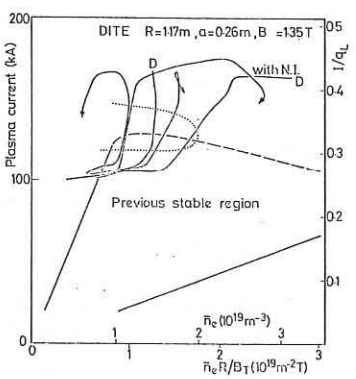

Fig. 1. Trajectory of various discharges in I v $\bar{n}$ space. Region of stable operation obtained previously (1) is shown. Dotted curve encloses area where enhanced m = 3 (kink) activity is observed.

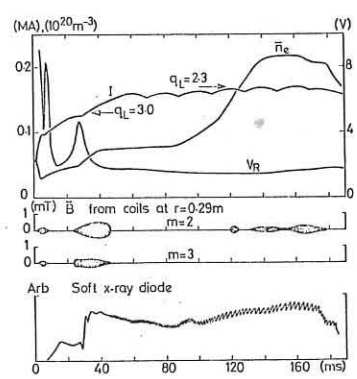

Fig. 2. Time behaviour of various parameters in a low-q discharge in deuterium.

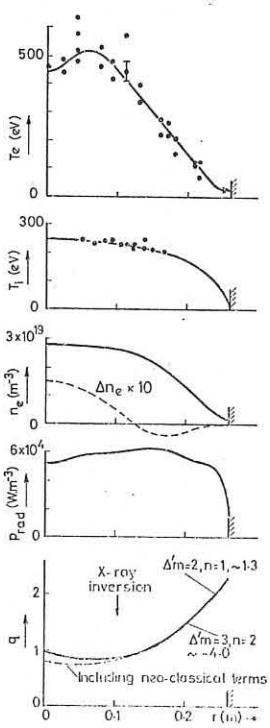

Fig. 3. Radial profiles of various parameters at t = 150 ms. The q profile shown is derived from the electron temperature, including neoclassical terms. Marked is the X-ray sawtooth oscillation inversion point, and the parameter Δ' from a tearing mode calculation (2).

52

EP12

MEASUREMENTS OF ELECTRON CYCLOTRON EMISSION ON T-10

A.A. Bagdasarov*, W.H.M. Clark, A.E. Costley‡, E.P. Gorbunov* and G.F. Neill‡

Culham Laboratory, Abingdon, Oxon, OX14 3DB, UK
(Euratom/UKAEA Fusion Association)

* The I.V. Kurchatov Institute of Atomic Energy, Moscow, U.S.S.R.
‡ The National Physical Laboratory, Teddington, UK

ABSTRACT

Measurements of the electron cyclotron emission from the T-10 tokamak plasma are presented. From these the spatial profiles of the electron temperature are deduced and compared with measurements from Thomson scattering. In general there is good agreement but in some cases structure is observed on the profiles. It is possible that this is due to the presence of trapped electrons. Attempts to measure the emission during experiments on ECRH were unsuccessful because of interference, but we can conclude that ECRH does not leave the electron velocity distribution disturbed after the pulse.

EXPERIMENTAL ARRANGEMENT

In this paper we report results of a joint UK/USSR experiment on the T-10 tokamak where the primary objective was to measure the spectrum of electron cyclotron emission and to deduce the spatial profile of the electron temperature. Attempts were also made to measure the emission during electron cyclotron resonance heating (ECRH) experiments on the plasma.

Radiation emitted from the outside of the tokamak at 10° to the equatorial plane was transmitted by over-moded waveguides (dia. > 10 x maximum wavlength) to a rapid-scan polarization type interferometer[1] fitted with a liquid helium cooled indium antimonide detector. The instrument measures the emission spectrum in the frequency range $50 < f < 500$ GHz, that is $f_{ce} < f < 6f_{ce}$ for toroidal flux density $B_T = 3.0$ T, where f_{ce} is the electron cyclotron frequency. The time resolution is ~ 14 ms and the spectral resolution $\tilde{>}$ 7 GHz. A dedicated minicomputer system (SADA) is used to control the interferometer remotely, and to analyse, display and record the data in the time interval between shots (typically 10 mins). The interferometer was calibrated with single frequency microwave sources and with a black body source at liquid nitrogen temperature.

In addition, the emission around fixed frequencies was measured with a Fabry-Perot interferometer operating in first order with a resolving power $\tilde{>}$ 20. A multi-element low pass filter is included in the device to prevent transmission of the higher orders. In principle, the time resolution of this device is determined by the bandwidth of the detector ($\tilde{<}$ 300 kHz) but for the measurements reported here the radiation was amplitude modulated at 200 Hz to minimize effects due to pick-up.

Some preliminary measurements were also made with a scanning Fabry-Perot interferometer where one of the plates was vibrated at 100 Hz. With this device it is possible to measure the emission in narrow regions of the spectrum, e.g. $1.8\ f_{ce} < f < 2.2\ f_{ce}$, with a spectral resolving power ~ 20 and a time resolution ~ 5 ms.

RESULTS

Two types of plasma discharges were investigated. In type I, $B_T = 3.0$ T, plasma current I_g ~ 400 kA, typical line-average electron density $\bar{n}_e \sim 2 \times 10^{19}$ m^{-3} and electron temperature T_e ~ 800 eV. For type II, $B_T = 1.5$ T, I_g ~ 200 kA, $\bar{n}_e \sim 1.5 \times 10^{19}$ m^{-3} and T_e ~ 1.2 keV.

Under conditions I the emission spectra are usually of the form shown in Fig. 1. Since for these conditions the plasma is optically thick for most of the second harmonic (see Fig. 2) it should be possible to determine the spatial dependence of the electron temperature by using the usual frequency to space transformation[2]. An example is shown in Fig. 3 along with the corresponding Thomson scattering points. The profiles obtained at other times on the same shot are also shown. We note that the agreement is generally good but that the profile from cyclotron emission is slightly narrower. This is possibly due to a reduction in optical depth and therefore a departure from black-body conditions in the wings of the line.

One interesting feature is the apparent structure on the line which under some circumstances can be relatively large. The plasma emission results suggest that this may be real, although at present the signal-to-noise on the calibration is insufficient to be sure of the exact shape. In view of the high thermal conductivity along the magnetic surfaces it is unlikely that this represents real structure in the temperature profile. One possible explanation is emission by trapped electrons, i.e. localised suprathermals, and it is interesting to note that independent soft X-ray measurements have shown that such particles exist in T-10 particularly on the outside of the plasma (i.e. at major radii > 1.5 m)[3].

Under conditions II similar spectra are obtained but in this case the deduction of the electron temperature profile is less reliable because of cut-offs in the emission due to finite density effects[4]. Nevertheless, the profiles still seem to be in approximate agreement with Thomson scattering, possibly because of the spatial averaging in the emission measurement arising from antenna pattern, frequency resolution and refraction effects.

With experiments on ECRH at the second harmonic extraordinary mode under type II conditions no measurements could be made during the heating pulse (peak power $\tilde{<}$ 250 kW, duration $\tilde{<}$ 50 ms) because of severe pick-up. However, measurements made immediately before and after the pulse showed little change in the spectrum, as shown in Fig. 4. No heating effect was observed but this is probably because the time delay for the system to recover from the pick-up was of the same order as the energy confinement time (~ 15 ms under these conditions). Nevertheless, it is possible to conclude that the heating does not produce distortions to the electron velocity distribution lasting longer than 15 ms. It will be necessary to use a system specifically designed for minimum sensitivity to radiative and electrical pick-up to obtain measurements during the heating pulse.

ACKNOWLEDGEMENTS

We wish to thank Drs Berlizov, Dnestrovskii, Notkin and Razumova for information and useful discussions, Dr B. Walker for supplying the Fabry-Perot interferometers and the T-10 tokamak group for their co-operation.

REFERENCES

(1) A.E. Costley and J. Chamberlain, Conf. on Precision Electromagnetic Measurements, IEE, No 113, 210 London (1974).
(2) F. Engelmann and M. Curatolo, Nuclear Fusion 13 (1973) 497.
(3) K.A. Razumova and D. Marty, Private communication.
(4) C.M. Celata and D.A. Boyd, Nuclear Fusion 19 (1979) 423.
(5) Yu. N. Dnestrovskii, D.P. Kostomarov and N.V. Skrydlov, Sov. Phys. Tech. Phys. 8 (1964) 691.

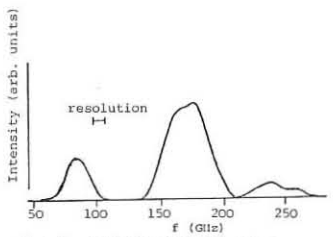

Fig. 1. Emission spectrum under type I conditions.

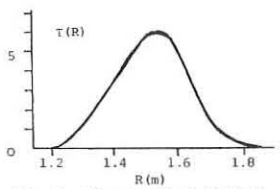

Fig. 2. Plasma optical depth τ as a function of major radius R calculated using expressions derived from Ref. (5) and probable density and temperature profiles. We note that it should be possible to determine $T_e(R)$ in the range $1.3 < R < 1.7$ m from emission measurements.

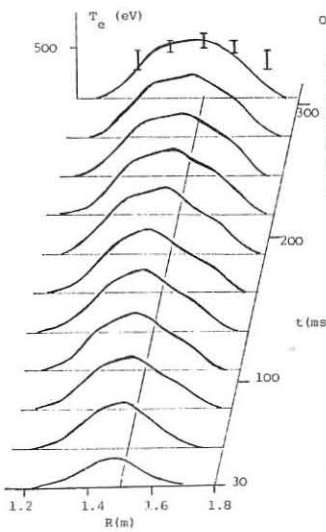

Fig. 3. $T_e(R,t)$ deduced from emission measurements and comparison with Thomson scattering. Emission profile is normalised to Thomson profile at R = 1.5 m.

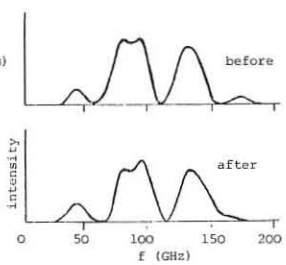

Fig. 4. Spectrum just before (~ 15 ms) and just after (~15 ms) the ECRH heating pulse (power ~ 120 kW, duration = 20 ms).

POLARIZATION AND MILLISECOND SPECTRAL MEASUREMENTS OF ELECTRON CYCLOTRON EMISSION FROM DITE TOKAMAK

D.J. Campbell[+], W.H.M. Clark, A.E. Costley[*], P.J. Fielding, L.C. Robinson[*], G.D. Tait[‡] and B. Walker[*]

Culham Laboratory, Abingdon, Oxon, OX14 3DB, UK
(Euratom/UKAEA Fusion Association)

+ University of Sydney, Sydney, Australia
* Division of Electrical Science, National Physical Laboratory, Teddington, U.K.
‡ University of Maryland, College Park, Maryland U.S.A.

ABSTRACT

Measurements of electron cyclotron emission (ECE) spectra from DITE tokamak on a millisecond timescale are reported along with the corresponding electron temperature profiles. Preliminary measurements of the Stokes parameters for the polarization of the emission at the second harmonic are also reported. A theoretical expression for the angular variation of the optical depth of each mode of polarization of the second harmonic in a finite density plasma is used to qualitatively explain the low degree of polarization observed.

MILLISECOND MEASUREMENTS

The measurement of ECE spectra from tokamak discharges using fourier-transform spectroscopy is becoming a routine diagnostic[1,2]. If the emission is due to thermal electrons the radial electron temperature profile may be determined from the line profile of an optically thick harmonic[3]. On the DITE tokamak a vibrating mirror interferometer, with a scanning time of 14 ms, is used for this purpose. Repetitive measurements in shorter timescales have proved difficult[4]. Here we report spectral measurements taken with a novel Michelson interferometer, where the scanning device is a rotating mirror providing a scanning time of 1 ms and repetition rate of 100 Hz. In Fig. 1 the spectra measured by both instruments for similar steady state discharges show good agreement, (magnetic field = 2 T, mean density = 4.5×10^{13} cm^{-3} and peak electron temperature from Thomson scattering = 700 eV). Figure 2 shows a sequence of electron temperature profiles determined from spectra measured (from several shots) in the early transient phase of the DITE discharge. The plasma is assumed to be optically thick in the central region, (field = 2 T, density = 1×10^{13} cm^{-3}, temperature = 1 keV). Interference prevented measurements from being made during the first 10 ms. The same detector (a hot electron bolometer) is used for both instruments but is not yet calibrated accurately. This may account for the apparent asymmetry in the profiles.

POLARIZATION MEASUREMENTS

Previous measurements have not completely determined the polarization of the ECE[5,6]. If the x and y components of the electric field vector of a monochromatic wave propagating in the z-direction are given by

$$E_x = E_{xo}\cos(\omega t - kz + \delta_x) \qquad E_y = E_{yo}\cos(\omega t - kz + \delta_y)$$

then the polarization may be completely defined by the four Stokes parameters:

$$I = E_{xo}^2 + E_{yo}^2 \qquad M = E_{xo}^2 - E_{yo}^2$$

$$C = 2E_{xo}E_{yo}\cos(\delta_x - \delta_y) \qquad S = 2E_{xo}E_{yo}\sin(\delta_x - \delta_y)$$

where for a monochromatic wave: $I - \sqrt{M^2 + C^2 + S^2} = 0$. For a beam composed of an incoherent ensemble of waves in a narrow spectral bandwidth the totals of the Stokes parameters are such that

$$I_t - \sqrt{M_t^2 + C_t^2 + S_t^2} = I_t - I_p = I_o.$$

Thus the beam intensity is composed of a polarized component I_p and an unpolarized component I_o such that the degree of polarization

$$P = \frac{I_p}{I_o + I_p}.$$

With a fixed frequency (112 GHz) polarimeter consisting of a Fabry-Perot interferometer (bandwidth 3 GHz), rotating polarizer and a quarter-wave plate, we have determined the Stokes parameters for radiation at the second harmonic from the centre of a discharge under conditions similar to those of Fig. 2, viz:

$$I = 4.5 \pm 1.5 \qquad M = 4 \pm 1 \qquad C = 0 \pm 1.5 \qquad S = -1.0 \pm 1.5.$$

With the magnetic field along the x-axis, this means that $p = (25 \pm 10)\%$ of the radiation is elliptically polarized with the major axis at $(90 \pm 10)^\circ$ to the x-axis, $E_x/E_y = (0.2 \pm 0.3)$ and the more probable sense is left-handed. The measurement uncertainties are consistent with plane polarization in the extraordinary mode and should be significantly reduced with an improved version of the polarimeter presently under construction.

THEORY

If the optical depth τ, for radiation in the resonant layer is such that $\tau \gg 1$ then the intensity of ECE corresponds to the black body level[7]. For the second harmonic under typical tokamak conditions $q = (\omega_{pe}/\omega)^2 \lesssim 1$. Hence instead of the very low density, ($q \ll 1$), theory[3] used to estimate $\tau_{o,e}$ for the ordinary (o) and extraordinary (e) modes we use the general expression for the ℓth harmonic cyclotron damping in a plasma of finite density[8] and the usual slab model for the resonant layer[3]. Thus for the second harmonic:

$$\tau_{o,e} = 4\pi^2\left(\frac{kT}{m_o c^2}\right)\frac{R}{\lambda}\,G(q,\theta)\cos\beta$$

where: R = major radius, λ = free space wavelength, T = electron temperature, θ is the angle between the wave vector and the magnetic field and β is the angle between the wave vector and the Poynting vector.

$$G(q,\theta) = 3qn^3\sin^2\theta\,\frac{[n^4\sin^2\theta - n^2(1-q)(1+\cos^2\theta) + 2(1-2q)(1-q-n^2\sin^2\theta)]}{2(1-2q)(3-2q)(1-q-n^2) - qn^2(1+\cos^2\theta)}$$

where $n = n_{o,e}(q,\theta)$ is the cold plasma refractive index. The neglect of relativistic line-broadening is valid for $n\cos\theta \gtrsim \sqrt{kT/mc^2}$, typically $\theta \lesssim 88^\circ$. Figure 3 shows a plot of $G(\theta)$ for $q = 0.1$ and 0.2 (for which $\cos\beta \simeq 1$) indicating that although $\tau_o \ll \tau_e$ for $\theta \simeq 90^\circ$, for $\theta \simeq 70^\circ$ $\tau_o \sim \tau_e$.

In the experiment the antenna receives radiation over angles $87^\circ < \theta \lesssim 90^\circ$. The angular variations of $\tau_{o,e}(\theta)$ are insufficient to explain the low degree of polarization observed unless a significant amount of black body radiation in the o-mode from $\theta \gtrsim 70^\circ$ is refracted by the plasma into the antenna. Numerical computations of $\tau_{o,e}$ along refracted ray paths confirm that this effect can bring about substantially unpolarized emission at $\theta = \pi/2$, previously attributed to polarization scrambling by wall reflections[1].

REFERENCES

(1) A.E. Costley, R.J. Hastie, J.W.M. Paul and J. Chamberlain, Phys. Rev. Lett. 33 (1974) 758.
(2) F.J. Stauffer and D.A. Boyd, Infrared Physics, 18 (1978) 755.
(3) F. Englemann and M. Curatolo, Nuclear Fusion 13 (1973) 497.
(4) D.V. Bartlett, A.E. Costley and L.C. Robinson, Infrared Physics, 18 (1978) 749.
(5) A.E. Costley and TFR Group, Phys. Rev. Lett. 38 (1977) 1477.
(6) I.H. Hutchinson and D.S. Komm, Nuclear Fusion 17 (1977) 1077.
(7) V.I. Pakhomov, V.F. Aleksin and K.N. Stepanov, Sov. Phys. Tech. Phys. 6 (1962) 856.
(8) A.I. Akhiezer et al "Plasma Electrodynamics" Vol 1, Pergamon Press, (Oxford, 1975).

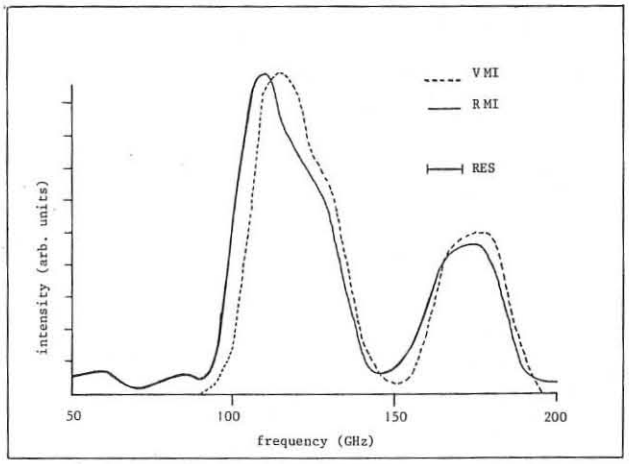

Fig. 1. Comparison between spectra from vibrating mirror interferometer (VMI) and rotating mirror interferometer (RMI). RES is the frequency resolution of both instruments.

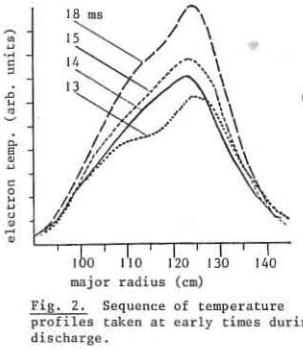

Fig. 2. Sequence of temperature profiles taken at early times during discharge.

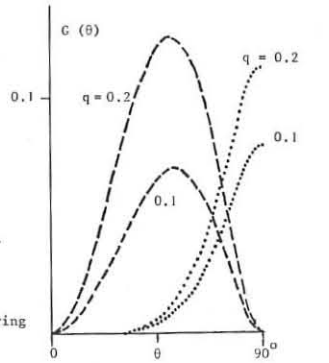

Fig. 3. The function $G(\theta)$ for $q = 0.1$ and $q = 0.2$. Dashed line o-mode, dotted line e-mode.

EP15

D_α SPECTRAL PROFILE MEASUREMENTS ON TFR PLASMAS

TFR GROUP

Presented by P. PLATZ

ASSOCIATION EURATOM-CEA SUR LA FUSION
Département de Physique du Plasma et de la Fusion Contrôlée
Centre d'Etudes Nucléaires
Boite Postale n° 6. 92260 FONTENAY-AUX-ROSES (FRANCE)

Abstract : High resolution ($d\lambda$ = 0.1 Å) profile measurements of D_α are done with a high-throughput, high-finesse (F = 30) scanning Fabry-Perot interferometer. In a typical discharge a superposition of a narrow and a broad component with an intensity ratio of 1 : 3 is observed and interpreted as due to a two-component velocity distribution at 1 eV and 30 eV respectively. With pure D_2 filling gas, the H_α/D_α intensity ratio is normally near or below the threshold of detection (6 %).

A Burleigh RC 110 interferometer is used at a ramp amplitude of 3 interference orders and a ramp duration of 100 ms. A He-Ne laser is used for adjustment (finesse = 30). The D_α line is isolated by an interference filter (FWHM 20 Å). Observations are mainly done in the R-direction at 80° with respect to the toroidal field. A π-polarizer permits the almost complete suppression of the σ-components (the width of the π-component due to the fine-structure is 0.1Å /1/).

Fig. 1 shows a typical low-resolution (0.3 Å) result of a (200 kA, 40 kG, D_2)-discharge (two successive scans are superposed). The profile may be decomposed into a narrow component (NC), a broad component (BC) and residues from $D_\alpha\sigma$ and $H_\alpha\pi$. The BC has almost constant width throughout the discharge (the first 10-20 ms excepted) and, in the present case, fits well to a Gaussian distribution at 28 eV. The interpretation of the NC is somewhat uncertain due to instrumental reasons. More insight into the NC is got at higher resolution (0.1 Å) accepting some overlapping of the BC interference orders. Fig. 2 shows such a scan for a (150 kA, 43 kG, D_2)-discharge. Here, the NC is nearly Gaussian with shot-to-shot variations of the FWHM from ≃ 0.3 Å to 0.41 Å. After correcting for the fine-structure and the instrumental function this leads to 0.5 - 1.2 eV. However, in another series under similar conditions, a non-Gaussian NC with several reproducible features has been observed (Fig. 3). This structure may be an indication for the molecular origin of the slow neutrals in these discharges. Similar D_α (and H_α) profiles have been observed in experiments on the dissociation of D_2 (H_2) by electron impact /2-4/ and are well explained by the discrete values of the kinetic energy of the dissociation fragments at electron impact energies ≥ 30 eV. However, the existence of the BC is incompatible with the present knowledge of the molecular potential curves and is therefore interpreted as due to the kinetic energy of plasma particles after backscattering from the walls.

With a well discharge-cleaned (i.e. oxygen free) wall surface and SS limiters, the H_α/D_α ratio is generally near or below the threshold of detection (≃ 6 %, depending on the D_α line radiance) ; Fig. 1. A slight increase may be observed at the end of long series of shots. However, when using a four-section limiter with the top and bottom sectors made of moderately discharge-cleaned carbon, the H_α/D_α ratio increases from a few % to 50 % in 100 - 200 ms. These observations agree well with mass spectroscopy.

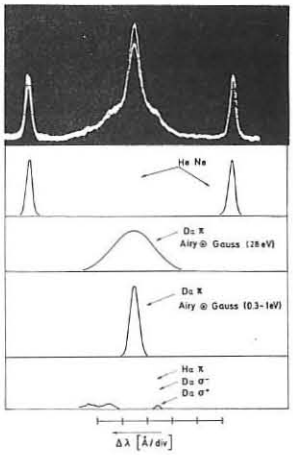

Fig. 1

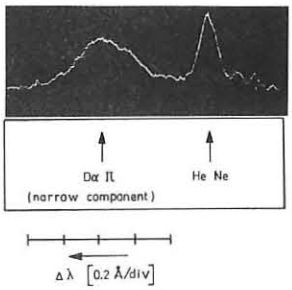

Fig. 2

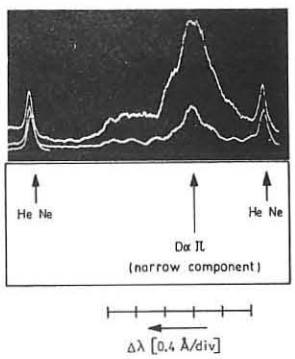

Fig. 3

/1/ P.C. Norem, PPL - Report, MATT-286 (1964).
/2/ R.S. Freund et al., J. Chem. Phys. 64, 1122 (1976).
/3/ K. Ito et al., Chem. Phys., 17, 35 (1976) and 21, 203 (1977).
/4/ L. Julien et al., J. Phys. B, 6, L 196 (1973).

NONLINEAR PHENOMENA BY THE TOKAMAK HELICAL MODE EVOLUTION

N.V. Ivanov, A.M. Kakurin

I.V. Kurchatov Institute of atomic energy

Moscow, USSR

ABSTRACT: By means of phenomenological tO-1 tokamak oscillogram analysis a set of differential equations, describing a magnetic pickup signal, is derived.

It is known, that helical mode amplitudes of tokamak plasma either slightly change in time or pulsate around their average levels /1/. Such an amplitude behaviour shows a nonlinear nature of helical modes, because permanent or pulsatory self-oscillatory regimes are impossible in linear systems. The investigation of helical mode nonlinear evolution is necessary for comprehension of feedback /2/ action peculiarities.

The pickup trace (Fig. 1) shows oscillations with frequency of 20 khz and periodically changing amplitude. The amplitude pulsation period is about 0.5 msec, the pulsations form is characterized by relativelly slow increase and swift quenching.

We consider the poloidal magnetic field perturbations as

$$B_\theta(t) = \tilde{B}_\theta(t)\cos\Omega t, \qquad (1)$$

ignoring the mode frequency variations. The amplitude evolution is described by

$$d\tilde{B}_\theta/dt = \gamma\,\tilde{B}_\theta . \qquad (2)$$

Let us assume, that γ time variations are not independent, but are conditiond by $\tilde{B}_\theta(t)$ behaviour. Let $\tilde{B}_\theta(t)$ and $\gamma(t)$ dependencies be determined by a closed set of equations, which we shall try to find from the experimental data.

The pulsed form of $\tilde{B}_\theta(t)$ shows absence of a simple tie between instant $\tilde{B}_\theta$ and γ values. The magnetic pickup trace and corresponding $\tilde{B}_\theta(t)$ and $\gamma(t)$ dependences are shown in Fig. 2. As it follows from the analysis of oscillogram series, there is a tie between $\tilde{B}_\theta$ and a product of $d\gamma/dt$ and some γ function, the tie remains invariable in time. This conclusion is illustrated by Fig. 3, in which a series of instant $d\gamma/dt$ upon $\tilde{B}_\theta$ dependens, each obtained for fixed γ value, is shown.

It is convenient to take into account some w value:

$$\frac{dw}{dt} = \frac{dw}{d\gamma}\cdot\frac{d\gamma}{dt}, \qquad (3)$$

$$w = 0 \quad \text{if} \quad \gamma = 0, \qquad (4)$$

so that

$$dw/dt = \tilde{B}_{\theta c} - \tilde{B}_\theta , \qquad (5)$$

where $\tilde{B}_{\theta c} \approx 5$ G.

Using Fig. 3 we obtain dw/dt as γ function. The result, shown in Fig. 4, gives approximately

$$dw/d\gamma = 10^{-8}/(1-10^{-4})^2 , \qquad (6)$$

that is

$$\gamma = \gamma_{max}\,\frac{10^4 w}{1+10^4 w} , \qquad (7)$$

where $\gamma_{max} = 10^4$ sec^{-1}.

So we have derived a set of equations (2),(5),(7), describing helical mode amplitude time evolution. $\tilde{B}_\theta(t)$ dependence, obtained from (1) by means of (2),(5),(7) numerical calculation, is shown in Fig. 5.

The phenomenologically derived (2),(5),(7) set of equations is in agreement with the next simple interpretation. The helical mode benaves as a self-excited oscillation with inertial nonlinearity. The growth rate γ depends on plasma parameter combination, which in it's turn changes under the mode influence. This parameter combination is characterized by w value. By w increase, γ goes to it's maximum value, which coincide with the tearing mode /3/ growth rate:

$$\gamma \sim \sqrt[5]{\Omega_A^2\,(c^2/4\pi^5 a^2)^3} \qquad (8)$$

for our experimental conditions. The pulsed regime is due to γ inertia. Similar pulsed generation of self-oscillators with inertial nonlinearity is well known for electronic generators with thermistors /4/ and for lasers /5/.

Helical mode amplitude pulses are in time correlation with tokamak voltage spikes, the voltage decreases while the mode amplitude increases (Fig.1,2,6). It means that there is a voltage and dw/dt time correlation. The plasma current being constant, it shows a tie between w and total(including magnetic) plasma energy. Magnetic energy depends on plasma current profile, which both conditions $\int\gamma$ value / 8 / and changes under helical mode influence.

REFERENCES

1. H.P.Furth, Nuclear Fusion, 15 ,487 (1975).
2. V.V.Arsenin et al, Plasma Physics and Controlled Nuclear Fusion Research. 7-th Conf.Proceedings. Innsbruck,1978,IAEA-CN-37/N-1.
3. H.P.Furth, J.Killeen, M.N.Rosenbluth, Phys.Fluids,6, 459 (1963).
4. В.А.Котельников, А.М.Николаев, "Основы радиотехники", Гос.изд-во лит-ры по вопросам связи и радио. Москва, 1954, с.262-266.
5. А.М.Ратнер, "Спектральные пространственные и временные характеристики лазера", изд-во "Наукова думка", Киев, 1968, стр.109-111.
6. С.В.Мирнов, И.Б.Семенов, Атомная энергия,30, 20 (1971).
7. V.S.Vlasenkov et al, 6-th European Conf.on Controlled Fusion and Plasma Physics. Contributed papers. Moscow 1973, p.55.
8. H.P.Furth, P.H.Rutherford, H.Selberg, Phys.Fluids,16, 1054 (1973).

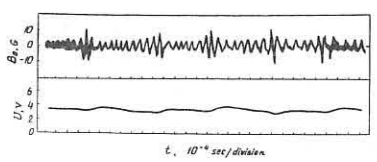

Fig.1. Magnetic pickup B_θ (absolute callibration given for a frequency of 20 khz) and tokamak discharge voltage U traces.

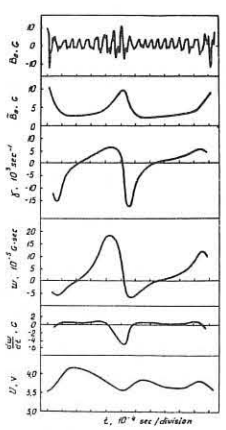

Fig.2. Magnetic pickup trace and time dependences of mode amplitude $\tilde{B}_\theta$, growth rate γ, w, dw/dt and discharge voltage U.

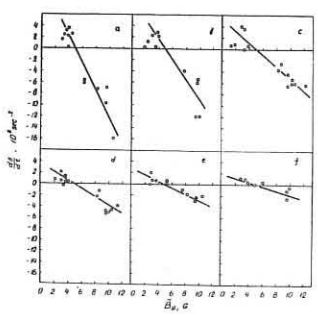

Fig.3. $d\gamma/dt$ versus mode amplitude for fixed γ values: a- $\gamma = -5\ 10^3$sec^{-1}, b- $\gamma = -2.5\ 10^3$sec^{-1}, c- $\gamma = 0$, d- $\gamma = 1.5\ 10^3$sec^{-1}, e- $\gamma = 3\ 10^3$sec^{-1}, f- $\gamma = 4.5\ 10^3$sec^{-1}.

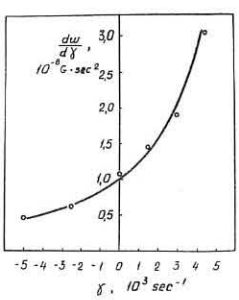

Fig.4. dw/dγ versus γ.

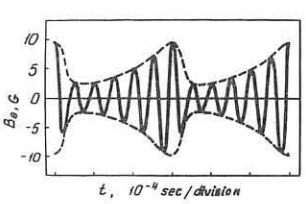

Fig.5. Calculated $\tilde{B}_\theta$ (t) dependence.

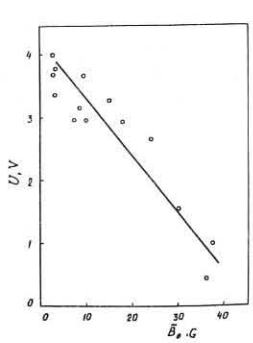

Fig.6. Discharge voltage versus mode amplitude (instant values).

EP17

Ballooning Stable Profiles in Circular Tokamaks

D. Lortz, J. Nührenberg

Max-Planck-Institut für Plasmaphysik, 8046 Garching bei München

Federal Republic of Germany

Abstract: The ballooning stability properties of axisymmetric equilibria are characterized by a ballooning unstable band in the plane poloidal ß vs. shear. For equilibria with nearly circular cross-section ballooning stable ß-values of about 8% below the unstable band and of about 25% above the unstable band are found.

Recently, ballooning instabilities, as obtained from the ballooning instability equation [1,2] have gained much interest and it has been shown [3] that the ballooning stability properties of self-consistent axisymmetric equilibria are characterized by a ballooning unstable band in the plane poloidal ß vs. shear. We have developed a code which evaluates the ballooning instability criterion over the whole plasma cross-section of any given axisymmetric equilibrium. Here, this code is applied to equilibria with circular cross-section near the magnetic axis and $\iota = 1$ on the magnetic axis. Two classes of equilibria are considered: Class 1. Analytic equilibria with linear profiles $p' = -ß_p(0) + p_1 T$ (T normalized poloidal flux function), $ff' = -ß_p(0) - 1 + \gamma_1 T$, which are obtained by separation of variables [4], have vanishing triangularity and quadrangularity near the magnetic axis, and contain three free parameters $ß_p(0) = 1 - \dot{I}_\phi(0)/\dot{J}_\chi(0)$, $S(0) = 2\pi^2 R^3 \dot{q}(0)/q(0)$, p_1. Class 2. A new class of numerical equilibria with independently prescribable nonlinear profiles (as an example $p' = -ß_p(0) + p_1 T + p_2 T^2$, $ff' = ß_p(0) - 1 + \gamma_1 T + \gamma_2 T^2$ is used) for which the angularities in all orders of a numerical aspect ratio expansion to arbitrary order are put to zero.

First, we consider equilibria above the ballooning unstable band. With $ß_p(0) = 2$, $S(0) = 3$, $p_1 = 5$, $p_2 = \gamma_2 = 0$, the Class 2 equilibrium is ballooning stable over the whole cross-section and has a ß-value of 25% and $\iota \sim 2$ at the boundary. Fig. 1 shows flux surfaces of this configuration.

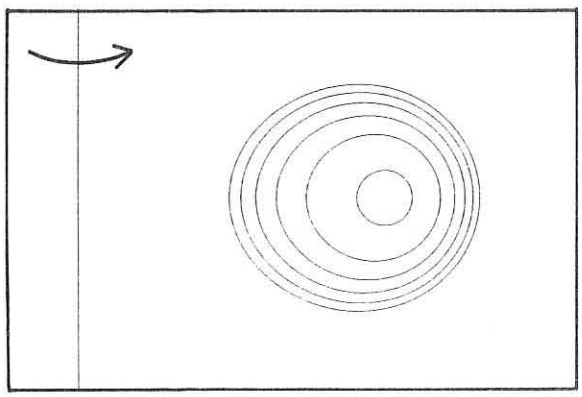

Fig. 1

A similar equilibrium of Class 1, $ß_p(0) = 3.5$, $S(0) = 6$, $p_1 = 9.6875$, was mode analyzed with the help of ERATO [5] with respect to internal modes and found to be unstable to a mode with toroidal mode number $N = 3$. This appears to be the first example of an unstable internal mode in a configuration stable to ballooning modes as obtained from the ballooning instability equation. Thus, we conjecture that high-ß ballooning stable equilibria of this type found above the instability band are unstable to internal modes.

Second, we consider equilibria below the ballooning unstable band. Choosing $ß_p(0)$ and $S(0)$ marginal (i.e. on the lower boundary of the unstable band) an optimization of ß with respect to $ß_p$ of equilibria which are ballooning stable over the whole cross-section was carried out in Class 1. The result, which was obtained with 2 as lower bound on the aspect ratio, shows that $ß_p \approx .4$ is optimal, as illustrated in Fig. 2.

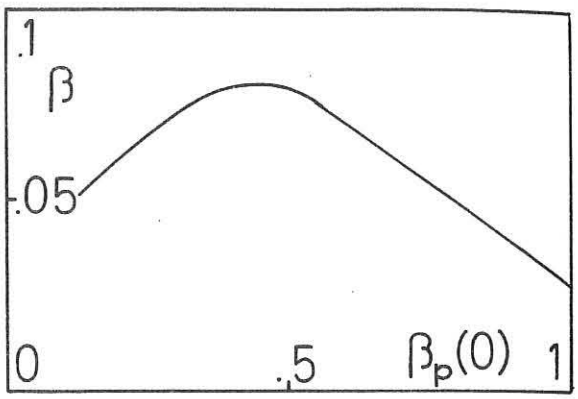

Fig. 2

Flux surfaces of the case $ß_p(0) = .4$ (ß = 8%) are shown in Fig. 3.

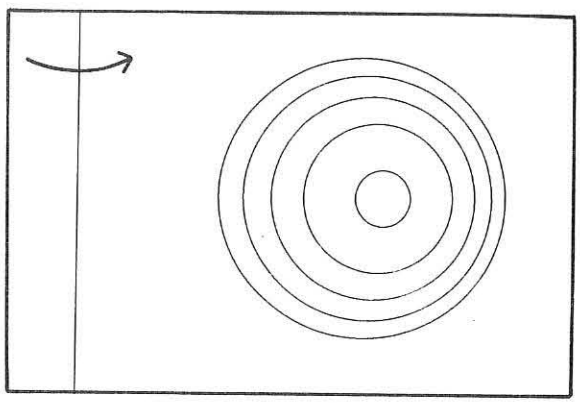

Fig. 3

For this equilibrium, $\iota \sim .8$ at the boundary, so that instability with respect to external modes has to be expected and was indeed verified with ERATO.

We conclude that also below the unstable band the ballooning instability is not limiting the ß-value realistically. In contrast to the situation above the unstable band, here, as far as we know, only the external modes limit the ß-values obtainable. A particular class of external modes, the peeling modes, is investigated in the paper "On the peeling instability" of this conference. Starting from an equilibrium of Class 2 of the above type [$ß_p(0) = .4$, $S(0) = 1.04625$, $p_1 = \gamma_1 = 0$] peeling marginality ($p' = ff' = 0$) is obtained with $p_2 = 10$, $\gamma_2 = 15$ at $T = .2$, where $\iota \sim 1/3$, so that probably no external modes will be found. The ß-value is 3%.

Acknowledgement. Discussions with Drs. R. Gruber and W. Kerner on the use of ERATO are gratefully acknowledged.

References

[1] Dobrott, D., Nelson, D., Green, J., Glasser, A., Chance, M., Frieman, E., Phys. Rev. Lett. 39 943 (1977).

[2] Connor, J., Hastie, R., Taylor, J.B., Phys. Rev. Lett. 40 (1978) 396.

[3] Lortz, D., Nührenberg, J., Nucl. Fusion, to appear

[4] Lortz, D., Nührenberg, J., IAEA-CN-33/A12-2, Vienna (1975) 439.

[5] Berger, D., Bernard, L.C., Gruber, R., Troyon, F., paper C3, 2nd European Conf. on Comp. Phys., Garching (1976).

"This work was performed under the terms of the agreement on association between Max-Planck-Institut für Plasmaphysik and EURATOM".

Ripple Loss of Fast Ions in a Large Tokamak

K. Tani, H. Kishimoto and S. Tamura

Division of Large Tokamak Development, JAERI
Tokai, Ibaraki, Japan

Abstract Ripple loss of fast ions in a large Tokamak is investigated in detail by means of a Monte-Calro simulation code. Coupled processes of trapping into and detrapping from ripple wells are essential in the fast ion ripple loss mechanism.

§1. Introduction Neutral beam injection into a large Tokamak suffers from the surface trapping of the injected beams. A quasi-perpendicular injection permits sufficient beam penetration. However this injection geometry is associated with an increase in the ripple loss of fast ions. Hence detailed studies on ripple loss processes are required.

§2. Model The Monte-Carlo simulation code[1], which was developed for describing fast ion behaviors in an axisymmetric field such as Tokamak, has been extended so as to involve the effects relating to a non-axisymmetric configuration. This code has been used to analyse the ripple loss of fast ions in a large Tokamak. The magnetic field is given by $\vec{B} = \vec{B}_\psi(r,\theta,\psi) + \vec{B}_\theta(r,\theta)$, where B_ψ is the toroidal magnetic field and B_θ the poloidal one. They are represented as followings:

$$B_\psi = B_t(R_0/R)(1+\delta\cos N\psi) \quad , \quad B_\theta = (R_0/R)B_p(r).$$

Here, B_t is the toroidal field on the magnetic axis (R_0), B_p the poloidal field defined by a current profile $j = j_0(1-r^2/a^2)$, N the number of the toroidal coils, δ the amplitude of the toroidal field ripple, respectively. In case of JT-60, $\delta = \delta_0 \cdot \delta_1(r)\cos\theta$ is obtained for $\theta \lesssim \pi/2$[2]; δ_0 is the peak of the ripple field and δ_1 is given by polynomials of r/a ($\delta_1 \sim (r/a)^4$). In the present calculations, charge exchange processes are excluded and the plasma parameters are assumed to be radially uniform with $T_e = T_i = 1$ keV, $n_e = 2\times10^{19}\,m^{-3}$ and $Z_{eff} = 2$ near the plasma periphery. We investigate the ripple loss processes by changing the toroidal field strength B_t under a condition of constant q_a(=3.5). The birth point of fast ions (protons) is set at r/a=0.9 with a pitch angle of 10°, and the energy is 75 keV.

§3. Results and Discussions Typical contours of fast ion drift orbit are shown in Fig. 1(a) and (b) in case of JT-60 (δ_0=0.5%). Two kinds of ripple-associated loss processes are found. These are the ripple-trapped drift loss (Fig. 1(a)) and the banana orbit loss (Fig. 1(b)). The latter comes from the ripple-enhanced banana drift[3], the detrapping from the ripple well and the collisional banana drift.

We first focus our attention to the ripple-trapped drift loss. The energy fraction of fast ions due to this loss process is denoted by G_{rt}. If the detrapping process is excluded artificially in the computations, the ripple-trapped drift loss is increased and given by G'_{rt}. The dependences of G_{rt} and G'_{rt} on B_t are shown in Fig. 2 where δ_0=1%. Therefore the difference between G'_{rt} and G_{rt} results from the detrapping effect of the ripple-trapped ions. In a high B_t region ($B_t \geq 5$T), G_{rt} shows an inverse proportionality to B_t. This relation is defined by the ripple-trapped drift velocity ($v_z = mv_\perp^2/2B_tR$). In a low B_t region ($B_t < 5$T), G_{rt} shows a slight dependence on B_t and it probably arises from the detrapping effect due to the increase of the banana size. When the magnitude of the ripple field δ_0 is changed, G'_{rt} is not influenced significantly but G_{rt} varies according as $G_{rt} \propto \delta_0^2$.

In order to study the detrapping process in more details, we count the detrapping times N_{dtr} and the trapping times N_{tr}. The ratio of N_{dtr} to N_{tr} (solid curve) is given in Fig. 3 as function of B_t. Number of detrapping times has its minimum near $B_t \sim 6$T. This fact is fairly consistent with the B_t dependence of $G'_{rt}-G_{rt}$ in Fig. 2. If the pitch-angle scatterings are excluded artificially for the trapped particles, the ratio of N_{dtr} to N_{tr} varies as shown by the dotted line in Fig. 3. The difference between the solid line and the dotted one indicates the number of detrapping times due to the pitch-angle scattering and it increases in the high B_t region. The detrapping from the ripple well without scattering arises from the spatial inhomogeneity of the ripple well.

The collisional banana orbit loss G_{so} decreases monotonically with an increase of B_t as illustrated in Fig. 2. This result can be explained by the decrease of the banana size with an increased B_t. When a ripple field exists, the banana orbit loss is enhances by the banana drift motion[3] and the detrapping from the ripple well. The banana orbit loss in a ripple field results in the curve denoted by G_{ro} in Fig. 2. The curve of G_{ro} is similar to that of G_{so}. If the detrapping effect is not taken for the ions trapped in the ripple well, the banana orbit loss without detrapping G'_{ro} decreases. The difference between G_{ro} and G'_{ro} corresponds to the detrapping effect. In contrast with the ripple-trapped loss, the ripple-associated banana orbit loss increases when the ripple field becomes small from δ_0=1% to 0.5%.

§4. Conclusions

1. Ripple-associated loss particles can be categolized in two groupes; the ripple-trapped loss particles and the ripple enhanced banana orbit loss particles
2. The ripple-trapped loss is significantly influenced by the detrapping process from the ripple well and decreases with the ripple field strength.
3. The banana orbit loss is strongly enhanced by the ripple-associated banana drift motion as well as the detrapping of the ripple trapped particles.

Acknowledgements The authers thank for the continuous encouragement of Drs. S. Mori, Y. Iso and M. Yoshikawa. Valuable discussion with Drs. M. Tanaka, M. Azumi, T. Tuda and T. Takizuka is also acknowledged.

References

1. K. Tani, et al., Proc. Joint Varenna-Grenoble International Symposium on Heating in toroidal Plasma, vol. 1 (1978) 31.
2. T. Nishio, et al., JAERI-M 7846 (1978) (presented in Japanese)
3. J. N. Davidson, Nuclear Fusion 16 (1976) 731.

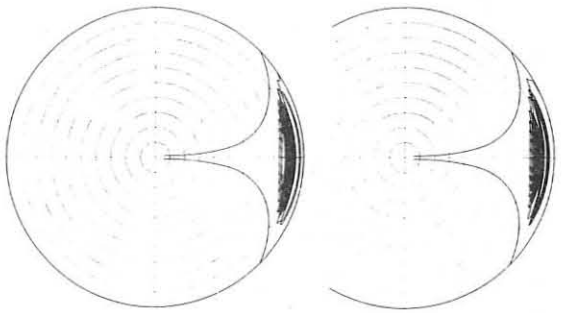

(a) ripple-trapped loss (b) ripple-associated banana orbit loss

Fig.1 Contours of fast ion orbit in case of δ_0=0.5%.

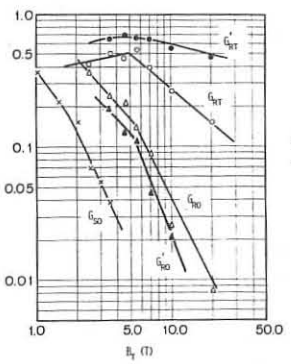

Fig.2 Fractional energy of ripple-associated loss particles as function of toroidal field strength in case of δ_0=1%.

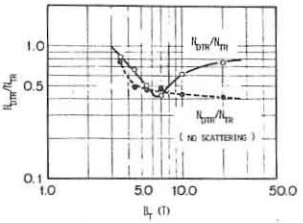

Fig.3 Ratio of detrapping times to trapping times in case of δ_0=1%.

EP19

Numerical Study of the Internal Kink Mode in Tokamaks

W. Kerner, Max-Planck-Institut für Plasmaphysik, D-8046 Garching, FRG
EURATOM - Association
R. Gruber, F. Troyon, CRPP-EPFL, Lausanne, Switzerland

Abstract

A numerical study of the internal kink mode is performed for a family of tokamak equilibria with circular cross-section and parabolic current profile. If the β_p values are sufficiently small the internal kink mode becomes stable.

Introduction

The internal kink mode is examined in the context of ideal MHD theory using the ERATO /1/ code. Growth rates and eigenfunctions of the normal modes are computed by extremizing the Lagrangian of the system connected with linearized perturbations. The "internal kink modes" are defined here as modes with a toroidal wave number n=1 leaving the plasma boundary unperturbed. Besides the relevance to tokamak experiments, there is a challenging aspect in the numerical complexity of this problem. Since the growth rates of these modes are very small, a high resolution of the numerical scheme is required. This numerical study is complementary to analytical results /2-5/. It is well known that these analytical calculations differ strongly in the results, especially concerning the β_p stabilization of the internal kink mode. In our opinion it seems worthwhile to resolve this controversy by providing the numerically obtained solution to the problem.

Equilibrium

Because of the high accuracy required in the numerical calculation a family of very accurate equilibria (Lortz and Nührenberg /6/) is used. These equilibria are characterized by the pressure p and the poloidal current profile $T = rB_\phi$:

$$\frac{dp}{d\psi} = -p_0\,(1 - \psi/\psi_L), \qquad \frac{T\,dT}{d\psi} = \gamma_0\,(1 - \psi/\psi_L), \tag{1}$$

with p_0 and γ_0 as constants.

The toroidal current density vanishes at the plasma boundary ($\psi = \psi_L$). The external kink mode is then stable for q on axis greater or about unity ($q_0 \gtrsim 1.0$). The flux function ψ is computed with a separation ansatz

$$\psi(r,z) = v(r) + w(r)\cos kz \tag{2}$$

leading to Coulomb wave functions. This solution can be computed at any grid point, which enables us to perform the mapping from Cartesian to flux coordinates accurately.

The equilibria considered have circular flux surfaces near the magnetic axis. We cannot prescribe the shape of the plasma boundary, but we have to adjust the parameters to get the desired shape. The parameters have been chosen such that for a large aspect ratio these equilibria have an almost circular cross-section and a parabolic current profile.

In the following study the profiles (eq. (1)) are kept fixed, and the cross-section is (almost) circular. The following quantities are varied:

q_0 q on axis,
β_p ($= 8\pi \int p\,df / I^2$) beta poloidal,
ϵ^{-1} aspect ratio

Results

The aspect ratio is chosen large $\epsilon^{-1} = 8.4$ in order to allow a detailed comparison with the analytical results.

A satisfactory resolution of the eigenfunctions is obtained by using a non-equidistant s mesh ($s \propto \sqrt{\psi}$) with a strong accumulation around the q = 1.0 and the q = 2.0 surface, if the latter is located inside the plasma.

For $\epsilon^{-1} = 8.4$ and $\beta_p = 1.0$ the eigenvalues as a function of q_0 (the value of the safety factor on axis) have two marginal points, an upper and a lower one:

$q_u = 0.975 < 1.0$,
$q_l = 0.61$ with $q_s = 1.5$ (q_s = q on surface).

The internal kink mode has inside the q = 1.0 surface in terms of Fourier components a dominant $\ell = 1$ component, whereas at the q = 2.0 surface it is a pure $\ell = 2$ mode. The normal component of the displacement vector is large inside the q = 1.0 surface with a steep gradient at the q = 1.0 surface.

The fact that the lower value corresponds exactly to $q_s = 1.5$ shows the stabilizing effect of the $\ell = 2$ Fourier component on the eigenfunction. Note that the upper marginal point is smaller than unity. This interesting result is to be checked against the analytical results. We perform a detailed comparison with Bussac et al. /2/. In their paper the following definition of β_p was used:

$$\beta_p^B(r_0) = 2\int_0^{r_0} (r/r_0)^2\,(-dp/dr)\,dr \Big/ B_\theta^2(r_0) \approx \beta_p\left(1 + 0.33\,(r_0/a)^2\right)/4 \tag{3}$$

which leads to the approximate values for our class of equilibria. The radius of the q = 1.0 surface is denoted by r_0 and the plasma radius by a. In Fig. 1 the stability limit of Ref. /2/ for a parabolic current profile is plotted. If the value of β_p^B for an equilibrium is smaller than $\beta_{cr.}^{Bussac}$, there is stability, otherwise instability. In this diagram the crosses denote the β_p^B values for the parameters used in the numerical stability calculation. For $\beta_p = 1.0$ there is according to /2/ stability for $q_0 = 1.0$, which means $r_0 = 0$.

There is very good agreement in the marginal point given by the analytical and numerical analysis with $q_u = 0.975$. The marginal points obtained numerically are indicated by the dots in the figure. The lower stability limit q_l is not obtained by /2/. This is expressed by the " ? " on the extrapolated $\beta_{cr.}^{Bussac}$ values. For $\beta_p = 1.2$ marginal stability is given by $q_0 = 1.0$ in agreement with /2/. If we further increase the β_p value the upper limit remains $q_u = 1.0$, but the growth rates of the unstable modes increase and q_l changes.

In order to check the β_p stabilization we keep q on axis fixed -$q_0 = 0.8$ and 0.9 - and vary β_p. The β_p values for marginal stability are

$\beta_p^{cr.} = 0.63$, for $q_0 = 0.8$,
$\beta_p^{cr.} = 0.70$, for $q_0 = 0.9$.

These values agree perfectly with those of Bussac et al.. For β_p values less than $\beta_p^{cr.}$ (including $\beta_p \to 0$) we find the internal kink mode to be stable - in contrast to the results of Ref. /4/. Summarizing the large aspect ratio calculations, we are able to confirm the entire curve for marginal stability of Ref. /2/.

Finally, we change the aspect ratio from 8.4 to 2.5. If the q = 1.0 surface is very close to the axis the stability limit is unchanged. The $\beta_p^{cr.}$ values for $q_0 = 0.8$ and 0.9 are shifted to somewhat smaller values compared with the large aspect ratio cases.

References

/1/ Berger, D., Bernard, L.C., Gruber, R. and Troyon, F., Plasma Physics and Contr. Fusion Research (Proc. 6th Int. Conf. Berchtesgaden, 1976)2, Vienna (1977), 411

/2/ Bussac, M.N., Pellat, R., Edery, D., Soule, J.L., Physical Rev. Lett. 35 (1975), 1638

/3/ Pao, Y.-P., Physics of Fluids 19 (1976), 1796

/4/ Galvao, R.M.O., Sakanaka, P.H., Shigueoka, H., Phys.Rev.Lett. 41 (1978), 870

/5/ Zacharov, Fiz, Plazmy 4 (1978), 898

/6/ Lortz, P., Nührenberg, J.
Plasma Physics and Contr. Fusion Research (Proc. 5th Int. Conf. Tokyo, 1974), 1, Vienna (1975), 439

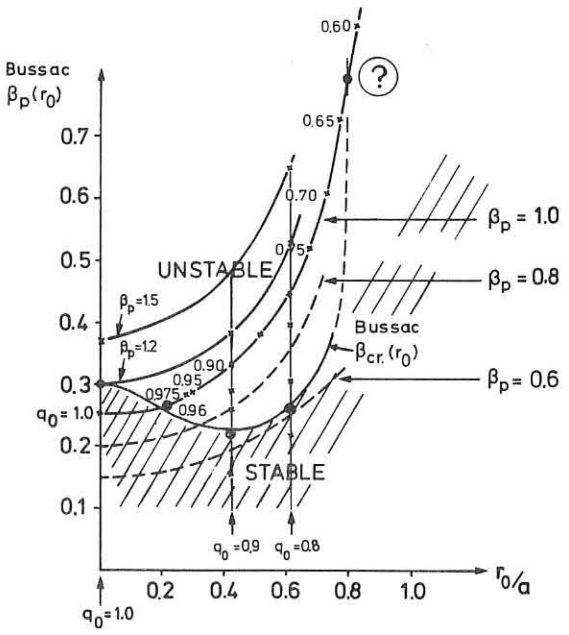

Fig.1: Comparison with analytical results
r_0: radius of q = 1.0 surface

ELECTRIC FIELD AND SLOWING-DOWN EFFECTS ON RELATIVISTIC CHARGED PARTICLE MOTION IN TOKAMAKS

H.P. Zehrfeld, G. Fußmann, B.J. Green*
Max-Planck-Institut für Plasmaphysik, EURATOM-IPP Association, D-8046 Garching, Federal Republic of Germany
* At present JET Joint Undertaking, Abingdon, Oxon., U.K.

Abstract: We consider relativistic guiding center motion of charged particles in magnetic fields consistent with toroidal tokamak equilibrium. For peaked current distributions and sufficiently high particle energies the occurrence of drift separatrices is observed. They are calculated and their relevance to charged particle confinement and injection in tokamaks is considered.

Toroidal Equilibrium and Relativistic Drift Equations: Analytical expressions for magnetic fields consistent with toroidal tokamak equilibrium in terms of current and pressure distributions are available from the customary approach involving the basic differential equation for the poloidal magnetic flux in a large aspect-ratio approximation which gives results correct to first order in inverse aspect-ratio /1/. The magnetic surfaces are represented by non-concentric tori of circular cross-section and are nested in an outermost one of small radius a and large radius R_o. For pressure and toroidal current we assume the following class of distributions

$$p = p_o(1-\rho^2)^n \quad , \quad I = I_T(1-(1-\rho^2)^{m+1}) \tag{1}$$

where $\rho = r/a$ is the normalized poloidal cross-sectional radius of a magnetic surface, p_o the plasma pressure on the magnetic axis and I_T the total toroidal plasma current. n and m are arbitrary positive integer exponents describing the peakedness of the distributions. The resulting equilibrium is characterized by the poloidal magnetic flux

$$G = \frac{1}{2}\mu_o R_o I_T \sum_{k=1}^{m+1} \frac{1}{k}(1-(1-\rho^2)^k) \tag{2}$$

and a displacement function $\Delta(\rho)$ describing the outward shift of the magnetic surfaces. Besides on ρ, Δ depends on the parameters n and m in (1) and on the poloidal beta value $\beta_p = 8\pi^2 \cdot a^2 p_o/(n+1)\mu_o I_T^2$ (for more details see /2/).

Closer investigation of the guiding center equations reveals that, for the considered equilibria, the poloidal trace of a guiding center orbit is given by a solution of the equations

$$\frac{d\mathbf{x}}{dt} = \frac{e\,\Delta^*(\gamma,\alpha)}{\gamma m_o q A} R\, \nabla\xi \times \nabla G^* \tag{3}$$

$$G^* \equiv G - \mu_o I_T R A\, \Delta^*(\gamma,\alpha), \quad \Delta^*(\gamma,\alpha) \equiv -\frac{(\gamma^2-1)^{1/2}}{2A}\frac{I_A}{I_T}\left\{1-\frac{\gamma_s^2-1}{\gamma^2-1}\sin^2\alpha\right\}^{1/2} \tag{4}$$

Here $\mathbf{x}$ is the guiding center position, e is the charge and m_o the rest mass of a particle, q is the safety factor at r=a, ξ is the angle about the axis of symmetry divided by 2π, R the distance from this axis and A the aspect-ratio R_o/a. Further, $I_A = 4\pi m_o c/\mu_o e$ is the Alfven current and α is the initial pitch angle. γ is the relativistic parameter, which in terms of the particle kinetic energy E_k is given by $\gamma = 1+E_k/m_o c^2$. We wish to consider solutions of (3) for two particular problems, where we specify γ (or, equivalently, E_k) as functions of time.

Electric Field and Current-Flattening Effects on Runaway Motion: The toroidal electric field essential to tokamak operation causes γ to increase according to

$$\frac{d\gamma}{dt} = -\frac{eU}{m_o c^2}\frac{I_T}{I_A}\frac{A\,\Delta^*}{\pi\gamma}\frac{c}{R} \tag{5}$$

where U is the loop voltage. Taking into account the smallness of $eU/m_o c^2$ the acceleration process is accompanied by only a quasistatic increase of the particle kinetic energy. In that case and for

$$\Delta^*(\gamma,\alpha) < \frac{1-(1-\lambda^2)^{m+1}}{\lambda(1+\Delta'(\lambda))} \equiv \Delta_s^*(\lambda) \tag{6}$$

the poloidal locus of charged particle motion is found to be an envelope of closed drift orbits at constant kinetic energy, whose cross-sectional area is constant. Fig.1 shows the geometry for magnetic and for drift surfaces through a given point $(R,z)=(R_o+a.(\lambda+\Delta(\lambda)),0)$. Figs.2 and 3 show results for typical PULSATOR parameters. Fig.2 shows the drift surface migration due to the toroidal electric field, fig.3 illustrates the effect of a complete current-flattening resulting in an additional runaway outward drift at constant energy over the radial distance $\Delta\lambda$.

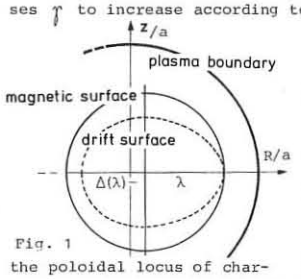

Fig. 1

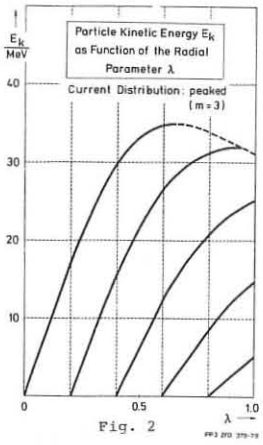

Fig. 2

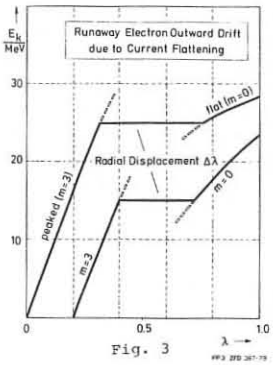

Fig. 3

The Problem of Particle Injection and of Slowing-Down: For non-flat current distributions there is a finite region inside of the outermost magnetic surface with radially decreasing poloidal magnetic field. In this region, for energies $E_k = m_o(\gamma-1)c^2$, such that $\Delta^*(\gamma,\alpha) = \Delta_s^*(\lambda)$ applies, a stagnation point appears at $(R,z)=(R_o+a.(\lambda+\Delta(\lambda)),0)$. Fig.4 shows drift surfaces in the neighbourhood of such a point in ASDEX (E_k=2 MeV, m=3, 12 orbital points correspond to one toroidal turn). Their geometry with trajectories leading into the plasma region suggests tangential injection for the purpose of heating. Depending on the stagnation point position λ the required energies can be obtained from the condition $\Delta^*(1+E_k/m_o c^2,\alpha) = \Delta_s^*(\lambda)$. Neglecting plasma displacement effects this simplifies to $E_k/\mathrm{MeV} = \Delta_s^* . A . I_T/16.7$ for relativistic electrons and to $E_k/\mathrm{eV} = 1.93.(A.\Delta_s^*.I_T.Z)^2/M$ for nonrelativistic ions (Z is the ion charge and M the mass number, I_T in kA), and $\Delta_s^* = B_p(R_o+a.\lambda,0)/B_p(R_o+a,0)$. For ASDEX, for example, we find for electrons 74-103 MeV, for deuterons 1.5-2.9 MeV (I_T= 300 kA). If we, in the case of ions, assume energy losses due to Coulomb collisions we can achieve deuteron trapping as illustrated in fig.5, however, only under the assumption of an unrealistically high density ($n_e = 10^{16}\mathrm{cm}^{-3}$). The corresponding slowing-down law is /3/

$$\frac{d\gamma}{dt} = -\frac{2(\gamma-1)}{t_s}\left\{1+\left(\frac{\gamma_c-1}{\gamma-1}\right)^{3/2}\right\} \tag{7}$$

(with the slowing-down time $t_s = t_s(T_e,n_e)$ and some critical γ-value γ_c). The introduction of anomalous energy loss processes would make the slowing-down more efficient. Here particle-wave interaction and beam-induced return currents come into question. For relativistic electrons the importance of these effects is known /4/, for high-energy ions a theoretical treatment can be found in /5/.

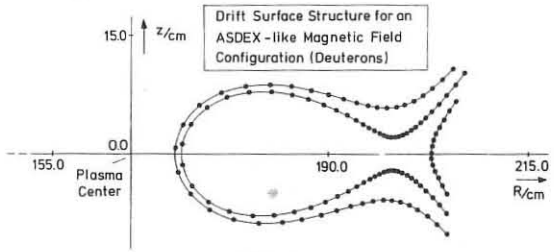

Fig. 4

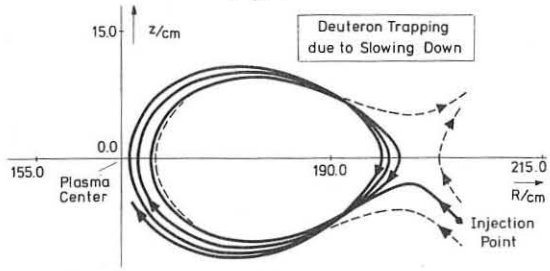

Fig. 5

1. V.D.Shafranov, "Reviews of Plasma Physics", Vol.2, N.Y. 1966
2. H.P.Zehrfeld, G.Fußmann, B.J.Green, Report IPP III/49, 1979
3. T.H.Stix, Plasma Physics 14 (1971) 367
4. J.Benford et al., Int.Conf.Pl.Phys.Contr.Th.Fus., Berchtesgaden (1976), IAEA-CN-35/G2-3
5. R.N.Sudan, Phys.Rev.Let. 37, 24(1976), 1613

EP21

CONTROL OF THE RADIAL POSITION OF A TOKAMAK PLASMA IN THE CURRENT RISE PHASE

B.J. Green, M.R. Perrone*, P. Noll, P. Dokopoulos+
JET Joint Undertaking, Abingdon, Oxon.
* Universita degli Studi di Lecce, Italy. + University of Salonika, Greece.

Abstract

It has been experimentally demonstrated that tokamak performance is much improved when the position of the plasma column is accurately controlled. In this paper we model the control of the radial position of a tokamak plasma in the current-rise phase, including many of the features of a real tokamak system, e.g. current-carrying elements which "screen" the plasma from the control field coils. Two models for this problem are presented and the results of calculation summarised.

Plasma Radial Position Control

Control of the radial plasma position is carried out by externally-applied vertical magnetic fields. The plasma displacement from a reference equilibrium position increases with the value of the induced plasma current so that a generalpositioning procedure is to regulate the vertical fields in step with the plasma current. However, in the early phase of a tokamak discharge when the plasma current is building up (current rise phase) stray fields (in particular those due to currents induced in the vacuum vessel) may be larger than the control field based on the value of the plasma current. Such a "stray" effect makes plasma radial position control in the current rise particularly difficult.

The actual problem in a real tokamak system involves not only a vacuum vessel but also toroidal field coils and their associated mechanical structure as well as the poloidal field coils themselves. All these elements can carry current and, together with the plasma, are electro-magnetically coupled, and the induced currents give rise to perturbing fields which affect the plasma position.

To achieve reasonable control of the plasma position, a detection circuit is used to monitor the position (and speed) of the plasma column. These signals can be amplified and fed-back to modify the control field appropriately.

Basic Equations

The vertical field $B_\perp$ required for the equilibrium of a large aspect-ratio, circular cross-section, toroidal plasma column carrying current I_p, at major radius R_0 and minor radius a is $B_\perp = (\mu_0 I_p/4\pi R_0)(\ln\frac{8R_0}{a} + \beta_p + \frac{\ell_i}{2} - \frac{3}{2})$ where β_p is the poloidal beta (ratio of mean plasma pressure to magnetic pressure of the poloidal field) and ℓ_i is related to the plasma internal inductance (i.e. plasma current distribution).

The actual vertical field at the plasma position due to currents (I_j) in the various circuit elements can be written as, $B_V(R) = \sum_j b_j I_j$, where $b_j(R)$ are the vertical fields at the plasma due to unit currents in each element.

The difference between B_V and $B_\perp$ provides the driving force on the plasma column. The plasma mass is so small that the equation of motion reduces to an "equilibrium" condition $B_V(R_0+x) = B_\perp(R_0+x)$ which for small displacements x from the reference position R_0 gives $x/R_0 = (B_\perp(R_0) - B_V(R_0))/(\frac{\partial B_V}{\partial R} - \frac{\partial B_\perp}{\partial R})_{R_0}$.

Now the electrodynamic equations governing the time evolution of currents (I_j) including the plasma current can be put in the form

$\dot{\phi}_j + \sum_i I_i R_{ij} = V_j$ (1), where ϕ_j is the effective flux of vertical magnetic field linking current-carrying elements so that $\phi_j = \sum_i L_{ji} I_i$. The fluxes are defined in such a way that the inductance coefficients L_{ji} satisfy $L_{ji} = L_{ij}$. The rate of change of flux linkage is due not only to the rate of change of currents I_j , but also to the radial shift velocity of the plasma ($\dot{x}$) and the radial variation of the inductances e.g. $\dot{L}_{jk} = \frac{dL_{jk}}{dt} = \dot{x}\frac{\partial L_{jk}}{\partial R}$.

The resistances R_{ij} are (i) the self-resistances R_{ii} which are the toroidal electrical resistances of elements carrying net toroidal current I_i ; and (ii) the cross-resistances R_{ij} $(i \neq j)$ which describe the effect that differential currents (zero net toroidal value) in a current-carrying element can be driven not only by the differential flux change over that element but also by the net flux change. This is to be considered for the all-metal vacuum vessel which carries a current distribution with both homogeneous and inhomogeneous parts.

The V_j are applied voltage terms and include the voltage applied to the tokamak primary windings and the voltage applied to the poloidal field coils (both equilibrium and feedback control).

The problem then involves the solution of the equation system (1) for the time evolution of each of the currents in the circuit elements. The system of equations isclosed as the voltages V_j are specified, (including any feed-back voltages), the resistances and inductances (and the radial derivatives) are specified, and the x and $\dot{x}$ terms can be expressed in terms of the dependant variables (I_j) using the $b_j(R)$ and their radial derivatives which are specified.

Models

The two different models which we have considered can be characterised as follows:

(A) The current-carrying elements of the system are replaced by equivalent large aspect-ratio toroidal shells (see fig. 1.) with particular surface current distributions $J + \tilde{J}\cos\theta$. This allows the b_j, L_{ji} and R_{ji} to be calculated analytically [1] in terms of the system geometry.

(B) The discrete nature of the current-carrying elements is retained (see fig. 2) and it is possible to include the presence of an iron core with a specified permeability distribution. For any particular (finite aspect-ratio) plasma equilibrium, 2-dimensional magnetostatic calculations evaluate the $b_j(R)$ (and their derivatives) (see fig. 3.) as well as the $L_{ji}(R)$ and their derivatives.

The circuit connections for the two models must be specified and determine the detailed form of (1). For both models, the numbers of turns of the poloidal field coils are taken into account as well as (i) a detection circuit, which from measurements of the plasma speed and position provides an electrical signal S and (ii) a feedback circuit which amplifies the signal S to provide a voltage V_A . These circuits are described by the equations:

$$\dot{S} + S/\tau_S = (G_1 x + G_2 \dot{x})/\tau_S \quad (2) \qquad \dot{V}_A + V_A/\tau_A = G_A S/\tau_A \quad (3)$$

where τ_S and τ_A are circuit time constants and G_1, G_2 and G_A are "gain" factors.

The problem is an initial-value one and the starting procedure adopted for both models is as follows: the circuit equations (without the plasma-coupling effects) are allowed to evolve until (time $t = t_B$) the vertical field at the reference position is that for which a plasma column carrying 10 kA current is in equilibrium at $x = 0$ i.e. $B_V(R_0, t_B) = B_\perp(I_p = 10\,kA, x = 0)$

For times $t \geq t_B$ the complete equation set is stepped forward in time until the completion of the current rise phase.

Results

The above models were applied to JET [2] and various studies were carried out:

(i) the variation of the time to breakdown t_B with poloidal field coils turns ratios and initial coil currents.

(ii) the achievement of adequate radial position control for given detection and amplification circuit time constants by the adjustment of the gain factors.

(iii) the sensitivity of control results to the model of plasma resistance.

Typical behaviour for the plasma column displacement is shown in Figs 4 and 5. The gas breakdown condition and plasma resistance model do influence the details of the position control problem, nevertheless appropriate control with moderate feedback power can be obtained over a wide range of operating conditions (poloidal field coil turns ratios and initial currents). For adequate control, both spatial ($\propto x$) and velocity ($\propto \dot{x}$) feedback were found to be necessary. The finite time constants for the detection and amplifier circuits did not prevent adequate control from being obtained. Both models exhibit similar qualitative behaviour, but because model B is more realistic (in that it allows for more complicated current distributions in circuit elements, and is more directly comprehensible in terms of the real ciruit lay-out), it is being extended to describe the plasma position control situation in the current flat top in the presence of a significant increase in plasma pressure (due to a non-ohmic heating method).

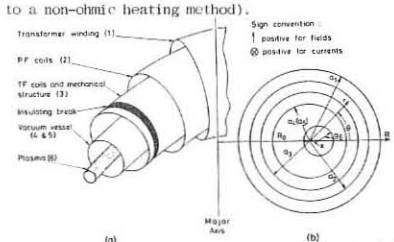

Fig.1 (a) The different current-carrying elements of Model A
(b) Model geometry with sign convention

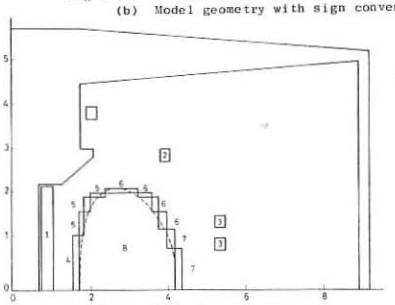

Fig.2 Model B of the iron core, vacuum vessel and poloidal field coils

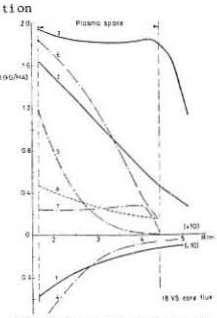

Fig.3 Vertical fields at R=0 for 1MA/turn in each circuit element

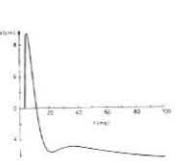

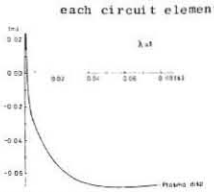

Time evolution of plasma column displacement

Fig.4 Model A

Fig.5 Model B

References

[1] B.J. Green, M.R. Perrone, P. Noll, submitted for publication.

[2] The JET Project - Design Proposal ,Commission of the European Communities Report EUR 5516e.

A STABLE ROUTE TO THE HIGH β_p REGIME

A Sykes, M F Turner
Culham Laboratory, Abingdon, Oxon, OX14 3DB, UK
(Euratom/UKAEA Fusion Association)

Abstract

Recent computational work has confirmed the existence of a second, high beta-poloidal, regime of stability to high-n ballooning modes. Here we examine the accessibility of this high β_p regime and show that it may be possible to reach it experimentally. Examples of TOSCA and JET equilibria are given and the $\bar{\beta}$ values obtainable are shown to be significantly higher than the 'optimised' values previously obtained particularly for high current operation.

INTRODUCTION

It has recently been found[1] that, for a certain family of equilibria, as β_p is raised (keeping the q-profile fixed in FCT fashion) the equilibria become high-n unstable as usual as $\varepsilon\beta_p \sim \frac{1}{2}$, but become stable again if β_p is increased sufficiently so that $\varepsilon\beta_p \gtrsim \frac{3}{2}$. Calculations of the stability of a model tokamak equilibrium with circular surfaces and no variation of the poloidal field on the surface (first considered in Ref. 2) indicate the existence of such a second stability region in a $s = \frac{rq'}{q}$ and $\alpha = \frac{2R}{B^2} p'q^2$ diagram (Fig.1), and the results of Ref.1 indicate that it may be a property of more realistic equilibria.

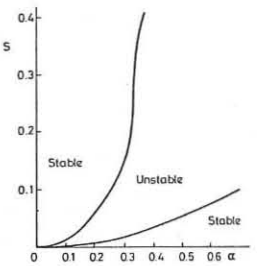

Fig.1

To investigate this region we use the family of equilibria described in[3]. An advantage of this family is that for a given fixed total current, β_p and q_o can be varied independently by a suitable choice of the parameters; and it has been shown[3,4] that low-n internal modes can be stabilised even at high β_p by re-arrangement of the current profile (conveniently characterised by the value of q_o). In this paper we define

$\bar{\beta} = 2\int p d\tau / \int B^2 d\tau$; $\beta_p = 2\int p d\tau / \int B_o^2 d\tau$; q_o = safety factor on axis; q_a = safety factor at plasma edge.

THE HIGH β_p STABLE REGIME

There are already indications[5,6] that high n modes can be partially stabilised by using the techniques that stabilise low n modes. Here we undertake a more systematic study, considering first a 5 : 1 aspect ratio device of circular section.

Fixing the total current to give $q_a \sim 3$, we vary β_p from 0.5 to 8.0. At each value of β_p, q_o is varied from 0.5 to 2, and for each equilibrium the high-n ballooning mode equation[2] is solved on each of a set of equi-spaced flux surfaces. (Note that raising q_o in this fashion is not a simple scaling: current is redistributed from the magnetic axis region, tending to produce hollow profiles).

In fact we find for this configuration that, provided the basic pressure profile is not too wide, high-n stability is obtained for each β_p if q_o exceeds some critical value, shown in Fig.2. From Fig.2 we can see that if a fixed q-profile is considered - with $q_o = 1.1$ for example - then the usual stable region exists if $\beta_p \lesssim 1$, followed by an unstable region if $1 < \beta_p < 6$, and a second region of stability if $\beta_p > 6$. This is similar to the result found in (1), and is analogous to moving horizontally in Fig.1.

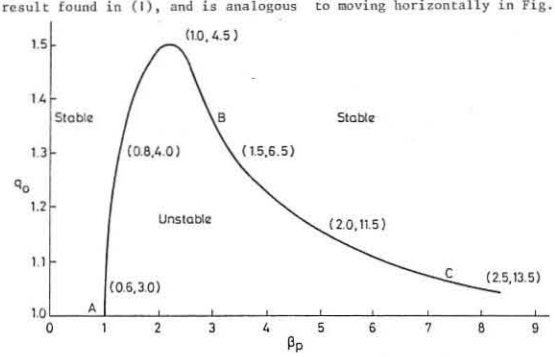

Fig.2 Critical q_o for stability vs β_p number pairs are $(\bar{\beta}\%, \beta(o)\%)$.

The relation between $\bar{\beta}$, $\beta(o)$ and β_p is given by the number pairs $(\bar{\beta}, \beta(o))$ alongside the curve of Fig. 2. The low β_p limit of stability (point A) has $\bar{\beta} \sim 0.6\%$; we see that $\bar{\beta}$ can increase to 2.5% at $\beta_p \sim 7$.

A STABLE ROUTE TO THE SECOND REGION

Usually, as in the above example, the second (high β_p) region of stability is reached after a period of instability. However Fig. 2 suggests that if, experimentally, large heating power could be applied to a discharge with a $q_o > 1.5$ hollow current profile (during the current rise?) to give high β_p, the current can then increase near the axis provided that q_o exceeds some critical value (~ 1.1 for the configuration of Fig. 2; possibly < 1 for other equilibria).

This then would provide a possible stable route. Whether the instability caused by a deviation from the route acts to restore stability, or grows to destroy the confinement, remains to be seen.

Fig. 3 may provide insight into the transition from the restrictive low β_p region to the high β_p regime. The full curves show the s,α values of each flux surface for equilibria A, B, C of Fig. 2. The shaded region is the unstable region of Fig. 1, and is relevant for unshifted circular flux surfaces. It is seen that the (stable) points of equilibrium A lie just to the left of this shaded region.

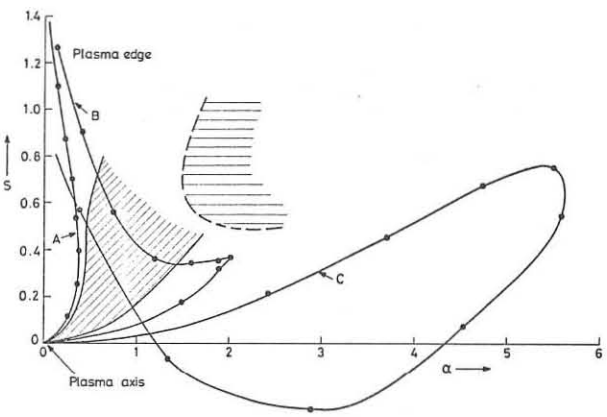

Fig. 3: s, α values on flux surfaces for stable equilibria A, B, C of Fig. 2.

Considering the extreme high-β_p case C, the outer flux surfaces appear to be in the shaded region but are in fact stable, as they have large displacement and ellipticity, and these effects are known by study of the model equation (2) to shift the unstable region in the direction indicated by the dashed region. The inner flux surfaces of C have a smaller displacement, and approach the origin underneath the original shaded area.

HIGH β EQUILIBRIA IN JET AND TOSCA

We find that at a current of 4.7 MA ($q_a \sim 6$), JET is stable to high n modes at $\bar{\beta} = 4.5\%$, $\beta_p = 3$: this value is slightly higher than the 'optimised' value obtained in [5]. However at high current (9.4 MA, $q_a \sim 3$) significant increases are possible: although the low β_p limit has $\bar{\beta} = 2\%$ at $\beta_p = 0.3$ (lower than the optimised result given in [5]), the high β_p regime allows $\bar{\beta} = 12\%$ at $\beta_p = 3$.

Similar results are found for TOSCA[7], here taken as having a plasma of 4 : 1 aspect ratio and circular section. At large current ($q_a = 1.4$), the low β_p limit has $\bar{\beta} \sim 1\%$ at $\beta_p \sim 0.3$ and there are indications that the experiment may be near this lower limit. However the high-β_p regime allows $\bar{\beta} = 5\%$ at $\beta_p = 2$.

CONCLUSIONS

We have demonstrated a possible route to the high β_p regime of ideal, high-n ballooning mode stability. The corresponding $\bar{\beta}$ values attained are significantly higher than previous estimates and are very similar to the values predicted by the low-n internal mode stability condition.

ACKNOWLEDGEMENTS

We thank J. Connor, R.J. Hastie, D.C. Robinson and J.B. Taylor for help and encouragement.

REFERENCES

(1) H.R. Strauss et al., to appear in Phys. Rev. Lett.
(2) J.W. Connor, R.J. Hastie, J.B. Taylor, Phys. Rev. Lett. 40, (1978) 396.
(3) A. Sykes, J.A. Wesson, S.J. Cox, Phys. Rev. Lett. 39, 12 (1977) 757.
(4) R. Gruber et al., Innsbruck Conference IAEA-CN-37/K-2.
(5) A. Sykes, M.F. Turner, P.J. Fielding, F.A. Haas, Innsbruck Conference, IAEA-CN-37/K-5.
(6) S. Rousset, R. Gruber, F. Troyon, to appear in ZAMP.
(7) R. Birch et al., 9th European Conference on Controlled Fusion and Plasma Physics.

EP23

PELLET REFUELLING OF A DIVERTOR TOKAMAK

L.W. Jørgensen and P.E. Stott*

Culham Laboratory, Abingdon, Oxon, OX14 3DB, UK
(Euratom/UKAEA Fusion Association)

INTRODUCTION. Experiments with the DITE Bundle Divertor have demonstrated the need for a new means of refuelling a diverted discharge in order to replace the particles exhausted by the divertor and thus maintain a constant density[1]. Refuelling with gas puffed into the torus has been shown to be inefficient because a large fraction of the gas is ionised in the divertor scrape-off layer and immediately exhausted leaving only a small fraction to penetrate and refuel the centre of the discharge. Increasing the input of gas to counteract this loss results in increased recycling between the plasma boundary and the wall which in turn results in increased desorption of impurities.

Injection of solid hydrogen pellets has been proposed as a method of refuelling a future fusion reactor, and the technique has been demonstrated recently in an experimental tokamak[2]. A pellet with sufficiently high velocity will penetrate the scrape-off layer with only a small loss of material and will refuel the centre of the discharge. A pellet acceleration device based on a light gas gun system is being constructed for DITE. Initially, the plan is just to accelerate a single cylindrical pellet with a diameter and length of about 400 μm to a velocity of about 400 m/s with the purpose of testing ablation models and studying the effect of injecting fresh fuel across the divertor scrape-off layer. SI-units are used throughout this paper except when stated otherwise. Temperatures are given in eV.

PELLET ABLATION RATE. Many different models of pellet ablation in a hot plasma have been presented[3]. The most recent models assume that a neutral cloud of gas is established around the pellet[4,5] and the pellet ablation rate is determined by the maintenance of cloud thickness equal to the penetration depth of the plasma electrons. Comparing the different models for pellet-plasma interaction with the few available experimental results of pellet injection show[2,3,6,7] that in present day tokamaks the pellet-plasma interaction can be explained by this neutral cloud model.

The results of the different neutral cloud models have been compared[7] and it is concluded that the ablation rates which they predict have almost identical scaling. Hence we will use the following convenient "average" pellet ablation rate for a spherical pellet

$$\dot{r}_p = - f\, r_p^{-2/3}\, n_e^{1/3}\, T_e^{5/3} \qquad \ldots (1)$$

where r_p is the instant pellet radius; n_e and T_e are the plasma electron density and temperature; f is a material constant; $f_{H_2} = 8 \times 10^{-14}$; $f_{D_2} = 5.6 \times 10^{-14}$.

We will assume linear profiles for the plasma density $n_e = n_{eo}(1 - r/a)$ and temperature $T_e = T_{eo}(1 - r/a)$ where a is the minor radius of the torus. Inserting these profiles in Eq.(1) using $v_p t = a - r$, where v_p is the pellet velocity, gives

$$r_p = \left(r_{po}^{5/3} - \frac{5}{9} f \frac{a\, n_{eo}^{1/3}\, T_{eo}^{5/3}}{v_p} (1 - r/a)^3\right)^{3/5} \qquad \ldots (2)$$

and a pellet penetration depth of

$$d = \left(\frac{9}{5f}\right)^{1/3} a^{2/3}\, n_{eo}^{-1/9}\, T_{eo}^{-5/9}\, r_{po}^{5/9}\, v_p^{1/3} \qquad \ldots (3)$$

where r_{po} is the initial radius of the pellet.

For non-perpendicular (to the toroidal magnetic field) pellet injection the perpendicular component of the velocity vector is used in Eqs.(2) and (3). In order to derive an ablation equation as (1) it is necessary to assume[4,5] that the number of pellet atoms, N_p, is small compared to the total number of plasma ions, N, otherwise the presence of the pellet in the plasma will significantly change the plasma density and temperature, which in turn will change the ablation rate of the pellet.

Figure 1 shows the pellet penetration depth versus the pellet velocity for different plasma parameters. We have shown also the value of the ratio $N_p/N = 2n_s r_{po}^3/\pi a^2 R\, n_{eo}$, where n_s is the atomic density of solid hydrogen; R is the major radius of the torus. It is seen that these relatively slow pellets have penetration depths deeper than the scrape-off layer, but smaller than the distance to the centre of the plasma.

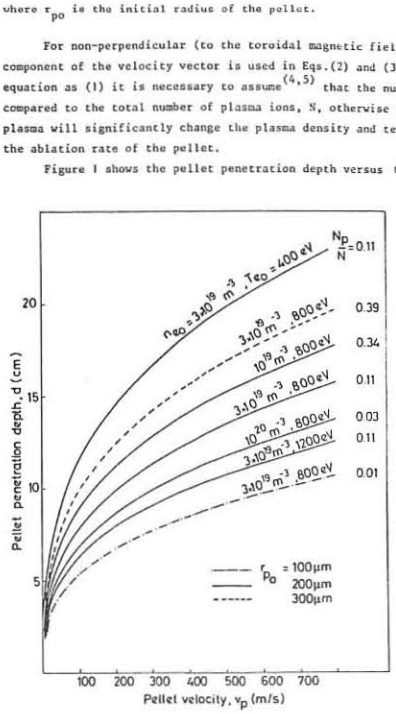

Fig. 1. Pellet penetration depth

DEPOSITION OF THE PELLET MATERIAL

Besides estimating the pellet penetration depth it is very important to see how the ablated material is deposited in relation to the plasma density profile.

The Ablating Pellet as a Point Source. In this section we assume the pellet to be a point source emitting atomic ions and electrons with a rate given by Eq.(1). Due to the magnetic field configuration, the amount of ablated hydrogen ions in a toroidal shell with radius r and thickness dr is $n_s 4\pi r_p^2 |\dot{r}_p| dt$, and as the parallel transport of ionised material is large we will assume these ions fill the toroidal shell uniformly, so that the density is:

$$n_p(r) = \frac{n_s\, 4\pi r_p^2 |\dot{r}_p| dt}{2\pi r\, dr\, 2\pi R} = \frac{f\, n_s}{\pi R\, r\, v_p} r_p^{4/3}\, n_e^{1/3}\, T_e^{5/3}. \qquad \ldots (4)$$

In Fig. 2 we show in the curves marked $\delta = 0$ the resulting plasma density profile for a typical set of parameters. It is seen that even for low values of N_p/N there will be rather high local plasma density perturbations; with peak values of $n_p/n_e \approx 3N_p/N$.

Ionisation Radius of the Ablation Cloud. In the previous section we assumed the pellet to be a point source of atomic ions and electrons but this is not entirely correct since the pellet-plasma model we use is based on the development of a neutral cloud of hydrogen molecules around the pellet. This cloud is heated by the energetic plasma electrons which drive the molecules outwards until they reach the point where they are ionised. The dominant ionisation process is $H_2 + e \rightarrow H_2^+ + 2e$[8]. The point at which most of the molecules are ionised is defined as the "ionisation radius", r_I[5]. It is shown that: $r_I/r_p \gg 1$; r_I is almost independent of the values of r_p; and r_I decreases for increasing plasma density and increases for increasing plasma temperature.

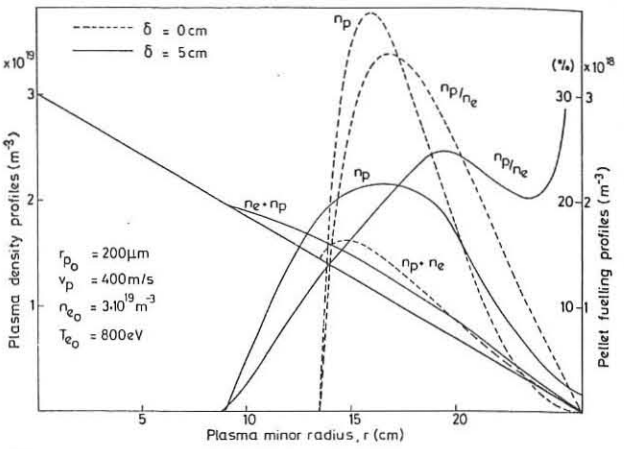

Fig. 2. Ablated pellet material profiles

After ionisation the H_2^+ ions are constrained to follow the magnetic field lines. The dominant process is then dissociation, $H_2^+ + e \rightarrow H^+ + H^0 + e$. The mean free path length for this process is somewhat smaller than the value of r_I. Hence the overall picture is that the pellet material results in equal numbers of cold ions and neutral atoms smeared out over a region $(r - \delta, r + \delta)$ where $\delta \gtrsim r_I$. Assuming a uniform production rate of ions within this interval we have for $d > \delta$

$$n_p(r) = \frac{\int_{t1}^{t2} \frac{dr}{2\delta} n_s\, 4\pi r_p^2 |\dot{r}_p| dt}{2\pi r\, dr\, 2\pi R} \qquad \ldots (5)$$

where $t_1 = 0$ for $a - \delta \le r \le a$; $\quad \frac{a - \delta - r}{v_p}$ for $r \le a - \delta$

$t_2 = \frac{a + \delta - r}{v_p}$ for $a - d + \delta \le r$; $\quad \frac{d}{v_p}$ for $r \le a - d - \delta$.

In order to carry out this integration we shall simply assume a constant value of δ which is reasonably well justified since the pellet travels towards both higher plasma density and temperature[5]. Hence from Eq.(5) we find

$$n_p(r) = - \frac{n_s}{6\pi R\, \delta\, r} [r_p^3]_{t1}^{t2} \qquad \ldots (6)$$

where r_p is given in Eq.(2). Figure 2 shows how the fuelling profile and resulting plasma density profile are changed when taking into account a finite radius of the ablation cloud. The fuel is spread out and a larger fraction of the fuel is deposited deeper in the plasma. This also results in a smaller local plasma perturbation, $n_p/n_e|_{max} \sim 2\, N_p/N$.

TRANSPORT OF NEUTRAL PELLET ATOMS. In this section we deal with the transport of the neutrals which originate from the ablating pellet. We include these neutrals as a source term, $S_n(r)$ in a steady-state recycling code for neutral plasma particles. The cold neutrals from the pellet charge-exchange with hot plasma ions and the resulting hot neutrals are able to penetrate deep into the plasma. Because the charge-exchange cross-section is several times larger than the ionisation cross-section, several generations of hot neutrals are possible before the final ionising collision occurs. The steady-state approximation is valid in cases where the pellet repetition time, (Δt) is only a few times larger than the pellet ablation time so that we can assume $S_n(r) \approx \frac{1}{2} n_p(r)/\Delta t$, where $n_p(r)$ is given from Eq.(6). This expression will, of course, be better fulfilled for several pellet launchers distributed around the torus. Figure 3 shows the results of the calculations for the same case as in Fig. 2.

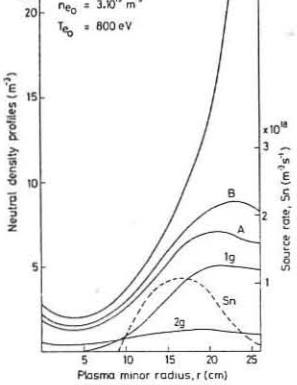

Fig. 3. Neutral density profiles calculated for a pellet injection rate normalised to one pellet per second. Values for an injection rate of η pellets per second can be obtained by multiplying these results by a factor η. The curve S_n shows the source rate of cold neutrals (energy 10 eV) from the ablating pellet. The curves 1g and 2g show the first and second generations of more energetic neutrals produced by charge-exchange. Three boundary conditions are compared: (A) a non-reflecting wall which traps all incident neutrals; (B) a partly-reflecting wall from which neutrals are reflected with reduced energy and with an energy dependent reflection coefficient; (C) a partly reflecting wall as (B) plus gas desorption. A cold (10 eV) neutral is released to replace every incident neutral which is trapped on the wall.

CONCLUSIONS. It is shown that relatively slow pellets (about 300 - 600 m/s) penetrate beyond the divertor scrape-off layer but do not reach the centre of the plasma. However, if the finite size of the pellet ablation cloud is taken into account, a large fraction of the fuel is deposited much deeper in the plasma and there is less local plasma density perturbation. Half of the ablated pellet ends up as neutral atoms and steady-state transport calculations show that these atoms penetrate even deeper into the plasma resulting in a significant neutral density at the centre of the plasma.

REFERENCES
(1) S.J. Fielding et al, 8th Europ. Conf. on Controlled Fusion, Prague (1977) 1, 36.
(2) S.L. Milora et al, Phys. Rev. Letts. 42 (1979) 97.
(3) Proc. Fusion Fuelling Wksp. (Princeton) U.S. Dept. of Commerce, CONF-771129 (1978).
(4) D.F. Vaslow, IEEE Transaction on Plasma Science, 5 (1977) 12.
(5) P.B. Parks et al, Nuclear Fusion 17 (1977) 539.
(6) C.A. Foster et al, Nuclear Fusion 17 (1977) 1067.
(7) L.W. Jørgensen and A.H. Sillesen, Ablation of Solid Hydrogen in a Plasma, Submitted for publication in J. Phys. D.
(8) R.L. Freeman and E.M. Jones, Atomic Collision Processes in Plasma Physics Experiments I + II, CLM-R 137 (1974) and CLM-R 175 (1977).
(9) G.M. McCracken and P.E. Stott, Nuclear Fusion (to be published), CLM-P573

* Present address: JET Joint Undertaking, Abingdon, Oxon, OX14 3EA.

EP24

Nonlinear Theory of Collisional Drift-Waves in Toroidal Geometry and Anomalous Skin Effects in Tokamaks

André Rogister and Günter Hasselberg

Institut für Plasmaphysik der Kernforschungsanlage Jülich GmbH, Ass. EURATOM-KFA, D-5170 Jülich, Federal Republic of Germany

Collisional drift waves in a sheared magnetic field which are stable in cylindrical geometry /1-3/ may become unstable in Tokamak configuration when the shear damping is nullified by strong toroidal coupling. The stability of long toroidal wavelength modes, the most dangerous from the point of view of particle and energy transport, is essentially governed by the sign of $\eta_e \equiv d\ln T_e/d\ln N$. These modes which are unstable for reversed electron temperature and density gradients ($\eta_e < 0$) are of particular significance for many fusion problems such as the initial current rise, the fueling phase by injection of cold gas, and the cold plasma mantle concept. For example, the rapid experimental disappearance of the temperature maximum near the plasma boundary during the current rise (anomalous temperature skin effect) and of the outer density maximum during fueling (anomalous density skin effect) are indications of anomalous particle diffusion, thermal conduction and/or electrical resistivity which could be the result of wave transport.

In this paper, the nonlinear theory of collisional drift waves in a sheared magnetic field is developed in the framework of weak turbulence theory and in the strong toroidal coupling approximation (ballooning limit). A self-consistent estimate of the turbulence level results. The anomalous particle and heat fluxes are then evaluated and compared to the neoclassical fluxes. The dominant nonlinear effect is to increase the radial width of the eigenmode and consequently to decrease the destabilizing role of electron collisions while increasing the role of ion Landau damping. Stationary turbulence level obtains when the latter balances the residual growth rate.

The electrostatic potential $\phi(x,\theta,\zeta)$ is written in the form

$$\phi_\ell(x,\theta)=\exp\{i\ell[\zeta-\int_{\theta_o}^{\theta}\nu(r_o,\theta')d\theta']\}\hat{\phi}_\ell(x,\theta);\quad \hat{\phi}_\ell(x,\theta)=\sum_m \exp[im(\theta+\theta_o)]\,\hat{\phi}_{\ell,m}(x)$$

where $\hat{\phi}_\ell$ is a slow function of $x \equiv r-r_o$ and, because of toroidicity, of θ; ℓ is the toroidal mode number, $\zeta(\theta)$ is the toroidal (poloidal) angle, $\nu(r,\theta)\equiv rB_\zeta/RB_\theta$ describes the differential rotation of a field line, r_o is the position of a rational surface defined by $\ell\int_{\theta_o}^{2\pi}\nu(r_o,\theta)(d\theta/2\pi)\equiv \ell q(r_o)=n$ (n entire), q is the safety factor, and θ_o is an arbitrary angle in the vicinity of which the mode is localized poloidally. In the following we shall assume $\theta_o = 0$ or π ($|\theta|<\pi/2$ corresponds to the inside of the torus) for reasons of simplicity. The distance between neighbouring rational surfaces is $\Delta x = [\ell q\partial\ln q\,(r_o)/\partial r_o]^{-1} \equiv r_q/\ell q$; for linear density and temperature profiles, periodicity in x requires $\hat{\phi}_{\ell,m}(x) = \hat{\phi}_\ell(m+\ell qx/r_q)$. We expect the eigenvalue equation to become nonlinear for wave amplitudes $e\phi_{\ell,m}/T_e \approx G_{\ell,m} \sim \epsilon \equiv a_i/r$ where a_i is the ion Larmor radius.

There results from a straightforward calculation the following nonlinear equations

$$(D+P)a_s^2\frac{\partial^2 G_{\ell,m}}{\partial x^2} - \frac{k_\parallel'^2 c_s^2}{\omega^{*2}_{e,\ell}}(x+\frac{m}{k_\theta\sigma})^2 G_{\ell,m} + (\frac{\delta\omega_\ell}{\omega^*_{e,\ell}}A - Q_\ell)\,G_{\ell,m} = A\frac{i\mu x^2_{t,\ell}}{(k_\theta\sigma x+m)^2+ip\,x^2_{t,\ell}}\,G_{\ell,m} \qquad (2)$$

where $\sigma \equiv r/r_q$ is the shear parameter, $A \equiv [1+(1+\eta_i)\,\tau\,]^{-1}$, $\mu \equiv -\zeta q/r$ is the poloidal mode number, $D_\ell = (1/k_\theta a_s\sigma)^2(r_N/R_o)(1-2\sigma)\cos\theta_o - 1$, $\tau = T_i/T_e$, $\omega^*_{e,\ell} = -(cT_e/eBj k_\zeta/r_N$ is the diamagnetic drift frequency, $r_N^{-1} = d\ln N/dr$, $a_s = c_s/\Omega_i$, $c_s = (T_e/m_i)^{1/2}$, and $\delta\omega_\ell$ is the eigenvalue. Further

$$P \equiv \frac{1}{3}r_N^2\sum_{\ell',m'} k_\theta'^2|G_{\ell',m'}|^2;\quad Q_\ell \equiv \frac{1}{3}k_\theta^2 a_s^2 r_N^2\sum_{\ell',m'}\left|\frac{\partial G_{\ell',m'}}{\partial x}\right|^2; \qquad (3)$$

$\mu = -0.6\,\eta_e$ if $\nu_{ee}/\nu_{ei} \ll 1$, p is of order unity, and $x^2_{t,\ell} \equiv (m_e\nu_{ei}/m_i\omega^*_{e,\ell})\cdot(Br\omega^*_{e,\ell}/B_\theta c_s)^2$.

The right-hand-side of the equation represents the linear electron response. (For simplicity we have only retained the part proportional to the temperature gradient. It is noted that except for a numerical factor, the electron response in Eq. (2) agrees with Eq. (3) of Ref. 2.) The left-hand-side of the equation represents the nonlinear ion response including inertia, motion along the field lines, magnetic curvature and finite Larmor radius effects, and nonlinear ion Landau damping including both the Compton ("bare" particle) and the shielding cloud contributions. The matrix elements have been estimated in the limit of small Larmor radius, i.e. $k_\theta^2 a_s^2 < 1$ and assuming $r_N/R_o < 1$. Not surprisingly the nonlinear terms of Eq. (2) agree with those of Ref. /4/ in the limit where the modes overlap many rational surfaces. The linear ion response was previously obtained in /5/ including the toroidal terms.

Noting that P and Q_ℓ are approximately constant since the modes overlap many rational surfaces, Eq. (2) has the same structure as the linear equation solved in /1-3/ by the method of matched asymptotic expansion. This is possible if

$$\sqrt{D+P}\;(k_\theta a_s\sigma)^2\frac{B}{B_\theta}\left|\frac{r_q}{r_N}\right| \gg x^2_{t,\ell} \qquad (4)$$

For $(k_\theta\sigma x+m)^2 \gg x^2_{t,\ell}$, Eq. (2) reduces to Kummer's Equation; for $(k_\theta\sigma x+m)^2 \ll x^2_{t,\ell}$, it becomes the hypergeometric differential equation.

The eigenvalue, obtained by matching the two asymptotic solutions, is given to a good approximation by

$$a = \frac{1}{4}\{-\frac{\delta\omega_\ell}{\omega^*_{\ell,e}}[1+\tau(1+\eta_i)]^{-1}+Q_\ell\}\Lambda(\frac{B}{B_\theta})^2(\frac{r_q}{r_N})^2 a_s^2+\frac{1}{2}(s_\ell+\frac{1}{2}) = 0 \qquad (5)$$

where s_ℓ is the solution of

$$s_\ell(s_\ell-1) = i\mu x^2_{t,\ell}[1+\tau(1+\eta_i)]^{-1}\frac{1}{k_\theta^2\sigma^2}\Lambda^2(\frac{B}{B_\theta})^2(\frac{r_q}{r_N})^2 a_s^2$$

with $R_e s_\ell > 1$ and Λ is the positive root of $(D+P)\Lambda^2 a_s^2 = (B_\theta r_N/Br_q)^2$ provided $s_\ell - 1 > \Lambda^{1/2}(x_{t,\ell}/k_\theta\sigma)$ ("strong collisionality limit" of Ref. 2). The growth rate $\gamma_\ell \equiv -i\delta\omega_\ell$ is then given by

$$\gamma_\ell = 2\,\mathrm{Im}\,s_\ell\,\omega^*_{\ell,e}\,[1+\tau(1+\eta_i)]\,\Lambda^{-1}(\frac{B_\theta}{B})^2(\frac{r_N}{r_q})^2 a_s^{-2} \qquad (6)$$

It is readily verified, by going back to the definition of s_ℓ (with $\mathrm{Re}\,s_\ell > 1$) and $x^2_{t,\ell}$ that instability occurs for $\mu > 0$; thus inverted temperature gradients ($\eta_e < 0$) are destabilizing. It is also obvious that the growth rate decreases with increasing turbulence, and perhaps more important that the width of the eigenmode increases. This may go on until

$$\langle(x+\frac{m}{k_\theta\sigma})^2\rangle \simeq \Lambda^{-1} \sim \frac{1}{k_\theta^2\sigma^2}\frac{B^2}{B_\theta^2}(\frac{r\omega^*_{e,\ell}}{c_s})^2 \equiv \frac{B^2}{B_\theta^2}\frac{r_q^2}{r_N^2}a_s^2 \qquad (7)$$

at which point increased convection of energy by shear from the unstable region to the region where ion Landau damping occurs will balance the residual growth rate. We shall assume and verify later that when (7) approximately holds, $P \simeq (k_\theta,_m a_s\sigma)^{-2}\,|(r_N/R_o)(1-2\sigma)|$ where $k_{\theta,m}$ is the minimum value of k_θ for which the condition that the mode overlaps many rational surfaces is still satisfied. Then, from (7)

$$P \simeq \frac{B^2}{B_\theta^2}\frac{r_q^2}{r_N^2} \qquad (8)$$

The condition for the mode to overlap many rational surfaces and the assumption $k_\parallel c_e < \nu_{ei}$ lead to the inequalities

$$\frac{B_\theta}{B}\left|\frac{r_N}{r_q}\right|P^{-\frac{1}{2}} \ll (\frac{\nu_{ei}R_o q}{c_e})^2 \gg (k_\theta a_s\sigma)^2 \gg \frac{B_\theta}{B}\left|\frac{r_N}{r_q}\right|P^{-\frac{1}{2}} \qquad (9)$$

and it is easily verified that the assumption leading to (8) holds. It is noted that the range of toroidal mode numbers satisfying (9) is non-zero only in the Pfirsch-Schlüter regime ($\nu_{ei}R_o q/c_e > 1$).

Considering now anomalous particle and heat transport, we have found that particles and heat flow towards regions of lower density and temperature respecitvely. The ratio of anomalous to neoclassical time scales is approximately, both for particle and heat transport,

$$\frac{\tau_a^{-1}}{\tau_{N.C.}^{-1}} \sim |\eta_e|\frac{R_o^2}{r_N^2}\sigma^{-2} \qquad (10)$$

The estimate (10) shows that the anomalous transport is easily more than one order of magnitude faster than neoclassical. The collisional drift ballooning modes are thus candidates to explain the experimental observations whereby temperature profiles which are strongly peaked outwards within a monotonically decreasing density distribution as should be expected during the initial current rise (temperature skin effect), or reciprocally strong outward peaked density profiles in a smooth T_e distribution as expected during fueling (density skin effect), are not observed.

In concluding, it is noted that the nonlinear theory developed here readily applies to other types of drift ballooning modes in axisymmteric toroidal geometry.

References

/1/ A. Rogister and G. Hasselberg, IAEA-CN-37/W-6(A), Vol. 1, 809,1979
/2/ J.G. Cordey, E.M. Jones and D.F.H. Start, Culham Report CLM-P551 (1978)
/3/ L. Chen, P.N. Guzdar, J.Y. Hsu, P.K. Kaw, C. Oberman, and R. White, Nucl. Fus. 19, 373 (1979)
/4/ G. Hasselberg, A. Rogister, and A. El-Nadi, Phys. Fluids, 20, 982, 1977
/5/ W.M. Tang, Nucl. Fus. 18, 1089, 1978

EP25

TRANSPORT CALCULATIONS FOR THE APPROACH TO IGNITION IN JET

M L Watkins and A Gibson
The JET Joint Undertaking, Abingdon, Oxfordshire, OX14 3EA

Abstract: The approach to ignition in the JET apparatus is assessed using a one-dimensional transport model that includes impurity effects. The results are presented in terms of the parameter, $Y = P_\alpha/(P_{loss}+|\dot{E}|)$, which tends to unity as alpha particles dominate the energy balance both in steady state and evolving plasmas. While Y is limited to values $\lesssim$ 10% with basic performance levels of heating, Y $\gtrsim$ 60% is achieved with power levels that correspond to the proposed extended performance capability in JET [1].

1. Introduction: We report the results of radial transport calculations for a plasma that is heated by neutral injection to conditions of thermonuclear interest in the equivalent circular cross-section JET configuration. Earlier work [2] indicated that for anomalous transport losses that scaled as pseudo-classical or Pfirsch-Schluter plasmas characterised by temperatures ~5 keV and densities ~$7\times10^{19}m^{-3}$ could be achieved with 10 MW of injected power, provided that 3 MW (at low energy) were used to control the impurity influx by maintenance of a Cool Plasma Mantle that surrounds the hot core.

The present calculations extend from basic power levels to the higher input power levels characteristic of the proposed extended performance parameters in JET (Table I). Electron transport models are chosen to be in accord with recent experimental results [3,4].

2. Physical Model (Essentially as in [2], except as indicated below)

2.1 Electron and fuel ion fluxes and electron thermal flux represented by anomalous diffusion coefficients (Table I). The coefficient in the N-model is chosen to approximate ALCATOR data [3]. The exponents in the NT-model are chosen to give a fit to data in [5] but constrained to be both proportional to density and temperature, and consistent with [6]. The coefficient is chosen to agree with high temperature PLT data [4].

2.2 A multi-regime neo-classical model for the fuel ion thermal transport.

2.3 A collison-dominated neo-classical model for the particle and thermal transport of a single impurity species. ∇T terms in the particle flux are set to zero.

2.4 All ions have the same local temperature. For the impurity calculations reported here the electron and ion temperatures are assumed to be equal. Results with decoupled temperatures will be presented at the conference.

2.5 Escaping particles are assumed to recycle at the boundary and be returned to the plasma with an energy distribution determined by the reflection properties of the wall. The penetration of the neutral flux is calculated using a diffusion approximation in which the population is exponentially attenuated into the plasma.

2.6 Injected neutral particles are assumed to penetrate the plasma using the model of Riviere [7], with an effective penetration length that takes into account proton ionisation and charge transfer on impurity ions according to the prescription of [8]. The injected power is apportioned between electrons and ions. The finite width of the beam is approximated by modification of the source terms for radii, r < 0.2m.

2.7 The sole source of impurities is assumed to be sputtering [9] of iron impurity ions from the wall as a result of outgoing fluxes of both fuel ions and charge-exchanged neutrals. All impurities accumulate within the plasma.

2.8 Additional to bremsstrahlung radiation losses the mean state of ionisation and the radiation efficiency are calculated using the results of [10].

2.9 Alpha particle power from the calculated slowing down of the beam and from plasma thermonuclear reactions is evaluated assuming a 50:50 mixture of D-T. The alpha particles are slowed down instantaneously and power is apportioned to electrons and ions as in §2.6 above.

3. Summary of Results

The approach to ignition in the JET apparatus is assessed in terms of the variation with the central ion temperature ($\hat{T}_i$) of the parameters $\hat{n}_{20}\tau$ and $Y = P_\alpha/(P_{loss}+|\dot{E}|)$, where $\hat{n}_{20}$ is the central density (x $10^{20}m^{-3}$), and τ, P_α, P_{loss}, $|\dot{E}|$ are defined in the interior of the plasma (radii, r <0.63m) to be respectively the energy confinement time(s), the α-power production, the power loss by conduction and radiation and the magnitude of the rate of change of internal energy. The results are obtained for different plasma compositions (different starting densities and purity), beam powers and energies, and plasma transport (Table I) and are summarised below:

3.1 In most of the cases reported, the Y-value shown is with the additional heating source still on. Whether or not a large Y-value will lead to ignition when the additional heating is switched off depends upon the consequent profile relaxation which can take many seconds.

3.2 With the basic power level in a pure plasma (i.e. impurity source switched off and level set to zero)conditions close to ignition (i.e. temperature escalation with no external power source) cannot be obtained with the N-model but can be obtained with the NT-model. The point plotted (A in figs. 1 and 2) has Y = 0.8 and $\hat{T}_i$ would continue to increase if the beam were to be switched off.

3.3 With extended power level in a pure plasma ignition is obtained readily with the N-model, provided that the beam is on for ~ 2.5s at full power (Point B in figs. 1 and 2).

3.4 In the cases with sputtered iron impurity the temperature profiles are more peaked than in the pure cases: the total input power is eventually radiated by impurities in the edge region.

3.5 With power levels appropriate to the basic performance, the best performance is obtained at low densities ($\bar{n}$ building up from 0.26 x $10^{20}m^{-3}$ to 0.6 x $10^{20}m^{-3}$) and gives Y ~ 0.08, $\hat{T}_i$ ~ 6 keV and $\hat{n}_{20}\tau$ ~0.8.

3.6 With the extended power level and the N-model, beam powers and energies that correspond to similar ion powers (Table I) produce comparably good approaches to ignition. Y ~ 0.7 is obtained for β ~ 3%.

3.7 With the extended power level and the NT-model, Y ~ 0.84 is obtained with β ~ 4% when the beam is switched off(2.5s). Temperature escalation is obtained even with sputtered iron as the impurity. (Point C in figs. 1 and 2).

3.8 With modest amounts ($\lesssim$ 12 MW) of yet unspecified heating that couples efficiently(with a parabolic power density profile) to the inner 0.5m radius plasma, Y ~ 0.75 with β ~6% is obtained. The temperature is still increasing and would continue to do so if the heating source were to be switched off. (Point D in figs. 1 and 2).

4. Model Variants

The results of moderating the impurity influx by the formation and maintenance of a Cool Plasma Mantle for these model calculations will be presented at the conference. There are indications that gas-puffing can affect the initial build-up of impurities, but that using carbon as the sputtered impurity can lead to a build-up of highly ionised carbon in the edge layers which can prevent beam penetration.

5. References

[1] "The JET Project-Design Proposal" EUR-5516e(R5) (1976) 467.
[2] Gibson A and Watkins M L, VIII European Conf on Controlled Fusion and Plasma Physics 1 (1977) 31.
[3] Gaudreau M, et al, Phys Rev Letts 39 (1977) 1266.
[4] Eubank H, et al, VII Int Conf on Plasma Physics and Cont Nuclear Fusion Research, Innsbruck (1978) Paper IAEA-CN-37-C-3.
[5] Pfeiffer W and Waltz R E, Nuclear Fusion 19 (1979) 51.
[6] Connor J W and Taylor J B, Nuclear Fusion 17 (1977) 1047.
[7] Riviere A C, Nuclear Fusion 11 (1971) 363.
[8] Olson R E, et al, Phys Rev Letts 41 (1978) 163.
[9] Behrisch R, et al, J Nucl Mat 60 (1976) 321.
[10] Post D E, et al, At Data Nucl Tables, 20 (1977) 397.

TABLE I

Machine Parameters			Transport Losses [3]
Major Radius,	R	2.96m	N-Model $\kappa_{e1}=0.5/\bar{n}_{20}$ [$m^{-2}s^{-1}$]
Minor Radius,	a	1.62m	NT-Model $\kappa_{e2}=K/\bar{n}_{20}T$[$m^{-2}s^{-1}$]for $\kappa_{e1}>\kappa_{e2}$
Toroidal Field,	B	3.45T	where $K = 2\times10^{-5}/a^{0.35}R^{1.2}I^{-0.2}$
Toroidal Current,	I	4.8 MA(3.0MA)	D=0.25 κ_{e1} or 0.25 κ_{e2}

Beam Specification Species: Hydrogen [H^+] or deuterium [D]

Total Power (MW) [Species]	Principal Component: Power (MW)	Principal Component: Energy (kV)	Approximate ion power (MW) into the neutraliser	Key to Curves in Fig.1 and 2
17.5 [H]	10	80	75	— — —
39.0 [D]	26	120	120	—·—·—
45.0 [D]	26	160	194	- - - - -
62.5 [D]	42	120	194	———

Initial Density Specification

Radial, r, variation of density n_{20} in units of 10^{20} m^{-3}: $n_{20}(r)=\hat{n}_{20}[1-0.9(r/a)^8]$

$\hat{n}_{20}$ and $\bar{n}_{20}$ are peak and average densities

The symbol key applies to Figs.1 and 2

$\hat{n}_{20}$	$\bar{n}_{20}$	Symbol
1.0	0.88	•
0.75	0.66	□
0.50	0.44	○
0.30	0.26	×
0.15	0.13	△

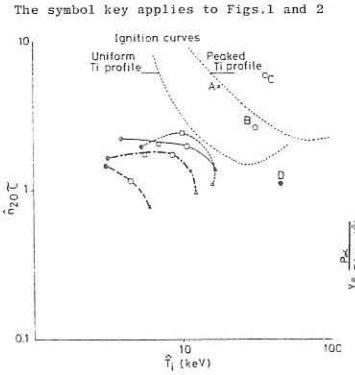

Fig.1 Variation with central ion temperature, $\hat{T}_i$(keV) of $\hat{n}_{20}\tau$ where $\hat{n}_{20}$ is the density on axis in units of $10^{20}m^{-3}$ and τ is the energy confinement time(s) in the interior (radius, r=0.63m).

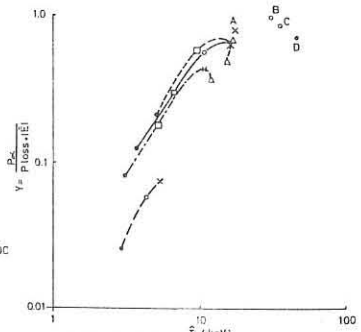

Fig.2 Variation with central ion temperature, $\hat{T}_i$(keV) of the parameter, Y, defined in the interior (radius,r=0.63m).

EP26

THE LOSS OF INJECTED IONS DUE TO SPATIAL FIELD RIPPLE IN TOKAMAKS

J. G. Cordey, UKAEA, Culham Laboratory, Abingdon, Oxon, England
W. G. F. Core and A. Gibson, the JET Joint Undertaking, Abingdon, Oxon, England, OX14 3EA.

The loss of injected fast ions from tokamak confinement systems has been intensively investigated in the literature[1]. In this paper we examine a further loss mechanism[2] that is due to the energetic ions being scattered during the slowing down process into the toroidal field ripples. To assess this loss process we restrict our treatment to confinement systems that conform to the following assumptions:

(i) The usual simplified model tokamak where the resulting confining magnetic field can be approximated by

$$B \sim B_\phi \sim B_o(1 - \varepsilon\cos\theta - h(r)\cos N\phi) \qquad ..(1)$$

where B_o is the magnetic field on the magnetic axis, $\varepsilon = r/R$ the aspect ratio, R the major radius of the magnetic axis, θ the poloidal angle, $h(r)$ the magnitude of the ripple field at minor radius r, N the number of toroidal field coils, and ϕ is the angular distance along the magnetic axis.

(ii) The ripple field component is independent of poloidal angle and takes the familiar form $h(r) = h(a)(r/a)^\lambda$, where $h(a)$ is the magnitude of the ripple field at the plasma edge $r = a$, λ is a constant and describes the variation of ripple with minor radius and is sufficiently large to limit the effect of the ripples to a radial depth $d = a - r$ of the plasma edge region.

(iii) The orderings $h(a) \ll \varepsilon < 1$, and $0 < d \ll a$, are applicable.

From the guiding centre equations in the drift approximation, it is readily shown that the motion between collisions can be completely characterised by the equation of energy,

$$\frac{1}{2}mV_{\shortparallel}^2 = E - \mu B, \qquad ..(2)$$

and the invariance of the toroidal canonical momentum J which for a particle moving in a tokamak with uniform current density can be written in the form,

$$J = \frac{r^2}{2a}\rho_{i\theta} + \sigma\frac{B_o}{R}\left\{1 - \frac{\mu B}{E}\right\}^{\frac{1}{2}}. \qquad ..(3)$$

Where $\sigma = \pm 1$, E the ion energy, $V_{\shortparallel}$ the velocity along the magnetic field B, $\mu = mv_\perp^2/2B$ the magnetic moment, and $\rho_{i\theta}$ the total Larmor radius in the poloidal magnetic field at the plasma edge. To complete our description of the ion behaviour during the slowing down process, we assume in addition that:

(iv) The scattering is predominantly small angle so that the usual drift kinetic Fokker-Planck prescription for the collisional evolution of the energetic ion is applicable.

(v) The orderings, $\tau_B \ll \tau_s$, $\delta \ll \Delta \ll \sqrt{2\varepsilon}$, and $V_D/d \ll \tau_s^{-1}$, where τ_B is the usual "banana" orbit bounce time, τ_s the Spitzer slowing down time, δ and Δ are the width and separation of the ripple trapping regions in velocity space respectively, and V_D is the guiding centre drift velocity of the ripple trapped ion.

Starting from the usual drift kinetic equation[3] in the velocity space variables V, $\zeta = V_{\shortparallel}/V$, and bounce averaging, gives

$$\frac{1}{V^2}\frac{\partial}{\partial V}\left\{(V^3+V_c^3)f_B\right\} + \beta\left(\frac{V_c}{V}\right)^3\frac{\partial^2 f_B}{\partial\zeta^2} = -\tau_s S \qquad ..(4)$$

for the inter ripple well particle distribution function f_B.

For the ripple trapped particle distribution function f_R, we neglect back-scattering from the ripple wells into the "banana" regions of velocity space so that the Fokker-Planck equation in this region reduces to

$$\frac{1}{V^2}\frac{\partial}{\partial V}\left\{(V^3+V_c^3)f_R\right\} - V_D\tau_s\frac{\partial f_R}{\partial r} = 0 \qquad ..(5)$$

Where V_c is the critical velocity and β a function of the plasma parameters.

Our method of solution for the ripple trapping loss process is first to determine the width of the ripple trapping regions δ, and their separation in velocity space Δ. We then solve the drift kinetic equation in the inter-well region. Imposing the boundary conditions, continuity of f and particle flux leads directly to a boundary-layer solution for the ripple trapped particle distribution.

The regions in velocity space in which the particles are ripple trapped are determined as follows. A particle initially in the median plane $\theta = 0$, with pitch $\xi_m = V_{\shortparallel}/V$ such that it is just reflected at the ripple well maximum $\theta = \theta_m$ defines the edge of a particular trapping region. The width of the loss region in velocity space is then given by the increment in pitch δ consistent with reflection in the interval $\theta_m < \theta < \theta_{m+1}$ such that the particle becomes localised and trapped.

Consider a particle reflecting in the toroidal field gradients. Let the magnetic field at the reflection point r,θ_b be $B(r,\theta_b)$ and at $r + \Delta r$, θ_m be $B(r + \Delta r, \theta_m)$ then the condition that particle be ripple-trapped is $B(r + \Delta r,\theta_m) \geq B(r,\theta_b)$. Where Δr is the radial width of the orbit at the ripple well maximum $\theta = \theta_m$. Writing $\theta_b = \theta_m + \Delta\theta$, expanding, using the energy equation Eq.(2), invoking the invariance of J Eq.(3), and introducing the simplified model field Eq.(1) gives for the width δ of the ripple trapping region in velocity space associated with the ripple well at $\theta = \theta_m$,

$$\delta \sim 2\left\{\frac{i\theta\,\lambda\,h(a)}{a\,\xi_m}\right\}^2 . \qquad ..(6)$$

The separation of consecutive ripple trapping regions $\Delta = \xi_{m+1} - \xi_m$ on a magnetic surface is calculated in a similar manner, we have

$$\Delta = \frac{\pi}{Nq}\sqrt{2\varepsilon}\cos\left(\frac{\theta_m}{2}\right) . \qquad ..(7)$$

where q is the safety factor and $2/Nq$ is the ripple well period.

In order to solve the system of equations (4),(5) we consider a fast ion population injected at an initial velocity V_o between consecutive ripple loss regions so that on introducing the variable $\xi = \eta\Delta$, Eqn.(4) becomes

$$\frac{1}{V^2}\frac{\partial}{\partial V}\left\{(V^3+V_c^3)f_B\right\} + \frac{\beta}{\Delta^2}\left(\frac{V_c}{V}\right)^3\frac{\partial^2 f_B}{\partial\eta^2} = -\tau_s S(\eta)\frac{\delta(V-V_o)}{V^2}, \qquad ..(8)$$

with $S(\eta) = 1$; $0 \leq \eta \leq 1$, and $f_B = 0$; $V > V_o$. Integration of Eqn.(5) through ripple trapping region in velocity space gives the following constraint on the distribution function f_B at the boundaries $\eta = 0$, $\eta = 1$,

$$-\frac{2\beta}{\delta\Delta}\left(\frac{V_c}{V}\right)^3\frac{\partial f_B}{\partial\eta} = V_D\tau_s\frac{\partial f_R}{\partial r} . \qquad ..(9)$$

Substitution of the appropriate Fourier representations for the distribution function f_B and source function S in Eqns (8),(9), then using the method of Laplace transformation in the variable r, gives the following solution for situations that are typical of the next generation heating systems i.e. $V_c^3 \gg \Delta^2 V_o^3$. We have

$$f_R = \frac{S\tau_s}{V^3 + V_c^3}\exp\left\{-\frac{\kappa}{V_o^4}\int_V^{V_o}\frac{V^6 dV}{V^3 + V_c^3}\right\} \qquad ..(10)$$

where $\kappa = \frac{\delta V_D \tau_s}{\Delta d}$.

The effect of ripple trapping on neutral injection heating in a next generation device can now be accessed. We take the JET parameters, $R = 2.96$ m, $a = 1.25$ m, $d = 0.15$ m, $I_p = 3$ MA, $r = 32$, $q = 6$, $\lambda = 11$, $h(a) \sim 2\%$, $n_e = 5 \times 10^{19} m^{-3}$, and consider proton injection at 80 kV, and 40 kV accelerating voltages. Using Eq.(10), the flux of energetic ions, and energy flux to the vessel wall is calculated as a function of mean boundary layer electron temperature $\langle T_e \rangle$ for particles that are ionised onto banana orbits in the ripple trapping region of the plasma, Figs. 1 and 2.

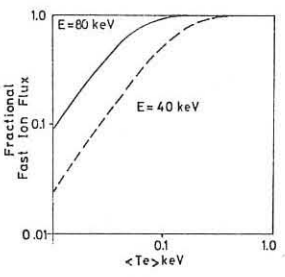

Fig. 1

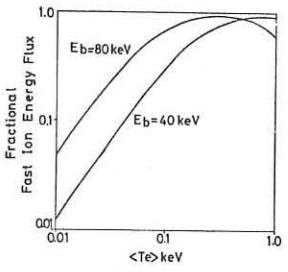

Fig. 2

Fig.3. In order to estimate the corresponding impurity production rate we take the sputtering emission spectrum of $(H^+ \rightarrow F_e)$; $f_s = 1.43 \times 10^{-2}(E/2+/2/E)^2)^{-2}\exp(-0.017E)$. [4] where E is the incident proton energy. The impurity generation is then determined in a similar manner to the ion, and energy fluxes.

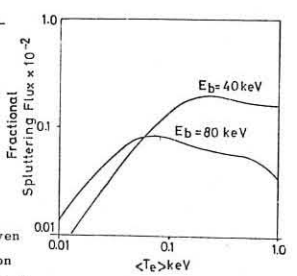

Fig. 3

In this paper we have shown that even at relatively low values of edge electron temperature e.g.($\langle T_e \rangle \sim 50$eV), a substantial fraction of the particles (50%) and power (20%) that is deposited in the ripple trapping region of the plasma is lost. Calculations of consequent impurity production indicate that injection directly into a ripple trapping region having $\langle T_e \rangle \sim 50$eV gives a production rate comparable to that calculated [5] due to diffusing and charge exchanged particles alone.

REFERENCES

[1](Rome, J.A., et al Nuclear Fusion 14 (1974)
(Rome, J.A., et al Nuclear Fusion 16 (1976)
[2] Lister, G., Post, D., Goldston, R., Monte Carlo, Calculations for Neutral Beam Heating of Tokamaks, U.S E.R.D.A. Contract E(11-17 3073)
[3] Cordey, J.G., Nuclear Fusion 16 (1976)
[4] Hotson, E., Private Communications
[5] Watkins, M.L. VIII European Conf. on Controlled Fusion and Plasma Physics 1 (1977)31.

EP27

A Multi-Region Global Transport Model for Tokamaks

W.G.F. Core and T.E. Stringer, UKAEA/JET

JET Joint Undertaking, Abingdon, Oxon, OX14 3EA, United Kingdom

Global transport models can provide a crude guide to the plasma evolution for a fraction of the computing time required by a full one-dimensional (1-D) simulation. Their greatest weakness is the prediction of impurity influx. This is largely determined by the outer annulus of plasma, whose properties may differ considerably from the main plasma core. A further defect is that the temperature and density profiles must be specified a priori, to allow the various energy sources and sinks to be averaged over the cross-section. In practice, these profiles are themselves determined by the sources and sinks, and may change during the evolution. The 3-region global code to be described takes account of both these effects.

Fig.1 shows typical density and temperature profiles obtained by numerical simulation of the plasma evolution using 1-D transport codes, e.g. [1]. Similar profiles are observed experimentally. Impurity radiation is the dominant loss mechanism over the relatively cool edge region, balanced mainly by energy transport out of the hot core. This radiation dominated annulus is represented by region 3 of our model. Its inner boundary b(t), is characterised by the temperature above which impurity radiation is small [2]. If iron is the dominant impurity, b(t) is defined as the radius at which the temperature equals 200 eV. Because of the relatively high collision frequency, the ion and electron temperatures are assumed equal in region 3. The temperature is taken to increase linearly with edge distance from a low value at the plasma boundary at r = b(t).

Fig. 1

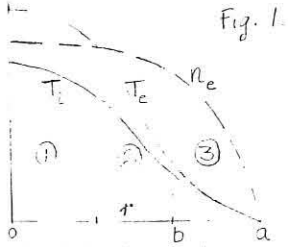

The temperature profile for the j^{th} species over the central region is taken in the form

$$T_j(r,t) = [T_{jo}(t) - 0.2]\,[1 - r^2/b^2]^{\gamma_j(t)} + 0.2 \text{ keV} \qquad (1)$$

To obtain equations for $\gamma_j(t)$ the sharpness parameter, the central region is divided into an inner core (region 1), $o<r<b/2$, and an intermediate annulus (region 2), $b/2<r<b$. Separate global energy conservation equations are used for each of the three regions, with allowance for the heat conduction between them. For example, the electron energy equation for the intermediate region has the form

$$\frac{3}{2}\frac{d}{dt}(\overline{nT_e})_2 = P_{Be2} + P_{\alpha e2} + P_{\Omega 2} + P^e_{in2} - P^e_{out2} + P_{ie2} - P_{rad2} - \frac{1}{b}\frac{db}{dt}\left[3(\overline{nT_e})_2 - 4(nT_i)_b + (nT_i)_{b/2}\right] \qquad (2)$$

when P_{Be} = beam and RF power, $P_{\alpha e}$ = α-heating, P_Ω = ohmic power, P_{ie} = ion-electron collisional transfer, P_{rad} = radiated power. In each term the local power to the electrons is integrated over the region, and divided by the volume. P_{in} and P_{out} are the energy conduction and convection into and out of the region, divided by the volume. This energy flux between the inner and intermediate regions is $\pi b \chi_j \partial T_j/\partial r$, where χ_e is one of the empirical results and χ_i is neoclassical. The corresponding heat flux between the intermediate and outer regions is taken to be $1.5\,[(nT_j)_{12} - (nT_j)_b]V_{12}/\tau_{Ej12}$, where $(\overline{nT_j})_{12}$ is the pressure averaged over the central (inner + intermediate) region, $(nT_j)_b$ the pressure at r = b, $V_{12} = 2\pi^2 R_o b^2$, and τ_{Ej12} is the energy confinement appropriate to the central regions. The term in db/dt is the change in mean energy of the intermediate region due to the moving boundaries.

Since the electron density profile does not generally show any regional structure, this is assumed to follow a simple form over the entire plasma, i.e.,

$$n(r,t) = n_o(t)\;\;[1 - 0.9\,r^2/a^2] \qquad (3)$$

Hence we have only one global equation for the evolution of n_o,

$$\frac{d\bar{n}_e}{dt} = -\frac{\bar{n}_e(1-R_c)}{\tau_p} + R_B + R_G \qquad (4)$$

where $\bar{n}_e = 0.55\,n_o$, R_c = boundary recycling coefficient, τ_p = electron confinement time, R_B and R_G are the mean electron sources due respectively to the injected beam and to gas feed or other refueling method.

The large difference in radiated power between region 2 and 3 results from the rapid decrease in line radiation above a certain temperature. There is no corresponding abrupt change in the impurity density profile $n_I(r) = \Sigma_j n_{Ii}(r)$, summed over all ionisation states of the species. Thus one might hope to average n_I over the entire cross-section, and describe it by a single global equation.

$$\frac{\partial \bar{n}_I}{\partial t} = -\frac{\bar{n}_I}{\tau_I} + S_I \qquad (5)$$

where τ_I is the confinement time and S_I the sputtered influx divided by the plasma volume. However, experiment indicates that impurity confinement within a narrow edge region (whose depth is less than region 3) is substantially shorter than over the rest of the plasma. It has been estimated [3] that only about 20% of the sputtered influx penetrates this region. Since the processes are not well understood, no attempt is made to represent this rapid recycling layer. As a first approximation, the mean impurity density over the rest of the plasma is described by Eqn. [5] with the right side replaced by $S_I/5$ (the estimated net influx from the recycling layer). Over the main part of the plasma the net effect of neoclassical and anomalous transport should give relatively long confinement, and the loss term from this region is neglected. S_I is found by estimating the fast neutral flux striking the wall. This flux results from charge exchange of slow neutrals recycled at the walls.

The radial impurity distribution is needed to evaluate the electron energy loss by line radiation. A first approximation is based on the observation, from both experiments and 1-D numerical simulations, that Z_{eff} tends to be relatively constant over most of the cross section. Thus we assume for each impurity species

$$n_I Z_I^2 \equiv \Sigma_j n_{Ij} Z_j^2 = n_{Io} Z_{Io}^2\,(1 - 0.9\,r^2/a^2) \qquad (6)$$

where $Z_{Io}^2 = Z_I^2$ at r = o. Z_I^2 may be obtained as a function of local temperature from published data [4], assuming coronal equilibrium. A simple analytic approximation to the variation, $Z_I^{-2} = (C_I + T_e)/A_I^2\,T_e$, is used to allow analytic integration of n_I over the cross section. This is combined with approximations for the radiation rate per impurity ion to evaluate the total line radiation from each region.

We now consider the simultaneous solution of the global continuity equations for electrons and impurities, and the energy conservation equations for each region.

Integration over each region gives $(\overline{nT_j})_s = n_o F_s[T_{jo}, \gamma_j, b]$, hence the left side of each energy equation has the form

$$\frac{d}{dt}(\overline{nT_j})_s = F_s\frac{dn_o}{dt} + n_o\left\{\frac{\partial F_s}{\partial T_{jo}}\frac{dT_{jo}}{dt} + \frac{\partial F_s}{\partial \gamma_j}\frac{d\gamma_j}{dt} + \frac{\partial F_s}{\partial b}\frac{db}{dt}\right\} \qquad (7)$$

The number of equations is 6 + the number of impurity species. These equations are integrated numerically to follow the time evolution of n_o, b, T_{io}, T_{eo}, γ_i, γ_e, and n_I. The width of region 3 is determined primarily by the balance between heat conduction into, and impurity radiation out of, this region. If the first is greater, the hot region eats into the cooler edge. The ratio of the energy sources in the inner and intermediate regions determines the sharpness of the temperature profile for each species, while the total heat input determines the peak temperatures.

The main object is to study the evolution of the edge region and its effect on the impurity content. Sputtering of impurities results mainly from the hot neutral flux, originating from charge-exchange in the hot core. It has been proposed [5] that sputtering could be greatly reduced by control of the edge region. A cool plasma mantle, which screens the wall from hot neutrals and whose temperature is below the sputtering threshold, could be formed by a low energy neutral beam [5].

Application of this code to JET and to existing tokamaks will be illustrated. The code allows a rapid scan of parameter space, to supplement the more reliable, but more costly, 1-D simulations. It should also help elucidate the dominant physical processes.

Acknowledgement

We would like to thank A. Gibson, who suggested a multi-region model, for his comments and interest.

References

[1] D.F. Duchs, D.E. Post and P.H. Rutherford Nuc. Fusion 17 (1977) 565.

[2] P.H. Rebut and B.J. Green, Pl. Phys. and Con. Fusion Research II 3, IAEA Vienna, 1977.

[3] Equipe TFR. Pl. Phys. and Con. Fusion Research, I, 127, IAEA Vienna, 1975.

[4] D.E. Post et al, Atomic Data and Nuclear Data Tables 20, (1977) 397.

[5] A. Gibson and M.L. Watkins, VIII European Conf. on Controlled Fusion and Pl. Phys. 1 (1977) 31.

BEAM-INDUCED CURRENTS IN TOROIDAL PLASMAS

D F H Start, J G Cordey and E M Jones
Culham Laboratory, Abingdon, Oxon, OX14 3DB, UK
(Euratom/UKAEA Fusion Association)

ABSTRACT A Fokker-Planck treatment of the effects of trapped electrons on beam induced currents has been developed for the 'banana' regime of collisionality and large aspect ratio tokamaks. The theory is extended to tokamaks of arbitrary aspect ratio using a model operator to simulate electron-electron collisions.

INTRODUCTION The kinetic theory of beam-induced currents developed by Cordey et al[1] has been successful in reproducing the observed[2] scaling of the current with electron temperature. The techniques developed in that theory are used in the present paper to calculate the effect on the current of electron trapping in the toroidal field gradient of a tokamak for plasmas in the 'banana' regime of collisionality. For large aspect ratio tokamaks a Fokker-Planck treatment is employed which uses the full electron collision operator. It is shown that for the high temperature regime of present day tokamaks the theory agrees with the calculation of Connor and Cordey[3] who used a model operator to simulate electron-electron collisions. With this justification the model operator is used to calculate the effect of trapping for tokamaks of arbitrary aspect ratio.

FOKKER-PLANCK THEORY The injection of fast ions is taken to produce a small perturbation of the electron distribution function which is written $f_e = F_{me} + f'_e$ where F_{me} is the Maxwellian distribution. The perturbation f'_e satisfies the electron Fokker Planck equation

$$C_{eb}(F_{me}, f_b) + C_{ei}(f'_e, F_{mi}) + C_{ee}(f'_e, F_{me}) + C_{ee}(F_{me}, f'_e) = \frac{\xi v}{r}\frac{B_\theta}{B}\cdot\frac{\partial f'_e}{\partial \theta} \qquad (1)$$

where C is the linearised collision operator, $\xi = v_{||}/v$ and f_b is the fast ion distribution function. The solution of eq(1) for the 'banana' regime of collisionality can be obtained to order $\varepsilon^{\frac{1}{2}}$ in the inverse aspect ratio ($\varepsilon = r/R$) in the form[4] $f'_e = f^o + h^o + f^*$ where f^o is the distribution function for no trapped electrons, h^o is a localised function in the trapped particle region and f^* is a non-localised correction term of order $\varepsilon^{\frac{1}{2}}$. In terms of the current, h^o and f^* describe the reduction of the back electron current due to (a) the reduction in the number of current carrying electrons and (b) the increased friction on the passing electrons due to collisions with the trapped electrons. The functions h^o and f^* are related to f^o by eqs(56) and (60) of ref.4. Expanding f^o, h^o and f^* in terms of Legendre polynomials and writing $a_1 = \langle h^o_1 \rangle + \langle f^*_1 \rangle$, where $\langle h^o_1 \rangle$ and $\langle f^*_1 \rangle$ are the flux surface averages the first order Legendre coefficients, leads to the integro-differential equation

$$a''_1 + P(x)a'_1 + Q(x)a_1 - \frac{16}{3\pi^{\frac{1}{2}}\Lambda}\left[xI_3(x) - 1.2xI_5(x) - x^4(1-1.2x^2)(I_o(x) - I_o(\infty))\right] = R(x) \qquad (2)$$

where $x = v/v_c$ and P, Q, Λ and I_n are defined in ref.1. Equation (2) is identical to that of Cordey et al[1] for the case of no trapped particles except that the term R(x) depends on f^o_1

$$R(x) = -1.46\varepsilon^{\frac{1}{2}} f^o_1 \left[xE' + (2x^2-1)E + 2Z_{eff}x^2\right]/\Lambda x^2 \qquad (3)$$

The equation for no trapped particles was solved numerically to obtain f^o_1 using a two point boundary value code[1]. This distribution function was then used to calculate R(x) in eq(2) which was also solved numerically using the two point boundary value code. The results are shown in Fig.1 where the ratio F of the net current (fast ion plus reverse electron current) to the fast ion current is plotted against $(v_e/v_b)^2$ where v_e is the electron thermal velocity and v_b the beam velocity. Clearly small amounts of trapping ($\varepsilon \lesssim 0.1$) are sufficient to produce large changes in the net circulating current. For present day tokamak experiments the result can be expressed in the form

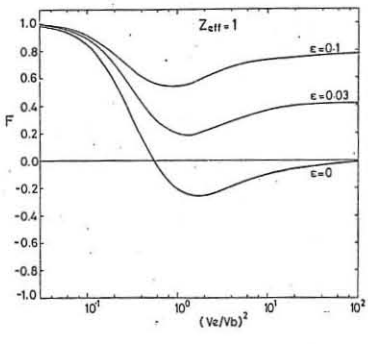

Fig.1 Ratio of net current to fast ion current as a function of v_e^2/v_b^2.

$$F = 1 - \frac{Z_b}{Z_{eff}}\left(1 + 1.2\frac{v_b^2}{v_e^2}\right) + 1.46\varepsilon^{\frac{1}{2}} A\left(Z_{eff}, \frac{v_b}{v_e}\right)\frac{Z_b}{Z_{eff}}\left(1 + 1.2\frac{v_b^2}{v_e^2}\right)$$

At high electron temperatures the function $A(Z_{eff}, 0)$ agrees to within a few per cent of that obtained from the model operator calculation of Connor and Cordey[3]. With this justification the model operator has been used to calculate the effect of trapped electrons on the current for all values of ε. Using a proceedure similar to that of Connor et al[5] the ratio F is found to be

$$F = 1 - \frac{4}{3\pi^{\frac{1}{2}}} Z_b I\left\{\int_o^\infty x^{\frac{3}{2}}\frac{\nu_{ei}}{\nu_e} e^{-x}dx + \frac{I\int_o^\infty \frac{\nu_{ee}}{\nu_e} e^{-x}dx \int_o^\infty x^{\frac{3}{2}}\frac{\nu_{ee}}{\nu_e} e^{-x}dx}{\int_o^\infty \frac{\nu_{ee}}{\nu_{ei}} e^{-x}dx - I\int_o^\infty \frac{\nu_{ee}^2}{\nu_e} e^{-x}dx}\right\} \qquad (4)$$

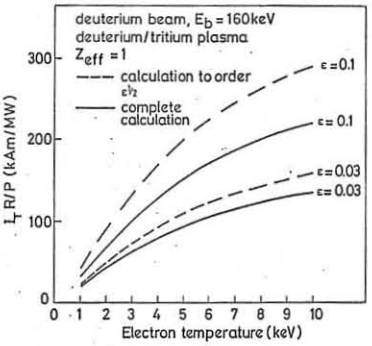

Fig.2 Comparison of the Fokker-Planck and model operator calculations of the net circulating current for deuterons injected into a deuterium/tritium plasma.

where the integral I and the collision frequencies ν_{ee} and ν_{ei} are defined in ref.5 and $\nu_e = \nu_{ee} + Z\nu_{ei}$. The integrals appearing in eq(4) have been evaluated numerically. The results have been combined with the fast ion distribution of Cordey and Haas[6] to calculate the net circulating current I_T per megawatt of neutral power P injected into a tokamak plasma of major radius R. In Fig. 2 this current is plotted against electron temperature for 160 keV deuterons injected into a deuterium/tritium plasma of density 10^{14} cm^{-3}. For comparison the results obtained with the Fokker Planck treatment to order $\varepsilon^{\frac{1}{2}}$ are also shown. For $\varepsilon = 0.1$ this latter calculation overestimates the current by about 25%. The model operator calculation has been used to obtain the neutral beam injection power required to drive the plasma currents in the PLT, JET and TFTR tokamaks, and the results are shown in Table 1. These powers are of similar magnitude to the beam heating powers for these devices.

CONCLUSION The effect of trapped electrons on beam driven currents has been obtained to order $\varepsilon^{\frac{1}{2}}$ using a Fokker-Planck calculation. It is found that the net current is a sensitive function of the inverse aspect ratio for all values of v_e/v_b. At high electron temperatures the results justify the use of a model operator to simulate electron-electron collisions and this has enabled the calculation to be extended to all values of ε.

Table 1 NEUTRAL INJECTION POWER REQUIRED FOR BEAM-DRIVEN OPERATION OF PRESENT DAY AND NEAR-TERM TOKAMAKS

	PLT (H^o, H^+)	JET (D^o, D^+-T^+)	TFTR (D^o, D^+-T^+)
$\bar{n}_e$ (10^{14} cm^{-3})	0.4	0.5	0.5
$\bar{T}_e$ (keV)	2.0	5.0	5.0
ε_o (keV)	40	160	120
Z_{eff}	2	2	2
I_p (MA)	0.45	3.0	2.5
P (MW)	4.7	24	19

REFERENCES

[1] Cordey J G, Jones E M, Start D F H, Curtis A R and Jones I P, (1979) Nucl. Fusion 19 249

[2] Start D F H, Collins P R, Jones E M, Riviere A C and Sweetman D R, (1978) Phys.Rev.Letters 40 1497

[3] Connor J W and Cordey J G (1974) Nucl. Fusion 14 185.

[4] Hazeltine R D, Hinton F L and Rosenbluth M N (1973) Phys. Fluids 16 1645

[5] Connor J W, Grimm R C, Hastie R J and Keeping P M (1973) Nucl. Fusion 13 11

[6] Cordey J G and Haas F A (1977) in Plasma Physics and Controlled Nuclear Fusion Research (Proc. 6th Int. Conf., Berchtesgaden 1976) 2 IAEA Vienna 423

EP29

Effect of Lower Hybrid Wave Turbulence on
Tearing Mode Instability

A.K. Sundaram* and A. Sen,
Physical Research Laboratory, Ahmedabad, India

In a tokamak plasma, the free energy sources associated with the current, density gradient, etc., drive a wide spectrum of instabilities in the plasma. Of these, the low frequency long wavelength MHD type waves affect the gross motion of the plasma column and in a sense determine the stability characteristics of the discharge. The higher frequency shorter wavelength fluctuations, on the other hand, influence the microscopic behavior of the plasma e.g. its heat conductivity, resistivity, viscosity, etc. It is of interest then to study the mutual interaction or the influence of one kind of wave activity on the other. In particular, we study the influence of high frequency microturbulence on the MHD activity of a tokamak plasma. In this context, we investigate the behavior of resistive tearing mode[1] (specifically for the case, m=1) in the presence of lower hybrid wave turbulence[2].

Our calculations are based on the simple MHD model for the resistive tearing mode carried out in a cylindrical geometry with an equilibrium field, $\vec{B}_0 = (0, B_\theta(r), B_z)$ and an electrostatic lower hybrid (LH) field, $\phi_0(\vec{r},t) = \sum_{\vec{k}} \phi_{\vec{k}} \exp(i\vec{k}\cdot\vec{r} - i\omega t) + c.c.$, where $(\omega,\vec{k})$ satisfies the linear lower hybrid dispersion relation, $\omega^2 = \omega_{LH}^2(1 + k_z^2 m_i/k_\perp^2 m_e)$. Assuming the level of fluctuations to be low, so that only terms to order $|\phi_k|^2$ need be retained, we consider the interactions among the low frequency tearing mode $(\Omega,\vec{q})$ and sideband LH modes at $\Omega+\omega$, $\vec{q}+\vec{k}$. The dominant nonlinear contribution to the sideband equations arises from the $(\vec{v}_T \cdot \nabla)\vec{v}_{LH}$ and the $\vec{v}_{LH} \times \vec{B}_T$ terms in the equations of motion. Here $\vec{v}_T, \vec{B}_T$ are the perturbed velocity and magnetic fields of the tearing mode and $\vec{v}_{LH}$ is the pump induced high frequency velocity. To describe the tearing mode, we use the single fluid MHD equations and the Maxwell equation. The MHD equations are derived from the two fluid model where the appropriate nonlinear coupling terms are taken into account by using the sideband equations. The predominant nonlinear coupling term is the $(\vec{v}_\perp\cdot\nabla)\vec{v}_\parallel$ term in the electron equation, where $\vec{v}_\perp$ is the $\vec{E} \times \vec{B}$ drift velocity experienced by the electrons in the LH field. Then, defining the potentials ϕ and ψ by the relations, $\vec{v}_T = \hat{z}\times\nabla\phi$, $B_T = \hat{z} \times \nabla\psi$ and seeking the mode perturbations of the type $\sim Q(r)\exp i(m\theta + q_z z - \Omega t)$, the modified set of coupled equations for the inner layer becomes

$$\phi_1'' + x\psi_1'' = \mu\phi_1''' + \nu\psi_1''' \qquad (1)$$

$$\phi_1 + (\psi_1/x) = \alpha(1+S_o/x)\,\phi_1'' + [\beta+(\bar{\eta}+S_o\beta)/x]\psi_1'' \qquad (2)$$

where primes denote the differentiation with respect to x, $\phi_1 = \phi/x_A V_A$, $\psi_1 = \psi/B_z x_A$, $\bar{\eta} = i\eta c^2/4\pi\Omega x_A^2$, $S_o = r_s/x_A$, $x = (r-r_s)/x_A$, $x_A = \Omega/q_\parallel' V_A$, $q' = (dq_\parallel/dr)_{r=r_s}$ and $q_\parallel = q_z + \frac{B_\theta(r)}{rB_z}$. Here V_A and η are the Alfven velocity and Spitzer's resistivity and r_s, the mode-rational surface. The quantities μ, ν, α and β are the turbulent contributions and will be defined later. Treating the turbulent terms perturbatively and writing $E = x\frac{d\psi_1}{dx} - \psi_1$, we obtain, from Eqs. (1) and (2), a single equation in E:

$$[f(x)E']' + (\mu-\nu/x)E' + E(1-1/x^2) = C_1 \qquad (3)$$

where $f(x) = (\bar{\eta}+S_o\beta)/x^2 + (\beta-S_o\alpha)/x - \alpha$ and C_1 is a constant. In the limit, $\mu=\nu=\alpha=\beta=0$, Eq. (3) agrees with the one derived by Hazeltine and Strauss[1] for the m=1 mode. To ensure proper matching with the outer layer solutions, we require C_1 to be zero and therefore we only need to concern ourselves with the homogeneous part of Eq. (3). We proceed to solve it by employing a variational technique[3]. Using a transformation, $E = (1/\sqrt{f})E_1 \exp\{\int(\mu - \nu/x)dx/f\}$, Eq. (3) reduces to a self adjoint form. Then, it can easily be shown that the functional

$$S = \int_{-\infty}^{\infty} dx \left\{ -\left(\frac{dE_1}{dx}\right)^2 + \left[\frac{1}{f}\left(1 - \frac{1}{x^2}\right) - \frac{1}{2}\frac{f''}{f} + \frac{1}{4}\frac{f'^2}{f^2} - \frac{1}{4}\frac{(\mu - \frac{\nu}{x})^2}{f^2} - \frac{1}{2}\frac{\nu}{x^2 f}\right] E_1^2 \right\} \qquad (4)$$

is variational, in that $\delta S = 0$ yields the equation in E_1. Choosing a trial function, $E_1 = \sqrt{f}\exp(-\lambda x^2/2)$ with $\mathrm{Re}(\lambda/x_A^2) > 0$. We obtain the function, $S(\lambda)$. Then a simultaneous solution of $S(\lambda) = \frac{dS}{d\lambda} = 0$ will now give us the dispersion relation. To obtain such a relation we need to evaluate the nonlinear terms which are proportional to a resonant term, $\frac{1}{\varepsilon_+} + \frac{1}{\varepsilon_-}$, ($\varepsilon_\pm \equiv \varepsilon(\Omega \pm \omega, \vec{q} \pm \vec{k})$ being the dielectric response function). We use the adiabatic approximations $|\vec{q}| \ll |\vec{k}|$ and $|\Omega| \ll |\omega|$ to expand $\varepsilon_\pm$ around $(\omega,\vec{k})$ and consider only the nonresonant type of interaction ($\Omega \ll \vec{q}\cdot\vec{v}_{gk}$, $\vec{v}_{gk}$ being the group velocity of LH waves). Thus, the expressions for α, β, μ and ν simplify to

$$\alpha \simeq -2i\left(\frac{m_e}{m_i}\right)\frac{q_z V_A}{\Omega\omega_e\omega_{LH}x_A}\sum_{\vec{k}}\frac{k_\perp^3}{k_z^2}\frac{c^2k_\perp^2|\phi_k|^2}{B_z^2}$$

$$\beta = -\frac{iq_z}{\bar{\Omega}\Omega_e x_A}\sum_{\vec{k}}\frac{k}{k_z}\frac{c^2k_\perp^2|\phi_k|^2}{B_z^2} \qquad (5)$$

$$\mu = -(\omega_{pi}/Cq_z)\alpha \quad \nu \simeq -(\omega_{pi}/Cq_z)\beta$$

With these simplifications, the dispersion relation will now be obtained in two convenient limits.

Case (i): For $|S_o\sqrt{\lambda}| > 1$, the dispersion relation takes the simple form

$$\left\{1-(\beta/2S_o)(\omega_{pi}^2/c^2q_z^2)\right\}\left\{1+\bar{\eta}+\beta(S_o - \omega_{pi}/Cq_z)\right\} = 0 \qquad (6)$$

Both roots of Eq. (6) are oscillating damped modes. The root corresponding to the first factor is a heavily damped quasimode while the second factor yields the turbulence modified version of the tearing mode (for β=0), one can recover the classical result[1], $\gamma = (\eta c^2/4\pi)^{1/3}(q_\parallel' v_A)^{2/3}$ from it). Setting $\Omega = \Omega_R + i\gamma$ and assuming $\gamma \ll \Omega_R$ the second factor can be solved to give

$$\gamma \simeq (q_\parallel' v_A c)^{2/3}\left\{(\eta/4\pi) - (q_z r_s/\Omega_e)\sum_{\vec{k}}\frac{k_\perp^3|\phi_k|^2}{k_z B_z^2}\right\}^{1/3} \qquad (7)$$

The turbulent term in γ easily exceeds $\eta/4\pi$ for small levels of fluctuations ($W_k/\eta_0 T \sim 10^{-6}$) and for typical tokamak parameters (Te ~ 1kev, B = 25KG, a/R ~ 1/3). Thus the tearing mode is stabilized in this limit and in addition has a real frequency induced by the fluctuations.

Case (ii): Next, the limit $|S_o\sqrt{\lambda}| < 1$ corresponds to a broad spatial extent of the eigenmode (wider than x_A) and the dispersion relation becomes

$$1 + \frac{\omega_{pi}^2}{2c^2q_z^2}\alpha = 0,\quad 1 + \bar{\eta} + \beta\{S_o(1-\omega_{pi}^2/c^2q_z^2) - (\omega_{pi}/cq_z)\} = 0 \qquad (8)$$

The first equation yields a new unstable mode with growth rate

$$\gamma \simeq (q_\parallel' v_A^2/2)^{1/2}\left\{(m_e/m_i)(\omega_{LH}/\Omega_e)\sum\frac{k_\perp^3}{k_z^2 q_z}\frac{k_\perp^2|\phi_k|^2}{B_z^2}\right\}^{1/2} \qquad (9)$$

and a comparable real frequency. This is again a quasimode which is solely driven by the fluctuations and it grows at a rate comparable to the classical resistive growth rate for moderate levels of fluctuations. From the second equation, we get

$$\gamma \simeq (q_\parallel' v_A c)^{2/3}\left\{\eta/4\pi - (q_s r_s/\Omega_e)(1-\omega_{pi}^2/c^2q^2)\sum_{\vec{k}}\frac{k_\perp^3|\phi_k|^2}{k_z B_z^2}\right\}^{1/3} \qquad (10)$$

The growth rate is similar to the one derived in the previous limit (Eq. (7) except for the factor $(1-\omega_{pi}^2/c^2q_z^2)$ multiplying the $q_z r_s$ term. Thus if $\omega_{pi}/cq_z < 1$, this again leads to a damped mode and in this case only the slowly growing quasimode can exist. For $\omega_{pi}/cq_z > 1$, however, the mode can become unstable and assume a large growth rate due to the turbulent contribution. Since $\omega_{pi}/cq_z \sim 4.4 \times 10^{-8} R\sqrt{n_0}$, where R is the major radius, this condition is easily satisfied for moderate sized machines (R ~ 30cms) and typical tokamak densities of $\sim 10^{14}\,cm^{-3}$. For $W_k/\eta_0 T \sim 10^{-6}$, taking $q_\parallel' \sim a^{-2}$ and using the parameters quoted earlier, the mode growth rate is of the order of $\sim 10^6\,sec^{-1}$ with a correspondingly large real frequency. The growth rate time is thus comparable to disruptive time scales for rather modest turbulence levels.

To summarize, we have discussed an important nonlinear effect that significantly influences the evolution of tearing modes. Physically, the random spectrum of these fluctuations act as pump waves which can parametrically excite or suppress the tearing modes through the nonlinear ponderomotive force effect.

*Presently at Fusion Research Center, The University of Texas at Austin

1. R.D. Hazeltine and H.R. Strauss, Phys. Fluids 21, 1007(1978).
2. A.A. Oomens et. al., Phys. Rev. Lett. 36,255(1976); A.T. Lin and J.M. Dawson, Phys. Fluids 21, 109(1978).
3. R.D. Hazeltine and D.W. Ross, Phys. Fluids 21, 1140(1978).

Numerical Study of the ideal-MHD Stability of Spheromaks

P. Gautier, R. Gruber, F. Troyon
Centre de Recherches en Physique des Plasmas - EPFL Lausanne
Association "Confédération Suisse - EURATOM".

W. Kerner, K. Lackner, W. Schneider
Max-Planck-Institut für Plasmaphysik.

Abstract : The ideal MHD stability of a family of hollow oblate spheromaks is numerically studied. The maximum value of β is obtained by shaping the force-free current such that q on axis is 1 and by surrounding the plasma with a shell at a distance of the order of .2 to .35 of the plasma radius. The limiting β increases with the size of the hole.

A spheromak is defined here as an axisymmetric equilibrium in which the toroidal field vanishes at the plasma surface (1). We study numerically the ideal MHD stability of a class of spheromaks to extend the analytic results reported in (1). This family is caracterized by the shape of the plasma surface, given in the usual cylindrical coordinate system r, z, ϕ,

$$\frac{z^2}{r^2+z^2}\left\{ J_{3/2}(\sqrt{r^2+z^2}) + \varepsilon \frac{4r^2-z^2}{r^2+z^2} J_{5/2}(\sqrt{r^2+z^2}) \right\} = \delta,$$

where ε and δ (excluded flux) are free parameters which fix the elongation and the size of the central hole (aspect ratio), and by the two source functions, $T\frac{dT}{d\psi}$ and $\frac{dp}{d\psi}$, in the Grad-Shafranov equation. For the toroidal flux, we choose

$$T^2(\psi) = T_o^2 \hat{\psi} (1+a\hat{\psi}),$$
$$\hat{\psi} \equiv \psi - \psi_s,$$

where ψ_s is the value of the flux at the surface, and T_o a normalizing factor which enters only as a multiplicative constant in the growthrate. The only free parameter is a, which caracterizes the force-free current profile. At low β values, the contribution to the current of the second source term $dp/d\psi$ is very small so that the toroidal current profile, and thus the q profile, is essentially fixed by the parameter a. Increasing a leads to a hollowing of the current profile and to a corresponding increase of q_o. A typical current profile and the corresponding q profile are shown in fig. 1. The original spheromak is recovered for ε=0, δ=0 and a=0, which gives a spherical plasma surface. A positive ε elongates the plasma while a negative ε compresses the plasma into an oblate ellipsoid. For δ≠0 the topology of the plasma changes into a toroidal configuration with a hole on the main axis, the size of which increases with δ.
In reference (1) it is shown that only an oblate spheromak can be stable against internal modes. This result is obtained by an analytic treatment limited to δ=0, ε<<1, a=0 and p≡0. We have verified it numerically with a small hole (δ=0.05) and assume it is true in all cases.
Our study is limited to a family of oblimaks with ε=-.3, varying only δ and a. All the calculations have been done with the spectral code ERATO.

Internal modes stability

As seen before, oblimaks with a=0 and $\frac{dp}{d\psi}$=0 are stable. The q profile is flat in the center and drops to zero at the edge. On axis, $q \equiv q_o$, is always less than 1. A pressure $dp/d\psi \neq 0$ may introduce instabilities. The Mercier criterion can be written as

$$M_1(\psi) + \frac{dp}{d\psi} M_2(\psi) > 0$$

where M_1 and M_2 are flux averages which depend weakly on $\frac{dp}{d\psi}$ as long as β<<1 and do not vanish in the limit $dp/d\psi$=0. For a=0, $M_2(\psi)>0$ and since $M_1(\psi)>0$ the Mercier criterion provides a pressure gradient limit

$$\frac{dp}{d\psi} > - M_1/M_2.$$

This limit vanishes on the axis linearly with ψ and increases monotonically towards the edge. An integration gives the limiting value for β (1).
We now introduce the additional term a in the force-free current. Increasing a, and thus q_o, decreases $M_2(\psi)$, giving a higher limiting value of β. When q_o becomes larger than 1, M_2 changes sign in the vicinity of the axis, and if a and q_o are further increased the Mercier criterion does not provide a β limitation. The ballooning criterion is in principle more stringent than Mercier, coinciding with it on the magnetic axis. We have not found, up to the highest values of β tested, any ballooning instabilities beyond the Mercier limit, with an integration range of 80 π.
The upper limit on a and q_o comes from an internal n=1 kink instability. For q_o>1, the singular surface q=1 lies in the plasma and an internal kink appears localized within the q=1 surface. The exact value of q_o corresponding to the onset of this instability is close to 1 but we cannot assert that it is exactly 1. It is sufficiently close to the value where $M_2(0)$ changes sign to consider them as identical in which case there is a maximum value of β which can be stably confined : choose a such that q_o=1, and $\frac{dp}{d\psi}$ such that Mercier is marginal everywhere. For technical reasons we have represented $dp/d\psi$ by a polynomial expression (ψ=0 on axis)

$$\frac{dp}{d\psi} = -\alpha_1 \psi$$

and adjusted α_1 to satisfy Mercier everywhere. Our β values are then underestimated. Figure 2 shows, for a particular case, the comparison between the value of $dp/d\psi$ which would make Mercier marginal and the optimized analytic profile. Figure 3 shows the optimized value of β as a function of the size of the hole δ. We do not know yet how it varies with the elongation ε.

Free boundary modes

Without a shell all the equilibria considered are unstable to external kinks. For the optimized equilibria found above we have verified their stability with ERATO for n=0,1,2,3 and 4 as the shell is progressively moved away from the plasma surface. The mode n=1 is the first to become unstable. The critical distance is between .20 and .40 of the plasma radius. Because of the non-vanishing current density at the edge, free boundary high-n modes are expected to be always unstable. A smoothing of the current discontinuity should easily solve this problem.

This work has been suported in part by the Swiss National Science Foundation.

Reference

(1) 'Low-Aspect-Ratio Limit of the Toroidal Reactor : The Spheromak'; M.N. Bussac, H.P. Furth, M. Okabayshi, M.N. Rosenbluth, and A.M. Todd, Plasma Physics and Controlled Nuclear Fusion Research (Proc. 7th Int. Conf. Innsbruck, 1978) IAEA-CN-37/X1.

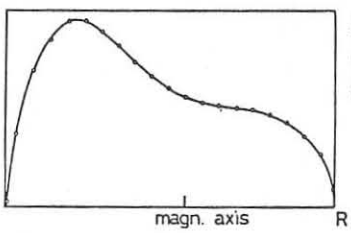

Fig. 1A : Typical profile (ε=-.3, δ=.2) of the toroidal current density (arbitrary units) across the mid plane Z = 0.

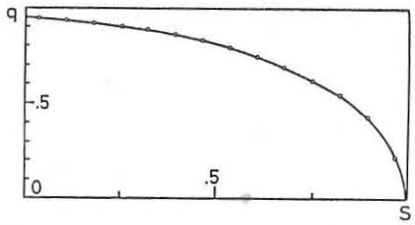

Fig. 1B : Corresponding q profile ($s = \sqrt{\frac{\psi}{\psi_s}}$).

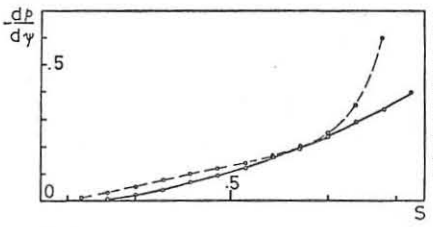

Fig. 2 : Comparison between the pressure gradient which would make Mercier criterion marginal everywhere (---) and the optimized analytic expression for which Mercier is marginal around s=.7 (——).

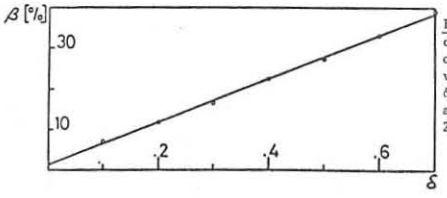

Fig. 3 : The dependence of the average optimized β value versus δ.
δ=.7 corresponds to an aspect ratio of 2.4.

EP31

Studies of Resonant Absorption of Alfvén Waves by Means of an Evolution Code

B. Balet, K. Appert, R. Gruber, R. Keller, F. Troyon, and J. Vaclavik

Centre de Recherches en Physique des Plasmas
Ecole Polytechnique Fédérale de Lausanne, Association Suisse - Euratom
21, Av. des Bains, CH-1007 Lausanne / Switzerland

Abstract : An evolution code based on well known spectral stability codes is described. Its validity for an excitation in the Alfvén continuum is discussed. The energy build-up and the spatial repartition of the energy in Alfvén resonant absorption heating is considered.

In recent years much progress has been made in numerical methods which are applicable to the ideal MHD stability problem in one and two dimensions {1, 2}.

$$\rho \ddot{\underline{\xi}} = \underline{F}(\underline{\xi}) \quad , \tag{1}$$

where ρ is the plasma mass density, $\underline{\xi} = (\xi_r, \xi_\theta, \xi_z)$ the displacement from the equilibrium and $\underline{F}$ the ideal MHD restoring force. In the so-called spectral codes use is made of sophisticated finite element methods for the discretization of eq. (1) or rather its corresponding eigenvalue problem. The resulting equation has the form

$$-\omega^2 \underline{\underline{B}} \cdot \underline{x} = \underline{\underline{A}} \cdot \underline{x} \quad . \tag{2}$$

In the above $\underline{x}$ is the vector representing the ensemble of all nodal values of $\underline{\xi}$ on a given spatial mesh. $\underline{\underline{B}}$ and $\underline{\underline{A}}$ represent the mass and the potential energy matrix, respectively. The idea for the evolution code was then to use the entire structure of the spectral codes by just stepping the equation

$$\underline{\underline{B}} \cdot \ddot{\underline{x}} = \underline{\underline{A}} \cdot \underline{x} + \underline{s}(t) \tag{3}$$

ahead in time where $\underline{s}(t) = \sin \omega_o t$ represents a source term which models a current in an antenna situated in the vacuum between the plasma and an outer conducting wall.

The one-dimensional spectral code THALIA {3} which solves eq. (2) for cylindrically-symmetric equilibria has been modified to solve eq. (3). For the purpose of this paper it has been applied to an equilibrium characterized by $B_z = 1$, $B_\theta/r = .3 - .3r^2 + .1r^4$ and $\rho = 1.01 - r^2$ in dimensionless units, where the plasma radius is unity. B_z and B_θ are the magnetic field components. Zero pressure on the plasma boundary results in a β-value of 5% on the axis. The conducting wall is at 1.5. The azimuthal and longitudinal wave numbers m and k of the plasma motion, $\xi \sim \exp(im\theta + ikz)$, are input values given, physically, by the antenna structure. Toroidal geometry can be simulated by expressing the longitudinal wave number in terms of the toroidal wave number n and the major radius R : $k = n/R = 0.3$.

After some initial checks where global modes in the fast magnetosonic branch have been excited, attention has been turned towards excitation with frequencies in the continuous Alfvén branch ω_A. As it has been shown in {1} the finite element discretization leads to a dense discrete spectrum as approximation for the continuum. The frequency spacing $\Delta\omega$ is directly given by the spacing of the spatial mesh Δr according to

$$\rho\omega_A^2 = (kB_z + mB_\theta/r)^2 \quad . \tag{4}$$

Each spatial mesh point has a corresponding discrete frequency and a pseudo-singular eigenmode peaking on this mesh-point. It may be anticipated that the code should correctly model the physical evolution up to times of the order $2\pi/\Delta\omega$. Later the discrete structure of the continuum should manifest itself by giving wrong results.

A typical evolution is shown in Fig. 1. The parameters chosen are m = 1, k = 0.3 and $\omega_o = .6$ leading to a resonant surface at $r_s = .32$. The maximum excitation does not occur initially at r_s as one might expect but progresses slowly towards it. The nearer r_s lies to the axis, the longer it takes the energy to get there.

According to the stationary calculations {4} which predict a simple resistive impedance for a plasma excited in a continuum, we should find that the energy stored in the plasma motion on the average increases linearly in time. This is exactly the case for times $t < 2\pi/\Delta\omega$, where $\Delta\omega$ has to be taken at the resonant surface for a non-equidistant ω-mesh. During this time the amplitude of ξ_r at the plasma-vacuum-interface stays constant. At later times ξ_r grows linearly and eventually starts to beat, showing that at these times the numerical "continuum" is represented by only one resonant or nearly resonant mode. The energy stored in the plasma motion accordingly shows a non-physicel quadratic growth when the pump frequency ω_o coincides with one of the discrete Alfvén frequencies. This validity limit of our code is a general limit which cannot be overcome by any evolution code which is based on a spatial discretization.

By taking the slope $W = dE/dt$ of the energy during its linear growth we obtain the power W delivered to the plasma. In Fig. 2 the convergence properties of this quantity are shown for a varying number N of mesh points. In this calculation $\omega_o = .98$ with $r_s = .9$ as a consequence. It is satisfying to see that using a coarse mesh such as the one with N = 10, the result deviates not more than 15% from the exact value.

In Fig. 3 the ratio of the delivered power W over the square of the radial displacement at the boundary ξ_{r_r} is shown. This quantity is a measure of the quality of the coupling. We also show the prediction of a simple theoretical model {5} which assumes that ξ_r on the axis equals ξ_r on the boundary for m = 1. This assumption is verified numerically at the point $r_s = 0.85$, where the results coincide. This graph tells us that resonant absorption of Alfvén waves permits one to heat the interior of the plasma at the expense, however, of a lower coupling than in the case of "skin"-heating.

In Fig. 4 we consider the absorption in the case of m = 2 where for low frequencies two resonant surfaces are present. This fact is demonstrated in the lower part of the figure where the local Alfvén frequency is plotted versus radius. In the upper part we show the coupling parameter W/ξ_r^2 separately evaluated for the two radial intervals $0 \leq r \leq .8$ and $.8 \leq r \leq 1$.

The results for four different pumping frequencies are shown. First of all one remarks that the m = 2 excitation, at least in the equilibrium chosen, does not couple as well to the interior of the plasma as does the m = 1 excitation. Secondly one can see that the presence of an outer resonant layer does not preclude the inner layer from being heated. This result may give rise to a certain optimism concerning the toroidal case where several layers are always present.

This work was supported by the Swiss National Science Foundation.

REFERENCES

{1} K. Appert et al. J. Comp. Phys. 18 (1975) 284

{2} R. Gruber, J. Comp. Phys. 26 (1978) 379

{3} K. Appert et al., Comp. Phys. Comm. 10 (1975) 11

{4} J. Tataronis and W. Grossmann, Nucl. Fusion 16 (1975) 87

{5} R. Keller, LRP 104/76, CRPP Lausanne, June 1976

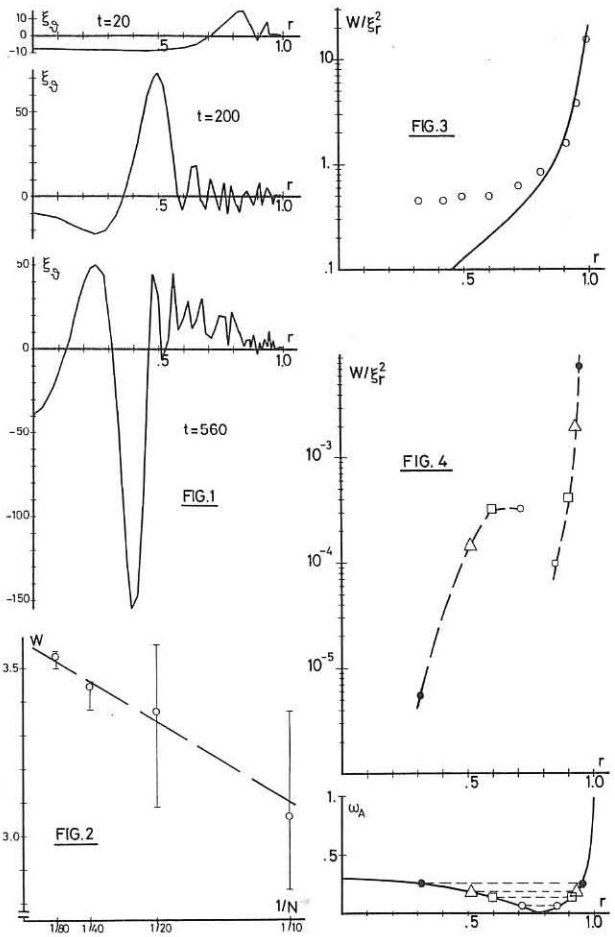

EP32

FREE-BOUNDARY EQUILIBRIUM OF A HIGH-β TOKAMAK

J.P. Goedbloed
Association Euratom-FOM, FOM-Instituut voor Plasmafysica
Rijnhuizen, Jutphaas, The Netherlands

ABSTRACT. A fast and accurate method for the solution of free-boundary equilibria is obtained.

The problem of global equilibrium and stability of sharp-boundary high-β tokamaks has been studied previously for arbitrary plasma cross-sections of prescribed shape.[1-4] In these studies the equilibrium was completely fixed by giving the value of the parameter $\varepsilon\beta_p \equiv 2p/\langle B_p\rangle^2$ and the shape of the plasma surface on which skin-currents are flowing. The equilibrium problem in that case consists in solving Laplace's equation on a two-dimensional domain with given values of the flux function and its normal derivative at the plasma boundary. This problem is ill-posed, but it leads to a well-defined equilibrium limit:

$$\varepsilon\beta_{p,crit} = \frac{1}{2}\langle\sqrt{(x(\theta)-\Delta)/a+1}\rangle^{-2}. \qquad (1)$$

Here, the brackets indicate averaging with respect to arc length, $x(\theta)$ is the horizontal distance of a point on the cross-section to the centre of the tube, Δ is the shift of the centre of the plasma, and a is the half-width. This limit on the poloidal beta arises as a result of the existence of a separatrix of the vacuum magnetic field, which has reached the plasma surface when $\varepsilon\beta_p$ has the value given in Eq. (1).

The existence of a separatrix, the location of the associated stagnation points, and the specific form of Eq. (1) are due to the fact that the shape of the plasma cross-section is imposed, which leads to an ill-posed problem. This shows up in a very sensitive dependence of the location of the stagnation points on the specific form of the cross-section chosen: small changes in the shape lead to big changes in the location of the stagnation points and, hence, in the value of the rotational transform parameter q. To remedy the latter pathology, in a previous publication[4] we already advocated the replacement of the parameter q by a parameter q*, measuring the toroidal current. The purpose of the present investigation is to remove the ill-posed character of the problem altogether by turning to the original physical question, viz. the determination of the plasma cross-section for a given shape of the outer conducting wall and to investigate whether and how the poloidal beta is limited in that case.

For a circular wall this free-boundary problem may be cast in the form of an integral equation for the poloidal field at the plasma vacuum boundary:

$$\oint \left[G(g(\theta),\theta;g(\theta'),\theta') + C\right]u(\theta')d\theta' = 0. \qquad (2)$$

The kernel is the Green's function $G(r,\theta;r',\theta')$ for a circular domain evaluated at the plasma boundary $r = g(\theta)$:

$$G(\theta,\theta') = \frac{1}{2\pi}\ln\sqrt{\frac{g^2(\theta)-2g(\theta)g(\theta')\cos(\theta-\theta')+g^2(\theta')}{1-2g(\theta)g(\theta')\cos(\theta-\theta')+g^2(\theta)g^2(\theta')}}. \qquad (3)$$

The function $u(\theta)$ provides the angular dependence of the poloidal field $b_p(\theta)$:

$$u(\theta) = \sqrt{g^2+\dot{g}^2}\,\sqrt{1+\tfrac{1}{4}k^2(g\cos\theta-\Delta-a)/a} \sim \sqrt{g^2+\dot{g}^2}\,b_p(\theta). \qquad (4)$$

Here, k^2 is a parameter of unit range associated with the poloidal beta:

$$\varepsilon\beta_p = \tfrac{1}{4}k^2\oint\sqrt{g^2+\dot{g}^2}\,d\theta/\oint u\,d\theta. \qquad (5)$$

The constant C turns out to be an eigenvalue parameter determined by periodicity requirements on $u(\theta)$.

The problem consists of determining the shape function $r = g(\theta)$ such that the solution to the integral equation (2) provides the correct angular dependence of $u(\theta)$ given in Eq. (4), i.e., the kernel of the integral equation is unknown here. Thus, although Eq. (2) is linear, we still wind up with a non-linear problem for which no guaranteed method of solution exists.

The solution $r = g(\theta)$ is fixed by fixing the points $g(0) = \Delta + a$ and $g(\pi) = \Delta - a$. The parameter k^2 is then determined, so that the problem only has two free parameters, viz. a and Δ (or k^2, or $\varepsilon\beta_p$), corresponding to freedom in choice of the plasma area and of the poloidal beta.

Previous investigations of the free-boundary problem[5-7] were based on an iterative procedure where the equilibrium equations were solved by guessing the shape of the plasma boundary. At each step in the iterative procedure the boundary is then displaced with an amount proportional to the unbalance in the total pressure at the boundary. This method turned out to be extremely inaccurate and often led to divergence. Since we also intend to investigate the stability of these equilibria we, a priori, decreed that the relative error in the field should not exceed 10^{-5}. This accuracy could not be reached with this method.

A successful modification of the problem stated in Eqs. (2) - (4) consists of applying a conformal mapping $z = z(w)$ from the $z = re^{i\theta}$-plane to the $w = se^{it}$-plane, in such a way that the image of the wall is a circle and the image of the plasma boundary becomes a curve centred around the origin. Such a mapping conserves the form of the Eqs. (2) and (3). For a circular wall it is provided by the simple bilinear transformation $z = (w+\delta)/(1+\delta w)$, where the interior point $z = \delta$ of the plasma is mapped onto the origin and the fixed points $z = \Delta \pm a$ transform into the fixed points $w = \pm\rho$.

The technique of conformal mapping also provides us with a simple method to treat free-boundary equilibria for walls of arbitrary cross-section. All that is required there is the contruction of a conformal mapping $z = z(w)$ of an arbitrary domain onto the unit disk. The existence of such a mapping is guaranteed by the Riemann mapping theorem, whereas the explicit numerical construction may be obtained by several methods.[8] We have developed a new method which is also exploited in the stability analysis.

After the conformal transformation the problem is ideally suited for a Fourier representation in the new angle t, where we have to keep only very few harmonics (typically in the order of 10) to accurately represent the field. This method also exhibits the reason for the above-mentioned failure to provide accurate answers. It turns out that, in the iteration procedure, the response to changes in the higher harmonics of the boundary is much higher than that due to the lower harmonics. If all harmonics are treated on an equal footing this frequently leads to divergence. By damping the response to the higher harmonics artificially through a judiciously chosen damping factor a fastly converging scheme was obtained, where the required accuracy of 10^{-5} was reached in 10 - 15 iterations.

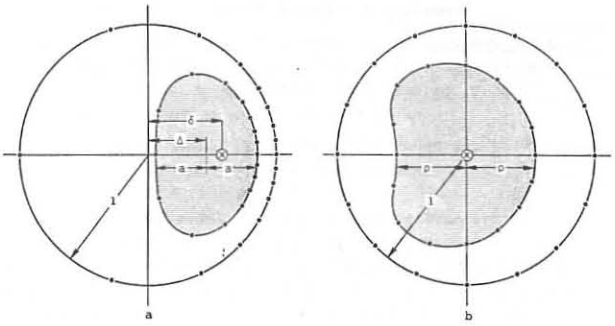

Fig. 1. Free-boundary equilibrium for a = .4, Δ = .45, for which $\varepsilon\beta_p$ = .595.
a. Original z-plane, b. image w-plane.

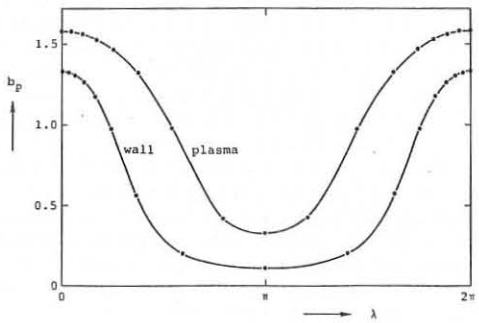

Fig. 2. Poloidal field as a function of arclength λ.

In Fig. 1 a typical example is exhibited of a free-boundary equilibrium in a range of $\varepsilon\beta_p$ where a separatrix would be close to the wall in the original ill-posed problem leading to Eq. (1). We have also indicated the computational grid, which is equidistant in the angle t. (Only 16 of the 128 points that were used are shown.) It is clear that the conformal mapping leads to a distribution of angular grid-points that is quite optimal for this problem.

The variation of the poloidal field at the plasma boundary and at the wall is shown in Fig. 2. If one fixes the parameter a and increases Δ (i.e., $\varepsilon\beta_p$) the fields develop an ever wider minimum on the inside of the torus so that all the poloidal field is squashed to the outside of the torus. In the fixed-boundary problem, increasing $\varepsilon\beta_p$ leads to an inward motion of the separatrix untill the stagnation point hits the plasma boundary. It is an easy matter to show that this cannot happen in the free-boundary case, since b_p at the wall cannot develop a zero as long as b_p is still positive definite at the plasma boundary. Hence, a separatrix could only suddenly appear at the plasma boundary without having arrived there by a continuous motion from the outside. Unfortunately, whether this actually happens could not be traced in the computation because the obtained accuracy is rapidly lost when Δ is increased beyond the value given in Fig. 1. So, the question raised at the beginning of this paper is not definitely answered, but on the way to an answer we did obtain a rapid and accurate method to find high-beta free-boundary equilibria.

ACKNOWLEDGEMENT. This work was supported by FOM, ZWO, and Euratom.

REFERENCES:

1. J.P. Freidberg and F.A. Haas, Phys. Fluids 16 (1973) 1909; 17 (1974) 440.
2. L.E. Zakharov. Nucl. Fusion 13 (1973) 595.
3. M. Kito and T. Honma, J. Phys. Soc. Jap. 41 (1976) 1749.
4. D.A. D'Ippolito, J.P. Freidberg, J.P. Goedbloed, and J. Rem, Phys. Fluids 21 (1978) 1600.
5. E. Martensen, Acta Math. (1963) 75.
6. D.C. Stevens, Phys. Fluids 17 (1974) 222.
7. B. Steffen, dissertation Göttingen (1975).
8. R.D. Richtmeyer, private communication.

EP33

Numerical Studies of MHD Instabilities*

J. L. Johnson,† M. S. Chance, R. L. Dewar, A. H. Glasser, R. C. Grimm, J. M. Greene, S. C. Jardin, J. Manickam, A. E. Miller, D. A. Monticello, A. M. M. Todd, K. E. Weimer, and R. B. White

Plasma Physics Laboratory, Princeton University
Princeton, New Jersey 08544 USA

At relatively high values of β, pressure-driven ballooning modes are not radially localized, but form channels leading from the center of the plasma to the edge.[1] This observation has motivated much computational effort[2] and has led to significant analytic advances in the limit of large azimuthal mode number.[3] Recent analyses using analytic equilibrium models with circular but nonconcentric magnetic surfaces and working near the magnetic axis have indicated that at sufficiently high β these high-n ballooning modes become stabilized.[4] The purpose of this communication is to discuss some numerical calculations that confirm this observation using numerically generated equilibria which show that the stabilization is not due to simplifications associated with the model, and to study ways of using this stabilization mechanism for future tokamak design. Some of this work has already been published.[5]

The mechanism responsible for this second region of stability can be understood with a rough model where instability should be expected when the energy associated with field line curvature, $p\xi^2/aR$, is larger than the magnetic field bending energy, $B^2\xi^2/L^2$. Here p/a measures the pressure gradient, R the major radius, and L the connection length or the distance along a field line between regions of favorable and unfavorable curvature. For the standard low-β tokamak ordering $L \sim qR$ with q the safety factor, we find instability if $\beta > a/q^2R$. At high β the Shafranov shift moves the magnetic axis out close to the plasma surface, drastically increasing the poloidal field locally, and shortening the connection length. Thus, at some value of β, field line tension introduces a new stable region. Since this effect is exaggerated by the circular cross section model, it is important that verification be made with exact numerical equilibria.

This was first done using a large aspect ratio tokamak approximation to obtain equilibria and the localized ballooning mode theory to investigate stability. Typical results are given in Fig. 1, where we plot the unstable region for $n \to \infty$ modes for a low shear model where $q_a/q_o \sim 2$ and p varies as $(\psi - \psi_a)^4$ with ψ the toroidal flux.

Comparison with exact numerical equilibria using the PEST code showed good agreement with this model. Results for a series with $1 < q < 2.5$ and $p = p_o\{[1 + 3(\psi - \psi_a)]^{1/2} - 1\}^4$ are given in Fig. 2. Here the growth rates were evaluated using a perfectly conducting surface boundary condition rather than with the localized ballooning mode model.

Efforts have been made to get into the high-β stable regime from a stable low pressure system through a flux-conserving tokamak scheme by increasing the pressure in such a way that the localized ballooning mode criterion shows at least marginal stability everywhere. This has not been successful for high shear systems with a circular outer plasma surface, but such a transition can easily be made in reasonably D-shaped configurations.

Stability in this high-β regime has only been demonstrated for perturbations where the plasma surface is held fixed. Growth rates for both fixed and free boundary modes are plotted in Fig. 3 for the same parameters as in Fig. 1. The unstable growth rates tend to saturate as β increases. The modes can be stabilized with a conducting wall reasonably far from the plasma.

Since more control of the free boundary modes may be needed, it is useful to investigate the effect of changing the shape of the current distribution on the stable regions that occur near rational values of q_a. For sufficiently low β, toroidicity has little effect on the width of these windows. As shown in Fig. 4, increasing β rapidly closes the stable windows. The width of the stable window and the pressure needed to close it are functions of the current profile and the aspect ratio. Peaking the profile increases the region of stability, as does lowering of the aspect ratio. Careful shaping of the current could further improve the critical β for maintaining stability up to moderate β values as noted above.

---

*Work supported by the United States Department of Energy Contract No. EY-76-C-02-3073.

†On loan from Westinghouse Reasearch and Development Center, Pittsburgh, PA, USA.

1. A. M. M. Todd et al., Phys. Rev. Lett. 38, 826 (1977).
2. A. M. M. Todd et al., Nucl. Fusion 19, 743 (1979).
3. D. Dobrott et al., Phys. Rev. Lett. 39, 943 (1977); J. W. Connor et al., Phys. Rev. Lett. 40, 396 (1978).
4. C. Mercier, IAEA 1978 Innsbruck meeting, paper CN-37-p-3-2; L. E. Zakharov, IAEA 1978 Innsbruck meeting CN-37-p-3-1; B. Coppi et al., Nucl. Fusion 19, 715 (1979).
5. H. Strauss et al., Princeton Plasma Physics Laboratory Report PPPL-1535, April, 1979.

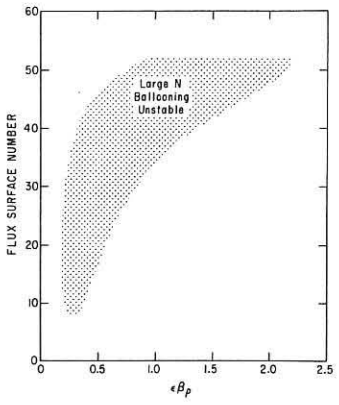

Fig. 1

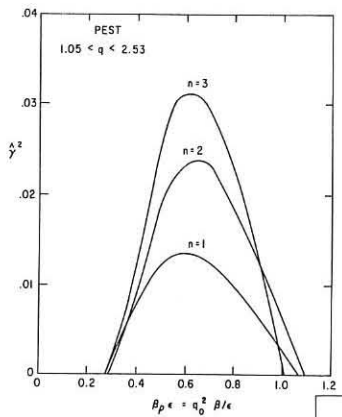

Fig. 2

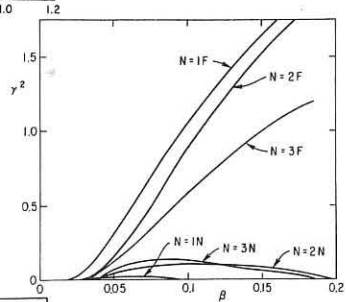

Fig. 3

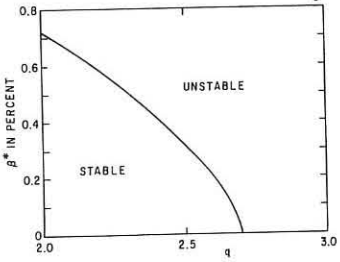

Fig. 4

STUDIES OF PARTICLE AND ENERGY BALANCE OF IONS IN TOKAMAKS T-4 AND TUMAN-2a BY METHODS OF CORPUSCULAR PLASMA DIAGNOSTICS.

V.V.Afrosimov, E.L.Berezovsky, A.B.Izvozchikov, A.I.Kislyakov, M.P.Petrov, A.V.Khudoleyev

Ioffe Physico-Technical Institute, USSR Academy of Sciences, Leningrad.

Abstract. Using experimental data obtained on T-4 and Tuman-2a with the help of the complex methods of corpuscular plasma diagnostics an analysis of particle and energy balance of ions is carried out through the numerical solution of transfer equations.

Diagnostic complexes installed in T-4 and Tuman-2a permitted to obtain data on the space distribution of density $n_p(r)$ and temperature $T_i(r)$ of plasma ions. In T-4 these measurements were carried out by analyzing the flux of fast atoms resulting from charge-exchange of the plasma ions on the artificial taget produced by injection of fast deuterium atoms into the hydrogen plasma [1]. Energy analysis of spectra of fast charge-exchange atoms enables to obtain distribution $T_i(r)$ presented in Fig. 1-a. By the value of atomic fluxes formed on the artificial target local ion densities were determined (Fig. 1-b). Absolute values of ion densities were found from the value of atomic beam attenuation at passing through the plasma.

Diagnostic devices in Tuman-2a enable to simultaneously carry out multichord probing of the plasma column by fast atom beams as well as multichord analysis of charge-exchange atomic beams from the plasma [2]. Registration of atomic fluxes was made in the direction perpendicular to the tore equator plane. In this case essentially decreased the influence of the trapped ions drift on the shape of radial ion temperature profile. The obtained distributions $T_i(r)$ and $n_pL(r)$ are presented in Fig. 2-a,b. It should be noted that in tokamak Tuman-2a a short plateau of plasma density (~ 2 msec) was observed after which density drop began proceeding untill the end of the discharge.

Numerical solution of particle and energy transfer equations was used for analyzing the results obtained. To determine diffusion coefficient D on tokamak Tuman-2a we have considered non-stationary diffusion equation

$$\frac{\partial n}{\partial t} + \frac{1}{r}\frac{\partial}{\partial r}\left(r D \frac{\partial n}{\partial r}\right) = A_i$$

where A_i is the source of ions determined by ionization of the flux of atoms from the wall. The flux value was obtained from the absolute values of the charge-exchange atomic flux from the plasma. For T-4 a stationary type of this equation was used as within the operating conditions the main part of the discharge took place at a constant plasma density. As a diffusion coefficient D pseudoclassical expression was used:

$$D^{pseudo} = k \cdot 3.3\cdot 10^{-5} \ln\Lambda \, \frac{n q^2 R^2}{T_e^{1/2} r^2 B_t^2} Z_{eff}, \quad k = 0.3 \div 3$$

The calculation showed that the best agreement with the experiment (dashed zones in Fig.1-b and 2-b whose width is defined by the error in determining the values of the atomic flux from the wall $n_0(a)$, Z_{eff} and $q(a)$) for the two devices is observed at $k \approx 1$.

Stationary heat equation was used to analyze the energy balance of ions

$$\frac{1}{r}\frac{\partial}{\partial r}\left(n_p r \chi_i \frac{\partial T_i}{\partial r}\right) = Q_{ei} - Q_c - Q_D$$

in which the left part represents the heat losses due to heat conductivity, Q_{ei} is heat transfer from electrons to ions and Q_c and Q_D are heat losses due to charge-exchange and diffusion, respectively.

Neoclassical coefficients in the form given in [3] were used as heat conductivity coefficients

The calculated ion temperature profiles are given in Fig. 1-a and 2-a as dashed zones.

In Fig.1-b and 2-b are presented the calculated values of power densities Q and full power flow P for the cylinder with radius of heating and heat losses due to different mechanisms. As is seen for both the devices in the main part of the plasma column heat losses by ions are determined by the heat conductivity and only in the plasma periphery at $r/a > 0.7$ the main role in the heat balance is played by charge-exchange and diffusion.

Thus, application of complex methods of corpuscular diagnostics permitted to obtain space distributions of density and temperature of plasma ions and to minimize the scope of the hypothetical data necessary for numerical simulation of transfer processes in plasma.

The analysis of particle and energy balance of ions showed that for devices with various plasma parameters particle transfer is determined by the pseudoclassical diffusion with the same adjusting coefficient $k \approx 1$. At the same time heat transfer is of classical character defined by energy transfer from electrons to ions at Coulomb collisions and heat loss due to neoclassical heat conductivity in the major portion of the plasma column.

References

1. E.V.Aleksandrov, V.V.Afrosimov, E.L.Berezovsky, et al. "Pisma v JETP", 29, 3, 1979.
2. V.V.Afrosimov, E.L.Berezovsky, A.I.Kislyakov, et al., "Pisma v JETP", 28, 472, 1978.
3. M.Bernard, EUR-CEA-FC-891, 1977.

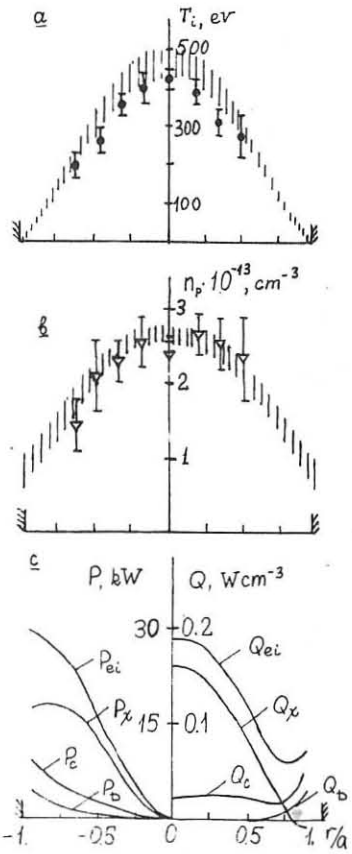

Fig. 1

T - 4

R = 90 cm, a = 15 cm.
I = 90 kA, B_t = 31 kG
$T_e(0)$ = 1 keV

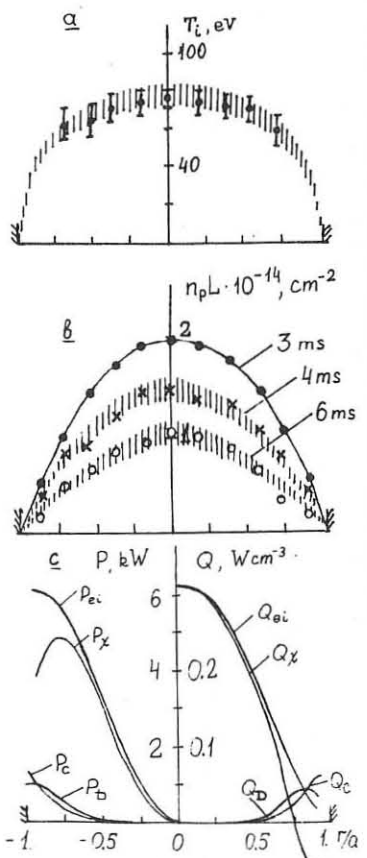

Fig. 2

Tuman-2a

R = 40 cm. a = 8 cm
I = 10 kA, B_t = 8 kG
$T_e(0)$ = 450 eV

AUTHOR INDEX

Aamodt, R.E. D3.1
Afrosimov, V.V. EP34
Ahlstrom, H.G. E1.7
Akiyama, H. AP31
Aliev, Yu.M DP20
Anderson, D. AP17
Anderson, D.T. BP28
Andrjukhina, E.D. BP29
Appert, K. BP9, EP31
Armstrong, W.T. DP5
Arsenin, V.V. AP32
Arunasalem, V. B2.7, D2.5
Asaishi, T. BP19
Ashby, D.E.T.F. AP14
Atkinson, D.W. A2.6
Axon, K.B. EP9, EP11
Azizov, E.A. B3.5

Bagdasarov, A.A. EP12
Bailey, V. DP29
Baity, F.W. A2.1
Baker, D.A. DP7
Baldock, P. DP6
Balet, B. EP31
Balmer, J.E. DP23
Baranowski, J. DP22
Barkhudarov, E.M. AP26
Barnes, C. D2.5
Barrero, A. DP26
Bartiromo, R. B2.5
Bartolik, B. DP11
Basov, N.G. E1.8
Bates, S.C. B2.2
Baxter, G.A. EP9
Becker, G. EP4
Bein, B.K. DP17
Bekiarian, A. E1.6
Benford, J. DP29
Berezhetskii, M.S. BP29
Berezovskii, V.R. AP26
Berezovsky, E.L. EP34
Berger, R.L. E1.2
Bernabei, S. B2.7
Bernard, A. E1.6
Bernard, L.C. A3.6
Bertalot, L. DP14
Bhatnagar, V.P. E2.3
Bieniosek, F.M. A2.1
Bilbao, L. DP14
Bingham, R. BP9, BP11
Birch, R. B2.1
Bitter, M. B2.7
Bittoni, E. E2.2
Blank, A.B. BP32
Bloch, M.A. BP29
Bobeldijk, C. DP9
Bol, K. B2.6, D2.5
Bond, D.J. E1.3
Bonnal, J.F. E2.5
Bornatici, M. BP12, BP13
Borrass, K. DP16
Bosia, G. E2.3
Boyd, D. B2.7
Bracco, G. E2.5
Bradley, J.E. A2.6
Brambilla, M. E2.1
Brederlow, G. E1.4
Breton, C. E2.5
Bretz, N. B2.7
Brodmann, R. E1.4
Brouquet, P. A2.5
Brownell, J.H. D3.3
Bruzzone, H. DP14
Buratti, P. B2.5
Buresi, E. E1.6
Burkhardt, L.C. DP7
Bush, C.E. B2.2
Bussac, J.P. E2.5
Byers, J.A. D3.1
Byrne, R.N. DP2

Cabral, J.A.C. AP16
Calderon, M. E2.3
Campbell, D.J. EP13
Campbell, P.M. E1.2
Cano, R. AP6
Canobbio, E. E2.4
Capes, H. A3.7
Carolan, P.G. DP4
Carpenter, K.H. A2.1
Catto, P.J. D3.1
Cavallo, A. AP6
Chance, M.S. A3.1, EP33
Chang, C.L. EP1
Chang, C.T. AP15
Charatis, G. E1.2
Chelidze, T.Ya. AP26
Chodura, R. A2.3
Choi, P. DP6
Christiansen, J.P. DP1
Chu, C.K. DP2
Chyrczakowski, S. DP22
Cissoko, G. A3.7
Clark, W.H.M. EP9, EP12, EP13
Cobble, J.A. A2.1
Cohen, S. B2.7, D2.2, D2.5
Colchin, R.J. A2.1, B2.2
Cole, H.C. AP3
Colestock, P.L. B2.3, B2.7
Condit, W.C. AP34
Connor, J.W. A3.4
Connor, K.A. AP22, A2.1
Cooke, L. E1.5
Cooper, W.A. B2.2
Cordey, J.G. AP13, E2.2, EP26
Core, W.G.F. EP26, EP27
Costley, A.E. EP12, EP13
Coumans, J.J.H. AP21
Cox, M. E2.2
Cutler, T.A. B3.1

Dalhed, H. D2.5
Dandl, R.A. A2.1
Dangor, A.E. DP6, DP28
Darius, I. E2.3
Daughney, C. D2.5
Dautray, R. E1.6
Davis, S. B2.3, B2.6, B2.7, D2.5
Davison, P.J.N. A2.6
Dawson, J. DP19
Daybelge, U. AP18, AP20
Decroisette, M. E1.6
Dellis, A.N. A2.6
Delobeau, F. E1.6
DeLucia, J. D2.5
Derr, J.A. BP28
Desoppere, E. E2.3
Dewar, R.L. A3.1, EP33
Dikij, A.G. BP31, BP32
Dimock, D. B2.7, D2.5
Djachenko, V.V. B2.4
Dokopoulos, P. EP21
Donaldson, T.P. DP23
Downward, J.G. E1.2
Drake, J.F. EP1
Drake, J.R. AP25
Drauaux, J. E2.5
Driemeyer, D. AP34
Dunlap, J.L. B2.2
Durvaux, M. A2.5
Dyabilin, K.S. BP29
Dyer, G.R. B2.2
Dylla, F. B2.7, D2.2, D2.5
Dymoke-Bradshaw, A.K.L. DP28

Eames, D. B2.7
Eason, H.O. A2.1
Edlington, T. AP13
Edmonds, P.H. B2.2
Efthimion, P.C. B2.3, B2.7, D2.5
Eidmann, K. E1.4
Engelhardt, W. D2.1, EP5, EP6
Engelmann, F. BP12, BP13
England, A.C. B2.2
Es'kov, A.G. DP35
Eubank, H.P. B2.3, B2.6, B2.7
Evans, R.G. E1.3, E1.5

Fahrbach, H.U. DP3
Faulkner, J.E. BP27
Favorsky, A.P. DP34
Fedjanin, O.I. BP29
Fedotov, S.I. E1.8
Fielding, P.J. EP13
Fielding, S.J. EP8
Fletcher, W.H.W. AP13
Folkierski, A. DP6
Fonck, R. D2.5
Foster, C.A. B2.2
Fowler, T.K. B1.3
Frieman, E.A. BP1
Frolov, A.A. DP20
Fujisawa, N. B1.2, D2.3
Fujita, J. AP1
Fujiwara, M. A2.2
Funato, Y. BP19
Furth, H.P. B1.4
Fussmann, G. D2.1, EP5, EP20

Galbraith, D.L. AP28
Gary, S.P. BP10
Gasilov, V.A. DP34
Gautier, P. EP30
Gelashvili, G.V. AP26
Gell, Y. AP10
Gentilino, A. DP14
Gerber, K.A. DP31
Gernhardt, J. D2.1, EP5, EP6
Gibson, A. EP25, EP26
Gill, R.D. EP9
Gilligan, J. AP34
Gladd, N.T. EP1
Glasser, A.H. A3.1, BP1, EP33
Glaze, J.A. E1.7
Glock, E. D2.1, EP5
Glowienka, J.C. A2.1
Goedbloed, J.P. EP32
Goeler, S von D2.1, EP5, EP6
Golant, V.E. B2.4
Goldston, R.J. B2.3, B2.6, B2.7
Goloviznin, V.M. DP34
Gorbunov, E.P. EP12
Gormezano, C. A2.5

Goto, Y. BP19
Gottardi, N. D2.1, EP5
Gourlan, C. DP14
Gowers, C.W. B2.1
Gradov, O.M. DP20
Granneman, E.H.A. DP32
Gray, D.R. E1.3
Grebenshchikov, S.E. BP29
Green, B.J. EP20, EP21
Greene, J.M. EP33
Gregory, B. A2.5
Grek, B. D2.5
Gresillon, D. AP19
Greve, P. B3.6
Gribanov, A.Yu. BP32
Grimm, R.C. EP33
Grisham, L.R. B2.3, B2.6, B2.7
Gross, R.A. EP3
Gruber, O. EP4
Gruber, R. A3.3, BP11, BP25, EP19, EP3O, EP31
Guillaneux, P. E1.6
Gullickson, R.L. DP14
Gupta, R.P. B3.3
Gusev, V.K. B2.4
Gutarev, Yu.V. A2.7
Gu, Y D3.7

Haan, P.H. de DP32
Haas, F.A. B2.1
Hacker, H. BP26
Hai, S. AP35
Hall, T.A. E1.5
Hamasaki, S. B3.4
Hamberger, S.M. BP20, BP21
Harafuji, K. BP19
Hares, J.D. E1.3
Harris, J.H. BP29
Hasegawa, A. BP5
Hasselberg, G. EP24
Haste, G.R. A2.1
Hastie, R.J. A3.4
Hatakeyama, R. B3.2
Haumann, J. B3.6
Hawryluk, R.J. B2.3, B2.6, D2.5
Hedrick, C.L. A2.1, BP34
Helava, H. DP29
Hellsten, T. AP4, BP7
Helton, F.J. A3.6
Hemsworth, R.S. AP3, EP9
Henderson, T.M. E1.2
Hendricks, C.D. DP27
Hermegger, F. A2.3
Hertzberg, A. DP19
Hesketh, K.W. A3.4
Hess, W. A2.5
Hickok, R.L. A2.1, AP22
Hinnov, E. B2.7, D2.5
Hiroe, S. A2.1
Hogan, J.T. B2.2
Hojo, H. BP2
Holzhauer, E. DP3
Hopman, H.J. DP32
Hosea, J.C. B2.6, B2.7
Hosking, R.J. BP6
Hosokawa, M. A2.2
Hovey, J. B2.3
Howe, H.C. B2.2
Howell, R.B. DP7
Hsuan, H. B2.7, D2.5
Hugill, J. EP9, EP11
Hugrass, W.N. AP23
Hwang, D. B2.7

Ichtchenko, G. A2.5
Iguchi, H. A2.2
Ikegami, H. A2.2
Inutake, M. B3.2
Irie, M. D2.5
Ishii, K. AP27
Isler, R.C. B2.2
Itoh, S. AP1
Ivanov, N.V. EP16
Izvozchikov, A.B. EP34

Jacobsen, R. D2.5
Jacobson, A. DP7
Jaeckel, H. A2.5
Jaeger, E.F. A2.1, BP34
Jaenicke, R. BP23
Jankowicz, Z. DP11
Janssen, G.A.M. DP32
Janssen, P.A.E.M. BP4
Jardin, S.C. EP33
Jassby, D.L. B2.3
Jayakumar, R. DP32
Jennings, W.C. AP22
Jernigan, T.C. B2.2
Jerzykiewicz, A. DP11
Jessup, B. A2.5
Jobes, F. B2.7
Johnson, D.W. B2.3, B2.7, D2.5
Johnson, J.W. DP4, EP33
Johnson, L. D2.5
Johnson, P.C. A2.6
Johnson, R.R. E1.2
Jones, E.M. AP13, EP28
Jones, I.R. AP23
Jones, P.A. B2.1
Jørgensen, L. EP23
Jurgens, B. DP32

Kadota, K. AP1
Kadysh, I.Ya. AP8
Kahan, E. DP6
Kaita, R. B2.7
Kakurin, A.M. EP16
Kalinichenko, S.S. AP9
Kalygin, A.G. DP35
Kammash, T. AP28
Kareev, Ju.A. B3.5
Karger, F. D2.1, EP5
Karttunen, S.J. BP3
Kasai, S. D2.3
Kato, M. B3.6
Kato, Y. E1.1
Kawahata, K. AP1
Kawasumi, Y. AP1
Keller, R. EP31
Kerner, W. A3.3, BP25, EP19, EP30
Kerslick, G.S. DP28
Ketterer, H.E. B2.2
Key, M.H. DP25, E1.3, E1.5
Kholnov, Yu.V. BP29
Khudoleev, A.V. BP29, EP34
Kilkenny, J.D. DP25, E1.3
Kim, J. B2.2
King, P.W. B2.2
Kirochkin, Yu.A. BP18
Kirov, A.G. AP8
Kishimoto, H. EP18
Kislyakov, A.I. EP34
Kitajima, S. BP19
Kladov, S.V. BP29
Klüber, O. D2.1, EP5
Koch, R. E2.3

Kock, L.C.J.M. de D2.6
Kogoshi, S. A2.6
Komori, A. B3.2
Konkashbaev, I.K. B3.5
Konoshima, S. D2.3
Köppendörfer, W. DP3
Kornev, B.I. BP29
Kosarev, P.M. AP33
Kotsubanov, V.D. BP31
Krall, N.A. B3.4
Kravchin, B.V. BP31
Kroegler, H. DP14
Kruckewitt, T. BP28
Kulaga, A.E. BP31
Kunze, H.-J. B3.6
Kuo, S.P. A2.1
Kurilko, P.I. AP9
Kuroda, T. AP1
Kurtmullaev, R.Kh. DP34, DP35
Kuthy, A. AP25
Kyrie, A.Yu. DP20

Lackner, K. A3.3, D2.1, DP16, EP5, EP30
Ladrach, P. DP23
Larionov, M.M. B2.4
Larionova, N.F. BP29
Latsko, E.M. BP32
Lawson, J. B2.7
Lazar, W.H. A2.1
Lazarus, E.A. B2.2
Lebedev, A.D. B2.4
Lee, R.W. DP25
Lees, D.J. A2.6
Lewis, C.L.S. DP25, E1.5
Liberman, B. E2.1
Linford, R.K. DP5
Lipson, J. DP5
Lisak, M. AP17
Lisitano, G. D2.1, EP5, EP7
Lister, G. BP13, BP28, DP9
Lomas, P.J. A2.6
Long, J.W. DP4, DP9
Loring, C.M. B2.2
Lortz, D. EP17, BP8
Lotz, W. BP22
Liu, C.S. EP1
Lunin, H.F. BP29
Lunney, J.G. DP25, E1.3, E1.5
Lyon, J.F. B2.2
Lysoivan, A.I. AP9

McBride, J.B. B3.4
McCracken, G.M. D2.2, D2.5
McCurdy, H.C. B2.2
McGuire, K. B2.1, D2.7
McNeil, D. B2.7
Maeda, H. D2.5
Maeno, M. D2.3
Magee, C.W. D2.2
Magne, R. A2.5
Malfliet, W. BP15
Malutin, A.I. DP35
Manes, K.R. E1.7
Manickam, J. EP33
Mansfield, D. D2.5
Marshall, T.C. EP3
Mase, H. AP27
Matsumoto, O. AP31
Matsuoka, K. AP1
Matsuura, K. AP1
Matusiak, A. DP11

Mayer, F.J. E1.2
Mayer, H.M. D2.1, EP5
Mazzucato, E. B2.7
Meade, D. D2.5
Medley, S.S. B2.6, B2.7
Meer, A.F.G. van der DP9
Meisel, D. D2.1, EP5
Meleta, E.A. AP8
Melzacki, K. DP22
Menon, M.M. B2.2
Mercier, C. A3.7
Meservey, E.B. B2.6, B2.7
Messiaen, A.M. E2.3
Michelis, C. de E2.5
Mihalczo, J.T. B2.2
Mijamoto, K. AP1
Mikhailov, Yu.A. E1.8
Miley, G.H. AP34, DP10
Miller, A.E. EP33
Miller, R.L. A3.6
Milora, S.L. B2.2
Minardi, E. DP16
Mirin, A.A. B2.3, EP9
Mirma, K. E1.1
Mittioli, M. E2.5
Miyanaga, N. E1.1
Moncur, N.K. E1.2
Monticello, D.A. EP33
Moore, A. DP25, E1.5
Moore, R.W. A3.6
Moreau, D. E2.1
Morera, J.P. A3.7
Moresco, M. A2.5
Morse, E. AP34
Moses, R.W. DP10
Mueller, D. B2.7, D2.5
Mulser, P. E1.4
Münich, M. DP3
Murakami, M. B2.2
Murmann, H. D2.1, EP5, EP6
Musinski, D.L. E1.2

Nagao, S. BP19
Nakach, R. AP10
Navarrot, A.P. B2.2
Nazarov, N.I. AP9
Nebel, R.A. DP10
Neidigh, R.V. B2.2
Neill, G.F. EP12
Neilson, G.H. B2.2
Neuhauser, J. A2.3, DP3
Newton, A.A. DP4
Neyatani, J. BP19
Nguyen, T.-K. A2.5
Nicolai, A. AP24
Nikandrov, L.B. B3.5
Nishida, Y. AP27
Nishihara, K. E1.1
Nishikawa, K. BP2
Noda, N. AP1
Noll, P. EP21
Novikov, Yu.M. DP15
Nowikowski, J. DP11
Nuckolls, J.H. E1.7
Nührenberg, J. BP8, EP17

Oberson, R. E2.5
Oepts, D. DP9
Ohkawa, T. B1.5
Ohkubo, K. AP1
Ohnuma, T. BP2
Oka, Y. AP1
Okabayashi, M. D2.5
Okada, O. D2.5
Olivain, J. AP19
Oomens, A.A.M. DP9
Oost, G. van E2.3
Ott, W. BP27
Overbey, D.R. B2.2
Owens, K. D2.5

Pacher, G. A2.5
Pacher, H. A2.5
Panarella, E. B3.3
Panov, D.A. AP33
Paré, V.K. B2.2
Paul, J.W.M. EP8, EP9
Pearlstein, L.D. D3.1
Pearson, D. E2.3
Pegoraro, F. BP14
Peng, Y.-K.M. B2.2
Percival, J.B.B. EP9
Perepelkin, N.F. BP31
Perrone, M.R. EP21
Pesic, S.S. E2.1
Peterson, L.F. BP20, BP21
Petrov, M.P. EP34
Petsch, R. E1.4
Phillips, M.G.R. AP23
Picraux, S.T. D2.2, D2.5
Piekaar, H.W. A2.5
Pieroni, L. B2.5
Piotrowicz, V.A. DP4
Piret, C. E2.3
Platts, D.A. DP5
Platz, P. EP15
Podda, S. DP14
Pohl, F. EP6
Pokroev, A.G. BP18
Ponte, N.S. B2.2
Popov, S.N. BP29
Pots, B.F.M. AP21, BP17
Potter, D.E. DP6
Powell, B.A. EP9, EP11
Powers, L.V. E1.2
Prentice, R. EP9, EP11
Proshletsov, A.P. DP35

Qiu, N. D3.7
Quon, B.H. A2.1

Rabinski, M. DP11
Rager, J.P. DP14
Ramette, J. E2.5
Rau, F. BP22
Razdobarin, G.T. B2.4
Rehker, S. BP28
Reisse, J.M. E1.6
Rem, J. DP8
Rewoldt, G. BP1
Richards, R.K. A2.1
Ringler, H. A2.4
Riviere, A.C. AP13
Roberts, K.V. DP1
Robinson, D.C. B2.1, BP6, D2.7, EP13
Robouch, B.V. DP14
Robson, A.E. DP31
Rogister, A. EP24
Rognlien, T.D. B3.1
Röhr, H. DP3
Rolland, P. D3.2
Rose, P. DP19
Rosenbluth, M. D3.1
Rossnagel, S.M. D2.2, D2.5
Rouchko, L.F. AP8
Rutgers, W.R. A2.5
Rybalko, V.F. BP32
Sadowski, M. DP22
Sakamoto, I. BP19
Sakurai, K. AP1
Salomaa, R.R.E. BP3
Saltmarsh, M.J. B2.2
Samoilov, V.P. BP32
Sanderson, J.J. BP10
Sanmartin, J.R. DP26
Sanuki, H. BP2
Sasaki, N. BP19
Sato, K. AP1
Sato, N. B3.2
Sauthoff, N. B2.7, D2.5
Sbitnikova, I.S. BP29
Scherbakov, A.G. AP33
Schechter, D.E. B2.2
Schep, T.J. BP14
Scherbinin, O.N. B2.4
Schilling, G. B2.3, B2.6, B2.7
Schivell, J. B2.7
Schlüter, A. A2.3
Schmidt, G. B2.7, D2.5
Schmidt, J. D2.5
Schneider, W. BP25, EP30
Schofield, A.E. DP7
Schram, D.C. AP21, BP17
Schramm, G. DP3
Schwarz, H. DP21
Schwarzenbach, A.P. DP23
Segall, S.B. E1.1
Segre, S. B1.1
Selden, A.C. A2.6
Semenov, V.N. DP34, DP35
Sen, A. EP29
Serebreny, G.A. B2.4
Sesnic, S. D2.1, EP5
Sethian, J.D. DP31
Sgro, A.G. DP7
Sharp, L.E. BP20, BP21
Shashkov, M.Yu. DP34
Shatford, P.A. A2.6
Sherwood, E.G. DP5
Shimada, M. D2.3
Shohet, J.L. BP28
Shoji, T. A2.2
Shpigel', I.S. BP29
Shukla, P.K. BP5
Shvets, O.M. AP9
Sigel, R. E1.4
Silver, E. D2.5
Simpkins, J.E. B2.2
Sinman, A. DP30
Sinman, S. DP30
Sinnis, J. D2.5
Sitt, B. E1.6
Sivo, A. B2.7
Skladnik-Sadowska, E. DP22
Sklizkov, G.V. E1.8
Skovoroda, A.A. AP33
Slade, P.D. DP6
Slatter, D.C. E1.2
Siebert, L.D. E1.2
Slavnyj, A.S. BP31, DP22
Söldner, F. A2.5
Solodovchenko, S.I. BP32
Solomon, D.E. E1.2
Sommer, J. DP3
Sosnin, N.A. DP34
Spalding, I.J. A2.6
Spatschek, K.H. BP5
Spector, D.N. DP31
Speth, E. BP27
Spies, G. BP7
Spindler, G. E1.4
Spong, D.A. BP34
Staib, P. D2.5

Stamatakis, T. A2.6
Start, D.F.H. AP13, EP28
Stauffer, F. B2.7
Stefan, V. BP16
Steinmetz, K. DP14
Stepanov, K.N. AP9, BP18
Sternlieb, A. DP24
Stewart, L.D. B2.3
Stirling, W.L. B2.2
Stodiek, W. B2.6, B2.7
Stooksberry, R. B2.3, B2.6, B2.7
Stork, D. AP3
Storm, E.K. E1.7
Stott, P.E. EP23
Strachan, J.D. B2.3, B2.7, D2.5
Strelkov, P.S. DP32
Stringer, T.E. EP27
Sugita, K. BP19
Suckewer, S. B2.7, D2.5
Sukachov, A.V. AP8
Summers, D.D.R. EP11
Sundaram, A.K. EP29
Sunka, P. DP28
Suprunenko, V.A. A2.7, BP31
Surko, C.M. AP19
Suzuki, N. D2.3
Swain, D.W. B2.2
Sykes, A. B2.1, EP22

Tait, G. B2.7, EP13
Takeda, S. AP31
Taktakishvili, M.I. AP26
Tamura, S. EP18
Tanahashi, S. AP1
Tang, W.M. BP1
Tani, K. EP18
Tarasenko, V.F. AP9
Tarvin, J.A. E1.2
Tataronis, J.A. BP28
Taylor, J.B. A3.4
Telesca, G. E2.3
Tendler, M. DP18
Tenney, F. D2.5
Tennfors, E. AP4
Terashima, Y. AP1
Thomas, C.E. B2.2, E1.2
Thomas, P.R. A2.6
Thomson, H. B2.7
Todd, A.M.M. EP33
Toi, K. AP1
Tolstolutskij, A.G. DP15
Toner, W. E1.3
Tonon, G.-F. A2.5
Towner, H.H. B2.3
Tozuka, F. BP19
Troyon, F. A3.3, BP11, BP25, EP19, EP30, EP31
Truc, A. AP19
Tsai, C.C. B2.2
Tsakiris, G. E1.4
Tsintsadze, N.L. AP26
Tudisco, O. B2.5
Turner, M.F. B2.1, EP22

Uckan, T. A2.1
Uehara, K. D2.3
Ugniewki, S. DP22
Ullrich, L. B3.6
Ulrickson, M. B2.6

Vaclavik, J. BP9, EP31
Vandenplas, P.E. E2.3
Varandas, C.A.F. AP16
Vasil'ev, M.P. BP31
Vedel, J.M. E1.6
Vojtsenya, V.S. BP32
Volk, R. E1.4
Volkov, E.D. BP32
Voronov, G.S. BP29
Vukovic, S. DP20

Wagner, F. D2.1, EP5
Walker, A.C. A2.6
Walker, B. EP13
Wampler, W.R. D2.2, D2.5
Ward, J.M. E1.5
Ward, S. A2.6
Watanabe, H. BP19
Watanabe, M. BP2
Watanabe, T. BP2
Watkins, M.L. EP25
Watteau, J.P. E1.6
Watts, M.R.C. DP4
Webb, S.J. DP6
Weber, H.P. DP23
Weber, P.G. EP3
Wegrowe, J.-G. A2.5
Weibel, E.S. BP9
Weimer, K.E. EP33
Weinstein, B.W. DP27
Werkoff, F. A3.7, AP6
Weynants, R.R. E2.3
White, T.L. A2.1
White, R.B. EP33
Wilgen, J.B. B2.2
Wilhemsson, H. AP17
Wilson, C.M. EP11
Wing, W.R. B2.2
Witkowski, S. E1.4
Woo, J.T. AP22
Wootton, A.J. B2.1, EP8, EP11
Worsham, R.E. B2.2

Yabe, T. E1.1
Yamamoto, T. D2.3
Yamanaka, C. E1.1
Ye, Y. AP35
Yu, M.Y. BP5

Zehrfeld, H.P. EP5, EP20
Zhang, W. AP35
Zhil'tsov, V.A. AP33
Zolototrubov, I.M. DP15
Zolotovitskaya, Eh.S. BP32
Zurro, B. B2.2
Zykov, V.G. DP15